ROCK AVALANCHES

EDITED BY: O. Adrian Pfiffner, John Joseph Clague, Reginald Leonhard Hermanns and Tim Davies

PUBLISHED IN: Frontiers in Earth Science

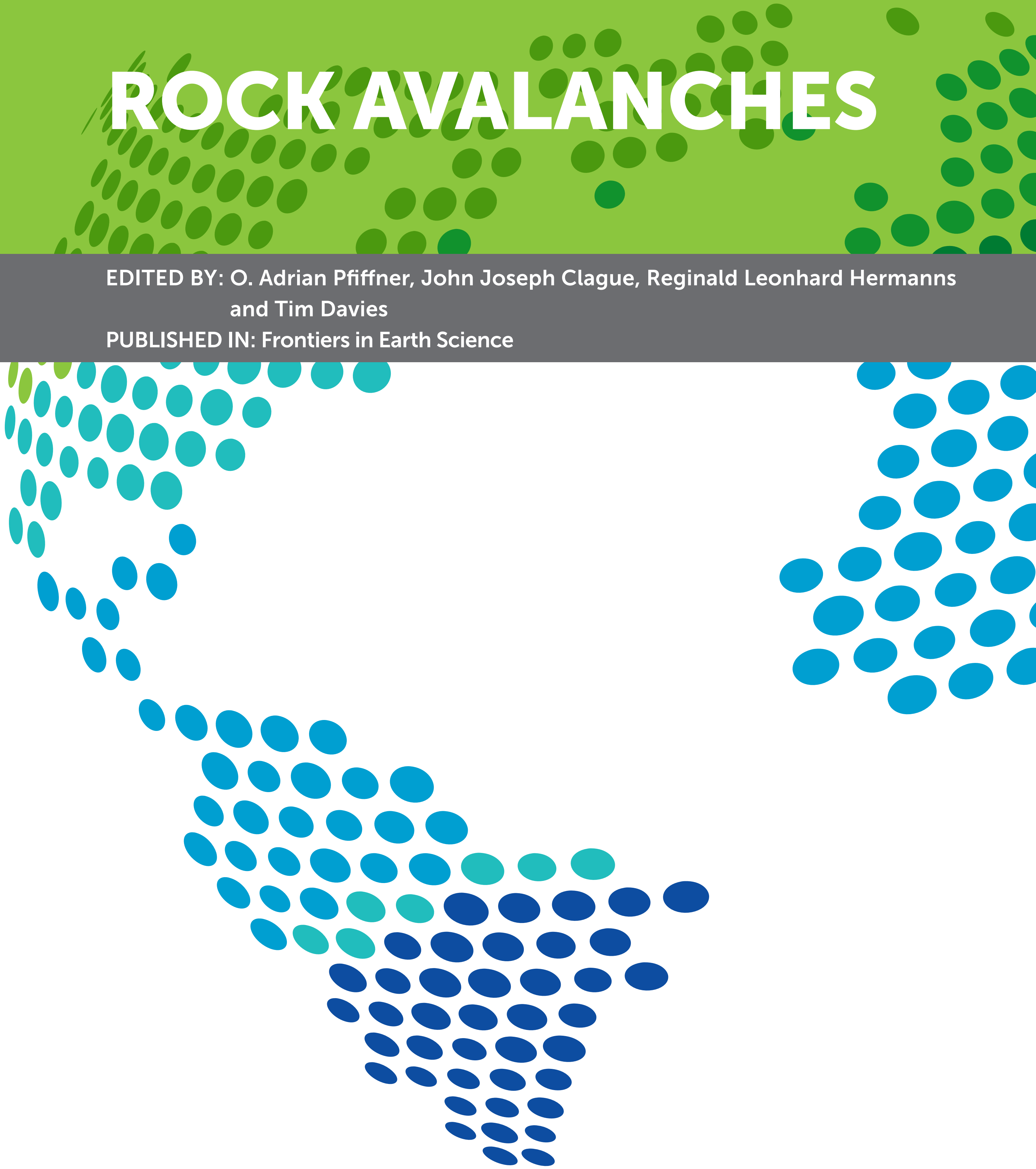

frontiers Research Topics

ISSN 1664-8714
ISBN 978-2-88966-614-0
DOI 10.3389/978-2-88966-614-0

About Frontiers

Frontiers is more than just an open-access publisher of scholarly articles: it is a pioneering approach to the world of academia, radically improving the way scholarly research is managed. The grand vision of Frontiers is a world where all people have an equal opportunity to seek, share and generate knowledge. Frontiers provides immediate and permanent online open access to all its publications, but this alone is not enough to realize our grand goals.

Frontiers Journal Series

The Frontiers Journal Series is a multi-tier and interdisciplinary set of open-access, online journals, promising a paradigm shift from the current review, selection and dissemination processes in academic publishing. All Frontiers journals are driven by researchers for researchers; therefore, they constitute a service to the scholarly community. At the same time, the Frontiers Journal Series operates on a revolutionary invention, the tiered publishing system, initially addressing specific communities of scholars, and gradually climbing up to broader public understanding, thus serving the interests of the lay society, too.

Dedication to Quality

Each Frontiers article is a landmark of the highest quality, thanks to genuinely collaborative interactions between authors and review editors, who include some of the world's best academicians. Research must be certified by peers before entering a stream of knowledge that may eventually reach the public - and shape society; therefore, Frontiers only applies the most rigorous and unbiased reviews.
Frontiers revolutionizes research publishing by freely delivering the most outstanding research, evaluated with no bias from both the academic and social point of view. By applying the most advanced information technologies, Frontiers is catapulting scholarly publishing into a new generation.

What are Frontiers Research Topics?

Frontiers Research Topics are very popular trademarks of the Frontiers Journals Series: they are collections of at least ten articles, all centered on a particular subject. With their unique mix of varied contributions from Original Research to Review Articles, Frontiers Research Topics unify the most influential researchers, the latest key findings and historical advances in a hot research area! Find out more on how to host your own Frontiers Research Topic or contribute to one as an author by contacting the Frontiers Editorial Office: frontiersin.org/about/contact

ROCK AVALANCHES

Topic Editors:
O. Adrian Pfiffner, University of Bern, Switzerland
John Joseph Clague, Simon Fraser University, Canada
Reginald Leonhard Hermanns, Geological Survey of Norway, Norway
Tim Davies, University of Canterbury, New Zealand

Citation: Pfiffner, O. A., Clague, J. J., Hermanns, R. L., Davies, T., eds. (2021). Rock Avalanches. Lausanne: Frontiers Media SA. doi: 10.3389/978-2-88966-614-0

Table of Contents

frontiers in Earth Science

EDITORIAL
published: 09 February 2021
doi: 10.3389/feart.2021.651642

Editorial: Rock Avalanches

O. Adrian Pfiffner[1]*, **Reginald L. Hermanns**[2], **Tim R. Davies**[3] and **John J. Clague**[4]

[1]Institute of Geological Sciences, University of Bern, Bern, Switzerland, [2]NORGES GEOLOGISKE UNDERSØKELSE, Geohazard and Earth Observations, Trondheim, Norway, [3]School of Earth and Environment, University of Canterbury, Christchurch, New Zealand, [4]Department of Earth Sciences, Simon Fraser University, Burnaby, BC, Canada

Keywords: rock avalanches, dating rock avalanches, landscape evolution, fragmentation, run-out

Editorial on the Research Topic

Rock Avalanches

This Research Topic *Rock Avalanches* gathers high-quality original research articles, reviews and technical notes on the nature and mechanics of large rock avalanches with long run-out and associated secondary features such as lakes dammed by rock avalanche deposits.

Rock avalanches have volumes of millions of m^3 or more, and large ones have major impacts on landscapes related to their source areas, travel paths and deposits. Key questions of rock avalanches include triggers and causes, mechanisms of long runout and the morphology of the rock avalanche deposits. Seismic shaking and extreme weather events are important triggering mechanisms, but some rock avalanches lack an obvious trigger. An important causative factor is the pre-existing structure of the displaced rock mass. The mechanisms of transport depend on the slope angle and shape of the sliding surface, the nature of the substrate on which the avalanche moves and the internal deformation that the rock avalanche is undergoing. The rock type and structure of the base of the rock avalanche is in many instances of paramount importance in the motion of the disintegrating rock mass. Several possibilities of how mobility and run-out are enhanced can be envisaged: 1) a mechanically weak layer within the rock mass from which the rock avalanche broke away, 2) strain softening by disintegration near the base and within the moving rock avalanche, 3) travel on ice or water-saturated unconsolidated sediment, and 4) energy transformation due to dynamic fragmentation. Analysis of the size and distribution of fragments within rock avalanche deposits, together with deposit morphology, provide insights into the internal deformation that accompanies the motion and final emplacement of the rock avalanche. All these factors contribute to the long run-out of rock avalanches, which augment the area of impact and hence landslide hazard.

This Research Topic adds to the state of knowledge of large rock avalanches and their impact on landscapes and society. It comprises contributions dealing with more generic questions of rock avalanches as well as case studies from very different places throughout the world.

GENERIC PAPERS

Knapp and Krautblatter present a theoretical analysis of energies involved in the movement of rock avalanches. Energy sources in the disintegration phase are potential (gravitational), elastic and kinetic energy. Energy sinks are friction, inelastic collision, entrainment, compressional deformation, chemical energy consumption, phase transitions, dust production, bouncing, sound, microseismicity and momentum of the solid-fluid transition. A better understanding of energy transformation and dissipation during disintegration, and of the residual kinetic energy of the rock avalanche, are keys to the mechanical and dynamic properties related to run-out.

Edited and reviewed by:
Derek Keir,
University of Southampton,
United Kingdom

****Correspondence:***
O. Adrian Pfiffner
adrian.pfiffner@geo.unibe.ch

Specialty section:
This article was submitted to
Structural Geology and Tectonics,
a section of the journal
Frontiers in Earth Science

Received: *10 January 2021*
Accepted: *14 January 2021*
Published: *09 February 2021*

Citation:
Pfiffner OA, Hermanns RL, Davies TR and Clague JJ (2021) Editorial: Rock Avalanches.
Front. Earth Sci. 9:651642.
doi: 10.3389/feart.2021.651642

Secondary sediment mass flows in the so-called splash zone are often poorly preserved in the morphologic and stratigraphic record of rock avalanches but can be of considerable size when the rock avalanche impacts on valley fill sediments. Not including this secondary mass flow in the hazard zone can lead to a substantial underestimation of the total risk of a rock slope failure. Mitchel et al. present a probabilistic model of how to estimate the area affected by these secondary mass flows that is based on 32 well-documented rock avalanches, most of them since 2010. Out of 13 post-2010 events nine produced a sediment mass flow.

An important task in landslide hazard assessment is estimating the volume likely to be released at each potential landslide site. For dealing with a large number of sites, Chih-Yu et al. propose an automated tool using volume-constrained smooth minimal surfaces (differentiable surfaces that enclose a given landslide volume with the minimal surface area) to approximate the landslide failure surfaces. The method is tested on 24 known landslides and is able to generate acceptable failure surfaces. A set of assessment indices is employed to measure the fitness of the predictions, and the prediction fitness is compared with the landslide scarp geometry.

CASE STUDIES

Rock slope failures in most glaciated mountain chains yield almost exclusively young, mostly Holocene ages. In this study by McColl, a 50–100 × 10^6 m^3 rock avalanche in the glaciated Rangitata Basin in Canterbury, New Zealand reveals a pre-Holocene age of >16 ka (and likely >20 ka), making it the oldest reported alpine rock avalanche in New Zealand, and one of the oldest last-glaciation rock avalanches reported worldwide. The study confirms that while rock avalanches were occurring in the Southern Alps early in the last period of deglaciation, evidence for them persists only in the few environments that have conditions favourable for preservation.

Lagmay et al. report a devastating rock avalanche that occurred in 2018 in Naga City (Philippines). The rock avalanche initiated as translational slide in limestone lying on a weak base of sandstone and siltstone. As the failed rock mass gained momentum, its front accelerated and disintegrated into jigsaw–cracked blocks embedded in a non-graded matrix. Hummocks and large tilted toreva blocks are evidence of the acceleration and long run-out of the faster-moving front of the rock avalanche. The unexpectedly long run-out resulted in the loss of at least 78 lives.

Entrainment of substrate along the path of rock avalanches has often been observed. This back analysis by Chen et al. of the 2017 Xinmo rock avalanche using discrete element methods (3DEC) indicates that entrainment by plowing due to the impact of the rock avalanche outweighs the effect of basal abrasion. In addition, the model shows that the plowing causes first a deceleration of the movement until the entrained material contributes to the increase of the velocity by adding potential energy. A good fit of the run-out model with the observed magnification factor (2) indicates the suitability of such models for entrainment analysis.

Cihan et al. studied the Akdag rock avalanche, one of the largest known of such deposits in Turkey. The failure occurred along the contact zone of carbonates over flysch sediments and springs along this intersection suggest that water played a central role in conditioning the slope for failure. Using terrestrial cosmogenic nuclides, the authors show that the main event with a volume of $3 * 10^8$ m^3 occurred 8.3 ± 1.4 ka years ago followed by a second event with much smaller volume 1.1 ± 0.2 ka ago.

Von Wartburg et al. studied a rock avalanche in northern Italy. The unusual morphology of the deposit with scarps, ridges and lineaments, was previously thought to indicate multiple events. The authors show that it was rather a single event, which occurred at 4.8 ± 0.5 ka. By comparing with analog experiments, they conclude that the deposit morphology is the result of emplacement along the complex valley floor, including run-up and gravitational spreading of the moving mass.

The relation of rock avalanche deposits in the upper Ferret Valley with the 1717 historic Triolet rock avalanche in the Mont Blanc massif have long been in dispute as organic material related to the deposit resulted in varying ^{14}C ages. Encouraged by 19 ^{10}Be ages confirming that the deposits relate to that event Hajdas et al. sampled a stratigraphic succession of detritic and organic material in four pits within the disputed rock avalanche deposit. Out of 36 samples for AMS ^{14}C dating eight ages on wood fragments result in an age of ~1,650–1950 AD. In the absence of any other historic events reported from this valley this confirms that the deposit indeed is related to the historically reported event in 1717.

The Flims deposit, the largest in Europe, offers an opportunity to investigate the failure process as the source zone is well exposed and accessible. Well constrained engineering geology analyses of the pre-failure and triggering conditions allow inferences to be drawn about the release of the mass and the transition to a long-runout event. Low-strength marl–like layers suggest that failure could have been seismically or meteorologically triggered. The analyses by Aaron et al. also show that some mechanism to reduce strength immediately following failure is required to explain the mobility of the event.

Moreiras reviews the genesis of a previously studied chaotic deposit in the Blanco River basin (Argentina Andes) that has been interpreted as a either a debris flow or glacial deposit. The author conducted a detailed sedimentological and geomorphic study of the deposit and concludes that it was emplaced by a huge rock avalanche that traveled nearly 27 km and descended 4,700 m in altitude. Optically stimulated luminescence (OSL) ages on alluvial sediments associated with the landslide deposit suggest an age of ~35–39 ka for the event. The rock avalanche may have been triggered by an earthquake, given the presence of a nearby active fault system and a cluster of seven Late Pleistocene rock avalanches in the region.

Pacheco et al. studied the distal portion of the oldest rock avalanche deposit in Yosemite Valley, which they dated to about 16.1 ka using the cosmogenic ^{10}Be. They identified the interface between the rock avalanche deposit and underlying late Pleistocene glaciofluvial sediments using ground penetrating radar (GPR) and electrical resistivity tomography (ERT) methods. Their findings provide an improved understanding of the sedimentation history in Yosemite Valley, inform hazard and risk assessment in the national park, and show the value of geophysical methods for three-dimensional investigation of buried landslide deposits.

Bessette-Kirton and Coe created an inventory of rock avalanches in a 3,700 km^2 area of the Saint Elias Mountains (Alaska) to differentiate between the frequency of landslides related to the geologic and active tectonic setting of the region, and landslides triggered by climate change. They found a temporal cluster of 41 rock avalanches that happened between 2013 and 2016 and correlated with above-average air temperatures. Most of these rock avalanches initiated from bedrock ridges in probable permafrost zones, suggesting that permafrost degradation could be an important factor contributing to rock-slope instability in the region.

AUTHOR CONTRIBUTIONS

All authors listed have made a substantial, direct and intellectual contribution to the work, and approved it for publication.

ACKNOWLEDGMENTS

We thank all authors for their valuable contribution to this Research Topic, the reviewers who shared their precious time to improve the manuscripts, the members of the Frontiers Team and the Editor in chief for their help at different stages of preparing this collection of papers.

frontiers
in Earth Science

ORIGINAL RESEARCH
published: 22 April 2020
doi: 10.3389/feart.2020.00103

The Anomalously Old Bush Stream Rock Avalanche and Its Implications for Landslide Inventories in Dynamic Landscapes

Samuel T. McColl*

Geosciences Group, School of Agriculture and Environment, Massey University, Palmerston North, New Zealand

Previous dating of rock slope failures in most glaciated mountain chains has revealed almost exclusively young, mostly Holocene ages. In this study, a rock avalanche in the glaciated Rangitata Basin in Canterbury, New Zealand is mapped, described, and dated, revealing a pre-Holocene age of failure. The geomorphology and characteristics of the rock avalanche, named here as the Bush Stream Rock Avalanche, were assessed from field mapping and photogrammetric analyses. To assess the age of the rock avalanche, *in situ* cosmogenic ^{10}Be exposure dating was applied to boulders on the deposit. The geomorphological mapping shows that the morphology of the head scarp and deposit of the rock avalanche are distinct from the surrounding landscape, much of which appears to be glacial in origin. The rock avalanche traveled about 4 km, with a volume of 50–100 M m^3, and appears to have temporarily blocked Bush Stream. The dated boulders suggest an age of >16 ka (and likely >20 ka), making it the oldest reported alpine rock avalanche in New Zealand, and one of the oldest last-glaciation rock avalanches to be reported worldwide. Deep depressions, possibly kettle holes, in the deposit are indicative of runout over a glacier (or associated dead ice), but any glacier present at the time must have been small and probably decaying. The excellent preservation was likely favored by a small catchment located on the dry lee side of the Two Thumb Range which dampened glacial and fluvial activity. The study confirms that rock avalanches were being produced in the Southern Alps early in the last glaciation or early period of deglaciation, but that evidence for them likely exists only in the rare environments that have conditions favorable for preservation. Preservation potential in most of the Southern Alps is low, with older deposits readily buried or eroded by New Zealand's high rates of erosion, aggradation, and dynamic processes. Unless methods can be developed to identify missing older events, we are hampered in our ability to understand the frequency, and therefore causes, of large slope failures in the Southern Alps and in other highly dynamic alpine landscapes.

Keywords: mass movement, glacial geomorphology, cosmogenic surface exposure age dating, landform preservation, New Zealand, two thumb range

OPEN ACCESS

Edited by:
Tim Davies,
University of Canterbury, New Zealand

Reviewed by:
José DARROZES,
UMR 5563 Géosciences Environnement Toulouse (GET), France
Fabio Matano,
Italian National Research Council, Italy

Correspondence:
Samuel T. McColl
s.t.mccoll@massey.ac.nz

Specialty section:
This article was submitted to Quaternary Science, Geomorphology and Paleoenvironment, a section of the journal Frontiers in Earth Science

Received: *30 January 2020*
Accepted: *23 March 2020*
Published: *22 April 2020*

Citation:
McColl ST (2020) The Anomalously Old Bush Stream Rock Avalanche and Its Implications for Landslide Inventories in Dynamic Landscapes. Front. Earth Sci. 8:103. doi: 10.3389/feart.2020.00103

INTRODUCTION

In mountainous landscapes rock slope failures (RSFs) are a major hazard (Froude and Petley, 2018) and contributor to erosion and sediment generation (Korup et al., 2007; Korup, 2008). This is especially true in tectonically active mountains where high uplift rates and seismic activity generate abundant RSFs (Korup, 2005; Tatard et al., 2010; Görüm, 2019). This propensity may be further heightened in glaciated mountains where glacially steepened relief combined with glacier recession, periglacial activity, and glacial isostasy can trigger or further prime slopes for failure (McColl, 2012). The hazardous potential of RSFs and their apparent efficacy as a landscape process is largely inferred from examination of their modern-day topographic signatures, documented historical events, and often-incomplete inventories. Any attempts to reliably quantify or model their hazard or roles in landscape processes needs to be founded upon robust empirical data that captures representative information about their location, frequency, magnitude, characteristics, and their preparatory factors or triggers through time (i.e., over longer than historical timescales; Korup and Clague, 2009). This requires rich inventories of dated RSFs that can be compared against records of other landscape processes (e.g., climate, glacial activity, seismicity). However, in humid and tectonically active mountains, high sediment yield and dynamic landscape processes rapidly erode or mask RSF deposits and remove evidence. This can occur through burial by fluvial, glacial, or other mass movement sediments, reworking of deposits by glaciers or rivers, or obscuring by vegetation or water bodies (Cook et al., 2013; Dunning et al., 2015; Bainbridge, 2017; Schleier et al., 2017). This makes examining longer-term trends in RSF activity challenging, especially prior to the last deglaciation. Furthermore, while the frequency of RSF activity in the historical past tends to be better documented, pre-historical patterns of RSF activity, which may reflect major shifts in climate or other disturbance events (e.g., earthquakes), need the application of absolute dating methods (Pánek, 2019). Despite the recent upturn in the number of RSFs that have been dated worldwide, there are still few mountains in which the populations of known RSFs have been extensively and robustly dated (McColl, 2012; Pánek, 2014, 2019). In places where RSFs have been dated, new insights have emerged (see Pánek, 2019 for a review). For example, the age distributions of postglacial RSFs in the Scottish Highlands suggest the likelihood of a period of high-magnitude earthquakes induced by glacioisostasy (Ballantyne et al., 2014). To develop accurate RSF models and hazard forecasts, we need to recognize, reduce, and account for preservation bias, and expend effort in dating the RSFs we recognize in the landscape. As an incremental advance toward this goal, the aim of this present study is to describe and date a large rock avalanche deposit in the New Zealand Southern Alps. The RSF, named here as Bush Stream Rock Avalanche (BSRA), is mapped and its morphology and geometry analyzed from the field observations and aerial photography. The age of the event is assessed using cosmogenic nuclide exposure dating. The results suggest that, while its size and occurrence are not exceptional, its age, the depositional environment in which it was emplaced, and its preservation in the landscape are unusual for glaciated mountains.

STUDY SITE AND SETTING

The BSRA is situated within the Bush Stream catchment, a tributary of the Rangitata River, in the Canterbury High Country of New Zealand's Southern Alps (−43.72; 170.75; **Figure 1**). The (∼ 2.5 km^2) rock avalanche deposit (∼1200–1500 m asl) occupies part of a small intermontane basin between the southern-central Two Thumb Range to the west and the smaller Sinclair Range to the east (**Figure 1C**). The rock avalanche fell from the northern slopes of a ridge connecting the two ranges (**Figure 1C**). The ranges are composed of Permian-Triassic Rakaia Terrane greywacke (sandstone and mudstone) (Cox and Barrell, 2007), with local peaks exceeding elevations of 2000 m above sea level. The block-faulted ranges are located some 55 km east of the plate boundary (Alpine Fault), on the Pacific Plate, and with the active Fox Peak and Forest Creek reverse faults within a few kilometers of the rock avalanche source area. Recurrence intervals for major earthquakes ($>M_w$ 7) on these faults may be 2000–3000 years (Stahl et al., 2016a,b). Stirling et al. (2012) estimate a regional probabilistic peak ground acceleration of 0.7–0.8 g over a 2500-year return time. Earthquake shaking is therefore a likely trigger for RSFs in this steep terrain.

The modern climate of the basin and surrounding hills is sub-alpine to alpine, with areas of rock and scree exposed on higher slopes, and tussock grasses and alpine vegetation in the lower basin. In the lee of the main topographic divide between the western and eastern alps and the Two Thumb Range, this area of the Southern Alps is relatively dry compared to other parts of the central alps which can reach 15 m of average annual rainfall (Kerr et al., 2011). The Bush Stream basin has an annual rainfall of ∼1.5 m (from 1972–2016), and median annual average temperatures of 7°C in the lower elevations to below 2°C on the higher peaks (from 1981–2010), estimated from 500 m grids of interpolated rainfall and temperature data (New Zealand Institute of Water and Atmospheric Science [NIWA]). There are no climate stations in the basin to validate these estimates, with the nearest being ∼13 km away. It is unknown what proportions of the precipitation falls as rain and snow, but some snow accumulation occurs in the winter months, as indicated by satellite imagery. Active periglacial processes (sub-zero temperature fluctuations) are likely to affect the higher slopes. Rock glaciers have been mapped in the Two Thumb ranges and some in the higher, northern parts of the range are likely still active where permafrost presence is modeled (Sattler, 2016; Sattler et al., 2016). No glaciers presently exist in the central Two Thumb range but there are cirque glaciers (mostly >1900 m asl) and a few small valley glaciers (terminating >1200 m asl) in the northern part of the range, 20–30 kilometers farther north.

Glacial activity was far more extensive during the Otira Glaciation (∼65–11.5 ka; Barrell, 2011) in the Two Thumb Range (Brook et al., 2006) and wider Rangitata Catchment with the limits of the Rangitata Glacier extending to the Rangitata Gorge

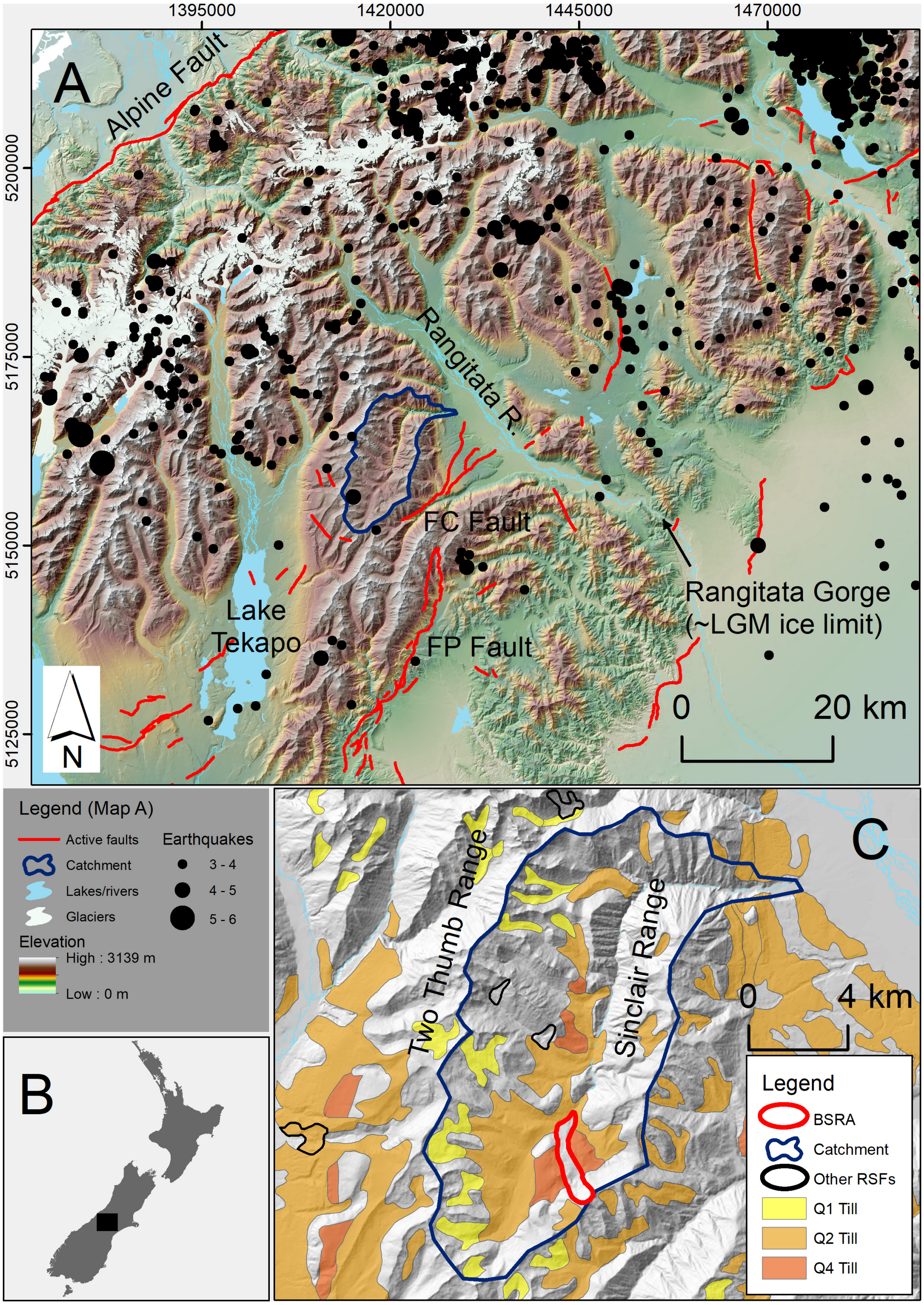

FIGURE 1 | (A) Location of Bush Stream catchment (blue outline), a tributary of the Rangitata River, within the eastern Southern Alps of New Zealand. Identified active faults are shown in red, sourced from the Institute of Geological and Nuclear Sciences (GNS Science) active faults database; http://data.gns.cri.nz/af/. The Alpine Fault, Forest Creek (FC) Fault, and Fox Peak (FP) Fault are labeled. The location of earthquakes (>M3) within the past 30 years (1990–2020) are shown from the GeoNet Earthquake Catalog, with indicated magnitude; the method of magnitude estimate varies in the catalog. The extant glaciers are shown in white. The approximate LGM extent of the Rangitata Glacier was at the Rangitata Gorge (labeled on map). The topographic data (colored hillshade model) are from LINZ: https://data.linz.govt.nz/. **(B)** Map of New Zealand with the location of Map A shown by the black rectangle. **(C)** Map showing the general topography of the Bush Stream catchment [same blue polygon as in Map **(A)**] with the Bush Stream Rock Avalanche (red polygon) and other landslides in the area (black polygons), along with the location of glacial sediments (till gravels) as mapped by Cox and Barrell (2007).

(<500 m asl) (Barrell, 2011; Shulmeister et al., 2018). Little is known of the extents of valley ice in Bush Stream basin, but evidence of glacial activity in the area is represented by cirque basins and till deposits (Cox and Barrell, 2007; Brook et al., 2008). Tills inferred to be of Late Pleistocene Age (Marine Isotope Stage [MIS] 2; 12–24 ka and MIS 4; 59–71 ka) are mapped in the Bush Stream basin while tills inferred to be of Late Pleistocene to Holocene Age (MIS 1–2; 1–14 ka) are mapped in the cirques above the Bush Stream basin (Cox and Barrell, 2007; **Figure 1C**). Like in many other parts of the Southern Alps (Kirkbride and Matthews, 1997; Brocklehurst and Whipple, 2007), the glacial activity in the Rangitata and tributary catchments has likely contributed to the generation of relief and steep rock slopes (Brook et al., 2008). Glacial steepening and growth of relief, along with deglaciation (e.g., glacial debuttressing, degradation of permafrost) are preparatory factors for rock slope failure (McColl, 2012). Consequently, rock slopes around Bush Stream may have experienced heightened instability conditions as a result of the Otira Glaciation and its transition toward Holocene conditions. Several RSFs and rock avalanches have been mapped in the Two Thumb ranges, but the BSRA appears to be the largest of these. The BSRA had first been mapped by Cox and Barrell (2007), who inferred it to be of Holocene age. It fell from a north-west facing slope in the southern part of the Bush Stream catchment (**Figure 1C**), likely from glacially modified slopes.

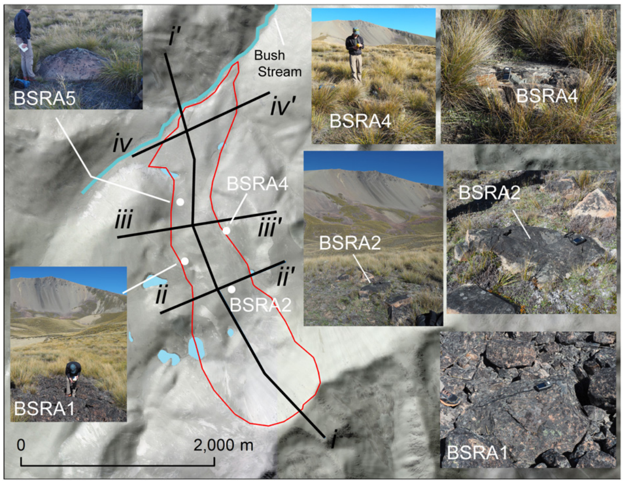

FIGURE 2 | Approximate extent of the Bush Stream Rock Avalanche (red outline; see **Figure 1C**) with locations of the long-section (black line i) spanning the length of the rock avalanche and cross-sections of the deposit (black lines; proximal ii; central iii; and distal iv), and ^{10}Be sample locations (white dots labeled BSRA#) with corresponding photos showing sampled boulder or surrounding ground. Lakes are indicated in blue. The base image of the main map is a semi-transparent LINZ 8 m hillshaded DEM overlaid onto LINZ aerial imagery.

MATERIALS AND METHODS

Topographic Data

The best existing topographic data for the area was the Land Information New Zealand (LINZ) national 8 m digital elevation model (DEM) which is based on interpolation of photogrammetrically derived 20 m contours. To provide a higher resolution topographic data set for mapping the rock avalanche deposit extent, visualization of the deposit morphology, and terrain analysis, a new topographic dataset was produced using Structure from Motion (SfM) photogrammetry. A photogrammetry survey was undertaken in March 2016 using a Phantom three Professional remotely piloted aircraft, capturing ∼1250 photos from 100–120 m above ground level, and mostly overlapping at better than 60% side and 70% forward overlap with a combination of nadir and oblique images. Seventeen ground control points (1 m canvas squares) were distributed on and around the rock avalanche deposit, and surveyed with a Trimble R10 GNSS receiver that was differentially corrected against the Mount John Observatory (MTJO) continuous GNSS station (at a 37 km baseline distance). The 2016 New Zealand Geoid Model was used to convert ellipsoidal elevations to orthometric heights, providing all survey data heights relative to the 2016 New Zealand Vertical Datum (NZVD2016), which approximates sea level. Differential correction resulted in point precisions of better than 0.08 m (horizontal and vertical) with an accuracy estimated to be better than 0.1 m (H&V) after accounting for error in GPS receiver pole placement on the ground control centroid. SfM photogrammetry processing was done with Agisoft Metashape 1.5.2. The initial alignment was done using the highest accuracy settings, the sparse cloud was edited to remove tie points of high uncertainty and georeferencing was applied prior to camera optimization and dense cloud generation. The ground control point RMS error was 0.43 m with a min. and max. error of 0.09 and 1.10 m, respectively. A 0.5 m digital surface model (DSM) was produced along with an orthophoto mosaic. No independent topography data were collected in the field to assess the accuracy of the SfM model, so forty manually selected check points were used to evaluate the consistency between the SfM-derived DSM and the national 8 m DEM (which has a stated accuracy of 90% of well-defined points falling within ±10 meters vertically). The min, RMS and max vertical differences of the forty check-points were 0.1, 7.7, and 14.0 m, respectively, with 95% of points having a difference of less than 8.2 m, consistent with the uncertainties estimated for the 8 m DEM. The SfM data were therefore deemed to be of sufficient accuracy for use in the geomorphological mapping and coarse-scale terrain analyses of this study.

Geomorphological Mapping and Rock Avalanche Geometry

The outline of the rock avalanche deposit, major topographic features (scarps or depressions), and hydrological features (streams or drainage lines) were mapped using a hillshade model derived from the 0.5 m DSM, an orthophoto mosaic (from the SfM), and from field observations. The complete source area of the rock avalanche was not captured in the photogrammetric survey (SfM DSM), so the 8 m LINZ DEM was used for mapping and terrain analysis of the rock avalanche source area. The planimetric areas for both source area and the deposit were measured. A long-section from the top of the source area to the inferred most-distal extent of the rock avalanche was drawn and the pre-existing travel path was roughly interpolated (Section *i* in **Figure 2**). The travel angle (fahrböschung) was calculated [$\tan^{-1}$ (fall height/runout length)] and compared against travel angles for other rock avalanches of a similar size. Cross-sections were extracted for proximal, central, and distal parts of the deposit to help support the mapping of the deposit extent and estimates of deposit thickness for volume calculations. Deposit thickness was roughly estimated from the cross-sections, by manually interpolating the pre-existing topography (valley floor) between the deposit margins. This interpolation is less confident in the central and proximal parts of the deposit, but is more confident at the distal end where the pre-existing river terraces are visible and suggest a relatively planar surface may have existed. To account for the uncertainty in the position of the pre-existing ground surface, and subsequent loss of rock avalanche material from erosion, an upper and lower bound estimate of deposit thickness was adopted.

To estimate the volume of the rock avalanche three methods were used: (i) The cross-sections (**Figure 2**) were used to estimate an average (upper and lower bound) deposit thickness which was then multiplied by the mapped deposit area; (ii) An area-volume scaling relationship for rock avalanches (Figure 1 in Hungr, 2006) was used to estimate the likely volume of the rock avalanche from the mapped area of the deposit; (iii) The source scar volume was estimated by reconstructing the pre-failure topography of the source scar, assuming that the hillslope that failed was an approximately planar slope, similar to the adjacent north-eastern slope. An 8-m DEM was produced to represent this pre-failure topography and differenced against the present-day 8-m DEM to derive a volume for the scar. The volume of material removed from the scar will have undergone bulking from fragmentation, a process which can increase rock avalanche volumes by some 15–25% (Jiskoot, 2011). Therefore, the source volume was increased by 20% to provide a deposit-volume equivalent. Additional bulking from entrainment during transport was not considered but may have further increased the volume of the deposit. The scar volume analysis also ignores post-failure erosion (i.e., enlarging) of the scar or materials accumulated in the scar (i.e., reducing scar volume estimate), and in general likely provides a lower-bound estimate of volume vacated from the scar. While all three methods suffer from different uncertainties and assumptions, it is considered that the three methods provide a realistic range for the volume of the rock avalanche.

Cosmogenic Dating

To assess the age of rock avalanche deposit, *in situ* cosmogenic ^{10}Be exposure dating was applied to three boulders exposed on the surface of the rock avalanche (**Figure 2**). One further sample (BSRA4; **Figure 2**) was taken from a boulder originally considered to be part of the rock avalanche, but later thought to be part of an adjacent slope failure. Soil development and weathering appears to have obscured or disintegrated many of the boulders so there were few suitable boulders to choose from for sample selection. However, to reduce the chance of selecting boulders or boulder surfaces that would provide unrepresentative exposure ages, the following sampling criteria were followed: (i) the boulders were larger than 1 m in diameter; (ii) the boulders were on gently sloping or flat ground and therefore less likely to have rolled/toppled since their original emplacement; and (iii) the sampled surface of the boulder was more than 0.2 m above any surrounding soil; (iv) the sampled surface was weathered (i.e., not recently exposed or over-turned). All samples appeared to be of similar lithology – slightly to moderately weathered, orange-gray greywacke sandstone. An angle-grinder, hammer and chisel were used to chip off approximately 1.5–4 cm thick layers of rock from the boulder surfaces, targeting quartz veins where available. Skyline horizon surveys were made at each sampled boulder location with a inclinometer and compass, for use in correcting for the topographic shielding of cosmogenic radiation. Boulder position was measured with a Garmin hand held GPS, but boulder elevation was measured from the SfM DSM.

Quartz was isolated from the greywacke samples following standard mineral separation procedures, following crushing, sieving, and acid washing. Beryllium targets were prepared at GNS Science and Victoria University of Wellington, in New Zealand. The beryllium of samples and two process blanks was measured by the GNS Science Accelerator Mass Spectrometer. Two processing blanks (KV322 and KV332) were averaged and the correction was less than 1.6% ($1.8 \pm 0.3 \times 10^5$ a ^{10}Be). Exposure ages, using processing-blank corrected data, were calculated using the online exposure age calculator (version 3; Balco et al., 2008). Corrections for sample thickness and topographic shielding were applied, with the shielding factor assessed using the online topographic shielding calculator. Sample densities were assumed to be 2.7 g/cm^3, a typical value for New Zealand greywacke (Hatherton and Leopard, 1964). The Putnam et al. (2010) Boundary Stream Tarn Moraine, New Zealand ^{10}Be production-rate calibration was used along with the time-dependent "LSDn" scaling scheme used to scale for elevation and latitude. ^{10}Be ages presented in this study are not corrected for erosion or snow shielding, both of which might have reduced ^{10}Be production leading to apparently younger ages. However, while no data are available on erosion rates on greywacke or time-dependent variations in snow-cover for Bush Stream catchment, an estimate of their potential effect was assessed. For erosion, erosion rates of 0.5 cm/ka and 1 cm/ka were applied in the online exposure age calculator. To evaluate snow shielding, the surface cover correction tool of Jones et al. (2019) was used with a snow density of 0.27 g cm^{-3} and a snow depth of 25 and 50 cm (representing a time-averaged snow depth for the entire exposure history). Note, these values are not constrained by any data but are considered to be upper (conservative) estimates for erosion and snow cover.

RESULTS

Rock Avalanche Characteristics

The rock avalanche deposit covers an area of 2.2 M m^2 and traveled ∼4 km from the top of the concave source area (∼2003 m asl) to the distal most extent of the mappable deposit (∼1180 m asl), representing a fall height of about 820 metres

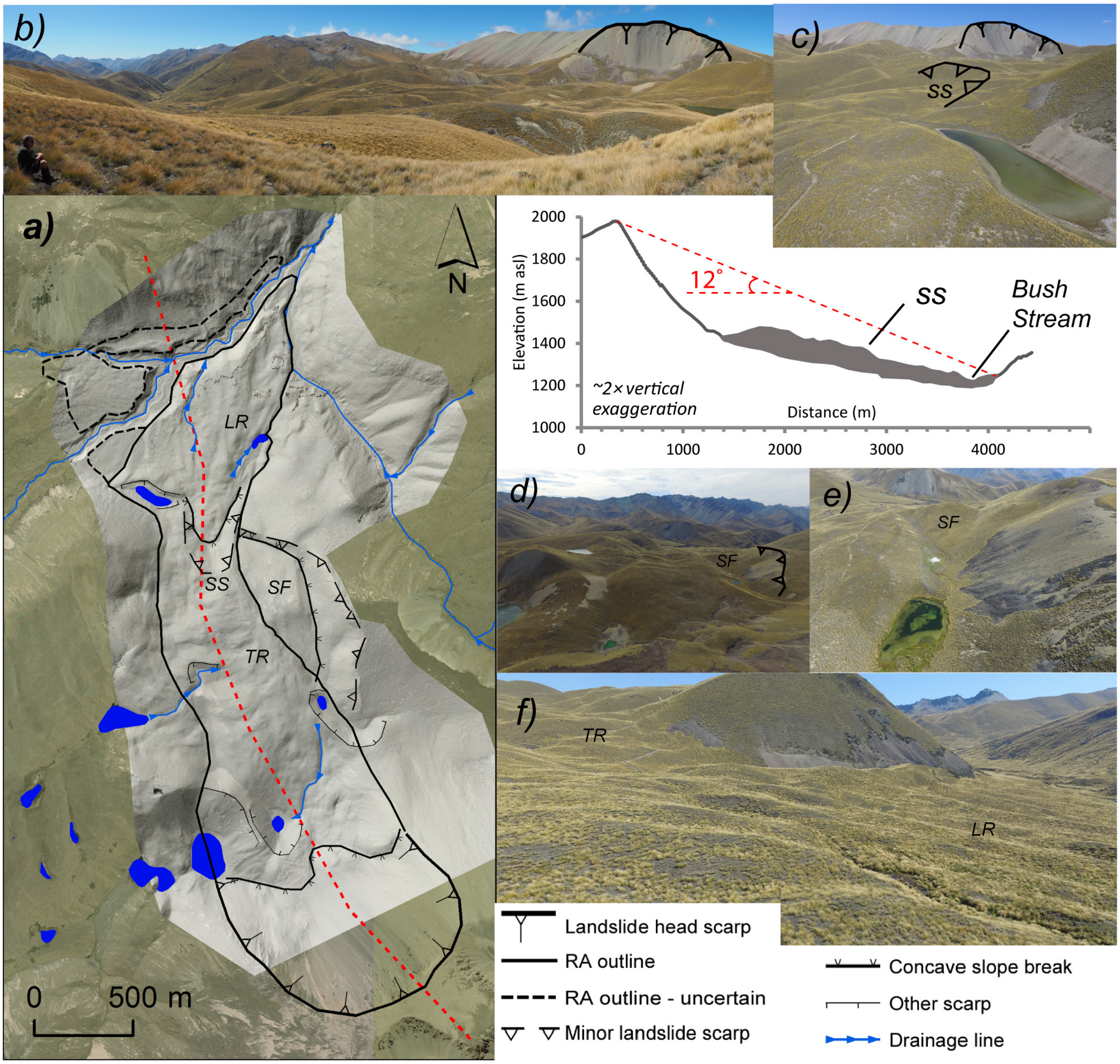

FIGURE 3 | (a) Geomorphological map of the Bush Stream Rock avalanche with corresponding long-section (dashed red line on map) with runout angle and inferred deposit shown in gray shading. Lakes are shown as blue on the map. The base image is the hillshaded 0.5 m SfM DEM on top of LINZ aerial imagery. LR = longitudinal ridges; SS = secondary scarp; SF = other slope failure; TR = transverse ridges. Supporting photos are provided to show some morphological features: **(b)** Photo taken from slope opposite distal end of deposit looking south toward the head scarp. **(c)** Photo looking southeast with view of the secondary scarp (SS) within the deposit. **(d)** Photo looking north-west along the rock avalanche deposit, taken from near the base of the head scarp, with several of the lakes visible, and the other slope failure (SF) abutting Bush Stream Rock Avalanche; **(e)** View looking north, with closer view of the other slope failure (SF); **(f)** View looking south-west from near the distal end of the deposit, showing narrow ridges (LR) aligned parallel to flow in the distal part of the deposit and shorter ridges (TR) aligned more transverse to flow in the mid reaches of the deposit.

and a travel angle (fahrböschung) of 12 degrees (**Figure 3**). The lateral margins of the deposit are mostly clearly distinguishable from the valley sides, especially on the eastern margin, expressed by a prominent edge that sharply contrasts with the pre-existing topography. The distal end of the deposit extends to the far side of Bush Stream, and appears to have super-elevated by some meters on the slopes at the northern side of Bush Stream, but its boundary is difficult to define. The rock avalanche likely blocked Bush Stream, and the stream has since cut through the deposit by 20–30 meters, providing one of the few exposures of the internal fabric of the deposit (**Figure 4**), which shows a poorly sorted, very angular to sub-angular diamicton with boulders through to fine particles. Rounded boulders and cobbles are visible in places at the base of the stream exposure, of similar nature to the modern boulders in Bush Stream. In most other locations little of the rock avalanche material is visible beneath the tussock grasses, with

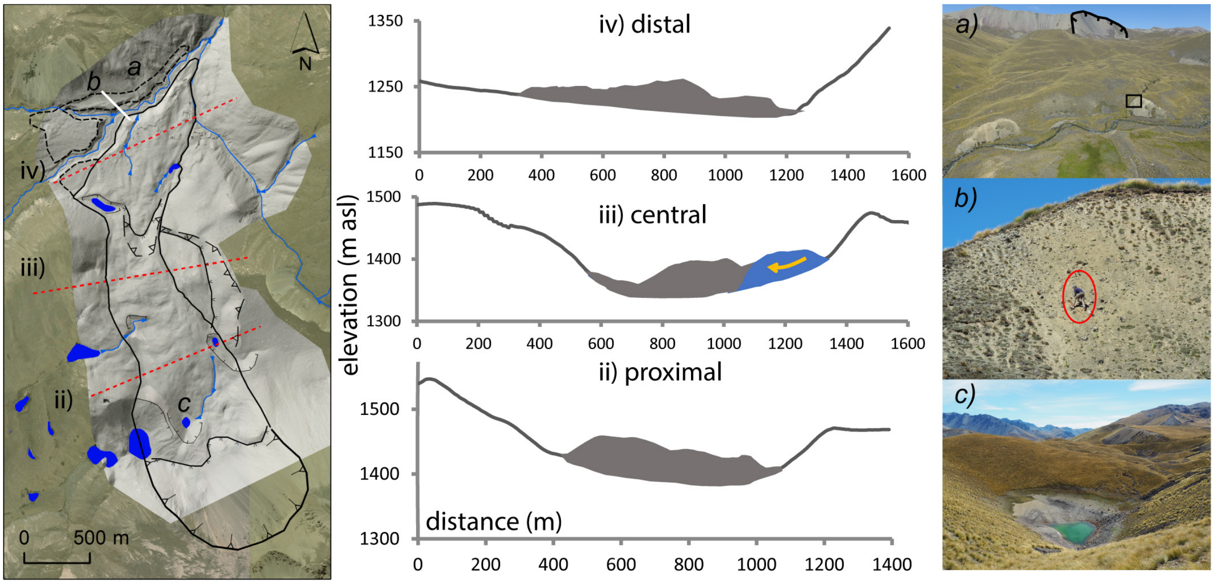

FIGURE 4 | Cross-sections ii-iv of rock avalanche deposit with locations of the sections and field photos indicated on map on the left. Photo **(a)** looking southwards with a view of Bush Stream in the middle distance and the source area crown (marked as black scarp) on the horizon. **(b)** Exposed rock avalanche sediments along Bush Stream (approx. photo position shown with black rectangle in photo **(a)**, showing the lack of stratification and poor sorting of deposit. **(c)** One of the depressions with a small lake within the rock avalanche deposit, with location indicated on the map on left.

shattered gravel- to small boulder-sized clasts visible in patches, but few large boulders, and no open-framework, large-boulder carapace typical of some rock avalanche deposits.

The body of the rock avalanche is undulating-hummocky with broad (30–100 m wide) but uneven ridges, which in the proximal and central deposit tend to be transverse to flow, and in the distal deposit are longitudinal to flow, narrower, and more elongate (**Figure 3**). The deposit appears (based solely on cross-section interpolation) to be approximately 20–70 meters thick in the upper to mid sections of the deposit, thinning to 20–30 m thick in the more distal section (**Figure 4**). A 10–50 m high arcuate-triangular secondary scarp (SS in **Figure 3**) separates the distal and mid-upper sections of the deposit, suggesting a secondary surge in the flow (see Strom, 2010), presumably as it dropped onto the Bush Stream floodplain and spread out due to a reduction in confinement. The lateral spreading may also explain the transition in this location to longitudinal ridges (see Dufresne and Davies, 2009). In several locations on the rock avalanche deposit there are (∼10–60 m) deep depressions, most of which host small lakes. The largest of these is in the south-western margin of the rock avalanche deposit (i.e., near the source area), but smaller depressions occur in the distal part of the deposit (**Figure 3**). These isolated depressions tend to deviate from the more subtle undulating-hummocky topography of the deposit.

The volume of the deposit calculated from the cross-section interpolation ranges between 71 and 107 M m^3. Using the area to volume scaling relationship (Figure 1 of Hungr, 2006) suggests a volume of ∼70 M m^3 using an area of 2.2 M m^2. The volume calculated for the source scar is smaller than both of these estimates. The reconstructed scar thickness is up to ∼120 m with an average of 44 m and planimetric area of 0.995 M m^2. That gives a volume of 43.8 M m^3, or 52.4 M m^3 after accounting for 20% bulking from fragmentation. Taken together, the volume of the original rock avalanche deposit is likely to have been between 50–100 M m^3. Both the (12°) travel angle and (4 km) runout length are within the expected range for rock avalanche volumes over this range (Hungr, 2006).

Another, smaller slope failure appears east of the rock avalanche deposit, defined by an approximately 1-km long and 30–120 m high arcuate head scarp above a displaced block (SF in **Figure 3**). The arcuate nature of the scarp and otherwise intact block of material suggests failure as a rotational debris slide or rotational rock slide – no suitable exposures allowed the nature of the materials at depth to be examined. The slope failure appears to be onlapped at the toe by the rock avalanche debris (**Figure 4**) with no obvious deformation of the rock avalanche deposit in this location, indicating that its movement/emplacement preceded (even if narrowly) the rock avalanche.

Cosmogenic Dating

The three boulders on the rock avalanche deposit have ^{10}Be exposure ages and external errors of 15.2 ± 0.5, 19.8 ± 0.5, and 20.1 ± 0.5 ka, and the boulder on the smaller slope failure east of the rock avalanche deposit has an exposure age of 16.6 ± 0.5 ka (**Table 1**). These ages do not account for erosion or shielding by snow cover. Applying erosion rates of 0.5 and 1 cm/ka, increases the ages by 1.1–1.8 ka (∼6-8%) and 2.4–4.3 ka (∼15–21%) respectively. Incorporating 25 and 50 cm of time-averaged snow-cover increases the ages by 0.7–0.9 (4–5%) and 1.4–1.8 ka (9–10%) respectively. The ages could therefore be some 10–30% older.

TABLE 1 | Cosmogenic ^{10}Be exposure age parameters and results. All samples were considered to have a density of 2.7 g cm^{-1}, a typical value for greywacke, and measured with the same AMS standard, 07KNSTD.

Sample name	Latitude	Longitude	Elevation (m asl)	Thickness (cm)	Shielding correction	Be-10 ± 1 σ (atoms g^{-1})	Age ± 1 σ (years) (external error in brackets)
BSRA1	−43.722	170.754	1429	2.5	0.998	197,013 ± 5,433	15,213 ± 421 (460)
BSRA2	−43.720	170.759	1434	2.0	0.996	265,082 ± 5,174	20,118 ± 395 (465)
BSRA4	−43.719	170.759	1408	3.5	0.997	210,106 ± 5,468	16,611 ± 434 (479)
BSRA5	−43.716	170.753	1343	1.5	0.994	241,861 ± 4,871	19,821 ± 401 (468)

To explain the ∼5 ka difference in exposure age between the youngest and the two older samples on the rock avalanche deposit, either the older samples both incorporate inherited ^{10}Be and/or the younger sample has a burial or erosion history that results in a lower ^{10}Be concentration. Hilger et al. (2019) have suggested that rock avalanches are prone to surface boulders with ^{10}Be inherited from previous exposure. This is due to rock avalanche materials typically not being vertically mixed during transport, resulting in a high chance of surface boulders being sourced from at or close to the original ground surface of the failed rock slope. This inheritance effect is smaller for older (>Holocene) RSFs on the assumption that glaciation or other processes sufficiently eroded, and therefore, reset the exposure history of the rock slope (Hilger et al., 2019). There is insufficient information to constrain ice thickness in the Bush Stream basin but likely parts of the rock slope were glacially eroded in the last glaciation given the evidence of glacial deposits (tills) mapped in the valley. Further, even if not significantly glacially eroded, the rockslope surface is likely to have undergone erosion by frost-weathering and rockfall processes, given its elevation (1600–2000 m asl) and steep gradient (>30 degrees; as measured for the adjacent unfailed hillslope). These erosion processes would have limited the amount of inherited ^{10}Be likely to be found in the rock avalanche samples.

Another explanation for the age difference is that the younger sample on the rock avalanche (BSRA1; 15.2 ± 0.5 ka) may have experienced ^{10}Be loss through erosion. The sample was taken from a boulder field in which boulders there were noted to be undergoing exfoliation/flaking, probably driven by frost weathering. Evidence of exfoliation was not noted for the other two rock avalanche samples, and therefore sample BSRA1 may have experienced higher erosion (i.e., removal of ^{10}Be). Differences in the prevalence of exfoliation may relate to differences in fracturing induced in the boulders by the rock avalanche process, or slight (unrecorded) lithological variations in the greywacke. The boulder may have also experienced slightly greater snow cover than the other rock avalanche samples (especially BSRA5), as it is relatively more low-lying. These factors together may explain the ∼5 ka difference in age.

The boulder (BSRA4) on the smaller slope failure east of the rock avalanche deposit has an exposure age of 16.6 ± 0.5 ka. If the interpretation of a rotational slide is correct for this slope failure, then the boulders on its surface are unlikely to have been disturbed during movement. In this case the sample age represents the age of the glacial sediment rather than the slope failure. The contact between the rotational slope failure and the rock avalanche indicates that the slope failure predates the rock avalanche. The age of 16.6 ± 0.5 ka therefore either suggests, like with BSRA1, there may have been erosion of the boulder (again supported by the observation of exfoliation flakes for this boulder), or it represents the timing of glacier retreat from this hillslope, and the rock avalanche is younger than ∼16.6 ka. If the latter, then it would lend more support to the two older (∼20 ka) samples from the rock avalanche having inherited ^{10}Be and a younger (e.g., 15 ka) age being more likely for the BSRA. However, like with BSRA1, it is entirely feasible that heightened erosion (from exfoliation weathering), and snow cover, could have resulted in an exposure age younger than the older samples from the rock avalanche.

DISCUSSION

Implications for Rock Avalanche Inventories

Whether the younger ^{10}Be age or the two older ^{10}Be exposure ages are more representative of the age of the rock avalanche, the rock avalanche is an anomalously old rock avalanche for the Southern Alps and many other glaciated mountains globally (McColl, 2012), especially if the effects of erosion and snow cover are included (i.e., they are 10–30% older). Green Lake Landslide in Fiordland (∼350 km to the south-west), may be the only other rock slope failure/avalanche in the Southern Alps that is known to (perhaps) have a pre-Holocene age (of 12–13 ka; Hancox and Perrin, 2009). Its preservation is likely partly owed to the very sizeable nature of the deposit – having a volume of 27 km^3. All other pre-historic dated, disrupted RSFs and rock avalanche deposits in the New Zealand Southern Alps are of Holocene age (Bainbridge, 2017), with only four of those occurring in the Early Holocene (Whitehouse and Griffiths, 1983; Lee et al., 2009), and 13 within the Mid-Holocene (Whitehouse and Griffiths, 1983; Hancox et al., 2013; Sweeney et al., 2013; McColl et al., 2019). Another 50 or so are dated from the Late-Holocene with increasing apparent frequency, and more than 100 historically recorded events have occurred since the 1800s (Bainbridge, 2017). Whitehouse and Griffiths (1983) and Bainbridge (2017) recognize that the apparent increase in frequency of events in New Zealand is not a real increase in frequency. Rather, it reflects a strong censoring of mass movement deposits from the humid and tectonically active Southern Alps as a result of the rapid erosion, modification, burial, or masking of deposits by glaciers, rivers, sediments and vegetation. Further to that, while several hundred deposits are mapped, absolute-age information exists for only 66% or so and most of those are historical events within the past 100 years (Bainbridge, 2017). The BSRA is therefore extremely old in the context of other dated mass movements in the Southern Alps, confirming that older events do exist but are likely to be no longer visible or simply not dated yet. The rapid censoring of deposits in New Zealand make it difficult to assess the true frequency of such events, and therefore make it difficult to reliably examine environmental processes driving changes in RSF activity. In contrast, in tectonically inactive mountains, such as the Scottish Highlands, post-glacial rock slope failure rates have been shown to be nearly five times higher prior to the Holocene, likely associated with enhanced seismicity (Ballantyne et al., 2014).

As more of the mapped deposits in the Southern Alps are dated, through greater application of absolute-age dating methods, there is potential to remove some of the age-bias and gaps in the frequency data. However, the development of other means of identifying and dating buried or reworked rock slope failure sediments may be necessary to reduce this bias sufficiently in order to draw meaningful evaluations of RSF frequencies. This will be necessary for supporting robust hazard assessments and for reliable assessment of the long-term bio-geomorphic impacts of rock avalanches or establishing of relationships between RSF frequency with that of climate changes or triggers such as earthquakes.

Insight Into the Depositional Environment and Climate of the Bush Stream Basin

The pre-Holocene timing of the rock avalanche means it occurred at a time when there was likely to still be a considerable volume of glacial ice in the Southern Alps and in the Rangitata Basin. While the local Last Glacial Maximum (LGM) in the Rangitata Catchment at c. 28 ka was earlier than the global LGM, the termination of the last glaciation was gradual from about 19–16 ka (Rother et al., 2014). Rother et al. (2014) suggest that substantial valley glaciers are likely to have been present in much of the Rangitata catchment until at least 15.8 ka. Mapping by Cox and Barrell (2007), albeit based on relative age assessment/geomorphic correlations, suggests that the rock avalanche fell onto tills of MIS 4 (∼59–71 ka) age, but that the distal end of the avalanche may have been emplaced onto tills of late glacial to Late Otira (MIS 2; 12–24 ka) age (**Figure 1C**). The data presented here suggests that the tills mapped near the distal end of the rock avalanche are at least older than 15–20 ka (i.e., older than the overlaying rock avalanche). The tills mapped as MIS 4 on the other hand may be younger (more likely MIS 2) than suggested by Cox and Barrell (2007). The boulder dated on the rotational slope failure east of the rock avalanche (BSRA4) has an age of at least 16 ka (likely several ka older after accounting for erosion and snow cover), and is most likely glacial sediment (as mapped by Cox and Barrell, 2007). The rotational movement of the slope failure does not appear to have caused disruption or deformation of the glacial materials, and even if the boulder was overturned during the slope failure (resulting in a younger exposure age), it is unlikely to be as old as MIS 4. This is supported by the observation of large depressions in the rock avalanche body. The depressions in the rock avalanche are much larger than the typical hummocky topography found on rock avalanches and which tend to show the inverse (i.e., large mounds rather than large holes). The depressions may be explained by the rock avalanche falling onto dead ice or an active glacier, either running over the glacier, or entraining blocks of the glacier, and the subsequent melt of the disintegrated ice blocks that produced "kettle holes". The largest kettle hole is on the western edge of the deposit, proximal to the source area where the rock avalanche deposit is inferred to be thickest. The depth of the lake occupying the bottom of this kettle hole is unknown but its surface is about 60 meters below the higher parts of the adjacent deposit, suggesting an ice thickness of some 60 m. If there was glacial ice (or at least "dead" ice) still present in the Bush Stream catchment at the time of the rock avalanche (c. 15–20 ka), it suggests that the glacial sediments mapped in this area are more likely of MIS 2 age.

An alternative explanation for the presence of the depressions in the deposit is that the depressions existed in the valley floor prior to the rock avalanche, possibly from older kettle holes produced by meltout of a sediment-covered glacier. However, a rock avalanche is likely to deposit sediment into any lake/depression it travels through, filling in those depressions. Therefore, it seems unlikely that these depressions existed, especially those below the rock avalanche source area where the deposit is thicker, prior to the rock avalanche. Although based on little data, taken together, the observation of the large depressions (kettle holes) and the age of the boulder on the rotational slide, provide some evidence that there was still glacier (dead?) ice present at the time of the rock avalanche, and that it was likely Late Otiran (MIS 2) in age.

If glacier ice is associated with the origin of the depressions, the remarkably good preservation of the rock avalanche deposit suggests that any glacier that the avalanche may have fallen onto was incapable of transporting or substantially modifying the RSF deposit, and it did not subsequently re-advance as far as the avalanche [e.g., during the Antarctic Cold Reversal (c. 14.7–13 ka), in which other glaciers in New Zealand advanced; Shulmeister et al., 2019]. When RSFs fall onto glaciers, they can increase the mass balance and induce an advance independent of climate, and the glaciers themselves are likely to modify RSF deposits, reworking the supraglacial sediment into moraines or entraining and modifying the sediment through active glacial transport processes (Shulmeister et al., 2009; Deline et al., 2015; Dunning et al., 2015; Reznichenko et al., 2015). There is no such morphological or sedimentological evidence to suggest that any of these processes (climate or mass movement-driven advance, or modification by glacial activity other than by dead-ice melt) occurred to any noticeable extent. These observations suggest the Bush Stream basin in the location of the rock avalanche at that time (15–20 ka) was either ice-free or had a glacier with a severely negative mass balance that was retreating, and that the rock avalanche did not sufficiently positively influence the glacier's mass balance.

These observations and the unusually good preservation of this deposit (for the Southern Alps), likely reflects the physiography of the Bush Stream basin. The catchment area of the basin above the rock avalanche is small (<45 km^2), and although with topography above the tree line, it has lower elevations than the northern part of the Two Thumb Range, and therefore likely had a relatively small accumulation area for snow. The position of the catchment in the lee side of the Two Thumb Range, in a low-precipitation region of the Southern Alps further would have resulted in perhaps lower-than-average snow accumulation. These factors combined probably limited the mass balance, length and flow rates of any valley glacier in the catchment such that by 15–20 ka when the BSRA fell, it was either retreated beyond that location or sufficiently small to cause no substantial modification. Likewise, while Bush Stream was able to breach and erode some of the distal end of the deposit that had temporarily dammed it, neither it nor other tributary streams have been sufficient to substantially remove or bury the deposit. This again, likely reflects the dry climate, small catchment, and consequent low competency of the streams.

The Causes of the Bush Stream Rock Avalanche

While the exact factors that caused the BSRA remain unknown, it is reasonable to speculate that the event was triggered by strong earthquake shaking. The bowl morphology of the source area that extends to the top of the ridge is typical of co-seismic RSFs (McSaveney et al., 2000). Further, there are no apparent structural features in the source scar that suggest obvious structural weakening (e.g., exposed dip-slope bedding planes, major persistent joints or faults). There is no evidence of secondary scarps or antiscarps above or adjacent to the source scars, which might indicate some pre-failure deformation and a progressive failure mechanism that could bring the slope to failure in the absence of a significant trigger. The Forrest Creek and Fox Peak faults are both within 10 km of the source area and paleo seismic evidence and modeling by Stahl et al. (2016b) suggests they are capable of generating earthquakes much stronger than the M_w 6 threshold for co-seismic triggering of major RSFs in New Zealand (Hancox et al., 2002). Paleo seismic records for the faults do not extend as far back in time as the BSRA, but given the recurrence intervals for the faults of less than 3000 years (Stahl et al., 2016b), they are likely to have generated multiple earthquakes over the past 20,000 years.

By the end of the last glaciation, the slope may have been primed for failure in an earthquake from steepening of the slope by glacier erosion and subsequent changes during the initial stages of deglaciation. The melting and complete or partial retreat of any glacier may have removed slope support (i.e., glacial debuttressing), exposed the rock slope to a new thermal regime with enhanced frost weathering, and possibly enhanced the intensity of any co-seismic shaking by increasing the topographic amplification of seismic waves (McColl et al., 2012). If the latter (i.e., paraglacial processes were operating and had contributed to slope priming) it provides a relatively rare example of an early (in the deglaciation history) rockslope response to glacier retreat (c.f. McColl, 2012; Hermanns et al., 2017), similar to only a small number of (>15 ka) RSFs in the Scottish Highlands where the timing of post-glacial RSFs is well-recorded (Ballantyne et al., 2014) and few other examples globally (Pánek, 2019).

CONCLUSION

The BSRA is the oldest known rock avalanche in the Southern Alps of New Zealand, occurring earlier than ∼16 ka (likely >20 ka). A volume of 50–100 M m^3 fell from the steep greywacke bedrock hillslope, producing a concave depression in the rock slope, and transitioned into a rock avalanche which traveled 4 km and temporarily blocked Bush Stream. Eventually the river breached the dam, as indicated by a deep channel through the distal end of the deposit. A travel angle of 12 degrees and runout distance of 4 km for the rock avalanche is typical for an event of this volume. The undulating, ridge-like morphology of the avalanche is also fairly typical of rock avalanches, except for the presence of several large lake-filled depressions. These depressions are interpreted to have formed from the melt out of glacier ice (dead ice) that the rock avalanche overrode and possibly entrained. Other than these depressions and fluvial erosion by Bush Stream, the avalanche is remarkably well preserved for its age, especially given the tendency for the Southern Alps to rapidly erase or obscure evidence of mass movements. Preservation of such a deposit suggests small, receded glaciers in the early stages of the regional deglaciation, and incompetent rivers with low sediment load and discharge. These factors likely reflect the relatively small size and very dry climate of the catchment in the lee of a mountain range. Given its age, the BSRA is an important (and extreme) data point in the New Zealand landslide inventory, and a reminder that older events can be found if we look in the right places.

DATA AVAILABILITY STATEMENT

Datasets are available on request: The data supporting the conclusions of this manuscript will be made available by the author (SM; https://orcid.org/0000-0002-2805-1761), without undue reservation, to any qualified researcher.

AUTHOR CONTRIBUTIONS

SM undertook the planning and collection of all field data (^{10}Be samples, aerial photography, dGPS data collection and post-processing), calculated the ^{10}Be exposure ages (after being provided with atom concentrations from GNS Science and Victoria University of Wellington cosmogenic laboratories), processed the SfM photogrammetry and undertook all geomorphological mapping, and interpretation. Field assistance and field photography was provided by Tom Brookman and Rob McGregor. SM prepared all figures and wrote the manuscript.

FUNDING

Funding was provided by a Massey University research grant RM17927.

ACKNOWLEDGMENTS

I would like to express my gratitude to Rob McGregor and Tom Brookman for their assistance with the fieldwork – for their photographs, help hauling gear and rocks, and their enthusiasm, meat-gathering, and wonderful company. I am grateful to Massey University for funding this research through a MURF grant (RM19927), and to Department of Conservation and staff for permission to carry out this research (Permits 49820-GEO and 49881-FIL). Dr. Jan Blahut is thanked for his proof-reading and helpful discussion. I am also grateful for the constructive feedback provided by reviewers José Darrozes and Fabio Matano.

REFERENCES

Bainbridge, R. (2017). *Lost Landslides: Rock-Avalanche Occurrence and Fluvial Censoring Processes on South Island*. New Zealand PhD Thesis, Northumbria University, Newcastle-upon-Tyne.

Balco, G., Stone, J. O., Lifton, N. A., and Dunai, T. J. (2008). A complete and easily accessible means of calculating surface exposure ages or erosion rates from 10Be and 26Al measurements. *Q. Geochronol.* 3, 174–195. doi: 10.1016/j.quageo.2007.12.001

Ballantyne, C. K., Sandeman, G. F., Stone, J. O., and Wilson, P. (2014). Rock-slope failure following Late Pleistocene deglaciation on tectonically stable mountainous terrain. *Q. Sci. Rev.* 86, 144–157. doi: 10.1016/j.quascirev.2013.12.021

Barrell, D. J. A. (2011). "Quaternary glaciers of New Zealand," in *Developments in Quaternary Science*, Vol. 15, eds J. Ehlers, P. L. Gibbard, and P. D. Hughes (Amsterdam: ScienceDirect), 1047–1064. doi: 10.1016/b978-0-444-53447-7.00075-1

Brocklehurst, S. H., and Whipple, K. X. (2007). Response of glacial landscapes to spatial variations in rock uplift rate. *J. Geophys. Res. F* 112:F02035.

Brook, M. S., Kirkbride, M. P., and Brock, B. W. (2006). Quantified time scale for glacial valley cross-profile evolution in alpine mountains. *Geology* 34, 637–640.

Brook, M. S., Kirkbride, M. P., and Brock, B. W. (2008). Temporal constraints on glacial valley cross-profile evolution: two thumb range, central Southern Alps. New Zealand. *Geomorphology* 97, 24–34. doi: 10.1016/j.geomorph.2007.02.036

Cook, S. J., Porter, P. R., and Bendall, C. A. (2013). Geomorphological consequences of a glacier advance across a paraglacial rock avalanche deposit. *Geomorphology* 189, 109–120. doi: 10.1016/j.geomorph.2013.01.022

Cox, S. C., and Barrell, D. J. A. (2007). Geology of the Aoraki area**:** institute of Geological and Nuclear Sciences 1:250 000 geological map 215. 271.

Deline, P., Hewitt, K., Reznichenko, N., and Shugar, D. (2015). "Chapter 9 - rock avalanches onto glaciers," in *Landslide Hazards, Risks and Disasters*, eds J. F. Shroder and T. Davies (Boston: Academic Press), 263–319. doi: 10.1016/b978-0-12-396452-6.00009-4

Dufresne, A., and Davies, T. R. (2009). Longitudinal ridges in mass movement deposits. *Geomorphology* 105, 171–181. doi: 10.1016/j.geomorph.2008.09.009

Dunning, S. A., Rosser, N. J., McColl, S. T., and Reznichenko, N. V. (2015). Rapid sequestration of rock avalanche deposits within glaciers. *Nat. Commun.* 6:8964. doi: 10.1038/ncomms8964

Froude, M. J., and Petley, D. (2018). Global fatal landslide occurrence from 2004 to 2016. *Nat. Hazards Earth System Sci.* 18, 2161–2181. doi: 10.5194/nhess-18-2161-2018

Görüm, T. (2019). Tectonic, topographic and rock-type influences on large landslides at the northern margin of the Anatolian Plateau. *Landslides* 16, 333–346. doi: 10.1007/s10346-018-1097-7

Hancox, G. T., Langridge, R. M., Perrin, N. D., Vandergoes, M., and Archibald, G. (2013). *Recent Mapping and Radiocarbon Dating of Three Giant Landslides in Northern Fiordland*. New Zealand: GNS Science, 52.

Hancox, G. T., and Perrin, N. D. (2009). Green Lake Landslide and other giant and very large postglacial landslides in Fiordland, New Zealand. *Q. Sci. Rev.* 28, 1020–1036. doi: 10.1016/j.quascirev.2008.08.017

Hancox, G. T., Perrin, N. D., and Dellow, G. D. (2002). Recent studies of historical earthquake-induced landsliding, ground damage, and MM intensity in New Zealand. *Bull. New Zealand Soc. Earthquake Eng.* 35, 59–95. doi: 10.5459/bnzsee.35.2.59-95

Hatherton, T., and Leopard, A. (1964). The densities of New Zealand rocks. *New Zealand J. Geol. Geophys.* 7, 605–625. doi: 10.1080/00288306.1964.10422108

Hermanns, R. L., Schleier, M., Böhme, M., Blikra, L. H., Gosse, J., vy-Ochs, S. I., et al. (2017). *Rock-Avalanche Activity in W and S Norway Peaks After the Retreat of the Scandinavian Ice Sheet*. Cham: Springer International Publishing.

Hilger, P., Gosse, J. C., and Hermanns, R. L. (2019). How significant is inheritance when dating rockslide boulders with terrestrial cosmogenic nuclide dating?—a case study of an historic event. *Landslides* 16, 729–738. doi: 10.1007/s10346-018-01132-0

Hungr, O. (2006). *Rock Avalanche Occurrence, Process and Modelling*. Dordrecht: Springer Netherlands.

Jiskoot, H. (2011). Long-runout rockslide on glacier at Tsar Mountain, Canadian Rocky Mountains: potential triggers, seismic and glaciological implications. *Earth Surf. Process. Landf.* 36, 203–216. doi: 10.1002/esp.2037

Jones, R. S., Small, D., Cahill, N., Bentley, M. J., and Whitehouse, P. L. (2019). iceTEA: tools for plotting and analysing cosmogenic-nuclide surface-exposure data from former ice margins. *Q. Geochronol.* 51, 72–86. doi: 10.1016/j.quageo.2019.01.001

Kerr, T., Owens, I., and Henderson, R. (2011). The precipitation distribution in the Lake Pukaki catchment. *J. Hydrol. New Zealand* 50, 361–382.

Kirkbride, M. P., and Matthews, D. (1997). The role of fluvial and glacial erosion in landscape evolution: the Ben Ohau Range, New Zealand. *Earth Surf. Process. Landf.* 22, 317–327. doi: 10.1002/(sici)1096-9837(199703)22:3<317::aid-esp760>3.0.co;2-i

Korup, O. (2005). Large landslides and their effect on sediment flux in South Westland, New Zealand. *Earth Surf. Process. Landf.* 30, 305–323. doi: 10.1002/esp.1143

Korup, O. (2008). Rock type leaves topographic signature in landslide-dominated mountain ranges. *Geophys. Res. Lett.* 35:L11402. doi: 10.1029/2008GL034157

Korup, O., and Clague, J. J. (2009). Natural hazards, extreme events, and mountain topography. *Q. Sci. Rev.* 28, 977–990. doi: 10.1016/j.quascirev.2009.02.021

Korup, O., Clague, J. J., Hermanns, R. L., Hewitt, K., Strom, A. L., and Weidinger, J. T. (2007). Giant landslides, topography, and erosion. *Earth Planet. Sci. Lett.* 261, 578–589. doi: 10.1016/j.epsl.2007.07.025

Lee, J., Davies, T., and Bell, D. (2009). Successive Holocene rock avalanches at Lake Coleridge, Canterbury, New Zealand. *Landslides* 6, 287–297. doi: 10.1007/s10346-009-0163-6

McColl, S. T. (2012). Paraglacial rock-slope stability. *Geomorphology* 15, 1–16. doi: 10.1016/j.geomorph.2012.02.015

McColl, S. T., Cook, S. J., Stahl, T., and Davies, T. R. H. (2019). Origin and age of The Hillocks and implications for post-glacial landscape development in the upper Lake Wakatipu catchment, New Zealand. *J. Q. Sci.* 34, 685–696. doi: 10.1002/jqs.3168

McColl, S. T., Davies, T. R. H., and McSaveney, M. J. (2012). The effect of glaciation on the intensity of seismic ground motion. *Earth Surf. Process. Landf.* 37, 1290–1301. doi: 10.1002/esp.3251

McSaveney, M. J., Davies, T. R., and Hodgson, K. A. (2000). "A contrast in deposit style and process between large and small rock avalanches," in *VIII ISL Cardiff, Landslides in Research, Theory and Practice*, (London: Thomas Telford).

Pánek, T. (2014). Recent progress in landslide dating: a global overview. *Progr. Phys. Geogr.* 39, 168–198. doi: 10.1177/0309133314550671

Pánek, T. (2019). Landslides and Quaternary climate changes—The state of the art. *Earth Sci. Rev.* 196:102871. doi: 10.1016/j.earscirev.2019.05.015

Putnam, A. E., Schaefer, J. M., Barrell, D. J. A., Vandergoes, M., Denton, G. H., Kaplan, M. R., et al. (2010). In situ cosmogenic 10Be production-rate calibration from the Southern Alps, New Zealand. *Q. Geochronol.* 5, 392–409. doi: 10.1016/j.quageo.2009.12.001

Reznichenko, N. V., Davies, T. R. H., and Winkler, S. (2015). Revised palaeoclimatic significance of Mueller Glacier moraines, Southern Alps, New Zealand. *Earth Surf. Process. Landf.* 41, 196–207. doi: 10.1002/esp.3848

Rother, H., Fink, D., Shulmeister, J., Mifsud, C., Evans, M., and Pugh, J. (2014). The early rise and late demise of New Zealand's last glacial maximum. *Proc. Natl. Acad. Sci. U.S.A.* 111:11630. doi: 10.1073/pnas.1401547111

Sattler, K. (2016). *Periglacial Preconditioning of Debris Flows in the Southern Alps*. New Zealand: Springer.

Sattler, K., Anderson, B., Mackintosh, A., Norton, K., and de Róiste, M. (2016). Estimating permafrost distribution in the maritime southern Alps, New Zealand, based on climatic conditions at rock glacier sites. *Front. Earth Sci.* 4:4. doi: 10.3389/feart.2016.00004

Schleier, M., Hermanns, R. L., Gosse, J. C., Oppikofer, T., Rohn, J., and Tønnesen, J. F. (2017). Subaqueous rock-avalanche deposits exposed by post-glacial isostatic rebound Innfjorddalen, Western Norway. *Geomorphology* 289, 117–133. doi: 10.1016/j.geomorph.2016.08.024

Shulmeister, J., Davies, T. R., Evans, D. J. A., Hyatt, O. M., and Tovar, D. S. (2009). Catastrophic landslides, glacier behaviour and moraine formation - A view from an active plate margin. *Q. Sci. Rev.* 28, 1085–1096. doi: 10.1016/j.quascirev.2008.11.015

Shulmeister, J., Thackray, G. D., Rittenour, T. M., Fink, D., and Patton, N. R. (2019). The timing and nature of the last glacial cycle in New Zealand. *Q. Sci. Rev.* 206, 1–20. doi: 10.1016/j.quascirev.2018.12.020

Shulmeister, J., Thackray, G. D., Rittenour, T. M., and Hyatt, O. M. (2018). Multiple glacial advances in the Rangitata Valley, South Island, New Zealand, imply roles for Southern Hemisphere westerlies and summer insolation in MIS 3 glacial advances. *Q. Res.* 89, 375–393. doi: 10.1017/qua.2017.108

Stahl, T., Quigley, M. C., and Bebbington, M. S. (2016a). Tectonic geomorphology of the Fox Peak and Forest Creek Faults, South Canterbury, New Zealand: slip rates, segmentation and earthquake magnitudes. *New Zealand J. Geol. Geophys.* 59, 568–591. doi: 10.1080/00288306.2016.1212908

Stahl, T., Quigley, M. C., McGill, A., and Bebbington, M. S. (2016b). Modeling earthquake moment magnitudes on imbricate reverse faults from paleoseismic data: fox peak and forest creek faults, South Island, New Zealand. *Bull. Seismol. Soc. Am.* 106, 2345–2363. doi: 10.1785/0120150215

Stirling, M., McVerry, G., Gerstenberger, M., Litchfield, N., Van Dissen, R., Berryman, K., et al. (2012). National seismic hazard model for New Zealand: 2010 update. *Bull. Seismol. Soc. Am.* 102, 1514–1542.

Strom, A. L. (2010). "Evidence of momentum transfer during large scale rockslides' motion. Geologically active," in *Proceedings of the Delegate Papers 11th Congress of the International Association for Engineering Geology and the Environment, Auckland, Aotearoa, 5-10 September 2010*, eds A. L. Williams, G. M. Pinches, C. Y. Chin, T. J. McMorran, and C. I. Massey (Auckland: CRC Press), 73–86.

Sweeney, C. G., Brideau, M. A., Augustinus, P. C., and Fink, D. (2013). "Lochnagar landslide-dam – Central Otago, New Zealand: geomechanics and timing of the event," in *Proceedings of the 19th NZGS Geotechnical Symposium*, Queenstown, 20–23.

Tatard, L., Grasso, J. R., Helmstetter, A., and Garambois, S. (2010). Characterization and comparison of landslide triggering in different tectonic and climatic settings. *J. Geophys. Res.* 115:F4.

Whitehouse, I. E., and Griffiths, G. A. (1983). Frequency and hazard of large rock avalanches in the central Southern Alps, New Zealand. *Geology* 11, 331–334.

Conflict of Interest: The author declares that the research was conducted in the absence of any commercial or financial relationships that could be construed as a potential conflict of interest.

frontiers
in Earth Science

ORIGINAL RESEARCH
published: 05 June 2020
doi: 10.3389/feart.2020.00164

Constraining the Age and Source Area of the Molveno landslide Deposits in the Brenta Group, Trentino Dolomites (Italy)

Jonas von Wartburg[1], Susan Ivy-Ochs[1,2], Jordan Aaron[1]*, Silvana Martin[3], Kerry Leith[1], Manuel Rigo[3], Christof Vockenhuber[2], Paolo Campedel[4] and Alfio Viganò[4]

[1] Department of Earth Sciences, ETH Zürich, Zurich, Switzerland, [2] Laboratory of Ion Beam Physics, ETH Zürich, Zurich, Switzerland, [3] Dipartimento di Geoscienze, Università di Padova, Padua, Italy, [4] Servizio Geologico della Provincia Autonoma di Trento, Trento, Italy

OPEN ACCESS

Edited by:
O. Adrian Pfiffner,
University of Bern, Switzerland

Reviewed by:
Regis Braucher,
UMR 7330 Centre Européen
de Recherche et d'Enseignement
de Géosciences de l'Environnement
(CEREGE), France
Jeff Moore,
University of Utah, United States

***Correspondence:**
Jordan Aaron
jordan.aaron@erdw.ethz.ch

Specialty section:
This article was submitted to
Structural Geology and Tectonics,
a section of the journal
Frontiers in Earth Science

Received: 19 March 2020
Accepted: 29 April 2020
Published: 05 June 2020

Citation:
von Wartburg J, Ivy-Ochs S,
Aaron J, Martin S, Leith K, Rigo M,
Vockenhuber C, Campedel P and
Viganò A (2020) Constraining the Age
and Source Area of the Molveno
landslide Deposits in the Brenta
Group, Trentino Dolomites (Italy).
Front. Earth Sci. 8:164.
doi: 10.3389/feart.2020.00164

Rock avalanches are low frequency natural hazards that can alter landscape morphology, and constraining the timing, volume and emplacement dynamics of pre-historic rock avalanches is crucial for understanding the hazards posed by these events. Here we perform cosmogenic nuclide dating, topographic reconstruction and runout modeling of the Molveno rock avalanche, located north of Lake Garda in the Province of Trento, Italy. The unique morphology of the deposits, which features numerous large scarps and prominent lineaments, have previously led researchers to interpret the Molveno rock avalanche as being the result of multiple events. Our results show that the Molveno rock avalanche had a volume of approximately 600 Mm^3, and failed from a prominent niche located on Monte Soran. ^{36}Cl cosmogenic nuclide dating results shows that the deposits were emplaced as a single event approximately 4.8 ± 0.5 ka, and suggests that the unique deposit morphology is due to the emplacement processes acting during and soon after failure. Numerical runout modeling shows that this morphology could have resulted from a combination of runup and extensional spreading of the debris along the complex valley floor topography. The ages we determined for this event are coincident with the nearby Marocca Principale rock avalanche (5.3 ± 0.9 ka), which may suggest a common trigger. Our results have important implications for interpreting the morphology of rock avalanche deposits, and contribute to the evolving understanding of rock avalanche processes in the Alps.

Keywords: rock avalanche, cosmogenic ^{36}Cl exposure dating, runout modeling, European Alps, geomorphic mapping

INTRODUCTION

Large rock avalanches are rare mass movements that can dramatically alter landscape morphology. Many rock avalanches have filled valleys and created landslide dammed lakes, and these catastrophic events can be a significant hazard to people and infrastructure located in the potential runout zone (Schwinner, 1912; Heim, 1932; Abele, 1974; Hovius et al., 1997; Korup and Tweed, 2007; Fort et al., 2009; Loew et al., 2017). Detailed studies of pre-historic landslides are important to understand the risk posed by these natural hazards, and understand post-glacial slope dynamics, landscape evolution, and paleoseismicity (Hovius et al., 1997; Hungr et al., 1999; Korup and Clague, 2009; Huggel et al., 2013; Grämiger et al., 2016; Ivy-Ochs et al., 2017a; Kremer et al., 2020; Singeisen et al., 2020). This requires knowledge of the volume, source area location and runout characteristics of these events, and inaccurate interpretations of these features can lead to misleading conclusions regarding rock avalanche hazard and mechanisms.

Rock avalanches are extremely rapid flows of fragmented rock that initiate as large slope failures (Hungr et al., 2014). Many rock avalanche deposits exhibit distinctive landforms, including longitudinal ridges, internal shear planes, and compressional and extensional features (Strom, 2006; Dufresne and Davies, 2009). Additionally, a characteristic stratigraphy, composed of a basal mixed zone, overlain by a highly fragmented body facies, and topped by a boulder carapace, is often observed in rock avalanche deposits (e.g., Dunning, 2004; Dufresne and Davies, 2009; Weidinger et al., 2014; Dufresne et al., 2016).

Dating of pre-historic events provides insights into rock avalanche triggering process, and facilitates comparisons to other dated landslides in the Alps. This helps to understand the temporal distribution of large mass movements during the Holocene and late Pleistocene (Prager et al., 2008; McColl, 2012), and to temporally relate the events with potential triggers and causes, such as earthquakes or climatic conditions (Ivy-Ochs et al., 2017b). Before many rock avalanches were dated, it was generally thought that they occurred within a few millennia after deglaciation, i.e., 18,000 years ago (Heim, 1932; Abele, 1974). This hypothesis implied that glacier debuttressing was a primary trigger of rock slope failure, an interpretation that has been called into question (McColl, 2012). More recently, surface exposure dating has revealed that many rock avalanches in the Alps occurred during the middle and late Holocene (Bigot-Cormier et al., 2005; Hippolyte et al., 2006; Cossart et al., 2008; Prager et al., 2008; Hippolyte et al., 2009; Le Roux et al., 2009; Ivy-Ochs et al., 2017a). Large landslides in the Alps show three periods of enhanced slope activity: 10–9, 5–3, and 2–1 ka, the latter especially for the Southern Alps (Prager et al., 2008; Zerathe et al., 2014; Ivy-Ochs et al., 2017a). Thus, most large landslides happened during the Holocene, at least 6000 years after the retreat of glaciers from the affected valleys, and many of them in quite recent time (Ivy-Ochs et al., 2017a).

The study of pre-historic rock avalanches has revealed that oversteepened valley flanks, and reduced support by glaciers, is one of several important causes, but not necessarily a trigger of rock avalanches (McColl, 2012; Grämiger et al., 2017). It is generally believed that a changing climate has an influence on landslide hazard, for example due to change in precipitation, and/or melting permafrost (Kellerer-Pirklbauer et al., 2012; McColl, 2012; Stoffel and Huggel, 2012; Huggel et al., 2013; Zerathe et al., 2014; Coe et al., 2018). In the Holocene, the climate became warmer and wetter, which may explain the three periods of enhanced slope activity described above (Prager et al., 2008; Ivy-Ochs et al., 2017a). However, for pre-historic rock avalanches it is challenging to detect climatic influence, due to their relatively low frequency (Huggel et al., 2013). Earthquake triggering has also been proposed to explain temporal clustering of pre-historic rock avalanches (McColl, 2012; Grämiger et al., 2016; Knapp et al., 2018; Köpfli et al., 2018).

In addition to providing important information about rock avalanche triggering mechanisms, the age and volume of large events are an important contribution to understanding the magnitude frequency relationship of rare events (Hovius et al., 1997), which are often missing in historic event cadasters (Hungr et al., 1999). However, if the deposits of a pre-historic event are mistakenly interpreted to be formed from multiple events, then the resulting magnitude-frequency relationship would be highly inaccurate. Finally, understanding the emplacement characteristics of past events contributes to understanding and predicting the mechanisms that govern rock avalanche mobility (e.g., Aaron and McDougall, 2019).

Thus, constraining the age, volume and emplacement dynamics of pre-historic case histories provides important insights into rock avalanche hazard and mechanisms. The aim of this study is to determine these parameters for the Molveno rock avalanche. The geomorphic characteristics of this site, which include large internal scarps, have led to a number of incompatible interpretations regarding the source location, age and number of events that make up the deposit. This makes it difficult to place the Molveno rock avalanche in a regional context and to interpret how this event contributes to the evolving understanding of rock avalanche processes in the Alps. To address these uncertainties, we perform detailed geomorphic mapping, cosmogenic nuclide dating, topographic reconstruction, and 3D runout analysis.

STUDY AREA

The study area, shown in **Figure 1**, is located in the lower Sarca Valley, north of Lake Garda in the Province of Trento, Italy. Molveno belongs to a cluster of large landslides (**Figure 1**). The oldest of these is Marocca Principale (5.3 ± 0.9 ka), located approximately 10 km away from Molveno (Ivy-Ochs et al., 2017a). Another nearby deposit is Tovel (<20 km away from Molveno), which is composed of at least two events (Ferretti and Borsato, 2004). Lavini di Marco (3.0 ± 0.4 ka) dates to the late Holocene (Martin et al., 2014). The other five dated landslides in Trentino are of historic age (Ivy-Ochs et al., 2017a).

Deposits of the Molveno rock avalanche(s) are situated in a NNE-SSW trending valley which is parallel to the Giudicarie fault system (Castellarin et al., 2005a). As shown on **Figure 1**, the study area is tectonically dominated by the southern Giudicarie fold and thrust belt (Castellarin et al., 2005a, 2006; Viganò et al., 2015). The Molveno Valley is dominated by a syncline, the fold axis of which is dipping toward SSW (Castellarin et al., 2005a). The Molveno Valley has an asymmetric profile, with a steep western flank, affected by scarp-fault-surfaces, and a gently dipping eastern flank which follows the orientation of stratification (Carton, 2017). Most large aquifers, and point-springs of high to very high capacity (100 to 500 l), are related to the Triassic dolomites of the Dolomia Principale formation

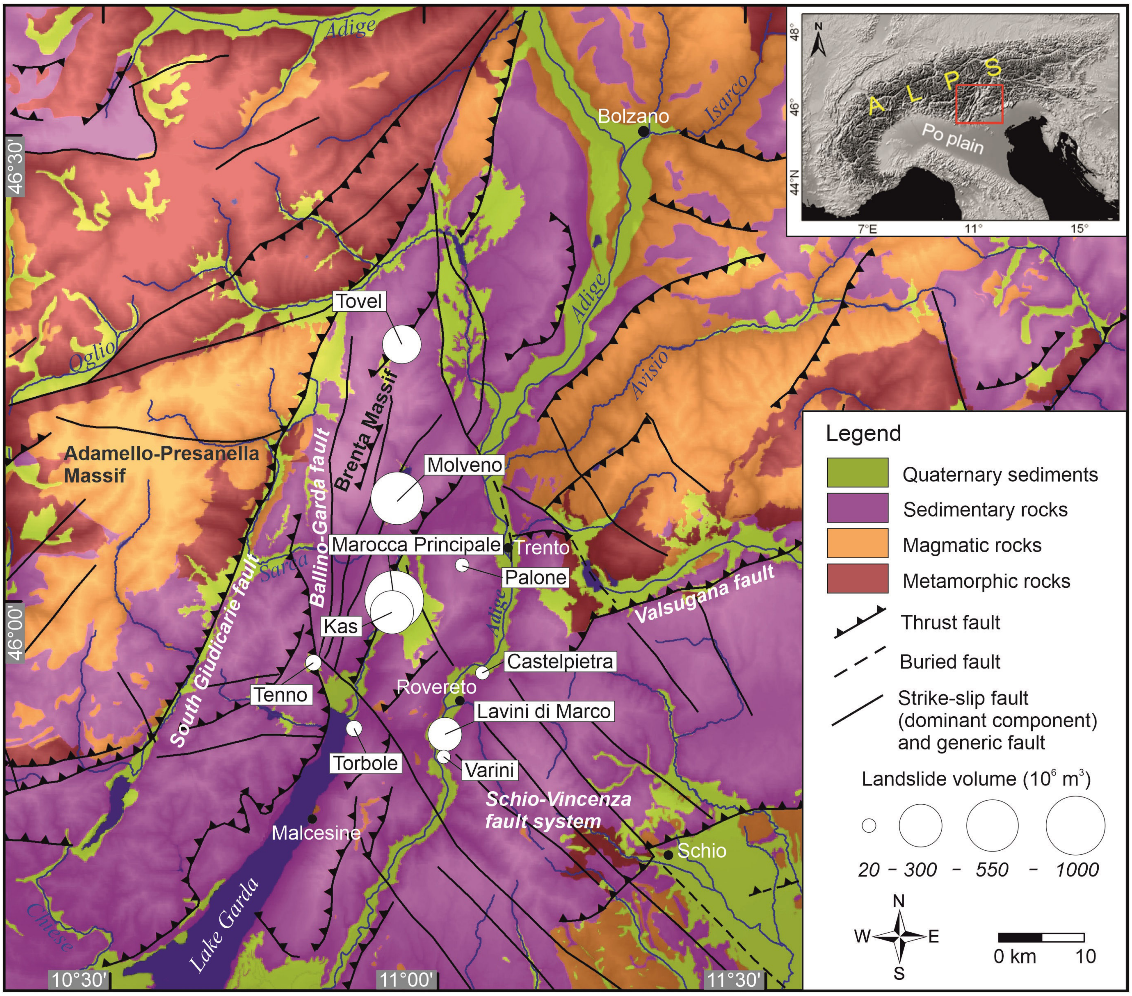

FIGURE 1 | Geological map showing rock avalanches in the province of Trento and their approximate size. Geologic data from the Geological Survey of Trento, CARG project database. Map modified from Ivy-Ochs et al. (2017a). The studied landslide is labeled as "Molveno."

and the overlaying Triassic limestones of the Calcari Grigi Group (Castellarin et al., 2005b).

The main lithologies of the study area are the typical formations of the Trentino carbonate platform, and the Molveno rock avalanche deposit consists mainly of oolitic limestone (Castellarin et al., 2005b). The Rotzo formation, which forms the base of the proposed source area, is known to have marly interbeds (Castellarin et al., 2005a).

Previous Work

The location of the source area, as well as the number of events that make up the Molveno rock avalanche deposits, has been debated by many authors (Lepsius, 1878; Damian, 1890; Trener, 1906; Schwinner, 1912; Trevisan, 1939; Marchesoni, 1954; Marchesoni, 1958; Fuganti, 1969; Abele, 1974; Chinaglia, 1992; Carton, 2017). Lepsius (1878) stated that the rock avalanche initiated on Monte Gazza, located on the western valley flank (**Figure 2C**). In contrast, Damian (1890) suggested that the rock avalanche initiated from Monte Soran (**Figures 2C, 3A**). Schwinner (1912) also suggested the source area was located on Monte Soran, and was the first to estimate the volume of the landslide, which he estimated to be between 300 and 500 Mm^3. Fuganti (1969) locates the source area, in contrast to Damian (1890) and Schwinner (1912), and in line with Lepsius (1878), at the eastern side of the valley at Monte Gazza (**Figures 2, 3C**), south of Pian delle Gaorne, in a prominent niche (**Figure 3D**). Chinaglia (1992) estimated the volume of the deposit to be 750 Mm^3, and suggested it was composed of four different landslides. One key aspect of this interpretation is that the prominent scarps featured in the debris (discussed in the following section) have been used as evidence that the deposits formed during several different events.

Radiocarbon dates associated with the Molveno rock avalanche have been reported by Marchesoni (1954, 1958). Marchesoni (1958) dated several logs obtained from Lago di Molveno when it was emptied for a hydropower project in 1951/52, and determined an age of 2908 ± 153 ^{14}C year BP (3441–2752 cal BP). In this work, several logs were sampled from

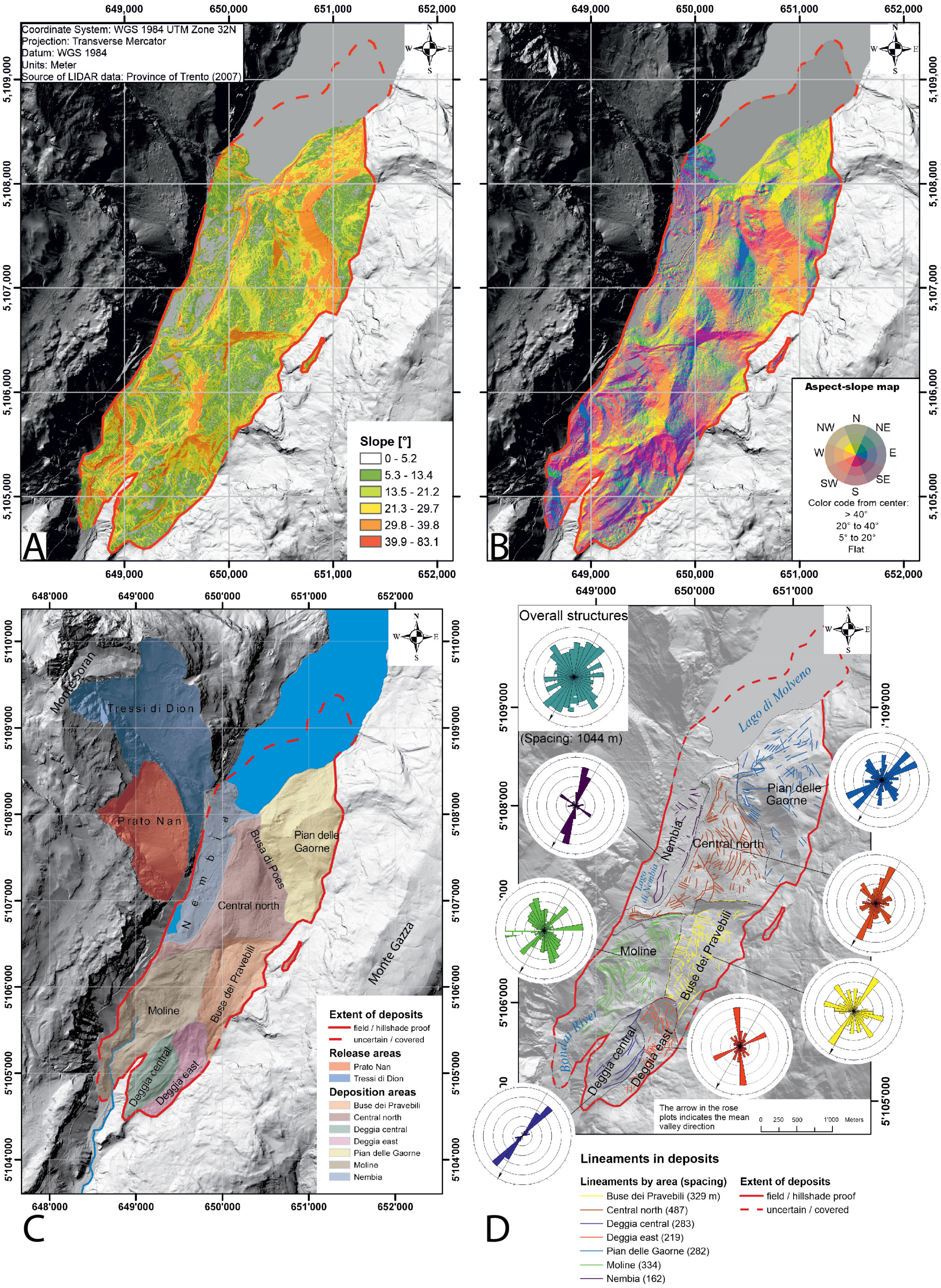

FIGURE 2 | (A) Slope map of the Molveno deposits. **(B)** Aspect map of the deposits. **(C)** Landslide regions. Deposition and release area. The red line encircles the mapped landslide deposits. The proposed release area is in the Northwest, it comprises Prato Nan and Tressi di Dion. **(D)** Lineament map of deposit structures. For each of the landslide areas lineaments were drawn on the aspect-slope map and hillshade. The lineaments are plotted length normalized as rose plots, i.e., the direction with greatest cumulative length is the longest rosette branch, and so on. A bin size of 10° was chosen. The concentric circles on each plot correspond to lineament length, with spacing the circles indicated on the legend. Map coordinate system: WGS 1984 UTM Zone 32N.

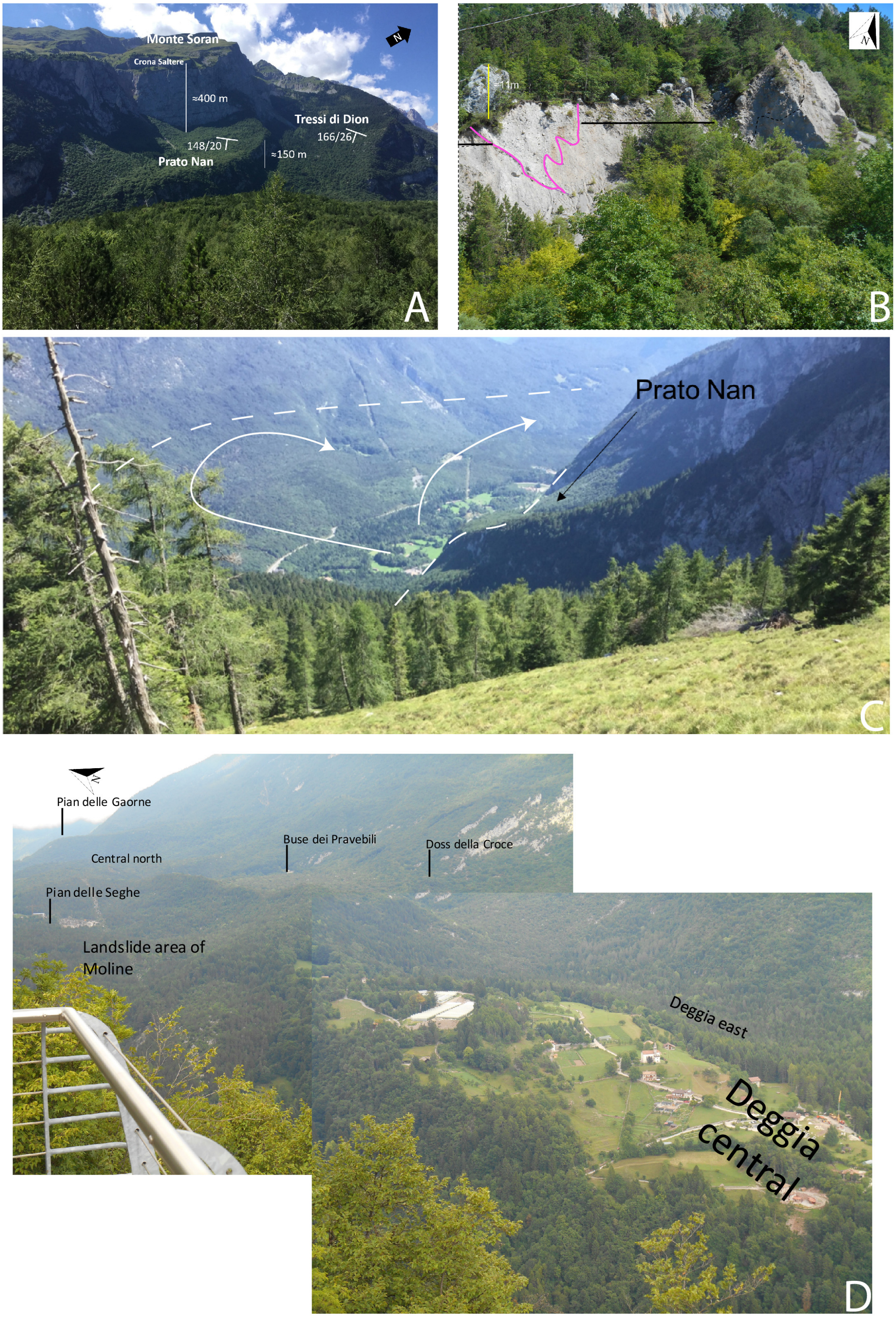

FIGURE 3 | (A) Image of rupture surface, showing both Prato Nan, and Tressi di Dion. **(B)** Outcrop of landslide deposits at Moline. Typical example of a carapace (large boulders on top) and strongly comminuted material inside the deposits. The carapace layer is indicated with a black line. The purple line shows a wedge-shaped pattern of coarser looking material. The boulder on top is around 11 m high (Photo: S. Ivy-Ochs). **(C)** Overview of the landslide looking from Tressi di Dion toward Pian delle Gaorne. **(D)** Overview of deposit zones.

a drowned forest, which was located on top of the deposits, and also a buried log (32 m below ground) from the construction site at the plain of Nembia, shown on **Figure 2C** (Marchesoni, 1954, 1958). The reported date is a composite date based on analysis of a single sample made up of several wood fragments, therefore it must be viewed with caution. The suggested age could also be constrained by other items used by human settlers, found further north on the lake floor, which are from into the Iron Age (Marchesoni, 1954).

GEOMORPHOLOGICAL ANALYSIS

We have performed geomorphic mapping of the site in order to document surficial features of the source zone and deposit. These provide field evidence to help understand the failure and emplacement of the Molveno rock avalanche. Our mapping included measurements of several geometric characteristics (such as planar area) of the source and deposit zone, a subdivision of the deposit into distinct geomorphic areas, and mapping of the location and extent of scarps, ridges and lineaments. This was done by manually digitizing all these features on a hillshade projection of available LiDAR data.

As will be summarized further in the section entitled "Reconstruction of pre-failure topography and volume analysis," we tested whether the emplacement characteristics of the event could be explained with a source area located on Monte Soran. This source location has a total planar area of approximately 2.74 Mm^2 and can be subdivided into a northern niche called Tressi di Dion that has an area of 1.74 Mm^2 and a southern niche called Prato Nan, covering 1.00 Mm^2. These source niches are shown on **Figures 2**, **3A,C**. The crown of the scarp has a total length of about 5000 m. The source reaches from 2360 m a.s.l. at the peak of Monte Soran down to around 900 m a.s.l., where an approximately 100 m high bedrock step separates it from the plain of Nembia. The slope of Tressi di Dion, with an average of 26°, is steeper than the slope of Prato Nan with 20°. Throughout the whole length of Prato Nan, very large boulders of up to 25 m diameter are found, which are interpreted as rock avalanche deposits (Castellarin et al., 2005a).

The deposition area of the landslide, shown on **Figures 3B,D**, is estimated to cover an area of 5.7 to 6.4 Mm^2. Between 0.5 and 1.2 Mm^2 are submerged in Lago di Molveno, based on mapping by Marchesoni (1954). The deposits are angular, well graded gravel with many large boulders, mainly on top, and many cobbles and blocks within the deposits.

As shown on **Figure 2C**, the deposit area is divided into seven separate areas, discussed below from North to South:

- Nembia, which is characterized by its flatness, large boulders and hillocks, and is surrounded by meadows. The flat areas are composed of lake sediments underlain by large boulders.
- Central North, which reaches from Lago di Molveno down to the ridge below the plain of Nembia. This region is defined by prominent trenches and depressions, and features numerous lineaments (**Figure 2D**). Large boulders cover the surface.
- Pian delle Gaorne, which is an elevated semicircular platform-like landform, located 200 m above Lago di Molveno. The entire plain is covered by large boulders and finer grained landslide debris. Most boulders are in the range of 5 to 15 m in diameter.
- Buse dei Pravebili, which is a topographic depression separated from the Central North zone by a 50 m high, 600 m long scarp. This area is partly covered by an alluvial fan, and features many large boulders.
- Moline, which contains a small settlement and limestone quarry. This area has been heavily modified by anthropogenic activities. An outcrop showing the sedimentology of the landslide deposits can be seen in the eroded landslide deposits above Moline (**Figure 3B**). A boulder carapace, consisting of boulders up to 11 m in diameter, can be observed at the surface (e.g., Dunning, 2004; Dufresne and Davies, 2009; Weidinger et al., 2014). However, large boulders are also found in the body facies. Within the deposits, slump structures can be seen (**Figure 3B** below the large boulder). Strongly comminuted material underlies the carapace layer. Below the 11 m high boulder, a wedge of sediment bound by an internal sliding plane is visible (marked in purple in **Figure 3B**).
- Deggia East, which is a forested, hummocky area, with hummocks that are on the order of 20 to 50 m in diameter. It is separated from Buse dei Pravebili by a 150 m high, 35° steep major scarp (**Figures 2A,B**).
- Deggia central, which is a settlement on a bedrock high at the centre of the valley. Based on bedrock outcrops and a construction site, the thickness of the landslide deposits here is estimated to be less than 10 m.

The deposit features numerous scarps and ridges (**Figures 2A,B**). These are especially prominent between the Central North and Buse dei Pravebili regions, as well as in Moline (**Figures 2A,B**). These features have been interpreted as evidence that the deposit is composed of multiple events (Chinaglia, 1992), and it was previously unknown if these features formed during or after the emplacement of the rock avalanche(s).

Another striking feature of the deposit is the presence of numerous lineaments within the debris. As shown on **Figure 2D**, the lineaments have two dominant orientations, one parallel to the presumed direction of motion and the other perpendicular. These features provide important dynamic information as they either align with the local direction of motion, or provide evidence for compression and extension during runout (Strom, 2006; Dufresne and Davies, 2009). These features are numerous in all deposition sectors, except for Nembia. The orientation of the two sets of lineaments is consistent in Nembia, Central North, and Buse dei Pravebili. Similarly, the orientations are consistent in Deggia East and Pian delle Gaorne. These observations are discussed further in section "Runout analysis," after the results of the cosmogenic nuclide exposure dating and runout analysis are presented.

COSMOGENIC NUCLIDE SURFACE EXPOSURE DATING

Constraining the age of the landslide is an important contribution to understanding the post-glacial dynamics, and to be able to correlate the timing of the landslide with possible triggers e.g., seismic crises or climatic conditions. Additionally, dating of boulders in the different landslide areas provides a direct means of establishing the number of landslides that the deposit is composed of. Since the deposit is composed of limestone, cosmogenic ^{36}Cl was used for dating. Cosmogenic nuclides are produced within minerals of rock surfaces exposed to cosmic rays. Measuring the concentration of the cosmogenic nuclide allows calculation of the time elapsed since boulder deposition (Ivy-Ochs and Kober, 2008).

During fieldwork, numerous boulders were examined for suitability for dating, using the criteria given by Ivy-Ochs and Kober (2008). The main considerations were that the block be large, weathering-resistant, and stand locally high in the landscape. Two sampling campaigns were conducted: The first campaign was in 2009 when three samples were collected, MO1 to MO3; two of these were successfully dated (for MO2, during measurement the ^{36}S counts were too high and measurement was stopped). In the second sampling campaign, in 2017, eight samples (MO4–MO11) were taken and all dated. Photos of select boulders are shown in **Figure 4**, and the locations of the samples are shown in **Figure 5**.

We followed the sample preparation procedure using isotope dilution as given by Ivy-Ochs et al. (2004). Rock samples were crushed to <0.4 mm, leached with water and dilute HNO_3, then dissolved completely with HNO_3 after addition of ^{35}Cl carrier. Sample AgCl was isolated and purified in a series of precipitation and dissolution steps. To avoid ^{36}S interferences during accelerator mass spectrometer (AMS) measurements, sulfur was removed through precipitation of $BaSO_4$ after addition of $Ba(NO_3)_2$. Measurement of both ^{37}Cl/^{35}Cl as well as ^{36}Cl/Cl ratios is with the 6 MV tandem accelerator at Ion Beam Physics, ETH Zurich. ^{36}Cl/Cl ratios were measured against the ETH internal standard K382/4N with a value of $^{36}\mathrm{Cl/Cl} = 17.36 \times 10^{-12}$ which has been calibrated to international AMS standards (Vockenhuber et al., 2019). Sample ratios were corrected for a blank value of 3.2×10^{-15}. Elemental concentrations (**Table 1**) as required for age calculations were determined commercially at Actlabs (Toronto, Canada).

Calculation of the ^{36}Cl exposure ages, applying all corrections, was conducted using an the in-house MATLAB© code developed at Ion Beam Physics ETH Zurich. A density of 2.4 g/cm^3 was used, and production rates were scaled to the boulder locations using the time dependent scaling model (Lm; Balco et al., 2008). Implemented equations, constants and production rates are given by Alfimov and Ivy-Ochs (2009). We used the calcium spallation production rate of 48.8 ± 3.4 ^{36}Cl atoms $g_{Ca}{}^{-1}$ year^{-1} and a contribution due to muon capture on Ca of 9.6% at the rock surface (Stone et al., 1996). For calculation of production of ^{36}Cl through low-energy neutron capture, a value of 760 ± 150 neutrons $g_{air}{}^{-1}$ year^{-1} was used (Alfimov and Ivy-Ochs, 2009). These values agree well with the ^{36}Cl production rates recently published by Marrero et al. (2016). Final age uncertainties (**Table 2** and **Figure 5**) include both analytical (one sigma) and production rate uncertainties. All production mechanisms are included in the age calculations. Shielding corrections were determined using ArcGIS from the digital terrain data.

The dating results show a cluster of boulder ages between 4.1 ± 0.3 to 5.5 ± 0.4 ka (**Table 2**), and a smaller cluster comprised of two dates, 2.1 ± 0.3 and 2.4 ± 0.2 ka. There is a clear spatial pattern for these ages. The two younger ages are from two closely situated boulders at Nembia (**Figure 5**). The other eight ages are from boulders found all across the Molveno deposits. The sampled boulders lie in the following areas (**Figure 5**): On Pian delle Gaorne three samples (MO4, 5, 6) whose ages range from 4.7 ± 0.3 to 5.1 ± 0.3 ka; In Central North, two samples date to 5.0 ± 0.6 ka (MO9), and 5.5 ± 0.4 ka (MO1); On Buse dei Pravebili, three samples (MO3, 7, 8) with ages between 4.1 ± 0.3 ka, and 4.9 ± 0.3 ka were determined. There is some scatter to these dates, however, in all three geographical areas at least one sample lies within the range of 4.9 ± 0.3 and 5.1 ± 0.4 ka. We therefore assume that all sampled geomorphological areas (**Figure 5**) are part of the same event with an average age of 4.8 ± 0.5 ka. All ages are included in the average except for MO10 and MO11 from Nembia.

Nembia (**Figure 2C**) is a distinct area due to its notable flatness reflecting the presence of lake sediments. Large landslide boulders are much younger (2.2 ka) than the rest of the deposits. These younger ages can be due to: (1) a later detachment by a second rock slide or rock avalanche, (2) shielding from cosmic rays after the event by sediment or water, or (3) loss of the top surface of the boulder by spalling. There is a small detachment zone in the bedrock above Nembia at the southwestern margin of Prato Nan, however, the lithology of Prato Nan does not match the lithology seen in the deposits at Nembia. Therefore, we consider the second possible explanation, shielding from cosmic rays, more likely.

There is no evidence for sediment covering the sampled surfaces. But in accordance with the presence of lake sediments underlying the plain, it is conceivable that water was previously covering the boulders, and a subsequent event led to drainage of the lake. The deposits south of Nembia, which form a transverse ridge have an elevation of around 815 m a.s.l. If they would have blocked the lake, the lake level would have had a maximum level of 815 m a.s.l. water cover, which would have been at least 10 m above both blocks, as MO11 is at 792 m a.s.l., and MO10 805 m a.s.l., would have provided sufficient shielding from cosmic rays. The production rate of ^{36}Cl in limestone is less than 5% of the surface value below 3 m depth (Steinemann et al., 2020). As attenuation is density dependent, water more than 9 m in depth would have provided sufficient shielding to reduce ^{36}Cl production to less than 5% of the non-shielded value.

Below Nembia no clear evidence of a catastrophic dam breach can be found, however, Evans et al. (2011), based on a database of landslide dam breaches, show a wide variety of breach

FIGURE 4 | Examples of boulders used for surface exposure dating (**Table 1**). Written informed consent was obtained from the individuals for the publication of any potentially identifiable images or data included in this article.

morphologies, often with no clear markers of a catastrophic event. The coherence of the two boulder dates suggests that 2.2 ka may be a good approximation for the timing of the breaching event and that both blocks were covered by enough water to shield them from cosmic rays. Accordingly, 815 m a.s.l. may well represent the elevation of the lake surface between 4.8 and 2.2 ka. Importantly, no geomorphological evidence of a discontinuity between the blocky deposits at Nembia and the main Molveno rock avalanche deposits can be found.

RECONSTRUCTION OF PRE-FAILURE TOPOGRAPHY AND VOLUME ANALYSIS

The volume of the rock avalanche(s) is a key element in the landslide analysis. It is an important parameter for understanding the dynamic behavior of the landslide, i.e., reach and velocity (Scheidegger, 1973), and also a main input parameter, for magnitude frequency relationships (Hungr et al., 1999). As described above, previous authors have estimated the volume

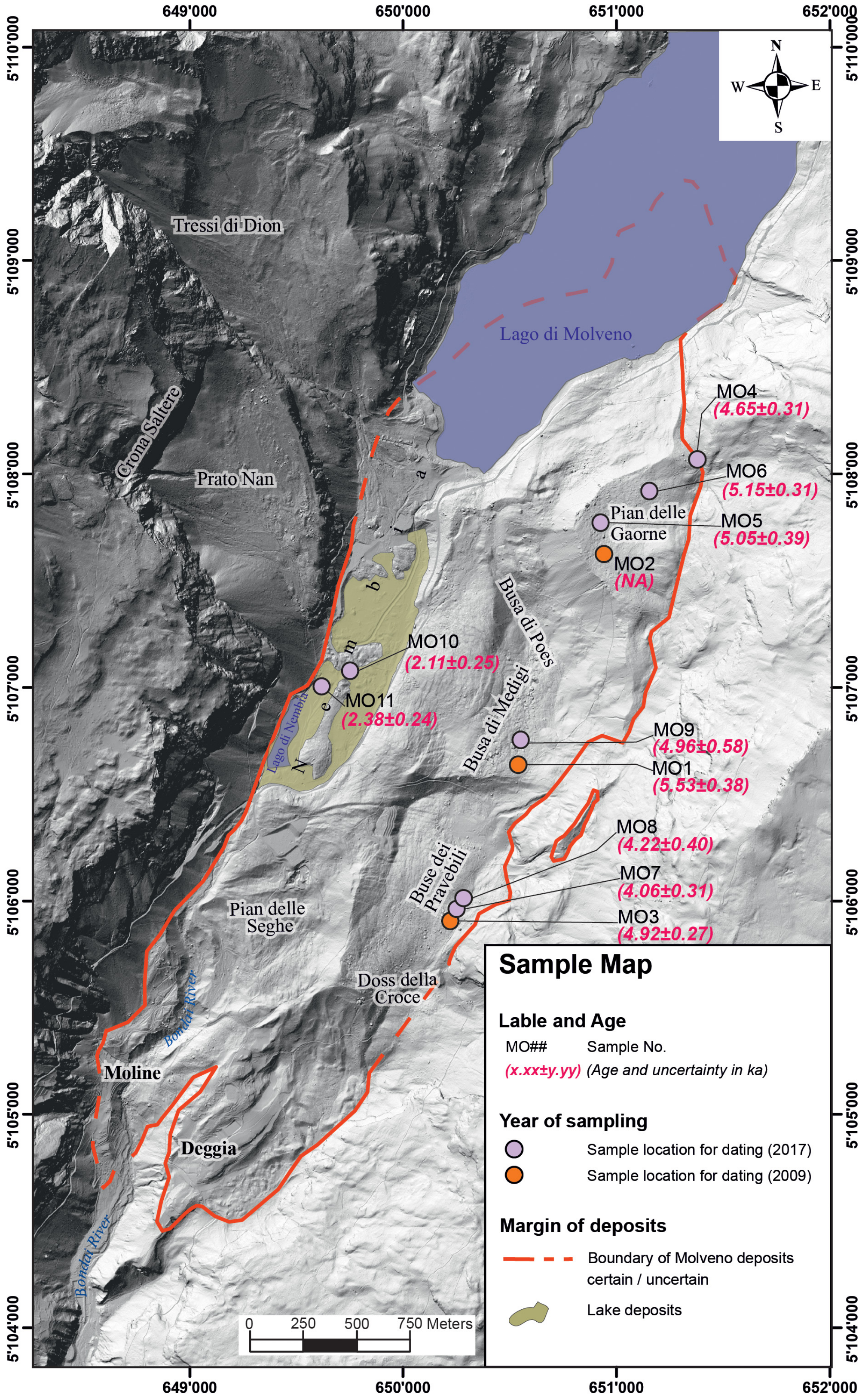

FIGURE 5 | Sample and ^{36}Cl exposure age map. All samples dated are shown in this figure (MO02 could not be dated due to too high ^{36}S counts during AMS). Coordinate system: WGS 1984 UTM Zone 32N.

TABLE 1 | Chemical composition of the samples used for cosmogenic nuclide dating.

	Sm	Gd	Th	U	Si02	Al203	Fe203(T)	MnO	MgO	CaO	Na20	K20	Ti02	P205
	ppm	ppm	ppm	ppm	w%	w%	w%	w%	w%	w%	w%	w%	w%	w%
MO 1	0.1	0.1	0.1	1.5	0.12	0.11	0.05	0.010	0.27	54.95	0.01	0.01	0.010	0.02
MO 2	0.1	0.1	0.0	2.0	0.06	0.07	0.07	0.010	0.24	55.16	0.01	0.01	0.010	0.01
MO 3	0.1	0.1	0.1	2.0	0.03	0.04	0.03	0.010	0.24	55.37	0.01	0.01	0.010	0.01
MO 4	0.2	0.3	0.1	0.6	0.23	0.09	0.06	0.004	0.61	55.98	0.03	0.02	0.004	0.29
MO 5	0.3	0.3	0.5	1.1	1.40	0.73	0.40	0.006	0.77	53.74	0.04	0.23	0.036	0.03
MO 6	<0.1	0.2	<0.1	0.3	<0.01	0.10	0.06	0.003	0.40	55.77	0.05	0.02	0.001	<0.01
MO7	0.3	0.3	0.3	1.3	0.18	0.22	0.07	0.003	0.61	55.35	0.04	0.06	0.009	<0.01
MO8	0.1	0.2	<0.1	0.6	0.07	0.14	0.07	0.003	0.49	55.62	0.06	0.03	0.002	0.01
MO 9	0.1	0.2	0.1	0.7	<0.01	0.13	0.05	0.003	0.57	55.65	0.03	0.04	0.004	0.01
MO 10	<0.1	<0.1	<0.1	0.4	<0.01	0.11	0.06	0.003	0.33	55.82	0.05	0.02	0.001	0.02
MO 11	<0.1	0.1	<0.1	0.3	<0.01	0.13	0.05	0.003	0.53	55.64	0.05	0.03	0.002	0.06

The here listed chemical components are the most important ones for the production rate of ^{36}Cl, i.e., also for the dating.

TABLE 2 | Sample data. Spatial location, orientation, thickness, chlorine concentration, and calculated ages.

	Lat (°N)	Long (°E)	Elevation (m a.s.l)	Samp. Thickn. (cm)	Shielding corr	Cl (ppm)	10^6 atoms ^{36}Cl/ (*g* rock)	Exposure age (ka)
MO1	46.0967	10.9475	920	5	0.947	15.5 ± 0.2	0.238 ± 0.014	5.53 ± 0.38
MO3	46.0902	10.9432	850	2	0.960	16.5 ± 0.1	0.209 ± 0.009	4.92 ± 0.27
MO4	46.1094	10.9588	1037	4	0.962	11.7 ± 0.1	0.222 ± 0.013	4.56 ± 0.31
MO5	46.1068	10.9529	1012	3	0.980	21.1 ± 0.3	0.247 ± 0.017	5.05 ± 0.39
MO6	46.1081	10.9559	1035.9	2.5	0.966	11.5 ± 0.0	0.253 ± 0.013	5.15 ± 0.31
MO7	46.0907	10.9436	849	5	0.937	13.6 ± 0.2	0.164 ± 0.011	4.06 ± 0.31
MO8	46.0912	10.9440	842	4.5	0.967	14.0 ± 0.1	0.177 ± 0.016	4.22 ± 0.40
MO9	46.0978	10.9478	899	3	0.912	16.3 ± 0.3	0.208 ± 0.023	4.96 ± 0.58
MO10	46.1009	10.9375	802	5	0.958	14.3 ± 0.1	0.085 ± 0.010	2.11 ± 0.25
MO11	46.1002	10.9358	792	5	0.886	15.4 ± 0.2	0.088 ± 0.009	2.38 ± 0.24

Two groups of ages are distinguished. The main body (4.8 ky) and a minor body (2.2 ky), marked brown in ***Figure 5****.*

of the landslide. However, the thickness of the deposits has not been previously estimated. A comparably minor uncertainty is the extent of the landslide into the lake. The pre-failure topographic surface is also a key input for the runout modeling, described below.

To estimate the volume of the source area, we manually modified the contour lines in the source area to provide a smooth transition with surrounding terrain. In the deposit area, a seismic survey, conducted while planning of the dam (Vecchia, 1953), was used to constrain the bedrock depth at Nembia, in the southern part of Lago di Molveno and in the area of Busa di Poes (**Figure 2C**). In addition to this, we have combined LiDAR data from the Province of Trento and an assumed pre-failure river profile for the valley to the estimated pre-failure surface. The volumes of the source and the deposition area were determined by differencing the present day topography with the reconstructed pre-event topography, and removing the volume of water assumed to be contained in the lake. For this, the contour map of the lake floor, presented by Vecchia (1953), was used. The calculated volumes are shown in **Table 3** and the reconstructed topography, as well as the source and deposit thicknesses, are shown in **Figure 6**.

Based on the back-analysis of various rock avalanche case studies, Hungr and Evans (2004) estimated a typical bulking factor (ratio of deposit volume to source volume) of 25%. Our reconstruction resulted in a bulking factor of 8%, which is somewhat lower. However, our reconstructed deposit volume fits well within the ranges estimated by previous authors [300–500 Mm^3 (Schwinner, 1912) to 750 Mm^3 (Chinaglia, 1992)]. Thus, given the uncertainties inherent in reconstructing pre-event topography, our source and deposit volumes are likely reasonable approximations of the pre-event conditions.

In our topographic reconstruction, the deposit is thickest at Pian delle Gaorne (**Figure 6**). There are two potential explanations for this. (1) Pian delle Gaorne is a bedrock high, covered with landslide debris. If this is the case, then we have overestimated the thickness of deposits in this area. However, there are no bedrock outcrops which would support this hypothesis. (2) Pian delle Gaorne is composed entirely of landslide deposits which remained more intact than the rest.

TABLE 3 | Calculated volumes of the source and deposition area of the rock avalanche of Molveno.

	Volume (Mm^3)
Deposit volume	600
Source mass	550

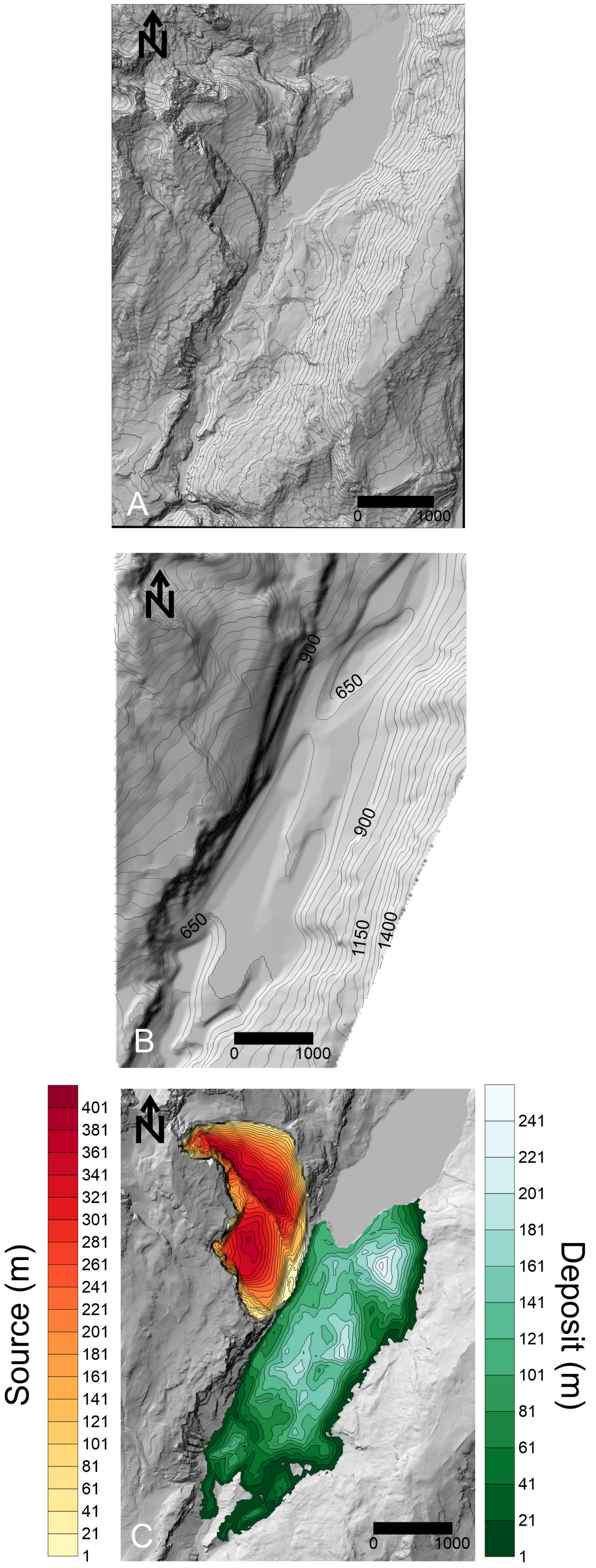

FIGURE 6 | **(A)** Present day topography (LiDAR data provided by province of Trento). **(B)** Reconstructed pre-failure topography. **(C)** Reconstructed source and deposit thickness, only material reconstructed above the present-day lake is shown.

That means it would have had high internal strength, however, there is also no direct evidence for this hypothesis. At the contact to the bedrock along the eastern valley side, a small ridge and a distinct depression through the whole length of the contact are visible (**Figure 2A**). This ridge and depression were interpreted to be signs for compression (e.g., Strom, 2006; Dufresne et al., 2016; Wolter et al., 2016), or run up and fall back (e.g., Evans et al., 1994).

Our estimated source volume can be used to compare the mobility of the Molveno rock avalanche to other large rock avalanches. A plot of fall height (H) divided by runout length (L) as a function of volume for the Molveno rock avalanche, as well as a large number of rock avalanche case histories assembled by Scheidegger (1973) and Li (1983) is shown in **Figure 7** (see inset for explanation of these two terms). As summarized in Heim (1932), the inclination of the line connecting the centers of mass of the source and deposit (red line on the inset of **Figure 7**) is equal to the basal friction angle, if the mass is assumed to move as a sliding block. Rock-on-rock sliding is expected to have a centre-of-mass fall height to runout length ratio of 0.6, and values lower than this indicate that additional mechanisms must reduce basal resistance (Scheidegger, 1973). The inclination of the line connecting the tip of the scarp to the toe of the deposit (H/L), approximates this angle, and is easier to measure in practice. Due to this, H/L serves as a useful empirical parameter for comparing mobility of different rock avalanches. As can be seen on **Figure 7**, the mobility of the Molveno rock avalanche was relatively low, compared to other rock avalanches of similar volume.

RUNOUT ANALYSIS

We perform semi-empirical runout modeling to simulate the impact area and deposit thicknesses, and to verify our proposed source geometry and location. For the simulations presented here, we used the depth averaged, 3D runout model Dan3D-Flex (Aaron and Hungr, 2016b). This model simulates the motion of an "equivalent fluid" over 3D terrain (Hungr, 1995). The rock avalanche is initially treated as a flexible block, able to translate, and rotate over 3D terrain. At a user specified time, the model transitions into a frictional fluid (McDougall and Hungr, 2004). The program features an open rheological kernel to calculate the basal resistance stress, and the parameters that govern the basal rheological model are calibrated. For the present analysis, we use the frictional and Voellmy rheologies, summarized in Hungr and McDougall (2009). The fluid portion of the model is a depth-averaged continuum dynamic model, incorporating an earth pressure theory similar to the classical Rankine earth pressure theory, where stresses linearly increase with depth (Savage and Hutter, 1989).

The parameters used for our best-fit model are listed in **Table 4**. **Figure 8** shows position and extent of the landslide at selected time intervals, **Figure 9** shows a number of cross sections through the results, and **Figure 10A** shows the final simulated deposit thicknesses and impact area. At $t = 0$ s the landslide is in its initial source niche. After 30 s the still coherent landslide mass hits the valley floor and disintegrates. At this

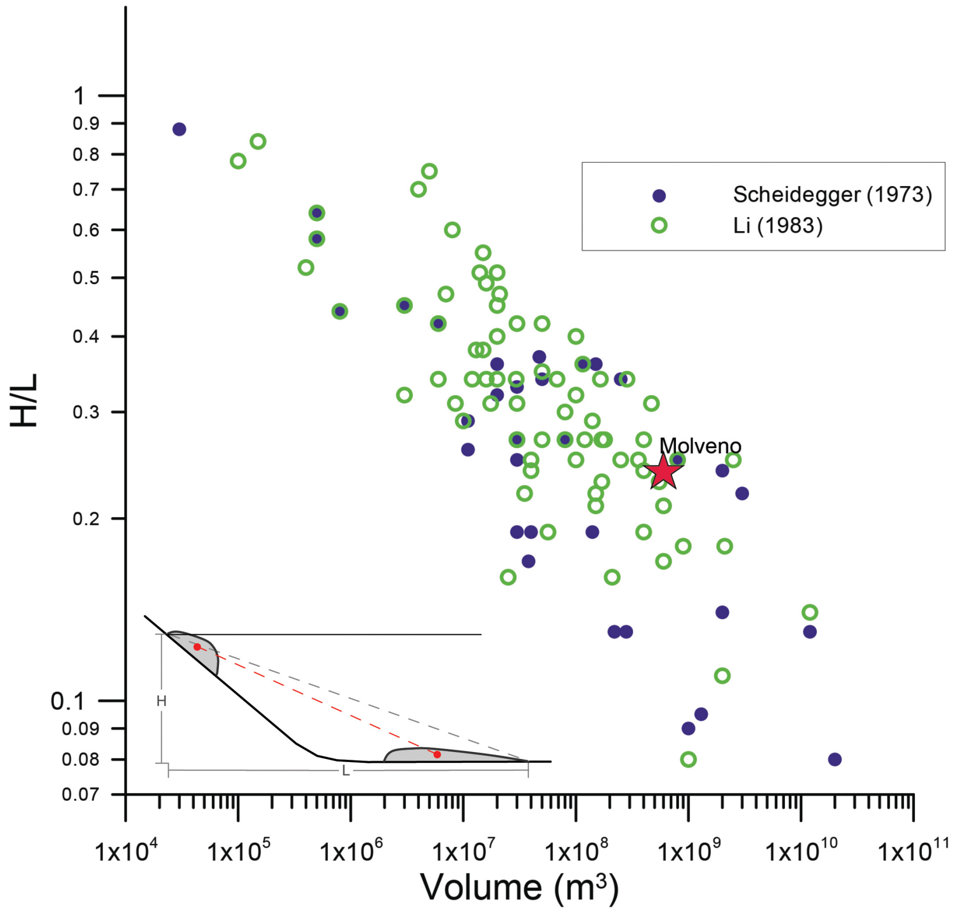

FIGURE 7 | Scheidegger-Plot (Volume vs. H/L; Scheidegger, 1973) extended by a dataset of Li (1983). The rock avalanche of Molveno is marked with a red star. The inset shows the definition of the fall height (H) and runout length (L).

point, the model changes from simulating frictional sliding of a rigid body to simulating a granular flow with the Voellmy rheology. At 60 s the landslide collides with the opposite valley, and spreads to the North and the South. This symmetrical spreading is not expected from field mapping, it is explained though by the large depression which was created at the location of present-day Lago di Molveno (see section "Reconstruction of pre-failure topography and volume analysis"). At t = 90 s the landslide mass starts to flow back from the eastern flank and has reached its maximum extent in the North, albeit not in the South. At around t = 120 s (**Figure 8**) the model has reached its maximum extent.

The maximum velocity of the slide is reached at 30 s, when the movement changes from rigid, frictional sliding to granular flow with a Voellmy rheology. The maximum modeled velocity as the mass crosses the valley floor is 90 m/s, comparably estimated as 83 m/s from field-observed runup on the opposing valley flank [using $v = \sqrt{2gh}$ (Fahnestock, 1978)]. Reported rock avalanche velocities range from about 42 to 150 m/s (Heim, 1932; Evans et al., 1994). The modeled run-up reaches up to 550 m above the reconstructed valley floor to around 1250 m a.s.l. This indicates that the modeled run-up at one location just south of Pian delle Gaorne, where the highest run-up was modeled (**Figure 9**), might be slightly overestimated.

The runout model well reproduced the extent of the landslide, with the exception of the northern part. The deposit thickness was reproduced reasonably well except in Pian delle Gaorne and Moline, where the simulated deposit is too thin (**Figures 9**, **10B**). There are several possible reasons for this: (1) Uncertainties in the pre-failure topography, as the highest difference between

TABLE 4 | Properties of path-materials for the best-fit model run.

	Sliding plane (source zone)	Disintegrated mass movement (deposition zone)
Rheology	Frictional	Voellmy
Unit weight (kN/m^3)	20	20
Friction angle (°)	12	–
Pore pressure coeff. (R_u; –)	0	–
Friction coefficient μ (–)	–	0.2
Turbulence coefficient ξ (m/s^2)	–	500
Internal friction angle (°)	35	35

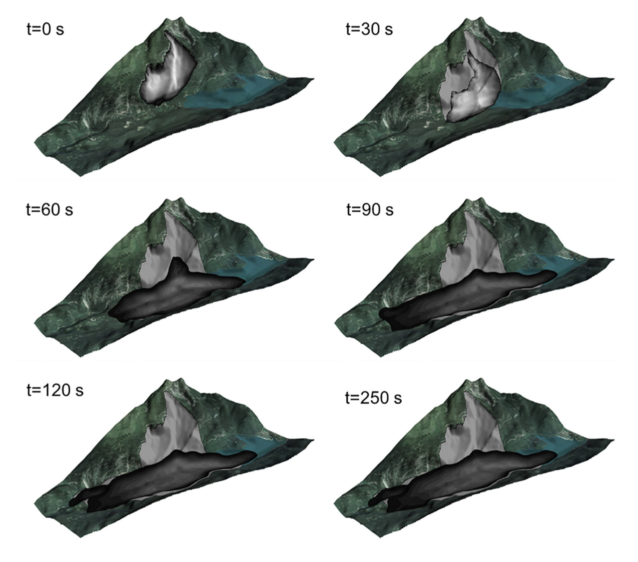

FIGURE 8 | Time series of runout. The first image at *t* = 0 s is showing the initial state. The first 30 s are in flexible mode that means the whole mass moves as intact body with a frictional rheology. After *t* = 30 s the model disintegrates and behaves as a Voellmy liquid. At *t* = 60 s the model runs up on Monte Gazza (opposite side of valley). At *t* = 90 s the model spreads more to *N* and *S*. At this time the landslide material already flowed back down from Monte Gazza. The gray colored area shows its maximum extent. At *t* = 120 s the maximum extent of the model is reached and only small changes in thickness and internal movement still happen. Photo by AGEA© 2011.

estimated and modeled thickness occurs on Pian delle Gaorne and the southern parts of the deposits where no seismic data were available. (2) Limitations of the numerical model, as the numerical technique used cannot simulate internal collapses where steep ridges are formed. This could potentially explain why the highest uncertainties lay in areas where the deposit creates steep ridges and deep depressions (Compare **Figure 10B** with **Figures 2A,B**). The calibrated parameters, shown in **Table 4**, are comparable with similar case studies (Aaron and McDougall, 2019).

The chosen friction angle of 12° for modeling the slide in the source area is low, however, it was well constrained by the absence of deposition in the source zone and matches values presented by Aaron and McDougall (2019). Cruden and Krahn (1978) measured ultimate friction angles as low as 14° along flexural slip planes found in the debris of the Frank slide, which had an approximate volume of 36.5 Mm^3. Aaron and McDougall (2019) showed with Dan3D modeling of a series of rock avalanches that friction angles of the sliding plane are inversely correlated with the volume of the slide. This may be related to breakage of asperities and extreme polishing of the sliding plane, which leads to a reduction of the friction angle to an ultimate friction angle (Cruden and Krahn, 1978). This process is dependent on normal stress and hence on the thickness of the sliding mass. Since the volume of the Molveno rock avalanche was significantly higher than volume of the Frank slide, an ultimate friction angle below 14° seems to be possible.

DISCUSSION

The combination of geomorphic mapping, runout modeling, and cosmogenic nuclide dating suggests that the Molveno rock avalanche occurred as one event, with the potential exception of the deposits at Nembia. Thus, the prominent internal scarps (**Figure 2**) must result from dynamic emplacement processes and do not provide evidence that the deposit is composed of multiple events. As shown on **Figure 8**, these features could be the result of extension of the moving debris along the irregular topography of the valley floor.

Our analysis has revealed several important preconditioning, preparatory, triggering, and emplacement factors that contributed to the Molveno rock avalanche (for a definition of these terms see McColl, 2012). The key preconditioning factors for the failure are the structural setting and the presence of marly interbeds with relatively weaker geotechnical properties. Lateral control of slope failure was along NW-SE oriented fractures that lie parallel to the Schio-Vicenza system (**Figure 1**). The basal rupture planes in both source niches are parallel to bedding, which has a mean dip angle of 23°(Castellarin et al., 2005a). Additionally, laboratory tests by Chinaglia and Fornero (1995) on the marly interbeds resulted in friction angles of approximately 25°. Thus, the slope was likely stable due to the presence of rock bridges.

Preparatory factors include glacial erosion, which steepened the valley and undercut the toe of the slope. This would have exposed the basal rupture plane, and likely contributed to time dependent strength degradation (e.g., Grämiger et al., 2017). However, the Molveno rock avalanche occurred 12,000 years after the valley was deglaciated, which suggests that other factors in addition to glacial debuttressing must have contributed to failure at this site. Heavy rain storms and wet climate in general have been suggested to be a possible trigger and driving factor for rock avalanches (Zerathe et al., 2014). Zerathe et al. (2014) found that many large landslides in the Western Alps are temporally related to a climatic period of high precipitation rates, with its peak at 4.2 ka. For the Austrian Alps a similar trend of landslides coinciding with a wetter period around the middle to late Holocene transition has been observed (Prager et al., 2008). Cycling of pore-water pressure due to frequent filling and draining of joints in the rock contributes to micro crack propagation and weakening of the rock mass (Gischig et al., 2016; Loew et al., 2017). Thus, heavy precipitation events or pore pressure changes due to seasonal climatic variations were likely an important preparatory factor for the Molveno rock avalanche (Gischig et al., 2016).

The trigger of the landslide could not be definitively constrained, however, the study area is known to be seismically active. Moderate earthquakes of magnitudes <6.0 have been documented (Basili et al., 2008), which are related to activity along the Giudicarie and the Schio-Vicenza fault systems (Viganò et al., 2013; Viganò et al., 2015). Dominant compression takes place along the Giudicarie and the Belluno–Bassano–Montello thrusts (Viganò et al., 2015). Strain is partitioned along the dominant right-lateral strike-slip faults of the Schio-Vicenza fault system (Viganò et al., 2015).

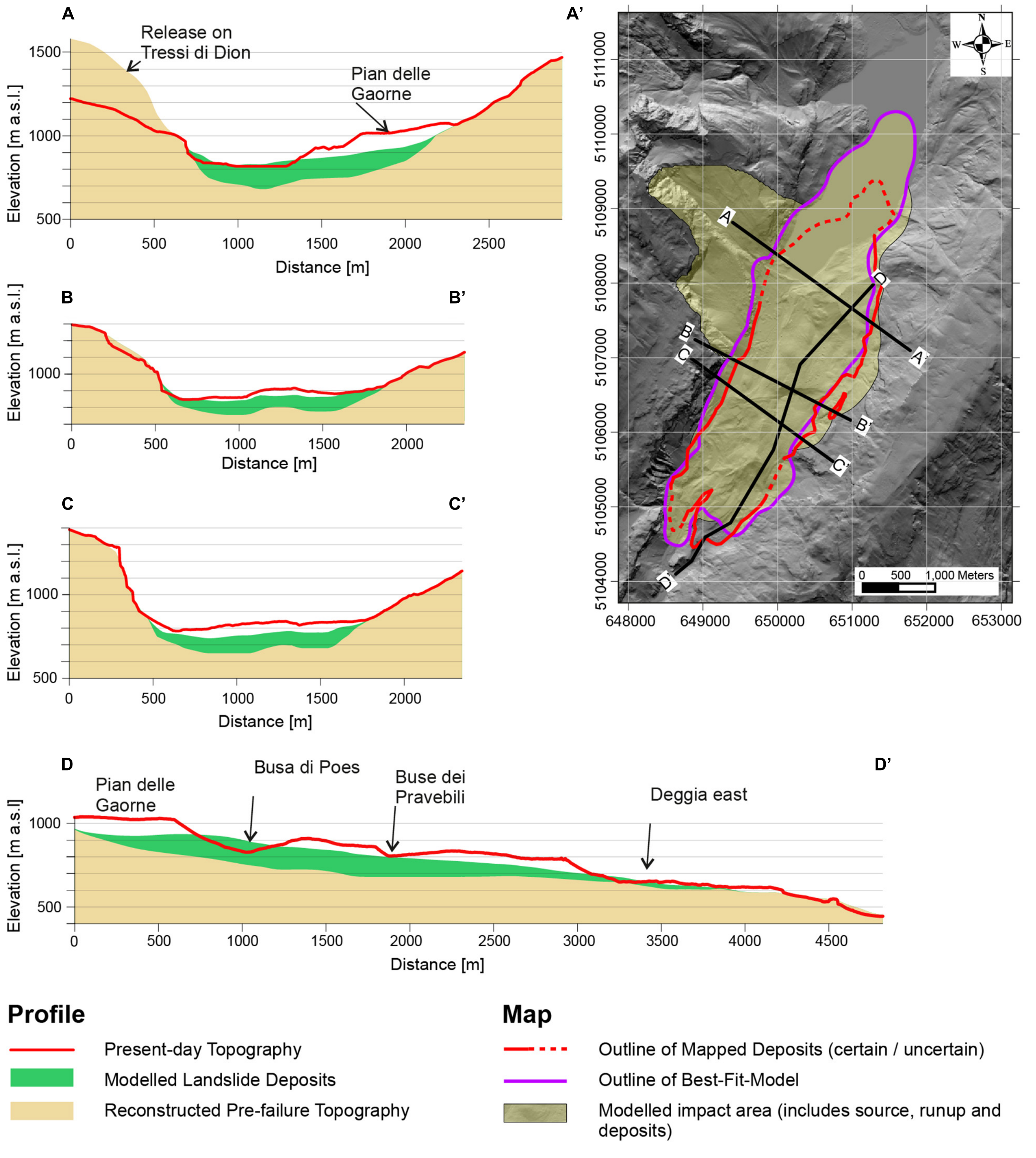

FIGURE 9 | Runout extent and thickness of modeled deposits. Best-fit model run. The modeled run-up on the eastern side could reproduce the mapped deposits and seems hence realistic. The southern margin is also quite well matched, except for the farther end of Deggia East. In the North the runout is too long into the lake. The thickness of the deposits does not match the estimated thickness of the pre-failure topography. Especially the thick deposit at Pian delle Gaorne cannot be reproduced.

A seismic trigger was also suggested for the nearby rock avalanches of Dro, Marocca Principale (5.3 ± 0.9 ka), and Kas (1.1 ± 0.2 ka; Ivy-Ochs et al., 2017a). As Marocca Principale is not only geographically close to Molveno but is also of the same age, within the uncertainties, a common seismic trigger is possible.

By combining geomorphic mapping, runout modeling and cosmogenic nuclide surface exposure dating, we can infer key

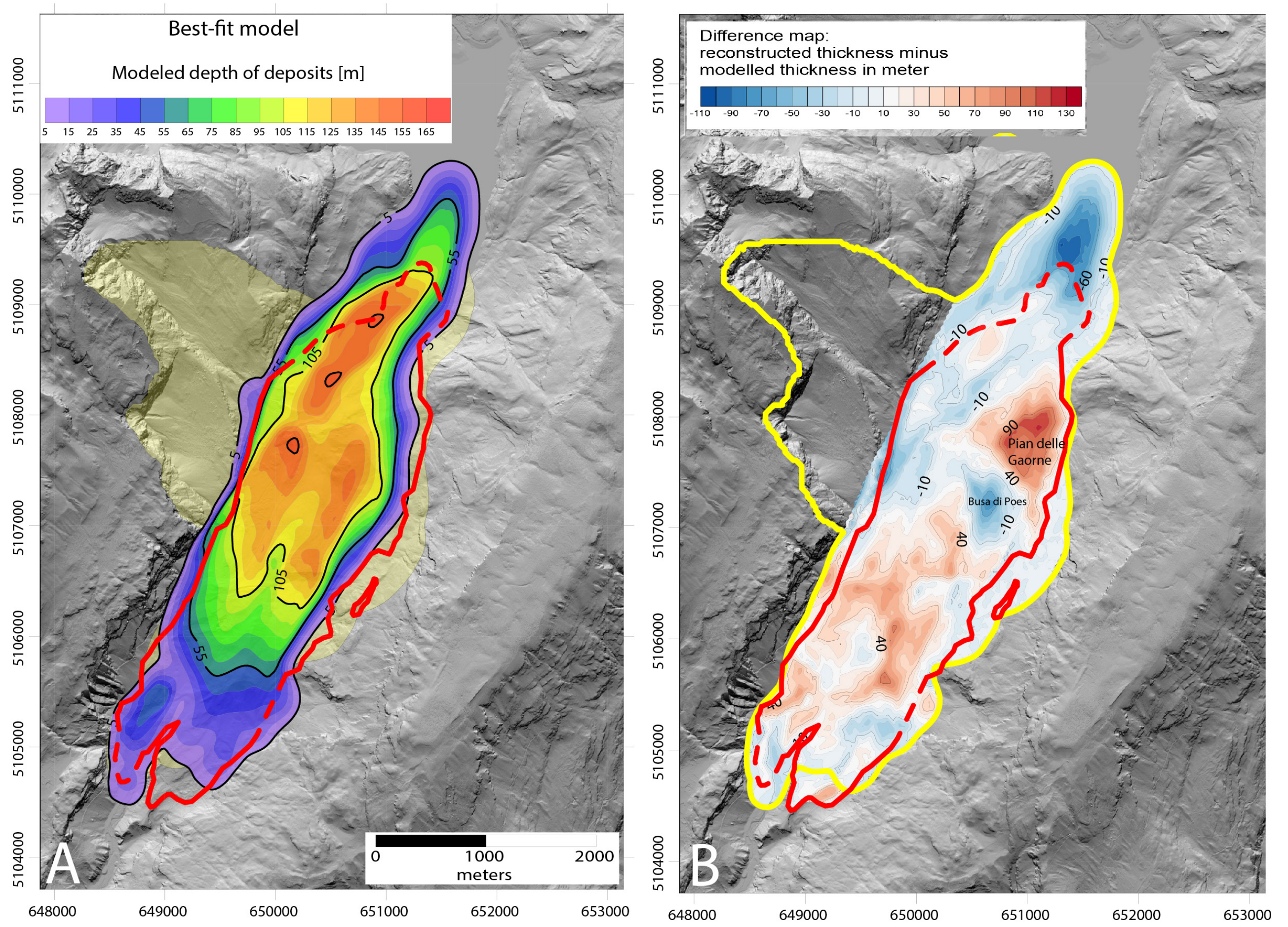

FIGURE 10 | (A) Depth map of the modeled deposits of the best-fit model. Contour interval is 10 m for the minor contour-lines and 50 m for the major contour-lines. The maximum impact area is marked in a pale yellow and the mapped landslide deposit is marked with a thick, red line. **(B)** Depth-difference-map between the estimated thickness when constructing the pre-failure topography and the modeled thickness of the best-fit model. The yellow outline indicates simulation results, and red indicates the mapped landslide deposits.

features regarding the dynamic characteristics of the Molveno rock avalanche. Dating suggests, that with the exception of Nembia (discussed above), all the deposit zones were emplaced simultaneously (at least within the uncertainties of the technique). Therefore, it is likely that the geomorphological features we mapped are evidence of dynamic runout processes. In Pian delle Gaorne, the inferred orientation of the direction of motion based on lineaments is different than the other zones except Buse dei Pravebili. This is consistent with direction of motion simulated by Dan3D-Flex, as runup and fallback are simulated in this area. Additionally, in Buse dei Pravebili, minor runup is also simulated, consistent with the rotated primary direction of the observed lineaments. In our simulations, strong depth gradients drive spreading along the valley, consistent with extensional features observed in the deposit. Finally, fall back ridges, similar to those observed at the Avalanche Lake Rock Avalanche (Aaron and Hungr, 2016a), can be seen in the areas of our simulated runup and fall back (**Figure 8**).

CONCLUSION

By combining cosmogenic ^{36}Cl exposure dating, detailed geomorphological mapping, volume reconstruction and numerical runout modeling, the constraints on the age and source area of the Molveno rock avalanche have been reconstructed. Cosmogenic ^{36}Cl dating combined with geomorphological mapping has shown that the main deposits are of the same age (4.8 ± 0.5 ka), with the exception of the deposits at Nembia, which have an age of 2.2 ± 0.2 ka. We speculate that in the Nembia area a lake of more than 10 m depth covered the deposits leading to the younger exposure dates. The age of the main event fits well within the middle Holocene peak in landslide activity, centering at 4.2 ka reported by other authors, and overlaps with the timing of the nearby Marocca Principale rock avalanche, within the dating uncertainties. Our geomorphic interpretation, confirmed by runout modeling, is that the landslide source area is located on Monte Soran, and that the many scarps, lineaments and ridges in the deposit occurred during rock avalanche emplacement.

DATA AVAILABILITY STATEMENT

All datasets presented in this study are available upon reasonable request.

AUTHOR CONTRIBUTIONS

JW performed the field work, laboratory analysis, numerical modeling and interpretation, and assisted with the writing. SI-O conceived of the study, and performed the field work, laboratory analysis, data interpretation and assisted with the writing of the manuscript. JA assisted with the numerical modeling and data interpretation and assisted with the writing of the manuscript. SM conceived of the study, assisted with field work and data interpretation, and assisted with the writing of the manuscript. KL assisted with numerical modeling, data interpretation, and writing the manuscript. MR assisted with field work and data interpretation, and assisted with the writing of the manuscript. CV performed laboratory analysis, data interpretation and assisted with the writing of the manuscript. PC provided data used in the study, assisted with the field work and data interpretation, and assisted with writing the manuscript. AV provided data, assisted with field work and interpretation, an assisted with writing

FUNDING

This project was in part funded by the Geological Survey of Trento Province and the University of Padova (Progetto di ricerca di Ateneo 2014 and CPDA140511).

ACKNOWLEDGMENTS

The Geological Survey of Trento Province kindly provided access to the DEM. We appreciate support of fieldwork, laboratory work and AMS measurements by the Laboratory of Ion Beam Physics, ETH Zürich. Comments from two reviewers substantially improved the manuscript.

REFERENCES

Aaron, J., and Hungr, O. (2016a). Dynamic analysis of an extraordinarily mobile rock avalanche in the Northwest Territories, Canada. *Can. Geotech. J.* 53, 899–908. doi: 10.1139/cgj-2015-0371

Aaron, J., and Hungr, O. (2016b). Dynamic simulation of the motion of partially-coherent landslides. *Eng. Geol.* 205, 1–11. doi: 10.1016/j.enggeo.2016.02.006

Aaron, J., and McDougall, S. (2019). Rock avalanche mobility: the role of path material. *Eng. Geol.* 257, 105126. doi: 10.1016/j.enggeo.2019.05.003

Abele, G. (1974). *Bergstürze in den Alpen: ihre Verbreitung, Morphologie und Folgeerscheinungen*. Ph.D. thesis, Universität Karlsruhe, Karlsruhe.

Alfimov, V., and Ivy-Ochs, S. (2009). How well do we understand production of 36Cl in limestone and dolomite? *Quat. Geochronol.* 4, 462–474. doi: 10.1016/j.quageo.2009.08.005

Balco, G., Stone, J. O., Lifton, N. A., and Dunai, T. J. (2008). A complete and easily accesible means of calculating surface exposure ages or erosion rates from 10Be and 26Al measurements. *Quat. Geochronol.* 3, 174–195.

Basili, R., Valensise, G., Vannoli, P., Burrato, P., Fracassi, U., Mariano, S., et al. (2008). The Database of Individual Seismogenic Sources (DISS), version 3: Summarizing 20 years of research on Italy's earthquake geology. *Tectonophysics* 453, 20–43. doi: 10.1016/j.tecto.2007.04.014

Bigot-Cormier, F., Braucher, R., Bourlès, D., Guglielmi, Y., Dubar, M., and Stéphan, J. F. (2005). Chronological constraints on processes leading to large active landslides. *Earth Planet. Sci. Lett.* 235, 141–150. doi: 10.1016/j.epsl.2005.03.012

Carton, A. (2017). "Large ancient landslides in trentino, northeastern alps, as evidence of postglacial dynamics," in *Landscapes and Landforms of Italy*, eds M. Soldati, and M. Marchetti, (Padua: Springer International Publishing AG).

Castellarin, A., Dal Piaz, G. V., Picotti, V., Selli, L., Cantelli, L., Martin, S., et al. (2005a). *Carta Geologica D'Italia - Tione di Trento - Foglio 59, 1:50000*. Firenze: APAT.

Castellarin, A., Dal Piaz, G. V., Picotti, V., Selli, L., Cantelli, L., Martin, S., et al. (eds) (2005b). *Note illustrative della carta geologica d'Italia, Foglio n. 059, Tione di Trento*. Firenze: APAT.

Castellarin, A., Vai, G. B., and Cantelli, L. (2006). The alpine evolution of the Southern Alps around the Giudicarie faults: a late cretaceous to early Eocene transfer zone. *Tectonophysics* 414, 203–223. doi: 10.1016/j.tecto.2005.10.019

Chinaglia, N. (1992). Le "Marocche" Della Bassa Valle del Sarca: scivolamenti Planari in unità calcaree stratificate. *I Conv. Naz. Giov. Ric. Geol. Appl.* 3, 47–56.

Chinaglia, N., and Fornero, E. (1995). Ipotesi sulla possibile evoluzione cinematica di un movimento profondo di versante: L'esempio del M. *Soran (Trentino meridionale). Mem. Soc. Geol. Ital.* 50, 101–108.

Coe, J. A., Bessette-Kirton, E. K., and Geertsema, M. (2018). Increasing rock-avalanche size and mobility in Glacier Bay National Park and Preserve, Alaska detected from 1984 to 2016 Landsat imagery. *Landslides* 15, 393–407. doi: 10.1007/s10346-017-0879-7

Cossart, E., Braucher, R., Fort, M., Bourlès, D. L., and Carcaillet, J. (2008). Slope instability in relation to glacial debuttressing in alpine areas (Upper Durance catchment, southeastern France): evidence from field data and 10Be cosmic ray exposure ages. *Geomorphology* 95, 3–26. doi: 10.1016/j.geomorph.2006.12.022

Cruden, D., and Krahn, J. (1978). "Frank Rockslide, Alberta, Canada," in *Rockslides and Avalanches, Vol 1 Natural Phenomena*, ed. B. Voight, (Amsterdam: Elsevier Scientific Publishing), 97–112.

Damian, J. (1890). Der Molvenosee in Tirol. *Petermann. Mitt.* 36, 262–270.

Dufresne, A., and Davies, T. R. (2009). Longitudinal ridges in mass movement deposits. *Geomorphology* 105, 171–118.

Dufresne, A., Prager, C., and Bösmeier, A. (2016). Insights into rock avalanche emplacement processes from detailed morpho-lithological studies of the Tschirgant deposit (Tyrol. Austria). *Earth Surf. Process. Landforms* 41, 587–602. doi: 10.1002/esp.3847

Dunning, S. A. (2004). *Rock Avalanches in High Mountains*. Ph.D. thesis, University of Bedfordshire, Luton.

Evans, S. G., Hermanns, R. L., Strom, A., and Scarascia-Mugnozza, G. (2011). *Natural and Artificial Rockslide Dams*. Berlin: Springer Science & Business Media.

Evans, S. G., Hungr, O., and Enegren, E. G. (1994). The Avalanche Lake rock avalanche, Mackenzie Mountains, Northwest Territories, Canada: description, dating, and dynamics. *Can. Geotech. J.* 31, 749–768. doi: 10.1139/t94-086

Fahnestock, R. K. (1978). "Chapter 5 - Little Tahoma Peak Rockfalls and avalanches, Mount Rainier, Washington, U.S.A," in *Developments in Geotechnical Engineering*, ed. B. Voight, (Amsterdam: Elsevier).

Ferretti, P., and Borsato, A. (2004). Geologia e geomorfologia della Valle e del Lago di Tovel. *Studi Trent. Sci. Nat. Acta Biol.* 81, 173–187.

Fort, M., Cossart, E., Deline, P., Dzikowski, M., Nicoud, G., Ravanel, L., et al. (2009). Geomorphic impacts of large and rapid mass movements: a review. *Géomorphologie* 15, 47–64.

Fuganti, A. (1969). Studio geologico di sei grandi frane di roccia nella regione Trentino-Alto Adige. *Mem. Mus. Trid. Sc. Nat.* 17, 1–72.

Gischig, V., Preisig, G., and Eberhardt, E. (2016). Numerical Investigation of Seismically Induced Rock Mass Fatigue as a Mechanism Contributing to the Progressive Failure of Deep-Seated Landslides. *Rock Mech. Rock Eng.* 49, 2457–2478. doi: 10.1007/s00603-015-0821-z

Grämiger, L. M., Moore, J. R., Gischig, V. S., Ivy-Ochs, S., and Loew, S. (2017). Beyond debuttressing: Mechanics of paraglacial rock slope damage during repeat glacial cycles. *J. Geophys. Res. Earth Surf.* 122, 1004–1036. doi: 10.1002/2016JF003967

Grämiger, L. M., Moore, J. R., Vockenhuber, C., Aaron, J., Hajdas, I., and Ivy-Ochs, S. (2016). Two early Holocene rock avalanches in the Bernese Alps (Rinderhorn, Switzerland). *Geomorphology* 268, 207–221. doi: 10.1016/j.geomorph.2016.06.008

Heim, A. (1932). *Bergsturz und Menschenleben*. Zürich: Frez&Wasmuth Verlag.

Hippolyte, J. C., Bourlès, D., Braucher, R., Carcaillet, J., Léanni, L., Arnold, M., et al. (2009). Cosmogenic 10Be dating of a sackung and its faulted rock glaciers, in the Alps of Savoy (France). *Geomorphology* 108, 312–320. doi: 10.1016/j.geomorph.2009.02.024

Hippolyte, J. C., Brocard, G., Tardy, M., Nicoud, G., Bourlès, D., Braucher, R., et al. (2006). The recent fault scarps of the Western Alps (France): Tectonic surface ruptures or gravitational sackung scarps? A combined mapping, geomorphic, levelling, and 10Be dating approach. *Tectonophysics* 418, 255–276. doi: 10.1016/j.tecto.2006.02.009

Hovius, N., Stark, C. P., and Allen, P. A. (1997). Sediment flux from a mountain belt derived by landslide mapping. *Geology* 25, 231–234.

Huggel, C., Allen, S., Clague, J. J., Fischer, L., Korup, O., and Schneider, D. (2013). "Detecting potential climate signals in large slope failures in cold mountain regions," in *Landslide Science and Practice*, eds C. Margottini, P. Canuti, and K. Sassa, (Heidelberg: Springer).

Hungr, O. (1995). A model for the runout analysis of rapid flow slides, debris flows, and avalanches. *Can. Geotech. J.* 32, 610–623. doi: 10.1139/t95-063

Hungr, O., and Evans, S. G. (2004). Entrainment of debris in rock avalanches: an analysis of a long run-out mechanism. *GSA Bull.* 116, 1240–1252. doi: 10.1130/b25362.1

Hungr, O., Evans, S. G., and Hazzard, J. (1999). Magnitude and frequency of rock falls and rock slides along the main transportation corridors of southwestern British Columbia. *Can. Geotech. J.* 224–238. doi: 10.1139/t98-106

Hungr, O., Leroueil, S., and Picarelli, L. (2014). The Varnes classification of landslide types, an update. *Landslides* 11, 167–194. doi: 10.1007/s10346-013-0436-y

Hungr, O., and McDougall, S. (2009). Two numerical models for landslide dynamic analysis. *Comput. Geosci.* 35, 978–992. doi: 10.1016/j.cageo.2007.12.003

Ivy-Ochs, S., and Kober, F. (2008). Surface exposure dating with cosmogenic nuclides. *Quat. Sci. J.* 57, 179–209.

Ivy-Ochs, S., Martin, S., Campedel, P., Hippe, K., Alfimov, V., Vockenhuber, C., et al. (2017a). Geomorphology and age of the Marocche di Dro rock avalanches (Trentino, Italy). *Quat. Sci. Rev.* 169, 188–205. doi: 10.1016/j.quascirev.2017.05.014

Ivy-Ochs, S., Martin, S., Campedell, P., Hippe, K., Vockenhuber, C., Carugati, G., et al. (2017b). "Geomorphology and age of large rock avalanches in Trentino (Italy): Castelpietra," in *Advancing Culture of Living with Landslides. WLF 2017*, eds M. Mikoš, V. Vilímek, Y. Yin, and K. Sassa, (Cham: Springer), doi: 10.1007/978-3-319-53483-1_41

Ivy-Ochs, S., Synal, H.-A., Roth, C., and Schaller, M. (2004). Initial results from isotope dilution for Cl and 36Cl measurements at the PSI/ETH Zurich AMS facility. *Nucl. Instrum. Methods Phys. Res. Sect. B* 22, 623–627. doi: 10.1016/j.nimb.2004.04.115

Kellerer-Pirklbauer, A., Lieb, G. K., Avian, M., and Carrivick, J. (2012). Climate change and rock fall events in high mountain areas: numerous and extensive rock falls in 2007 at Mittlerer Burgstall, Central Austria. *Geogr. Ann. Ser. A* 94, 59–78. doi: 10.1111/j.1468-0459.2011.00449.x

Knapp, S., Gilli, A., Anselmetti, F. S., Krautblatter, M., and Hajdas, I. (2018). Multistage rock-slope failures revealed in lake sediments in a seismically active Alpine region (Lake Oeschinen, Switzerland). *J. Geophys. Res. Earth Surf.* 123, 658–677. doi: 10.1029/2017JF004455

Köpfli, P., Grämiger, L. M., and Moore, J. R. (2018). The Oeschinensee rock avalanche, Bernese Alps, Switzerland: a co-seismic failure 2300 years ago? *Swiss J. Geosci.* 111, 205–219. doi: 10.1007/s00015-017-0293-0

Korup, O., and Clague, J. J. (2009). Natural hazards, extreme events, and mountain topography. *Quat. Sci. Rev.* 28, 977–990. doi: 10.1016/j.quascirev.2009.02.021

Korup, O., and Tweed, F. (2007). Ice, moraine, and landslide dams in mountainous terrain. *Quat. Sci. Rev.* 26, 3406–3422.

Kremer, K., Gassner-Stamm, G., Grolimund, R., Wirth, S. B., Strasser, M., and Fäh, D. (2020). A database of potential paleoseismic evidence in Switzerland. *J. Seismol.* doi: 10.1007/s10950-020-09908-5

Le Roux, O., Schwartz, S., Gamond, J. F., Jongmans, D., Bourles, D., Braucher, R., et al. (2009). CRE dating on the head scarp of a major landslide (Séchilienne, French Alps), age constraints on Holocene kinematics. *Earth Planet. Sci. Lett.* 280, 236–245. doi: 10.1016/j.epsl.2009.01.034

Lepsius, R. (1878). *Das Westliche Südtirol: Geologisch Dargest*. Berlin: W. Hertz.

Li, T. (1983). A mathematical model for predicting the extent of a major rockfall. *Z. Geomorphol.* 27:473482.

Loew, S., Gschwind, S., Gischig, V., Keller-Signer, A., and Valenti, G. (2017). Monitoring and early warning of the 2012 Preonzo catastrophic rocklope failure. *Landslides* 14, 141–154. doi: 10.1007/s10346-016-0701-y

Marchesoni, V. (1954). Il lago di Molveno e la foresta riaffiorata in seguito allo svaso. *Studi Trent. Sci. Nat.* 31, 9–24.

Marchesoni, V. (1958). La datazione col metodo del Carbonio 14 del lago di Molveno e dei resti vegetali riemersi in seguito allo svaso. *Studi Trent. Sci. Nat.* 2, 95–98.

Marrero, S. M., Phillips, F. M., Caffee, M. W., and Gosse, J. C. (2016). CRONUS-Earth cosmo-genic36Cl calibration. *Quat. Geochronol.* 31, 199–219. doi: 10.1016/j.quageo.2015.10.002

Martin, S., Campedel, P., Ivy-Ochs, S., Viganò, A., Alfimov, V., Vockenhuber, C., et al. (2014). Lavini di Marco (Trentino, Italy): 36Cl exposure dating of a polyphase rock avalanche. *Quat. Geochronol.* 19, 106–116. doi: 10.1016/j.quageo.2013.08.003

McColl, S. T. (2012). Paraglacial rock-slope stability. *Geomorphology* 153, 1–16. doi: 10.1016/j.geomorph.2012.02.015

McDougall, S., and Hungr, O. (2004). A model for the analysis of rapid landslide motion across three-dimensional terrain. *Can. Geotech. J.* 41, 1084–1097. doi: 10.1139/t04-052

Prager, C., Zangerl, C., Patzelt, G., and Brandner, R. (2008). Age distribution of fossil landslides in the Tyrol (Austria) and its surrounding areas. *Nat. Hazards Earth Syst. Sci.* 8, 377–407. doi: 10.5194/nhess-8-377-2008

Savage, S. B., and Hutter, K. (1989). The motion of a finite mass of granular material down a rough incline. *J. Fluid Mech.* 199, 177–215. doi: 10.1017/S0022112089000340

Scheidegger, A. E. (1973). On the prediction of the reach and velocity of catastrophic landslides. *Rock Mech.* 5, 231–236.

Schwinner, R. (1912). Der Mte. Spinale bei Campiglio und andere Bergstürze in den Südalpen. *Aust. J. Earth Sci.* 5, 127–197.

Singeisen, C., Ivy-Ochs, S., Wolter, A., Steinemann, O., Akçar, N., Yesilyurt, S., et al. (2020). The Kandersteg rock avalanche (Switzerland): integrated analysis of a late Holocene catastrophic event. *Landslides*. doi: 10.1007/s10346-020-01365-y

Steinemann, O., Ivy-Ochs, S., Grazioli, S., Luetscher, M., Fischer, U. H., Vockenhuber, C., et al. (2020). Quantifying glacial erosion on a limestone bed and the relevance for landscape development in the Alps. *Earth Surf. Process. Landforms*. 45, 1401–1417. doi: 10.1002/esp.4812

Stoffel, M., and Huggel, C. (2012). Effects of climate change on mass movements in mountain environments. *Prog. Phys. Geogr. Earth Environ.* 36, 421–439. doi: 10.1177/0309133312441010

Stone, J. O. H., Allan, G. L., Fifield, L. K., and Cresswell, R. G. (1996). Cosmogenic chlorine-36 from calcium spallation. *Geochim. Cosmochim. Acta* 60, 679–692. doi: 10.1016/0016-7037(95)00429-7

Strom, A. (2006). *Morphology and Internal Structure of rockslides and Rock Avalanches: Grounds and Constraints for their Modelling*. Dordrecht: Springer, 305–326.

Trener, G. B. (1906). Geologische aufnahme im nördlichen abhang der presanellagruppe. *J. K. K. Geol. Reichsanst.* 56, 405–496.

Trevisan, L. (1939). *Il Gruppo di Brenta:(Trentino occidentale)*. Rome: Istituto poligrafico dello Stato.

Vecchia, O. (1953). Recherches geophysiques pour un barrage au Lac de Molveno. *Riv. Geofisica Appl.* 14, 73–85.

Viganò, A., Scafidi, D., Martin, S., and Spallarossa, D. (2013). Structure and properties of the Adriatic crust in the central-eastern Southern Alps (Italy) from local earthquake tomography. *Terra Nova* 25, 504–512. doi: 10.1111/ter.12067

Viganò, A., Scafidi, D., Ranalli, G., Martin, S., Della Vedova, B., and Spallarossa, D. (2015). Earthquake relocations, crustal rheology, and active deformation in the central–eastern Alps (N Italy). *Tectonophysics* 661, 81–98. doi: 10.1016/j.tecto.2015.08.017

Vockenhuber, C., Miltenberger, K. U., and Synal, H. A. (2019). 36Cl measurements with a gas-filled magnet at 6 MV. *Nucl. Instrum. Methods Phys. Res. Sect. B* 455, 190–194. doi: 10.1016/j.nimb.2018.12.046

Weidinger, J. T., Korup, O., Munack, H., Altenberger, U., Dunning, S. A., Tippelt, G., et al. (2014). Giant rockslides from the inside. *Earth Planet. Sci. Lett.* 389, 62–73. doi: 10.1016/j.epsl.2013.12.017

Wolter, A., Stead, D., Ward, B. C., Clague, J. J., and Ghirotti, M. (2016). Engineering geomorphological characterisation of the Vajont Slide, Italy, and a new interpretation of the chronology and evolution of the landslide. *Landslides* 13, 1067–1081. doi: 10.1007/s10346-015-0668-0

Zerathe, S., Lebourg, T., Braucher, R., and Bourlès, D. (2014). Mid-Holocene cluster of large-scale landslides revealed in the Southwestern Alps by 36Cl dating. Insight on an Alpine-scale landslide activity. *Quat. Sci. Rev.* 90, 106–127. doi: 10.1016/j.quascirev.2014.02.015

Conflict of Interest: The authors declare that the research was conducted in the absence of any commercial or financial relationships that could be construed as a potential conflict of interest.

frontiers
in Earth Science

ORIGINAL RESEARCH
published: 30 June 2020
doi: 10.3389/feart.2020.00224

Understanding Failure and Runout Mechanisms of the Flims Rockslide/Rock Avalanche

Jordan Aaron*[1]*, *Andrea Wolter*[1,2], *Simon Loew*[1] and *Stefan Volken*[1,3]

[1] Department of Earth Sciences, Geological Institute, ETH Zürich, Zurich, Switzerland, [2] Engineering Geology, GNS Science, Lower Hutt, New Zealand, [3] Geoformer igp AG, Brig-Glis, Switzerland

The Flims rockslide/rock avalanche (FRRA) is the largest long runout landslide in Europe. This event provides a unique opportunity to study the pre-failure and failure behavior of a large rock slope, as both the source zone and deposit of this event are accessible. In this study, we perform engineering geological and geomorphic field mapping as well as stability and runout modeling in order to explore the preconditioning and triggering factors that resulted in failure of this event, and to infer the mechanisms that governed its runout. By combining these analyses, we qualitatively comment on the mechanisms that lead to the transition from a rockslide to a long runout, catastrophic rock avalanche. Our engineering geological and geomorphic field mapping has revealed that the FRRA failed along a sliding zone that features numerous, large scale steps. Previous work at the site, as well as new analysis of thin sections, has revealed the presence of marl-like layers within the failed stratigraphic unit. Our stability analysis shows that the presence of low strength layers at the depth of the rupture surface is required for failure to initiate, and that failure could be triggered either by strong seismic shaking, elevated pore-water pressures, or a combination of both. The results of the runout analysis show that this event likely remained coherent for a large portion of its motion, and that liquefaction of alluvial sediments at the toe of the slope may have enhanced the runout distance of this rock avalanche. Combining the mapping, stability and runout modeling has shown that the basal shear strength required for the runout analysis is ∼6°–10° lower than that back-analyzed for the stability of this event. Thus, a mechanism to reduce strength along the rupture surface immediately following the initial instability was required for catastrophic failure of this event. This mechanism is poorly understood at present, but is likely crucial for understanding the transition from an initially stable slope to a catastrophic, long runout rock avalanche.

Keywords: Flims rockslide/rock avalanche, engineering geological mapping, failure mechanisms, runout modeling, initial coherence, rock slope failure

Edited by:
Tim Davies,
University of Canterbury, New Zealand

Reviewed by:
Andreas Von Poschinger,
Bavarian Environment Agency, Germany
Giovanni Battista Crosta,
University of Milano-Bicocca, Italy

****Correspondence:***
Jordan Aaron
jordan.aaron@erdw.ethz.ch

Specialty section:
This article was submitted to Structural Geology and Tectonics, a section of the journal Frontiers in Earth Science

Received: *25 March 2020*
Accepted: *27 May 2020*
Published: *30 June 2020*

Citation:
Aaron J, Wolter A, Loew S and Volken S (2020) Understanding Failure and Runout Mechanisms of the Flims Rockslide/Rock Avalanche. Front. Earth Sci. 8:224. doi: 10.3389/feart.2020.00224

INTRODUCTION

Rockslides that undergo sudden failure and transition into flow-like rock avalanches are among the most catastrophic landslide types. Understanding the mechanics governing failure and runout of these events is important to quantify the risk to people and infrastructure, and to understand how they alter landscapes. The Flims rockslide/rock avalanche (FRRA) is the largest long runout landslide in Europe. The age and deposit stratigraphy of the event have been studied extensively, however, relatively little work has been done to quantitatively investigate the source zone initiation and runout mechanisms that acted during this catastrophic event. Given its large volume, well-constrained deposit extent, and accessible location, this event provides a unique opportunity to study the transition of a rockslide into a catastrophic rock avalanche.

The drivers of rock slope failure are often divided into three categories (Glade and Crozier, 2004): (1) preconditioning factors, such as structural setting (e.g., Agliardi et al., 2001), (2) preparatory factors, such as damage propagation due to minor seismic activity (e.g., Gischig et al., 2016; Wolter et al., 2016), and (3) triggering factors, such as heavy rainfall and earthquakes. Structural preconditioning factors are often investigated through field mapping and remote sensing methods, such as photogrammetry (e.g., Wolter et al., 2016; Clayton et al., 2017). One preconditioning factor often implicated in large-scale dip slope failures in the Alps is the presence of thin, low strength layers, such as marl interbeds within a limestone sequence (Thuro and Hatem, 2010; Grämiger et al., 2016). Preparatory and triggering factors are often investigated using numerical models, in order to simulate damage accumulation over long timescales (Gischig et al., 2011), as well as the effect on short-term slope stability of transient triggering conditions (Preisig et al., 2016).

Once a rockslide has failed, several runout scenarios are possible, which depend on site specific phenomena. The rockslide may displace a few meters or tens of meters (Glueer et al., 2019), disintegrate over a number of hours (Schneider et al., 1993), or transition into a catastrophic, flow-like rock avalanche (Coe et al., 2016). If catastrophic failure occurs, a rockslide may initially slide for a significant distance, translating and rotating over 3D topography, before fragmenting and becoming flow-like (Davies et al., 1999; De Blasio, 2011; Bowman et al., 2012; Aaron and Hungr, 2016b; Moore et al., 2017). Aaron and McDougall (2019) have shown that the bulk basal shear strength that acts on the rupture surface of rock avalanches soon after failure appears to be dependent on the volume of the rock avalanche. These friction angles are often 5°−10° lower than that required for static stability (Aaron and Hungr, 2016a). Hungr and Evans (2004) noted that the failed mass typically increases its volume by about 25% as the initial rock slope fragments and becomes flow-like. This increase in volume dissipates any pre-failure pore pressures present within the failed rockslide, meaning that other mechanisms, including those that may cause pore pressure to increase again, must explain these low basal strengths.

Once fragmented, the resulting flow spreads out as a frictional fluid, with high internal strength corresponding to intergranular friction (Hungr, 2017). Rock avalanche deposits exhibit distinctive sedimentological features, which can be used to infer dynamic characteristics of rock avalanche motion (e.g., Pollet and Schneider, 2004). Examination of the sedimentology of rock avalanche deposits has revealed that the comminuted rock avalanche debris often preserves the source stratigraphy, and features numerous internal shear planes (e.g., Dufresne et al., 2016). A mixing zone is often present at the base of rock avalanche debris, where the rock avalanche has incorporated slope substrate. Taken together, these observations suggest that rock avalanches move as a high internal strength body overriding a low strength basal layer, without turbulence.

In this paper, we present a detailed analysis of the FRRA. We perform geologic and geomorphic mapping, engineering geological rock mass characterization and terrestrial digital photogrammetry. The field data is used to investigate the geologic structures controlling failure, and the geometry and lateral constraints of the failure surface. We then incorporate this data into two-dimensional stability and three-dimensional runout modeling. The stability modeling results are used to quantitatively investigate failure of the rockslide, as well as the effects of various triggers, such as increases in pore water pressure and seismic loading. A preliminary version of this work was presented by Volken et al. (2016). Runout modeling is used to quantify the strength loss required in the source zone for catastrophic failure, and to understand basal and internal mechanisms that may have acted during runout to produce the observed deposit stratigraphy. We then qualitatively combine the results from the stability and runout modeling to interpret the mechanisms that lead to the transition of this event from a rockslide to a rock avalanche.

SITE DESCRIPTION

Since we analyze the preconditioning and triggering factors, as well as emplacement characteristics, of this event, we will refer to it as the Flims Rockslide/Rock Avalanche (FRRA), following the classification of Hungr et al. (2014). The FRRA has been the subject of numerous studies, reviewed by Poschinger et al. (2006). Here we briefly summarize some of the previous work, as well as our own observations, relevant to the present study.

The study area is located in eastern Switzerland, between Tamins and Ilanz in the Vorderrhein Valley (**Figure 1**). This valley trends east-west and follows the tectonic boundary between the Helvetic and Penninic zones of the Alps. The bedrock in the study area comprises para-autochthonous Mesozoic sedimentary rocks of the Panära, Mirutta, and Tschepp nappes, overlying crystalline basement of the Aar Massif. The stratigraphic sequence involved in the FRRA belongs to the Jurassic and Cretaceous Tschepp Nappe, and includes (from bottom to top) carbonates of the Quintnerkalk, Öhrlikalk, Kieselkalk, Drusberg, and Schrattenkalk units. These units have a complex tectonic history, and were affected by multiple deformation events. A regional thrust fault (Glarus Thrust) separates Permian Verrucano metasediments from the carbonates on the top of Flimserstein.

The FRRA was first dated by Poschinger and Haas (1997) using radiocarbon dating of wood found within the event deposits, and subsequently by Deplazes and Anselmetti (2007) using radiocarbon dating of organics found in lake deposits. The event was subsequently dated by Ivy-Ochs et al. (2009) using cosmogenic ^{36}Cl and ^{10}Be. These studies resulted in an event age of ∼8900 years BP, and suggested that the FRRA occurred as a single event. This age corresponds to the early Holocene, a warmer and wetter period (Ivy-Ochs et al., 2009).

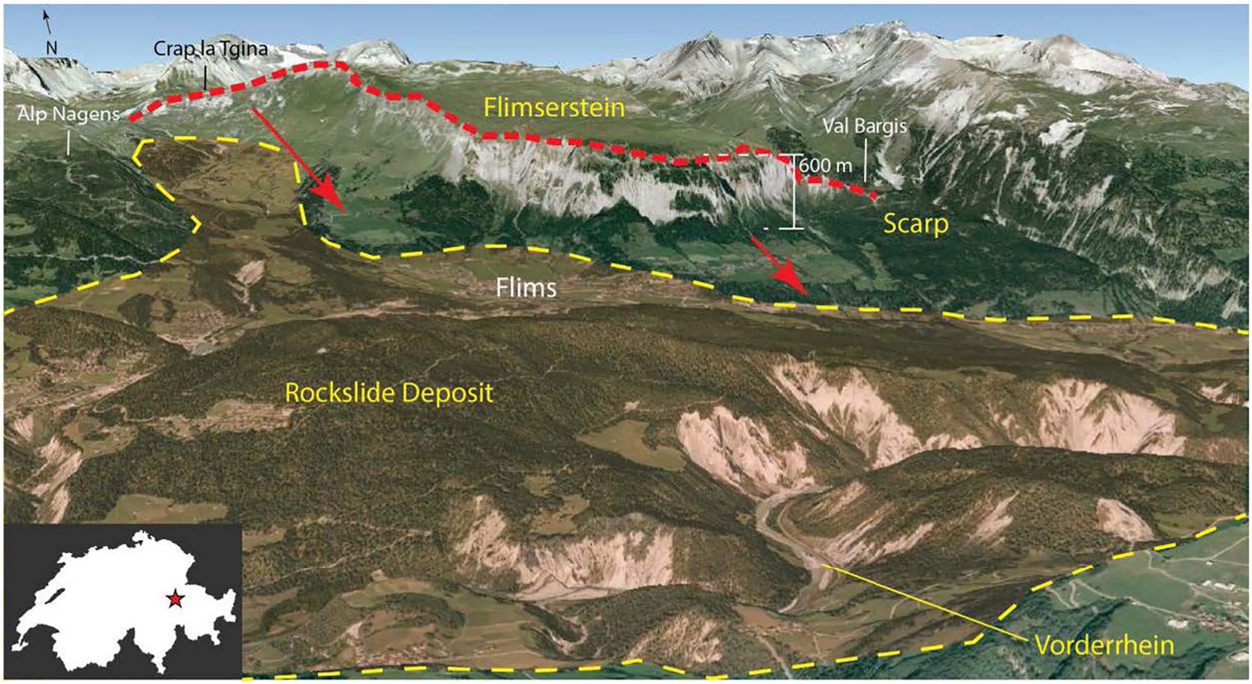

FIGURE 1 | Overview of the study area (Imagery: Google Earth, 2009).

Caprez (2008) provides what is, to the authors knowledge, the most detailed estimate of the volume of both the source zone and deposit of the FRRA. The deposit was subdivided into fragmented rock deposits in the valley, fragmented rock deposits on the rupture surface, mobilized alluvium (which formed the Bonaduz Gravel, discussed below), and fragmented rock deposits that have been eroded by the Vorderrhein river after emplacement of the debris. Based on estimates of the deposit volume in these zones, Caprez (2008) suggested that the volume of fragmented rock is 10.1–10.8 km^3, which includes an estimate of 1.48 km^3 of debris that has been eroded by the Vorderrhein River after emplacement of the event. A further 0.7 km^3 of alluvium was estimated to be mobilized. Caprez (2008) reconstructed the volume in the source zone, which resulted in an estimate of ~7.2 km^3. The bulking factor, defined as the ratio of the volume of fragmented rock to the initial source volume is therefore ~1.5, which Caprez (2008) noted was higher than for other rock avalanches (a typical value of 1.25 is given in Hungr and Evans, 2004). As noted above, bulking is caused by the creation of pore space in the rock avalanche debris due to disaggregation along pre-existing joint planes, and fragmentation of intact rock.

The stratigraphy of the Flims deposit is complex, but has been divided into two main facies (Pollet and Schneider, 2004; Poschinger et al., 2006). These include a well-structured, internal facies, and a coarse upper facies, consistent with the facies model presented in Dufresne et al. (2016). The internal facies is intensely fractured; however, features of the source stratigraphy are preserved in the comminuted debris, despite being displaced several kilometers (Pollet and Schneider, 2004). The internal facies is separated by discrete internal shear planes, leading to a proposed "slab-on-slab" kinematic model for the displacement of the rockslide debris (Pollet et al., 2005).

The Bonaduz Gravel, comprising well-graded, coarse-grained material, outcrops on the eastern flank of the rock avalanche deposits and presents a unique feature associated with the FRRA event (Pavoni, 1968; Poschinger et al., 2006; Poschinger and Kippel, 2009; Calhoun and Clague, 2018). The most recent interpretation of the Gravel (Calhoun and Clague, 2018) suggests emplacement during a massive hyperconcentrated flow, triggered by the Flims rock avalanche impacting a lake. Of particular importance to the present study is an outcrop mapped at Trin station, where Bonaduz Gravel flows up through rockslide debris, providing field evidence for liquefaction of these alluvial sediments.

Morphology of the Source Zone

We have undertaken geologic and geomorphic mapping in order to interpret the morphology of the source zone, and the likely pre-failure stratigraphy of the FRRA. The headscarp and eastern lateral scarp of the FRRA are well-defined. The headscarp is 1800 m long and has a relatively low relief of ~40 m. The western lateral margin of the FRRA is poorly defined; however, a bouldery ridge is located above Platta, corresponding to the assumed margin (**Figure 2**). The L-shaped eastern lateral scarp is ~8500 m long and follows the cliffs of the Flimserstein (**Figure 2**). These cliffs have heights of 30–45 m in the headscarp area, and reach heights between 400 and 500 m at the front of the Flimserstein. The impressive side scarp of the FRRA is about 4450 m long, and has a height of over 500 m. This feature extends from Fil de Cassons in the north to Piz Aulta in the south (**Figure 2**) and

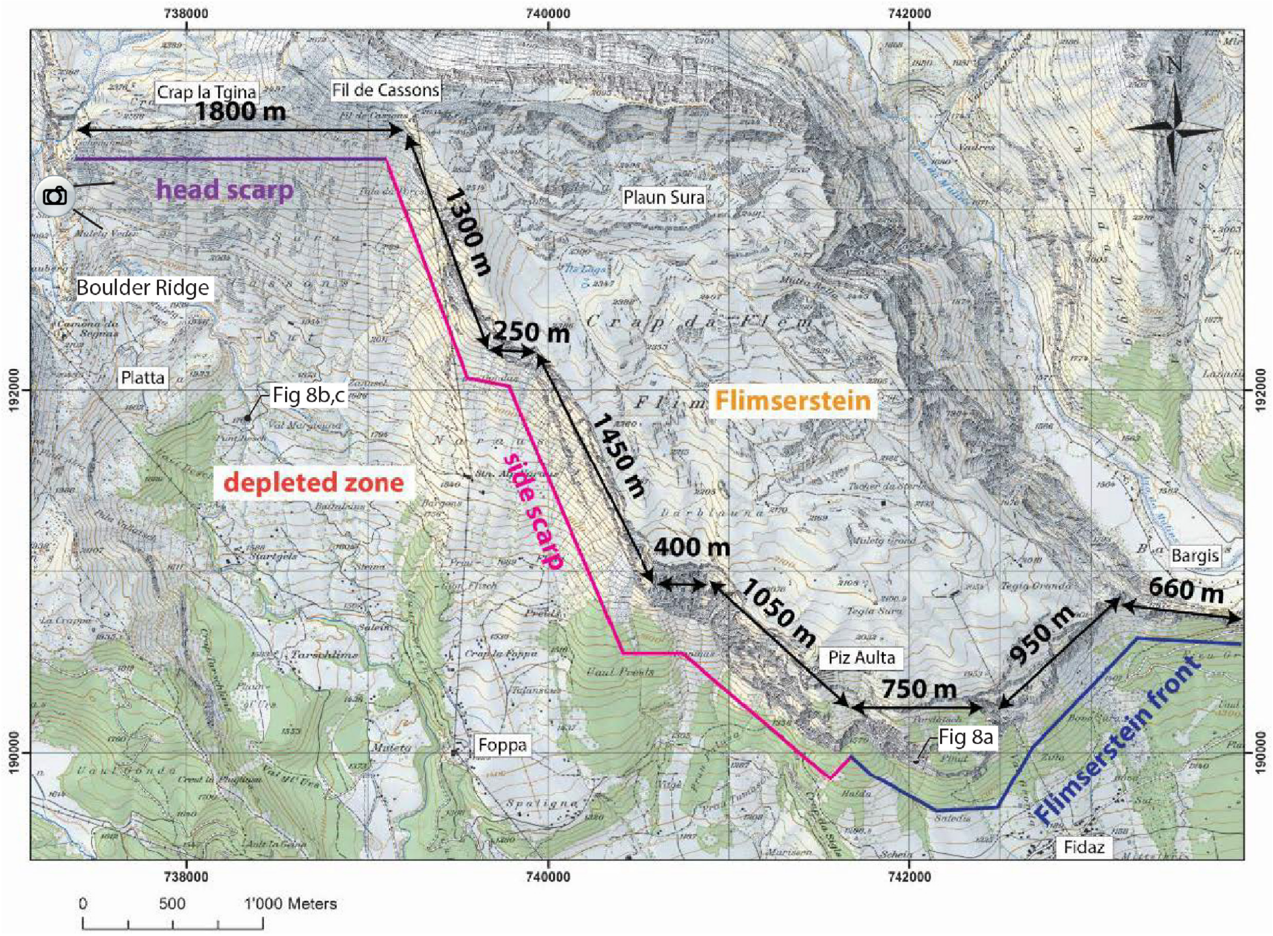

FIGURE 2 | The Flims Rockslide scarp, separated into its headscarp, lateral scarp, and the front of the Flimserstein. The location of where the image shown on **Figure 3**, top was taken is shown above Platta.

has three dominant dip directions: (i) SW in the northern and mid sections (dip direction 240°–250°), (ii) SSW in the southern section faces (dip direction 220°), and (iii) S in some intermediate steps that are each less than 400 m in length (Volken et al., 2016).

As shown on **Figure 3**, the entire stratigraphic sequence is visible in the side scarp, and tectonic faults are visible in the Cretaceous carbonate units. These faults do not all appear to continue in the underlying Quintnerkalk. The faults at Fil de Cassons and Pala da Porcs show signs of tectonic movement. Faults also appear on the surface of Flimserstein (Volken et al., 2016). An interpreted geological cross section is shown in **Figure 3**, based on Volken (2015).

The main zone of depletion (**Figure 2**) is framed by the scarps and deposit of the FRRA. This zone features exposures of the sliding surface scar, rockslide deposits and colluvial material. Deplazes (2005) described the upper region of the depleted zone in detail. The sliding zone of the FRRA is located within the Quintnerkalk, which contains marl layers of 5–15 cm thickness (Buechi and Mueller, 1994). These marl layers are not very obvious in the field, but have been found in subsurface drillings (Buechi and Mueller, 1994). The sliding zone includes several very persistent (>1 km long) SW-NE to E-W oriented steps with heights up to 80–150 m. Thus, the rupture zone is not a discrete, single surface, and it likely exploits multiple horizons within the source stratigraphy. Dip directions of the sliding planes within the sliding zone range from 135° to 205°, and dip angles from 10° to 30°.

MATERIALS AND METHODS

Rock Mass Characterization and Engineering Geomorphological Mapping

The rock masses involved in the FRRA were characterized through field investigations, such as mapping, scanlines, and spot measurements, laboratory and *in situ* testing, and mapping on aerial LiDAR and orthoimagery and long-range terrestrial digital photogrammetry models (cf. **Figure 4**).

Field mapping included a description of lithology, weathering grade, water condition, and geological strength index (GSI), as well as measurement and characterization of discontinuities. Discontinuity characterization included dip, dip direction,

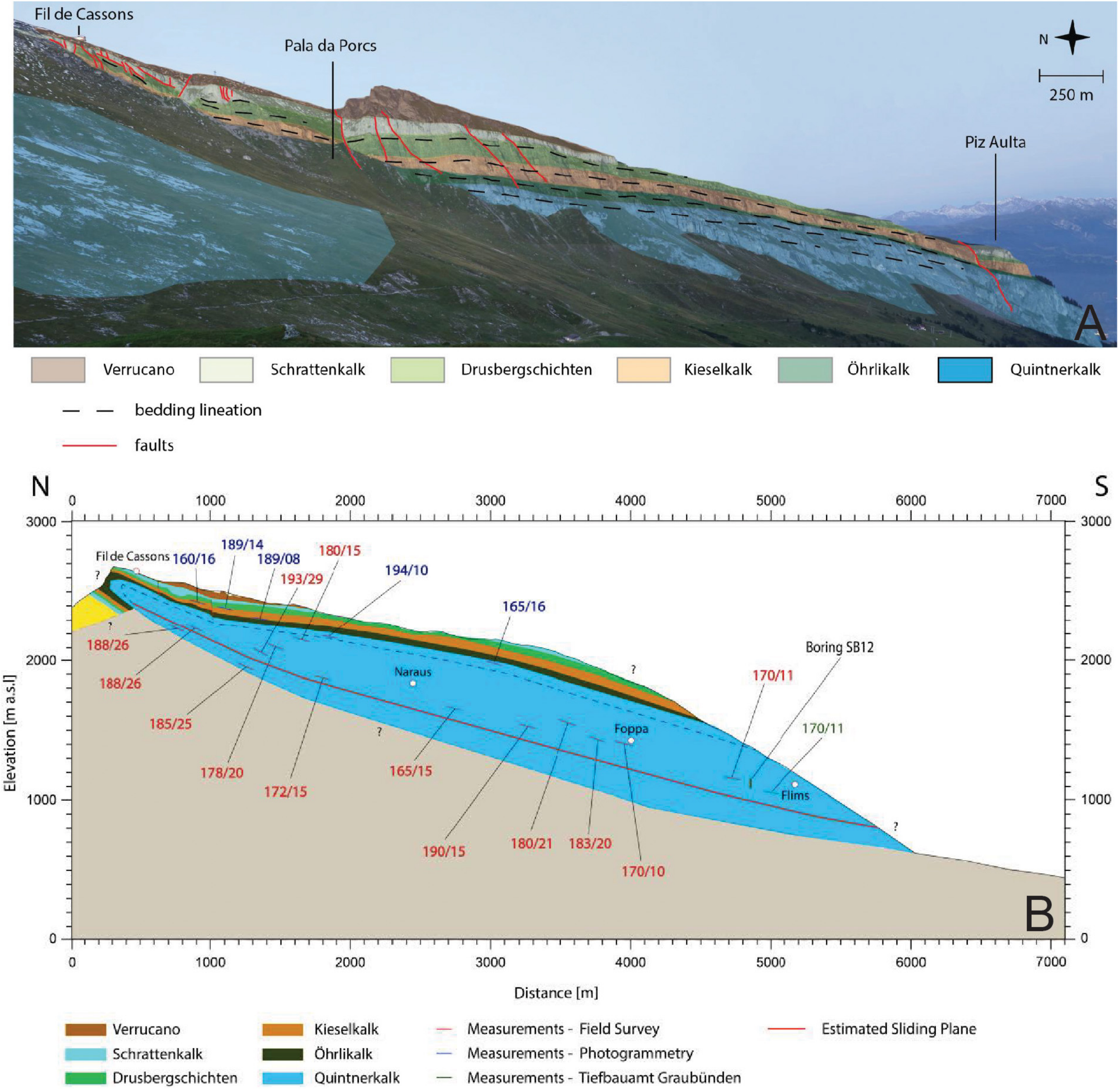

FIGURE 3 | Top: Image of the side scarp, showing site stratigraphy and steep faulting. The location of where this image was taken is shown on **Figure 2**. **Bottom:** Reconstructed geological profile with bedding plane orientations; the section line is shown on **Figure 4**.

spacing, roughness, persistence, and aperture. Four scanlines along the side scarp and one on the surface of Flimserstein, as well as 223 spot measurements, were completed. In total, 431 discontinuities were measured and characterized in the field. Field and laboratory testing included Schmidt Hammer, Brazilian and Point Load tests on each of the lithological units (Quintnerkalk, Oerhlikalk, Kieselkalk, Drusbergschichten, Schrattenkalk, and Verrucano). Two thin sections of potential marl layers and the Flims basal sliding zone were analyzed to compare the properties of the sliding body and the equivalent *in situ* rock masses.

Given the large study area and mostly inaccessible outcrops, we created 10 long-range terrestrial photogrammetry models, using a Canon 6D camera with a 70 mm focal length lens and a Nikon D80 camera with a 135 mm lens. The imagery data was processed with the 3DM Analyst Suite (AdamTechnology, 2015), and georeferenced using control points measured with a Vectronix AG tachymeter. Overall accuracy ranged from 1.6 to 29 cm depending on distance to the face (55–1000 m). Mapping of discontinuity orientations and dimensions was conducted in 3DM, with a total of 1132 discontinuities mapped. Imagery of the surface of Flimserstein captured

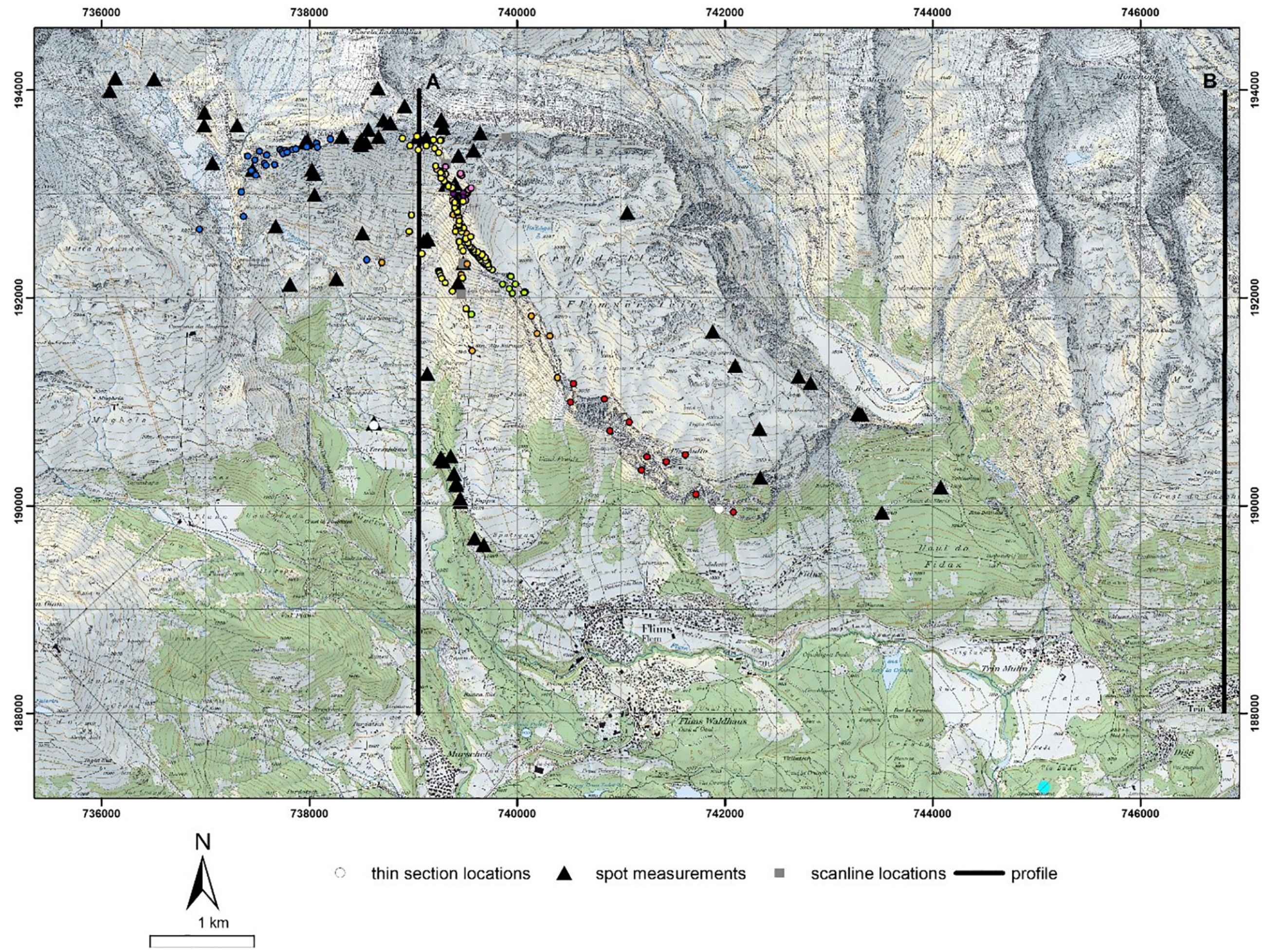

FIGURE 4 | Locations of spot measurements, scanlines, and profiles. Profile B was used to reconstruct the pre-failure surface along profile A, given similar slope geometries. Profile A was used as the modeling profile (see section below). Colored points are reference points used in the 10 photogrammetry models, represented as different colors for each model generated.

using a Hexacopter XR6-mounted Sony ILCE-6000 with a focal length of 19 mm supported terrestrial photogrammetry interpretations.

Engineering geomorphology mapping of the depletion zone of the FRRA and Flimserstein included identification of persistent tectonic structures, slope changes (concave, convex), and morphological features and processes.

Stability Modeling

To analyze the possible kinematic mechanisms, preconditioning factors and triggering mechanisms of the FRRA, we applied kinematic, limit equilibrium, and finite element (FEM) analysis. These analyses are the first of the FRRA; hence our aim was to test hypotheses related to the overall stability of the initiation zone using equivalent conceptual models, not to produce detailed models. In particular, we assessed (i) the need for an equivalent weak layer in the stratigraphy to initiate failure, (ii) the role of pre-existing discontinuities in governing failure kinematics, and (iii) the influence of high pore pressures and seismic loading as potential triggering mechanisms. As we use two-dimensional models, we do not explicitly capture the effect of lateral constraints on failure. Additionally, our model cross section does not intersect any large steps in the sliding surface, so we do not explicitly consider the role these steps may have played. Consideration of these more detailed aspects is beyond the scope of the present analysis.

Kinematic analyses were conducted in DIPS (RocScience, 2015), and provided initial constraints on the kinematic behavior of the FRRA, including a first estimate of the strength required to initiate planar sliding. The limit equilibrium and finite element models, performed using the numerical models Slide and Phase2/RS2 (RocScience, 2015), provided an estimate of the influence of weak layers on the stability of the slope, and the role of elevated pore pressures as a potential triggering mechanism. Finally, more advanced FEM simulations were used to further investigate how pre-existing discontinuities influence failure kinematics, as well as how seismicity may have acted as a triggering mechanism.

TABLE 1 | Material and discontinuity properties used for the Slide and Phase2 models.

Property	Simulated material			
	QU	**WQL**	**WML**	**JTS**
GSI	80–50	40–10	40–10	–
γ (kN/m^3)	26	26	26	–
φ (°)	39–31	28–18	28–15	25
c (MPa)	10.5–5.7	4.9–2.2	2–0.6	1/0.1
σ_T (MPa)	2.5–0.3	0.1–0	0.1–0	0.5/0.1
σ_{ci} (MPa)	115	115	115	–
m_i	10	10	10	–
MR	500	500	175	–
E (MPa)	50,000	50,000	15,000	–
j_{kn} (GPa/m)	–	–	–	10
j_{ks} (GPa/m)	–	–	–	1

*GSI, Geological Strength Index; γ, unit weight; φ, friction angle; c, cohesion; σ_T, tensile strength; σ_{ci}, uniaxial compressive strength; m_i, Hoek-Brown constant; MR, modulus ratio; E, Young's modulus; j_{kn}, joint normal stiffness; j_{ks}, joint shear stiffness. QU = Quintnerkalk, with properties associated with GSI = 80 applied below the sliding zone and incrementally decreasing to GSI = 50 at the surface. WQL, Weak Quintnerkalk Layer; WML, Weak Marl Layer; JTS, Joints (see **Figure 5** for locations of zones and discontinuities). Note that the second values listed for friction angle, cohesion and tensile strength are residual values.*

For the two-dimensional Slide and Phase2 models, a pre-failure cross-section was reconstructed based on Caprez (2008), as well as the geometry of the surrounding topography. Pre-failure geological contacts and the estimated sliding surface were projected onto this profile based on structural measurements. The resulting cross-section is shown in **Figure 3B**.

Since this is a prehistoric event, material properties needed for our stability models are difficult to directly measure. Therefore, we based the properties used in our models on a combination of field and laboratory data, literature values and back-analysis. Our approach was to initially test models that were parameterized using our field and laboratory data, and then adjust certain parameters, such as basal resistance, until failure is simulated to occur. The back-analysis results indicate the strength required for failure, and, as in the case of the potential role of weak layers in the site stratigraphy, can't be directly measured in the field and/or laboratory. We also conducted an extensive sensitivity analyses of multiple parameter combinations before arriving at the most likely equivalent modeling scenarios.

For the kinematic analysis, we initially assumed a friction angle of 35°, to test whether sliding failure would be expected assuming the strength properties of the massive, strong Quintnerkalk unit. Material properties used for the Slide and Phase2 models are presented in **Table 1**, and the location of the main rupture plane was specified based on field investigations. Two sets of material properties were assigned to the rupture plane: (i) weak Quintnerkalk, to test if failure could occur in the absence of a weak layer, and (ii) marl-like properties. All other units were grouped into a single unit and assigned Quintnerkalk properties. The limestones (Öhrlikalk, Kieselkalk, Drusbergschichten, and Schrattenkalk) have similar geomechanical properties, and both these units and the Permian Verrucano units only act as body forces. Bedding parallel planes of weakness were represented using the generalized anisotropic material function in Slide.

In Phase2, *in-situ* stresses were modeled as gravitational stresses, and materials were modeled as isotropic Mohr-Coulomb materials. Two methods were used to represent the rock mass: (i) equivalent rock mass strength properties using the GSI approach (Hoek, 2007), and (ii) direct integration of simplified fracture networks into the model. In both models, weathering and erosion were accounted for by using lower GSI values near surface (GSI = 50) than at the base of the model (GSI = 80).

Both high pore pressures and seismicity were considered as potential triggers. As data regarding pore pressures within the

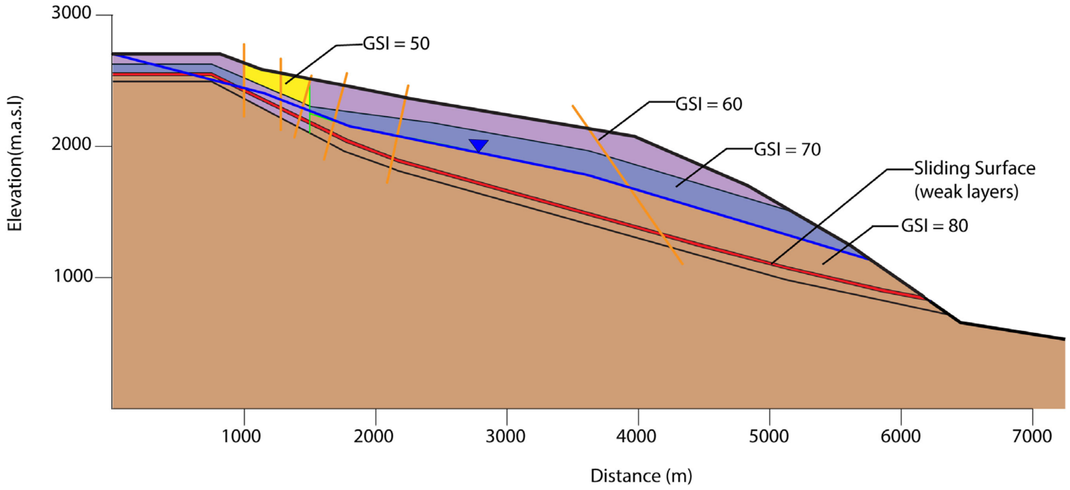

FIGURE 5 | Example of geometry and material properties of a GSI model in Phase2. Orange lines indicate discrete fault locations and the expected sliding surface, shown in red, is modeled either as disintegrated Quintnerkalk or a marl-like layer in all models. The blue line represents the assumed groundwater table position (about 100–300 m above the failure surface) in the "wet" case.

prehistoric failure cannot be obtained, we tested both high and low groundwater tables that are typical of fractured and karstified limestone aquifers in the Alps. The low water table was assumed to be below the failure surface, and hence would not have influenced failure; no groundwater level was included in models for this case. We assumed that the high water table lies between 100 and 300 m above the sliding zone, and generally follows the shape of the topography (**Figure 5**). The assumed high water table likely corresponds to a condition of elevated pore pressure within the sliding mass directly after a significant recharge event. The effect of seismicity as a potential trigger of the FRRA was analyzed using pseudo-static FEM simulations. The input seismic coefficients were selected based on the historical Churwalden earthquake, which occurred in 1295 ∼20 km south-east of the study site, and had an estimated magnitude of 6.5 (Schwarz-Zanetti et al., 2004). Using the methodology presented by Pyke (1991), this magnitude results in estimated seismic coefficients ranging between 0.1 and 0.3. These coefficients are in good agreement with those estimated for a 1:10,000 year return period earthquake in the study region by the Swiss Seismological Survey (Wiemer et al., 2016).

Runout Modeling

Runout modeling was performed using Dan3D-Flex (Aaron and Hungr, 2016b; Aaron et al., 2017). Initially, Dan3D-Flex simulates the motion of a "flexible block," which rotates and translates across 3D topography. At a user-specified time, the physics of the block changes to that of a frictional fluid, and the

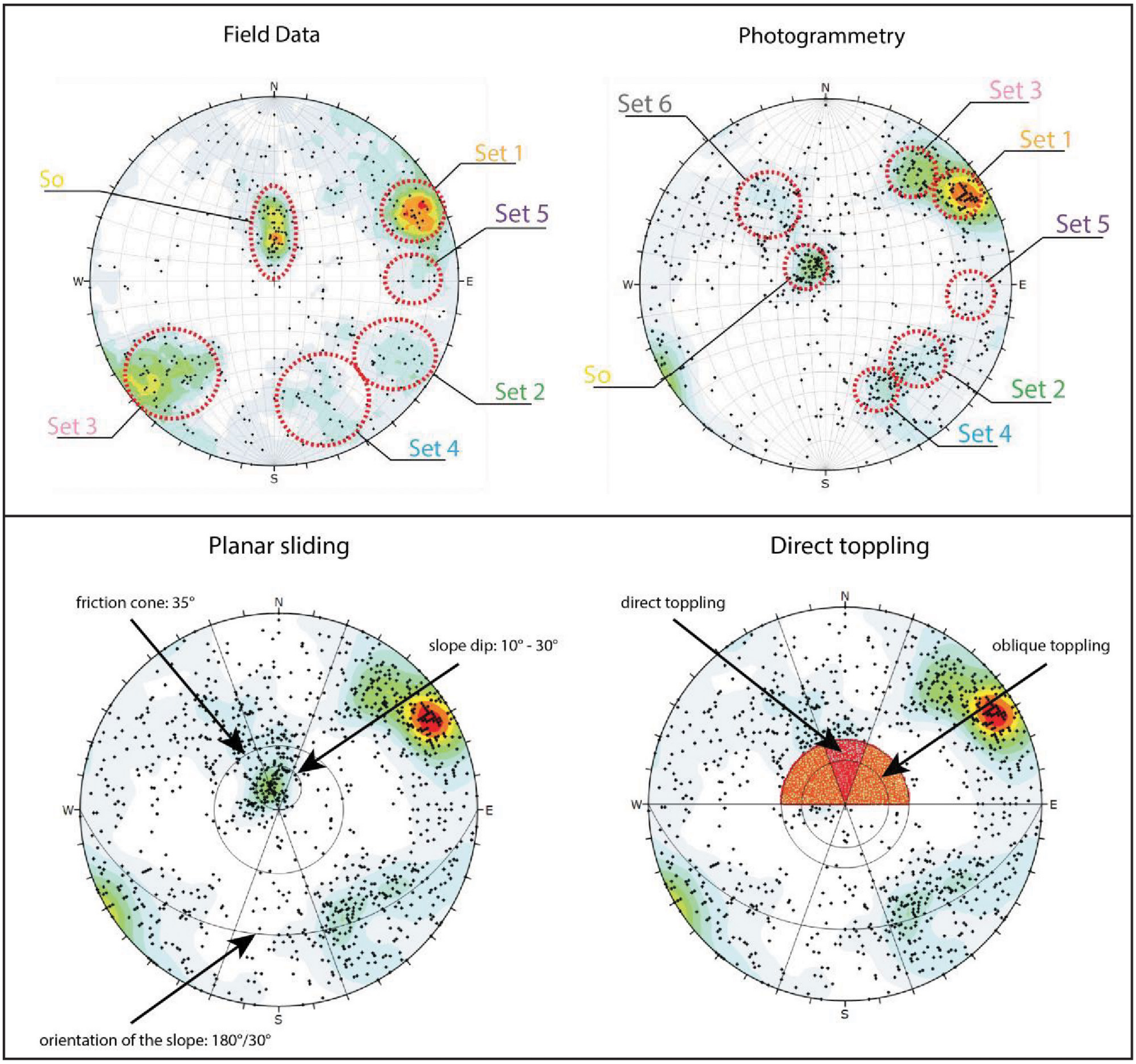

FIGURE 6 | Top: discontinuity measurements taken from the field and from photogrammetry. **Bottom:** Results of the kinematic analysis.

motion of the failed mass is simulated with the original Dan3D algorithm (McDougall and Hungr, 2004). By combining both a solid and fluid mechanics solver, Dan3D-Flex can, in a simplified way, simulate the initial sliding phase of motion, as well as the fluid phase after the mass has fragmented and turned flow-like. During the solid mechanics portion of the simulation, the motion of the block is governed by a simple basal rheology, and during the fluid mechanics portion motion is governed by both a basal and an internal rheology.

As input, Dan3D-Flex requires a topographic raster that represents the sliding surface, as well as a raster of the thickness of the initial source mass. To create these files, a topographic reconstruction was performed by manually modifying the present-day topography, based on **Figure 3B**, Caprez (2008) and our own geomorphic interpretation. The present-day topographic files used were based on 1m LiDAR data obtained from Swiss Topo. This resulted in the removal of 7.5 km^3 from the present-day topography, which when combined with the estimate of 1.5 km^3 eroded since deposition (Caprez, 2008), results in a deposit volume of 9 km^3. Our reconstruction of the source zone resulted in a volume estimate of 7.5 km^3. This results in a bulking factor of ∼1.2, comparable to but slightly lower than that estimated for other rock avalanches (∼1.25) by Hungr and Evans (2004). Our estimated deposit volume is ∼1 km^3 less than Caprez (2008), however, it well matches our estimated source volume, assuming a reasonable bulking ratio (volume increase due to expansion along pre-existing discontinuities and fragmentation of source material). Dan3D-Flex does not explicitly simulate the bulking process, so a source mass with a total source volume of 9 km^3 was used as input for the runout modeling.

Three sets of simulations were performed in the present work. The first used a single basal rheology, with parameters calibrated using the Bayesian calibration technique described in Aaron et al. (2019). Briefly, this methodology uses an extensive parametric sweep to determine the posterior distribution of the basal resistance parameters. The second set of simulations used two rheologies, a frictional rheology in the source zone and a Voellmy rheology along the path, to separate the basal resistance in the source zone from that provided by the valley fill (Aaron and McDougall, 2019). For this set of simulations, the friction angle was selected based on Aaron and McDougall (2019), and the Voellmy coefficients for the path were calibrated. The third simulation used the same zonation of rheologies from simulation 2, however, a source zone friction angle of 15° was selected based

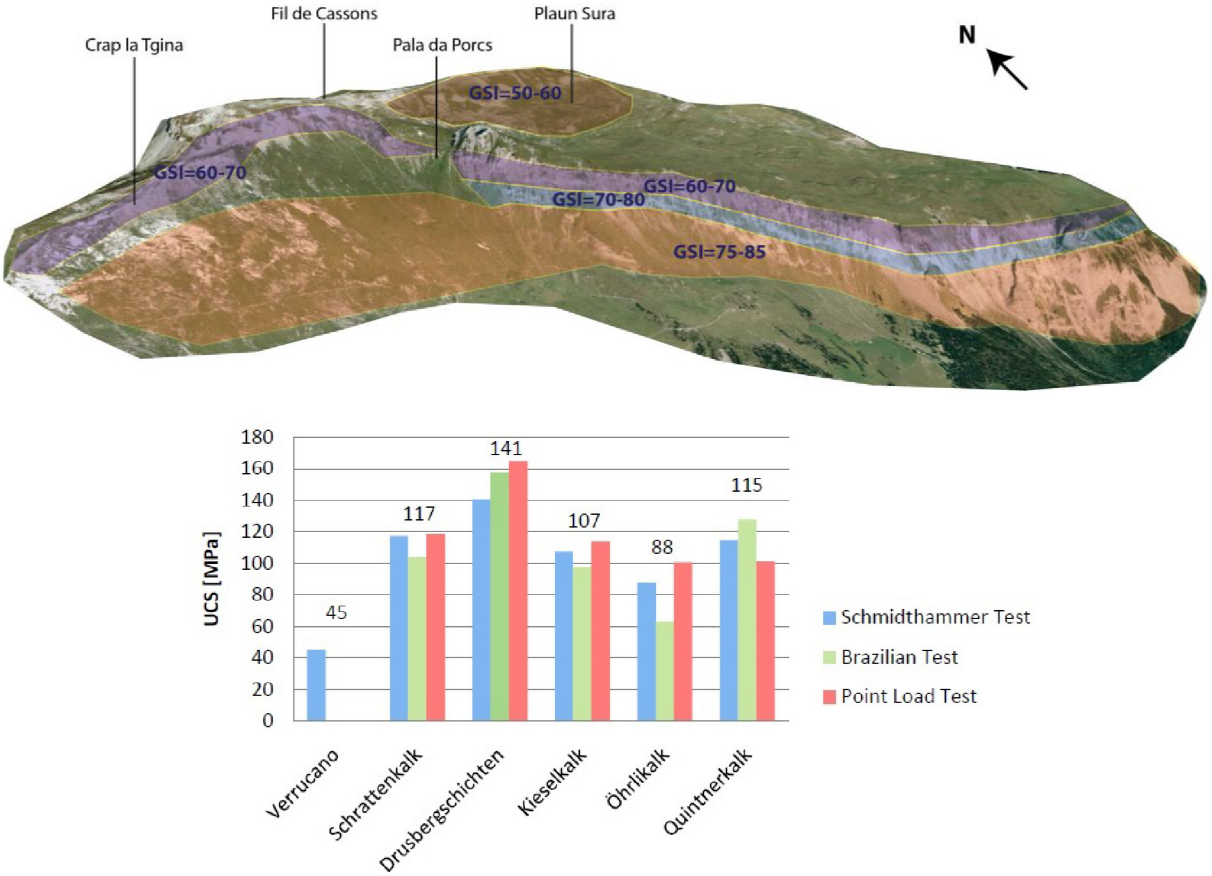

FIGURE 7 | Top: GSI (Geological Strength Index) domains in the study area, based on outcrop-scale field observations. The GSI generally increases with depth in the sequence (Imagery: Google Earth, 2009). **Bottom:** Unconfined compressive strength values derived from different strength testing methods. Mean values from averaging across tests for each lithology are indicated.

on the results of the rock mass characterization and stability analysis (**Table 1**). This set of simulations allows for the link to be made between the rock mass stability and runout characteristics.

RESULTS

Rock Mass Characterization and Engineering Geomorphological Mapping

The field and photogrammetry surveys resulted in over 1000 measurements, and six identified joint sets in addition to bedding (**Figure 6**). Bedding appears to be the dominant set, and is folded on both the local and regional scale. The dip of the bedding-parallel sliding surface scar is highest at the headscarp of the FRRA (30°), and decreases to 10° to the south. Sets 1 and 3 are common throughout the study area, whereas sets 2 and 4 are less common. Sets 5 and 6 are rarely found, and appear to be locally concentrated. Individual discontinuity orientations in sets 1, 2, 3, and 4 are consistent throughout the study area, whereas local variation was observed in the bedding and sets 5 and 6.

The rock masses in the study area are highly variable, ranging from fairly strong and massive to weak and highly fractured. As shown on **Figure 7**, outcrop-scale GSI values are related to lithology. The lowest GSI values (30–50) are found in the Verrucano unit, and the highest (75–85) are found in the massive Quintnerkalk. Our results also show that GSI values are affected by proximity to thrust faults and fold hinges.

Figure 7 summarizes the results of the Schmidt Hammer, Brazilian, and Point Load tests. The correlation of Altindag and Guney (2010) was used to transform Brazilian tensile strength into compressive strength. The strengths of the limestone units are between 80 and 150 MPa. The Drusbergschichten unit is the strongest (UCS = 141 MPa) and the Verrucano the weakest (UCS = 45 MPa). The Verrucano unit could not be tested in the laboratory as no suitable samples could be collected.

Thin sections of intact Quintnerkalk and the landslide body (cf. **Figure 4**) demonstrate the existence of marl-like layers within the Quintnerkalk (**Figure 8**). Microscopic clay bands are common at the level of the prehistoric failure zone. A thin section and outcrop image on the basal sliding surface (**Figures 8b,c**) shows comminuted limestone, with pulverized matrix, indicating high energy shear processes relatively close to the initiation zone.

The geomorphological map (**Figure 9**, top) highlights the large steps at the foot of the side scarp and front of Flimserstein. Steeply dipping faults are common in the study area, and generally follow orientations of discontinuity sets determined in the field and from remote sensing imagery (**Figure 9** bottom, and see below). Shallowly dipping thrust faults are likely present in the area, although they are not visible on the geomorphic map given orientation bias. Ongoing rockfall activity (Cabernard et al., 2004) and tectonic, glacial, periglacial, and karst processes have affected the Flimserstein and FRRA scarps and sliding surface scar. Other morphological features within the depletion zone of FRRA include gullies, small organic plains, and colluvial deposits (see also Caprez, 2008). The ridge of boulders on the western margin mentioned above (**Figure 2**) could be a remnant rockfall talus apron, or could have been deposited during the FRRA.

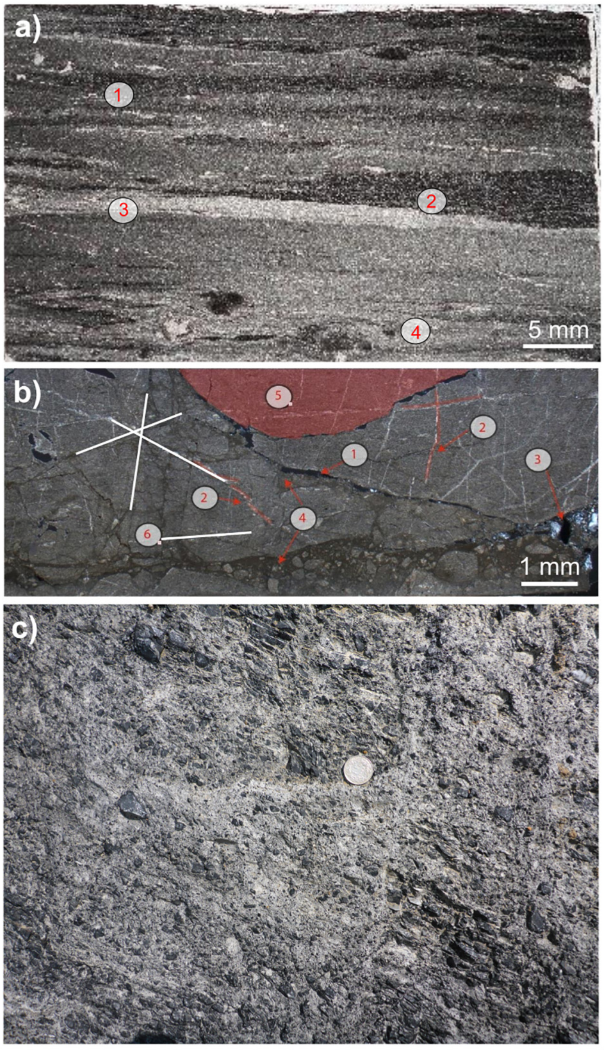

FIGURE 8 | (a) Thin section of *in situ* Quintnerkalk at the level of the Flims failure zone, at the southern margin of Flimserstein (cf. **Figure 4** for location). 1. marl layer, 2. fecal pellets (evidence of bioturbation), compressed during diagenesis, 3. calcite-rich layer, 4. bioturbated layer with larger calcite fragments. **(b)** Thin section taken at the contact between *in situ* Quintnerkalk and the failed mass at Punt Desch (cf. **Figure 2** for location). 1. voids, 2. calcite veins, 3. calcite, 4. cataclastic, comminuted limestone material, 5. limestone block, 6. (white lines) discontinuity sets. **(c)** Image of material at the basal sliding zone near Punt Desch, showing pulverized debris and polished fracture surfaces.

Stability Modeling

The results of the kinematic analyses are shown in **Figure 6**. These results show that occurrence of planar sliding requires a friction angle lower than 25°, indicating that a weaker lithology or layer must be present within the limestone to facilitate sliding. The limit equilibrium analysis indicates that the inclusion of a heavily disintegrated limestone layer (WQL in **Table 1**) within the massive Quintnerkalk unit does not lead to failure [Factor of Safety (FS) = 1.69 with a water table and 1.9 without]. Integration of a marl-like layer (WML in

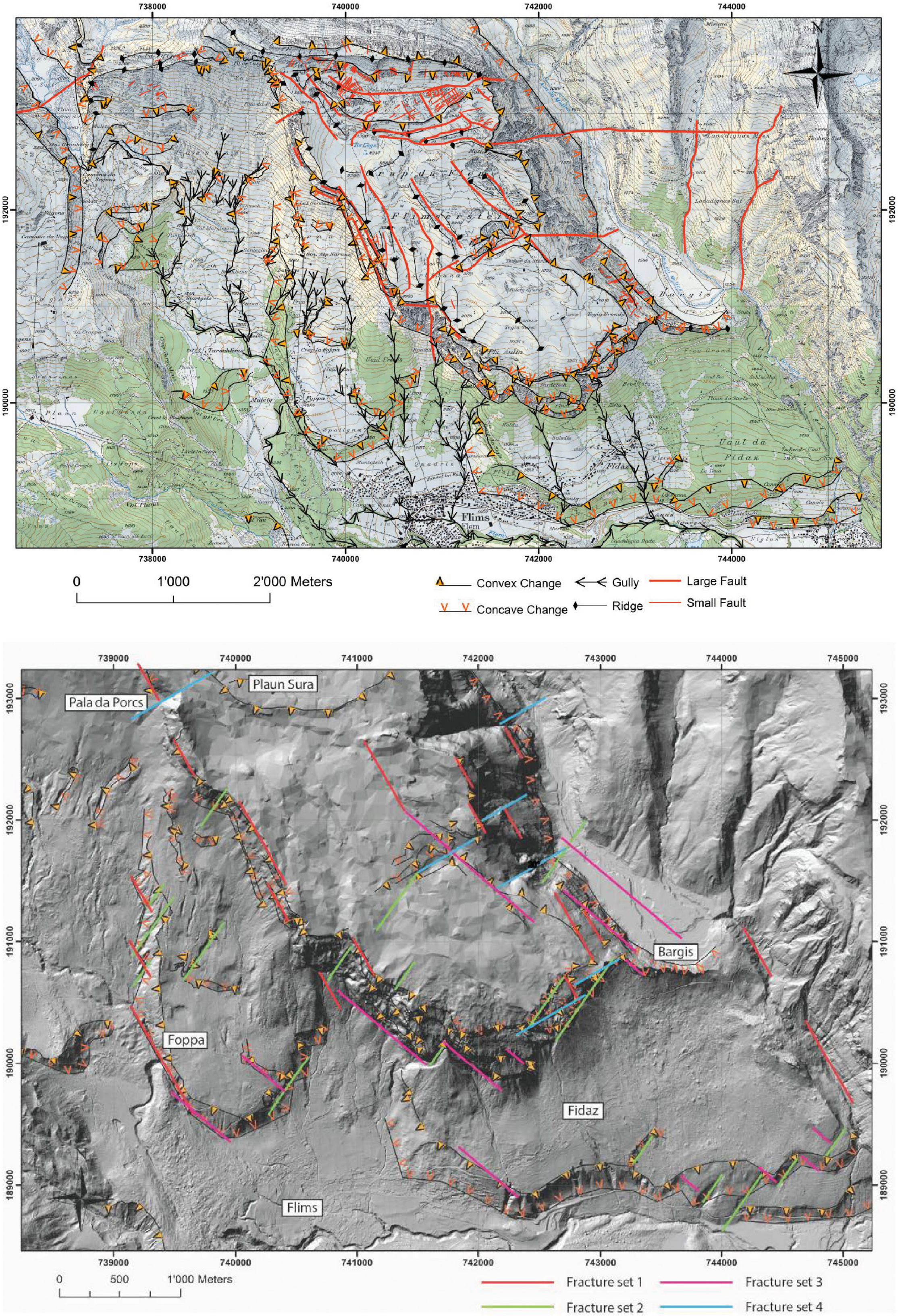

FIGURE 9 | Top: Geomorphological and structural geological map, indicating convex and concave changes in slope, gullies, ridges, and faults. **Bottom:** Surface expression of fracture sets 1–4 overlain on the geomorphology of the study area.

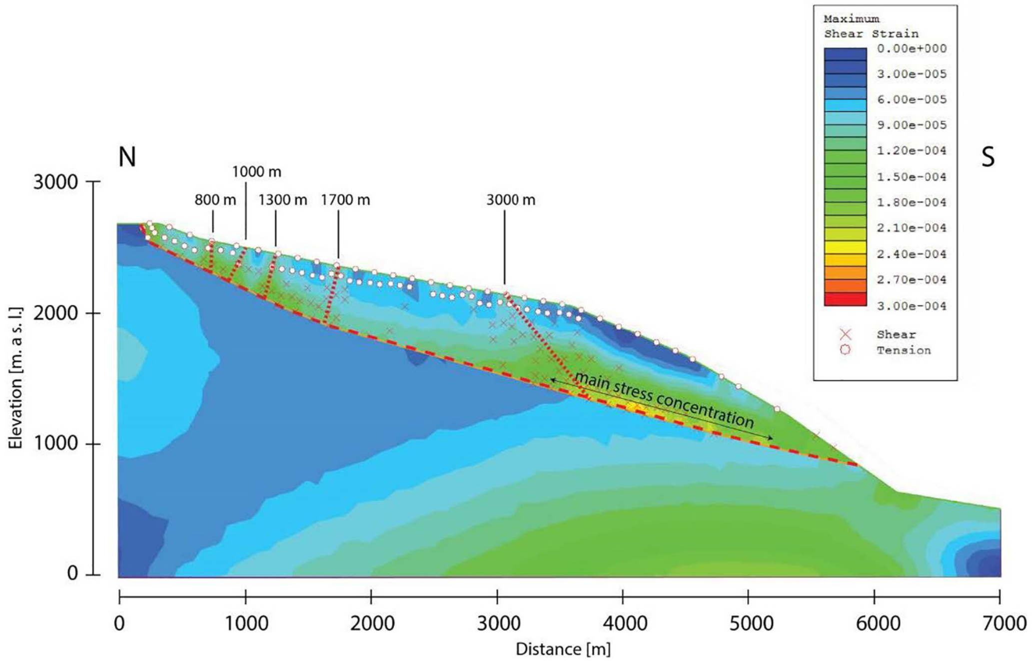

FIGURE 10 | Maximum shear strain plot in Phase2, indicating areas of high strain that could correspond to locations of secondary shear surfaces. These correlate well with field and remote sensing observations, as shown in **Figures 3A**, **9**.

Table 1), however, indicates *FS* = 1.0 (with water table) and *FS* = 1.2 (dry). The assumed water table location is indicated on **Figure 5**.

In Phase2, the critical strength reduction factor (SRF) results indicate that the slope is stable (critical SRF = 1.8 wet, 2 dry) when a weak Quintnerkalk layer with GSI = 10, φ = 18°, and c = 2 MPa is considered, corroborating the Slide results. However, when a marl layer equivalent is simulated, the critical SRF drops to 0.97 (with water table) and 1.16 (dry) when properties are GSI = 15, φ = 17°, and c = 0.7 MPa. The thickness of the weak sliding zone layer was also varied from 2 to 30 m to test the influence on stability. No significant differences were determined in model behavior.

Finally, the slope was subjected to seismic loading. The weak Quintnerkalk layer failed (critical SRF ∼1) with a seismic coefficient of 0.2 when GSI = 20 (φ = 22°, c = 3.2 MPa, σ_T = 0.028 MPa) properties were used. The marl-like layer failed when GSI = 50 (φ = 28°, c = 2 MPa, σ_T = 0.115 MPa).

Investigations on the development of secondary sliding surfaces show high shear stress concentrations mainly between 500 and 1800 m and 3000–6000 m along the horizontal axis (**Figure 10**). The assumed locations of the modeled secondary shear planes correlate with field observations of existing steeply dipping faults (**Figure 3**).

The potential secondary surfaces were integrated as discrete surfaces in subsequent models. In these models, shear strain was focused in the main sliding zone at the toe of the slope (**Figure 11A**). Tensile failure was induced at the top of Flimserstein. Total displacement contours (**Figure 11B**) for static models (no seismic loading) show that the southernmost fault observed in the models and in the field is an important boundary for movement – it acts to separate an active compartment of the failure from inactive compartments above. These results suggest that the toe of the slope must have failed first to provide kinematic freedom for the rest of the rock mass.

When seismic loading was included in this FEM model, total modeled displacement increased in general up to 1.5 m and was more evenly distributed throughout the sliding mass (**Figure 11C**). This result suggests that the compartments of the landslide could have failed contemporaneously during an earthquake.

A fracture network model, incorporating discontinuities explicitly, provided useful results for the possible kinematics and evolution of the landslide (**Figure 12**). The critical SRF of the model, including a water table but not seismic loading, is 1.33. It appears that the central part of the sliding mass underwent the most internal deformation and damage based on these preliminary models, perhaps indicating a Prandtl wedge transition zone. Additionally, **Figure 12** shows that the failure mass likely dilated along pre-existing discontinuities. This increase in volume would result in a subsequent decrease of pore-water pressure. When we modeled additional marl-like layers above and below the assumed failure surface, we found that the lowermost marl layer always showed the highest strain concentration, regardless of depth, and that strain increased with depth.

Runout Modeling

Runout modeling results from each of the three scenarios are presented in **Figure 13**. **Figure 14** shows simulated deposit

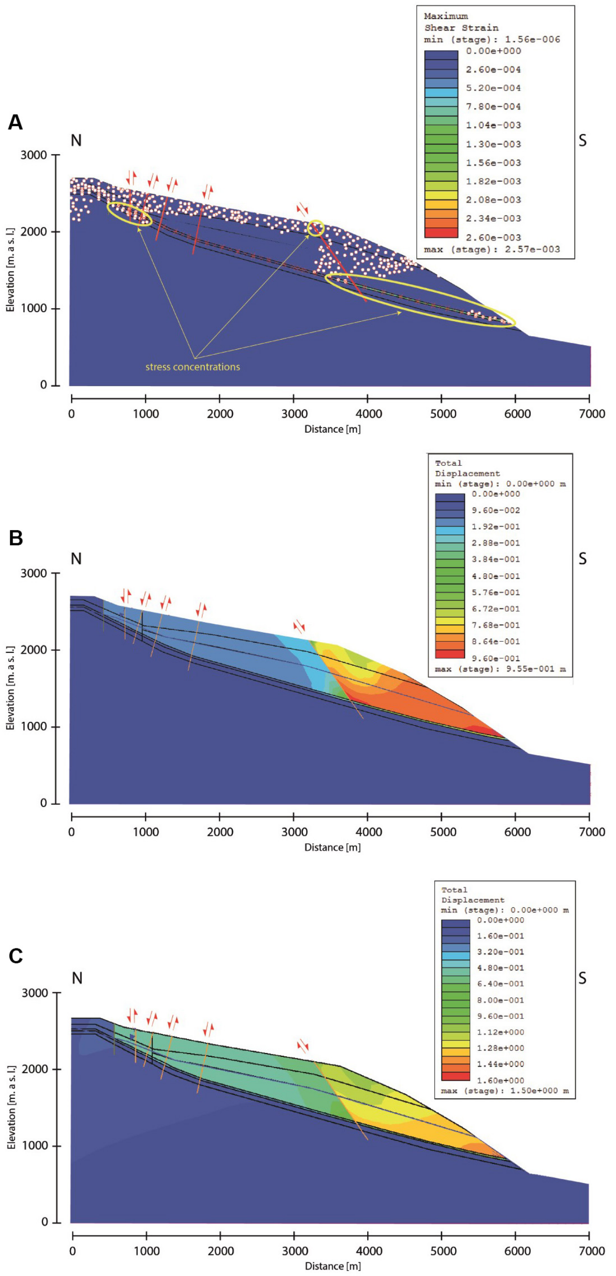

FIGURE 11 | (A) Maximum shear strain plot of simulation with secondary shear surfaces integrated as discrete planes in Phase2. The highest stress concentrations occur between the toe and the southernmost (rightmost) fault. In addition, increased strain values and tension failure occur between 500 and 1000 m distance and along the south-dipping, southernmost fault. **(B)** Total displacement plot for a static model, showing the importance of the southernmost fault as a compartment boundary. **(C)** Total displacement plot for a pseudo-static model with a seismic coefficient of 0.1.

depths at different times for the two-rheology simulation. Overall, the simulation results reproduce the observed impact area well, and deposition is simulated to be thickest in areas that match the thickest deposits estimated, based on the volume reconstruction. Simulated deposit thicknesses are lower than those estimated from the topographic reconstruction in many areas. This could be caused by underestimating the initial source volume with our topographic reconstruction. Since this estimate matches that made by Caprez (2008), the likely source of volume underestimation is underestimating the eroded volume by the Vorderrhein river.

The rigid motion distance that produces the best-fit results is 2.5 km. This parameter is discussed further in the following section. The posterior analysis revealed that the best-fit Voellmy parameters are a friction parameter of 0.16, and a turbulence parameter of 600. These values are the same for both the one rheology simulation and the valley floor material zone of the two-rheology simulation. The back-analyzed parameters for the valley floor fit well with those determined for a number of case histories that likely overran and liquefied saturated sediments (Aaron and McDougall, 2019). Cases in the database that had similar back-analyzed parameters include the Frank Slide, the Hope Slide, and the Rautispitz rock avalanche (Cruden and Krahn, 1978; Mathews and McTaggart, 1978; Nagelisen et al., 2015). The available data for the impact area and deposit distribution constrained the friction parameter well, however, a large range of turbulence parameters, between about 200 and 2000, all give similar results. Further refining this calibration would require estimates of velocity (Aaron et al., 2019), which would be difficult to make for this prehistoric case.

The best-fit source zone friction angle is 9°, which is low, but follows the volume-dependent trend for source zone friction angles presented in Aaron and McDougall (2019). We note that this value cannot be directly compared to more commonly presented measurements of H/L (e.g., Scheidegger, 1973; Li, 1983), as the H/L ratio includes the effect of path material. The source zone friction angle is well-constrained with available field data, as there is minimal deposition in the upper part of the source zone. Reproducing this observation requires a low friction angle. When a higher friction angle of 15° is used, which corresponds to that required for stability in our 2D stability models, the mass is simulated to remain in the source zone (**Figure 13D**).

DISCUSSION

Our analysis has revealed important information regarding the preparatory and triggering factors that governed the pre-failure behavior of the FRRA. Geomorphic and structural analyses show that the slide was structurally controlled – present-day features are bounded by discontinuities parallel to the discontinuity sets determined from rock mass characterization (**Figure 9**).

According to 2D modeling results, the presence of one or several weak layers, presumably marl layers, is required for sliding failure to occur. Such marl layers have been found in subsurface drilling at this site (Buechi and Mueller, 1994), and in outcrops and thin sections taken at the elevation of the sliding zone (**Figure 8**). However, at present only mm- to cm-thick layers have been identified, and our analysis results suggest that persistent weak layers must be present at multiple elevations

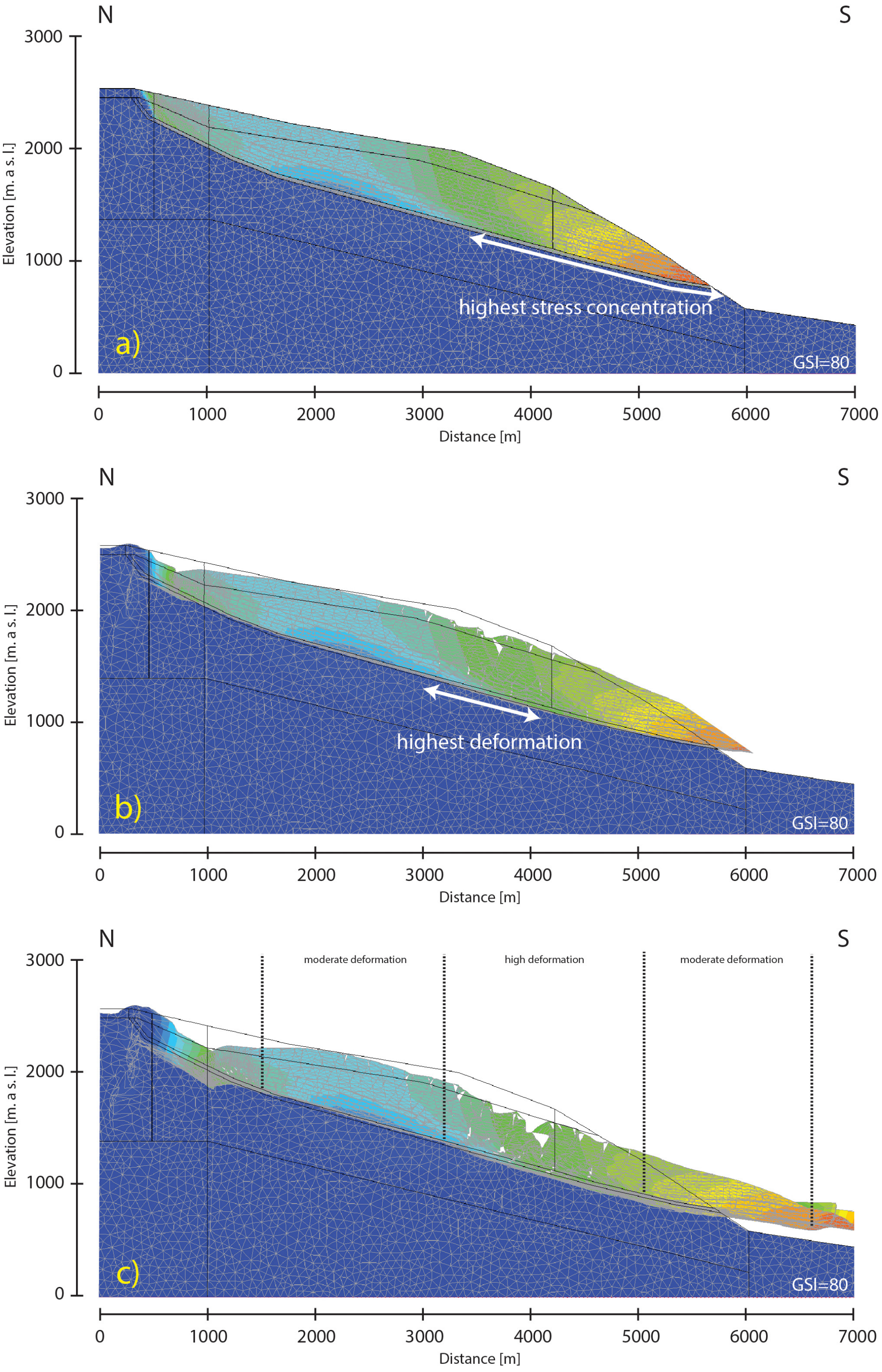

FIGURE 12 | Results of the fracture network model. **(a)** Displacement contours indicate highest movement between 3500 and 6000 m distance, where displacement increases toward the slope toe. **(b)** The headscarp and the middle part of the rockslide mass are subjected to extensional processes and sliding mass is separated into three compartments. **(c)** The rockslide body can be separated into higher (middle part) and lower (upper and lower parts) deformation regions.

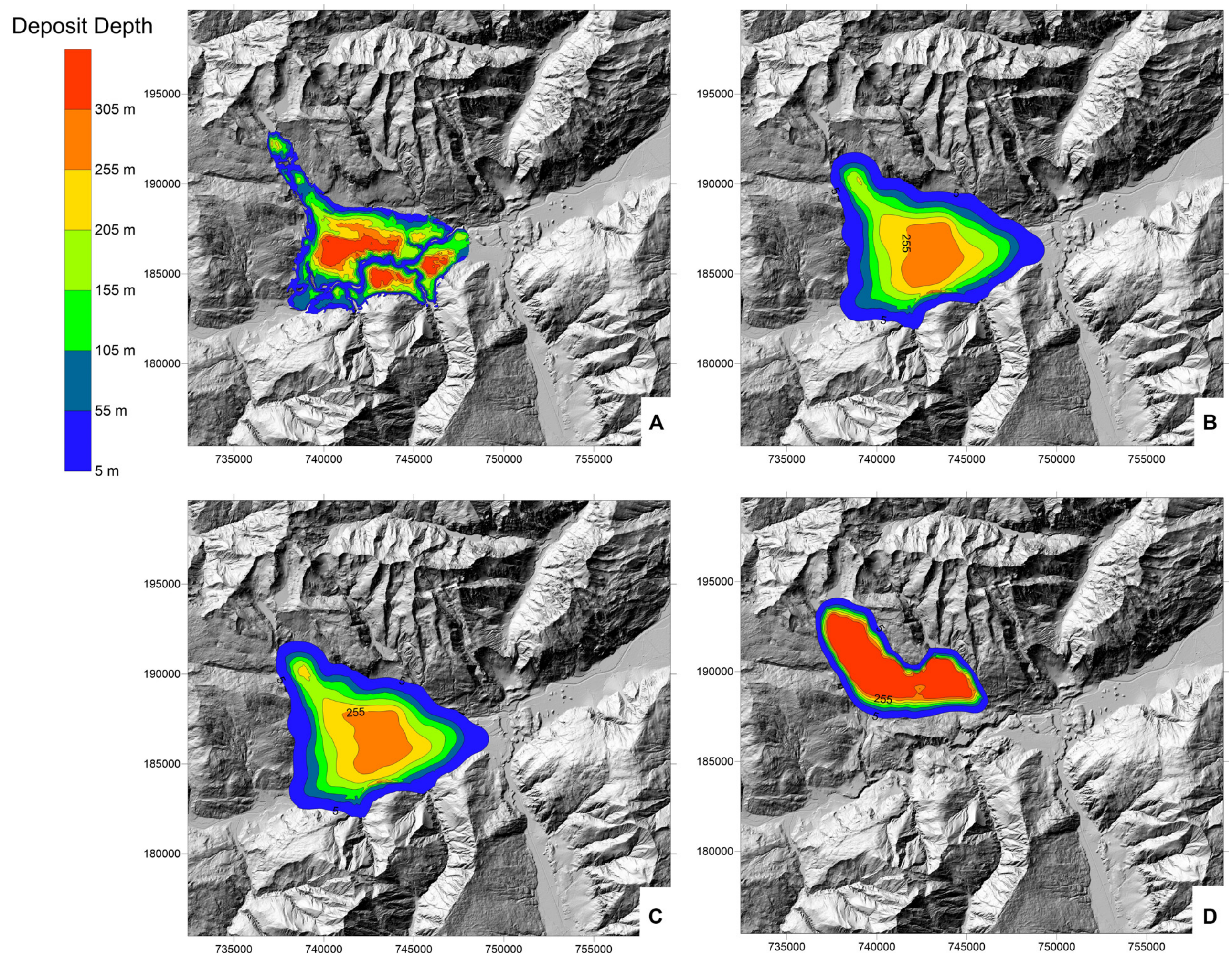

FIGURE 13 | Dan3D results for the three scenarios. **(A)** Reconstructed deposit depth. **(B)** Two-rheology simulation. **(C)** One-rheology simulation. **(D)** Simulation assuming only cohesion loss along the rupture plane occurred.

in the site stratigraphy (due to the stepped rupture surface) to explain failure. We note that the modeled layer thickness and depth did not significantly change simulation results, but that layer persistence was important. Including multiple marl-like layers in our models suggested that the deepest always showed the most strain, but other weak layers were strained as well. It is thus feasible that multiple closely spaced weak layers would lead to similar initiation behavior as one "equivalent" weakness zone. In reality, a combination of factors could have contributed to creating these persistent "weak layers" within the otherwise competent limestones: (i) multiple thin stratigraphic layers with increased content in sheet silicates and marl-like properties (low friction and cohesion), (ii) multiple weak layers resulting from tectonic activity, such as shearing along bedding-parallel marly limestone layers or fractures. Periodic loading from pore pressures cycles in karst systems and moderate seismic activity might have potentially propagated damage along these pre-existing planes of weakness. Failure within the limestones was possible only with strong seismic activity, and still required a weak limestone layer. Thus, our stability analysis demonstrates that weak layers are required for failure. These seem to be pre-existing lithological units, which may have been further weakened by shearing.

Our 2D stability analyses also suggest that a strong trigger is required for failure to occur, particularly if only a weak limestone layer is considered. This could either be through strong seismic shaking, or high pore-water pressures. Both Poschinger and Haas (1997) and Ivy-Ochs et al. (2009) note that the FRRA occurred during the early Holocene, when the climate was warmer and wetter. This cannot rule out a seismic trigger, however, as PGA values of 0.2–0.3 have been estimated with a 1:10,000 year return period in the study region by Wiemer et al. (2016).

Once the factor of safety of the rock slide dropped below one, our morphological observations and modeling results suggest that the FRRA was separated into several compartments, with the material closest to the Vorderrhein valley bottom failing first, allowing the material above to start to move. Steps in the failure surface suggest complex development of the surface, most

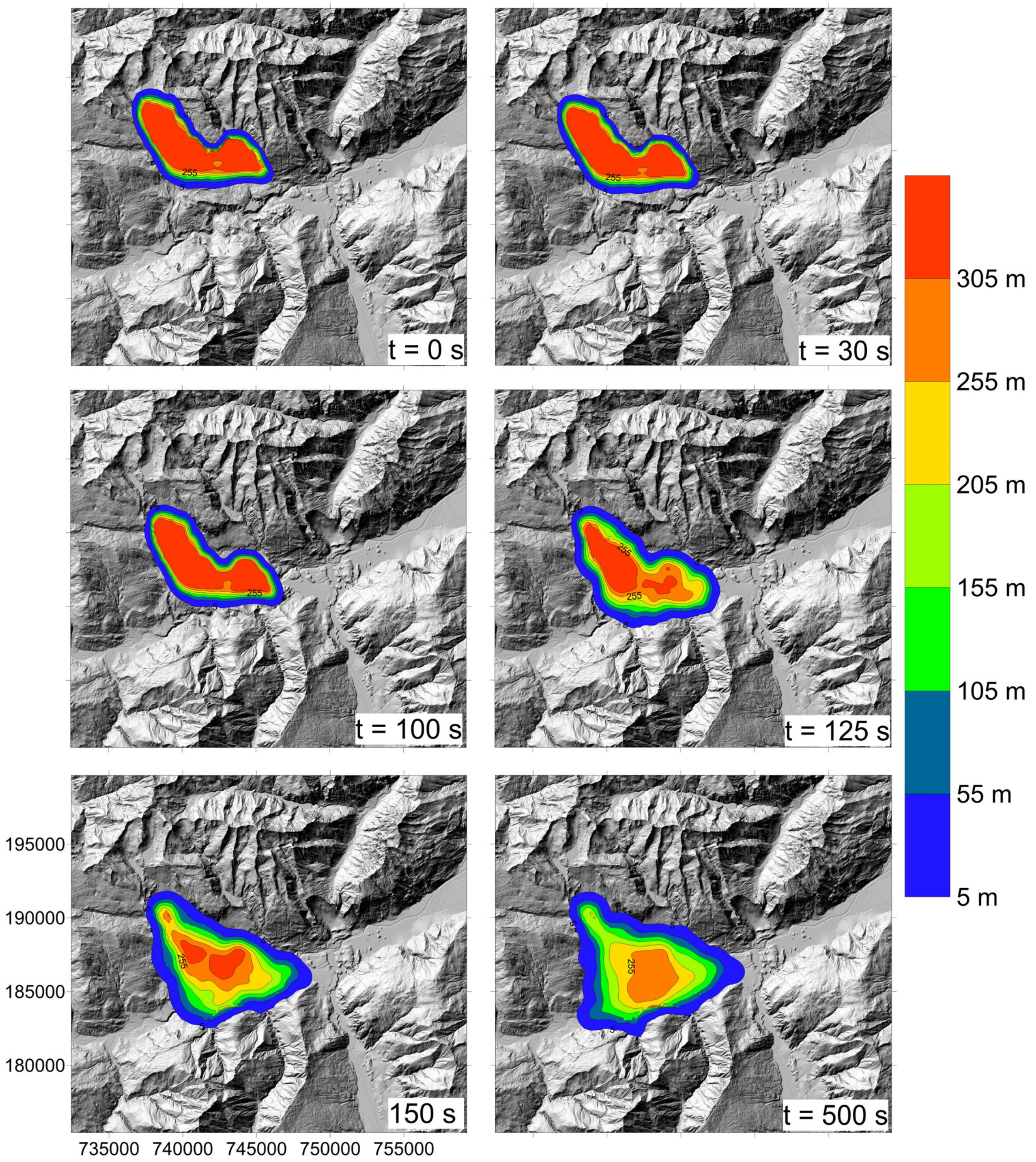

FIGURE 14 | Simulated deposit depths at different times during the simulation overlain on the post-event topography. The mass is specified to turn flow-like at 100 s.

likely including pre-existing, bedding-parallel discontinuities and brittle fracture of rock bridges.

As shown by comparing **Figures 13B,D**, catastrophic failure is not simulated to occur through loss of basal cohesion alone. The basal strength along the rupture plane must be reduced by 6°–10° in order for rapid acceleration and runout to occur. This mechanism must act soon after failure, or the mass will not rapidly accelerate. This requirement rules out many rock avalanche strength loss mechanisms, such as rapid undrained loading of saturated path material, as it must occur when the mass is still intact in the initial sliding phase. Some potential mechanisms by which this may occur include polishing and shearing of asperities (Cruden and Krahn, 1978), as well as frictional heating (Hu et al., 2018). It is interesting to note that in the absence of this immediate strength reduction, a catastrophic failure would have been unlikely to develop, and the morphology of the slope would have been more similar to that of a suspended rockslide, albeit closer to the valley floor than is typical of this landslide type. The lack of a catastrophic strength loss mechanism has been recently cited as a reason for the absence of a sudden failure of an accelerating rockslide responding to glacial retreat (Glueer et al., 2019).

Aaron and Hungr (2016b) note that the simulated impact area is relatively insensitive to the transition distance from flexible block to rock avalanche, provided that the transition from solid to frictional fluid occurs once the mass has started to vacate the source zone. The same is true of the present simulation of the Flims rock avalanche; however, we note that the deposit distribution is sensitive to this distance. We find that increasing the rigid motion distance increases the thickness of the deposit at the distal end, due to less internal deformation. Simulation of the thickest deposit points, observed based on the dissection of the debris by the Vorderrhein River (**Figure 13**), requires that the block travels ∼2.5 km as a rigid body, before behaving as a frictional fluid, with distributed internal shear.

Our numerical runout models likely represent two end members of rock avalanche motion, simulating either the sliding of an intact block, or flow of a material undergoing distributed and fully developed internal shearing. Field evidence suggests that the motion of the Flims rock avalanche was between these two extremes, and our simulation results reflect this. Thus, certain features of the model of "slab-on-slab" sliding proposed by Pollet et al. (2005) are qualitatively supported by our long rigid motion distance. However, our simulations require very low basal strength (discussed further in the following paragraph), and higher internal strength.

Calhoun and Clague (2018) suggest that there was a lake present at the toe of the slope, prior to the FRRA. The Bonaduz Gravel, now found in an extensive area surrounding the deposit, is likely composed of valley fill deposits originally located in this lake. Our runout analysis does not explicitly consider the effects of this lake, and momentum transfer that occurred when the rock avalanche impacted the lake and overrode and plowed the valley fill deposits (Jiang and LeBlond, 1992; Tinti et al., 2006; Si et al., 2018) are implicitly accounted for in the values of the calibrated basal resistance parameters. Our analysis does show that the Bonaduz Gravel would have been overridden and plowed by an ∼300 m thick wall of debris in ∼100 seconds. This substantial impact appears to have triggered a hyperconcentrated flow that traveled for ∼14 km (Calhoun and Clague, 2018).

When the valley fill deposits were overridden, they likely liquefied. This interpretation is supported by the presence of "Pavoni Pipes," as detailed in Pavoni (1968) and Calhoun and Clague (2018). This liquefied material likely accounts for the low basal resistance parameters required along the path to reproduce the observed runout, as our calibrated parameters are similar to other cases that overran saturated substrate (Aaron and McDougall, 2019). It is interesting to note that the basal resistance parameters determined for the Flims rock avalanche match those of these other case histories, despite a difference in volume of 4 orders of magnitude.

Thus, our results provide some interesting constraints on the preconditioning, triggering and runout behavior of the FRRA, which can be generalized to many other large rock slope failures. The main preconditioning factors for this event are the structural geology, and the presence of low strength layers. High pore pressures and/or strong (1:10,000 year) seismic shaking could have then triggered failure along thin marl-like layers. During failure, a mechanism, such as polishing or frictional heating would then have to immediately reduce the basal strength along the rupture plane by 6°–10°, to enable rapid acceleration and long runout. The mass would have moved in a coherent manner for about 2.5 km, impacting the pre-failure lake and liquefying the valley fill deposits through a combination of overriding and plowing. Overriding these liquefied sediments further increased the mobility of the rock avalanche, leading to a total impact area of ∼69 km^2.

CONCLUSION

We have performed a detailed analysis of the FRRA, the largest catastrophic failure in the European Alps. Our analysis included detailed engineering geomorphological mapping, two-dimensional stability and three-dimensional runout modeling. Our mapping and stability analysis show that this event was structurally controlled, that failure likely exploited weak, marl-like layers within the stratigraphic sequence and that either high pore pressures, seismic shaking or a combination of the two could have triggered failure. Our runout analysis suggested that liquefaction of alluvial sediments likely increased the runout of the event, however, catastrophic failure would not have occurred without a mechanism to reduce basal strength on the rupture plane by ∼6°–10°. The mechanisms by which this strength reduction occur are poorly understood at present, but appear to be crucial in explaining the occurrence of catastrophic failure at Flims, as well as many other rock avalanches around the world.

DATA AVAILABILITY STATEMENT

The raw data supporting the conclusions of this article will be made available by the authors, without undue reservation, to any qualified researcher.

AUTHOR CONTRIBUTIONS

JA helped to conceive of the study, performed the runout analysis, and assisted with writing the manuscript. AW conceived of the study, assisted with the geomorphic mapping and stability analysis, and assisted with writing the manuscript. SL helped to conceive of the study, assisted with results interpretation, and writing the manuscript. SV performed the stability analysis and geomorphic mapping, and assisted with writing the manuscript. All authors contributed to the article and approved the submitted version.

FUNDING

Funding for this work was provided by the Chair of Engineering Geology, Department of Earth Sciences, ETH Zürich.

ACKNOWLEDGMENTS

Thanks are due to Dr. Martin Ziegler and Dr. Matthew Perras for helping with the field data acquisition and sample preparation. We thank former BSc students Alicia Martinez for analyzing the thin sections, and Benjamin Ruf for his contributions to geomorphic mapping. Discussions with Andreas Von Poschinger, Jurgen Caprez, John Clague, and Adrian Pfiffner greatly improved this manuscript. Comments from two reviewers greatly improved this work.

REFERENCES

Aaron, J., and Hungr, O. (2016a). Dynamic analysis of an extraordinarily mobile rock avalanche in the Northwest Territories, Canada. *Can. Geotech. J.* 53, 899–908. doi: 10.1139/cgj-2015-0371

Aaron, J., and Hungr, O. (2016b). Dynamic simulation of the motion of partially-coherent landslides. *Eng. Geol.* 205, 1–11. doi: 10.1016/j.enggeo.2016.02.006

Aaron, J., and McDougall, S. (2019). Rock avalanche mobility: the role of path material. *Eng. Geol.* 257:105126. doi: 10.1016/j.enggeo.2019.05.003

Aaron, J., McDougall, S., Moore, J. R., Coe, J. A., and Hungr, O. (2017). The role of initial coherence and path materials in the dynamics of three rock avalanche case histories. *Geoenviron. Disasters* 4:5. doi: 10.1186/s40677-017-0070-4

Aaron, J., McDougall, S., and Nolde, N. (2019). Two methodologies to calibrate landslide runout models. *Landslides* 16, 1–14. doi: 10.1007/s10346-018-1116-8

AdamTechnology (2015). *3DM Analyst Suite*, 2.5.0 Edn.

Agliardi, F., Crosta, G., and Zanchi, A. (2001). Structural constraints on deep-seated slope deformation kinematics. *Eng. Geol.* 59, 83–102. doi: 10.1016/S0013-7952(00)00066-1

Altindag, R., and Guney, A. (2010). Predicting the relationships between brittleness and mechanical properties (UCS, TS and SH) of rocks. *Sci. Res. Essays* 5, 2107–2118.

Bowman, E. T., Take, W. A., Rait, K. L., and Hann, C. (2012). Physical models of rock avalanche spreading behaviour with dynamic fragmentation. *Can. Geotech. J.* 49, 460–476. doi: 10.1139/t2012-007

Buechi and Mueller, A. G. (1994). *A19 Oberalpstrasse Umfahrung Flims: Auflageprojekt Geologie, Hydrogeologie und Geotechnik*. INFO TBA: Chur.

Cabernard, V., Stoffel, M., and Monbaron, M. (2004). "Der Fidazer Felssturz von 1939: analyse and simulation," in *Turbulenzen in der Geomorphologie. Publikation zur Jahrestagung der Schweizerischen Geomorphologischen Gesellschaft, 27.–29. März 2003, Erstfeld. Mitteilungen der Versuchanstalt für Wasserbau, Hydrologie und Glaziologie*, Vol. 184, ed. H. E. Minor (Zürich: ETH Zürich), 1–12.

Calhoun, N. C., and Clague, J. J. (2018). Distinguishing between debris flows and hyperconcentrated flows: an example from the eastern Swiss Alps. *Earth Surf. Process. Landf.* 43, 1280–1294. doi: 10.1002/esp.4313

Caprez, J. (2008). *Das Flimser Bergsturzereignis 3D-Geländerekonstruktion und Volumenberechnungen mit Hilfe von GIS - Diplomarbeit*. Zürich: Universität Zürich.

Clayton, A., Stead, D., Kinakin, D., and Wolter, A. (2017). Engineering geomorphological interpretation of the Mitchell Creek Landslide, British Columbia, Canada. *Landslides* 14, 1655–1675. doi: 10.1007/s10346-017-0811-1

Coe, J. A., Baum, R. L., Allstadt, K. E., Kochevar, B. F., Schmitt, R. G., Morgan, M. L., et al. (2016). Rock-avalanche dynamics revealed by large-scale field mapping and seismic signals at a highly mobile avalanche in the West Salt Creek valley, western Colorado. *Geosphere* 12, 607–631. doi: 10.1130/GES01265.1

Cruden, D., and Krahn, J. (1978). *Frank Rockslide, Alberta, Canada*, ed. B. Voight (Amsterdam: Elsevier Scientific Publishing), 97–112.

Davies, T. R., McSaveney, M. J., and Hodgson, K. A. (1999). A fragmentation-spreading model for long-runout rock avalanches. *Can. Geotech. J.* 36, 1096–1110. doi: 10.1139/t99-067

De Blasio, F. V. (2011). Dynamical stress in force chains of granular media traveling on a bumpy terrain and the fragmentation of rock avalanches. *Acta Mech.* 221, 375–382. doi: 10.1007/s00707-011-0504-0

Deplazes, G. (2005). *Quartärgeologische Kartierung des Oberen Teils der Gleitfläche des Flimser Bergsturzes*. Zurich: ETH Zurich Engineering Geology.

Deplazes, G., and Anselmetti, F. S. (2007). Auf den spuren des flimser bergsurzes in lag la cauma und lag grond. *Geosci. Actuel* 3, 46–50.

Dufresne, A., Bösmeier, A., and Prager, C. (2016). Sedimentology of rock avalanche deposits – Case study and review. *Earth Sci. Rev.* 163, 234–259. doi: 10.1016/j.earscirev.2016.10.002

Gischig, V., Preisig, G., and Eberhardt, E. (2016). Numerical investigation of seismically induced rock mass fatigue as a mechanism contributing to the progressive failure of deep-seated landslides. *Rock Mech. Rock Eng.* 49, 2457–2478. doi: 10.1007/s00603-015-0821-z

Gischig, V. S., Moore, J. R., Evans, K. F., Amann, F., and Loew, S. (2011). Thermomechanical forcing of deep rock slope deformation: 1. Conceptual study of a simplified slope. *J. Geophys. Res.* 116, 1–18. doi: 10.1029/2011JF002006

Glade, T., and Crozier, M. J. (2004). "The nature of landslide hazard impact," in *Landslide Hazard and Risk*, eds T. Glade, M. Anderson, and M. J. Crozier (Hobken, NJ: John Wiley and Sons), 43–74.

Glueer, F., Loew, S., Manconi, A., and Aaron, J. (2019). From toppling to sliding: progressive evolution of the Moosfluh Landslide, Switzerland. *J. Geophys. Res.* 124, 2899–2919. doi: 10.1029/2019JF005019

Grämiger, L. M., Moore, J. R., Vockenhuber, C., Aaron, J., Hajdas, I., and Ivy-Ochs, S. (2016). Two early Holocene rock avalanches in the Bernese Alps (Rinderhorn. Switzerland). *Geomorphology* 268, 207–221. doi: 10.1016/j.geomorph.2016.06.008

Hoek, E. (2007). Practical rock engineering. *Environ. Eng. Geosci.* 14, 55–57. doi: 10.2113/gseegeosci.14.1.55

Hu, W., Huang, R., McSaveney, M., Zhang, X., Yao, L., and Shimamoto, T. (2018). Mineral changes quantify frictional heating during a large low-friction landslide. *Geology* 46, 223–226. doi: 10.1130/g39662.1

Hungr, O. (2017). "Chapter 9 - Runout Analysis," in *Guidelines for Mine Waste Dump and Stockpile Design*, eds M. Hawley, and J. Cunning (Clayton: CSIRO Publishing).

Hungr, O., and Evans, S. G. (2004). Entrainment of debris in rock avalanches: an analysis of a long run-out mechanism. *Geol. Soc. Am. Bull.* 116, 1240–1252. doi: 10.1130/B25362.1

Hungr, O., Leroueil, S., and Picarelli, L. (2014). The Varnes classification of landslide types, an update. *Landslides* 11, 167–194. doi: 10.1007/s10346-013-0436-y

Ivy-Ochs, S., Poschinger, A. V., Synal, H. A., and Maisch, M. (2009). Surface exposure dating of the Flims landslide, Graubünden, Switzerland. *Geomorphology* 103, 104–112. doi: 10.1016/j.geomorph.2007.10.024

Jiang, L., and LeBlond, P. H. (1992). The coupling of a submarine slide and the surface waves which it generates. *J. Geophys. Res. Oceans* 97, 12731–12744. doi: 10.1029/92JC00912

Li, T. (1983). A mathematical model for predicting the extent of a major rockfall. *Zeitschrift Geomorphol. Neue Folge* 27, 473–482.

Mathews, W. H., and McTaggart, K. C. (1978). Hope rockslides, british columbia, canada. *Develop. Geotech. Eng.* 14, 259–275. doi: 10.1016/B978-0-444-41507-3.50015-5

McDougall, S., and Hungr, O. (2004). A model for the analysis of rapid landslide motion across three-dimensional terrain. *Can. Geotech. J.* 41, 1084–1097. doi: 10.1139/t04-052

Moore, J. R., Pankow, K. L., Ford, S. R., Koper, K. D., Hale, J. M., Aaron, J., et al. (2017). Dynamics of the Bingham Canyon rock avalanches (Utah, USA) resolved from topographic, seismic, and infrasound data. *J. Geophys. Res.* 122, 615–640. doi: 10.1002/2016JF004036

Nagelisen, J., Moore, J. R., Vockenhuber, C., and Ivy-Ochs, S. (2015). Post-glacial rock avalanches in the Obersee Valley. Glarner Alps, Switzerland. *Geomorphology* 238, 94–111. doi: 10.1016/j.geomorph.2015.02.031

Pavoni, N. (1968). Uber die Entstehung der Kiesmassen in Bergsturzgebiet von Bonaduz-Reichenau (Graubünden). *Ecl. Geol. Helvetiae* 61, 494–500.

Pollet, N., Cojean, R., Couture, R., Schneider, J., Strom, A. L., Voirin, C., et al. (2005). A slab-on-slab model for the Flims rockslide (Swiss Alps). *Can. Geotech. J.* 42, 587–600. doi: 10.1139/T04-122

Pollet, N., and Schneider, J.-L. (2004). Dynamic disintegration processes accompanying transport of the Holocene Flims sturzstrom (Swiss Alps). *Earth Planet. Sci. Lett.* 221, 433–448. doi: 10.1016/S0012-821X(04)00071-8

Poschinger, A. V., and Haas, U. (1997). Der Flimser Bergsturz, doch ein warmzeitliches Ereignis? *Bull. Angewandte Geol.* 2, 35–46.

Poschinger, A. V., and Kippel, T. (2009). Alluvial deposits liquefied by the Flims rock slide. *Geomorphology* 103, 50–56. doi: 10.1016/j.geomorph.2007.09.016

Poschinger, A. V., Wassmer, P., and Maisch, M. (2006). "The flims rockslide: history of interpretation and new insights," in *Landslides from Massive Rock Slope Failure, NATO Science Series, IV, Earth and Environmental Sciences*, Vol. 49, eds S. Evans, G. Scarascia Mugnozza, A. L. Strom, and R. Hermans (Berlin: Springer), 329–356. doi: 10.1007/978-1-4020-4037-5_18

Preisig, G., Eberhardt, E., Smithyman, M., Preh, A., and Bonzanigo, L. (2016). Hydromechanical rock mass fatigue in deep-seated landslides accompanying seasonal variations in pore pressures. *Rock Mech. Rock Eng.* 49, 2333–2351. doi: 10.1007/s00603-016-0912-5

Pyke, R. (1991). *Selection of Seismic Coefficients for Use in Pseudo-Static Slope Stability Analyses*. Available at: https://tagasoft.com/seismic-coefficients/

RocScience (2015). *Phase2, Slide*. Toronto, ON: RocScience Inc.

Scheidegger, A. (1973). On the Prediction of the Reach and Velocity of Catastrophic Landslides. *Rock Mech.* 5, 231–236. doi: 10.1007/bf01301796

Schindler, C., Cuenod, Y., Eisenlohr, T., and Joris, C. L. (1993). Die Ereignisse vom 18. April und 9. Mai 1991 bei Randa (VS): ein atypischer Bergsturz in Raten. *Eclogae. Geol. Helv.* 86, 643–665.

Schwarz-Zanetti, G., Deichmann, N., Fäh, D., Masciadri, V., and Goll, J. (2004). The earthquake in Churwalden (CH) of September 3, 1295. *Ecl. Geol. Helvetiae* 97, 255–264. doi: 10.1007/s00015-004-1123-8

Si, P., Aaron, J., McDougall, S., Lu, J., Yu, X., Roberts, N. J., et al. (2018). A non-hydrostatic model for the numerical study of landslide-generated waves. *Landslides* 15, 711–726. doi: 10.1007/s10346-017-0891-y

Thuro, K., and Hatem, M. (2010). *The 1806 Goldau Landslide Event–Analysis of a Large Rock Slide, (Zehnder 1988)*. 3693–3700. Available at: http://www.geo.tum.de/people/thuro/pubs/2010_iaeg_goldau.pdf (accessed January 30, 2014).

Tinti, S., Pagnoni, G., and Zaniboni, F. (2006). The landslides and tsunamis of the 30th of December 2002 in Stromboli analysed through numerical simulations. *Bull. Volcanol.* 68, 462–479. doi: 10.1007/s00445-005-0022-9

Volken, S. (2015). *The Flims Rockslide: A New Perspective on Failure Mechanisms and Kinematics*. MSc Thesis, ETH Zurich, Zurich.

Volken, S., Wolter, A., and Loew, S. (2016). The Flims Rockslide: new investigations of the kinematics and mechanics using an integrated geotechnical approach. Landslides and Engineered Slopes. *Exp. Theor. Pract.* 2005, 1995–2000. doi: 10.1201/b21520-250

Wiemer, S., Danciu, L., Edwards, B., Marti, M., Fäh, D., Hiemer, S., et al. (2016). *Seismic Hazard Model 2015 for Switzerland (SUIhaz2015)*. Zurich: ETH Zurich, 164. doi: 10.12686/a2

Wolter, A., Gischig, V., Stead, D., and Clague, J. J. (2016). Investigation of geomorphic and seismic effects on the 1959 Madison Canyon, Montana, landslide using an integrated field, engineering geomorphology mapping, and numerical modelling approach. *Rock Mech. Rock Eng.* 49, 2479–2501. doi: 10.1007/s00603-015-0889-5

Conflict of Interest: SV was employed by geoformer igp AG during the preparation of this manuscript.

The remaining authors declare that the research was conducted in the absence of any commercial or financial relationships that could be construed as a potential conflict of interest.

The handling Editor declared a past co-authorship with one of the authors SL.

frontiers
in Earth Science

MINI REVIEW
published: 03 July 2020
doi: 10.3389/feart.2020.00263

Conceptual Framework of Energy Dissipation During Disintegration in Rock Avalanches

Sibylle Knapp and Michael Krautblatter*

Landslide Research Group, Technical University of Munich, Munich, Germany

Rock avalanches usually progress through three consecutive phases: Detachment (Phase 1), Disintegration (Phase 2), and Flow (Phase 3). While significant advances have been achieved in modeling Rock Avalanche Phase 1 (Detachment) and Phase 3 (Flow), the crucial link between both during Phase 2 (Disintegration) is still poorly understood. Disintegration of the detached rock mass is often initiated as soon as sliding starts, and *in situ* measurements are impossible due to the excessive energy release equivalent to multiple nuclear explosions. Better understanding the energy dissipation during Phase 2, and the resulting residual kinetic energy that propels the rock avalanche in Phase 3, is one of the keys to defining the mechanical properties of the avalanche in the runout zone and thus also the resisting force within the avalanche. This paper is a review of our knowledge of energy dissipation in rock avalanches with a focus on processes like friction, collision, fragmentation, comminution, entrainment and explosion during the phase of disintegration. We distinguish between energy sources and sinks and consider not only physical processes, but also chemical alterations that might occur at high temperatures. With that, we make a contribution to improve our understanding of Phase 2 "Disintegration," which is needed for accurately modeling rock avalanches and assessing their hazard potential.

Keywords: rock avalanche, energy dissipation, disintegration, fragmentation, heat, friction, chemical alteration

Edited by:
O. Adrian Pfiffner,
University of Bern, Switzerland

Reviewed by:
Jeffrey A. Coe,
United States Geological Survey (USGS), United States
Jia-wen Zhou,
Sichuan University, China
Aiguo Xing,
Shanghai Jiao Tong University, China

****Correspondence:***
Sibylle Knapp
sibylle.knapp@tum.de

Specialty section:
This article was submitted to Structural Geology and Tectonics, a section of the journal Frontiers in Earth Science

Received: *02 March 2020*
Accepted: *12 June 2020*
Published: *03 July 2020*

Citation:
Knapp S and Krautblatter M (2020) Conceptual Framework of Energy Dissipation During Disintegration in Rock Avalanches. Front. Earth Sci. 8:263. doi: 10.3389/feart.2020.00263

INTRODUCTION

Rock avalanches are defined as "extremely rapid, massive, flow-like motion of fragmented rock from a large rock slide or rock fall" (Hungr et al., 2014). Due to their high velocity, volume and runout distance, rock avalanches have a significant impact on human activities in mountain areas, can seriously damage infrastructure and settlements and can cause high numbers of casualties (Evans et al., 2006; Legros, 2006; Hewitt et al., 2008). Landslides resulting from large-scale rock-slope failures are especially hazardous; in the 20th century, disasters of this type have killed more than 50,000 people globally (Evans et al., 2006). As a consequence of increasing population density and the development of infrastructure in mountain areas, the number of elements at risk is growing and accelerating the vulnerability to landslide hazards (Fischer, 1999; Korup, 2005; Hungr, 2006; Legros, 2006). At the same time, the number of massive rock failures from permafrost warming appears to be increasing with potentially disastrous consequences especially when causing rock-ice avalanches with high mobility (Haeberli et al., 2004; Huggel, 2009; Huggel et al., 2012; Krautblatter et al., 2013; Krautblatter and Leith, 2015) or causing flooding after impacting lakes (Haeberli et al., 2016; Knapp et al., 2018).

Better understanding the disintegration (Phase 2; **Figure 1**) is key to defining mechanical properties like grain size composition and content of large blocks in the runout zone and therefore the hazard potential of rock avalanches. Current approaches based on Mohr–Coulomb friction models adequately describe the detachment processes (Phase 1; **Figure 1**) and its energy dissipation (Maddock, 1986) or the rock avalanche flow (Phase 3; **Figure 1**) utilizing fluid (Bingham) or snow avalanche (Voellmy) analogs with adequate parameterization (Hungr, 2006; Christen et al., 2010; Preuth et al., 2010; Pudasaini and Krautblatter, 2014; Pudasaini and Mergili, 2019). For Phase 2, some models on dynamic fragmentation were just developed (e.g., Zhao et al., 2017; Ghaffari et al., 2019), whereas other disintegration processes, e.g., heat transfer and phase transitions still represent major research gaps. This situation is mainly related to insufficient understanding of energy dissipation during Phase 2, and the resulting residual kinetic energy that propels the ensuing rock avalanche (Phase 3). The material properties of the avalanche result from these energetic processes and from the material being overrun. Only by understanding disintegration, will more precise modeling of rock avalanches and their hazard potential be possible. In this paper, we are going to primarily concentrate on the intrinsic properties of rock avalanches that influence disintegration, and we are going to focus on disintegration and energy dissipation in Phase 2, that is directly after the detachment.

ENERGY DISSIPATION DURING DISINTEGRATION

Disintegration Processes

Large rock-slope failures usually undergo different stages of downhill movement which may occur consecutively (Abele, 1974): (i) The rock mass moves as a coherent block, and translational shearing occurs along the contact of the bottom of the rock avalanche and the ground surface. (ii) Subsequently, differential movement of individual blocks initiates crushing of the original rock mass. (iii) If the coherent rock mass loses its internal cohesion and disintegrates intensely (shattering) it can evolve into a rapid granular flow (Pollet and Schneider, 2004), which is defined as the distributed shear motion of a group of clasts where individual grains interact with each other and with the boundaries of the moving flow (Dufresne and Davies, 2009). The result can be a highly fragmented (pulverized) rock mass which consists of angular grains of all sizes down to $<1\ \mu$m (**Figures 2A–D**; e.g., Davies and McSaveney, 2012).

To decipher individual processes during disintegration, two types of disintegration can be distinguished: (i) *static disintegration*, a collision-free process driven mainly by gravity, and (ii) *dynamic disintegration,* referring to particle comminution by grain-to-grain collisions driven by motion. Disintegration refers to fracturing by rapid changes in stress coupled with sudden (un-)loading caused by bending, transverse shearing or delamination of the rock mass creating large blocks, thin vertical slabs or, horizontal sheets, respectively (Erismann and Abele, 2001). Static disintegration is an essential precursor for dynamic disintegration as it creates fractures along which further relative shearing and fragmentation can occur. Shearing along predefined bedding and foliation planes induces shear crushing and the creation of a granular layer.

Energy Sources and Sinks

Energy dissipation in rock avalanches occurs by transformation of the total energy into thermal energy, acoustic energy or inelastic deformation energy (Nicoletti and Sorriso-Valvo, 1991), where due to the law of energy conservation, the final energy available for mechanical work is less than the initial amount. The energy release is often in the range of dozens to more than a thousand Hiroshima bombs (∼15 kt TNT or 63 TJ each) for large rock avalanches. Recent work also emphasizes the energy transfer into chemical reactions and phase transitions (Anders et al., 2010; Mitchell et al., 2015). Energy "release" and "consumption" describe the transfer of energy into a different form. Energy in rock avalanches is released by friction, collision and fracturing. Far from a continuous process, energy release is concentrated at points of impact with the ground surface and obstacles where major friction and disintegration of the rock mass is initiated (Erismann and Abele, 2001).

Field conditions constraining energy dissipation can be derived from (i) paleotopography (Nicoletti and Sorriso-Valvo, 1991), (ii) compressive and extensional flow structures in the rock-avalanche deposits (Hewitt, 2006; Dufresne and Davies, 2009; Dufresne et al., 2015), (iii) positions inside the flow recording differences between intact rock and major shear zones (Pollet et al., 2005), (iv) the sedimentological record (Yarnold, 1993; Weidinger et al., 2014) with (v) fine-sediment signatures (Reznichenko et al., 2012), and (vi) melting mineral formation (Weidinger and Korup, 2009). Referring to (i), Nicoletti and Sorriso-Valvo (1991) differentiate dissipation types and rates dependent on geomorphic controls along the runout path: The *low-energy dissipative type* refers to rock avalanches which are, for example, channelized in narrow valleys. Here, little potential energy is dissipated to other processes than kinetic energy, and mobility is enhanced. The *moderate-energy dissipative type* refers to radial spreading "free from lateral constraints," resulting in moderate mobility. Finally, the *high-energy dissipative type* describes running across a narrow valley and impacting against the opposite, at best perpendicular slope, which results in low mobility. Here, most initial energy is dissipated to energy sinks, and only little is left for the transfer into kinetic energy.

During disintegration, ∼20–50% of the potential energy is consumed (Locat et al., 2006; Haug et al., 2016). Considering multiple energy sinks in **Figure 1**, A–D (friction, inelastic collision, entrainment, and crustal deformation) cause heating to some degree, E and F (chemical energy consumption and phase transition) require latent energy for phase transitions, and G–I (dust production and bouncing, sound and microseismicity, and momentum exchange) act to export energy outside the impact/disintegration zone. The relative importance of D, G, H, and I (compression, dust production and bouncing, sound and microseismicity, and momentum exchange) has yet to be determined, but Erismann and Abele (2001) assumed that they are of minor importance. If A–C (friction, inelastic collision,

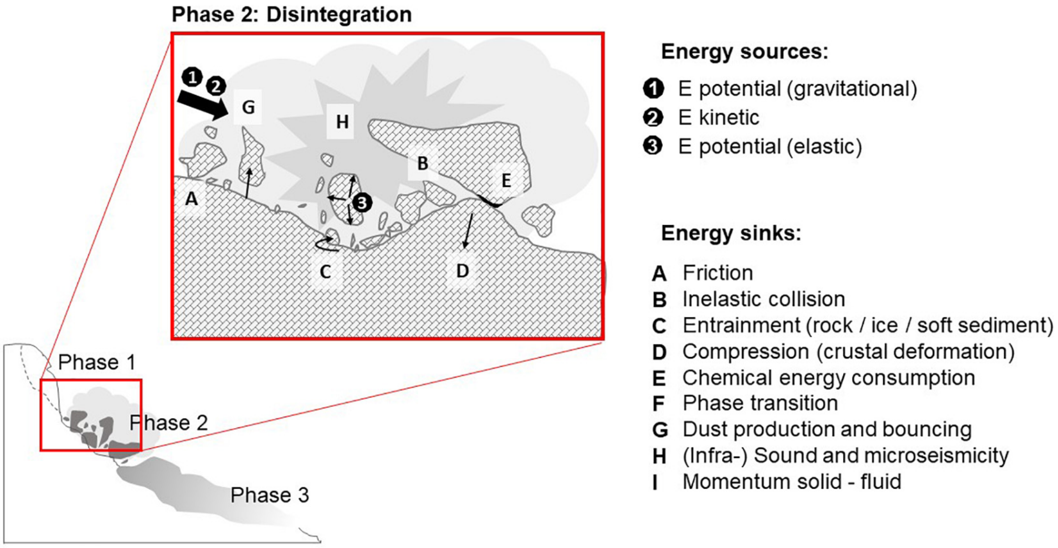

FIGURE 1 | Energy dissipation in Rock Avalanche Phase 2 (Disintegration). The primary energy input to the system is mostly derived from the potential/kinetic energy of the moving rock mass ("Energy sources"). "Energy sinks" cover different types of energy transformation, the majority of which involve heating. *(A) Friction*. *(B) Inelastic collision*: breaking at bonds stretching and friction. *(C) Entrainment*: plowing, scouring. *(D) Compression:* crustal deformation. *(E) Chemical energy consumption*: e.g., mineral transformation. *(F) Phase transition:* solid – fluid – gas, needs latent energy. *(G) Dust production and bouncing*. *(H) Sound and microseismicity. (I) Momentum exchange between solid and fluid phase*: energy dissipates to shock wave. The sediment record theoretically shows transitions linked to *(A)–(F)*. *(F)* and *(I)* may be present, but cannot be illustrated in the figure. Small arrows indicate direction of energy transfer.

and entrainment) have a major share in the energy dissipation and cause a mean frictional shear resistance whereas E–G (chemical energy consumption, phase transformation, and dust production) consume energy for phase transition, the rate of frictional heat generation per unit area Q is

$$\dot{Q} = \tau v - \phi = \mu_k \sigma_n v - \phi \tag{1}$$

where τ is the average frictional shear resistance, v is the average velocity, ϕ is the heat sink-rate due to latent heat, μ_k is the kinetic coefficient of friction and σ_n is the normal stress across the sliding plane (Maddock, 1986). Effective latent heat sinks could be from decarbonation of dolomite and calcite in sedimentary rock failures (Mitchell et al., 2015) or from phase transitions of water during melting and vaporization (De Blasio and Medici, 2017). The heat flow away from a source (e.g., a sliding plane) can be calculated by 1D-heat diffusion (Carslaw and Jaeger, 1959; Mitchell et al., 2015), where the temperature increase ΔT within the observed slip zone is

$$\Delta T\,(x,t) = \frac{1}{2\rho c\sqrt{\kappa\pi}} \int_0^t \frac{\tau(t')v(t') - \phi(t')}{\sqrt{t-t'}} e^{\frac{-x^2}{4\kappa(t-t')}}\, dt' \tag{2}$$

where x is the distance from the slip zone, t is time, ρ is mass density, κ is thermal diffusivity, c is heat capacity.

Physical Processes

Fragmentation/Collision/Comminution

Fragmentation describes the initiation and propagation of fractures and breaking apart and movement of grains (Turcotte, 1997). The related process energy is both linked to the length of the crack extension within existing grains (microcracking) and to the surface energy of the new created grains during comminution (Bieniawski, 1967; Hamdi et al., 2008). Fragmentation occurs as a *static* (Eberhardt et al., 2004; Wang et al., 2011; Zhang, 2016) or *dynamic* process (Pollet and Schneider, 2004; Crosta et al., 2007; Imre et al., 2010; Zhang et al., 2019). *Static fracture* occurs before any collision triggers the disintegration of a mass, whereas *dynamic fragmentation* shows more intense disintegration, e.g., in shear zones at the base of rock avalanches.

Grains fragment quickly under high local pressures and, thus, general intergranular effective stress and the frictional resistance to shear are reduced (Bowman et al., 2012). In laboratory experiments, the overburden strain-rate is directly related to the fragmentation process. If load is applied sufficiently quickly, particles will dynamically fragment and the kinetic energy of the resulting fragments will cause collisions with surrounding particles. Under dynamic disintegration, kinetic energy is dispersed through the system as colliding particles undergo further fragmentation (Rait and Bowman, 2010). The higher the spatial concentration of simultaneously-fragmenting grains, the lower the effective direct stress on the grain flow (Davies and McSaveney, 2009). Thereby, the basal sliding friction dissipates upward and laterally through the mass, which causes the slabs at the bottom to come to rest first. Thus, slabs higher in the moving mass travel further than the ones lower down (Erismann and Abele, 2001; Pollet and Schneider, 2004). Grain-to-grain collisions require an unconfined environment, in which particles can move freely. In such a case the highest levels of friction, crushing and collision occur in the lower part of a rock

FIGURE 2 | Examples of energy-related features in deposits of the Flims Rock Avalanche (Switzerland): **(A)** *Shattering* into cube-like, sharp-angled fragments of different size (cm-dm) in dark gray Helvetic limestone, secondarily cemented with white matrix of rock powder. **(B)** "Snapshot" of *pulverization* with multiple grain-internal layers of *micro-shearing*. **(C,D)** Grinding within a shear zone. **(E)** Entrained lump of lake sediment in the Bonaduz gravel deposits. **(F)** Vertical Pavoni pipes indicate rapid water discharge after deposition (person for scale).

avalanche due to high compressing forces and large differences in velocity between the moving particles and the ground (Erismann and Abele, 2001). Running on dry rock substrates, it is mainly fragmentation that leads to an increased travel length of the rock avalanche (Pollet and Schneider, 2004; McSaveney and Davies, 2007; Davies and McSaveney, 2009). After Haug et al. (2016), increased fragmentation mostly affects the front of a rock avalanche traveling further, whereas the center of mass crucial for energy considerations, is hardly displaced or decelerates. In comparison to previous papers stating that fragmentation accelerates the flow (Bowman et al., 2012; Langlois et al., 2015), Haug et al. (2016) confirmed that high fragmentation rather favors a more energy-efficient transport mode yielding longer runouts without acceleration.

In either case, fragmentation is considered an "energy sink" (Locat et al., 2006; Crosta et al., 2007; Haug et al., 2016). Haug et al. (2016) propose that static fragmentation may use up to 50% of the potential energy. Also, Ghaffari et al. (2019) postulate that the kinetic energy is only a small portion of dissipated energy during fragmentation, and the energy rather transfers into intergranular collision and friction. Thereby, it is important to note that the energy input for grain-internal "microcracking" weighs far more than for "macro-fragmentation," i.e., the formation of new grains (Ouchterlony et al., 2004; Hamdi et al., 2008). Zhao et al. (2017) quantify the energy dissipation by friction and plastic deformation to ∼90%, and the energy needed by bond breakage to <5%. Plus, the smaller the grain size becomes, the more energy is needed for comminution (Locat et al., 2006). The process of dynamic rock pulverization (**Figures 2A–D**) consumes massive amounts of energy, e.g., in gouge formation it sums up to 50% of earthquake energy (Wilson et al., 2005). During grinding, most energy (∼97%) is converted to heat, with only a small portion (<1%) actually contributing to fracturing (Spray, 1992).

Friction/Heat

Near the base of the moving rock mass, confining forces are largest and so the majority of frictional energy dissipation occurs in this zone (Pollet and Schneider, 2004). Disintegration and heating of the rock mass mainly arise (i) along well-defined persistent shear planes, or (ii) as a total disintegration of the whole mass. Shearing may be localized to a thin, discrete layer and frictional heating of bedrock may reduce basal strength (Hu et al., 2018, 2019; Hu and McSaveney, 2018). For (i), a high proportion of the energy release is focused on only a small proportion of the whole mass and will cause significant heating up to a partial melting of clasts, called *frictionite* (Heuberger et al., 1984; Erismann and Abele, 2001). As soon as particles are ∼1 μm and below, the amount of heat produced by their elastic and plastic deformation leads to their melting (Spray, 2005). In rare cases (i) this heating can cause centimetre-thick melting of rock and formation of frictionites at temperatures of 1700°C (Erismann et al., 1977; Weidinger et al., 2014). Discrete layers of more intense fragmentation contain *micro-breccias* and traces of partial melting (frictionite along shear planes; Schramm et al., 1998; Weidinger and Korup, 2009). For phase transitions, latent energy is absorbed. Besides, frictional shearing is controlled by the production and decay of random kinetic energy during gravitational work (Preuth et al., 2010). Random kinetic energy is referred to the random motion and inelastic interaction between the fragments; it is irreversible because it cannot perform mechanical work (Bartelt et al., 2006; Buser and Bartelt, 2009; Christen et al., 2010). For quantification, Schneider et al. (2010) argue that the total frictional work best correlates with the seismic signal of a rock (-ice) avalanche. The seismograph represents a small, but proportional fraction of this energy loss.

Erosion/Entrainment/Role of Water

There is an apparent increase in rock-avalanche mobility with volume (e.g., Heim, 1932; Scheidegger, 1973). The volume can be increased either by fragmentation up to 25–30% (Hungr and Evans, 2004; Crosta et al., 2007) or by the entrainment of substrate material. How enormous the effect of entrainment is, can be shown by the 2000 Tsing Shan event (Hong Kong), where a small volume of 150 m^3 of material grew to 1620 m^3 because of the strong erosion along the slope (Hungr and Evans, 2004). Entrainment strongly depends on the character of the path material (Crosta et al., 2009; Aaron and McDougall, 2019) and, for example, may cause high basal shear resistance and momentum loss, when overrunning bedrock or dry bed material (Iverson et al., 2011; Aaron et al., 2017; Whittall et al., 2017; Aaron and McDougall, 2019). In other cases, basal friction is reduced and mobility enhanced (Hungr and Evans, 2004; Aaron and Hungr, 2016; Coe et al., 2016). On the one hand, entrainment is an energy sink because the erosion, uptake and incorporation of material along the travel path by plowing, scouring or even surficial scratching (Hu and McSaveney, 2018) is mechanical work, accompanied by heating. On the other hand, the gain in weight increases the energy budget by acting as an energy source and must not be neglected. Water plays an important role for the amount and rate of entrainment and erosion (Iverson and Ouyang, 2015). Especially for rock avalanches traveling on ice (Huggel et al., 2008; Deline et al., 2015; Bessette-Kirton et al., 2018; Walter et al., 2020) or wet, soft sediments (e.g., lake sediments, **Figure 2E**), the increased pore pressure enhances the scour of the bed, reduces basal friction and causes velocity, mass and momentum to increase (Iverson et al., 2011; Iverson, 2016; Johnson et al., 2016). Pure ice has a basal friction which is about 75% lower than that of pure rock. Hence, in rock-ice avalanches, a ∼12.5% reduction of basal friction angle is observed for every 10% increase in ice content (Sosio et al., 2012). The intergranular direct stress between single grains is reduced by pore-water pressure, i.e., in initially wet sediment more overburden is necessary to start fragmentation than in dry sediment (Abele, 1997). Water may escape quickly after deposition like at the Flims Rock Avalanche (**Figure 2F**; Pavoni, 1968; Calhoun and Clague, 2018) but increasing temperature may cause water to be pressurized (Voight and Faust, 1982) and/or vaporized, as it is proposed for the Vajont Rockslide (Habib, 1975) or the Köfels Rockslide (De Blasio and Medici, 2017). For the melting of ice, a specific latent heat of 334 kJ/kg is needed, and for vaporization ∼2265 kJ/kg, which is almost seven times as much. There is a momentum exchange that consumes energy (Pudasaini and Krautblatter, 2014), and steam explosions are present, but probably camouflaged in the other energy dissipative processes. We have yet to understand the sedimentological imprint of steam explosions in the sediments.

Chemical Processes

Chemical processes are often neglected in the energy balance of rock avalanches. Novel friction experiments on carbonate rocks, for example, show that at velocities of several meters per second carbon dioxide starts to degas due to thermal decomposition induced by flash heating after only a few hundred microns of slip (Mitchell et al., 2015). This process creates vesicular degassing rims in dolomite clasts and crystalline calcite cement (Anders et al., 2010; Mitchell et al., 2015) and may allow the upper rock mass to slide over a "cushion" of pressurized material. Around 800–850°C, talc and dolomite start to decompose (Hu et al., 2018) and to produce high-pressure live steam and carbon dioxide (Habib, 1975; Hu et al., 2019). De Blasio and Medici (2017) found bubbles grown in the frictionites of the Köfels Rockslide, which they ascribe to water vapor, either due to seeping of vadose water through rock fissures prior to the rock-slope failure, or due to dehydroxylation of the mica, which occurs at ~700°C (Alexiades and Jackson, 1967). Also, the existence and relative increase of pyrophyllite on sliding surfaces indicate hydrothermal alteration around 450°C (Schäbitz et al., 2015). The accumulation of pyrophyllite at the sliding surface results in reduced shear strength. Also, graphitization (crystallization of amorphous carbon) was recognized in slip zones as phase transformation, which implies frictional heating due to rapid sliding (Oohashi et al., 2011). Graphite is well known as an effective solid lubricant in fault zones with a friction coefficient as low as that of smectite, $\mu = 0.1$ (Oohashi et al., 2014).

DISCUSSION OF RESEARCH NEEDS

Processes during the disintegration phases of rock avalanches are beyond observation, and we have very few analogs that show pressure and temperature conditions inside rock avalanches. Thus, it is likely that we neglect important processes such as steam explosions, partial melting, chemical transitions, and material explosion processes at high pressures.

To systematically decipher relevant processes in rock avalanches, we propose that the energy balance needs to be considered more seriously, since it will help us to reveal energy-relevant processes that we would otherwise neglect. Here we propose to balance the primary energy input to the system constrained by the potential/kinetic energy of the moving rock masses ("Energy sources"). "Energy sinks" include heating, friction, inelastic collision, entrainment, compression during crustal deformation, chemical energy consumption, phase transition solid – fluid – gas, dust production and bouncing as well as sound and microseismicity, and momentum exchange between solid and fluid.

Using an energy balance approach, we can attribute proportions of the energy transmission to certain processes and we can rule out others. However, for this approach, we have to find ways to accurately constrain the 3D deposition temperature of the rock avalanche by new methods as has been exemplified in a few cases in this paper. The influence of the substrate on types and rates of energy dissipation during disintegration and during the flow represent major research gaps and ask for more studies. For the hazard assessment of rock avalanches, it makes sense not only to differentiate between energy sources and sinks, but also to separate processes that favor mobility and runout length from those which may consume or release energy but do not essentially contribute to the hazard potential. Furthermore, we need to transfer the achievements gained in qualitative assessment toward a more quantitative approach.

Future research in the field should focus on analyzing spatial patterns of disintegration using surface mapping and 3D subsurface reconnaissance of rock slide/avalanche deposits using geophysical methods at varying scales. Sedimentological analyses reveal abundant information on internal processes, for instance high-stress comminution preserved in fine-sediment signatures (Reznichenko et al., 2012). There is a great demand for study cases with petrographic analysis at microscopic scale (Weidinger et al., 2014), and for such with cross sections through the debris (Locat et al., 2006).

Future research in the laboratory should focus on the implementation of disintegration scenarios in large-scale analog models to help better understand the impact of disintegration and heating on runout length. This way, a conceptual physical (and chemical) model of rock-avalanche disintegration in time and space may be set up in a first step, followed by the implementation in benchmark one- and two-phase runout models.

CONCLUSION

(1) Due to the law of energy conservation we have a superior tool to decipher processes we have yet neglected in rock avalanches: heating, friction, inelastic collision, entrainment, compression crustal deformation, chemical energy consumption, phase transition solid – fluid – gas, dust production and bouncing as well as sound and microseismicity generation and momentum exchange.
(2) Energy dissipation is concentrated in the disintegration zone where energy estimations indicate considerable heating above 100°C of significant portions of the rock mass.
(3) The spatial pattern of heating is characteristic for individual types of movement ranging from concentrated heating by friction along defined sliding planes to diffuse clustered heating in crushing zones near to obstacles.
(4) Massive entrainment where large rockslides drive into, or override, valley sediments also evidently causes crushing and very likely significant heating.
(5) Massive energy dissipation may leave a distinct sedimentological signal detectable in compressive and extensional flow structures, melting or new mineral formation, rock-avalanche structure, material composition, brecciation and fine-sediment signature.

AUTHOR CONTRIBUTIONS

SK drafted the work, substantially contributed to the conception and design of the work, and acquisition and analysis of literature/data for the work. MK substantially contributed to the concept and revised the work critically for important intellectual content and provided approval for publication. Both authors contributed to the article and approved the submitted version.

ACKNOWLEDGMENTS

The authors thank Dr. Andreas von Poschinger (Bavarian Environmental Agency, Germany), Prof. John Clague (Simon Fraser University, British Columbia, Canada), and Dr. Anja

Dufresne (RWTH Aachen, Germany) for longtime and intense discussions on rock avalanches in general, and the Flims Rock Avalanche and Tschirgant Rock Avalanche in particular. We also acknowledge the contributions by three reviewers that helped to improve this manuscript.

REFERENCES

Aaron, J., and Hungr, O. (2016). Dynamic analysis of an extraordinarily mobile rock avalanche in the Northwest Territories, Canada. *Can. Geotech. J.* 53, 899–908. doi: 10.1139/cgj-2015-0371

Aaron, J., and McDougall, S. (2019). Rock avalanche mobility: the role of path material. *Eng. Geol.* 257:105126. doi: 10.1016/j.enggeo.2019.05.003

Aaron, J., McDougall, S., Moore, J. R., Coe, J. A., and Hungr, O. (2017). The role of initial coherence and path materials in the dynamics of three rock avalanche case histories. *Geoenviron. Disasters* 4:5.

Abele, G. (1974). Bergsturze in den Alpen – Ihre Verbreitung, Morphologie und Folgeerscheinungen. *Wiss. Alpenvereinshefte* 25:247.

Abele, G. (1997). Rockslide movement supported by the mobilization of groundwater-saturated valley floor sediments. *Z. Geomorphol.* 41, 1–20.

Alexiades, C., and Jackson, M. (1967). Chlorite determination in clays of soils and mineral deposits. *Am. Mineral. J. Earth Planet. Mater.* 52, 1855–1873.

Anders, M. H., Fouke, B. W., Zerkle, A. L., Tavarnelli, E., Alvarez, W., and Harlow, G. E. (2010). The role of calcining and basal fluidization in the long runout of carbonate slides: an example from the Heart Mountain slide block, Wyoming and Montana, USA. *J. Geol.* 118, 577–599. doi: 10.1086/656383

Bartelt, P., Buser, O., and Platzer, K. (2006). Fluctuation-dissipation relations for granular snow avalanches. *J. Glaciol.* 52, 631–643. doi: 10.3189/172756506781828476

Bessette-Kirton, E. K., Coe, J. A., and Zhou, W. (2018). Using stereo satellite imagery to account for ablation, entrainment, and compaction in volume calculations for rock avalanches on glaciers: application to the 2016 Lamplugh rock avalanche in Glacier Bay National Park, Alaska. *J. Geophys. Res. Earth Surf.* 123, 622–641. doi: 10.1002/2017jf004512

Bieniawski, Z. (1967). Mechanism of brittle failure of rock Part I-Theory of fracture process. *Int. J. Rock Mech. Min. Sci. Geomech. Abstr.* 4, 395–406.

Bowman, E. T., Take, W. A., Rait, K. L., and Hann, C. (2012). Physical models of rock avalanche spreading behaviour with dynamic fragmentation. *Can. Geotech. J.* 49, 460–476. doi: 10.1139/t2012-007

Buser, O., and Bartelt, P. (2009). Production and decay of random kinetic energy in granular snow avalanches. *J. Glaciol.* 55, 3–12. doi: 10.3189/002214309788608859

Calhoun, N. C., and Clague, J. J. (2018). Distinguishing between debris flows and hyperconcentrated flows: an example from the eastern Swiss Alps. *Earth Surf. Process. Landforms* 43, 1280–1294. doi: 10.1002/esp.4313

Carslaw, H. S., and Jaeger, J. C. (1959). *Conduction of Heat in Solids*. Oxford: Oxford University Press.

Christen, M., Kowalski, J., and Bartelt, P. (2010). RAMMS: numerical simulation of dense snow avalanches in three-dimensional terrain. *Cold Regions Sci. Technol.* 63, 1–14. doi: 10.1016/j.coldregions.2010.04.005

Coe, J. A., Baum, R. L., Allstadt, K. E., Kochevar, B. F. Jr., Schmitt, R. G., Morgan, M. L., et al. (2016). Rock-avalanche dynamics revealed by large-scale field mapping and seismic signals at a highly mobile avalanche in the West Salt Creek valley, western Colorado. *Geosphere* 12, 607–631. doi: 10.1130/ges01265.1

Crosta, G., Imposimato, S., and Roddeman, D. (2009). Numerical modelling of entrainment/deposition in rock and debris-avalanches. *Eng. Geol.* 109, 135–145. doi: 10.1016/j.enggeo.2008.10.004

Crosta, G. B., Frattini, P., and Fusi, N. (2007). Fragmentation in the Val Pola rock avalanche, Italian Alps. *J. Geophys. Res. Earth Surf.* 112:F01006. doi: 10.1029/2005JF000455

Davies, T., and McSaveney, M. (2012). "Mobility of long-runout rock avalanches," in *Landslides: Types, Mechanisms and Modeling*, ed. J. J. Clague (Cambridge: Cambridge University Press), 50–58. doi: 10.1017/cbo9780511740367.006

Davies, T. R., and McSaveney, M. J. (2009). The role of rock fragmentation in the motion of large landslides. *Eng. Geol.* 109, 67–79. doi: 10.1016/j.enggeo.2008.11.004

De Blasio, F. V., and Medici, L. (2017). Microscopic model of rock melting beneath landslides calibrated on the mineralogical analysis of the Köfels frictionite. *Landslides* 14, 337–350. doi: 10.1007/s10346-016-0700-z

Deline, P., Hewitt, K., Reznichenko, N., and Shugar, D. (2015). "Rock avalanches onto glaciers," in *Landslide Hazards, Risks and Disasters*, eds J. F. Shroder, and T. Davies (Amsterdam: Elsevier), 263–319. doi: 10.1016/b978-0-12-396452-6.00009-4

Dufresne, A., and Davies, T. R. (2009). Longitudinal ridges in mass movement deposits. *Geomorphology* 105, 171–181. doi: 10.1016/j.geomorph.2008.09.009

Dufresne, A., Prager, C., and Clague, J. J. (2015). "Complex interactions of rock avalanche emplacement with fluvial sediments: field structures at the Tschirgant deposit, Austria," in *Engineering Geology for Society and Territory*, eds G. Lollino, A. Manconi, J. Clague, W. Shan, and M. Chiarle (Cham: Springer), 1707–1711. doi: 10.1007/978-3-319-09057-3_303

Eberhardt, E., Stead, D., and Coggan, J. (2004). Numerical analysis of initiation and progressive failure in natural rock slopes—the 1991 Randa rockslide. *Int. J. Rock Mech. Mining Sci.* 41, 69–87. doi: 10.1016/s1365-1609(03)00076-5

Erismann, T., Heuberger, H., and Preuss, E. (1977). Fused rock of kofels (tyrol) - frictionite generated by a Landslide. *Tschermaks Mineral. Petrogr. Mitteilungen* 24, 67–119. doi: 10.1007/Bf01081746

Erismann, T. H., and Abele, G. (2001). *Dynamics of Rockslides and Rockfalls*. Berlin: Springer.

Evans, S. G., Mugnozza, G. S., Strom, A. L., Hermanns, R. L., Ischuk, A., and Vinnichenko, S. (2006). "Landslides from massive rock slope failure and associated phenomena," in *Landslides from Massive Rock Slope Failure*, eds S.G. Evans, G. Scarascia Mugnozza, A. Strom, and R.L. Hermanns (Dordrecht: Springer), 03–52. doi: 10.1007/978-1-4020-4037-5_1

Fischer, K. (1999). *Massenbewegungen und Massentransporte in den Alpen als Gefahrenpotential: Symposion der Kommission für Geomorphologie der Bayerischen Akademie der Wissenschaften, München, am 24. und 25*. München: Borntraeger.

Ghaffari, H., Griffith, W., and Barber, T. (2019). Energy delocalization during dynamic rock fragmentation. *Geophys. J. Int.* 217, 1034–1046. doi: 10.1093/gji/ggz064

Habib, P. (1975). Production of gaseous pore pressure during rock slides. *Rock Mech.* 7, 193–197. doi: 10.1007/bf01246865

Haeberli, W., Buetler, M., Huggel, C., Friedli, T. L., Schaub, Y., and Schleiss, A. J. (2016). New lakes in deglaciating high-mountain regions–opportunities and risks. *Clim. Change* 139, 201–214. doi: 10.1007/s10584-016-1771-5

Haeberli, W., Huggel, C., Kääb, A., Zgraggen-Oswald, S., Polkvoj, A., Galushkin, I., et al. (2004). The Kolka-Karmadon rock/ice slide of 20 September 2002: an extraordinary event of historical dimensions in North Ossetia, Russian Caucasus. *J. Glaciol.* 50, 533–546. doi: 10.3189/172756504781829710

Hamdi, E., Romdhane, N. B., du Mouza, J., and Le Cleac'h, J. M. (2008). Fragmentation energy in rock blasting. *Geotech. Geol. Eng.* 26, 133–146.

Haug, ØT., Rosenau, M., Leever, K., and Oncken, O. (2016). On the energy budgets of fragmenting rockfalls and rockslides: insights from experiments. *J. Geophys. Res. Earth Surf.* 121, 1310–1327. doi: 10.1002/2014jf003406

Heim, A. (1932). *Landslides and Human Lives (Bergsturz und Menchenleben)*. Vancouver, BC: Bi-Tech Publishers.

Heuberger, H., Masch, L., Preuss, E., and Schröcker, A. (1984). Quaternary landslides and rock fusion in Central Nepal and in the Tyrolean Alps. *Mountain Res. Dev.* 4, 345–362.

Hewitt, K. (2006). "Rock avalanches with complex run out and emplacement, Karakoram Himalaya, Inner Asia," in *Landslides From Massive Rock Slope Failure*, eds S.G.Evans, G.S. Mugnozza, A. Strom, and R.L. Hermanns (Dordrecht: Springer), 521–550. doi: 10.1007/978-1-4020-4037-5_28

Hewitt, K., Clague, J. J., and Orwin, J. F. (2008). Legacies of catastrophic rock slope failures in mountain landscapes. *Earth Sci. Rev.* 87, 1–38. doi: 10.1016/j.earscirev.2007.10.002

Hu, W., Huang, R., McSaveney, M., Yao, L., Xu, Q., Feng, M., et al. (2019). Superheated steam, hot CO2 and dynamic recrystallization from frictional heat jointly lubricated a giant landslide: field and experimental evidence. *Earth Planet. Sci. Lett.* 510, 85–93. doi: 10.1016/j.epsl.2019.01.005

Hu, W., Huang, R., McSaveney, M., Zhang, X.-H., Yao, L., and Shimamoto, T. (2018). Mineral changes quantify frictional heating during a large low-friction landslide. *Geology* 46, 223–226. doi: 10.1130/g39662.1

Hu, W., and McSaveney, M. (2018). A polished and striated pavement formed by a rock avalanche in under 90 s mimics a glacially striated pavement. *Geomorphology* 320, 154–161. doi: 10.1016/j.geomorph.2018.08.011

Huggel, C. (2009). Recent extreme slope failures in glacial environments: effects of thermal perturbation. *Q. Sci. Rev.* 28, 1119–1130. doi: 10.1016/j.quascirev.2008.06.007

Huggel, C., Clague, J. J., and Korup, O. (2012). Is climate change responsible for changing landslide activity in high mountains? *Earth Surf. Process. Landforms* 37, 77–91. doi: 10.1002/esp.2223

Huggel, C., Gruber, S., Caplan-Auerbach, S., Wessels, R. L., and Molnia, B. F. (2008). "The 2005 Mt. Steller, Alaska, rock-ice avalanche: a large slope failure in cold permafrost," in *Proceedings of the 9th International Conference on Permafrost*, Alaska, 747–752.

Hungr, O. (2006). "Rock avalanche occurrence, process and modelling," in *Landslides from Massive Rock Slope Failure*, eds S.G.Evans, G.S. Mugnozza, A. Strom, and R.L. Hermanns (Dordrecht: Springer), 243–266. doi: 10.1007/978-1-4020-4037-5_14

Hungr, O., and Evans, S. G. (2004). Entrainment of debris in rock avalanches: an analysis of a long run-out mechanism. *Geol. Soc. Am. Bull.* 116, 1240–1252.

Hungr, O., Leroueil, S., and Picarelli, L. (2014). The Varnes classification of landslide types, an update. *Landslides* 11, 167–194. doi: 10.1007/s10346-013-0436-y

Imre, B., Laue, J., and Springman, S. M. (2010). Fractal fragmentation of rocks within sturzstroms: insight derived from physical experiments within the ETH geotechnical drum centrifuge. *Granular Matter* 12, 267–285. doi: 10.1007/s10035-009-0163-1

Iverson, R. M. (2016). Comment on "The reduction of friction in long-runout landslides as an emergent phenomenon" by Brandon C. Johnson et al. *J. Geophys. Res. Earth Surf.* 121, 2238–2242. doi: 10.1002/2016jf003979

Iverson, R. M., and Ouyang, C. (2015). Entrainment of bed material by Earth-surface mass flows: review and reformulation of depth-integrated theory. *Rev. Geophys.* 53, 27–58. doi: 10.1002/2013rg000447

Iverson, R. M., Reid, M. E., Logan, M., LaHusen, R. G., Godt, J. W., and Griswold, J. P. (2011). Positive feedback and momentum growth during debris-flow entrainment of wet bed sediment. *Nat. Geosci.* 4, 116–121. doi: 10.1038/ngeo1040

Johnson, B. C., Campbell, C. S., and Melosh, H. J. (2016). Reply to comment by Iverson on "The reduction of friction in long runout landslides as an emergent phenomenon". *J. Geophys. Res.* 121, 2243–2246. doi: 10.1002/2016jf004093

Knapp, S., Gilli, A., Anselmetti, F. S., Krautblatter, M., and Hajdas, I. (2018). Multistage rock-slope failures revealed in lake sediments in a seismically active Alpine region (Lake Oeschinen, Switzerland). *J. Geophys. Res.* 123, 658–677. doi: 10.1029/2017jf004455

Korup, O. (2005). Geomorphic hazard assessment of landslide dams in South Westland, New Zealand: fundamental problems and approaches. *Geomorphology* 66, 167–188. doi: 10.1016/j.geomorph.2004.09.013

Krautblatter, M., Funk, D., and Guenzel, F. (2013). Why permafrost rocks become unstable: a rock–ice-mechanical model in time and space. *Earth Surf. Process. Landforms* 38, 876–887. doi: 10.1002/esp.3374

Krautblatter, M., and Leith, K. (2015). "Glacier- and permafrost-related slope instabilities," in *The High-Mountain Cryosphere: Environmental Changes and Human Risks*, eds C. Huggel, M. Carey, J. J. Clague, and A. Kääb (Cambridge: Cambridge University Press), 147–165. doi: 10.1017/cbo9781107588653.009

Langlois, V. J., Quiquerez, A., and Allemand, P. (2015). Collapse of a two-dimensional brittle granular column: implications for understanding dynamic rock fragmentation in a landslide. *J. Geophys. Res.* 120, 1866–1880. doi: 10.1002/2014jf003330

Legros, F. (2006). "Landslide mobility and the role of water," in *Landslides from Massive Rock Slope Failure* (Dordrecht: Springer), 233–242.

Locat, P., Couture, R., Leroueil, S., Locat, J., and Jaboyedoff, M. (2006). Fragmentation energy in rock avalanches. *Can. Geotech. J.* 43, 830–851. doi: 10.1139/t06-045

Maddock, R. H. (1986). Frictional melting in landslide-generated frictionites (hyalomylonit) and fault-generated pseudotachylites. *Tectonophysics* 128, 151–153. doi: 10.1016/0040-1951(86)90316-1

McSaveney, M., and Davies, T. (2007). "Rockslides and their motion," in *Progress in Landslide Science*, eds K. Sassa, H. Fukuoka, F. Wang, and G. Wang (Dordrecht: Springer), 113–133. doi: 10.1007/978-3-540-70965-7_8

Mitchell, T. M., Smith, S. A., Anders, M. H., Di Toro, G., Nielsen, S., Cavallo, A., et al. (2015). Catastrophic emplacement of giant landslides aided by thermal decomposition: heart Mountain, Wyoming. *Earth Planet. Sci. Lett.* 411, 199–207. doi: 10.1016/j.epsl.2014.10.051

Nicoletti, P. G., and Sorriso-Valvo, M. (1991). Geomorphic controls of the shape and mobility of rock avalanches. *Geol. Soc. Am. Bull.* 103, 1365–1373. doi: 10.1130/0016-7606(1991)103<1365:gcotsa>2.3.co;2

Oohashi, K., Han, R., Hirose, T., Shimamoto, T., Omura, K., and Matsuda, T. (2014). Carbon-forming reactions under a reducing atmosphere during seismic fault slip. *Geology* 42, 787–790. doi: 10.1130/g35703.1

Oohashi, K., Hirose, T., and Shimamoto, T. (2011). Shear-induced graphitization of carbonaceous materials during seismic fault motion: experiments and possible implications for fault mechanics. *J. Struct. Geol.* 33, 1122–1134. doi: 10.1016/j.jsg.2011.01.007

Ouchterlony, F., Nyberg, U., Olsson, M., Bergqvist, I., Granlund, L., and Grind, H. (2004). Where does the explosive energy in rock blasting rounds go? *Sci. Technol. Energ. Mater.* 65, 54–63.

Pavoni, N. (1968). Über die Entstehung der Kiesmassen im Bergsturzgebiet von Bonaduz-Reichenau (Graubünden). *Ecol. Geol. Helvetica* 6, 494–500.

Pollet, N., Cojean, R., Couture, R., Schneider, J.-L., Strom, A. L., Voirin, C., et al. (2005). A slab-on-slab model for the Flims rockslide (Swiss Alps). *Can. Geotech. J.* 42, 587–600. doi: 10.1139/t04-122

Pollet, N., and Schneider, J. L. M. (2004). Dynamic disintegration processes accompanying transport of the Holocene Flims sturzstrom (Swiss Alps). *Earth Planet. Sci. Lett.* 221, 433–448. doi: 10.1016/s0012-821x(04)00071-8

Preuth, T., Bartelt, P., Korup, O., and McArdell, B. W. (2010). A random kinetic energy model for rock avalanches: eight case studies. *J. Geophys. Res.* 115: F03036. doi: 10.1029/2009JF001640

Pudasaini, S. P., and Krautblatter, M. (2014). A two-phase mechanical model for rock-ice avalanches. *J. Geophys. Res.* 119, 2272–2290. doi: 10.1002/2014jf003183

Pudasaini, S. P., and Mergili, M. (2019). A multi-phase mass flow model. *J. Geophys. Res.* 124, 2920–2942. doi: 10.1029/2019jf005204

Rait, K. L., and Bowman, E. T. (2010). "Dynamic fragmentation in rock avalanches: a numerical model of micromechanical behaviour," in *Numerical Methods in Geotechnical Engineering*, eds T. Benz and S. Nordal (London: Taylor & Francis Group), 435–440. doi: 10.1201/b10551-80

Reznichenko, N. V., Davies, T. R. H., Shulmeister, J., and Larsen, S. H. (2012). A new technique for identifying rock avalanche-sourced sediment in moraines and some paleoclimatic implications. *Geology* 40, 319–322. doi: 10.1130/g32684.1

Schäbitz, M., Janssen, C., Wirth, R., and Dresen, G. (2015). "Microstructural and geochemical evolution of sliding surfaces in landslides and comparisons with crustal fault zones," in *Proceedings of the EGU General Assembly 2015*, Vienna.

Scheidegger, A. E. (1973). On the prediction of the reach and velocity of catastrophic landslides. *Rock Mech.* 5, 231–236. doi: 10.1007/bf01301796

Schneider, D., Bartelt, P., Caplan-Auerbach, J., Christen, M., Huggel, C., and McArdell, B. W. (2010). Insights into rock-ice avalanche dynamics by combined analysis of seismic recordings and a numerical avalanche model. *J. Geophys. Res.* 115:F04026. doi: 10.1029/2010JF001734

Schramm, J. M., Weidinger, J. T., and Ibetsberger, H. J. (1998). Petrologic and structural controls on geomorphology of prehistoric Tsergo Ri slope failure, Langtang Himal, Nepal. *Geomorphology* 26, 107–121. doi: 10.1016/s0169-555x(98)00053-1

Sosio, R., Crosta, G. B., Chen, J. H., and Hungr, O. (2012). Modelling rock avalanche propagation onto glaciers. *Q. Sci. Rev.* 47, 23–40. doi: 10.1016/j.quascirev.2012.05.010

Spray, J. G. (1992). A physical basis for the frictional melting of some rock-forming minerals. *Tectonophysics* 204, 205–221. doi: 10.1016/0040-1951(92)90308-s

Spray, J. G. (2005). Evidence for melt lubrication during large earthquakes. *Geophys. Res. Lett.* 32:L07301. doi: 10.1029/2004GL022293

Turcotte, D. L. (1997). *Fractals and Chaos in Geology and Geophysics*. Cambridge: Cambridge university press.

Voight, B., and Faust, C. (1982). Frictional heat and strength loss in some rapid landslides. *Geotechnique* 32, 43–54. doi: 10.1680/geot.1982.32.1.43

Walter, F., Amann, F., Kos, A., Kenner, R., Phillips, M., de Preux, A., et al. (2020). Direct observations of a three million cubic meter rock-slope collapse with almost immediate initiation of ensuing debris flows. *Geomorphology* 351:106933. doi: 10.1016/j.geomorph.2019.106933

Wang, S., Sloan, S., Liu, H., and Tang, C. (2011). Numerical simulation of the rock fragmentation process induced by two drill bits subjected to static and dynamic (impact) loading. *Rock Mech. Rock Eng.* 44, 317–332. doi: 10.1007/s00603-010-0123-4

Weidinger, J. T., and Korup, O. (2009). Frictionite as evidence for a large Late Quaternary rockslide near Kanchenjunga, Sikkim Himalayas, India - Implications for extreme events in mountain relief destruction. *Geomorphology* 103, 57–65. doi: 10.1016/j.geomorph.2007.10.021

Weidinger, J. T., Korup, O., Munack, H., Altenberger, U., Dunning, S. A., Tippelt, G., et al. (2014). Giant rockslides from the inside. *Earth Planet. Sci. Lett.* 389, 62–73. doi: 10.1016/j.epsl.2013.12.017

Whittall, J., Eberhardt, E., and McDougall, S. (2017). Runout analysis and mobility observations for large open pit slope failures. *Can. Geotech. J.* 54, 373–391. doi: 10.1139/cgj-2016-0255

Wilson, B., Dewers, T., Reches, Z. E., and Brune, J. (2005). Particle size and energetics of gouge from earthquake rupture zones. *Nature* 434, 749–752. doi: 10.1038/nature03433

Yarnold, J. C. (1993). Rock-avalanche characteristics in dry climates and the effect of flow into lakes: insights from mid-Tertiary sedimentary breccias near Artillery Peak, Arizona. *Geol. Soc. Am. Bull.* 105, 345–360. doi: 10.1130/0016-7606(1993)105<0345:racidc>2.3.co;2

Zhang, M., Wu, L., Zhang, J., and Li, L. (2019). The 2009 Jiweishan rock avalanche, Wulong, China: deposit characteristics and implications for its fragmentation. *Landslides* 16, 893–906. doi: 10.1007/s10346-019-01142-6

Zhang, Z.-X. (2016). *Rock Fracture and Blasting: Theory and Applications*. Oxford: Butterworth-Heinemann.

Zhao, T., Crosta, G. B., Utili, S., and De Blasio, F. V. (2017). Investigation of rock fragmentation during rockfalls and rock avalanches via 3-D discrete element analyses. *J. Geophys. Res.* 122, 678–695. doi: 10.1002/2016jf004060

Conflict of Interest: The authors declare that the research was conducted in the absence of any commercial or financial relationships that could be construed as a potential conflict of interest.

frontiers
in Earth Science

ORIGINAL RESEARCH
published: 14 July 2020
doi: 10.3389/feart.2020.00211

Application Assessments of Using Scarp Boundary-Fitted, Volume Constrained, Smooth Minimal Surfaces as Failure Interfaces of Deep-Seated Landslides

Chih-Yu Kuo[1]*, *Pi-Wen Tsai*[2], *Yih-Chin Tai*[3], *Ya-Hsin Chan*[1], *Rou-Fei Chen*[4] and *Ching-Weei Lin*[5]

[1] Research Center for Applied Sciences, Academia Sinica, Taipei, Taiwan, [2] Department of Mathematics, National Taiwan Normal University, Taipei, Taiwan, [3] Department of Hydraulic and Ocean Engineering, National Cheng Kung University, Tainan, Taiwan, [4] Department of Geology, Chinese Culture University, Taipei, Taiwan, [5] Department of Earth Sciences, National Cheng Kung University, Tainan, Taiwan

OPEN ACCESS

Edited by:
Tim Davies,
University of Canterbury, New Zealand

Reviewed by:
Andrea Zanchi,
University of Milano-Bicocca, Italy
Susanta Kumar Samanta,
Jadavpur University, India

***Correspondence:**
Chih-Yu Kuo
cykuo06@gate.sinica.edu.tw

Specialty section:
This article was submitted to
Structural Geology and Tectonics,
a section of the journal
Frontiers in Earth Science

Received: 25 February 2020
Accepted: 20 May 2020
Published: 14 July 2020

Citation:
Kuo C-Y, Tsai P-W, Tai Y-C, Chan Y-H, Chen R-F and Lin C-W (2020) Application Assessments of Using Scarp Boundary-Fitted, Volume Constrained, Smooth Minimal Surfaces as Failure Interfaces of Deep-Seated Landslides. Front. Earth Sci. 8:211. doi: 10.3389/feart.2020.00211

More than 9,000 potential deep-seated landslide sites in the mountain ranges of Taiwan have been identified by a series of renewed governmental hazard mitigation initiatives after the 2009 Morakot typhoon. Among these sites, 186 sites have protection targets where thorough mitigation strategies are to be implemented. One of the important tasks in the hazard mitigation initiative is to estimate the volume, failure interface and related quantities of each landslide site. In addition, with this number of sites, an automated tool is needed to generate predictions at low operational costs. We propose to use volume-constrained smooth minimal surfaces to approximate the landslide failure interfaces. A volume-constrained smooth minimal surface in the current context is defined as a differentiable surface that encloses a given landslide volume with the minimal surface area. Although the stratigraphy and geological structures are omitted, the smooth minimal surface method is verified with 24 known landslides and is shown to be able to generate acceptable, approximated failure interfaces. A collection of assessment indices is employed to measure the fitness of the predictions. Finally, the prediction fitness vs. the landslide scarp geometry is investigated.

Keywords: deep-seated landslide, landslide volume-area relation, landslide failure surface prediction, FreeFem++ IpOPT, failure surface accuracy assessment

1. INTRODUCTION

Deep-seated landslides pose severe threats to human lives and property. Typhoon Morakot struck Taiwan in 2009 which brought approximately 2,500 mm of precipitation in 4 days to the southern parts of the island and triggered numerous landslides, debris flows and vast flooded areas. This catastrophic extreme climatic event caused more than 22,000 landslides. Among these mountainous hazards, more than 320 landslides were found in scarp areas larger than 10 ha (Lin et al., 2011). These large-volume landslides often lead to composite casualties. For example, the Hsiaolin landslide, after sweeping through the village in its course, formed a short-lived blockage dam, and the continuous inflow triggered follow-up dam-break debris flows (Dong et al., 2011; Li et al., 2011; Tsou et al., 2011). Similar rainfall triggered large scale deep-seated landslide examples and related research include those reported by Cardinali et al. (2002), Roering et al. (2005), Baroň et al. (2011), Chigira (2011), Xu et al. (2015), Vallet et al. (2015), and Lee et al. (2018).

Having learned from the Morakot typhoon landslides, Taiwan's government authorities officially defined the deep-seated landslides for administrative purposes according to their geometric measurements: volumes larger than 1×10^6 m^3, areas larger than 100 ha or depths deeper than 10 m (Lin et al., 2011; Chen et al., 2017). Using geometric measurements to classify the deep-seated landslides simplifies the administrative process and has been suggested in the literature (Roering et al., 2005; Lo, 2017). There are in fact other definitions of deep-seated landslides in different research contexts. For example, geologists may refer the term to slow moving large-scale landslides with failure surfaces occurring deep in a rock bed, or geotechnical engineers may refer it to landslides with failure surfaces below the underground water table. Nevertheless, as literally suggested, deep-seated landslides are usually associated with large slide volumes such that, in the present paper, we adopt the simple geometric definition for this type of landslides. Because of the large scale of the potential deep-seated landslides, the spatial geological variations, weathering effects and orogenic activities contribute to forming these sites. During long-term evolutionary processes, topographic features, such as crowns, bulges, and trenches, develop, and currently, these features can be detected by modern remote sensing techniques (Varnes, 1978; Chigira and Kiho, 1994; Chigira et al., 2013; Crosta et al., 2013; Lo, 2017). In a series of hazard mitigation initiatives implemented by the government starting from 2010 (Central Geological Survey, 2010) and continuing into the present (Soil Water Conserv. Bureau, 2017; Soil Water Conserv. Bureau, 2018), in which other sequential projects can be checked, airborne light detection and ranging (LiDAR), various satellite synthetic-aperture radar (SAR), and field investigations have been combined to survey the topographic surface activities (Lin et al., 2013, 2014; Tseng et al., 2013; Chen et al., 2015; Wu et al., 2017). Through these efforts, the scarp boundaries of the deep-seated landslides are identified according to the surface features. More than 9,000 potential deep-seated landslide sites have been found, and among them, 186 sites have protection targets (**Figure 1**). In the figure, a close-up view of ten sites in Ren'-ai Township, Nantou County, is shown. Along this direction, assessments of the landslide volume and influence area are to follow hazard mitigation planning.

In traditional geological engineering approaches, the factor of safety of the potential landslide site will then be calculated by using slope stability tools. The most well-known methods are the those based on the limit equilibrium concept, published by Bishop (1955), Mogenstern and Price (1965), and Janbu (1973). In these methods, the slope body above the prescribed failure interface is discretized into a number of vertical slices (free bodies), and a system of algebraic equations is derived according to the force and moment equilibrium, with an additional proposition of internal forces as closure conditions. Because the failure interface is a presumed input parameter in these limit equilibrium methods, there are a few empirical strategies for proposing the interfaces. These strategies include circular, piecewise linear, and other methods, and the choice is made according to the geological condition of the investigated site. The circular failure interface is the most widely employed because this shape is easily parameterizable and agrees with a large portion of common observations. Consequently, automatic iterative search schemes for the least stable interface are implemented in many analysis computation tools (e.g., Siegel, 1978). Once the least stable failure interface is obtained, the landslide depth and 2D volume can be estimated.

Although the analysis is convenient and straightforward, 2D slope stability can be performed on only one or a few heuristically selected representative profiles for each landslide site. Because of this limitation, the analysis may not provide sufficient information for deep-seated landslides in estimating landslide-influenced areas. For this purpose, the 3D scarp depth distribution of the slide mass, for example, is one of the essential quantities required to estimate the runout and spread of the landslide, and it is particularly important for rapid large-scale avalanches, whose motion can be largely influenced by the topographic conditions of the terrain (Kuo et al., 2011; Luca et al., 2016; Tai et al., 2019), and the references therein.

The concept of the factor of safety has long been the key concept in slope stabilization plans. Since the wide deployment of the aforementioned 2D methods, there have also been attempts to extend the slope stability analysis to general 3D terrains. Similar to the 2D limit equilibrium formulation, most of these methods require a priori failure surface; the derived system of equations is a statically indeterminate system, and additional conditions are needed to solve it. For example, in a study by Leshchinsky and Huang (1992a) and Leshchinsky and Huang (1992b), the landslide mass is assumed symmetric and variational optimization is adopted for searching the minimum factor of safety. Ignoring the shear stresses in the internal landslide mass (Ugai, 1985) showed that the failure profile is circular along the sliding direction. A two-directional moment equilibrium method was proposed by Huang and Tsai (2000) and Huang et al. (2002), which can directly determine the sliding direction, instead of presuming a sliding direction. Further improvements are made by including the complete momentum and moment equilibrium conditions (Zheng, 2012; Jiang and Zhou, 2018), in which examples of practical 3D applications are demonstrated. In the group of slope stability analysis methods, Hungr noted that the unbalanced force in the transverse direction of the potential landslide mass is responsible for the errors in the factor of safety (Hungr, 1987; Hungr et al., 1989). In contrast to the limit equilibrium concept, elasto-plastic approach is a full determinant method (Griffiths and Lane, 1999). The adoption of the full determinant method requires more complete underground material parameters and stratigraphic details, such that fitting the failure surface obtained by this type of method to the identified landslide scarp outlines may involve a series of procedural justifications of the material parameters and geological conditions. It has a different mechanical complexity beyond the present consideration and is not pursued further here.

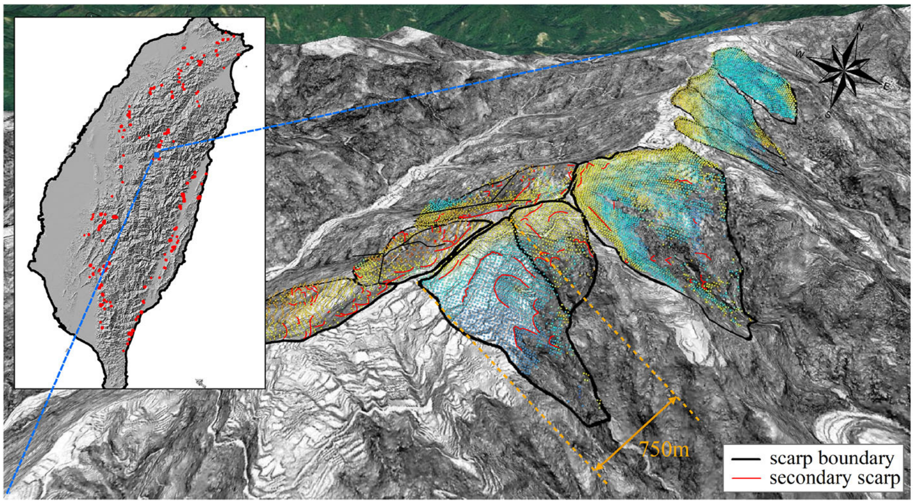

FIGURE 1 | The distribution of the 186 identified potential deep-seated landslide sites in Taiwan (inset panel, Soil Water Conserv. Bureau, 2018), and 10 examples of the scarp boundaries of the potential deep-seated landslides in Ren'-ai Township, Nantou County (Central Geological Survey, 2010). The dots in the scarp areas represent the line-of-sight deformation obtained by using the temporarily coherent point interferometry SAR (TCPInSAR) technique (Chen et al., 2017). Note that the length scale varies according to the 3D perspective.

Because the limit equilibrium approach for slope stability analysis yields a statically indeterminant system, additional empirical conditions, the failure surface and internal forces are needed to calculate the factor of safety. Unlike the 2D cases, there is a lack of systematic, convenient and commonly applied ways to form the 3D failure interfaces that fit the observed landslide scarps. However, simple spherical-shaped failure interfaces are often used as illustrative applications in developing 3D slope stability methods (Xing, 1988; Lam and Fredlund, 1993; Huang et al., 2002). Treating spherical surface sections as failure interface elements, a searching scheme has been proposed to construct the regional distribution of the factor of safety (Reid et al., 2000, 2001). Although the method does not focus on finding precise 3D matches of landslide scarps for individual sites, it has become increasingly popular in creating landslide susceptibility maps (Reid et al., 2015; Tran et al., 2018; Zhang and Wang, 2019).

In the examples of the identified potential deep-seated landslide sites in **Figure 1**, we can see that the scarp areas are identified by the closed polygons and the line-of-sight deformation obtained by using the temporarily coherent point interferometry SAR (TCPInSAR) technique somewhat indicates the landslide activity (Chen et al., 2017). In addition due to the large area that can cover topographic heterogeneous landscapes, each landslide site may contain multiple secondary failure structures, e.g., the cracks and minor scarps in **Figure 1** (Central Geological Survey, 2010). In landslide hazard mitigation plans with these types of information, a tool that it is able to generate 3D failure interfaces, conform with the surface scarps and provide related depth information for the landslide mass is required. Such a tool also provides great benefits for landslide sites, of which multiple secondary hazard scenarios are to be studied and managed. Furthermore, with the massive number of 186 potential landslide sites, the tool should be automated so that it can be operated at low costs.

As a tradeoff, the tool is aimed at providing predictions with satisfactory accuracy at small operational efforts but not necessarily with high degrees of precision. In this regard, we propose a simple method for computing the failure interfaces of deep-seated landslides, that is based on the minimization of a smooth surface that encloses a given landslide volume with the specified scarp boundary. The concept arises from the observations that (1), the scarp boundaries of potential deep-seated landslide sites often develop over time and become observable on the surface, for example crown fissures and flank scarps, and (2), landslide volume-area relations can be used to determine the volume from the scarp area. As a result, the average landslide depth is well-constrained, and the 3D failure interface and slide volume can be obtained.

In the proposed method, the geological settings and hydrogeological conditions of each landslide site are neglected. Geological settings include the rock texture, lithological stratas, rock cleavage or joint orientations, etc. These factors affect the intrinsic structure of the failure surfaces and landslide failure pattern. On the other hand, the hydrogeolocal conditions include the rainfall and underground water hydrology, which alter the force balance condition of the slide mass and trigger the landslide. Both geological settings and hydrogeological conditions are site specific details which lead to the deviations of the actual landslide failure surfaces from the predicted. However, to construct these details even for a single site may require extensive resources and investigations such that full coverage surveys and hazard monitoring for a population of landslides become virtually impossible. Under these circumstances, we defer the adoptation of any site specific detail to the present method.

Hence, it is an important task to establish the accuracy baseline of the method in the present paper, such that the paper is organized as follows: A brief introduction to the landslides used in the assessments is presented in section 2; The smooth minimal surface method and statistical assessment indices are described in sections 3 and 4, respectively; the applications of the method to two landslides and two conceptual examples are detailed in section 5 and **Appendix 1**, respectively, which includes the comparison of the predicted landslide failure interfaces to the actual failure interfaces and calculations of the assessment indices. Then, the application set is extended to include a total of 24 landslides, and their assessment indices are tabulated in section 6. With this amount of data, the accuracy bounds can be inferred.

2. LANDSLIDES IN THE STUDY AREA

In total, 24 deep-seated landslides were selected in the present study (Lin et al., 2011). They were all triggered by the excessive rainfall of the Morakot typhoon and are distributed in three different catchment areas in the southwest mountainous range of Taiwan. The first group, containing 11 sites, is located in the Cishan River catchment area, Jiaxian District, Kaohsiung City, as shown in **Figure 2**. All these landslides have areas larger than 10 ha, maximum depths over 10 m and, according to the definition from the Taiwanese government, are classified as deep-seated landslides. Among them, the sites labeled with HLIN prefixes are the scarps associated with the Hsiaolin landslides (Kuo et al., 2011; Tsou et al., 2011; Tai et al., 2019). The landslides are defined by using the 2005 and 2010 LiDAR 1 m resolution digital elevation maps (DEMs). The second and third groups of landslides are identified by the DF054 and DF081 prefixes, respectively (**Figure 3**). DF054 is in the Longjiao River catchment, Dapu Township, Chiayi County, and DF081 is in the Laonung River catchment, Maolin District, Kaohsiung City.

The geological structure and stratigraphy of these catchment areas are very briefly reviewed here as background information. Because of space limits, the geological maps of the three catchment areas are relegated to the **Supplementary Materials** of the paper and are made by referencing (Fei and Chen, 2013). To summarize, the landslide sites of the first group are distributed in three types of surface strata in the Cishan catchment area: Hunghuatzu Formation, Changchihkeng Formation, and Tangenshan Sandstone. These units are arranged chronologically, with the oldest formed in the late Miocene. The landslide sites of DF054 are in the Tangenshan Sandstone and Ailiaochiao Formation (early Pliocene). They consist of sedimentary rocks and are mainly composed of sandstones and shales, in which marine microfossils commonly occur. The third group, the DF081 landslides, is within Chaochou Formation, which is middle Miocene in age and occasionally interlaces with quartzite.

The landslide volumes ($\mathcal{V}$) and areas (Ω_p)[1] of the landslides are tabulated in **Table 1** and the data are plotted in **Figure 4A**. In the figure, the regression model is drawn and compared to the well-known equation from Guzzetti et al. (2009) and Klar et al. (2011). It is found that the present 24 landslides agree excellently with the fitted regression line. With these two quantities, we can calculate the equivalent radius: $\mathcal{R} = \sqrt{\Omega_p/\pi}$[2]. The characteristic length scale $2\mathcal{R}$, which is the equivalent diameter, will be used as the normalization length factor for statistical quantities varying in the horizontal or slopewise directions, such as the distance of the gravity centers between the actual and predicted landslide volume. In addition, two additional non-dimensional geometric parameters, the roundness $\mathfrak{r}_r$ and the sphericity $\mathfrak{r}_s$, can be defined with these measurements and the scarp boundaries.

We use standard mathematical definitions to define the two parameters. The roundness is defined as the ratio between the radius of the maximum inscribed circle of the scarp and that of the minimum circumscribed circle. Its values range between 0 and 1, with the two extreme values corresponding to an infinitely thin and perfectly circular shapes, respectively. For ellipses, the roundness reduces to the aspect ratio between the width and length. With this analogy, we can associate the roundness to the landslide aspect ratio, which commonly appears in the landslide literature. By adopting this general definition, calculation ambiguities for scarps with complicated shapes can be avoided. On the other hand, the sphericity $\mathfrak{r}_s$ is defined as the ratio of the surface area of a sphere of a volume $\mathcal{V}$ to the total surface area of the landslide mass $\mathcal{S}_0 + \mathcal{S}_b$ (the sum of the free surface $\mathcal{S}_0$ and the failure interface areas $\mathcal{S}_b$), i.e., $\mathfrak{r}_s = \pi^{1/3}(6\mathcal{V})^{2/3}/(\mathcal{S}_0 + \mathcal{S}_b)$. Its value also ranges from 0, an infinitely thin volume, to 1, a perfect sphere. Because the landslide thickness is usually much smaller than the other spanwise dimensions, the sphericity becomes a factor involving the landslide thickness and the slope[3]. These two parameters in the above definitions have long been applied in various landslide studies but have different terminologies, such as the width-length ratio and the depth-length ratio (Taylor et al., 2018).

There appears to be a relation between the roundness and sphericity with the present landslide inventory (**Figure 4B**). The data are somewhat evenly distributed in the range of the roundness and sphericity; i.e., no favorable clustering spots of data are found. Instead, the sphericity generally increases with increasing roundness. Among the sites, FID12 is likely a statistical outlier because of the distinctive gap between it and the other data. Inspecting the site in **Figure 2**, we find that the scarp boundary of FID12 appears to have a peculiar shape, colloquially a dumbbell shape, with landslide mass biasedly distributed at both end lobes but its relative roundishness reduces the sphericity. The site is likely composed of two distinguished landslides instead of an integrated one. We, however, do not perform further manipulations on this site other than simply exclude it from the accuracy assessments in section 6.

The other important landslide geometric parameters, such as the mean and maximum depths are calculated and listed in **Table 2** for facilitating the later accuracy assessments with the failure interface predictions. The related discussion will resume

---

[1] In common geological practice, Ω_p is measured on the horizontal projection of the landslide scarp, cf. **Figure 5**.

[2] $\mathcal{R}$, thus, is also defined on the horizontal projection plane, cf. **Figure 5**.

[3] Under the shallowness assumption, the total surface area $\mathcal{S}_0+\mathcal{S}_b$ is approximately $2\Omega_p$ divided by the directional cosine of the slope.

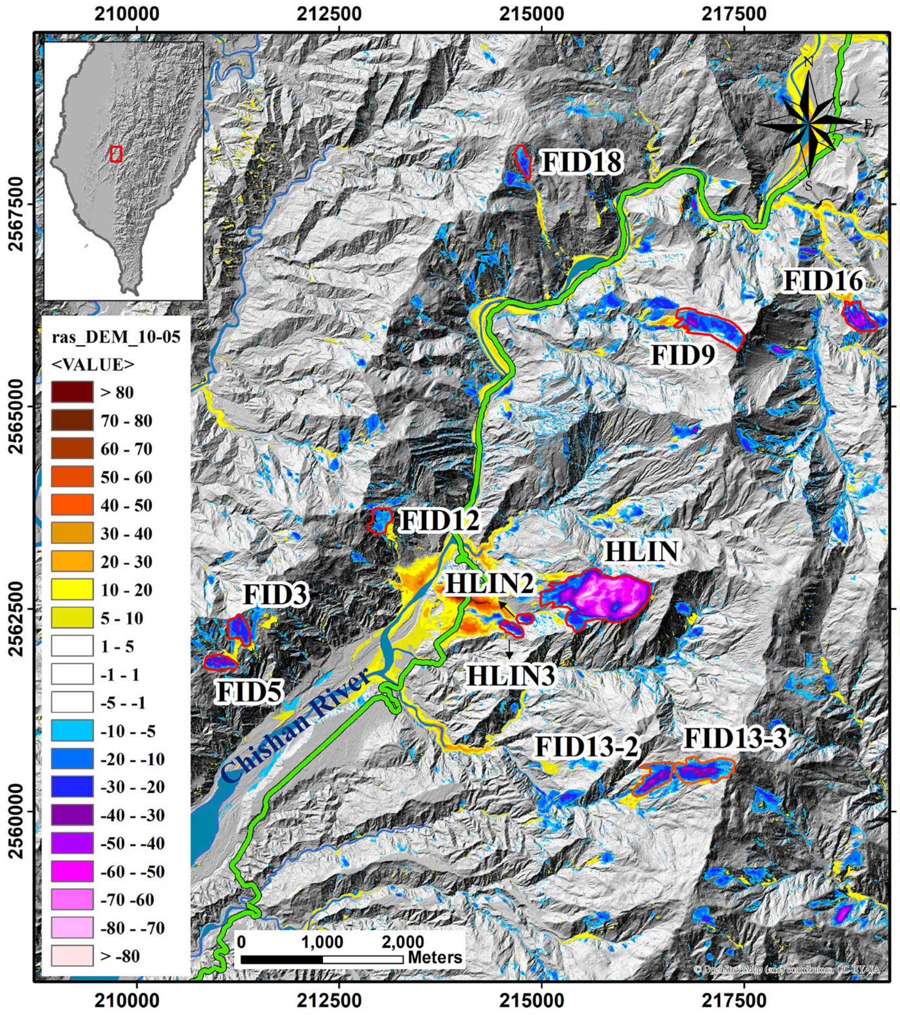

FIGURE 2 | Landslides in the Chishan River catchment, Jiaxian District, Kaohsiung City (Central Geological Survey, 2010). Negative values of the color legends indicate landslide scarp depths and the positive values indicate the deposit thickness in meters. The HLIN prefixes mark the Hsiaolin landslide and its associated landslides. The sites outlined in red solid lines are the deep-seated landslides investigated in the present study. The TWD97 coordinate system is used.

in section 6, after the description of the method of the smooth minimal surface, assessment indices and casewise applications.

3. SMOOTH MINIMAL SURFACE

Unlike the full mechanical approach involving fracturing or plasticity, the failure interface is not a determined result but a prescribed prerequisite. Based on observations, circular (2D) or spherical (3D) shaped failure surface profiles are usually applied for slopes with homogeneous and isotropic materials. To fit the application scenario, we relax the surface to a smooth minimal surface. In our application, the minimal smooth surface is obtained by giving an assumed failure volume $\mathcal{V}$ with the constraint that its boundary on the free surface matches that from geological field investigations. This type of surface is chosen because it has a close relation to the spherical failure surfaces in 3D slope slability analysis and can degenerate to the spherical surfaces for some special cases, cf. **Appendix 1**. Therefore it may also inherit the same property that the method fits better for slopes with isotropic and homogenous materials, following the same reasons of the traditional slope stability analysis.

Determining the smooth minimal surface is an optimization process. Let (x, y, z) be the Cartesian coordinates with z vertically pointing upwards, and let the failure interface $z_b \equiv z_b(x, y)$ be a smooth differentiable surface, as shown in **Figure 5**. Mathematically, the area of the surface can be calculated as

$$\mathcal{S}(z_b) = \int \sqrt{1 + ||\nabla z_b||^2}\, d\Omega_p, \tag{1}$$

such that the minimum surface can be acquired by minimizing (1) by varying z_b; i.e.,

$$\mathcal{S}_b = \min_{z_b} \mathcal{S}, \tag{2}$$

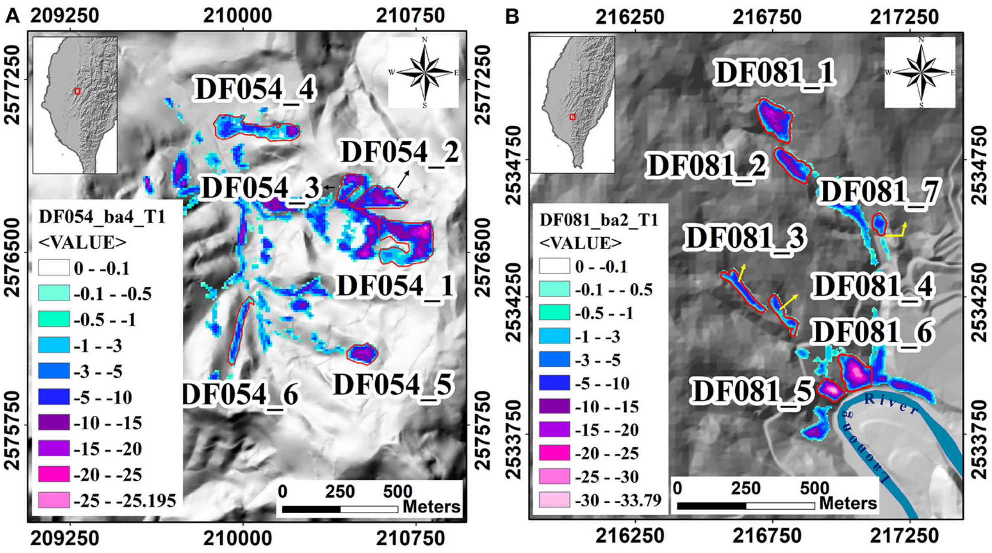

FIGURE 3 | Landslides in **(A)** the DF054 area, in the Longjiao River catchment, Dapu Township, Chiayi County and **(B)** the DF081 area in the Laonung River catchment, Maolin District, Kaohsiung City (Central Geological Survey, 2010). Negative values of the color legends indicate landslide scarp depths and the positive values indicate the deposit thickness in meters. The sites outlined in red solid lines are the deep-seated landslides investigated in the present study. The TWD97 coordinate system is used.

TABLE 1 | Landslide volume, area, equivalent radius, roundness, and sphericity.

Id	V, (m^3)	Ω_p, (m^2)	R, (m)	$\mathfrak{r}_r$	$\mathfrak{r}_s$
HLIN	21,100,000	628,000	447.0	0.413	0.255
HLIN-2	582,000	31,700	100.0	0.400	0.444
HLIN-3	288,000	19,900	79.6	0.538	0.462
FID3	1,420,000	72,800	152.0	0.588	0.353
FID5	1,150,000	58,000	136.0	0.442	0.362
FID9	2,900,000	214,000	261.0	0.303	0.201
FID12	503,000	66,600	146.0	0.744	0.182
FID13-2	2,130,000	114,000	190.0	0.378	0.310
FID13-3	3,040,000	175,000	236.0	0.352	0.253
FID16	2,210,000	93,600	173.0	0.473	0.335
FID18	573,000	46,800	122.0	0.339	0.306
DF054-1	271,000	35,700	107.0	0.417	0.218
DF054-2	113,000	14,400	67.7	0.381	0.307
DF054-3	58,400	7,100	47.5	0.492	0.377
DF054-4	89,800	24,100	87.6	0.253	0.177
DF054-5	68,700	8,600	52.3	0.611	0.351
DF054-6	31,400	9,500	55.0	0.129	0.223
DF081-1	96,300	12,800	63.7	0.485	0.299
DF081-2	50,400	8,480	51.9	0.402	0.291
DF081-3	22,300	6,000	43.7	0.182	0.240
DF081-4	12,800	5,000	39.9	0.215	0.206
DF081-5	63,400	5,050	40.1	0.584	0.506
DF081-6	119,000	11,400	60.2	0.599	0.402
DF081-7	10,300	3,020	31.0	0.616	0.301
EX1	1,061,000	42,500	116.3	0.862	0.488
EX2	3,810	897	16.9	0.884	0.554

*The parameters shaded in light colors indicate the normalized non-dimensional assessment indices. EX1 and EX2 are ideal benchmark cases for comparison and they are described in **Appendix 1**. The mean and maximum depths are tabulated in **Table 2**.*

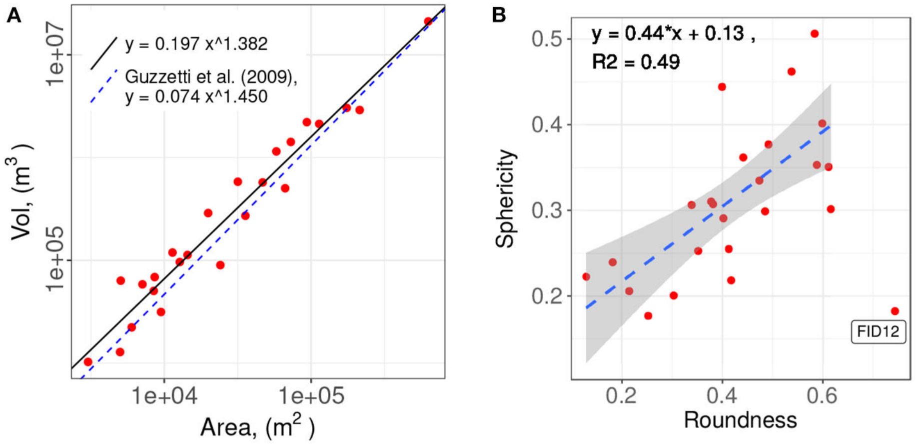

FIGURE 4 | (A) Landslide area and volume relation. **(B)** Roundness and sphericity relation. The gray area indicates the 95% confidence interval.

TABLE 2 | DEM grid size, depth-related quantities, and positional offsets of the maximum depth and gravity centers between the predicted and actual scarps.

Id	Δ, (m)	$\bar{\Delta}$, (%)	h^{act}_{max}, (m)	h^{pred}_{max}, (m)	$\bar{\mathcal{E}}_{max}$,(%)	h^{act}_{mean},(m)	h^{pred}_{mean},(m)	$\bar{\mathcal{E}}_{mean}$,(%)	d_{MD},(m)	$\bar{\mathcal{E}}_{MD}$,(%)	d_{GC},(m)	$\bar{\mathcal{E}}_{GC}$,(%)
HLIN	10.0	1.12	80.7	80.0	2.17	34.9	34.5	1.19	53.9	6.02	30.70	3.43
HLIN-2	10.0	4.98	44.9	39.3	30.38	18.5	18.2	1.52	192.0	95.74	24.40	12.15
HLIN-3	10.0	6.28	30.9	26.4	30.15	14.9	14.6	1.72	10.0	6.28	9.30	5.84
FID3	20.0	6.57	40.9	56.7	78.94	20.1	18.8	6.45	0.0	0.00	42.00	13.79
FID5	20.0	7.36	47.4	40.6	32.40	21.2	21.2	0.40	102.0	37.53	11.30	4.17
FID9	20.0	3.83	46.0	42.2	25.35	15.2	15.0	1.64	440.0	84.30	41.40	7.92
FID12	10.0	3.43	25.0	24.4	6.97	9.0	8.6	4.10	36.1	12.38	25.90	8.89
FID13-2	20.0	5.26	48.1	45.6	12.03	20.8	19.9	4.43	184.0	48.48	38.10	10.01
FID13-3	20.0	4.24	48.7	40.0	45.63	19.1	18.5	2.86	260.0	55.11	32.80	6.96
FID16	20.0	5.79	59.2	63.5	17.16	25.1	25.5	1.71	89.4	25.91	9.38	2.72
FID18	20.0	8.19	31.3	28.6	20.61	13.1	12.8	2.31	247.0	101.30	54.20	22.22
DF054-1	10.0	4.69	25.2	20.4	60.98	7.8	7.6	2.41	20.0	9.38	17.50	8.23
DF054-2	10.0	7.38	18.3	19.6	17.62	7.8	7.8	0.34	44.7	33.03	18.40	13.62
DF054-3	10.0	10.52	17.5	15.9	18.99	8.3	8.1	2.65	20.0	21.04	1.87	1.97
DF054-4	10.0	5.71	15.9	11.8	96.66	4.3	4.4	2.54	280.0	159.90	63.80	36.44
DF054-5	10.0	9.56	17.2	16.7	6.71	8.1	8.0	0.81	10.0	9.56	8.01	7.65
DF054-6	10.0	9.09	9.5	7.5	60.25	3.3	3.0	8.76	72.8	66.19	6.31	5.73
DF081-1	5.0	3.92	21.1	16.3	63.70	7.6	7.5	0.82	22.4	17.55	4.57	3.59
DF081-2	5.0	4.81	14.0	11.0	51.23	6.0	5.8	3.05	33.5	32.29	2.65	2.55
DF081-3	5.0	5.72	10.7	7.8	77.40	3.9	3.7	3.30	67.3	76.96	16.70	19.07
DF081-4	5.0	6.27	6.3	9.1	99.42	2.8	3.0	5.87	95.5	119.70	25.30	31.66
DF081-5	5.0	6.24	33.8	28.4	42.81	12.6	12.5	0.31	18.0	22.48	6.20	7.73
DF081-6	5.0	4.16	29.9	23.9	56.73	10.5	10.5	0.65	7.1	5.88	5.92	4.92
DF081-7	5.0	8.06	8.2	7.1	29.85	3.4	3.4	0.38	7.1	11.39	2.58	4.16
EX1	5.0	2.15	48.1	48.1	0.02	25.0	24.8	0.77	7.1	3.04	0.05	0.02
EX2	0.5	1.48	8.3	8.3	0.07	4.2	4.2	0.63	0.0	0.00	0.00	0.00

The parameters shaded in light colors indicate the normalized non-dimensional assessment indices. EX1 and EX2 are ideal benchmark cases and are described in ***Appendix 1****.*

subjected to the constraints

$$z_b = z_0 \text{ on } \Gamma, \qquad z_b \leq z_0 \text{ in } \Omega_p, \tag{3}$$

and

$$\mathcal{C}(z_b) \equiv \int (z_0 - z_b)\, d\Omega_p \ - \mathcal{V} = 0. \tag{4}$$

In the equations, ∇ is the 2D gradient operator $(\partial/\partial x, \partial/\partial y)$; Ω_p is the xy−projection area of the failure scarp area; and Γ is the boundary of Ω_p. The first constraint states that the boundary elevation of the failure interface is equal to the elevation of the free surface, $z_0 \equiv z_0(x, y)$; the scarp surface is below the free surface; and the second

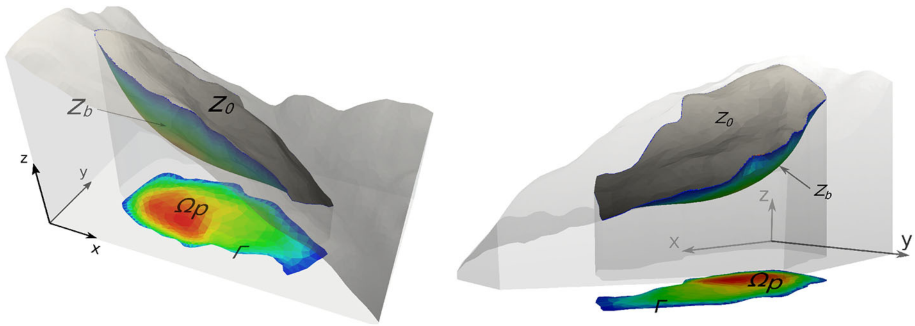

FIGURE 5 | Conceptual sketch, symbols, and coordinate system. The landslide site FID5, defined in **Figure 2** is used as an example. Symbols $z_0 \equiv z_0(x, y)$ and $z_b \equiv z_b(x, y)$ are the free surface and underground failure interfaces, respectively. Ω_p and Γ are the projection of the scarp area and outline on the xy plane, respectively. The scarp failure interfaces and depth are largely exaggerated for clarity in this sketch, and the color map conceptually indicates the scarp depth.

constraint states that the failure volume is the prescribed volume V.

The scheme is implemented in the open source finite element platform FreeFEM++, ver. 3.47 (or above) (Hecht, 2012), and the integrated Interior Point OPTimizer (IpOpt, Wächter and Biegler, 2006) optimization scheme in FreeFEM++ is applied to find the numerical solution. In the scheme, the Jacobian and Hessian matrices of the target function (1) are used to accelerate the numerical convergence:

$$\mathcal{S}'(z_b) \cdot [\hat{z}_b] = \int \frac{\nabla z_b \cdot \nabla \hat{z}_b}{\sqrt{1 + ||\nabla z_b||^2}}\, d\Omega_p, \tag{5}$$

and

$$\begin{aligned}\mathcal{S}''(z_b) \cdot ([\hat{z}_b], [\check{z}_b]) = & \int \left(\frac{\nabla \hat{z}_b \cdot \nabla \check{z}_b}{(1 + ||\nabla z_b||^2)^{1/2}} \right. \\ & \left. - \frac{(\nabla \check{z}_b \cdot \nabla z_b)(\nabla \hat{z}_b \cdot \nabla z_b)}{(1 + ||\nabla z_b||^2)^{3/2}} \right) d\Omega_p. \end{aligned} \tag{6}$$

The above two expressions are written with the help of the notation of the Fréchet derivative for facilitating the numerical scheme implementation (Vergez et al., 2016). Similarly, the Jacobian matrix of constraint (4) is

$$\mathcal{C}'(z_b) \cdot [\hat{z}_b] = -\int d\Omega_p = -\Omega_p. \tag{7}$$

Equations (5), (6), and (7) are evaluated at discrete points in each mesh element. Supporting external C++ functions are coded to handle the DEM, scarp boundary outline inputs and outputs to other software for geographic information systems (GIS), such as ArcGIS, qGIS, and GRASS. Initially, the outline is uniformly discretized with a prescribed number into a set of linear edges, and the mesh of the scarp area is generated. Then, the optimization (2) for the minimal surface is executed. Depending on the precision requirement of the mesh, multiple passes of mesh adaptation can be performed based on the calculated failure interface.

As seen in the formulation and calculation principle, the smooth minimal surface can be equivalently replaced with other mathematical surfaces, provided that they are phenomenologically reasonable and their descriptive expressions are available. It is also in principle possible to design transformations that can further manipulate the predicted failure surfaces to incorporate with site specific geological settings or hydrogeological conditions. Nevertheless, because the method is a phenomenological approach, the accuracy of the failure surface prediction has to be verified with actual landslide data. In what follows, we use the current smooth minimal surface to proceed the application example and accuracy assessment. The assessment indices and procedure are generic and applicable to future alternative failure surface prediction or transformation schemes.

4. ASSESSMENT INDICES

The proposed prediction method for the failure interface is purely mathematical. Intuitively, the failure interface is mimicked by a "soap-bubble" film that encloses the free surface at a specified volume $\mathcal{V}$. Because the film is uniquely defined, it becomes important to assess the fitness, i.e., the closeness between the film and the real failure interface and to establish the error bounds of the method.

Under the current approach, the area, volume and scarp boundary are kept identical for each landslide, and hence, the mean depth of the predicted landslide mass will be equal to the actual one, $(\mathcal{V}/\Omega_p)$, in principle. Nevertheless, because of the nature of discrete numerical data and computations, the discretization incurs digital errors, e.g., the DEM is presented at a resolution of grid size Δ and in the minimal surface calculation, forward and backward interpolation is performed between the DEM and mesh system. It is expected that this type of error is bounded by the precision of the mesh, such that we list the normalized grid size $\bar{\Delta}$ as an informative indicator, which is normalized with respect to the equivalent diameter $2\mathcal{R}$.

To compare the predicted and actual failure interfaces, we start by calculating and finding the crucial quantities in each of them: the mean and maximum scarp depths (h_{mean} and h_{max}, respectively) and the positions of the gravity center $\mathbf{r}_{\text{GC}}$ and

TABLE 3 | The modes, standard deviations of the prediction discrepancy $\delta(x, y)$, resultant regression parameters, and SSIMs.

Id	mode(δ),(m)	$\bar{\mathcal{E}}_{\mathrm{mode}}$, (%)	std(δ),(m)	$\bar{\mathcal{E}}_{\mathrm{std}}$, (%)	$\bar{\alpha}$	$\bar{\beta}$	R^2	SSIM
HLIN	−2.2	6.36	12.9	37.07	0.322	0.686	0.557	0.768
HLIN-2	1.6	8.43	8.6	46.33	0.392	0.617	0.416	0.849
HLIN-3	−2.0	13.76	4.5	30.14	0.128	0.887	0.684	0.913
FID3	−9.4	46.64	11.0	54.98	0.604	0.424	0.454	0.713
FID5	−0.7	3.51	7.3	34.51	0.087	0.916	0.618	0.864
FID9	4.7	30.72	9.0	59.26	0.398	0.612	0.330	0.715
FID12	−2.3	25.99	5.5	61.45	0.598	0.419	0.263	0.774
FID13-2	1.1	5.17	10.9	52.16	0.475	0.550	0.336	0.702
FID13-3	2.3	11.91	7.2	37.68	0.033	0.995	0.643	0.807
FID16	−4.7	18.68	10.8	42.95	0.392	0.598	0.645	0.777
FID18	6.9	52.47	9.4	71.61	0.725	0.282	0.063	0.677
DF054-1	−0.3	4.28	3.9	50.30	0.151	0.870	0.566	0.818
DF054-2	−0.4	4.72	5.5	69.49	0.659	0.342	0.177	0.748
DF054-3	−0.7	7.85	2.6	30.79	0.113	0.911	0.694	0.955
DF054-4	0.3	7.82	3.8	87.58	0.663	0.329	0.129	0.770
DF054-5	−0.1	1.15	3.1	38.84	0.114	0.893	0.595	0.919
DF054-6	−0.4	11.74	1.7	52.85	0.317	0.748	0.453	0.949
DF081-1	0.3	4.14	2.7	35.27	0.053	0.955	0.731	0.930
DF081-2	−0.8	13.25	3.5	58.10	0.240	0.783	0.323	0.839
DF081-3	−0.3	7.00	1.9	49.12	0.271	0.754	0.457	0.920
DF081-4	−0.2	5.52	2.0	69.94	0.533	0.441	0.477	0.892
DF081-5	0.0	0.10	4.6	37.03	0.020	0.983	0.760	0.898
DF081-6	−0.7	6.33	3.6	34.45	0.008	0.999	0.798	0.892
DF081-7	−0.8	24.52	1.1	31.27	0.094	0.903	0.751	0.977
EX1	−0.2	0.60	0.2	0.77	0.015	0.992	1.000	1.000
EX2	−0.0	0.13	0.0	0.59	0.012	0.994	1.000	1.000

The parameters shaded in light colors indicate normalized non-dimensional assessment indices. EX1 and EX2 are ideal benchmark cases described in ***Appendix 1****.*

maximum depth point $\mathbf{r}_{\mathrm{MD}}$. One can define the measures of discrepancy as the differences of these quantities between the predicted and actual landslide failure interfaces. To eliminate the landslide scale effect, the depthwise quantities are normalized with respect to the actual mean depth; i.e., $\bar{\mathcal{E}}_{\mathrm{mean}} = (h^{\mathrm{pred}}_{\mathrm{mean}} - h^{\mathrm{act}}_{\mathrm{mean}})/h^{\mathrm{act}}_{\mathrm{mean}}$, $\bar{\mathcal{E}}_{\max} = (h^{\mathrm{pred}}_{\max} - h^{\mathrm{act}}_{\max})/h^{\mathrm{act}}_{\mathrm{mean}}$, and the spanwise offsets of the gravity centers d_{GC} and maximum depths d_{MD} are then normalized with respect to the equivalent diameter; i.e., $\bar{\mathcal{E}}_{\mathrm{GC}} = d_{\mathrm{GC}}/(2\mathcal{R}) = |\mathbf{r}^{\mathrm{pred}}_{\mathrm{GC}} - \mathbf{r}^{\mathrm{act}}_{\mathrm{GC}}|/(2\mathcal{R})$, $\bar{\mathcal{E}}_{\mathrm{MD}} = d_{\mathrm{MD}}/(2\mathcal{R}) = |\mathbf{r}^{\mathrm{pred}}_{\mathrm{MD}} - \mathbf{r}^{\mathrm{act}}_{\mathrm{MD}}|/(2\mathcal{R})$. The superscripts $^{\mathrm{pred}}$ and $^{\mathrm{act}}$ obviously represent the model predictions and the actual measurements of these quantities. $\bar{\mathcal{E}}_{\mathrm{mean}}$ contains only the discretization error as discussed previously. $\bar{\mathcal{E}}_{\mathrm{GC}}$ and $\bar{\mathcal{E}}_{\mathrm{MD}}$ somewhat represent the bias of the depth distributions between the predicted and actual failure interfaces.

The ratio $\bar{\mathcal{E}}_{\max}$ is one of the assessment indices, which merely measures the difference between the maximum depths. The other assessment indices are the statistical properties associated with the prediction discrepancy. Let the prediction discrepancy be the difference between the actual and predicted scarp depths, $\delta(x, y) = h^{\mathrm{act}} - h^{\mathrm{pred}} = z^{\mathrm{pred}}_b - z^{\mathrm{act}}_b$, where $(x, y) \in \Omega_p$. The statistical properties that can be computed include the distribution function of the prediction discrepancy δ, its mode(δ) (the most frequent discrepancy), standard deviation std(δ), and their non-dimensionalized counterparts, $\bar{\mathcal{E}}_{\mathrm{mode}}$ and $\bar{\mathcal{E}}_{\mathrm{std}}$ (normalized with respect to $h^{\mathrm{act}}_{\mathrm{mean}}$). Note that std($\delta$) is virtually the root mean square error (RMSE) between the predicted and actual depths according to its computational principle (Kuo et al., 2011). For completeness, the linear regression model, $h^{\mathrm{act}} = \bar{\beta} h^{\mathrm{pred}} + \alpha$, is also calculated for each landslide site. To facilitate comparisons among landslides of different size scales, the intercept α of the regression model is again non-dimensionalized with respect to $h^{\mathrm{act}}_{\mathrm{mean}}$; i.e., $\bar{\alpha} = \alpha / h^{\mathrm{act}}_{\mathrm{mean}}$. Together with the slope $\bar{\beta}$ and the coefficient of determination R^2, these regression parameters are tabulated in **Table 3**.

The aforementioned statistical quantities are commonly applied in landslide studies. The limitations of these indices are that they rely on the fitness of a single point (e.g., $\bar{\mathcal{E}}_{\max}$, $\bar{\mathcal{E}}_{\mathrm{MD}}$), on the averaged properties of the scarp ($\bar{\mathcal{E}}_{\mathrm{mean}}$, $\bar{\mathcal{E}}_{\mathrm{GC}}$), or on the discrepancy distribution of the scattered grid data ($\bar{\mathcal{E}}_{\mathrm{mode}}$, $\bar{\mathcal{E}}_{\mathrm{std}}$, $\bar{\alpha}$, $\bar{\beta}$, R^2, etc.). To the authors' point of view, one important factor has not yet been properly addressed by these indices, and this factor is the likelihood of the patterns between the predicted and actual scarps. The pattern refers to the landslide depth distribution in the proximity of any given point in the scarp area, and this pattern is highly dependent on the neighboring area. The patterns are omitted in the former statistical indices because

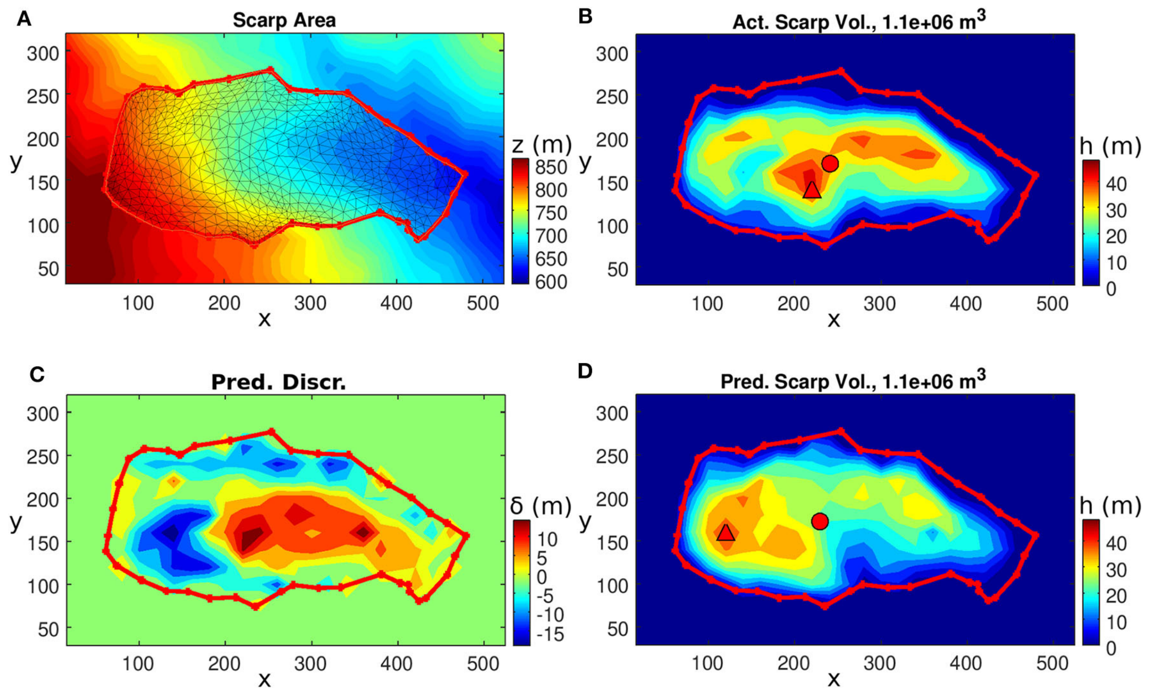

FIGURE 6 | Landslide FID5. *Clockwise from the upper-left figure*: **(A)** The topography, scarp outline and smooth minimal surface computational mesh. **(B)** The actual landslide depth. **(C)** The predicted landslide depth. **(D)** The prediction discrepancy $\delta(x, y)$. The solid red circle and triangle represent the gravity center and maximum depth location, respectively.

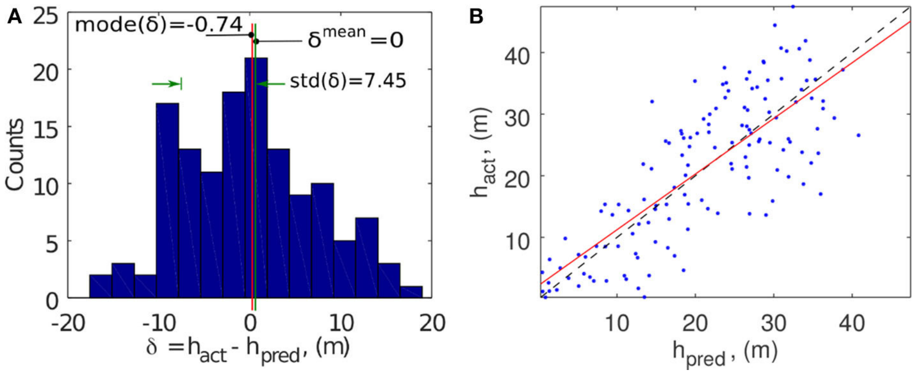

FIGURE 7 | Landslide FID5. **(A)** Histogram of $\delta(x, y)$, the graphical definition of mode(δ), std(δ) and the negligible mean depth discrepancy δ^{mean}. **(B)** Scatter plot and regression analysis of the predicted and actual depths.

the elevation of each mesh grid is treated as an independent random variable.

To include in the spatial topographic patterns into the current assessment, we adopt the so-called structural similarity index (SSIM), which was developed for and is commonly used in image studies for assessing qualities among various image-processing schemes (Wang et al., 2004). In the computation of this index, the value of each pixel of the image, or here, those of the grids in the scarp area, is replaced by the SSIM calculated in the vicinity window (grid) surrounding the pixel. For each window, the SSIM is defined as

$$\text{SSIM}(h^{\text{act}}, h^{\text{pred}}) = l(h^{\text{act}}, h^{\text{pred}})\ c(h^{\text{act}}, h^{\text{pred}})\ s(h^{\text{act}}, h^{\text{pred}}), \quad (8)$$

where the functions on the right hand side are defined as

$$\begin{aligned} l(h^{\text{act}}, h^{\text{pred}}) &= \frac{2h^{\text{act}}_{\text{mean}}\, h^{\text{pred}}_{\text{mean}} + C_1}{{h^{\text{act}}_{\text{mean}}}^2 + {h^{\text{pred}}_{\text{mean}}}^2 + C_1}, \\ c(h^{\text{act}}, h^{\text{pred}}) &= \frac{2h^{\text{act}}_{\text{std}}\, h^{\text{pred}}_{\text{std}} + C_2}{{h^{\text{act}}_{\text{std}}}^2 + {h^{\text{pred}}_{\text{std}}}^2 + C_2}, \\ s(h^{\text{act}}, h^{\text{pred}}) &= \frac{\sigma^{\text{act,pred}} + C_2/2}{h^{\text{act}}_{\text{std}}\, h^{\text{pred}}_{\text{std}} + C_2/2}. \end{aligned} \quad (9)$$

The symbols in the expressions are slightly modified to be consistent with those in the current work, such that $h^{\text{act}}_{\text{std}}$, $h^{\text{pred}}_{\text{std}}$ and

$\sigma^{\text{act,pred}}$ are the standard deviations of the actual and predicted scarp depths, respectively, and the cross variance $\sigma^{\text{act,pred}} = \left\{\int (h^{\text{act}} - h^{\text{act}}_{\text{mean}})(h^{\text{pred}} - h^{\text{pred}}_{\text{mean}})\, d\Omega_p\right\} / \Omega_p$. C_1 and C_2 are small constant parameters that stabilize the expressions for small denominators and their default values, as well as the window, are taken from Wang et al. (2004). The three expressions in (9) are for comparing the luminance, contrast and structural pattern in image studies but can be analogous to the comparison of the landslide scarp depth, the change in the depth and the pattern of the depth in the present study. Therefore, the SSIM should perform similarly as an assessment index to evaluate the fitness of the prediction. In the implementation, the SSIMs in the vicinity area of each grid are calculated with the help of the standard Gaussian window functions of signal processing and statistics. The window size is 10 DEM grids. The resultant SSIM for each landslide site is then defined as the average SSIM over the scarp area and takes a value between 0 and 1, where 0 indicates complete dissimilarity and 1 indicates perfect identicalness. Tests showed that the resultant SSIM does not sensitively depend on the window size and function. For further statistical theories and derivation details, interested readers are directed to the referenced literature.

5. APPLICATION EXAMPLES: FID5 AND FID18

In this section, application examples of the minimal surface method for two landslides are presented. There are also two additional benchmark cases for validating the minimal surface optimizations, but because of their simplicity, these benchmark cases are relegated to **Appendix 1**. The two real cases, one with a good prediction and the other with a fair prediction, are chosen and they are purposely selected to illustrate the comparison of the opposite predictions. The calculation of the statistical assessment indices are also explained in detail, particularly those operational procedures that are not thoroughly described in section 3 and section 4.

We start with the FID5 landslide. The FID5 site is on the slope of the west bank of the Cishan River and has a volume $\mathcal{V}$ of 1,167,000 m^3 and an average slope of 35.2°, inclined toward the E-NE direction. The DEM domain is 600×340 m, in the x and y directions, respectively, with a resolution of 20 m (normalized to $\bar{\Delta} = 7.36\%$). The 3D view of the site has been shown as a conceptual sketch in **Figure 5**. The post-landslide topography as well as the scarp boundary is plotted in **Figure 8A**. The projection area, Ω_p, of the scarp is then equal to $58,000$ m^2 and the equivalent radius $\mathcal{R} = 136.0$ m. These geometric dimensions lead to a roundness ratio $\mathfrak{r}_r$ of 0.442 and a spherical ratio $\mathfrak{r}_s$ of 0.362.

As the slope and scarp boundary are now defined, we proceed with the preparation of the input data set of the minimal surface optimization scheme. Because FreeFEM++ only provides unstructured triangular meshing for general shapes of computational domains, numerical interpolation algorithms are employed to convey the data between the structured DEM mesh and the unstructured FreeFEM++ computational grids. We do not have any compulsory reasons to adopt higher order accuracy interpolations for the present purpose; thus only first order interpolation algorithms are used.

When the DEM and scarp outline are input, parsed and interpolated, an initial unstructured mesh for the scarp domain Ω_p is constructed[4]. The P2 finite elements are used for data arrangement and manipulation. Then, the optimization routine for the minimal surface is executed. To extend the scarp prediction to future mechanical slope stability analyses, which may require a higher accuracy within the FreeFEM++ framework, we perform a second-pass mesh adaptation based on the scarp depth of the initial calculation with a mesh refinement precision error factor of 0.05[4]. The refined mesh for the smooth minimal surface calculation is superposed in **Figure 6A**. A high mesh density is found in the areas where the topography exhibits large variations, in this case, around the vicinity of the ridges and edges of the slope surface. After the smooth minimal surface is found, it is interpolated back to the structured DEM grids.

The actual and predicted landslide depths are shown in **Figures 6B,C**. The landslide has a maximum depth $h^{\text{act}}_{\text{max}}$ of 47.4 m and a mean depth $h^{\text{act}}_{\text{mean}}$ of 21.2 m. Their predicted counterparts are $h^{\text{pred}}_{\text{max}} = 40.6$ m and $h^{\text{pred}}_{\text{mean}}$ 21.2 m, respectively. These values lead to dimensionless discrepancies $\bar{\mathcal{E}}_{\text{max}} = 32.40\%$ and $\bar{\mathcal{E}}_{\text{mean}} = 0.40\%$, respectively. The prediction discrepancy distribution $\delta(x, y)$ is plotted in **Figure 6D**. The prediction overestimates the scarp depth in the part of the slope with higher elevation, such that $\delta(x, y)$ has two major oppositely signed zones aligned adjacently along the downslope direction. This distribution of $\delta(x, y)$ leads to the positions of both the maximum depth and gravity center of the landslide mass residing on the upper-slope side compared to the actual landslide mass. The positional offsets of the maximum depth and gravity center are $d_{\text{MD}} = 102.0$ m ($\bar{\mathcal{E}}_{\text{MD}} = 37.53\%$), and $d_{\text{GC}} = 11.3$ m ($\bar{\mathcal{E}}_{\text{GC}} = 4.17\%$).

The histogram of the prediction discrepancy $\delta(x, y)$ is plotted in **Figure 7A**. It depicts the frequency distribution of $\delta(x, y)$, and the distribution has an approximate symmetric triangular shape except for a minor peak at $\delta \approx -9$ m. Its mode, mode(δ), is approximately -0.7 m and the standard deviation, std(δ) is 7.3 m, leading to normalized discrepancy ratios of $\bar{\mathcal{E}}_{\text{mode}} = 3.51\%$ and $\bar{\mathcal{E}}_{\text{std}} = 34.51\%$. In **Figure 7B**, the scattered data of h^{pred} and h^{act} are plotted in the regression analysis and the resultant linear regression line is $h^{\text{act}} = 0.916h^{\text{pred}} + 1.84$, which provides the normalized intercept parameter $\bar{\alpha} = 0.087$. The coefficient of determination, R^2, is 0.618. The SSIM is 0.864, which is one of the cases with a high score, cf. section 6. In the SSIM computation, the default Gaussian window, of size 11×11 with a standard deviation of 1.5 cell sizes, is used. To compare with other cases, these statistical quantities are tabulated in both **Tables 2**, **3**.

FID18 is a landslide site near the Zion village. The landslide has a volume of 567,000 m^3, an area of 46,800 m^2, a maximum depth of 31.3 m, and a slope of 29.4° inclined toward the south. The roundness and sphericity are 0.339 and 0.306, respectively. The DEM has a spatial resolution of 20 m ($\bar{\delta} = 8.19\%$). After performing the smooth minimal surface calculation, the

---

[4] By BAMG, bidimensional anisotropic mesh generator with mesh refinement facility, integrated in FreeFEM++.

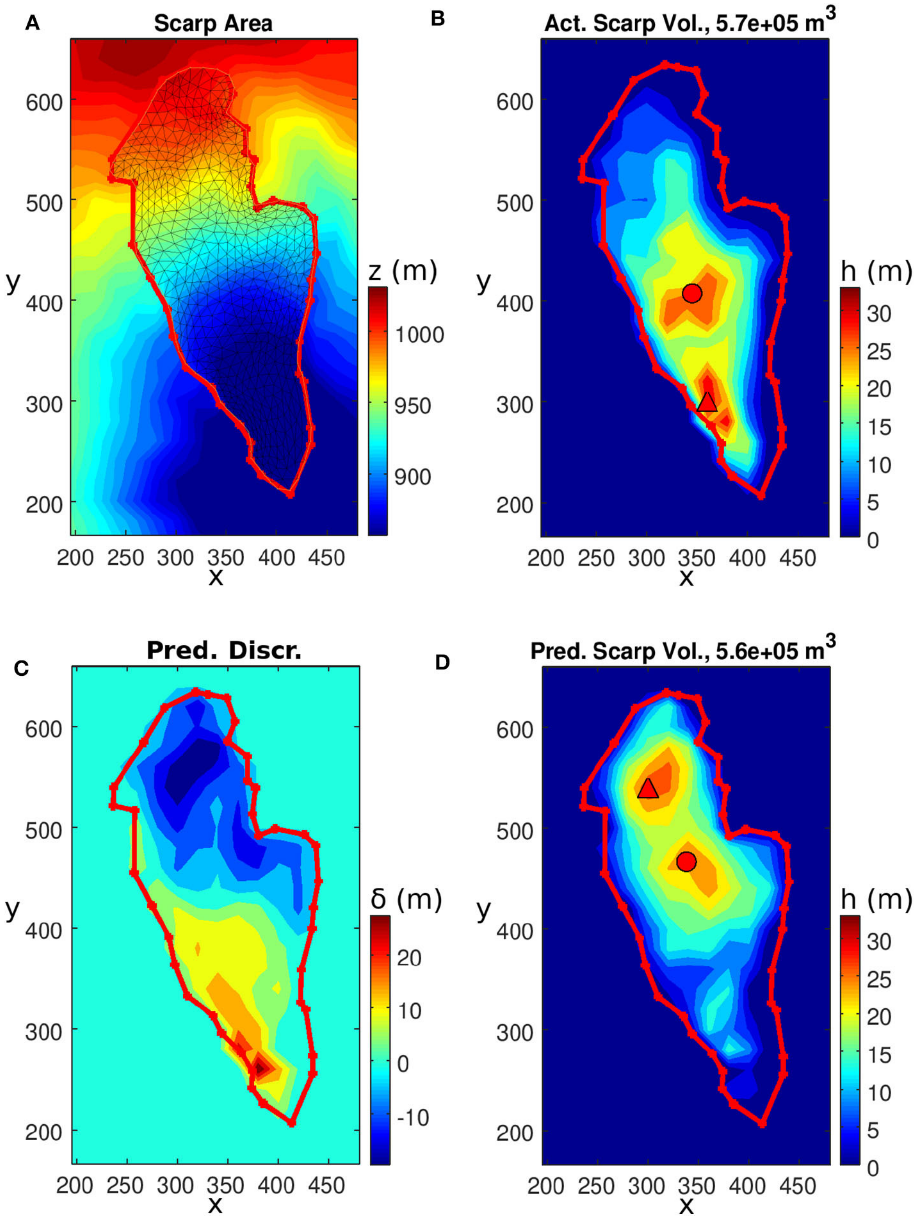

FIGURE 8 | Landslide FID18. *Clockwise from the upper-left figure* **(A)** The topography, scarp outline and smooth minimal surface computational domain. **(B)** The actual landslide depth and scarp outline. **(C)** The predicted landslide depth. **(D)** The prediction discrepancy $\delta(x, y)$. The solid red circle and triangle represent the gravity center and maximum depth location, respectively.

computational mesh, the actual, predicted depths and the prediction discrepancy are plotted in **Figure 8**. The panels are arranged the same way as in the previous FID5 case. Interestingly, the prediction also overestimated the landslide depth in the upper part of the slope and underestimated the lower part of the slope. Therefore, the prediction discrepancy also shows similar negative-positive-lobed prediction discrepancy zones along the downslope direction as in the previous case.

The accompanied discrepancy histogram and regression analysis are shown in **Figure 9**. The histogram indicates that the discrepancy has a flatter distribution with a few more irregular minor peaks than that of FID5. This case is identified as a poorer fit because the prediction also has relatively poor linear regression parameters compared to the actual data: the intercept $\bar{\alpha}$ (0.72, normalized with respect to $h^{\mathrm{act}}_{\mathrm{mean}}$) is large, $\bar{\beta}$ (0.28) deviates greatly from 1, and R^2 (0.063) is low. We found consistent indications from $\bar{\mathcal{E}}_{\mathrm{mode}}$ (52.47%), $\bar{\mathcal{E}}_{\mathrm{std}}$ (71.61%) and $\bar{\mathcal{E}}_{\mathrm{GC}}$ (44.44%), representing larger prediction discrepancies, wider deviations and larger offsets of the gravity center. The SSIM (0.677) also has one of the lowest scores. Nevertheless,

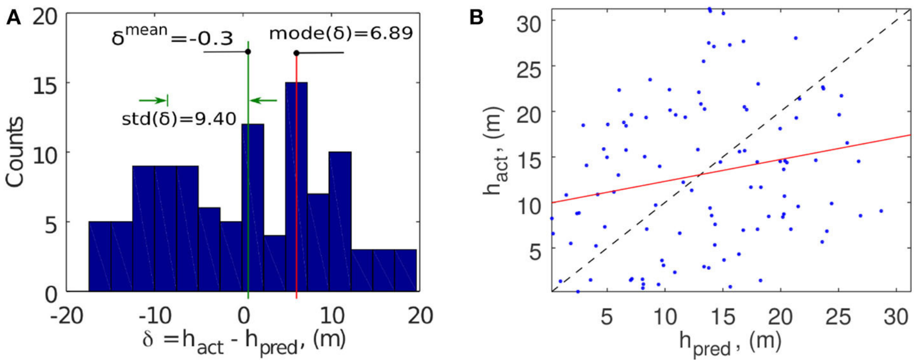

FIGURE 9 | Landslide FID18. **(A)** Histogram of $\delta(x, y)$ and the graphical definition of mode(δ), std(δ) and the negligible mean depth discrepancy δ^{mean}. **(B)** Scatter plot and regression analysis of the predicted and actual depths.

despite these comparatively subnormal indices, the prediction is only 2.31% for $\bar{\mathcal{E}}_{\mathrm{mean}}$ and a satisfactory 20.61% for $\bar{\mathcal{E}}_{\max}$, as both the scarp area and volume are constrained in the present failure surface prediction method such that the mean depth has interpolation errors only and the maximum depth is generally proportional to the mean depth (see section 6).

6. DEPLOYMENT TO THE FULL SET OF LANDSLIDES AND ASSESSMENTS

The method is applied to the 24 landslide sites defined in **Figures 2**, **3** and **Table 1**. The resolution of the DEMs varies from 5 to 20 m due to various preparation conditions, such as public release policies and the size of landslide sites. Though with these different resolution settings, the normalized grid size $\bar{\Delta}$ remains within 10% (**Table 2**). In the same table, the maximum and mean depths as well as the positional offsets of the maximum depths and gravity centers between the actual and predicted scarps are listed. To make visual comparisons, the depth-related quantities are plotted in **Figure 10**. The predicted and actual depths excellently match the diagonal lines in **Figure 10A**. Reorganizing the data, we find that there is also a linear relationship between the maximum and mean depths (**Figure 10B**). From the regression model, we have a gross guideline that the maximum scarp depth can be obtained by multiplying the mean scarp depth by a factor of 2.3.

The remaining assessment indices (i.e., the mode, standard deviation, regression parameters of the prediction discrepancy and the SSIM) are tabulated in **Table 3**. To comprehend at a glance the interrelationship among the assessment indices, we draw the box plots of the normalized indices in **Figure 11**. These indices are sorted in ascending order by their median values and are divided into two groups, of which the first group contains the slopewise quantities, normalized by $2\mathcal{R}$ and the second involves the depth-related quantities, normalized by $h^{\mathrm{act}}_{\mathrm{mean}}$. The discretization is determined by the DEM resolution, $\bar{\Delta}$, and its values in **Figure 11A**, are within 10% for the present data-sets. The values of the normalized mean prediction discrepancy, $\bar{\mathcal{E}}_{\mathrm{mean}}$ in **Figure 11B**, are small and are all within 10%, as expected. As argued in section 4, this finding is due to $\bar{\mathcal{E}}_{\mathrm{mean}}$ being constrained by the specified area and volume inputs to the method and the small values arise from the DEM discretization approach and interpolation scheme.

There are two assessment indices associated with the maximum scarp depth: the positional offset $\bar{\mathcal{E}}_{\mathrm{MD}}$ and discrepancy $\bar{\mathcal{E}}_{\max}$. The two indices both exhibit much larger spreads of their data values than the other indices. The positional offset of the gravity centers of the predicted and actual scarps is interestingly small approximately 6% (median value), dimensionally of $6\% \cdot 2\mathcal{R} \approx 0.12\mathcal{R}$. An important implication of this fact for future incorporation of the mechanical slope stability analysis is that the force balance condition of the predicted scarp mass (cf. free body diagram) may not significantly differ from the actual mass, and consequently, the landslide motion dynamics may bear a close similarity. Research into this proposition is beyond the scope of the present paper and will be reported in follow-up studies.

The index $\bar{\mathcal{E}}_{\mathrm{mode}}$ depicts the most frequent prediction discrepancy, and from this definition, it somewhat indicates the skewness of the frequency distribution of $\delta(x, y)$, cf. **Figures 7**, **9**. The moderate value range of $\bar{\mathcal{E}}_{\mathrm{mode}}$ (**Figure 11B**) suggests that the frequency distributions of the $\delta(x, y)$ histograms remain reasonably symmetric. As mentioned in section 4, the standard deviation index $\bar{\mathcal{E}}_{\mathrm{std}}$ equivalently describes the RMSE between the predicted and actual scarps. The box plot shows that the deviation is approximately 45 ± 10% of the mean scarp depth, or approximately 19 ± 4% of the maximum scarp depth, based on the regression model depicted in **Figure 10B**. These margins of $\bar{\mathcal{E}}_{\mathrm{std}}$ indicate that the present smooth minimal surface is satisfactory for predicting the landslide failure interfaces. **Figure 11C** presents the value range of the resultant regression parameters and the SSIM.

Finally, we comment on whether there is a relationship between the good predictions from the present method and the landslide scarps. The importance of the answer to this question is that it enables us to estimate the goodness of the prediction without needing to know the actual underground failure interface when the method is applied to hazard mitigation plans for potential landslide sites. For this purpose, the roundness is chosen as the parameter to describe the landslide scarp

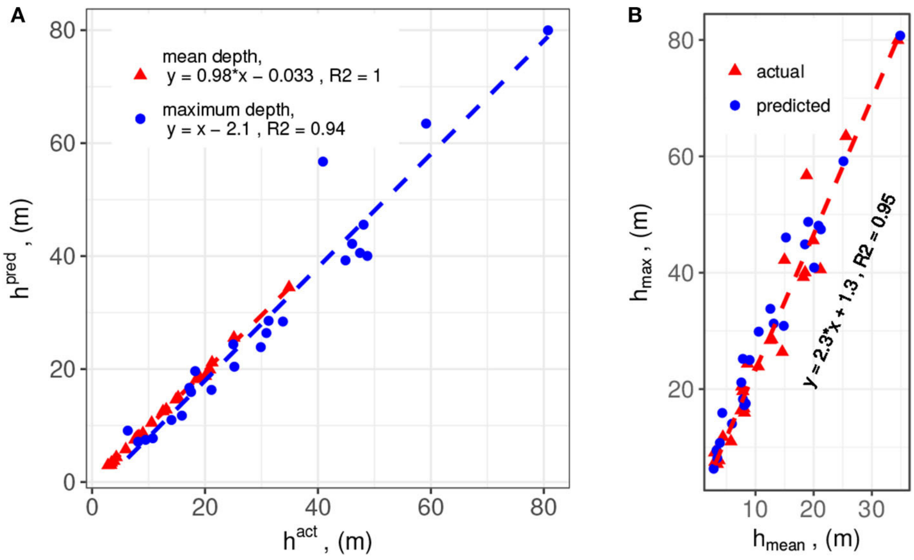

FIGURE 10 | Combined comparison between **(A)** the predicted and actual depths, and **(B)** the maximum and mean depths. The data sources and regression relations are marked in the figure legends.

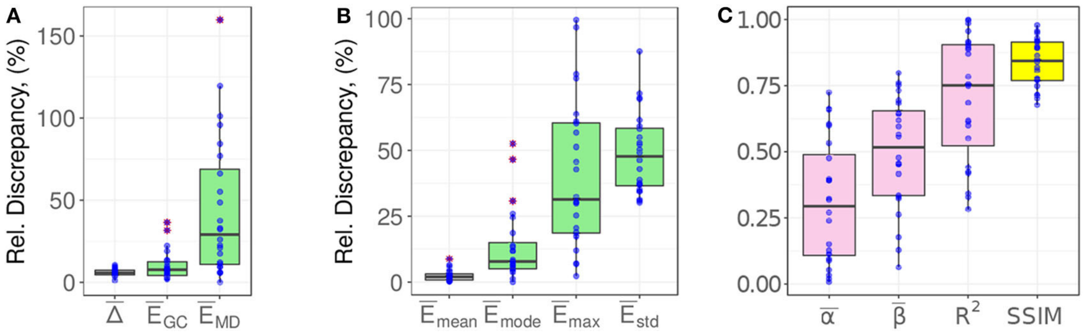

FIGURE 11 | Box plots for the assessment indices **(A)** $\bar{\Delta}$, $\bar{\mathcal{E}}_{\text{GC}}$ and $\bar{\mathcal{E}}_{\text{MD}}$, **(B)** $\bar{\mathcal{E}}_{\text{mean}}$, $\bar{\mathcal{E}}_{\text{mode}}$, $\bar{\mathcal{E}}_{\text{max}}$, and $\bar{\mathcal{E}}_{\text{std}}$, and **(C)** $\bar{\alpha}$, $\bar{\beta}$, R^2 and the SSIM. The normalization parameters are $2\mathcal{R}$ for the first group and $h^{\text{act}}_{\text{mean}}$ for the second group.

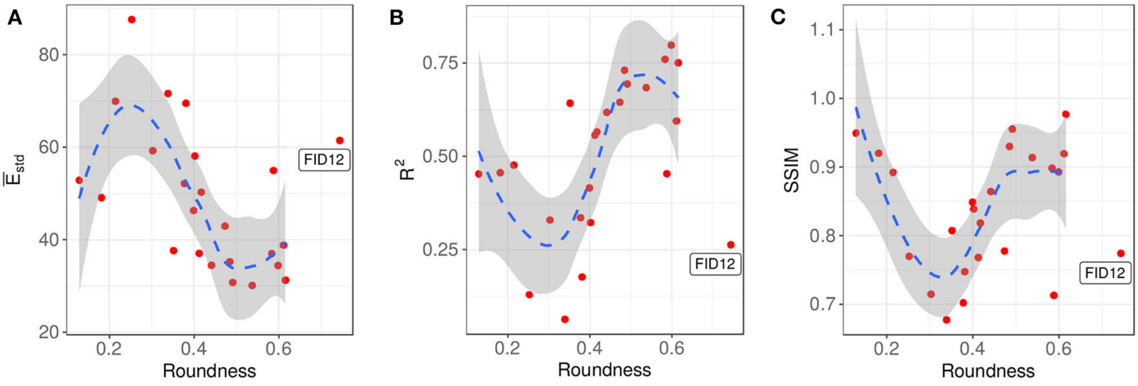

FIGURE 12 | Three selected normalized assessment indices vs. the landslide scarp roundness. The roundness vs. **(A)** $\bar{\mathcal{E}}_{\text{std}}$, **(B)** R^2, and **(C)** the SSIM. The dashed lines are obtained by LOESS regression, with a default span parameter of 0.75 (Cleveland et al., 1992). The gray shaded areas indicate 95% confidence intervals. FID12 is an outlier and is excluded from the regression analysis.

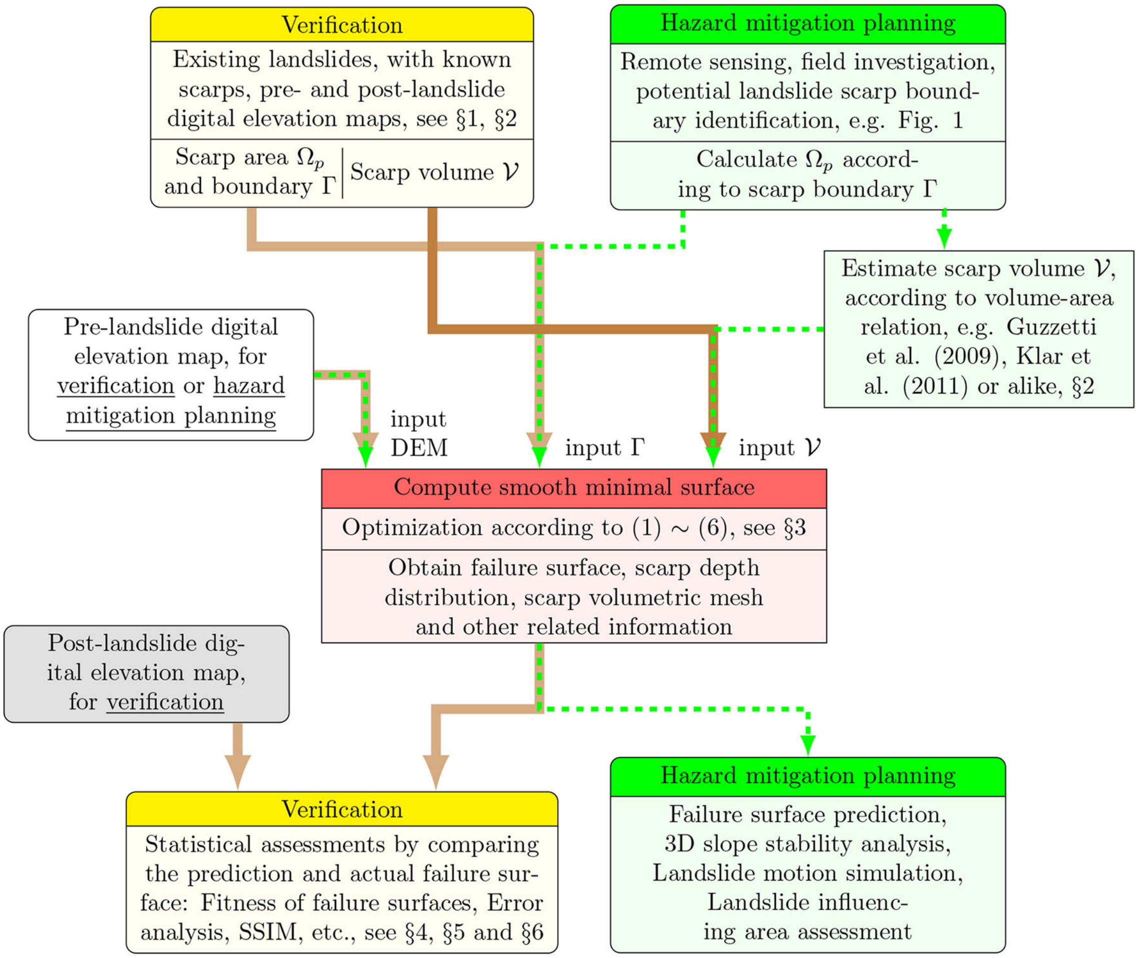

FIGURE 13 | Flowchart of the present model for both application scenarios: verification, blocks shaded in light yellows, and hazard mitigation planning, blocks in light greens. The current failure surface prediction model is in light red colors. For failure surface prediction verification, i.e., the main theme of the paper, the computational flow is led by the thick solid brown lines but, for hazard mitigation planning, it is led by the thin dashed green lines.

because this parameter is usually the first obtainable information from topographic surveys. After reviewing the collection of the assessment indices, we select $\bar{\mathcal{E}}_{\text{std}}$, R^2 and the SSIM to measure the fitness of the predictions. These three indices vs. the roundness are plotted in **Figure 12**. The locally estimated scatterplot smoothing (LOESS) technique (Cleveland et al., 1992), is then applied to determine their relationships with certain degrees of statistical confidence. One exception is made for the noted outlier FID12, cf. section 2, which is excluded from the LOESS analysis but is included in the figure for reference.

Comparing the three LOESS results, we can draw a consistent conclusion that the smooth minimal surface performs relatively poorer for a roundness of approximately 0.3. At this value, the standard deviation $\bar{\mathcal{E}}_{\text{std}}$ (RMSE) has the highest value whereas the coefficient of determination R^2 and structural similarity index SSIM have the lowest values. For values away from a roundness of 0.3, the landslide scarp becomes either slenderer or more circular. Intuitively, these two regimes have lower geometric complexity because they both degrade to simpler 2D-like scarps. The prediction fitness may thus be associated with the reduction in the geometric complexity. In fact, the same conclusion can be reached with the undiscussed $\bar{\alpha}$ and $\bar{\beta}$ parameters.

A note to keep in mind is that the conclusion drawn from the above assessments is based on the current simple smooth minimal surface approach for the failure surfaces. The geological settings and hydrogrological conditions are completely omitted. This arrangement is deliberate because it is essential at present to construct a baseline dataset with the simplest setting of the method. The dataset will be the foundation for future comparative studies if alternative failure surface prediction strategies are proposed. For example, the dataset will be used for improvement assessments when we design mathematical transformations to manipulate the failure surface predictions to accommodate site specific geological conditions. On the other hand, whether the current approach fits better for landslides in slopes with uniform rocks also remains to be investigated and the hypothesis can be examined by comparing to the baseline dataset. These related studies will be reported in upcoming papers.

7. CONCLUSION

Even with protection targets, a large number of potential deep-seated landslides in the mountain ranges were identified in a series of renewed hazard mitigation initiatives in Taiwan. When implementing successful, detailed hazard mitigation strategies, tasks such as the determination of the landslide influencing areas and the installation of a monitoring system, need the estimation of the landslide volumes, failure interfaces and other related information. Having observed that these deep-seated landslide sites are represented by polygons in the GIS and that there are regression relations between the landslide scarp areas and volumes, we propose to use smooth minimal surfaces to approximate the landslide failure interfaces. The smooth minimal surface is constructed by minimizing the surface area while keeping the enclosed volume fixed at the value obtained by the scarp area-volume relation. This type of surfaces is chosen because it is closely related to the commonly used spherical-shaped surfaces in slope stability analyses. Consequently, it is expected that the prediction may suit better for slopes with homogeneous and isotropic rocks.

The method, though still in its primitive form, has the potential to be applied to hazard mitigation plans in which higher tolerance in prediction errors is allowed. Therefore, one of the main themes of the paper is to establish the knowledge about the fitness and margins of errors for this method setting. The fitness of the prediction results was verified with 24 landslides that were triggered by excessive rainfall during the 2009 Morakot typhoon. A collection of assessment indices was reviewed and among these indices, the standard deviation $\bar{\mathcal{E}}_{\mathrm{std}}$ (equivalently, the RMSE), the regression parameters and the SSIM are shown to contain the information about the prediction discrepancy over the entire scarp domain for each landslide site. Using the present landslide dataset, the value range of the index $\bar{\mathcal{E}}_{\mathrm{std}}$ was found to be approximately 45 ± 10% of the mean scarp depth. The limited positional offset of the gravity center, $\bar{\mathcal{E}}_{\mathrm{GC}}$, indicates that the force balance condition may not significantly differ from the actual landslide mass. Finally, the relation between the prediction fitness and scarp geometry was determined: Better predictions are achieved for either slender or comparatively circular scarps. Overall, the indices reveal that the smooth minimal surface method is able to produce practical, acceptable predictions of deep-seated landslide failure interfaces, despite the omission of stratigraphy, geological structures and hydrogeological conditions.

The method is implemented with ease of use in mind such that operational costs are kept low and automation processes for a large number of landslide sites can be made possible. An additional benefit is that the method can simultaneously generate 3D computational meshes for the landslide scarp mass. These meshes can be applied to many subjects related to hazard mitigation plans. For example, for slope stability management, it is currently ongoing to develop 3D extended schemes for landslide volume and safety factor relations. Integrating with surface deformation data and material constitutive laws, slip displacements on the failure surface can be inversed for deep-seated landslides, in a somewhat similar way to dislocation model in tectonics. The volumetric mesh, or depth distribution, can also be used as the initial mass to perform landslide motion simulation to assess the influenced area. Summarizing the abovementioned potential applications and verification details presented in the present paper, we draw a combined flowchart in **Figure 13** for the two application scenarios of the method. The inputs and products of the method are explicitly indicated for each application scenario.

DATA AVAILABILITY STATEMENT

All datasets and computational codes generated for this study are included in the article/**Supplementary Material**.

AUTHOR CONTRIBUTIONS

All authors listed have made a substantial, direct and intellectual contribution to the work, and approved it for publication.

FUNDING

This work was supported in parts by grant no. MOST-106-2625-M-001-001- from the Ministry of Science and Technology and grant no. SWCB-108-10.10.1-S4 from the Soil and Water Conservation Bureau, of Taiwan, Republic of China.

ACKNOWLEDGMENTS

The authors thank Dr. Liu, Shou-Heng, Mr. Chen, and Yi-Zhong for their preparations of the DEMs and discussions.

SUPPLEMENTARY MATERIAL

The Supplementary Material for this article can be found online at: https://www.frontiersin.org/articles/10.3389/feart.2020.00211/full#supplementary-material

REFERENCES

Baroň, I., Řehánek, T., Vošmik, J., Musel, V., and Kondrová. (2011). Report on a recent deep-seated landslide at gírová mt., czech republic, triggered by a heavy rainfall: The gírová mt., outer west Carpathians; Czech Republic. *Landslides* 8, 355–361. doi: 10.1007/s10346-011-0255-y

Bishop, A. W. (1955). The use of slip circles in the stability analysis of slopes. *Geotechnique* 5, 7–17. doi: 10.1680/geot.1955.5.1.7

Cardinali, M., Paola, R., Guzzetti, F., Ardizzone, F., Antonini, G., Galli, M., et al. (2002). A geomorphological approach to the estimation of landslide hazards and risks in Umbria, Central Italy. *Nat. Hazards Earth Syst. Sci.* 2, 57–72. doi: 10.5194/nhess-2-57-2002

Central Geological Survey (2010). *Generation and QA/QC of LiDAR DEM in Heavy Disaster Area Induced by Typhoon Morakot in 2009 (in Chinese)*. Technical report, Cent. Geol. Survey Rep B.

Chen, R. F., Lee, C. Y., Yin, H. Y., Huang, H. Y., Cheng, K. P., and Lin, C. W. (2017). "Monitoring the deep-seated landslides by using ALOS/PALSAR satellite imagery in the disaster area of 2009 Typhoon Morakot, Taiwan," in *Advancing Culture of Living With Landslides-Vol. 3 Advances in Landslide Technology*, eds M. Miko, U. Arbanas, Y. Yin, and K. Sassa (Switzerland: Springer), 239–247. doi: 10.1007/978-3-319-53487-9_27

Chen, R. F., Lin, C. W., Chen, Y. H., He, T. C., and Fei, L. Y. (2015). Detecting and characterizing active thrust fault and deep-seated landslides in dense forest areas of southern Taiwan using airborne LiDAR DEM. *Remote Sens*. 7, 15443–15466. doi: 10.3390/rs71115443

Chigira, M. (2011). Geological and geomorphological characteristics of deep-seated catastrophic landslides induced by rain and earthquakes. *J. Chin. Soil Water Conserv*. 42, 265–278.

Chigira, M., and Kiho, K. (1994). Deep-seated rockslide-avalanches preceded by mass rock creep of sedimentary rocks in the Akaishi Mountains, central Japan. *Eng. Geo*. 38, 221–230. doi: 10.1016/0013-7952(94)90039-6

Chigira, M., Tsou, C. Y., Matsushi, Y., Hiraishi, N., and Matsuzawa, M. (2013). Topographic precursors and geological structures of deep-seated catastrophic landslides caused by Typhoon Talas. *Geomorphology* 201, 479–493. doi: 10.1016/j.geomorph.2013.07.020

Cleveland, W. S., Grosse, E., and Shyu, W. (1992). "Local regression models," in *Statistical Models in S*, eds J. M. Chambers and T. Hastie (Pacific Grove, CA: Wadsworth & Brooks/Cole), 624.

Crosta, G. B., Frattini, P., and Agliardi, F. (2013). Deep-seated gravitational slope deformations in the European Alps. *Tectonophys*. 605, 13–33. doi: 10.1016/j.tecto.2013.04.028

Dong, J. J., Li, Y. S., Kuo, C. Y., Sung, R. T., Li, M. H., Lee, C. T., et al. (2011). The formation and breach of a short-lived landslide dam at Hsiaolin Village, Taiwan - part I: post-event reconstruction of dam geometry. *Eng. Geo*. 123, 40–59. doi: 10.1016/j.enggeo.2011.04.001

Fei, L. Y., and Chen, M. M. (2013). *Geological Investigation & Database Construction for Upstream of Flood-Prone Area*. Central Geologic Survey.

Griffiths, D. V., and Lane, P. A. (1999). Slope stability analysis by finite elements. *Geotechnique* 49, 387–403. doi: 10.1680/geot.1999.49.3.387

Guzzetti, F., Ardizzone, F., Cardinali, M., R., M., and Valigi, D. (2009). Landslide volumes and landslide mobilization rates in Umbria, central Italy. *Earth Planet. Sci. Lett*. 279, 222–229. doi: 10.1016/j.epsl.2009.01.005

Hecht, F. (2012). New developments in Freefem++. *J. Numer. Math*. 20, 251–265. doi: 10.1515/jnum-2012-0013

Huang, C. C., and Tsai, C. C. (2000). New method for 3d and asymmetrical slope stability analysis. *J. Geotech. Geoenv. Eng*. 126, 917–927. doi: 10.1061/(ASCE)1090-0241(2000)126:10(917)

Huang, C. C., Tsai, C. C., and Chen, Y. H. (2002). Generalized method for three-dimensional slope stability analysis. *J. Geotech. Geoenv. Eng*. 128, 836–848. doi: 10.1061/(ASCE)1090-0241(2002)128:10(836)

Hungr, O. (1987). An extension of Bishop's simplified method of slope stability analysis to three dimensions. *Geotechnique* 37, 113–117. doi: 10.1680/geot.1987.37.1.113

Hungr, O., Salgado, F. M., and Byrne, P. M. (1989). Evaluation of a three-dimensional method of slope stability analysis. *Can. Geotech. J*. 26, 679–686. doi: 10.1139/t89-079

Janbu, N. (1973). "Slope stability computations," in *Embankment-dam Engineering, Casagrande Volume* (New York, NY: Wiley), 47–86.

Jiang, Q., and Zhou, C. (2018). A rigorous method for three-dimensional asymmetrical slope stability analysis. *Can. Geotech. J*. 55, 495–513. doi: 10.1139/cgj-2017-0317

Klar, A., Aharonov, E., Kalderon-Asael, B., and Katz, O. (2011). Analytical and observational relations between landslide volume and surface area. *J. Geophys. Res*. 116:F02001. doi: 10.1029/2009JF001604

Kuo, C. Y., Tai, Y. C., Chen, C. C., Chang, K. J., Siau, A. Y., Dong, J. J., et al. (2011). The landslide stage of the Hsiaolin catastrophe: simulation and validation. *J. Geophys. Res*. 116:F04007. doi: 10.1029/2010JF001921

Lam, L., and Fredlund, D. G. (1993). A general limit equilibrium model for three-dimensional slope stability analysis. *Can. Geotech. J*. 30, 905–919. doi: 10.1139/t93-089

Lee, C. F., Tsao, T. C., Huang, W. K., Lin, S. C., and Yin, H. Y. (2018). Landslide mapping and geomorphologic change based on a sky-view factor and local relief model: a case study in Hongye Village, Taitung (in Chinese). *J. Chin. Soil Water Conserv*. 49, 27–39. doi: 10.29417/JCSWC.201803_49(1).0003

Leshchinsky, D., and Huang, C. C. (1992a). Generalized slope stability analysis: interpretation, modification, and comparison. *J. Geotech. Eng*. 117, 1559–1576. doi: 10.1061/(ASCE)0733-9410(1992)118:10(1559)

Leshchinsky, D., and Huang, C. C. (1992b). Generalized three-dimensional slope-stability analysis. *J. Geotech. Eng*. 118, 1748–1764. doi: 10.1061/(ASCE)0733-9410(1992)118:11(1748)

Li, M. H., Sung, R. T., Dong, J. J., Lee, C. T., and Chen, C. C. (2011). The formation and breaching of a short-lived landslide dam at Hsiaolin Village, Taiwan–part II: Simulation of debris flow with landslide dam breach. *Eng. Geo*. 123, 60–71. doi: 10.1016/j.enggeo.2011.05.002

Lin, C. W., Chang, W. S., Liu, S. H., Tsai, T. T., Lee, S. P., Tsang, Y. C., et al. (2011). Landslides triggered by the 7 August 2009 Typhoon Morakot in southern Taiwan. *Eng. Geo*. 123, 3–12. doi: 10.1016/j.enggeo.2011.06.007

Lin, C. W., Tseng, C. M., Tseng, Y. H., Fei, L. Y., Hsieh, Y. C., and Tarolli, P. (2013). Recognition of large scale deep-seated landslides in forest areas of Taiwan using high resolution topography. *J. Asian Earth Sci*. 62, 389–400. doi: 10.1016/j.jseaes.2012.10.022

Lin, M. L., Chen, T. W., Lin, C. W., Ho, D. J., Cheng, K. P., Yin, H. Y., et al. (2014). Detecting large-scale landslides using Lidar data and aerial photos in the Namasha-Liuoguey Area, Taiwan. *Remote Sens*. 6, 42–63. doi: 10.3390/rs6010042

Lo, C. M. (2017). Evolution of deep-seated landslide at Putanpunas stream, Taiwan. *Geomatics Nat. Hazards Risk* 8, 1204–122. doi: 10.1080/19475705.2017.1309462

Luca, I., Tai, Y. C., and Kuo, C. Y. (2016). *Shallow Geophysical Mass Flows Down Arbitrary Topography*. (Switzerland: Springer). doi: 10.1007/978-3-319-02627-5

Mogenstern, N. R., and Price, V. E. (1965). The analysis of the stability of general slip surfaces. *Geotechnique* 15, 79–93. doi: 10.1680/geot.1965.15.1.79

Reid, M., Christian, S., and Brien, D. (2000). Gravitational stability of three-dimensional stratovolcano edifices. *J. Geophys. Res*. 105, 6043–6056. doi: 10.1029/1999JB900310

Reid, M., Christian, S., Brien, D., and Henderson, S. (2015). *Scoops3D-Software to Analyze 3D Slope Stability Throughout a Digital Landscape*. U.S. Geological Survey Techniques and Methods. doi: 10.3133/tm14A1

Reid, M., Sisson, T., and Brien, D. (2001). Volcano collapse promoted by hydrothermal alteration and edifice shape, Mount Rainier, Washington. *Geology* 29, 779–782. doi: 10.1130/0091-7613(2001)029<0779:VCPBHA>2.0.CO;2

Roering, J. J., Kirchner, J. W., and Dietrich, W. E. (2005). Characterizing structural and lithologic controls on deep-seated landsliding: implications for topographic relief and landscape evolution in the Oregon Coast Range, USA. *GSA Bull*. 117, 654–668. doi: 10.1130/B25567.1

Siegel, R. A. (1978). *STABL User Manual: a Description of the Use of STABL's Programmed Solution for the General Slope Stability Problem*. West Lafayette: Purdue University.

Soil Water Conservation Bureau (2017). *Monitoring and Analysis of Surface Deformation in Large-Scale Potential Areas by Using SAR Satellite Imagery (in Chinese)*. Technical report, SWCB-106-244, Taiwan.

Soil Water Conservation Bureau (2018). *Surface Displacement Observation and Deformation Analysis in Deep-Seated Landslide Areas Using InSAR Satellite (in Chinese)*. Technical report, Soil Water Conserv. Bureau Rep. SWCB-107-180, Taiwan.

Tai, Y. C., Heß, J., and Wang, Y. (2019). Modeling two-phase debris flows with grain-fluid separation over rugged topography: application to the 2009 Hsiaolin event, Taiwan. *J. Geophys. Res*. 124, 305–333. doi: 10.1029/2018JF004671

Taylor, F. E., Malamud, B. D., Witt, A., and Guzzetti, F. (2018). Landslide shape, ellipticity and length-to-width ratios. *Earth Surf. Proc. Landforms* 43, 3164–3189. doi: 10.1002/esp.4479

Tran, T. V., Alvioli, M., Lee, G., and An, H. U. (2018). Three-dimensional, time-dependent modeling of rainfall-induced landslides over a digital landscape: a case study. *Landslides* 15, 1071–1084. doi: 10.1007/s10346-017-0931-7

Tseng, C. M., Lin, C. W., Stark, C. P., Kiu, J. K., Fei, L. Y., and Hsieh, Y. C. (2013). Application of a multi-temporal, LiDAR-derived, digital terrain model in a landslide-volume estimation. *Earth Surf. Process. Landforms* 38, 1587–1601. doi: 10.1002/esp.3454

Tsou, C. Y., Feng, Z. Y., and Chigira, M. (2011). Catastrophic landslide induced by Typhoon Morakot, Shiaolin, Taiwan. *Geomorphology* 127, 166–178. doi: 10.1016/j.geomorph.2010.12.013

Ugai, K. (1985). Three-dimensional stability analysis of vertical cohesive slopes. *Soil Found*. 25, 41–48. doi: 10.3208/sandf1972.25.3_41

Vallet, A., Bertrand, C., Fabbri, O., and Mudry, J. (2015). An efficient workflow to accurately compute groundwater recharge for the study of rainfall-triggered deep-seated landslides, application to the Séchilienne unstable slope (western Alps). *Hydrology Earth Syst. Sci*. 19, 427–449. doi: 10.5194/hess-19-427-2015

Varnes, D. J. (1978). "Slope movement types and processes," in *Special Report 176: Landslides: Analysis and Control*, eds R. L. Schuster and R. J. Krizek (Washington, DC: Transportation and Road Research Board, National Academy of Science), 11–33.

Vergez, G., Danaila, I., Auliac, S., and Hecht, F. (2016). A finite-element toolbox for the stationary Gross-Pitaevskii equation with rotation. *Comp. Phys. Commun*. 209, 144–162. doi: 10.1016/j.cpc.2016.07.034

Wächter, A., and Biegler, L. T. (2006). On the implementation of a primal-dual interior point filter line search algorithm for large-scale nonlinear programming. *Math. Programming* 106, 25–57. doi: 10.1007/s10107-004-0559-y

Wang, Z., Bovik, A. C., Sheikh, H. R., and Simoncelli, E. P. (2004). Image quality assessment: from error visibility to structural similarity. *IEEE Trans. Image Process*. 13, 600–612. doi: 10.1109/TIP.2003.819861

Wu, R. Y., Chen, R. F., Yin, H. Y., Huang, H. Y., Cheng, K. P., and Lin, C. W. (2017). Assessment of deep-seated landslides using TCP-InSAR Interferometry (in Chinese). *J. Soil Water Conserv. Tech*. 11, 17–21.

Xing, Z. (1988). Three-dimensional stability analysis of concave slopes in plan view. *J. Geotech. Eng.* 114, 658–671. doi: 10.1061/(ASCE)0733-9410(1988)114:6(658)

Xu, Q., Li, W., Liu, H., Tang, R., Chen, S., and Sun, X. (2015). "Hysteresis effect on the deep-seated landslide by rainfall: The case of the kualiangzi landslide, China," in *Engineering Geology for Society and Territory - Volume 2*, eds G. Lollino, D. Giordan, G. B. Crosta, J. Corominas, R. Azzam, J. Wasowski, and N. Sciarra (Cham: Springer), 1557–1562. doi: 10.1007/978-3-319-09057-3_276

Zhang, S., and Wang, F. (2019). Three-dimensional seismic slope stability assessment with the application of Scoops3D and GIS: a case study in Atsuma, Hokkaido. *Geoenviron. Disasters* 6, 9–22. doi: 10.1186/s40677-019-0125-9

Zheng, H. (2012). A three-dimensional rigorous method for stability analysis of landslides. *Eng. Geol.* 145–146:30–40. doi: 10.1016/j.enggeo.2012.06.010

Conflict of Interest: The authors declare that the research was conducted in the absence of any commercial or financial relationships that could be construed as a potential conflict of interest.

frontiers
in Earth Science

ORIGINAL RESEARCH
published: 16 July 2020
doi: 10.3389/feart.2020.00293

A 36-Year Record of Rock Avalanches in the Saint Elias Mountains of Alaska, With Implications for Future Hazards

Erin K. Bessette-Kirton[1]* and Jeffrey A. Coe[2]

[1] Department of Geology and Geophysics, University of Utah, Salt Lake City, UT, United States, [2] Geologic Hazards Science Center, U.S. Geological Survey, Golden, CO, United States

Glacial retreat and mountain-permafrost degradation resulting from rising global temperatures have the potential to impact the frequency and magnitude of landslides in glaciated environments. Several recent events, including the 2015 Taan Fiord rock avalanche, which triggered a tsunami with one of the highest wave runups ever recorded, have called attention to the hazards posed by landslides in regions like southern Alaska. In the Saint Elias Mountains, the presence of weak sedimentary and metamorphic rocks and active uplift resulting from the collision of the Yakutat and North American tectonic plates create landslide-prone conditions. To differentiate between the typical frequency of landsliding resulting from the geologic and tectonic setting of this region, and landslide processes that may be accelerated due to changes in climate, we used Landsat imagery to create an inventory of rock avalanches in a 3700 km^2 area of the Saint Elias Mountains. During the period from 1984 to 2019, we identified 220 rock avalanches with a mean recurrence interval of 60 days. We compared our landslide inventory with a catalog of $M \geq 4$ earthquakes to identify potential coseismic events, but only found three possible earthquake-triggered rock avalanches. We observed a distinct temporal cluster of 41 rock avalanches from 2013 through 2016 that correlated with above average air temperatures (including the three warmest years on record in Alaska, 2014–2016); this cluster was similar to a temporal cluster of recent rock avalanches in nearby Glacier Bay National Park and Preserve. The majority of rock avalanches initiated from bedrock ridges in probable permafrost zones, suggesting that ice loss due to permafrost degradation, as opposed to glacial thinning, could be a dominant factor contributing to rock-slope failures in the high elevation areas of the Saint Elias Mountains. Although earthquake-triggered landslides have episodically occurred in southern Alaska, evidence from our study suggests that area-normalized rates of non-coseismic rock avalanches were greater during the period from 1964 to 2019, and that the frequency of these events will continue to increase as the climate continues to warm. These findings highlight the need for hazard assessments in Alaska that address changes in landslide patterns related to climate change.

Keywords: rock avalanche, Alaska, landslide inventory, landsat, saint elias mountains, frequency-magnitude

Edited by:
John Joseph Clague,
Simon Fraser University, Canada

Reviewed by:
Marten Geertsema,
Ministry of Forests and Range, Canada
Stefano Luigi Gariano,
Institute for Geo-Hydrological Protection (IRPI), Italy

***Correspondence:**
Erin K. Bessette-Kirton
erin.bessette.kirton@utah.edu

Specialty section:
This article was submitted to Quaternary Science, Geomorphology and Paleoenvironment, a section of the journal Frontiers in Earth Science

Received: *30 April 2020*
Accepted: *23 June 2020*
Published: *16 July 2020*

Citation:
Bessette-Kirton EK and Coe JA (2020) A 36-Year Record of Rock Avalanches in the Saint Elias Mountains of Alaska, With Implications for Future Hazards. Front. Earth Sci. 8:293. doi: 10.3389/feart.2020.00293

INTRODUCTION

Changes in landslide magnitude and frequency caused by rising temperatures are expected in mountainous, cryospheric terrain (e.g., Hock et al., 2019). This is especially true for rock slides and rock avalanches because their occurrence can be influenced by the degradation of ice (e.g., Gruber and Haeberli, 2007). Throughout this paper, we use the term "landslide" as a general term for all types of slope failures, and the term "rock avalanche" to describe rapid, flow-like landslides of fragmented rock that began as rock slides or rock falls (Hungr et al., 2014). Rock avalanches are considered rare events, with estimated frequencies for rock avalanches >20 Mm^3 or >1 km^2 for mountainous regions of 10,000 km^2 in Europe, New Zealand, and Canada ranging from 0.0002 to 0.0019 rock avalanches per year (526- to 5000-year recurrence intervals, Hungr and Evans, 2004). However, because recurrence intervals get longer as study area size gets smaller, and shorter as rock avalanche size gets smaller, these recurrence estimates are likely too short for individual sites, and too long for rock avalanches <20 Mm^3. In support of the second part of this statement, prior to the work by Hungr and Evans (2004); McSaveney (2002) estimated a frequency of 0.05 to 0.03 rock avalanches per year (a recurrence interval of 20–30 years) for rock avalanches >1 Mm^3 in the Southern Alps of New Zealand.

Because rock avalanches are common in cryospheric-mountainous terrain (e.g., Deline et al., 2015a) that is susceptible to degradation by warming from climate change (e.g., Beniston, 2003; Paul et al., 2004; Gruber and Haeberli, 2007; Fischer et al., 2012; Huss and Hock, 2015; Hock et al., 2019; Patton et al., 2019), studies of ice-degradation processes and their impact on slope stability (e.g., Fischer et al., 2006; Gruber and Haeberli, 2007; Krautblatter et al., 2013), as well as climate-induced changes in rock avalanche recurrence intervals and sizes, are active landslide research frontiers. For mountainous terrain, process research is generally of two types: studies on the degradation of mountain permafrost and the resulting impact on cohesion and pore pressure in rock slopes (e.g., Gruber and Haeberli, 2007), and studies investigating how the reduction and complete removal of glacial ice will impact steep rock slopes that were previously supported by ice (e.g., Grämiger et al., 2018). In the United States, Alaska is an emerging hot spot for such research because of abundant cryospheric terrain, annual (statewide) mean temperatures that have increased at a rate of 0.4°C (0.7°F) per decade since the 1970s (Walsh et al., 2014; Markon et al., 2018), and projected temperature increases (van Oldenborgh et al., 2013; Markon et al., 2018) that will be among the highest in the world.

Alaska is also tectonically active, and widespread rock avalanches are periodically triggered by earthquakes (e.g., Tarr and Martin, 1912; Post, 1967; Jibson et al., 2006). Uplift from tectonic plate collisions, especially in south-central Alaska, has likely weakened rocks, making them more susceptible to failure by both earthquake and non-coseismic triggers. Aside from earthquakes, climate related processes such as prolonged warming periods, freeze-thaw, rapid snowmelt, or intense or prolonged precipitation are common landslide triggers in cryospheric mountain regions. In addition, such factors have the capability to condition both earthquake-triggered and non-coseismic rock avalanches. An intriguing research question is related to the relative abundance and impact of rock avalanches from these different processes, as well as the compound effects that ice degradation will have on earthquake-triggered rock avalanches.

From a hazards and risk perspective, the question of how warming temperatures and changing patterns of precipitation as a result of climate change will impact rock avalanche frequency (recurrence intervals) and magnitude is important to consider because rock avalanches often entrain material and grow volumetrically as they travel downslope (e.g., Bessette-Kirton et al., 2018), travel long (>5 km) distances (Post, 1967; McSaveney, 1978; Evans and Clague, 1999; McSaveney, 2002; Huggel et al., 2005, 2007, 2010; Evans et al., 2009; Geertsema, 2012; Guthrie et al., 2012; Jacquemart et al., 2020), and can create cascading hazards (e.g., outburst floods or tsunamis) when they impact mountain lakes or fiords (Miller, 1960; Bessette-Kirton et al., 2017; Haeberli et al., 2017; Higman et al., 2018). These characteristics make rock avalanches a risk to humans in areas well downstream from locations where they initiate (e.g., Huggel et al., 2005; Evans et al., 2009; Duhart et al., 2019; Mergili et al., 2020; Walter et al., 2020).

Recent studies have suggested that rock avalanche recurrence intervals are becoming shorter in New Zealand (McSaveney et al., 2014, 2015) and Alaska (Coe et al., 2018), although the driving mechanisms for these changes are uncertain. In New Zealand's Southern Alps, McSaveney et al. (2014) and McSaveney et al. (2015) suggested that the shortened recurrence interval for rock avalanches >1 Mm^3 could be due to an increasing accumulation of strain in the crust since the last great earthquake, with mountain permafrost degradation being a possible contributing factor. In Alaska, Coe et al. (2018) found a temporal cluster of eight, large (total area >5 km^2), highly mobile rock avalanches that occurred during a 4-year period (2012–2016) of record-breaking winter and spring temperatures, and suggested that mountain permafrost degradation was a likely cause, but acknowledged that other factors such as accumulating crustal strain, glacial thinning, and increased precipitation may have contributed.

A difficulty of assessing changes in rock avalanche magnitude and frequency caused by climatic variations is a lack of long-term, systematically and consistently collected data sets that can be used to investigate such changes. Additionally, rock avalanches deposited on glaciers often have a short residence time and are rapidly reworked by glacial processes and snow cover (McSaveney, 2002; Hewitt et al., 2011; Reznichenko et al., 2011; Deline et al., 2015b; Dunning et al., 2015). These challenges highlight the difficulty of collecting long-term data that are of high and consistent quality. Several previous studies have utilized long-term records generated from satellite imagery (Schlögel et al., 2011; Uhlmann et al., 2013; Bessette-Kirton and Coe, 2016) and seismic data (Hibert et al., 2019) to assess changes to the frequency and magnitude of landslides, but, overall, such records are rare, especially in mountainous cryospheric terrain.

In this paper, we present and analyze a new 36-year (1984–2019) rock avalanche inventory (GIS map data are available in

Bessette-Kirton et al., 2020) from the high alpine, Saint (St.) Elias Mountains of southern Alaska. The St. Elias range lies at an active convergent tectonic plate boundary and is susceptible to rock avalanches (Petley, 2012; Evans and Delaney, 2014; Reid, 2017; Higman et al., 2018). We mapped rock avalanches in a 3700 km^2 area by systematically examining Landsat imagery, and analyzed trends in rock avalanche frequency and magnitude in the context of historical climate data from a local meteorological station. We determined if any rock avalanches could have been seismically triggered and compared our inventory with past events (coseismic and not) in neighboring areas of southern Alaska. Finally, we discuss the implications of our results for erosion rates and glacier dynamics in the region, and the effects of glacial thinning and permafrost degradation on rock avalanche failures in the St. Elias Mountains.

Study Area

The 3700 km^2 study area is located in southern Alaska, within Wrangell-St. Elias National Park and Preserve and along the south flank of the glaciated St. Elias mountain range between Icy Bay and Yakutat Bay (**Figure 1**). The St. Elias range is an accretionary terrane at the convergent (collisional) boundary between the northwestward moving Yakutat tectonic microplate and the North American tectonic plate (e.g., Winkler et al., 2000; Bruhn et al., 2004). The convergence rate between the plates is ∼40–50 mm/yr (e.g., Elliott et al., 2010, 2013) and overall exhumation within the orogen is estimated to be 2–3 mm/year, with localized exhumation >10 mm/year (Pavlis et al., 2012). Uplift within the study area from combined tectonic and isostatic forces ranges from 16 to 18 mm/yr (Larsen et al., 2004). Geologic units within the study area (e.g., see Winkler et al., 2000; Richter et al., 2005; Wilson et al., 2015) consist of folded and faulted rocks including: flysches, altered volcanic rocks, chert, carbonate, and granitic rocks of the Cretaceous Yakutat Group; mudstones, siltstones and sandstones of the Tertiary and Quaternary Yakataga and Tugidak Formations; Eocene siltstones and sandstones of eastern Prince William Sound; flysches, volcanic rocks, and graywackes of the Cretaceous Chugach accretionary complex; and marbles, schists, and phyllites of the Mississippian Kaskawulsh group.

The St. Elias study area lies within the largest connected glacier and icefield complex in continental North America (Muskett et al., 2003), and relief within the study area is extreme, ranging from sea level to Mount St. Elias at 5489 m within a distance of 19 km (**Figure 1**). Gruber (2012a,b) indicates that mountain permafrost is likely present in high elevation areas (see Gruber (2012b) for map data). Glaciers cover roughly 50% of the study area (**Figure 1**) and include interior valley (e.g., Seward), tidewater (e.g., Hubbard), and piedmont (e.g., Malaspina) glaciers. Erosion by glaciers is approximately equal to the rate of uplift (Spotila et al., 2004). Between 1972/1973 and 2000, thinning of 47 ± 5 m was observed in the ablation areas of the Malaspina Glacier, including the Seward lobe, and the Agassiz, Marvine, and Hayden Glaciers (Muskett et al., 2003). More recent surveys between 2007 and 2012 have shown several meters of local thickening per year for Seward Glacier and the upper part of Malaspina Glacier, and thinning rates of one to several meters per year elsewhere in the study area (Loso et al., 2014).

Several studies have documented landslides in the study area during the past century. Most recently, in October 2015 the Taan Fiord landslide (Dufresne et al., 2018; Haeussler et al., 2018; Higman et al., 2018) involved the collapse of 76 Mm^3 of material (Haeussler et al., 2018) from a previously identified, unstable mountain flank (Meigs and Sauber, 2000), onto the terminus of Tyndall Glacier and into Taan Fiord. This landslide generated a tsunami with a maximum onshore runup of 193 m (Higman et al., 2018). Prior to the Taan Fiord landslide, reported landslides in the study area included a rock avalanche that was detected seismically and occurred at the terminus of Hubbard Glacier at Disenchantment Bay (i.e., the northernmost part of Yakutat Bay, **Figure 1**) in 2012 (Petley, 2012), two rock avalanches in 1965 that were deposited on the Blossom (1.5 km^2 deposit area) and Marvine (1 km^2 deposit area) Glaciers (Post, 1967), a 3 Mm^3 rock-ice avalanche that was deposited on Marvine Glacier in 1983 (e.g., Schneider et al., 2011) and three large (6–10 Mm^3) rock avalanches triggered by a M 7.4 earthquake on February 28, 1979 that failed from rock slopes within 10 km of both sides of Seward Glacier (Cascade 1, 2, and 3 in Table 2 of Reid, 2017; see also Delaney and Evans, 2014; Evans and Delaney, 2014). In September 1899, coseismic rock avalanches throughout the St. Elias range were recorded in the aftermath of multiple large (M 7.8 to M 8.6, Stover et al., 1980) earthquakes that occurred in the Yakutat Bay area (Tarr and Martin, 1912; Evans and Clague, 1999). After making post-earthquake field observations in the region in 1905, Tarr and Martin (1912, p. 48) stated that rock and snow "avalanche tracks are far more abundant in the Yakutat Bay region than in any part of the thousand-mile mountainous inside passage from Seattle to Sitka" and attributed this abundance to their close proximity to active earthquake faults. Additionally, Tarr and Martin (1912) noted the locations of several rock avalanches near the coastline and indicated that multiple glaciers in the area experienced surging because of the amount of rock avalanche debris that was deposited on them during the earthquake.

MATERIALS AND METHODS

Inventory Mapping

The methods used in this work were replicated from Bessette-Kirton and Coe (2016) and Coe et al. (2018). Here, we provide a summary of the methodology and discuss some additional details that were necessary to consider for the St. Elias study area. We used 30-m resolution Collection 1 Level-1 Landsat imagery, which has been continuously collected since 1984, to create an inventory of rock avalanches in our study area from 1984 through 2019. To maintain consistency throughout the 36-year period of record we did not utilize the 15-m resolution panchromatic data that are available for Landsat 7 and Landsat 8 since these data are not available for earlier Landsat missions. The consistency and short acquisition time (∼16 days) of Landsat typically allowed us to examine at least one early summer (May or June) and one late summer (August or September) image from every year

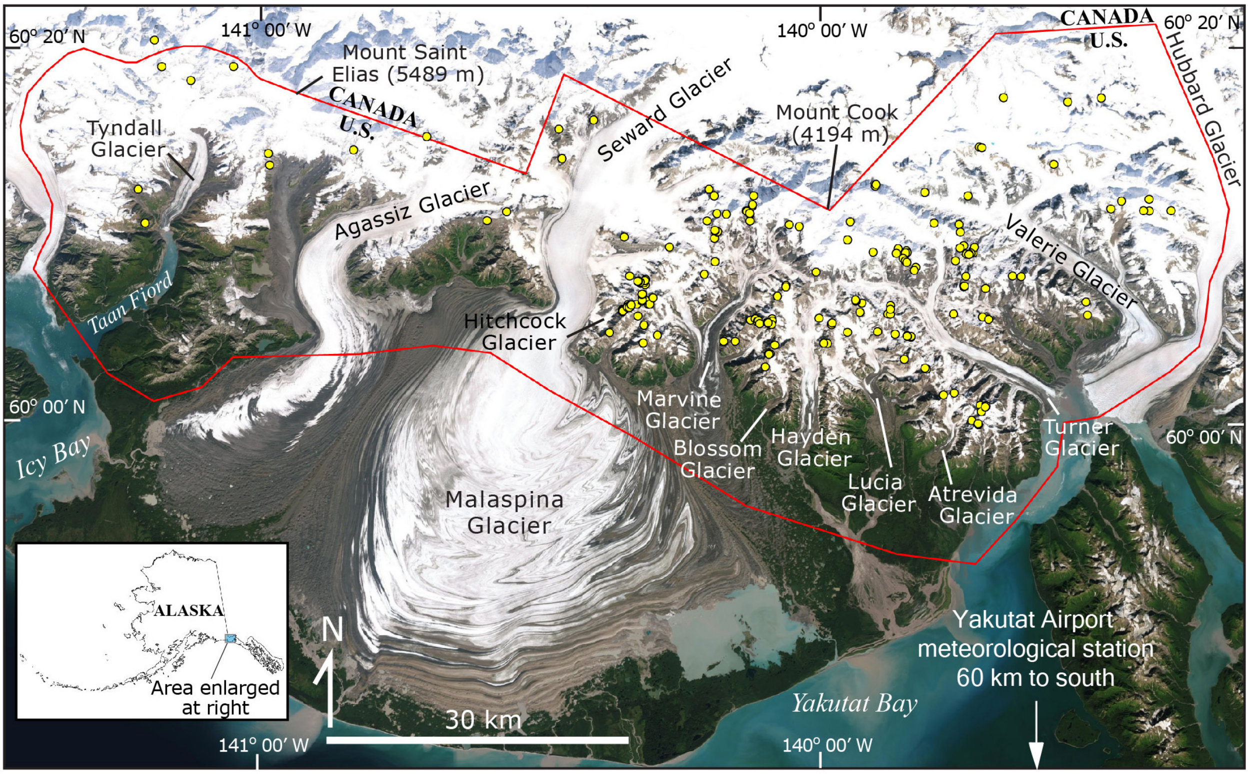

FIGURE 1 | Map of the Saint Elias study area (red polygon) in Alaska, showing locations of rock avalanches mapped between 1984 and 2019 (yellow dots).

(**Supplementary Table S1**). Within the period of record, 1989 was the only year for which coverage of the study area was incomplete, when imagery was only available for half of the study area. Whenever possible, we used the best quality, cloud-free imagery to improve our ability to identify rock avalanches, but in rare cases we were forced to use cloudy or poor quality (e.g., striping, poor lighting) images out of necessity (see Bessette-Kirton et al., 2020 for details).

We performed a grid search of the study area and identified rock avalanches at a scale of 1:60,000, and then mapped the total affected area (undifferentiated source and deposit areas) at a scale of 1:20,000. In addition to mapping total area polygons, we mapped headscarp points corresponding to the center of each rock avalanche headscarp, and travel distance lines, which reflect the maximum distance from the headscarp point to the farthest extent of visible rock avalanche deposits. Geographic information system (GIS) data are available from Bessette-Kirton et al. (2020) and here we include summary attributes for each mapped rock avalanche (**Supplementary Table S2**). Whenever possible, we used additional Landsat imagery (including fall and winter images) to map and constrain the date range for each event, and in a few cases, we also used DigitalGlobe imagery to further constrain rock avalanche dates (see **Supplementary Table S2**, Bessette-Kirton et al., 2020). We typically used false color images (band combinations 453 for Landsat 4, 5, 7, and 564 for Landsat 8) to systematically search the study area since the color contrast allowed for detection of events at a small scale. Subsequently, we used both true color and false color images (e.g., **Figure 2**) to map each event in detail. In some cases, good quality, true-color images allowed us to delineate disturbed source areas more easily than false color images, but contrast between disrupted or entrained snow and ice was often more noticeable in false color images.

We mapped rock avalanches by identifying lobate deposits that exhibited a high contrast with the surrounding surface and noticeable differences between progressive Landsat images. At the resolution of Landsat imagery (30 m), dark-colored rock avalanche deposits emplaced on glacier surfaces were much more readily identifiable than rock avalanche source areas. In addition, it was much more difficult to identify rock avalanche deposits with a high percentage (i.e., $>50\%$) of snow and ice that were emplaced on glaciers (i.e., because of low contrast with surrounding ice surfaces), rock avalanches that were disturbed by glacier movement, or rock avalanches that were predominantly deposited onto rock surfaces. We identified several events that fit these criteria, but our mapping methods could have caused us to miss additional events with these characteristics. Rock avalanches that occurred during the winter and were rapidly covered by snowfall and reworked before reappearing during the summer were particularly difficult to detect, and our inventory may have missed events with these characteristics.

Based on the size of events that could be consistently identified in 30-m resolution imagery, we used a total rock avalanche area of 0.1 km^2 as a minimum limit of detection.

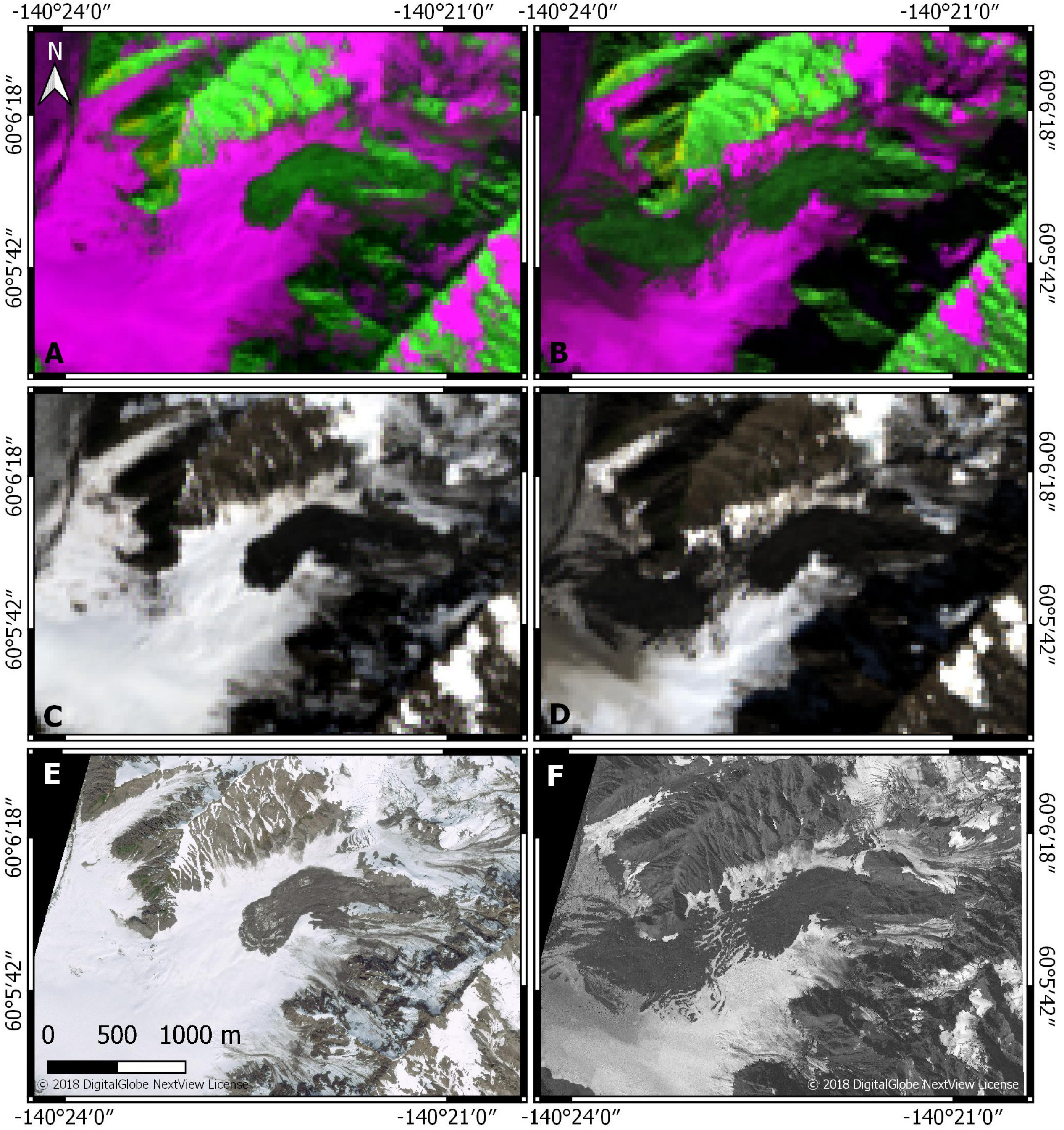

FIGURE 2 | (A) Landsat image acquired on 24 July 2018 (false color band combination RGB = 564) showing a fresh rock avalanche deposit (RA 212, event occurred between 8 June 2018 and 1 July 2018) and older rock avalanche deposits buried under snow on the surface of Hitchcock Glacier. **(B)** Landsat image acquired on 3 September 2018 showing the deposit of RA 212 starting to degrade and older rock avalanche deposits that have been uncoved by snow. **(C,D)** True color images of **(A,B)**, respectively. DigitalGlobe satellite images that were collected at similar times are shown in parts **(E)** 5 July 2018 and **(F)** 4 September 2018 for comparison.

Thus, we did not map rock falls or continuously active talus slopes in which relatively small movements were consistently visible. The accuracy with which we were able to map rock avalanches varied with image quality and terrain type. In general, headscarp locations were much more difficult to delineate than deposit areas because shadows were often present in areas of steep terrain, and contrasts between fresh failure surfaces and intact rock were more difficult to identify on bedrock ridges with partial or no snow cover (which was typical during the summer months). Thus, we estimated the absolute accuracy of deposit polygons and headscarp points to be ±50 m and ±150 m, respectively.

In the St. Elias study area, rock avalanches commonly occurred from source areas that had previously failed. We observed repeated failures with temporal spacing ranging from days to years, and thus developed the following criteria to classify rock avalanches originating from the same source areas. In a few cases, we observed repeated rock avalanche failures from the same location within a 1-month time period. When two rock avalanches occurred from the same source area location within a 1-month period of time, we classified the event as a "two-part" failure. These events were recognized on rare occasions when high-quality images were closely spaced in time, and we acknowledge that they consisted of a minimum of two parts but may have included more. The general lack of closely spaced imagery could have prevented us from identifying many more failures which happened in multiple parts. Furthermore, if an event occurred in multiple episodes, closely spaced imagery allowed us to detect a small event followed by a larger event, but not a large event followed by a small event (due to the lack of contrast between overlapping rock avalanche deposits). Therefore, two-part failures were mapped as separate events, but were counted together, as a single event for statistical analyses of rock avalanche rates.

In the case of rock avalanche failures that originated from the same source area but were separated by months or years, we used successive imagery to differentiate between old and new deposits. If a rock avalanche was found in an area where an older rock avalanche had previously been mapped, we compared the shapes and textures of the deposits to decide if the new event was distinct from the old event. Often, the shape of a new deposit was substantially different from that of older deposits. Recent deposits were usually characterized by smooth, lobate edges that contrasted sharply with the surrounding surface (**Figures 2A,C**), whereas old deposits typically had rough or uneven edges and sometimes became more visible throughout the summer as snow cover progressively melted (**Figures 2B,D**). After identifying all distinct rock avalanches, we used our headscarp accuracy limit of ±150 m to group rock avalanches with overlapping source areas into spatial clusters.

Earthquake Search

To identify rock avalanches that could have been triggered by earthquakes, we searched the U.S. Geological Survey earthquake catalog (U.S. Geological Survey, 2019, 2020) for $M \geq 4$ earthquakes that occurred within a distance of 1000 km from the headscarp location and coincided with the event date range of each rock avalanche in our inventory. We analyzed each resulting earthquake based on the magnitude-distance criteria established by Keefer (1984) and subsequently modified by Jibson (2013) to determine whether it could have triggered the rock avalanche. For example, based on these criteria, an earthquake that occurred 100 km away from the rock avalanche source area could have been a possible trigger if it was $M \geq 6.2$. In accordance with Coe et al. (2018), we used the conservative "disrupted landslides" criteria (i.e., the most susceptible type of landslide) of Keefer (1984) since we did not have prior knowledge of hillslope conditions. Disrupted landslides have experienced movement in the past and may, therefore, have established failure surfaces. Disrupted landslides are more sensitive to triggering by earthquakes than coherent landslides. For example, at a distance of 100 km from an earthquake epicenter, a disrupted landslide could be triggered by a smaller magnitude earthquake than the one required to trigger a coherent landslide.

Climate Analyses

We used climate data from the Yakutat Airport weather station (Lawrimore, 2017) to examine long-term temperature and precipitation trends in close proximity to the St. Elias study area. The Yakutat Airport weather station (59.512°, −139.6712°) is located 60 km southeast of the St. Elias study area and has a nearly complete data record dating back to 1948. We examined data from the 72-year period for which nearly continuous data were recorded at the station (1948–2019) to identify trends over the entire data record and also during the 36-year period corresponding to our rock avalanche inventory (1984–2019).

We used monthly temperature (minimum, maximum, and average), precipitation, and snowfall averages from 1948 to 2019 and 1984–2019 to track monthly, seasonal (multi-month), and yearly climate trends at the Yakutat Airport weather station. We used data from October 1-September 30 (water year) to represent annual climate intervals and evaluated trends in annual data using Mann-Kendall statistical tests (Hussain and Mahmud, 2019). The low elevation (10 m above sea level) and geographic position of the Yakutat Airport weather station undoubtedly contributed to differences in absolute temperature and precipitation values between the weather station and the higher elevation, mountainous terrain characteristic of the St. Elias study area. Because of this potential problem, we focused our analysis on long-term temperature and precipitation trends that may have influenced rock avalanche processes in the region, rather than examining absolute climate conditions for individual rock avalanche events. Furthermore, the presence of only one meteorological station in proximity to the St. Elias study area limited the extent of interpretations that we were able to make.

RESULTS

Rock Avalanche Inventory

Our inventory mapping revealed 220 rock avalanches in the St. Elias study area during the 36-year period between 1984 and 2019 (**Figure 1** and **Supplementary Table S2**). We did not observe other types of landslides during the period of record. On average, 6 rock avalanches occurred annually, with at least 2, and up to 14 events occurring each year (**Figure 3**). The greatest number of rock avalanches (per year) occurred during 2016 (14 rock avalanches, **Figure 3**). The longest period of consecutive years (four) with numbers of rock avalanches above the average of six, was from 2013 to 2016. Since we primarily used imagery to constrain the timing of rock avalanches in our inventory, most events were characterized by a range of possible event dates (**Supplementary Table S2** and **Figure 3A**). These ranges varied from several days to nearly 14 months. The only exceptions are a rock avalanche on the Hubbard Glacier in 2012 (RA 161, **Supplementary Table S2**; Petley, 2012), the

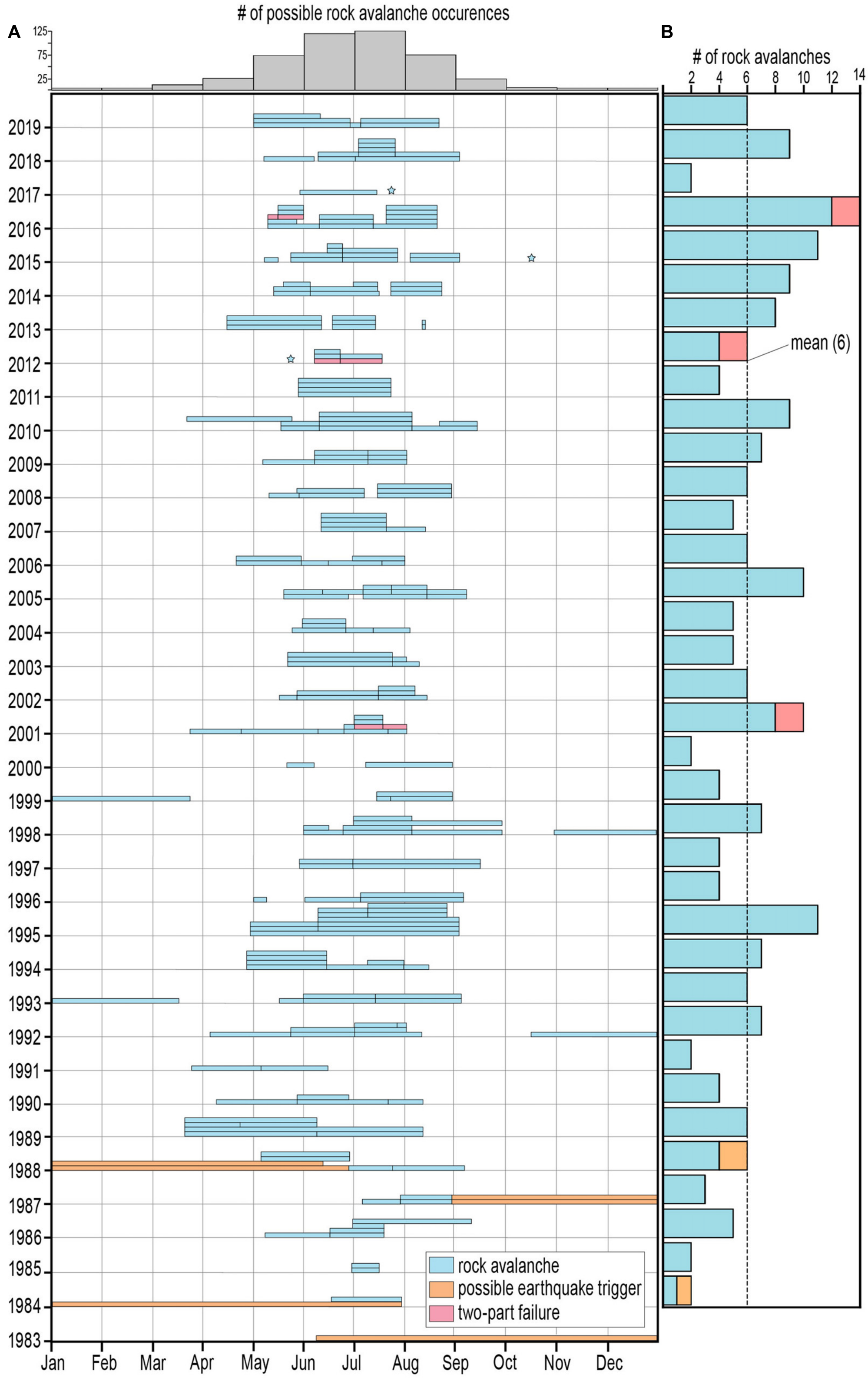

FIGURE 3 | (A) Chart showing the range of possible dates for 220 rock avalanches in the Saint Elias Mountains between 1984 and 2019 (center) and the number of possible rock avalanche events during each month of the year (top). Rock avalanches for which the exact event date is known are shown by stars. **(B)** Total number of rock avalanches that occurred annually during the period of record, with an overall mean of six rock avalanches per year.

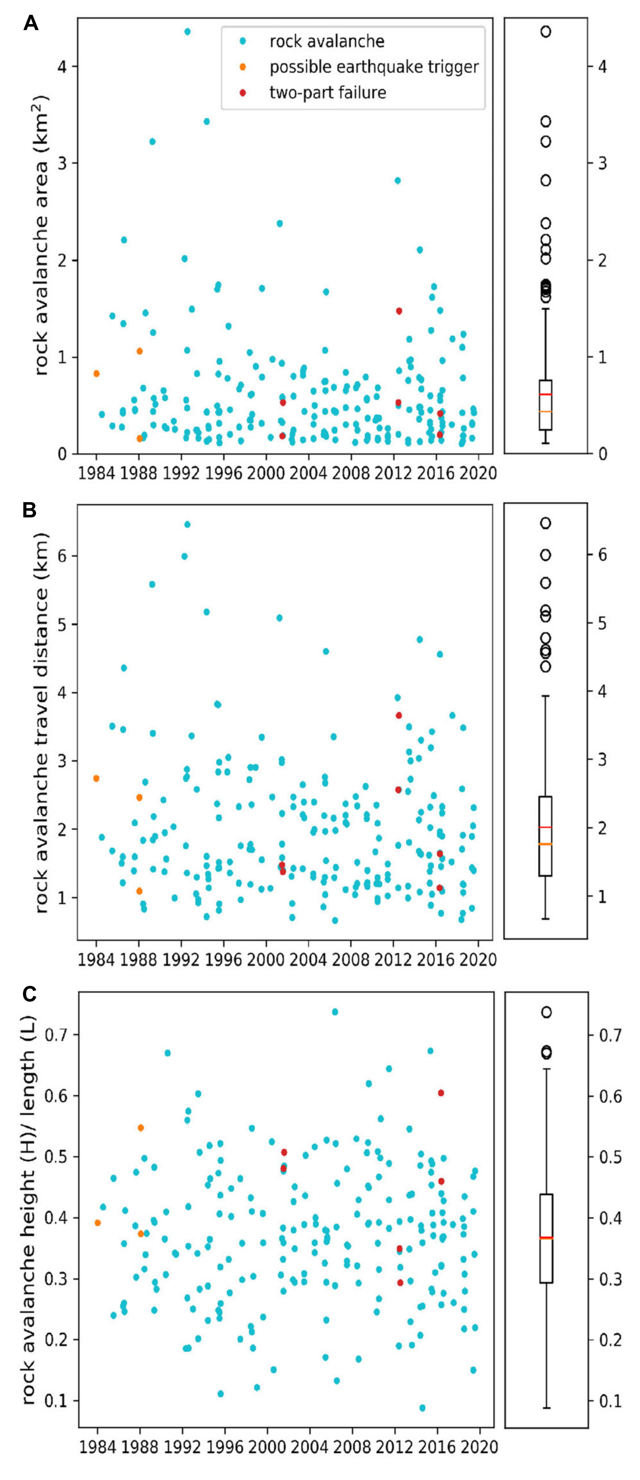

FIGURE 4 | Rock avalanche **(A)** area, **(B)** travel distance, and **(C)** ratio of fall height (H) to travel distance length (L) for rock avalanches in the Saint Elias study area during the period 1984–2019.

Taan Fiord landslide (RA 188, **Supplementary Table S2**), and a rock avalanche which occurred in 2017 (RA 204, **Supplementary Table S2**) for which we were able to confirm the exact date with seismic data analysis. Overall, the mean recurrence interval between rock avalanches was 60 days. However, rock avalanches were not evenly distributed throughout the year, but instead, occurred primarily during summer months, with 82% of all possible rock avalanche occurrences during May, June, July, and August (**Figure 3A**). During the period of record, the month with the highest number of possible rock avalanche occurrences was July (129; **Figure 3A**), and we observed no considerable changes in the occurrence dates of rock avalanches over time. We acknowledge that the observed predominance of summer season rock avalanches could be biased by the difficulty of detecting rock avalanches during winter months. We also acknowledge that this bias could have resulted in an undercounting of events.

Earthquake catalog search results yielded three rock avalanches (shown in orange in **Figure 3**) that could have been triggered by earthquakes (**Supplementary Table S3**). The absence of good quality imagery for these events limited our ability to narrow the range of possible event dates to fewer than 9–14 months (**Figure 3A**), which may have hindered the potential to rule out seismic triggers. Additionally, we identified three two-part failures (shown in red in **Figure 3**). Since any of the rock avalanches in our inventory could have also failed in multiple parts, we consider each two-part failure only once when quantifying rock avalanche rates and comparing rock avalanches to climate data. Additionally, possible earthquake-triggered landslides were not included in comparisons to climate data.

Rock avalanche areas (combined source and deposit areas) ranged from 0.1 to 4.4 km^2, with a median area of 0.4 km^2 (**Figure 4A**). Travel distances of rock avalanches ranged from 0.6 to 6.5 km with a median of 1.8 km (**Figure 4B**). The skewed distributions of area and travel distance indicate that most rock avalanches were small and had short travel distances. These distributions differed from the uniform distribution of rock avalanche mobility, measured by the ratio of fall height (H) to travel distance (L), which had a mean of 0.37 (**Figure 4C**). The examination of rock avalanche characteristics revealed no changes in area, travel distance, or mobility as a function of time.

Rock avalanches commonly initiated at or near bedrock ridges in probable permafrost zones (**Figure 5B**; Gruber, 2012b) were transported over mountainsides irregularly covered with snow and ice, and deposited onto either glacier accumulation zones or occasionally, gently sloping valley glaciers. Notably, the only rock avalanche in our inventory that did not predominantly run out onto a glacier was the Taan Fiord landslide, which partially deposited material onto Tyndall Glacier, but was mostly emplaced in Taan Fiord (Higman et al., 2018). We observed that rock avalanche deposits typically disappeared rapidly and were rarely identifiable in the years following an event unless they were uncovered by snowmelt at the end of a following summer (e.g., **Figure 2**). In some cases, we found that rock avalanche deposits were covered by snow or reworked within a few months after deposition (**Figure 6**). Some large rock avalanche deposits that traveled onto glacier ablation zones were visible on glaciers for multiple (up to 27) years after occurrence. The largest rock avalanche in our inventory (RA 33, **Supplementary Table S2**), which occurred in 1992 and had a total area of 4.4 km^2, was visible in imagery through 2019 (**Figure 7**). The movement rate of the

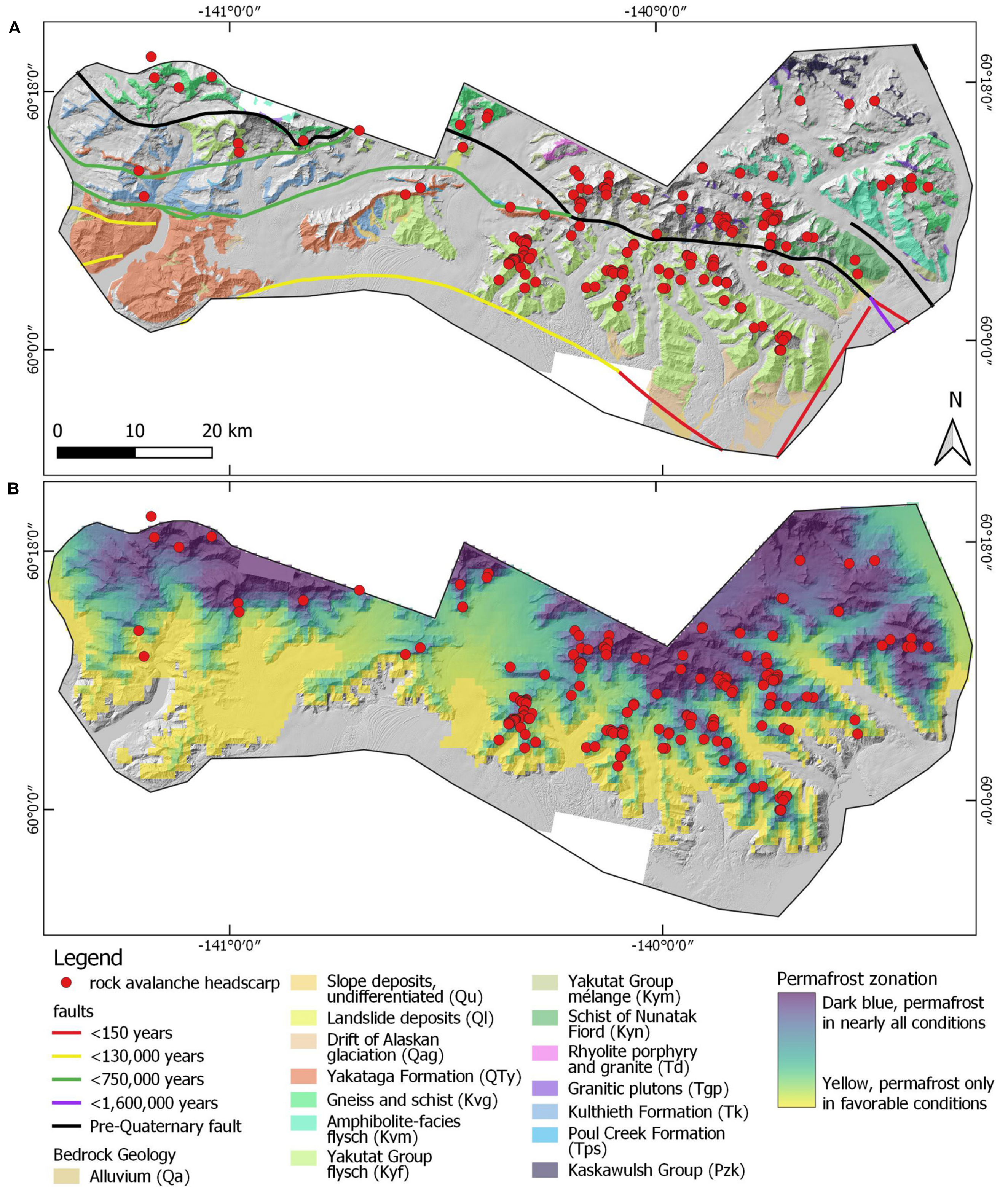

FIGURE 5 | (A) Map of the Saint Elias study area showing mapped rock avalanches, bedrock geology (Richter et al., 2005; Wilson et al., 2005) and fault locations (Koehler et al., 2012). Timing of most recent movement for each fault is shown. Geologic units have not been mapped in ice-covered areas, which account for ~68% of the study area. **(B)** Permafrost zonation map (Gruber, 2012b) of the Saint Elias study area showing the locations of rock avalanches that occurred between 1984 and 2019.

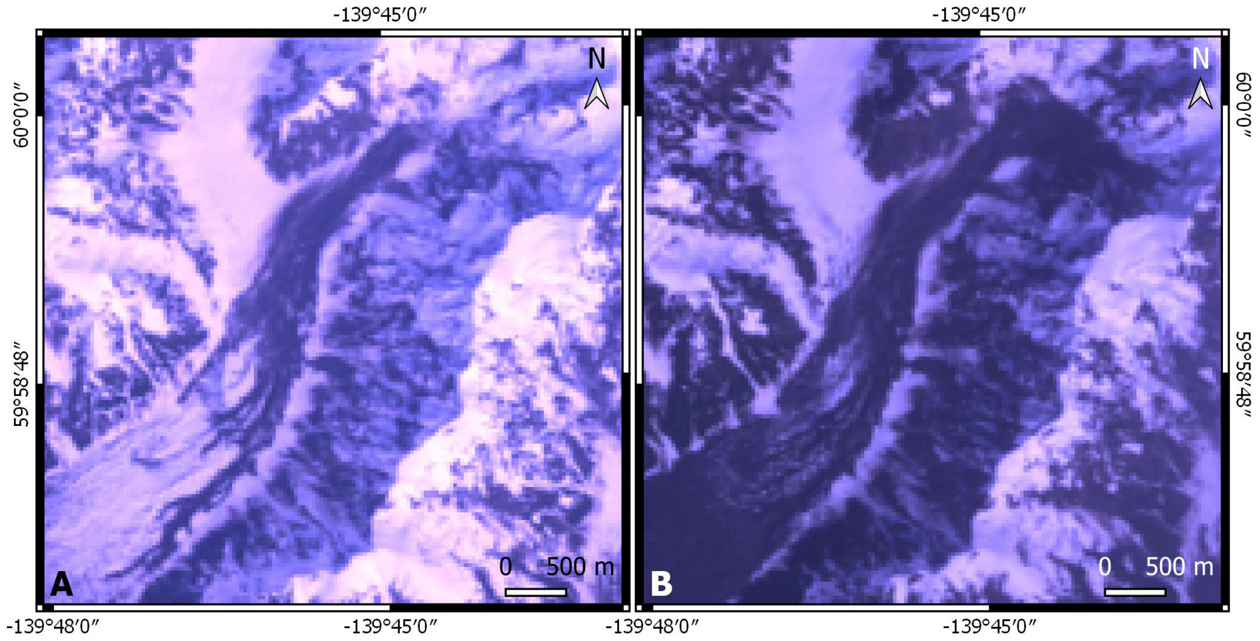

FIGURE 6 | Landsat images acquired on **(A)** 2 July 1992 and **(B)** 10 August 1992, showing the rapidly reworked deposit of RA 36 (event occurred between 4 April and 22 May 1992) on Atrevida Glacier.

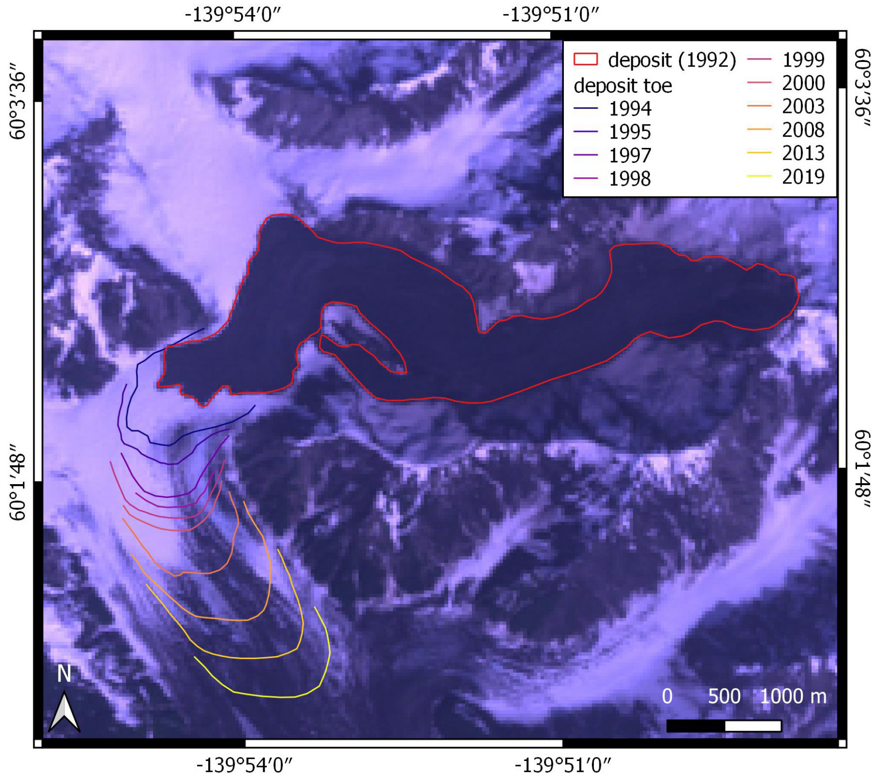

FIGURE 7 | Landsat image acquired on 10 August 1992 showing RA 33, which occurred between 25 July 1992 and 2 August 1992. In subsequent years, the rock avalanche toe was visible on the surface of Lucia Glacier, as shown by colored lines.

deposit terminus on the glacier surface varied between 65 and 250 m/year (**Supplementary Table S4**).

Rock avalanches initiated from a variety of rock types, but were particularly abundant to the east of Malaspina Glacier in the schist of Nunatuk Fiord (Kyn), flysch (Kyf) and mélange (Kym) of the Yakutat Group, and granitic plutons (Td, Tgp) which intruded Kyn and Kym (**Figure 5A**). Over half of all rock avalanches (131) originated in the flysch (Kyf) of the Yakutat Group (**Table 1**), which is the most areally extensive bedrock unit in the study area, underlying 34% of all non-ice-covered areas. The spatial density of rock avalanches in the flysch (Kyf) was 0.32 rock avalanches/km^2 (**Table 1**), which was relatively low compared to other geologic units. For example, the units with the highest spatial densities (1.3 rock avalanches/km^2) were the intrusive units (Td and Tgp; **Table 1**). The spatial density of rock avalanches in the schist of Nunatuk Fiord and other (non-flysch) units in the Yakutat Group ranged from 0.32 to 0.40 rock avalanches/km^2 (**Table 1**).

Spatial Rock Avalanche Clusters

Over half of the rock avalanches in our inventory (122; **Table 1**) initiated from source areas that failed repeatedly during the period of record. We identified 34 different source areas that contained between 2 and 14 distinct failures (i.e., spatial rock avalanche clusters). Spatial rock avalanche clusters occurred in rocks of the Yakutat Group (Kyf, Kyn, and Kym), intrusive units (Td and Tgp) and gneiss and schist (Kvg) of the Chugach terrane. Spatial clusters occurred in all geologic units with at least five failures, and nearly 70% of all failures in flysch (Kyf) of the Yakutat Group occurred in spatial clusters. Three rock avalanches that were documented in the study area prior to 1984 coincided with the locations of spatial clusters in our inventory. The exact location of two 1965 rock avalanches on Marvine and Blossom Glaciers (Post, 1967) are unknown, but approximately coincided with clusters c23 and c5, respectively (**Table 2**). A coseismic rock avalanche triggered by the 1979 St. Elias earthquake (Cascade 3; Delaney and Evans, 2014; Evans and Delaney, 2014; Reid, 2017) was located on Hitchcock Glacier (**Figure 1**) and coincided with cluster c12 (**Table 2**). Spatial rock avalanche clusters predominantly originated from slopes with north and west aspects, whereas single rock avalanches preferentially failed from south-southeast facing slopes (**Supplementary Table S2**, **Supplementary Figure S1**). We found no substantial differences between the deposit characteristics (area, travel distance, H/L) between rock avalanches that occurred in spatial clusters and those that did not.

Among all spatial clusters of rock avalanches, the timing of repeated events had no apparent pattern (**Figure 8**), although seven different clusters had events that occurred in consecutive years. The recurrence intervals for distinct spatial clusters ranged from just over a year (369 days) to more than 18 years (6572 days; **Table 2**). Overall, about 67% of basins in which rock avalanches occurred, had one event in the 36-year period of record. The other 33% of basins had multiple rock avalanches during the period of record (e.g., **Figures 9**, **10**). The source areas of spatial clusters c11 and c12 were located approximately 800 m apart and deposits from both clusters were emplaced in the same area of Hitchcock Glacier (**Figure 9**), making this the most active basin in the study area. The combination of seven failures from cluster c11, 14 failures from cluster c12, and spatially overlapping deposits from both clusters, resulted in a mean recurrence interval of 2 years (18 overlapping rock avalanche deposits in 36 years) for a small part of the Hitchcock Glacier (**Figures 9B**, **10**).

Climate Analyses

Mann–Kendall tests for temperature and precipitation during the 72-year period for which nearly continuous data were recorded at the Yakutat Airport weather station (1948–2019) yielded statistically significant ($p = 0.05$) increasing trends for average (slope = 0.028°C/year), maximum (slope = 0.028°C/year), and minimum (slope = 0.030°C/year) annual temperatures, a statistically significant ($p = 0.05$) decreasing trend for annual snowfall (slope = −3.5 mm/year), and no trend for precipitation. During the 72-year period, a warmer than average period began in 1977 and continued through 2019 (**Figure 11A**). This period was characterized by less than average snowfall (**Figure 11B**) but wide variations in overall precipitation (**Figure 11C**). Between 1977 and 2019, average annual temperatures exceeded the 72-year average 65% of the time, while minimum annual temperatures were above average 70% of the time. Total annual snowfall was below average during 79% of the years between 1977 and 2019. Beginning in about 1977, total precipitation was above average until the early 2000s, when precipitation decreased and remained below average through 2019 (**Figure 11C**).

The examination of monthly data throughout the period of record revealed seasonal discrepancies in the timing and magnitude of temperature changes. During the period between 1948 and 2019, winter (December through February) temperatures were generally more above average than summer temperatures. During the period of our rock avalanche inventory (1984–2019), January temperatures exceeded average by about twice as much as any other month (**Figure 12A**), and summer temperatures (May through August) also exceeded average more than temperatures during spring and fall months, although to a lesser extent than winter temperatures. Because winter and summer temperatures showed larger deviations from average during the period of our rock avalanche inventory, we used winter (December through February) and summer (June through August) seasonal averages to investigate temperature trends that may have affected rock avalanche processes.

During the period between 1984 and 2019, winter (December through February) and summer (June through August) temperatures were variably above and below the overall (1984–2019) mean (**Figures 12B,C**). Five-year moving average winter temperatures were above average for two or more consecutive years between 1986–1988, 1999–2006, and 2012–2017 (**Figure 12B**). Five-year moving average summer temperatures were similarly above average for two or more consecutive years between 2003–2006 and 2011–2017 (**Figure 12C**). The most recent and longest period during which both summer and winter temperatures were consistently above average coincided with a peak in rock avalanche activity that occurred between 2013 and 2016 (**Figure 12D**). In the future,

TABLE 1 | Characteristics of rock avalanches that occurred in the Saint Elias study area between 1984 and 2019 in varying bedrock formations (Richter et al., 2005).

Bedrock geology	Rock avalanches (#)	Rock avalanches (%)	Rock avalanches/Area (km^2)	Spatially clustered rock avalanches (#)	Single rock avalanches (#)
All	220	n/a	0.21	122	98
Yakataga formation (Qty)	3	1.4	0.01	0	3
Amphibolite-facies flysch (Kvm)	2	0.9	0.03	0	2
Gneiss and schist (Kvg)	19	8.6	0.18	2	17
Kulthieth formation (Tk)	3	1.4	0.04	0	3
Poul creek formation (Tps)	1	0.5	0.28	0	1
Granitic plutons (Tgp)	19%	8.6	1.30	7	12
Rhyolite porphyry and granite (Td)	8	3.6	1.31	5	3
Kaskawulsh group (Pzk)	1	0.5	0.06	0	1
Yakutat group mélange (Kym)	16*	7.3	0.40	7	9
Yakutat group flysch (Kyf)	131**%%	59.5	0.32	92	39
Schist of nunatak fiord (Kyn)	17	7.7	0.35	8	9

**Includes two-part failure. %Includes possible earthquake-triggered rock avalanche. **Includes 2 two-part failures. %%Includes two possible earthquake-triggered rock avalanches.*

additional climate data from multiple stations located in the study area or in similar terrain could aid in the understanding of climate-driven rock avalanche processes.

DISCUSSION

Comparison With Other Rock Avalanche Inventories

Recent works by Uhlmann et al. (2013) and Coe et al. (2018) present inventory data of rock avalanches in areas of southern Alaska that have terrain and climate characteristics that are similar to the St. Elias study area. Uhlmann et al. (2013) utilized Landsat imagery to identify and track the movement of rock avalanche deposits on glaciers in the Chugach Mountains between ∼1950–2008. The methods and data sources that we used in the St. Elias study area were identical to those used by Coe et al. (2018) in their study of rock avalanches in Glacier Bay National Park and Preserve (GBNPP) between 1984 and 2016. Rock avalanches in the St. Elias Mountains occurred seven times more frequently (**Figure 13A**), but were, on average, an order of magnitude smaller (**Figure 13B**) than rock avalanches in a 5000 km^2 area of GBNPP between 1984 and 2019 (Bessette-Kirton and Coe, 2016; Coe et al., 2018 and **Supplementary Table S5**). The average recurrence interval for rock avalanches in GBNPP was 437 days (30 rock avalanches), with an average of 0.8 rock avalanches occurring annually (Coe et al., 2018 and **Supplementary Table S5**). Similarly, Uhlmann et al. (2013) reported rock avalanche rates of 0.8–1.7 events/year in the Chugach Mountains (including rock avalanches triggered by earthquakes), which is about 4–8 times less frequent than non-coseismic rock avalanches in the St. Elias area.

We suspect that the large difference in the frequency of rock avalanches between the St. Elias and GBNPP study areas is due to differences in tectonic settings and rock types. The St. Elias area is undergoing rapid uplift due to compression from the collision of the Yakutat micro-tectonic plate and the North American tectonic plate. The GBNPP area is undergoing rapid uplift from viscoelastic rebound from post-Little Ice Age deglaciation, but lacks comparable active compression because it is located adjacent to a transform plate boundary between the Pacific and North American plates. In the St. Elias area, the presence of flysch (flysch of the Yakutat Group, Kyf), a weak rock type which is known to be highly susceptible to rock-slope failures in many parts of the world (e.g., Duman et al., 2005; Margielewski, 2006), likely contributed to the relatively high occurrence of rock avalanches. A comparable geologic unit is not present in GBNPP.

Although we observed differences in the total number and magnitude of events in the neighboring GBNPP study area, the timing and frequency changes observed in both study areas share important similarities. In both the GBNPP and St. Elias areas, a large departure from the average number of rock avalanches occurred between 2013 and 2016, a period during which regional temperatures were above average (**Figures 11A**, **12B–D**). During this period, the annual number of rock avalanches was, on average, 1.5 and 4 rock avalanches above the overall yearly average for St. Elias and GBNPP, respectively (**Figure 13A**). A smaller positive departure from average (0.5–3 rock avalanches) also occurred in both study areas between 1994 and 1996, which correlates to increased winter temperatures in the GBNPP study area (Coe et al., 2018), but no strong positive or negative temperature change at the Yakutat weather station (**Figures 11A**, **12B–D**). The rate of rock avalanches per year increased during the period of record for both study areas, with increases of 1.2 and 0.3 rock avalanches per year in St. Elias and GBNPP, respectively.

A comparison of rock avalanche frequencies between the St. Elias study area and mountainous regions in the European Alps, New Zealand Alps, and Canada (McSaveney, 2002; and Table 1 of Hungr and Evans, 2004) suggests that the frequency of rock avalanches in the St. Elias area is exceptional. For events larger than 1 km^2, the St. Elias study area had a rock avalanche frequency of 2.3 events/year/10,000 km^2 (30 events >1 km^2). This rate is >45 times higher than the rate of rock avalanches >1 Mm^3 in New Zealand (0.03–0.05 events/year,

TABLE 2 | Characteristics of 34 rock avalanche clusters (122 rock avalanche events) in the Saint Elias study area.

Rock avalanche cluster	Bedrock geology	Number of events	Mean recurrence interval between events (days)	Mean recurrence interval between events (years)
c1	Kvg	2	1835	5.0
c2	Kyf	4	1857	5.1
c3	Kyf	3	4386	12.0
c4	Kyf	3	3459	9.5
c5	Kyf	3	2024	5.5
c6	Kyf	6	1611	4.4
c7*	Kyf	7	1769	4.8
c8	Kyf	2	3301	9.0
c9	Kyf	2	2259	6.2
c10	Kyf	2	369	1.0
c11	Kyf	7	1878	5.1
c12*	Kyf	14	871	2.4
c13	Kyf	2	5044	13.8
c14	Kyf	3	3841	10.5
c15	Kyf	6	2051	5.6
c16	Kyf	2	5525	15.1
c17$^{\%}$	Kyf	3	3712	10.2
c18	Kyf	2	4034	11.1
c19	Kyf	2	1868	5.1
c20	Kyf	3	2906	8.0
c21	Kyf	7	1280	3.5
c22	Kyf	7	1588	4.4
c23	Kyf	2	4411	12.1
c24	Kym	3	5109	14.0
c25*	Kym	4	3071	8.4
c26	Kyn	4	1352	3.7
c27	Kyn	2	1456	4.0
c28	Kyn	2	4700	12.9
c29	Td	2	3285	9.0
c30	Td	2	2960	8.1
c31	Td	2	1483	4.1
c32	Tgp	3	1596	4.4
c33	Tgp	2	1080	3.0
c34	Tgp	2	6572	18.0

**Includes two-part failure. $^{\%}$Includes possible earthquake-triggered rock avalanche.*

McSaveney, 2002) and $>$1000 times higher than the frequencies (0.0002 to 0.0019 events/year/10,000 km^2) reported by Hungr and Evans (2004) for rock avalanches $>$20 Mm^3 or $>$1 km^2. Additionally, the St. Elias rate is 4 times greater than the frequency of rock avalanches greater than 1 km^2 in GBNPP (Coe et al., 2018 and **Supplementary Table S5**). Comparisons with rock avalanche frequencies in additional areas should be made as more systematically derived inventories become available.

Comparison With Coseismic Rock Avalanches in Alaska

Many of the rock avalanches that have been mapped and documented in southern Alaska have been triggered by earthquakes (Tarr and Martin, 1912; Miller, 1960; Post, 1967; Jibson et al., 2006, 2020; Delaney and Evans, 2014). In contrast, several large rock avalanches in Alaska during the last 15 years have attracted attention because they may have been conditioned by warming temperatures (Huggel et al., 2008, 2010). Additionally, in GBNPP non-coseismic rock avalanches (30 total; Bessette-Kirton and Coe, 2016; Coe et al., 2018, **Supplementary Table S5**) dominated the record of rock-slope failures during a period of relative earthquake quiescence between 1984 and 2019. This recent work suggests that a comparison between the number of rock avalanches triggered by earthquakes and those triggered by other sources would improve the understanding of the relative contribution of each type.

Since 1964, there have been three, large ($>$M 7.1) earthquakes that triggered widespread, well-documented landslides in southern Alaska: (1) the 1964 M 9.2 Anchorage earthquake (Hansen et al., 1966; Post, 1967); (2) the 2002 M 7.9 Denali earthquake (Eberhart-Phillips et al., 2003; Jibson et al., 2006); and (3) the 2018 M 7.1 Anchorage earthquake (Jibson et al., 2020). Nearly all of the landslides triggered in 2018 occurred at low altitudes and were not located in cryospheric terrain (Jibson et al., 2020). The 1964 and 2002 earthquakes triggered many rock avalanches in mountainous terrain similar to our study area (e.g., Post, 1967; Jibson et al., 2006; Schulz, in press). Two additional earthquakes in the late 20th century, one in 1958 and one in 1979, caused a few isolated, but notable landslides. The 1958 M 7.8 earthquake triggered a rock avalanche that entered Lituya Bay in GBNPP and caused a tsunami with a runup of 524 m (Miller, 1960). The 1979 M 7.2 St. Elias earthquake (Lahr et al., 1979) triggered three large (∼3–5 km^2) rock avalanches in the St. Elias study area (Delaney and Evans, 2014; Evans and Delaney, 2014). Although the epicenter of the 1979 St. Elias earthquake was located amidst the precipitous terrain of the St. Elias mountains (∼40 km from our study area) widespread rock avalanches were not triggered by the event (Lahr et al., 1979). However, since the earthquake occurred during the winter, the presence of ice-filled discontinuities could have resulted in increased cohesion of otherwise susceptible slopes (Gruber and Haeberli, 2007) or snowfall could have rapidly covered deposits, making them difficult to detect (e.g., Dunning et al., 2015).

At least 78 rock avalanches were triggered by the 1964 earthquake [Table 2 of Post (1967)], and approximately 1580 events were triggered by the 2002 earthquake (Schulz, in press). Summing these numbers in addition to the three 1979 St. Elias rock avalanches (we omitted the 1958 Lituya Bay rock avalanche since an inventory was not conducted for the earthquake), yields a crude minimum estimate of 1661 rock avalanches triggered by earthquakes in southern Alaska since 1964, or a mean of about 27 per year (1661/55 years) in an area with a size of 140,000 ± 30,000 km^2. The combined area of the St. Elias (3700 km^2) and GBNPP (5000 km^2) study areas is about 8700 km^2. The total number of non-coseismic rock avalanches in both areas between 1984 and 2019 is 244. Although we don't have systematic records of rock avalanches prior to 1984 in either of the study areas, we can compare with coseismic rock avalanches during the period from 1964

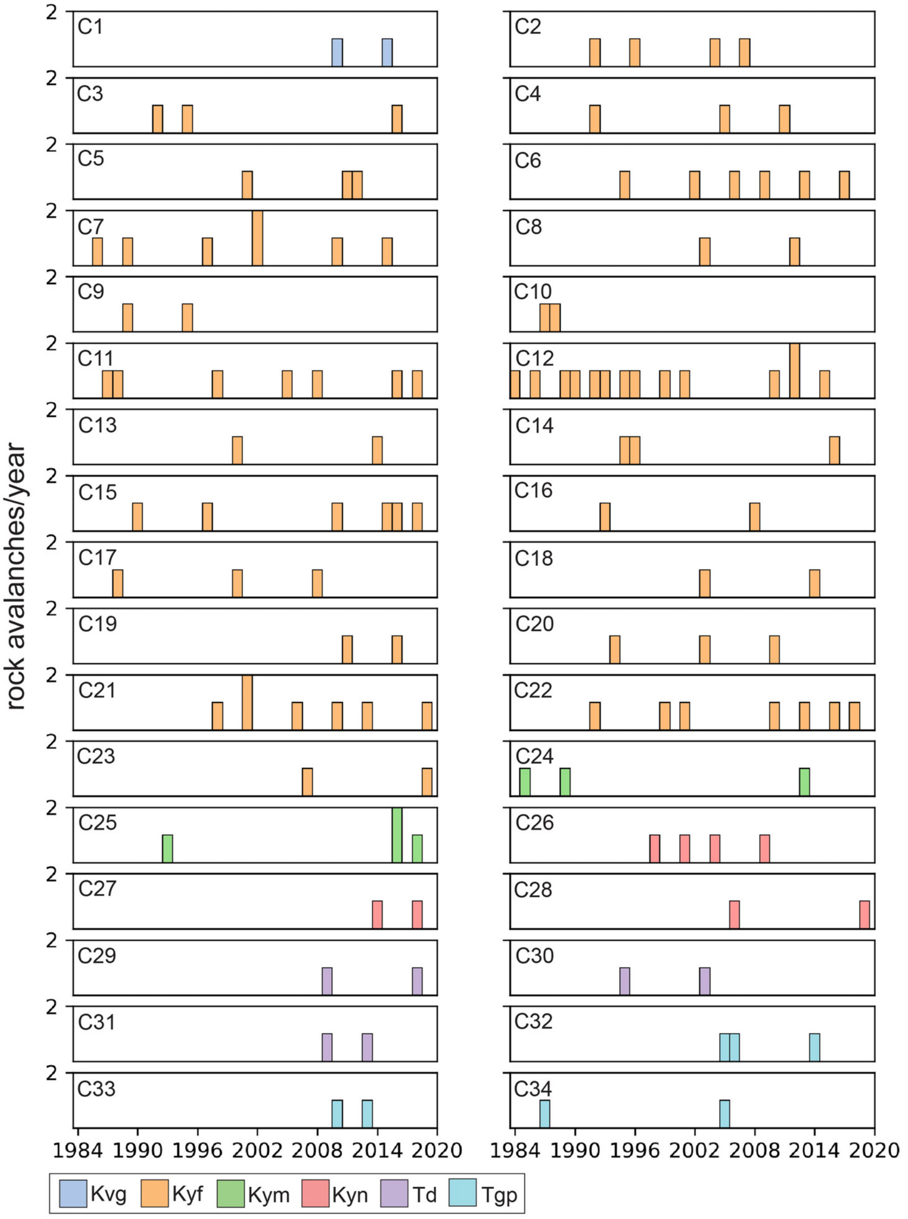

FIGURE 8 | Histograms showing the timing of clustered rock avalanche failures in the flysch (Kyf) and mélange (Kym) members of the Yakutat Group, schist of Nunatak Fiord (Kyn), gneiss and schist of the Chugach terrane (Kvg), granitic plutons (Tgp), and rhyolite porphyry and granite (Td) in the Saint Elias study area between 1984 and 2019.

to 2019 by assuming 244 as a minimum number of non-coseismic events. Thus, the minimum rate of non-coseismic rock avalanches for the St. Elias and GBNPP study areas was about 4 events per year (244/55 years). Normalizing the two means by area (27/year/140,000 ± 30,000 km^2 and 4/year/8,700 km^2) yields values of 0.0002 ± 0.00005/year/km^2 for earthquake-triggered rock avalanches, and 0.0005/year/km^2 for non-coseismic rock avalanches. These estimates suggest that, in cryospheric mountainous terrain since 1964, the area-normalized rate of non-coseismic rock avalanches was, at a minimum, about 2x greater than that of earthquake-triggered rock avalanches.

We acknowledge that a longer period of time may be needed to better characterize the frequency of rock avalanches triggered by earthquakes. Additionally, intense shaking from earthquakes can destabilize slopes, or cause marginally stable slopes to fail, and thus alter the frequency of subsequent non-coseismic rock avalanches (e.g., Shafique, 2020). The opposite effect would also be true, that is, future earthquakes could be more impactful because intense shaking could have a greater effect on slopes that are increasingly susceptible to failure as a result of glacial retreat or permafrost degradation; a phenomenon that has been demonstrated for the combination of

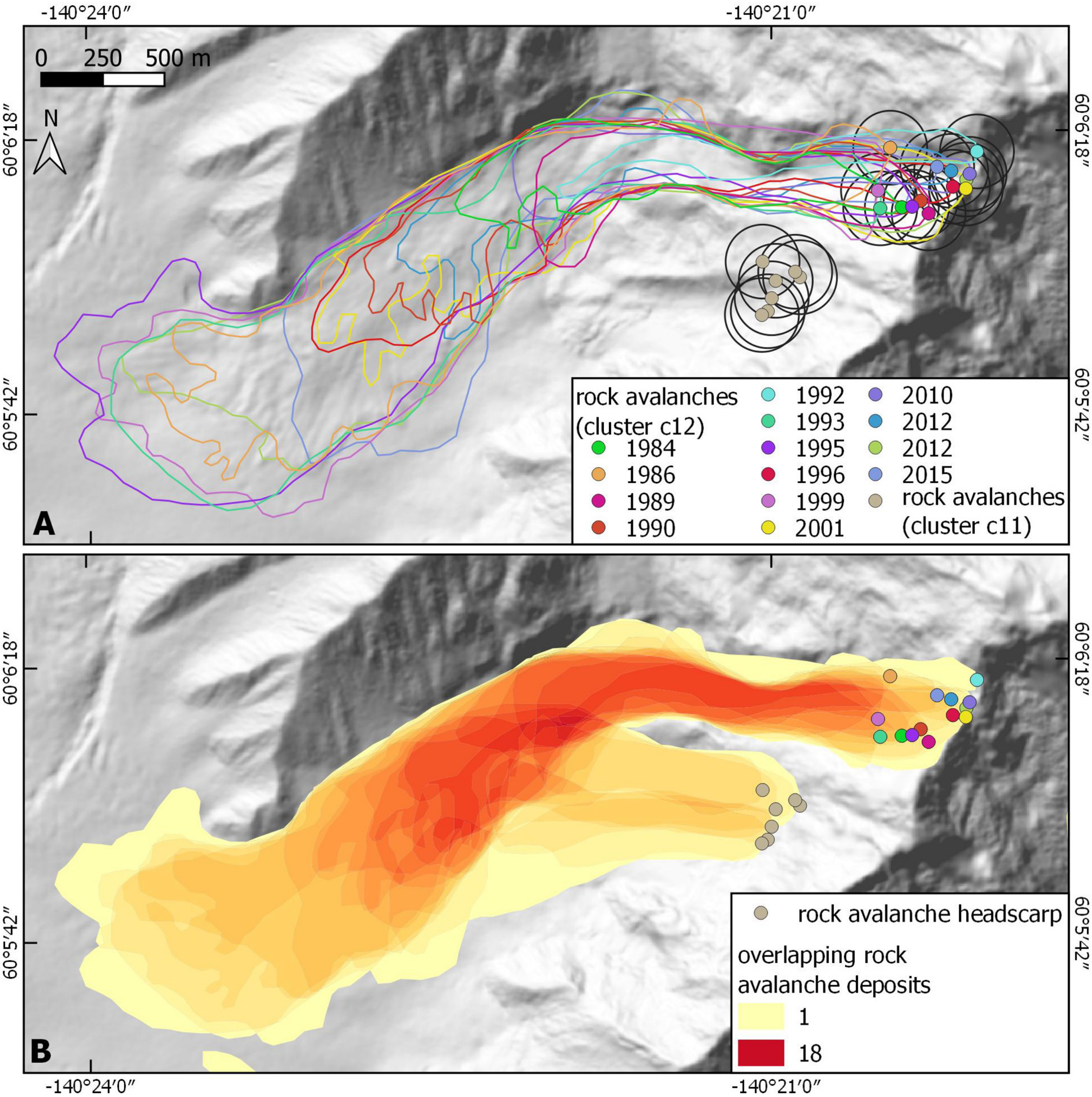

FIGURE 9 | (A) Closeup of the Hitchcock Glacier showing mapped headscarp locations for rock avalanche clusters c11 (gray dots) and c12 (colored dots) and deposits (colored lines) for cluster c12. Black circles denote a 150 m buffer zone around each headscarp point, indicating the extent of possible mapping error. **(B)** Heat map showing the number of overlapping rock avalanche deposits from clusters c11 (gray headscarp points) and c12 (colored headscarp points) on the Hitchcock Glacier.

earthquake shaking and increased precipitation in soil landslides (Bontemps et al., 2020). Overall, the relative number of rock avalanches is likely to increase in the future as a result of warming temperatures in mountain cryosphere environments (e.g., Huggel et al., 2010; McColl, 2012; Deline et al., 2015a; Coe et al., 2018). The distinct, overlapping temporal clusters of rock avalanche activity in the St. Elias (2013–2016) and GBNPP (2012–2016) study areas encompassed a 3-year period (2014–2016) of record-breaking warmth in Alaska (e.g., NOAA, 2017; Walsh et al., 2017), and demonstrate that this phenomenon has already begun to occur.

Implications for Glacier Composition and Dynamics

Supraglacial rock avalanches contribute to large-scale sediment fluxes of glaciated basins and can affect the movement and composition of the glaciers upon which they are deposited.

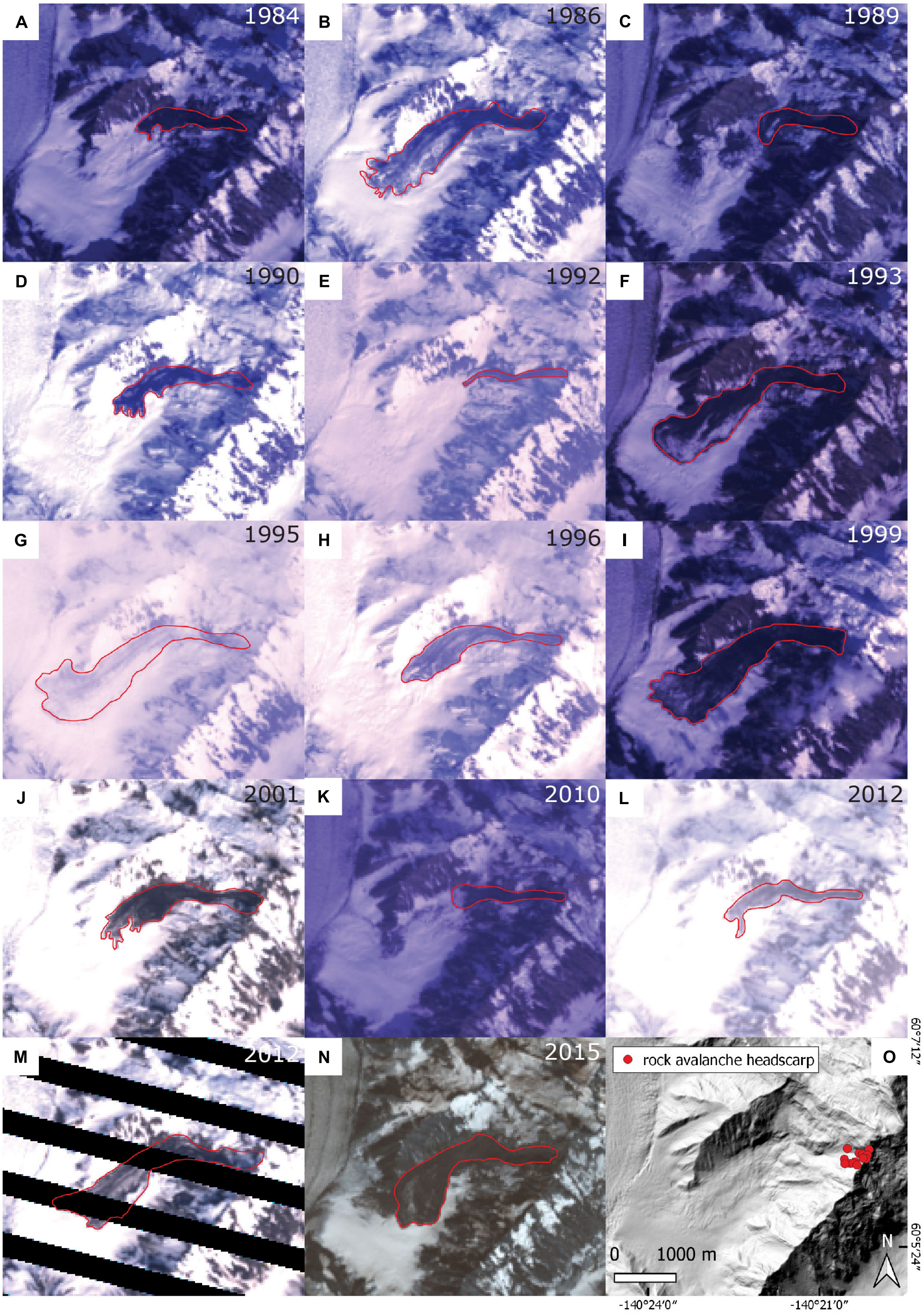

FIGURE 10 | Landsat imagery showing 14 mapped rock avalanches (cluster c12) on Hitchcock Glacier in the Saint Elias Mountains. Rock avalanches occurred in **(A)** 1984 (RA 2), **(B)** 1986 (RA 8), **(C)** 1989 (RA 24), **(D)** 1990 (RA 25), **(E)** 1992 (RA 37), **(F)** 1993 (RA 43), **(G)** 1995 (RA 51), **(H)** 1996 (RA 62), **(I)** 1999 (RA 78), **(J)** 2001 (RA 86), **(K)** 2010 (RA 149), **(L,M)** 2012 (RA 158 and RA 159), and **(N)** 2015 (RA 182). **(O)** Hillshade (derived from a 5 m digital elevation model (DEM; U.S. Geological Survey, 2012) of Hitchcock Glacier and the surrounding area showing the locations of rock avalanche headscarps. Note: the IFSAR-derived DEM was acquired in 2012 and the deposit of RA 159 is apparent in the hillshade.

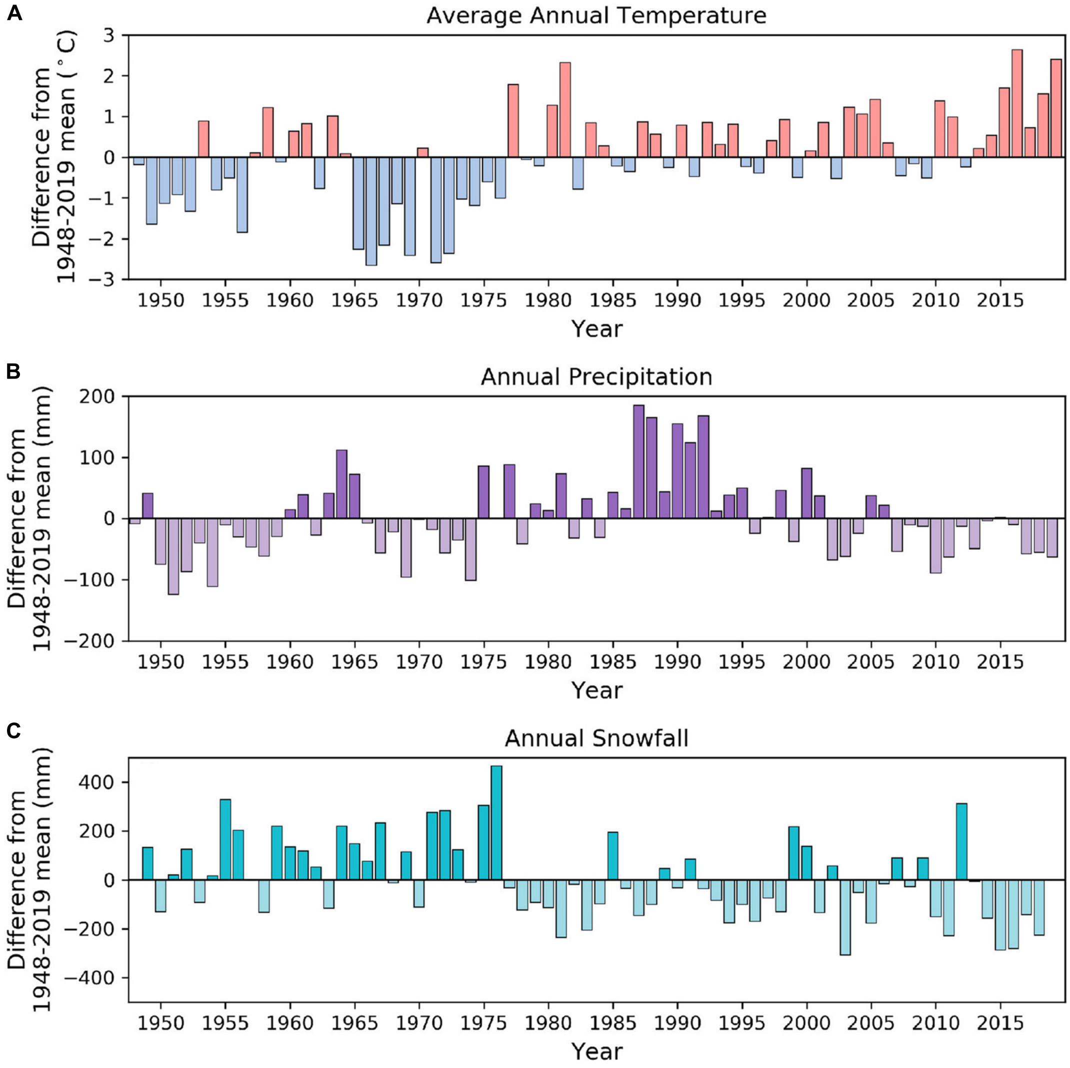

FIGURE 11 | Deviation from 1948 to 2019 mean **(A)** average annual temperature, **(B)** annual precipitation and **(C)** annual snowfall at the Yakutat Airport weather station in southern Alaska.

The presence of rock avalanche debris (with a thickness of at least 10 cm) on glaciers insulates underlying surfaces and can reduce ice ablation by between 25 and 100% (Jiskoot, 2011; Reznichenko et al., 2011; Bessette-Kirton et al., 2018). Conversely, the presence of a dust layer or very thin deposits (<2 cm), can increase the rate of ice ablation (Jiskoot, 2011). Rock avalanche deposits can also cause changes in glacier velocities (e.g., McSaveney, 1975; Shugar et al., 2012) and glacial surges have been observed following rock avalanche emplacement (Tarr and Martin, 1912; Deline, 2009). The interactions between rock avalanche debris and glacier dynamics depend in part on the location of deposition with respect to the accumulation and ablation zones of the glacier (Hewitt et al., 2011). Rock avalanches that are deposited in the accumulation zone may be covered by snow and substantially reworked before appearing in the ablation zone (Uhlmann et al., 2013; Dunning et al., 2015), while rock avalanches that are deposited directly on, or travel far enough to reach the ablation zone, more commonly remain visible on the glacier surface for multiple years (Uhlmann et al., 2013).

In the St. Elias study area, all of the rock avalanches in our inventory, with the exception of the Taan Fiord landslide, were emplaced entirely on ice and did not travel beyond glacial margins. Most rock avalanches were deposited on glacier accumulation zones and were subsumed within a year or less. A few large rock avalanches (e.g., **Figure 7**) were deposited in ablation zones and could be traced moving down glacier for several to tens of years. The recognition of a large number of rock avalanches that were deposited predominantly in glacier accumulation zones and were rapidly covered by snow and reworked by glaciers, contrasts to many past studies which were able to trace rock avalanche deposits for years to decades after occurrence (Jiskoot, 2011; Shugar et al., 2012; Uhlmann et al., 2013;

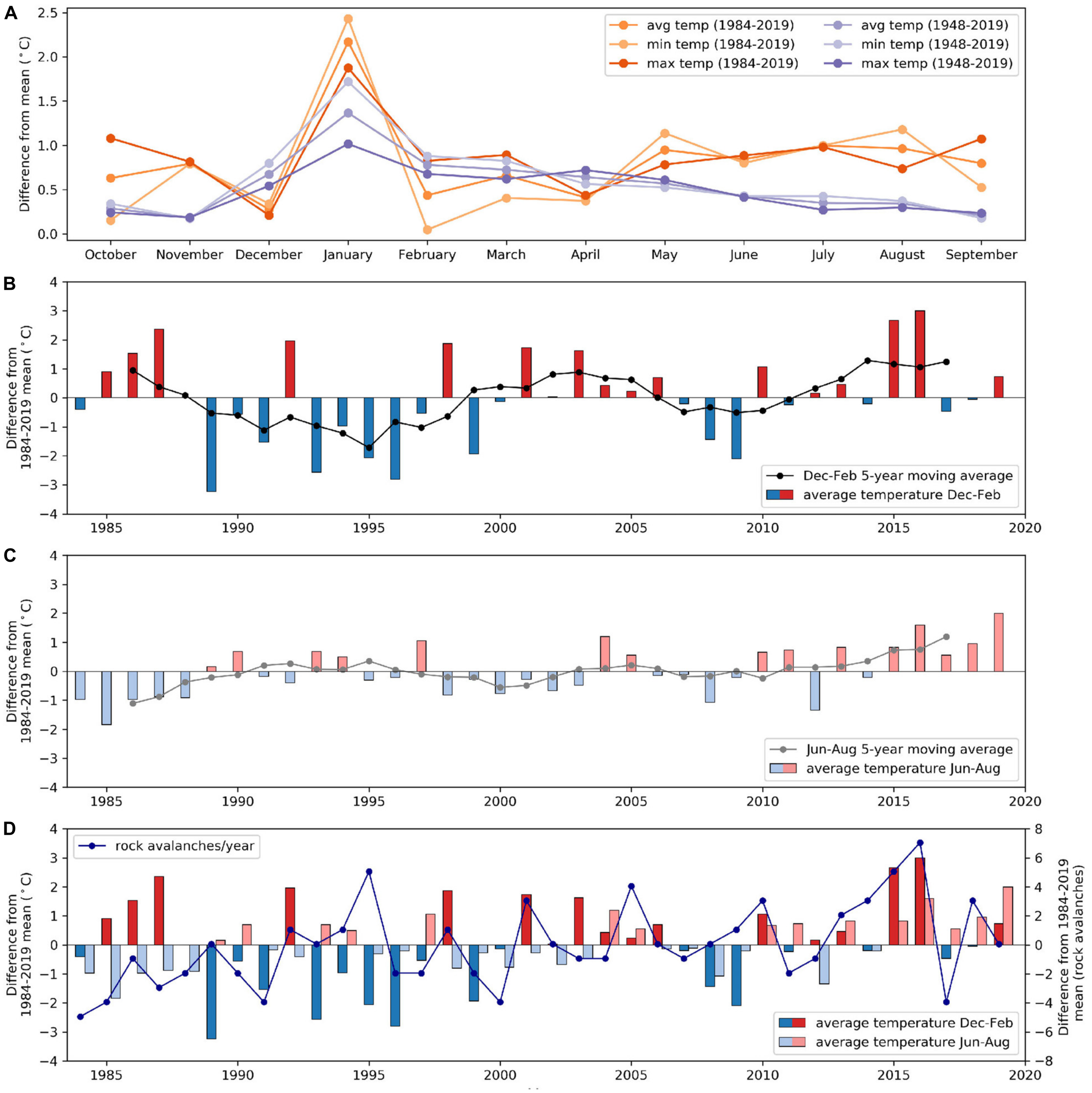

FIGURE 12 | (A) Deviations from the 1948–2019 (purple) and 1984–2019 (orange) mean monthly temperatures (average, minimum and maximum) at the Yakutat Airport weather station in southern Alaska. Difference from 1984 to 2019 mean temperature for average **(B)** winter (December-February) and **(C)** summer (June-August) temperatures. **(D)** Comparison of the number of rock avalanches per year and average winter (December-February) and summer (June-August) temperatures during the period from 1984 to 2019 in the Saint Elias study area. Rock avalanche data do not include possible earthquake-triggered events (three) and each two-part failure is only counted once.

Dufresne et al., 2019). This finding highlights the possibility that numerous rock avalanches in glaciated areas may go undetected without systematic examination of repeat satellite imagery. Furthermore, there may be additional, largely unquantified contributions to glacier sediment flux from the incorporation of rock avalanche deposits in glacier accumulation zones, that cannot be traced at the surface, but which influence glacier movement and composition (Deline, 2009; Dunning et al., 2015).

While it is not possible to directly quantify the sediment flux of rock avalanches that disappeared in accumulation zones and may have reappeared at a later time in glacier ablation zones, we can estimate rock slope erosion rates based on the magnitude and frequency of mapped landslides and an estimated deposit area and thickness. In accordance with similar calculations made for rock avalanches deposited on glaciers in the Chugach Mountains of southeast Alaska (Uhlmann et al., 2013), we used an estimated deposit thickness of 2–3 m for rock avalanches in the St. Elias

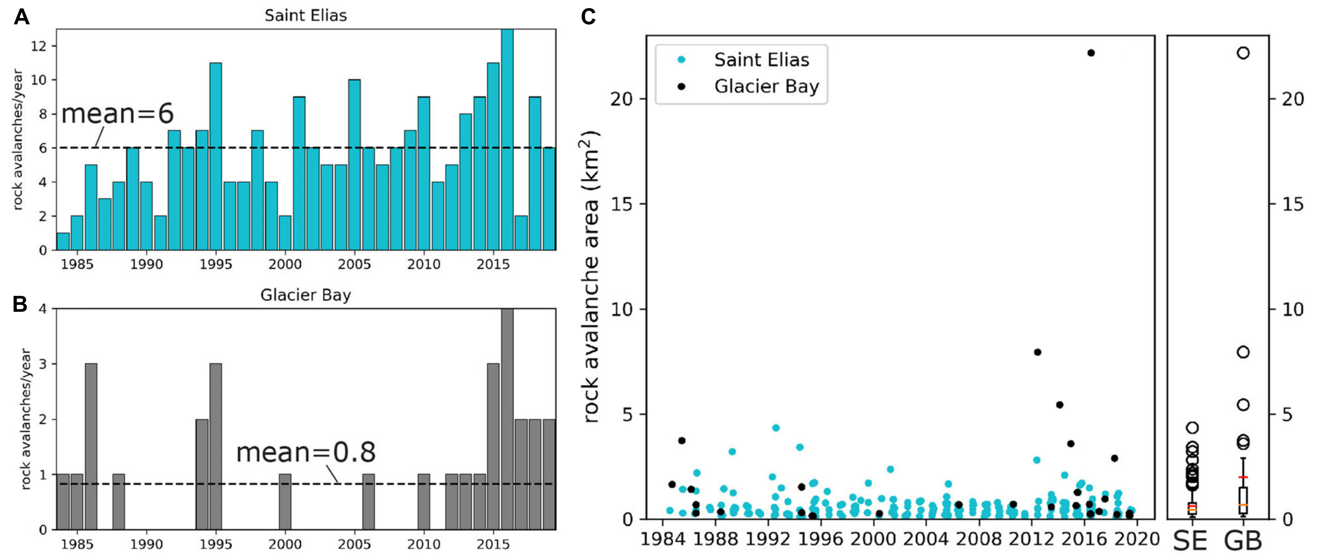

FIGURE 13 | Histograms showing the distribution of rock avalanches per year in the **(A)** Saint Elias (SE) and **(B)** Glacier Bay National Park and Preserve (GB) study areas. Data for GB are from Bessette-Kirton and Coe (2016) and **Supplementary Table S5**. **(C)** Comparison of rock avalanche areas for 214 and 30 rock avalanches in the SE and GB study areas, respectively, between 1984 and 2019. Rock avalanche data for the Saint Elias study area do not include possible earthquake-triggered events (three) and each two-part failure is only counted once.

study area. Additionally, since our inventory mapping quantifies total (source and deposit) rock avalanche areas, we estimated rock avalanche deposit areas as 80% of total rock avalanche areas. For a conservative estimate, we calculated average annual erosion rates using the entire 3700 km^2 study area instead of using only the area of landslide-prone slopes, as was done by Uhlmann et al. (2013). The average rock erosion rate in the St. Elias study area ranged from 0.7 to 1.0 mm/year, which was, on average ∼20% higher than similarly calculated rates of 0.5–0.8 mm/year for GBNPP (rock avalanche data from Coe et al., 2018 and **Supplementary Table S5**) and reported rates of 0.5–0.7 mm/year (Arsenault and Meigs, 2005; Uhlmann et al., 2013) for the Chugach Mountains.

Sediment yields from tidewater glaciers in southern Alaska are among some of the highest worldwide (Koppes and Hallet, 2006). Basin-wide sediment yields for the Seward Malaspina glacier system ranged between 5 and 10 mm/year (Jaeger et al., 1998; Sheaf et al., 2003), with localized erosion rates of up to 20 mm/year in high flow velocity areas of Seward Glacier (Headley et al., 2012). At Tyndall Glacier at the head of Taan Fiord, basin-wide erosion rates between 1961 and 2014 were estimated at 26 ± 5 mm/yr, (Williams and Koppes, 2019). Rock slope erosion rates due to rock avalanches in the St. Elias study area are about an order of magnitude lower than estimated rates of total sediment production (glacial erosion plus rock avalanche debris), a finding that is similar to that from the Chugach Mountains (Uhlmann et al., 2013). Nonetheless, the sediment yield from rock avalanche debris is not insignificant and could account for up to 20% of basin-wide sediment flux. Furthermore, the role of incorporated rock avalanche debris is important for an overall understanding of glacier dynamics and mass balance (e.g., Deline, 2009; Reznichenko et al., 2011; Dunning et al., 2015; Tielidze et al., 2020), which are important considerations for the response of glaciers to climate changes (Larsen et al., 2007; Burgess et al., 2013) and the role of meltwater in sea level rise, particularly in places like the Gulf of Alaska (Berthier et al., 2010).

Rock Avalanche Mechanisms

Rapid deglaciation and isostatic rebound following the Little Ice Age (Muskett et al., 2003; Larsen et al., 2004; Hewitt et al., 2011), in addition to rapid tectonic uplift, exhumation, and glacial erosion (Elliott et al., 2010; Pavlis et al., 2012) have predisposed many of the steep slopes composed of weak lithologic materials in the St. Elias Mountains to failure. The Taan Fiord landslide has been attributed to debutressing due to rapid ice loss at the outlet of the Tyndall Glacier (Higman et al., 2018). While this mechanism may be prevalent in coastal areas that are presently devoid of ice (Meigs and Sauber, 2000; Koppes and Hallet, 2006), our inventory highlights the ubiquity of rock-slope failures on inland, glaciated slopes. Only 2 of 220 landslides in our inventory (RA 161 and RA 188) occurred in ice-free areas along the coast, prompting further evaluation of the processes that condition landslides from higher-elevation glaciated slopes throughout the remainder of the study area.

Glacial thinning within the study area has been predominantly observed at low elevations in glacier ablation zones (Arendt et al., 2002; Muskett et al., 2003). In addition, the high surface velocities (up to 5 m/day) measured on glaciers within the St. Elias study area (Headley et al., 2012; Burgess et al., 2013; Waechter et al., 2015) have been partially attributed to large accumulation rates from the high elevation basins that feed glaciers (Burgess et al., 2013). Thus, the fact that the majority of the rock avalanches in our inventory initiated from bedrock ridges in probable permafrost zones (**Figure 5B**) and traveled onto glacial accumulation zones, suggests that ice loss due to permafrost degradation, as opposed to glacial thinning, could be a dominant factor contributing to rock-slope failures in the high elevation areas of the St. Elias Mountains. Previous work on permafrost degradation and its influence on rock-slope stability indicates that the advection of heat via the movement of water in fractures can promote the thawing of ice, which leads to an increase in effective stress, a reduction in rock-mass strength, and the destabilization of rock masses (e.g., Gruber and Haeberli, 2007; Noetzli and Gruber, 2009; Fischer et al., 2010; Hasler et al., 2011). We acknowledge that our results could be biased by a possible lack of detection of rock avalanches in areas where glacier thinning and retreat were taking place (because they were less likely to have traveled over ice at, and downslope from, glacier termini). However, even if this were the case, the large number of rock avalanches that initiated from bedrock ridges in glacier accumulation areas suggests that the likely influence of permafrost degradation cannot be ignored.

Additional clues to processes controlling rock avalanche occurrence in southern Alaska can be found in the similarities between results from the St. Elias and GBNPP study areas. The primary similarity is that both sites had temporal clusters of exceptional rock avalanche activity during multi-year periods of above normal temperatures (2013–2016), with much of the temperature anomaly associated with the prevalence of above normal winter temperatures. These data suggest that warmer than normal winter temperatures are an antecedent condition needed to promote the initiation of exceptional rock avalanche activity later in the spring and summer. These antecedent conditions likely weaken rock masses and make them more susceptible to failure when air temperatures exceed freezing. A notable difference between rock avalanches in the St. Elias and GBNPP study areas during the period between 1984 and 2019 is the prevalence of spatial rock avalanche clusters in the St. Elias area. Disparities in lithology and tectonic setting, as previously discussed, likely contribute to the difference in overall rock avalanche activity in addition to the commonality of repeated failures in the St. Elias area. However, field work, localized climate data, and in situ monitoring, would help gain a better understanding of spatial clusters and the conditioning processes influencing rock avalanches in the St. Elias Mountains.

CONCLUSION

We mapped and analyzed 220 rock avalanches that occurred from 1984 through 2019 in a 3700 km^2 area of the tectonically active St. Elias Mountains of southern Alaska. During the 36-year period of record, the frequency of large rock avalanches (>1 km^2) in the study area was 2.3 rock avalanches/year/10,000 km^2, which is more than 1000 times larger than rates for similarly sized (>1 km^2) rock avalanches documented by Hungr and Evans (2004) in Europe, New Zealand, and Canada. We observed a distinct temporal cluster of 41 rock avalanches from 2013 through 2016. This temporal cluster occurred during a period of above average air temperatures (including the three warmest years on record in Alaska, 2014–2016), and corresponds to a temporal cluster of rock avalanches during a similar period (2012–2016) in an area of Glacier Bay National Park and Preserve (about 220 km to the southeast). The majority of rock avalanches in the St. Elias inventory occurred from high-elevation inland terrain, highlighting permafrost degradation as opposed to glacial thinning as a dominant driving factor for the majority of failures in this area. Our work suggests that the area-normalized rate of non-coseismic rock avalanches was at least 2× greater than that of earthquake-triggered rock avalanches in southern Alaska from 1964 to 2019. Additionally, all available evidence indicates that frequencies of non-coseismic rock avalanches will continue to increase as climates continue to warm in the future. While the St. Elias study area is remote, events such as the Taan Fiord landslide and tsunami underscore the importance of understanding the processes that control changes in landslide frequency and magnitude in cryospheric mountainous terrain.

DATA AVAILABILITY STATEMENT

All datasets presented in this study are included in the article/**Supplementary Material** and in Bessette-Kirton et al. (2020).

AUTHOR CONTRIBUTIONS

EB-K conducted the inventory data collection and analysis. JC consulted on inventory collection and analysis. EB-K and JC contributed equally to the manuscript preparation. All authors contributed to the article and approved the submitted version.

ACKNOWLEDGMENTS

We thank Michael Loso and two Frontiers in Earth Science reviewers for their insightful and constructive reviews that helped improve our manuscript. Janet Slate provided helpful editorial improvements. Ian Kellogg, Chloe Roth, Shyanne Wilson, Luke Jeter, and Caleb Smith from Colorado School of Mines helped with preliminary data collection that was advantageous to the development of the project. We also thank Kate Allstadt for seismic data analyses that confirmed the date of RA 204. Any use of trade, firm, or product names is for descriptive purposes only and does not imply endorsement by the United States Government.

SUPPLEMENTARY MATERIAL

The Supplementary Material for this article can be found online at: https://www.frontiersin.org/articles/10.3389/feart.2020.00293/full#supplementary-material

REFERENCES

Arendt, A. A., Echelmeyer, K. A., Harrison, W. D., Lingle, C. S., and Valentine, V. B. (2002). Rapid wastage of Alaska glaciers and their contribution to rising sea level. *Science* 297, 382–386. doi: 10.1126/science.1072497

Arsenault, A. M., and Meigs, A. J. (2005). Contribution of deep-seated bedrock landslides to erosion of a glaciated basin in southern Alaska. *Earth Surf. Proc. Land.* 30, 1111–1125. doi: 10.1002/esp.1265

Beniston, M. (2003). Climatic change in mountain regions. A review of possible impacts. *Clim. Chang.* 59, 5–31. doi: 10.1007/978-94-015-1252-7_2

Berthier, E., Schiefer, E., Clarke, G. K. C., Menounos, B., and Rémy, F. (2010). Contribution of Alaskan glaciers to sea-level rise derived from satellite imagery. *Nat. Geosci.* 3:92. doi: 10.1038/NGEO737

Bessette-Kirton, E., Allstadt, K., Godt, J., and Pursley, J. (2017). *Preliminary Analysis of Satellite Imagery and Seismic Observations of the Nuugaatsiaq Landslide and Tsunami, Greenland*. Available online at: https://www.usgs.gov/natural-hazards/landslide-hazards/science/preliminary-analysis-satellite-imagery-and-seismic?qt-science_center_objects = 0#qt-science_center_objects (accessed April 29, 2020).

Bessette-Kirton, E. K., and Coe, J. A. (2016). *Inventory of Rock Avalanches In Western Glacier Bay National Park And Preserve, Alaska, 1984-2016: A Baseline Data Set For Evaluating The Impact Of Climate Change On Avalanche Magnitude, Mobility, and Frequency*. Reston, VA: U.S. Geological Survey.

Bessette-Kirton, E. K., Coe, J. A., and Kellogg, I. N. (2020). *Inventory Data Of Rock Avalanches In The Saint Elias Mountains Of Southeast Alaska, Derived From Landsat Imagery (1984-2019)*. Reston, VA: U.S. Geological Survey.

Bessette-Kirton, E. K., Coe, J. A., and Zhou, W. (2018). Using stereo satellite imagery to account for ablation, entrainment, and compaction in volume calculations for rock avalanches on glaciers: application to the 2016 Lamplugh rock avalanche in Glacier Bay National Park, Alaska. *J. Geophys. Res. Earth Surf.* 123, 622–641. doi: 10.1002/2017JF004512

Bontemps, N., Lacroix, P., Larose, E., Jara, J., and Taipe, E. (2020). Rain and small earthquakes maintain a slow-moving landslide in a persistent critical state. *Nat. Commun.* 11, 1–10. doi: 10.1038/s41467-020-14445-3

Bruhn, R. L., Pavlis, T. L., Plafker, G., and Serpa, L. (2004). Deformation during terrane accretion in the Saint Elias Orogen, Alaska. *Geol. Soc. Am. Bull.* 116, 771–787. doi: 10.1130/B25182.1

Burgess, E. W., Forster, R. R., and Larsen, C. F. (2013). Flow velocities of Alaskan glaciers. *Nat. Commun.* 4:2146. doi: 10.1038/ncomms3146

Coe, J. A., Bessette-Kirton, E. K., and Geertsema, M. (2018). Increasing rock-avalanche size and mobility in Glacier Bay National Park and Preserve, Alaska detected from 1984-2016 Landsat imagery. *Landslides* 15, 393–407. doi: 10.1007/s10346-017-0879-7

Delaney, K. B., and Evans, S. G. (2014). The 1997 mount munday landslide (British Columbia) and the behaviour of rock avalanches on glacier surfaces. *Landslides* 11, 1019–1036. doi: 10.1007/s10346-013-0456-7

Deline, P. (2009). Interactions between rock avalanches and glaciers in the Mont Blanc massif during the late Holocene. *Quat. Sci. Rev.* 28, 1070–1083. doi: 10.1016/j.quascirev.2008.09.025

Deline, P., Gruber, S., Delaloye, R., Fischer, L., Geertsema, M., Giardino, M., et al. (2015a). "Chapter 15, ice loss and slope stability in high-mountain regions," in *Snow and Ice-Related Hazards, Risks, And Disasters*, eds W. Haeberli, C. Whiteman, and J. F. Shroder ((Amsterdam: Elsevier), 521–561. doi: 10.1016/B978-0-12-394849-6.00015-9

Deline, P., Hewitt, K., Reznichenko, N., and Shugar, D. (2015b). "Rock avalanches onto glaciers," in *Landslide Hazards, Risks, And Disasters*, eds T. Davies and J. F. Shroder (Amsterdam: Elsevier), 263–270. doi: 10.1016/B978-0-12-396452-6.00009-4

Dufresne, A., Geertsema, M., Shugar, D. H., Koppes, M., Higman, B., Haeussler, P. J., et al. (2018). Sedimentology and geomorphology of a large tsunamigenic landslide, Taan Fiord, Alaska. *Sediment. Geol.* 364, 302–318. doi: 10.1016/j.sedgeo.2017.10.004

Dufresne, A., Wolken, G. J., Hibert, C., Bessette-Kirton, E. K., Coe, J. A., Geertsema, M., et al. (2019). The 2016 lamplugh rock avalanche, alaska: deposit structures and emplacement dynamics. *Landslides* 16, 2301–2319. doi: 10.1007/s10346-019-01225-4

Duhart, P., Sepúlveda, V., Garrido, N., Mella, M., Quiroz, D., Fernández, J., et al. (2019). "The Santa lucia landslide disaster, Chaitén-Chile: origin and effects," in *Debris-Flow Hazards Mitigation: Mechanics, Monitoring, Modeling, and Assessment, Proceedings of the 7th International Conference on Debris Flow Hazards Mitigation*, eds J. W. Kean, J. A. Coe, P. M. Santi, and B. K. Guillen (Golden, CO: Association of Environmental & Engineering Geologists Special Publication), 653–660. doi: 10.25676/11124/173159

Duman, T. Y., Çan, T., Emre, Ö, Keçer, M., Doðan, A., Ateş, Ş, et al. (2005). Landslide inventory of northwestern Anatolia, Turkey. *Eng. Geol.* 77, 99–114. doi: 10.1016/j.enggeo.2004.08.005

Dunning, S. A., Rosser, N. J., McColl, S. T., and Reznichenko, N. V. (2015). Rapid sequestration of rock avalanche deposits within glaciers. *Nat. Commun.* 6:7964. doi: 10.1038/ncomms8964

Eberhart-Phillips, D., Haeussler, P. J., Freymueller, J. T., Frankel, A. D., Rubin, C. M., Craw, P., et al. (2003). The 2002 Denali fault earthquake, Alaska: a large magnitude, slip-partitioned event. *Science* 300, 1113–1118. doi: 10.1126/science.1082703

Elliott, J., Freymueller, J. T., and Larsen, C. F. (2013). Active tectonics of the St. Elias orogen, Alaska, observed with GPS measurements. *J. Geophys. Res. Solid Earth* 118, 5625–5642. doi: 10.1002/jgrb.50341

Elliott, J. L., Larsen, C. F., Freymueller, J. T., and Motyka, R. J. (2010). Tectonic block motion and glacial isostatic adjustment in southeast Alaska and adjacent Canada constrained by GPS measurements. *J. Geophys. Res.* 115:B09407. doi: 10.1029/2009JB007139

Evans, S. G., Bishop, N. F., Smoll, L. F., Murillo, R. V., Delancy, K. B., and Oliver-Smith, A. (2009). A re-examination of the mechanism and human impact of catastrophic mass flows originating in Nevada Huascarán, Cordillera Blanca, Peru in 1092 and 1970. *Eng. Geol.* 108, 96–118. doi: 10.1016/j.enggeo.2009.06.020

Evans, S. G., and Clague, J. J. (1999). "Rock avalanches on glaciers in the Coast and St. Elias Mountains, British Columbia," in *Proceedings of the 13th Annual Vancouver Geotechnical Society Symposium*, Vancouver.

Evans, S. G., and Delaney, K. B. (2014). "Catastrophic mass flows in the mountain glacial environment," in *Snow and Ice-Related Hazards, Risks, And Disasters*, eds W. Haeberli, C. Whiteman, and J. F. Shroder (Amsterdam: Elsevier), 563–606. doi: 10.1016/b978-0-12-394849-6.00016-0

Fischer, L., Amann, F., Moore, J., and Huggel, C. (2010). Assessment of periglacial slope stability for the 1988 Tschierva rock avalanche (Piz Morteratsch, Switzerland). *Eng. Geol.* 116, 32–43. doi: 10.1016/j.enggeo.2010.07.005

Fischer, L., Kääb, A., Huggel, C., and Noetzli, J. (2006). Geology, glacier retreat and permafrost degradation as controlling factors of slope instabilities in a high-mountain rock wall: the Monte Rosa east face. *Nat. Hazard Earth Syst.* 6, 761–772. doi: 10.5194/nhess-6-761-2006

Fischer, L., Purves, R. S., Huggel, C., Noetzli, J., and Haeberli, W. (2012). On the influence of topographic, geological and cryospheric factors on rock avalanches and rockfalls in high-mountain areas. *Nat. Hazards Earth Syst. Sci.* 12, 241–254. doi: 10.5194/nhess-12-241-2012

Geertsema, M. (2012). "Initial Observations of the 11 June 2012 Rock/Ice Avalanches, Lituya Mountain, Alaska," in *Conference: The First Meeting of ICL Cold Region Landslides Network*, Harbin, China. doi: 10.13140/2.1.2473.5682

Grämiger, L. M., Moore, J. R., Gischig, V. S., and Loew, S. (2018). Thermomechanical stresses drive damage of Alpine valley rock walls during repeat glacial cycles. *J. Geophys. Res. Earth Surf.* 123, 2620–2646. doi: 10.1029/2018JF004626

Gruber, S. (2012a). Derivation and analysis of a high resolution estimate of global permafrost zonation. *Cryosphere* 6, 221–233. doi: 10.5194/tc-6-221-2012

Gruber, S. (2012b). *Global Permafrost Zonation Index Map*. Available online at: http://www.geo.uzh.ch/microsite/cryodata/pf_global/ (accessed April 29, 2020).

Gruber, S., and Haeberli, W. (2007). Permafrost in steep bedrock slopes and its temperature-related destabilization following climate change. *J. Geophys. Res.* 112:F02S18. doi: 10.1029/2006JF000547

Guthrie, R. H., Friele, P., Allstadt, K., Roberts, N., Evans, S. G., Delaney, K. B., et al. (2012). The 6 August 2010 Mount Meager rock slide-debris flow, Coast mountains, British Columbia: characteristics, dynamics, and implications for hazard and risk assessment. *Nat. Hazard Earth Syst.* 12, 1277–1294. doi: 10.5194/nhess-12-1277-2012

Haeberli, W., Schaub, Y., and Huggel, C. (2017). Increasing risks related to landslides from degrading permafrost into new lakes in de-glaciating mountain ranges. *Geomorphology* 293, 405–417. doi: 10.1016/j.geomorph.2016.02.009

Haeussler, P. J., Gulick, S. P. S., McCall, N., Walton, M., Reece, R., Larsen, C., et al. (2018). Submarine deposition of a subaerial landslide in Taan Fiord, Alaska. *J. Geophys. Res. Earth Surf.* 123, 2443–2463. doi: 10.1029/2018JF004608

Hansen, W. R., Eckel, E. B., Schaem, W. E., Lyle, R. E., George, W., and Chance, G. (1966). The Alaska Earthquake of March 27, 1964, Field investigations and reconstruction effort. *U.S. Geol. Survey Prof. Pap.* 541:111.

Hasler, A., Gruber, S., Font, M., and Dubois, A. (2011). Advective heat transport in frozen rock clefts—Conceptual model, laboratory experiments and numerical simulation. *Permafr. Periglac. Process.* 22, 387–398. doi: 10.1002/ppp.737

Headley, R., Hallet, B., Roe, G., Waddington, E. D., and Rignot, E. (2012). Spatial distribution of glacial erosion rates in the St. Elias range, Alaska, inferred from a realistic model of glacier dynamics. *J. Geophys. Res.* 117:F03027. doi: 10.1029/2011JF002291

Hewitt, K., Clague, J. J., and Deline, P. (2011). "Catastrophic rock slope failures and mountain glaciers," in *Encyclopedia of Snow, Ice and Glaciers, Encyclopedia of Earth Sciences Series*, eds V. P. Singh, P. Singh, and U. K. Haritashya (Dordrecht: Springer), doi: 10.1007/978-90-481-2642-2_615

Hibert, C., Michéa, D., Provost, F., Malet, J.-P., and Geertsema, M. (2019). Exploration of continuous seismic recordings with a machine learning approach to document 20?yr of landslide activity in Alaska. *Geophys. J. Int.* 219, 1138–1147. doi: 10.1093/gji/ggz354

Higman, B., Shugar, D. H., Stark, C. P., Ekström, G., Koppes, M. N., Lynett, P., et al. (2018). The 2015 landslide and tsunami in Taan Fiord, Alaska. *Sci. Rep.* 8:12993. doi: 10.1038/s41598-018-30475-w

Hock, R., Rasul, G., Adler, C., Cáceres, B., Gruber, S., Hirabayashi, Y., et al. (2019). "High mountain areas," in *IPCC Special Report on the Ocean and Cryosphere in a Changing Climate*, eds H.-O. Pörtner, D. C. Roberts, V. Masson-Delmotte, P. Zhai, M. Tignor, E. Poloczanska, et al. (Geneva: IPCC).

Huggel, C., Caplan-Auerbach, J., Waythomas, C. F., and Wessels, R. L. (2007). Monitoring and modeling ice-rock avalanches from ice-capped volcanoes: a case study of frequent large avalanches on Iliamna Volcano, Alaska. *J. Volcanol. Geoth. Res.* 168, 114–136. doi: 10.1016/j.jvolgeores.2007.08.009

Huggel, C., Gruber, S., Caplan-Auerbach, J., Wessels, R. L., and Molnia, B. F. (2008). "The 2005 Mt. Steller, Alaska, rock-ice avalanche: a large slope failure in cold permafrost," in *Proceedings of the 9th International Conference on Permafrost*, Fairbanks.

Huggel, C., Salzmann, N., Allen, S., Caplan-Auerbach, J., Fischer, L., Haeberli, W., et al. (2010). Recent and future warm extreme evens and high-mountain slope stability. *Philos. Trans. R. Soc.* 368, 2435–2459. doi: 10.1098/rsta.2010.0078

Huggel, C., Zgraggen-Oswald, S., Haeberli, W., Kääb, A., Polkvoj, A., Galushkin, I., et al. (2005). The 2002 rock/ice avalanche at Kolka/Karmadon, Russian Caucasus: assessment of extraordinary avalanche formation and mobility, and application of QuickBird satellite imagery. *Nat. Hazard Earth Syst.* 5, 173–187. doi: 10.5194/nhess-5-173-2005

Hungr, O., and Evans, S. G. (2004). The occurrence and classification of massive rock slope failure. *Felsbau* 22, 16–23.

Hungr, O., Leroueil, S., and Picarelli, L. (2014). The Varnes classification of landslide types, an update. *Landslides* 11, 167–194. doi: 10.1007/s10346-013-0436-y

Huss, M., and Hock, R. (2015). A new model for global glacier change and sea-level rise. *Front. Earth Sci.* 3:54. doi: 10.3389/feart.2015.00054

Hussain, M., and Mahmud, I. (2019). Pymannkendall: a python package for non parametric Mann Kendall family of trend tests. *J. Open Source Softw.* 4:1556. doi: 10.21105/joss.01556

Jacquemart, M., Loso, M., Leopold, M., Welty, E., Berthier, E., Hansen, J. S. S., et al. (2020). What drives large-scale glacier detachments? Insights from Flat Creek glacier, St. Elias Mountains, Alaska. *Geology* 48, 703–707. doi: 10.1130/G47211.1

Jaeger, J. M., Nittrouer, C. A., Scott, N. D., and Milliman, J. D. (1998). Sediment accumulation along a glacially impacted mountainous coastline: north-east Gulf of Alaska. *Basin Res.* 10, 155–173. doi: 10.1046/j.1365-2117.1998.00059.x

Jibson, R. W. (2013). "Mass-movement causes: earthquakes," in *Treatise on Geomorphology, v. 7, Mountain and Hillslope Geomorphology*, eds J. Shroder, R. A. Marston, and M. Stoffel (San Diego: Academic Press), 223–229.

Jibson, R. W., Grant, A. R., Witter, R. C., Allstadt, K. E., Thompson, E. M., and Bender, A. M. (2020). Ground failure from the anchorage, Alaska, earthquake of 30 November 2018. *Seismol. Res. Lett.* 91, 19–32. doi: 10.1785/0220190187

Jibson, R. W., Harp, E. L., Schulz, W., and Keefer, W. K. (2006). Large rock avalanches triggered by the M 7.9 Denali Fault, Alaska, earthquake of 3 November 2002. *Eng. Geol.* 83, 144–160. doi: 10.1016/j.enggeo.2005.06.029

Jiskoot, H. (2011). Long-runout rockslide on glacier at Tsar Mountain, Canadian rocky mountains: potential triggers, seismic and glaciological implications. *Earth Surf. Proc. Land.* 36, 203–216. doi: 10.1002/esp.2037

Keefer, D. K. (1984). Landslides caused by earthquakes. *Geol. Soc. Am. Bull.* 95, 406–421.

Koehler, R. D., Burns, P. A. C., and Combellick, R. A. (2012). *Quaternary Faults And Folds In Alaska: A Digital Database: Miscellaneous Publication MP 141*. Fairbanks: Alaska Division of Geological & Geophysical Surveys.

Koppes, M., and Hallet, B. (2006). Erosion rates during rapid deglaciation in Icy Bay, Alaska. *J. Geophys. Res. Earth Surf.* 111, 1–11. doi: 10.1029/2005JF000349

Krautblatter, M., Funk, D., and Günzel, F. K. (2013). Why permafrost rocks become unstable: a rock-ice mechanical model in time and space. *Earth Surf. Process. Land.* 38, 876–887. doi: 10.1002/esp.3374

Lahr, J. C., Plafker, G., Stephens, C. D., Fogleman, K. A., and Blackford, M. E. (1979). *Interim report on the St. Elias, Alaska Earthquake of 28 February 1979*. Reston, VA: U.S. Geological Survey.

Larsen, C. F., Motyka, R. J., Arendt, A. A., Echelmeyer, K. A., and Geissler, P. E. (2007). Glacier changes in southeast Alaska and northwest British Columbia and contribution to sea level rise. *J. Geophys. Res. Earth Surf.* 112:F01007. doi: 10.1029/2006JF000586

Larsen, C. F., Motyka, R. J., Freymueller, J. T., Echelmeyer, K. A., and Ivins, E. R. (2004). Rapid uplift of southern Alaska caused by recent ice loss. *Geophys. J. Int.* 158, 1118–1133. doi: 10.1111/j.1365-246X.2004.02356.x

Lawrimore, J. (2017). *Dataset Description Document, Global Summary of the Month/Year Dataset*. Silver Spring, MD: National Oceanic and Atmospheric Administration.

Loso, M., Arendt, A., Larsen, C., Rich, J., and Murphy, N. (2014). *Alaskan National Park Glaciers - Status And Trends*. Final Report: natural Resource Technical Report NPS/AKRO/NRTR—2014/922. Fort Collins: U.S. National Park Service.

Margielewski, W. (2006). Structural control and types of movements of rock mass in anisotropic rocks: case studies in the polish Flysch Carpathians. *Geomorphology* 77, 47–68. doi: 10.1016/j.geomorph.2006.01.003

Markon, C., Gray, S., Berman, M., Eerkes-Medrano, L., Hennessy, T., Huntington, H., et al. (2018). "Alaska," in *Impacts, Risks, and Adaptation in the United States: Fourth National Climate Assessment*, eds D. R. Reidmiller, C. W. Avery, D. R. Easterling, K. E. Kunkel, K. L. M. Lewis, T. K. Maycock, et al. (Washington, DC: U.S. Global Change Research Program), 1185–1241. doi: 10.7930/NCA4.2018.CH26

McColl, S. T. (2012). Paraglacial rock-slope stability. *Geomorphology* 153-154, 1–16. doi: 10.1016/j.geomorph.2012.02.015

McSaveney, M. J. (1975). *Sherman Glacier Rock Avalanche Of 1964: Its Emplacement And Subsequent Effects On The Glacier Beneath It*. Ph.D. thesis, The Ohio State University, Columbus, OH.

McSaveney, M. J. (1978). "Sherman glacier rock avalanche, Alaska, U.S.A," in *Rockslides and Avalanches, 1: Natural Phenomena, Developments in Geotechnical Engineering 14A*, ed. B. Voight (Amsterdam: Elsevier), 197–258.

McSaveney, M. J. (2002). "Recent rockfalls and rock avalanches in Mount Cook National Park, New Zealand," in *Catastrophic landslides: Effects, Occurrence, And Mechanisms, Geological Society of America Reviews in Engineering Geology*, eds S. G. Evans and J. V. DeGraff (Boulder: Geological Society of America), 35–70.

McSaveney, M. J., Cox, S. C., and Hancox, G. T. (2014). *Seeking a Credible Cause Of The Recent Increase In Rock-Avalanche Frequency in New Zealand's Southern Alps*. San Francisco: American Geophysical Union.

McSaveney, M. J., Cox, S. C., and Hancox, G. T. (2015). Increasing rock-avalanche frequency correlates with increasing seismic moment release in New Zealand's Southern Alps. *Geophys. Res. Abstr.* 17:EGU2015-8074.

Meigs, A., and Sauber, J. (2000). Southern Alaska as an example of long-term consequences of mountain building under the influence of glaciers. *Quat. Sci. Rev.* 19, 1543–1562.

Mergili, M., Mergili, M., Jaboyedoff, M., Pullarello, J., and Pudasaini, S. P. (2020). Back calculation of the 2017 Piz Cengalo-Bondo landslide cascade with r.avaflow: what we can do and what we can learn. *Nat. Hazard Earth Sys.* 20, 505–520. doi: 10.5194/nhess-20-505-2020

Miller, D. J. (1960). Giant waves in Lituya Bay Alaska. *U.S. Geol. Surv. Prof. Pap.* 354, 51–86.

Muskett, R. R., Lingle, C. S., Tangborn, W. V., and Rabus, B. T. (2003). Multi-decadal elevation changes on Bagley Ice Valley and Malaspina Glacier, Alaska. *Geophys. Res.* 30, 1–4. doi: 10.1029/2003GL017707

NOAA (2017). *United States National Climate Report - Annual 2016*. Silver Spring, MD: NOAA.

Noetzli, J., and Gruber, S. (2009). Transient thermal effects in Alpine permafrost. *Cryosphere* 3, 85–99. doi: 10.5194/tc-3-85-2009

Patton, A. I., Rathburn, S. L., and Capps, D. M. (2019). Landslide response to climate change in permafrost regions. *Geomorphology* 340, 116–128. doi: 10.1016/j.geomorph.2019.04.029

Paul, F., Kääb, A., Maisch, M., Kellenberger, T., and Haeberli, W. (2004). Rapid disintegration of alpine glaciers observed with satellite data. *Geophys. Res.* 31:L21402.

Pavlis, T. L., Chapman, J. B., Bruhn, R. L., Ridgway, K., Worthington, L. L., Gulick, S. P. S., et al. (2012). Structure of the actively deforming fold-thrust best of the St. Elias orogen with implications for glacial exhumation and three-dimensional tectonic processes. *Geosphere* 8, 991–1019.

Petley, D. (2012). *Another Teleseismic Landslide- This Time In Alaska On Monday 21st May 2012*. Available online at: https://blogs.agu.org/landslideblog/2012/05/24/another-teleseismic-landslide-this-time-in-alaska/ (accessed April 29, 2020).

Post, A. (1967). *Effects of the March 1964 Alaska earthquake on glaciers*. U.S. Geological Survey Professional Paper 544-D. Reston, VA: U.S. Geological Survey.

Reid, M. (2017). *Landslide Hazard And Climate Change In The Mountain Glacial Environment of Northwest North America*, Masters thesis, University of Waterloo, Waterloo, ON.

Reznichenko, N. V., Davies, T. R., and Alexander, D. J. (2011). Effects of rock avalanches on glacier behaviour and moraine formation. *Geomorphology* 132, 327–338.

Richter, D. H., Preller, C. C., Labay, K. A., and Shew, N. B. (2005). *Geology of Wrangell-Saint Elias National Park and Preserve, South Central Alaska: U.S. Geological Survey Scientific Investigations Series Map SIM-2877*. Reston, VA: U.S. Geological Survey.

Schlögel, R., Torgoev, I., De Marneffe, C., and Havenith, H. (2011). Evidence of a changing size-frequency distribution of landslides in the Kygyz Tien Shan, central Asia. *Earth Surf. Proc. Land.* 36, 1658–1669. doi: 10.1002/esp.2184

Schneider, D., Huggel, C., Haeberli, W., and Kaitna, R. (2011). Unraveling driving factors for large rock-ice avalanche mobility. *Earth Surf. Proc. Land.* 36, 1948–1966. doi: 10.1002/esp.2218

Shafique, M. (2020). Spatial and temporal evolution of co-seismic landslides after the 2005 Kashmir earthquake. *Geomorphology* 362:107228. doi: 10.1016/j.geomorph.2020.107228

Sheaf, M., Serpa, L., and Pavlis, T. L. (2003). Exhumation rates in the St. Elias Mountains, Alaska. *Tectonopysics* 367, 1–11. doi: 10.1016/S0040-1951(03)00124-0

Shugar, D. H., Rabus, B. T., Clague, J. J., and Capps, D. M. (2012). The response of black rapids glacier, Alaska, to the Denali earthquake rock avalanches. *J. Geophys. Res.* 117:F01006.

Spotila, J. A., Buscher, J. T., Meigs, A. J., and Reiners, P. W. (2004). Long-term glacial erosion of active mountain belts: example of the Chugach-St. Elias Range, Alaska. *Geology* 32, 501–504. doi: 10.1130/G20343.1

Stover, C. W., Reagor, B. G., and Wetmiller, R. J. (1980). Intensities and isoseismal map for the St. Elias earthquake of February 28, 1979. *B. Seismol. Soc. Am.* 70, 1635–1649.

Tarr, R. S., and Martin, L. (1912). Earthquakes at Yakutat Bay, Alaska in September, 1899. *U.S. Geol. Surv. Prof. Pap.* 69:135.

Tielidze, L. G., Bolch, T., Wheate, R. D., Kutuzov, S. S., Lavrentiev, I. I., and Zemp, M. (2020). Supra-glacial debris cover changes in the Greater Caucasus from 1986 to 2014. *Cryosphere* 14, 585–598.

U.S. Geological Survey (2019). *Libcomcat, Version 1.0. GitHub Repository*. Reston, VA: U. S. Geological Survey.

U.S. Geological Survey (2020). *ANSS Comprehensive Earthquake Catalog (ComCat) Documentation*. Reston, VA: U. S. Geological Survey.

U.S. Geological Survey (2012). *USGS NED Original Product Resolution (OPR) AK IFSAR*. Available online at: http://ned.usgs.gov/ (accessed April 1, 2020).

Uhlmann, M., Korup, O., Huggel, C., Fischer, L., and Kargel, J. S. (2013). Supra-glacial deposition and flux of catastrophic rock-slope failure debris, south-central Alaska. *Earth Surf. Proc. Land.* 38, 675–682. doi: 10.1002/esp.3311

van Oldenborgh, G. J., Collins, M., Arblaster, J., Christensen, J. H., Marotzke, J., Power, S. B., et al. (2013). "Annex I: atlas of global and regional climate projections," in *Climate Change 2013: The Physical Science Basis. Contribution of Working Group I to the Fifth Assessment Report of the Intergovernmental Panel on Climate Change*, eds T. F. Stocker, D. Qin, G.-K. Plattner, M. Tignor, S. K. Allen, J. Boschung, et al. (Cambridge: Cambridge University Press), 1311–1393.

Waechter, A., Copland, L., and Herdes, E. (2015). Modern glacier velocities across the Icefield Ranges, St Elias Mountains, and variability at selected glaciers from 1959 to 2012. *J. Glaciol.* 61:228. doi: 10.3189/2015JoG14J147

Walsh, J., Wuebbles, D., Hayhoe, K., Kossin, K., Kunkel, K., Stephens, G., et al. (2014). "Chapter 2: our changing climate," in *Climate Change Impacts in the United States: The Third National Climate Assessment*, eds J. M. Melillo, T. C. Richmond, and G. W. Yohe (Washington, DC: U.S. Global Change Research Program), 19–67.

Walsh, J. E., Bieniek, P. A., Brettschneider, B., Euskirchen, E. S., Lader, R., and Thoman, R. L. (2017). The exceptionally warm winter of 2015/16 in Alaska. *J. Clim.* 30, 2069–2088. doi: 10.1175/JCLI-D-16-0473.1

Walter, F., Amann, F., Kos, A., Kenner, R., Phillips, M., de Preux, A., et al. (2020). Direct observations of a three million cubic meter rock-slope collapse with almost immediate initiation of ensuing debris flows. *Geomorphology* 351:106933. doi: 10.1016/j.geomorph.2019.106933

Williams, H. B., and Koppes, M. N. (2019). A comparison of glacial and paraglacial denudation responses to rapid glacial retreat. *Ann. Glaciol.* 60, 151–164. doi: 10.1017/aog.2020.1

Wilson, F. H., Hults, C. P., Mull, C. G., and Karl, S. M. (2015). Geologic map of Alaska. *U.S. Geol. Surv. Sci. Invest. Map* 3340:197.

Wilson, F. H., Labay, K. A., Shew, N. B., Preller, C. C., and Mohadjer, S. (2005). *Digital data for the geology of Wrangell-Saint Elias National Park and Preserve, Alaska. U.S. Geological Survey Open-File Report 2005-1342*. Reston, VA: U.S. Geological Survey.

Winkler, G. R., MacKevett, E. M., Plafker, G. Jr., Richter, D. H., Rosenkrans, D. S., and Schmoll, H. R. (2000). A geologic guide to Wrangell-saint Elias National Park and Preserve, Alaska, a tectonic collage of northbound terranes. *U.S. Geol. Surv. Prof. Pap.* 161:166.

Conflict of Interest: The authors declare that the research was conducted in the absence of any commercial or financial relationships that could be construed as a potential conflict of interest.

frontiers
in Earth Science

ORIGINAL RESEARCH
published: 17 July 2020
doi: 10.3389/feart.2020.00267

The Plata Rock Avalanche: Deciphering the Occurrence of This Huge Collapse in a Glacial Valley of the Central Andes (33° S)

Stella M. Moreiras[1,2]*

[1] *IANIGLA, Institute of Snow, Glaciology and Environmental Science, Mendoza, Argentina,* [2] *Cátedra Edafología, Facultad de Ciencias Agrarias, Universidad Nacional de Cuyo, Mendoza, Argentina*

This paper reviews the genesis of a chaotic deposit in the Blanco River basin (BRB) in the Argentine Andes that has been interpreted to be either of debris flow or glacial origin. A detailed sedimentological and geomorphic study of the deposit was undertaken to determine its origin. Glacial landforms in the source area of the deposit contrast markedly to those in neighboring valleys of the BRB. The lack of moraines and the presence only of rock glaciers in the headwaters of the Angostura Valley suggest that a glacier might have been destroyed by a rock avalanche in the Late Pleistocene. The deposit itself has the characteristics of rapid deposition by a huge ($\leq 10^5$ m^3) rock avalanche sourced on the eastern slope of Mount Plata (5,956 m asl). The rock avalanche traveled a distance of 26.6 km and descended 4,700 m in altitude. The optically stimulated luminescence (OSL) ages on alluvial sediments associated with the landslide deposits suggest that the rock avalanche occurred ∼35–39 ka ago. The rock avalanche may have been triggered by an earthquake, given that the active Carrera fault system extends across the basin and there is a cluster of seven Late Pleistocene rock avalanches in the region.

Keywords: rock avalanche, Late Pleistocene, Central Andes, Argentina, sedimentology

Edited by:
John Joseph Clague,
Simon Fraser University, Canada

Reviewed by:
Fabio Matano,
National Research Council (CNR), Italy
Cristina Maria Pinto Gama,
University of Évora, Portugal

Correspondence:
Stella M. Moreiras
moreiras@mendoza-conicet.gob.ar

Specialty section:
This article was submitted to Quaternary Science, Geomorphology and Paleoenvironment, a section of the journal Frontiers in Earth Science

Received: *28 January 2020*
Accepted: *15 June 2020*
Published: *17 July 2020*

Citation:
Moreiras SM (2020) The Plata Rock Avalanche: Deciphering the Occurrence of This Huge Collapse in a Glacial Valley of the Central Andes (33° S). Front. Earth Sci. 8:267. doi: 10.3389/feart.2020.00267

INTRODUCTION

Researchers often argue about the origin of chaotic sedimentary deposits in high mountains (Abele, 1984; Hewitt, 1999; Hewitt et al., 2011). Landslide deposits assumed to be of glacial origin have evoked erroneous paleoclimatic interpretations. In the Central Andes, for example, landslide deposits originally interpreted to be glacial have been reinterpreted in recent years (Antinao and Gosse, 2009; Sepúlveda and Moreiras, 2013; Hermanns et al., 2015; Moreiras and Sepúlveda, 2015).

Near the area of this study, such reinterpretation began much earlier with the seminal work of Dessanti (1946) and Polanski (1953, 1963, 1961), who debated the genesis of a chaotic deposit called the Quemado Conglomerate, which extends down to 1,200 m asl. If the conglomerate were glacial in origin, glaciers would have to have reached the foothills of the Andes. Polanski (1953, 1963) emphatically argued that Pleistocene glaciers could not have reached below 1,800 m asl, whereas Groeber (1951, 1955) defended the existence of such extensive advances. This discussion continued two decades later when the "cenoglomerate," a chaotic mass of boulders lacking internal structure in the Blanco River basin (BRB) which Polanski (1966) interpreted to be the deposit of a huge debris flow, was reinterpreted as till of the Angostura glacial advance (Wayne and Corte, 1983; Wayne, 1984). Based on relative methods (e.g., rock varnish on blocks, degree of weathering, and soil development), these authors proposed an Early Pleistocene age for a glacier that reached 1,500 m asl in the BRB. Later, Wayne (1990) returned to Polanski's original viewpoint.

This paper reviews and reconsiders the deposits described by Polanski (1966) and Wayne (1984, 1990) based on new detailed stratigraphic studies of the "cenoglomerate" in the BRB. As the source of the deposit has never been clear, I analyzed landforms in the formerly glaciated headwaters of the basin. Globally, main efforts for deciphering landform genesis are focused on characterizing the deposit features, while a general geomorphological study for understanding the genesis of certain landform is overlooked. This study highlights the necessity of integrating sedimentology and geomorphology when attempting to discriminate glacial and landslide.

SETTING OF THE BLANCO RIVER BASIN

The Blanco River basin (BRB) has an area of 150 km^2 and is located on the eastern slope of the Plata Range in the Argentine Central Andes. The slopes are steep, and the peaks reach to more than 5,000 m asl; the elevations drop gradually to the north (**Figure 1**). The basin is drained by the Blanco River and its tributaries (Angostura and Vallecitos rivers), and the southern Alto Las Vegas sub-catchment is drained by the Mulas River (Drovandi et al., 2010; Massone et al., 2016) (**Figure 1**). The Blanco River, with a mean annual flow of 1 m^3/s (Massone et al., 2016), has season variability due to snowmelt during late spring and summer.

This part of the Andes is semiarid. The climate is forced by the Southern Arid Diagonal, which prevents tropical air masses from the Atlantic from reaching the region. Westerlies from the Pacific Ocean, however, generate snowfall of about 240 mm/year (snow water equivalent) in mountain areas during the South Hemisphere winter (June–August) and rainfall in the foothills during summer (December–February) (Norte, 1995). The Vallecitos (2,470 m asl) and the Las Aguaditas (2,200 m asl) meteorological stations report a mean annual temperature of 5 and 7.6°C and a mean annual precipitation of 294 and 450 mm, respectively (Wayne, 1984). The mean annual temperature is below 0°C at about 3,200 m asl, which is the lower limit of Andean permafrost (Corte and Grosso, 1993). The permafrost reaches depths of about 90 cm at 4,500 m asl (Trombotto, 1991, 2002; Trombotto and Borzotta, 2009). Rock glaciers attest to the periglacial conditions at these high elevations (Brenning et al., 2005; Drewes et al., 2018). Glaciers reach down to 4,700 m asl in some valleys; debris-covered glaciers are common due to the arid environment conditions in the Central Andes (Corte and Espizúa, 1981; Espizúa, 1982; Corte and Grosso, 1993; Buk, 2002).

GEOLOGICAL FRAMEWORK AND NEOTECTONIC ACTIVITY

The Plata Range is part of the Andean Frontal Cordillera morphotectonic unit and was uplifted during the Andean Orogeny 12–18 Ma ago (Giambiagi et al., 2003). The basement of the Frontal Cordillera comprises Devonian metasedimentary rocks of the Vallecitos Series (Heredia et al., 2012) and Carboniferous–Permian marine pelite of the Loma de los Morteritos and El Plata formations (Caminos, 1965) (**Figure 2**). The basement rocks are overlain by a thick sequence of Permo-Triassic volcanic rocks of the Choiyoi Group, which were erupted in an extensional environmental during a final stage of subduction (Llambías et al., 1993; Kleiman and Japas, 2009). Granitic rocks were also intruded into the crust at this time. The Choiyoi Group also includes sedimentary units (Tambillos and Mal Pais formations). The sequence continues with a thick pile of Triassic continental fluvial deposits and subordinate volcanic rocks emplaced within the Cuyo rift basin (Rio Mendoza, Potrerillos, Cacheuta, and Rio Blanco formations). These Triassic rocks are overlain by conglomerates of the Jurassic Papagallos Formation. Paleogene and Lower Neogene rocks are mainly represented by sandstones of the Mariño Formation in lower piedmont areas (Caminos, 1965). This Mariño Formation is overlain by a thin succession of poorly stratified coarse conglomerate of the Mogotes Formation of late Pliocene age (Irigoyen et al., 2000, 2002).

Quaternary deposits are present within BRB valleys and in the piedmont region. Moraines have been identified in the higher parts of some valleys (Wayne and Corte, 1983; Wayne, 1984; Moreiras et al., 2017). Recently, some of these moraines have been dated using surface exposure cosmogenic methods as ∼8–25 ka and are probably linked to the Last Glacial Maximum. One moraine in the Mulas River valley yielded an age of ∼40 ka (Moreiras et al., 2017). Near the study area, the Penitentes glaciation was dated ∼30 ka in the Mendoza River valley (Espizúa and Bigazzi, 1998; Espizúa, 1999); however, Late Pleistocene climatic conditions remain uncertain for the region.

The Carrera fault system extends along the eastern margin of the Plata Range and is the main structure responsible for the uplift of the Frontal Cordillera (Caminos, 1965) (**Figure 1**). This system comprises north-trending imbricated reverse faults with eastern vergence (Polanski, 1972). The Arenales fault thrusts granitic intrusive rocks over the volcanic rocks of Choiyoi Group, and the Médanos fault displaces rocks as young as Neogene (Folguera et al., 2004; Casa et al., 2010). The Rio Blanco fault offsets Pliocene and Quaternary strata, and the El Salto fault has uplifted three pediment levels of Quaternary age (Casa et al., 2010). The offset Quaternary alluvial fans (Cortés et al., 1999, 2006; Borgnia, 2004; Casa, 2005, 2009; Casa et al., 2010) and a cluster of seven Late Pleistocene rock avalanches in the northern Plata Range (Moreiras, 2006; Fauqué et al., 2009; Moreiras et al., 2015) provide evidence that the Carrera fault system remains active (**Figure 2**). Different levels of alluvial terraces have been identified in the lower piedmont portion of the study area (Polanski, 1963) and have been attributed to the uplift of the Frontal Cordillera (Rodríguez and Barton, 1993; Casa, 2005).

METHODOLOGY

The motivation for this study was understanding the genesis of a chaotic deposit that had been previously and ambiguously interpreted to be till (Wayne and Corte, 1983; Wayne,

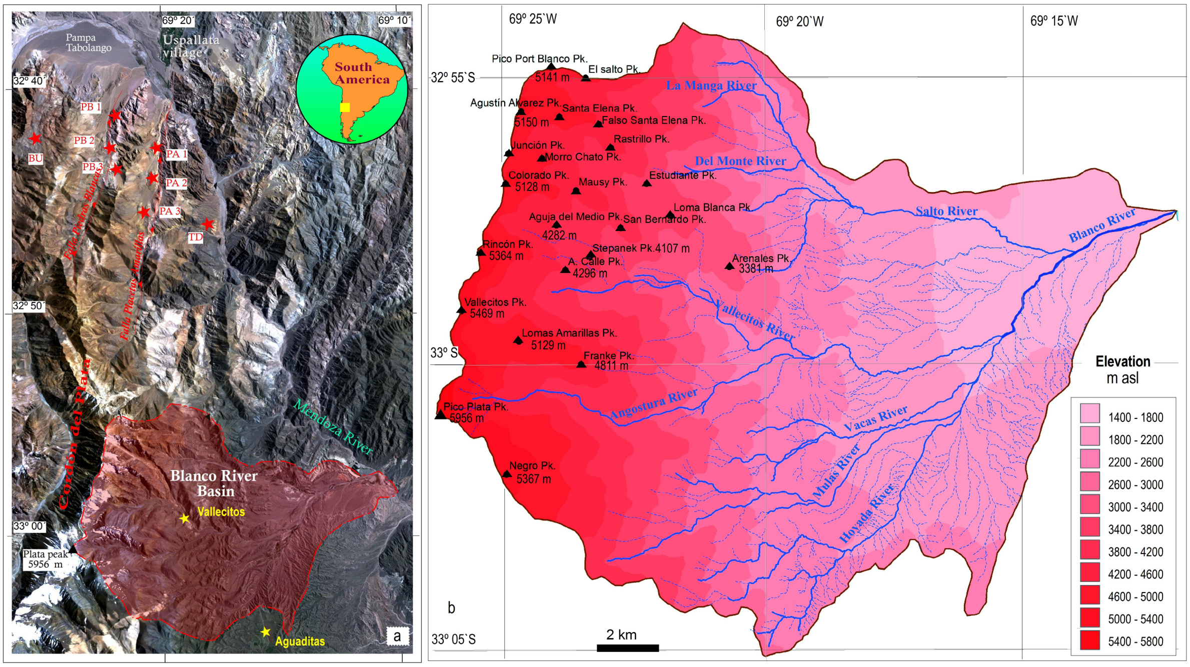

FIGURE 1 | Study area location at 33°S: **(a)** the Blanco River Basin (BRB) on the eastern slope of the Plata Range (polygon in red) and its relative position with a cluster of rock avalanches studied in the northern extreme of Plata Range. Rock avalanches are represented by red stars: BU, Burro rock avalanche; PB, Piedras Blancas rock avalanches: PB1, PB2, PB3; PA, Placetas Amarillas: PA1, PA2, PA3; TD, Tigre Dormido rock avalanche. Yellow stars indicate meteorological stations of Vallecitos and Aguaditas. **(b)** Digital elevation model of the Plata Range showing highest peaks and the catchment area of the BRB integrated by the main central branch of the Blanco River including the Angostura and Vallecitos rivers, the sub-catchments the Alto Manantiales integrated by the Salto, Manga, del Monte and Chacay rivers, and the southern subcatchment denominated Alto Las Vegas integrated by Mulas river.

1984) or a debris flow deposit (Polanski, 1961, 1966). To resolve this disagreement, I initially carried out a geospatial analysis of the study area based on remotely sensed imagery. A geomorphological map of the main Quaternary deposits and landforms was done using pairs of 1,963 airphotos, Landsat satellite images, and Google Earth imagery. The map shows bare and debris-covered glacier ice, rock glaciers, and snow patches, following the classification of Janke et al. (2015) (**Figure 3**). Moraines and outwash and alluvial deposits were also mapped. The map was verified during the field sessions carried out between 2012 and 2015.

The cenoglomerate chaotic deposit was studied in the field using methods taken from Abele (1984); Hewitt (1999), and Reznichenko et al. (2012). Specifically, observations were made in terms of fabric, grain size, boulder lithology, size, and roundness, matrix percentage, stratigraphic context, and the presence or the absence of striations.

Stratigraphic profiles were described at different locations within the BRB (**Figure 3**) in an effort to find possible facies differences along the depositional path. Even though rock avalanche deposits are chaotic in nature, they typically exhibit characteristics indicative of rapid motion, fragmentation, and abrupt deposition, for example, jigsaw-like fracturing of large clasts, inverse grading, sheared or mylonitized layers, mixed facies, a matrix with fractal-like particle size distribution, and deformed or liquefied substrates (e.g., Cruden and Hungr, 1986; Gates, 1987; Yarnold and Lombard, 1989; Dunning, 2006; Prager et al., 2012; Weidinger et al., 2014; Wang et al., 2015, 2018; Dufresne et al., 2016; Strom and Abdrakhmatov, 2018; Zeng et al., 2019). The principal morphological parameters of the cenoglomerate were estimated, and its isolated remnants were mapped to establish the original extent of the deposit and to provide a rough estimate of its volume.

The alluvial sediments underlying and overlying the cenoglomerate were dated using optically stimulated luminescence (OSL) techniques to establish the age of the deposit. Radiocarbon dating was not possible because the sediments on the BRB lack organic matter. OSL dating determines the time since the last exposure to daylight of quartz or feldspar grains in unheated sediments (Aitken, 1998; Rhodes, 2011). I collected samples for OSL dating by cleaning a vertical exposure and then inserting plastic tubes 25 cm long and 70 mm in diameter horizontally into the sediment by hammering. The ends of the tubes were sealed with aluminum foil and the tubes were wrapped with a black plastic bag. In the lab, sediment immediately surrounding the primary sample was collected to calculate the ß contribution to the dose rate, and a second sub-sample was taken 10–30 cm from the primary sample to calculate the Y dose rate component (Antinao et al., 2013).

Sand-sized grains were analyzed because silt is more likely to move vertically within a profile, a process that increases the chances of mixed-age grain populations within a given

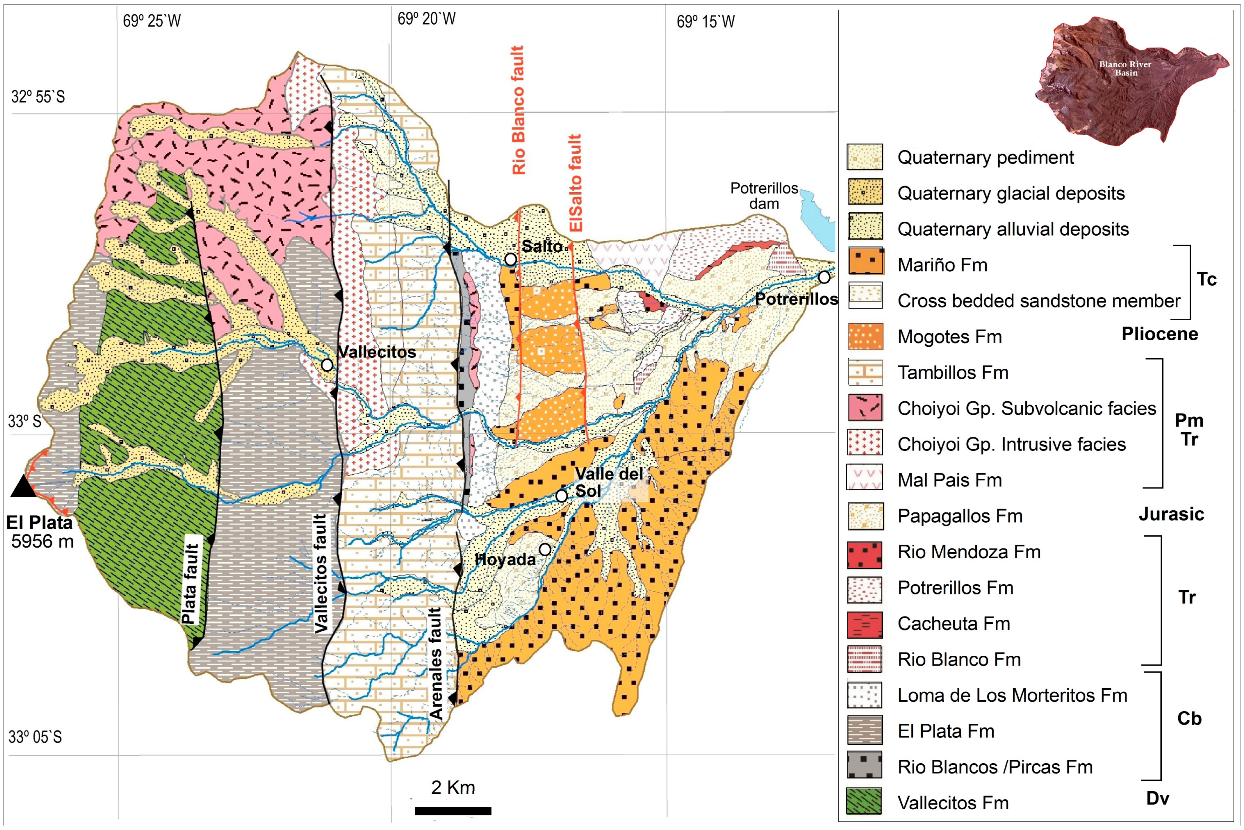

FIGURE 2 | Quaternary, Tertiary (Tc), Pliocene, Jurassic, Permo-Triassic (PmTr), Triassic (Tr), Carboniferous (Cb), and Devonian (Dv) lithological units outcropping in the BRB with the main structures of the Carrera fault system responsible for the Frontal Cordillera uplift. Rio Blanco (RBF) and Salto (SF) active faults are mapped in red color. The probable source area of the Plata rock avalanche is indicated in red line the headwater of the Angostura Valley at the Plata Mount (5,956 m asl). Dots indicate main villages.

stratum (e.g., Berger et al., 2004). Both quartz and feldspar grains were dated. Values of water (relation between of the weight of wet sample/dry sample) were estimated based on data for similar sediments in similar climatic settings, with an estimated uncertainty of ±0.02 (Antinao et al., 2013). The potassium value (K_2O) for material around the quartz grains was established with an estimated uncertainty set to ±0.05%. The value of K_2O was set to zero for dose rate calculations in the case of quartz separates, while the value of K_2O at 10 ± 2% was used for the feldspar data. Total (C_t) and thorium (C_{th}) count rates were established from finely powered samples by the thick-source-alpha-particle-counting (Huntley and Wintle, 1981). These values were inserted directly into the age equations of Berger (1988), with the internal dose rate components set to zero. Cu is equal to the total count (C_t) minus the thorium count (C_th). A cosmic ray component, basically a function of burial depth, was estimated using the algorithm of Prescott and Hutton (1994).

The dose rate was calculated using the conversion factors given by Adamiec and Aitken (1998) and the equations of Berger (1988). Attenuation of ß radiation across the sand grain was accounted for by using attenuation factors from Aitken (1985). An estimated small internal dose rate in quartz of 0.05 ± 0.03 Gy/ka was added to the calculated dose rate (**Table 1**).

The ages reported here stem mainly from single-grain aliquots, indicated by "single grain" in **Table 2**. A grain size attenuation factor for the beta dose was taken from Mejdahl (1979). The preheating temperature for the single-aliquot regenerative dose approach was held for 10 s (Murray and Wintle, 2000). A signal-readout temperature of 125°C was employed for quartz, whereas sequential measurements at 50°C (whole disc. IRSL) and 225°C (post-IR single-grain IRSL) were used for feldspar. The dose estimation used for age determination is based on the minimum age model (MAM) or the central age model (Galbraith et al., 1999).

RESULTS

Deposit Sedimentology and Stratigraphy

The deposit that motivated this study has been described as a greenish–grayish chaotic deposit found along the main branch of the Blanco River (site 6, **Figure 3**). However, the deposit also crops out elsewhere in the BRB, including Angostura Valley (sites 1–3), Blanco River valley (sites 4–7), and along the Vacas River (site 8) (**Figure 3**). The deposit is up to 8.5 m thick at higher sites in the Angostura Valley but is generally much thinner

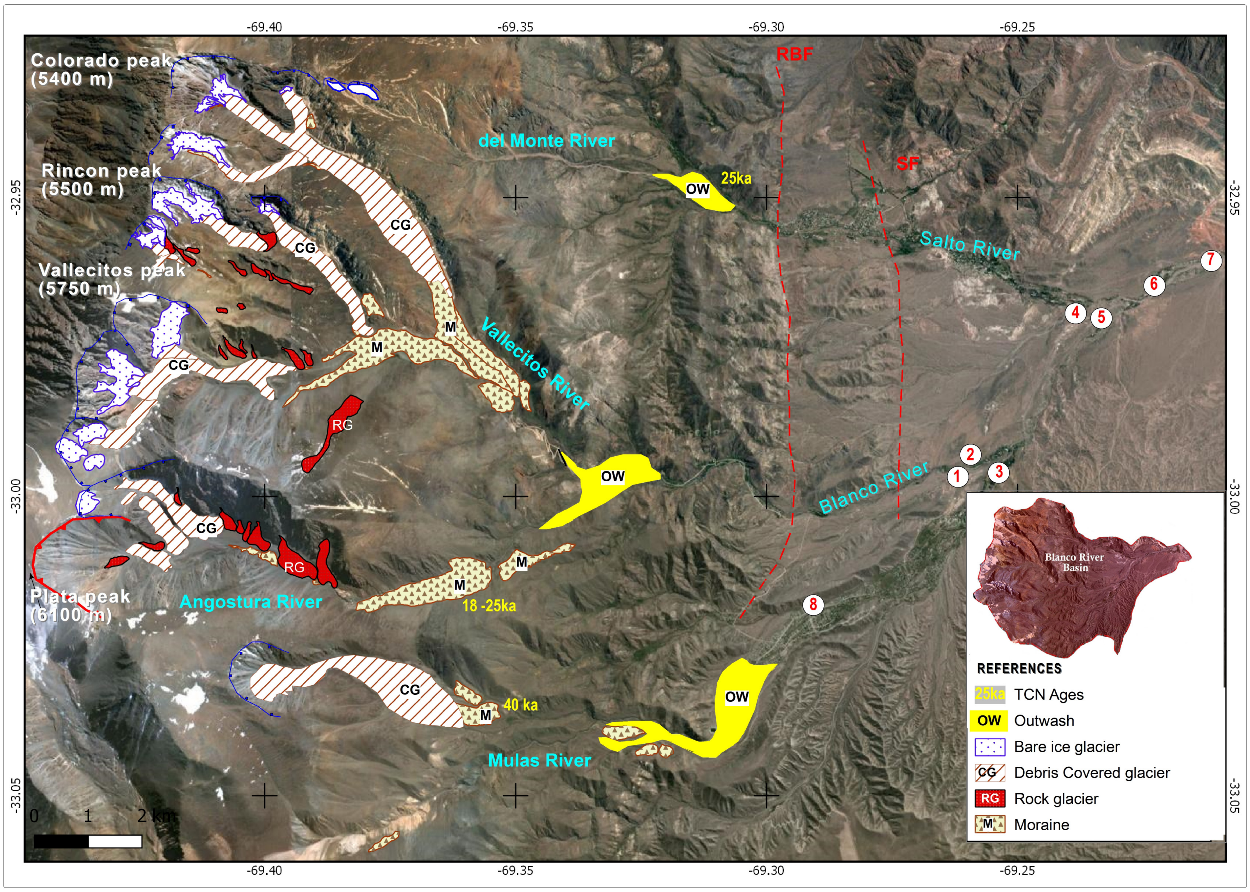

FIGURE 3 | Google image showing main landform of the BRB: bare ice glaciers; debris-covered glaciers, rock glaciers, moraines, and outwash deposits. The 10 Be ages of the Salto outwash and moraines of Angostura and Mulas rivers are in yellow letters (after Moreiras et al., 2017). Note that the Angostura valley has preserved relict moraines at the headwaters but uncovered glacier in the highest peak of the Plata peak (5,956 m asl) is missed. RBF, Rio Blanco fault and SF, Salto fault mapped in red lines. Number indicates places where the rock avalanche outcrops.

TABLE 1 | Dose rates (Gy/ka) for feldspar and quartz grains.

Sample[a]	Water	K_2O %	C_t ($ks^{-1}\cdot cm^2$)	C_{th} ($ks^{-1}\cdot cm^2$)	DCR (Gy/ka)	Dose rate (Gy/ka)	
						Feldspar	Quartz
CP-VS03.12 (1)	0.10	1.90	0.430 ± 0.004	0.201 ± 0.013	0.195	2.88 ± 0.19	2.26 ± 0.06
CP-VS03.12 (2)	0.10	1.92	0.404 ± 0.006	0.159 ± 0.016			
CP-SA-07.12 (1)	0.10	2.46	0.660 ± 0.005	0.292 ± 0.016	0.156	3.9. ± 0.20	3.17 ± 0.08
CP-SA-07.12(2)	0.10	2.07	0.934 ± 0.008	0.241 ± 0.023			

[a] *The first row of data (1) comprises data for sediment immediately surrounding the primary sample used to calculate the ß contribution to the dose rate, while the second row (2) represents data for samples taken 10–30 cm away from the primary sample used to calculate the Y dose rate component.*

(<3.5 m) in the Blanco Valley where it is unconformably overlain by alluvial fan sediments. The clasts in the deposit are up to 3 m in size (mean diameter = 0.5 m) and are mainly derived from the Carboniferous El Plata Formation. More than 98% of blocks are gray sandstone, conglomerate, and phyllite of this unit. The clasts of an altered gabbro, although only about 2% of the deposit, contribute to the greenish matrix color. The clasts are angular to subangular and show no evidence of having been rounded during transport. They bear no striations or other evidence of a glacial origin. Although the deposit is typically massive, inverse grading and weak bedding were noted in some outcrops. The matrix content ranges from 20 to 40%. The matrix is dominantly sand-sized, but gravel was noted in some sections. The chaotic deposits comprise two main lithofacies. The finer facies ("a") has a brownish-grayish color, with clasts <0.5 m in size, and a high matrix content. It forms the lowest part of the deposit at some sites. In contrast, lithofacies "b" has a greenish–grayish color, with larger blocks (up to 3 m).

TABLE 2 | Single-grain equivalent dose (DE) and estimated ages for the sand samples (preferred age in bold).

Sample	Grain size (μm)	Preheat	Mode (°C)	DE (Gy)	Age estimate (10^3 years before 2012)
CP-VS03.12	210–250	260/220	Single-grain (SG) quartz	84.2 ± 9.374 (minimum age model, MAM)	37.26 ± 4.26
				159.8 ± 13.54 (central age model, CAM)	70.71 ± 6.28
		250	SG feldspar	114.3 ± 8.365(MAM)	**39.68 ± 3.89**
				220.5 ± 13.37 (CAM)	76.54 ± 6.81
CP-VA07.12	250–300	260/220	SG quartz	113.8 ± 8.7 (MAM)	**35.90 ± 2.89**
				159.6 ± 11.31 (CAM)	50.35 ± 3.79
		250	SG feldspar	116.4 ± 4.91 (MAM)	29.85 ± 1.98
				163.2 ± 9.46 (CAM)	41.85 ± 3.24
				180.2 ± 7.328 (CAM)	46.21 ± 3.02

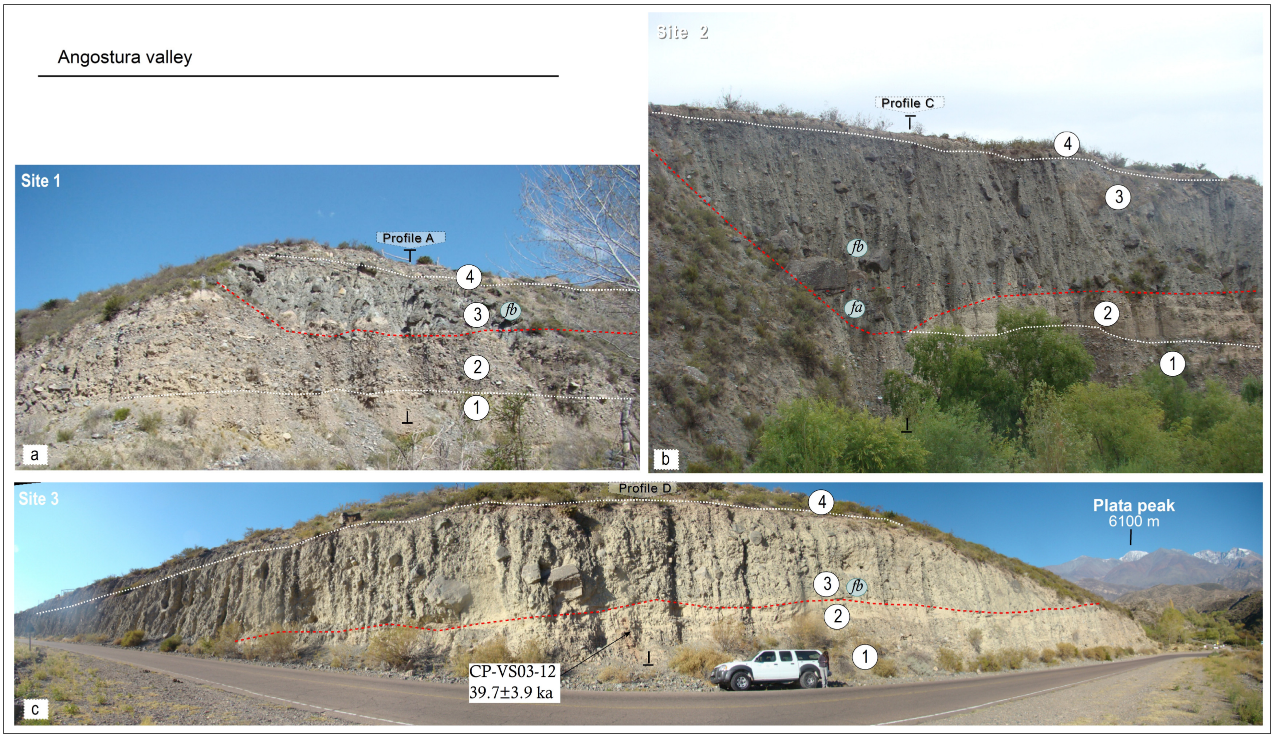

FIGURE 4 | Cross sections along the Angostura Valley where the Plata rock avalanche outcrops: **(a)** Cross section at site 1 where the profile A was described on the right margin of the Angostura valley. Units: 1. corresponds to basal fluvio-glacial deposits, 2. alluvial deposits, 3. the Plata rock avalanche, and 4. A 0.7 m thick-alluvial layer (see **Figure 5**). The profile B was described 300 m from profile A. **(b)** Cross section at site 2 where the profile C was described on the left margin of the Angostura valley. Units: 1. gravel alluvial deposits, 2. finer alluvial deposits, 3. the Plata rock avalanche with erosive basal contact, and 4. alluvial layer (see **Figure 5**). **(c)** Cross-section at site 3 just in front site 2 where the profile D was described on the right margin of the Angostura valley. Units: 1. gravel alluvial deposits, 2. finer alluvial deposits from where the sample CP.VS 03.12 was taken, 3. the Plata rock avalanche, and 4. alluvial layer (see **Figure 5**). Facies a (fa) and facies b (*fb*).

Site 1, Stratigraphic Profile A ~1,780 m asl

This section is a road cut at the margin of the Angostura Valley and was created during the construction of the road to Vallecitos (**Figure 4a**), which is basal glaciofluvial gravel consisting mainly of clasts of sedimentary and metamorphic rocks derived from Carboniferous and Devonian formations that crop out in the headwaters of the valley. It is overlain by the massive chaotic deposit, which here is 2–3 m thick and contains blocks of the Carboniferous El Plata Formation up to 2.5 m in size within a sandy matrix. The chaotic deposit is covered by 0.7 m of alluvium with carbonate-coated clasts (**Figure 5**).

Site 1, Stratigraphic Profile B ~1,800 m asl

This natural exposure is 300 m upstream of profile A. The chaotic deposit is 8 m thick at this site (**Figure 5**), and the fluvial deposits noted at the previous site are absent here. Blocks within the chaotic deposit reach up to 2.5 m in size and lie within a sandy matrix that constitutes 20–40% of the deposit. Most of the

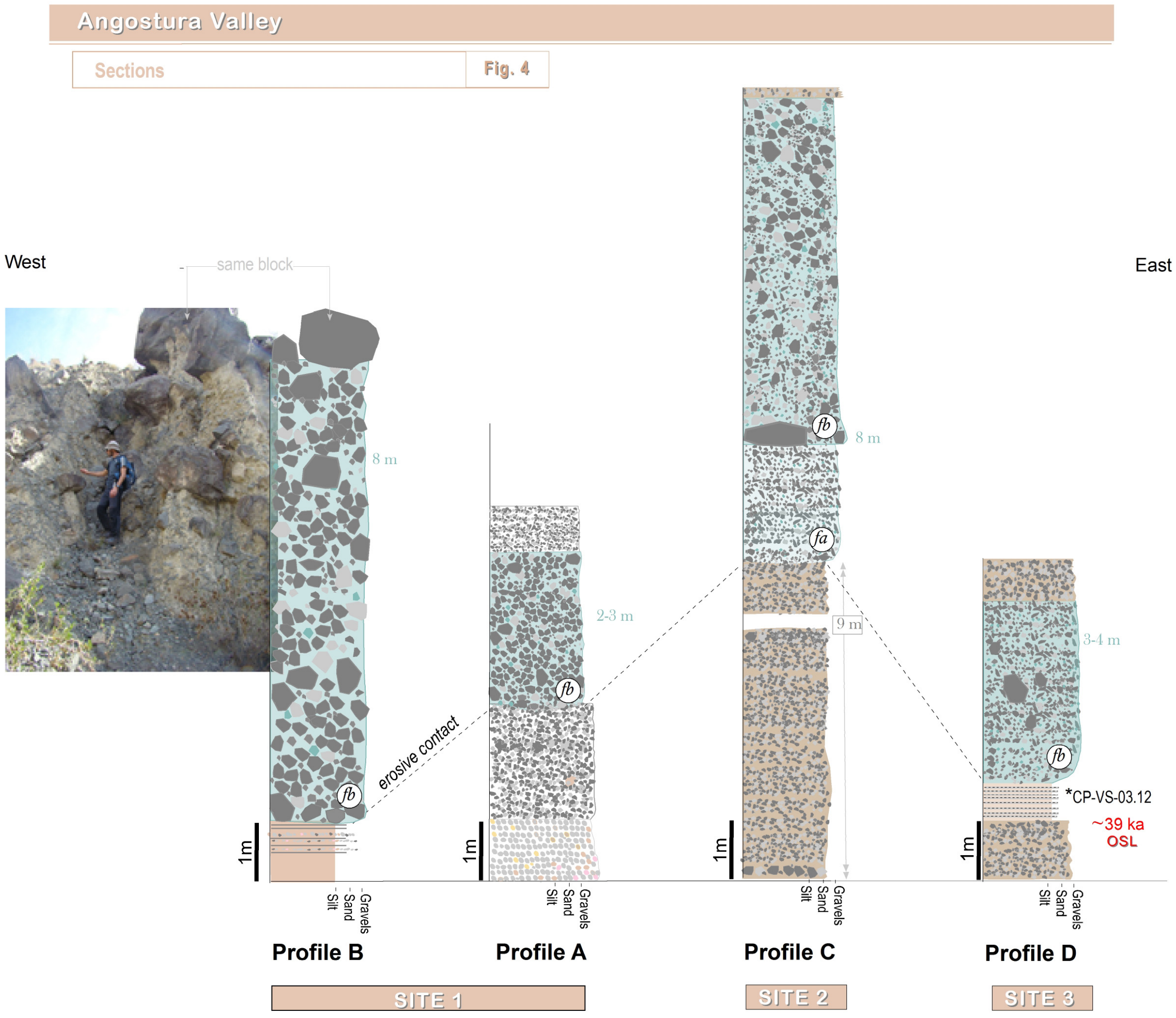

FIGURE 5 | Graph of sedimentological profiles described in sites 1, 2, and 3 along the Angostura Valley showing presence of facie a (*fa*) *or* facie b (*fb*) (see pictures in **Figure 4**). The photo on the left corresponds to the top of the profile B with a person as scale.

blocks are El Plata breccia, sandstone, and pelites; some clasts of sedimentary rocks derived from the Loma de los Morteritos Formation are also present, as are pebbles (1%) of granite and silicified rocks 2–4 cm in diameter. The deposit is massive but shows the same inverse grading with the largest blocks near the top of the exposure.

Site 2, Stratigraphic Profile C ∼1,750 m asl

Section C is a 17-m-high natural exposure in an incised Quaternary alluvial terrace in the Angostura Valley (**Figure 4b**), which is up to 9 m of coarse fluvial gravel and with clasts up to 0.5 m in diameter forming the lower half of the exposure. This sequence changes laterally: an upper finer muddy layer overlies a coarser layer (**Figure 5**). The chaotic deposit, which is 8 m thick here, overlies the alluvium across an erosional contact. It comprises the two lithofacies mentioned above: basal facies with high matrix content and blocks < 0.5 m in diameter (lithofacies a) and an upper grayish-green facies with less matrix content, mainly sand, and larger blocks (up to 2 m in size) (lithofacies b). The contact between the two facies is gradational. No stratification or block imbrication is visible in the section.

Site 3, Stratigraphic Profile D ∼1,750 m asl

Site 3 is an exposure along the road to Valle del Sol in the Angostura Valley. About 1 m of alluvium (**Figures 4c**, **5**) is present at the base of the exposure. It consists of intercalated layers of sand and silt with some gravel lenses with heterogeneous compositions (pelite, volcanite, and metamorphic rocks) (2–4 cm in diameter). Sample CP-VS03.12 was extracted from this unit for OSL dating. The alluvium is overlain across an erosional contact by 3–4 m of the chaotic deposit, with boulders reaching 2 m across and a sandy matrix that constitutes 10–20% of the mass. The chaotic deposit is unconformably overlain by alluvium consisting of sub-rounded clasts of Devonian metamorphic rocks (mainly gneiss), rhyolite, andesite, and granite, as well as clasts of the same composition as the blocks in the underlying chaotic deposit (**Figure 5**).

Site 4, Stratigraphic Profile E ∼1,580 m asl

This exposure is located along the Blanco River at the junction of the roads to El Salto and Vallecitos. At this site, the chaotic deposit is 4.5–6 m thick and has a marked greenish–grayish color (**Figure 6a**). The blocks are 0.4–0.7 m in size and are set in a sandy matrix that forms 40% of the deposit. The chaotic deposit lies within a paleochannel incised into older alluvium and is covered by up to 1.5 m of reddish alluvium across an irregular contact (**Figure 7**). The upper alluvium unit was sampled for OSL dating (sample CP-SA07.12).

Site 5, Stratigraphic Profile F ∼1,540 m asl

Up to 2.4 m of glaciofluvial gravel containing rounded and sub-rounded boulders up to 0.60 m in diameter form the lower part of the road cut at site 5 in the Blanco Valley (**Figure 6b**). This deposit lies within a paleochannel incised into the Tertiary Mariño Formation. The boulders are mainly volcanic and intrusive rocks of the Permo-Triassic Choiyoi Group (andesite, gabbro, rhyolite, and granite) but include some Carboniferous pelite and sandstone. About 30% of the deposit is a sandy matrix.

The glaciofluvial unit is overlain by 0.8 m of the chaotic deposit with its typical greenish–grayish color. Blocks up to 2 m in size are set in a matrix that constitutes 40% of the deposit. About 98% of the blocks are sedimentary rocks of the Plata Formation. The chaotic deposit is overlain successively by 1–2.5 m of glaciofluvial gravel with rounded boulders of a variety of lithologies and 0.4 m of alluvial fan deposits (**Figure 7**).

The chaotic deposit shows a thicker thickness (4 m) in section F’, described to be 10 m from previous section F (**Figure 6b**). Here the boulder sizes are up 2 m in diameter, predominating the largest blocks near the top of the unit, and the matrix content reaches 35%. A 1-m-thick fluvial glacial level and 0.7-m-thick alluvial deposits are overlying the chaotic deposit (**Figures 6b**, **7**).

Site 8, Stratigraphic Profile G ∼1,800 m asl

This 11-m-high section is located at the north margin of the Vacas valley (**Figure 8**). About 3.5 m of the greenish–grayish

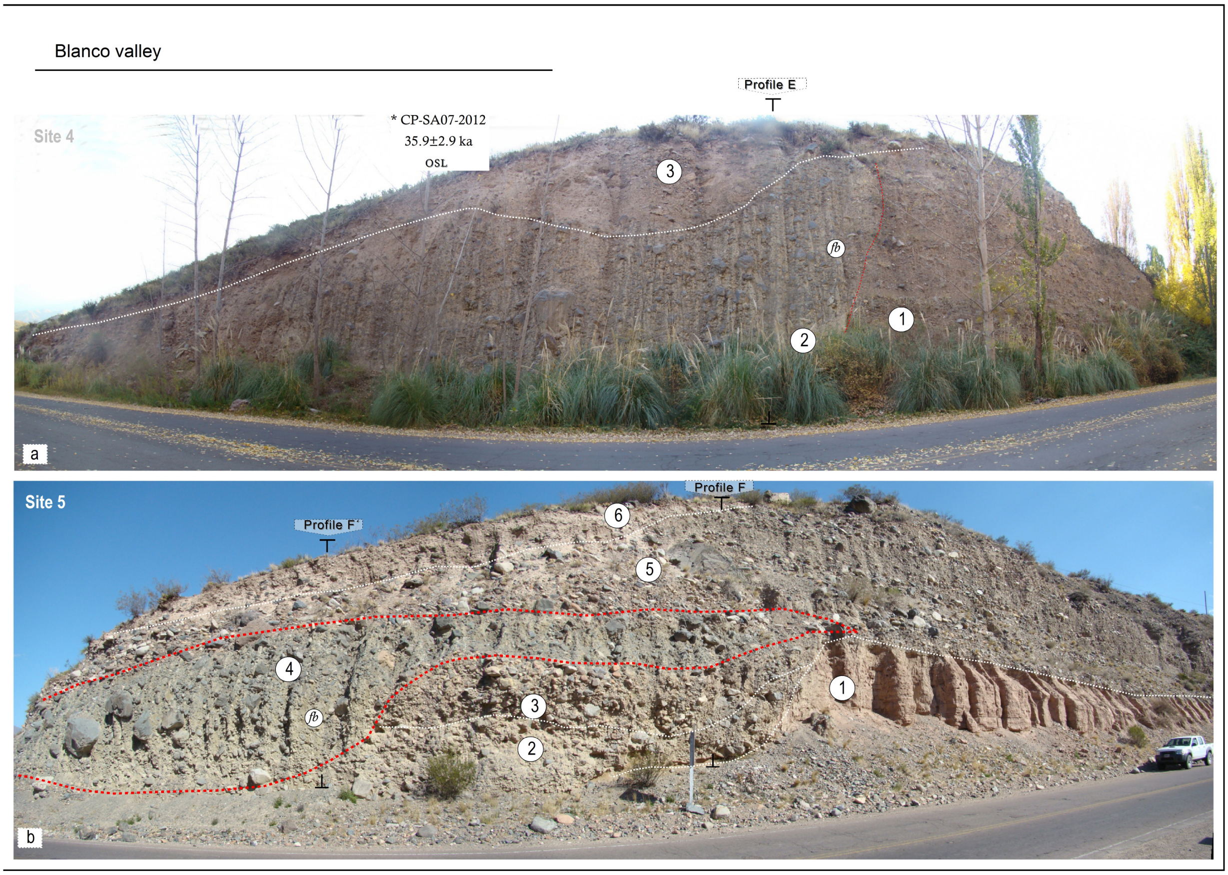

FIGURE 6 | Cross sections along the Blanco River where the Plata rock avalanche outcrops: **(a)** Cross section at site 4 where unit 1 corresponds to gravel alluvial deposits, 2. the Plata rock avalanche with apparent vertical lamination due to vertical erosion (*fb* is facie b), and 3. finer alluvial deposits where the sample CP-SA07.12 was taken for OSL dating. **(b)** Cross section in site 5 where unit 1 corresponds to Tertian outcroppings, 2. and 3. paleo-channel deposits, 4. the rock avalanche, 5. outwash deposit, and 6. alluvial deposits. See profiles on **Figure 7**.

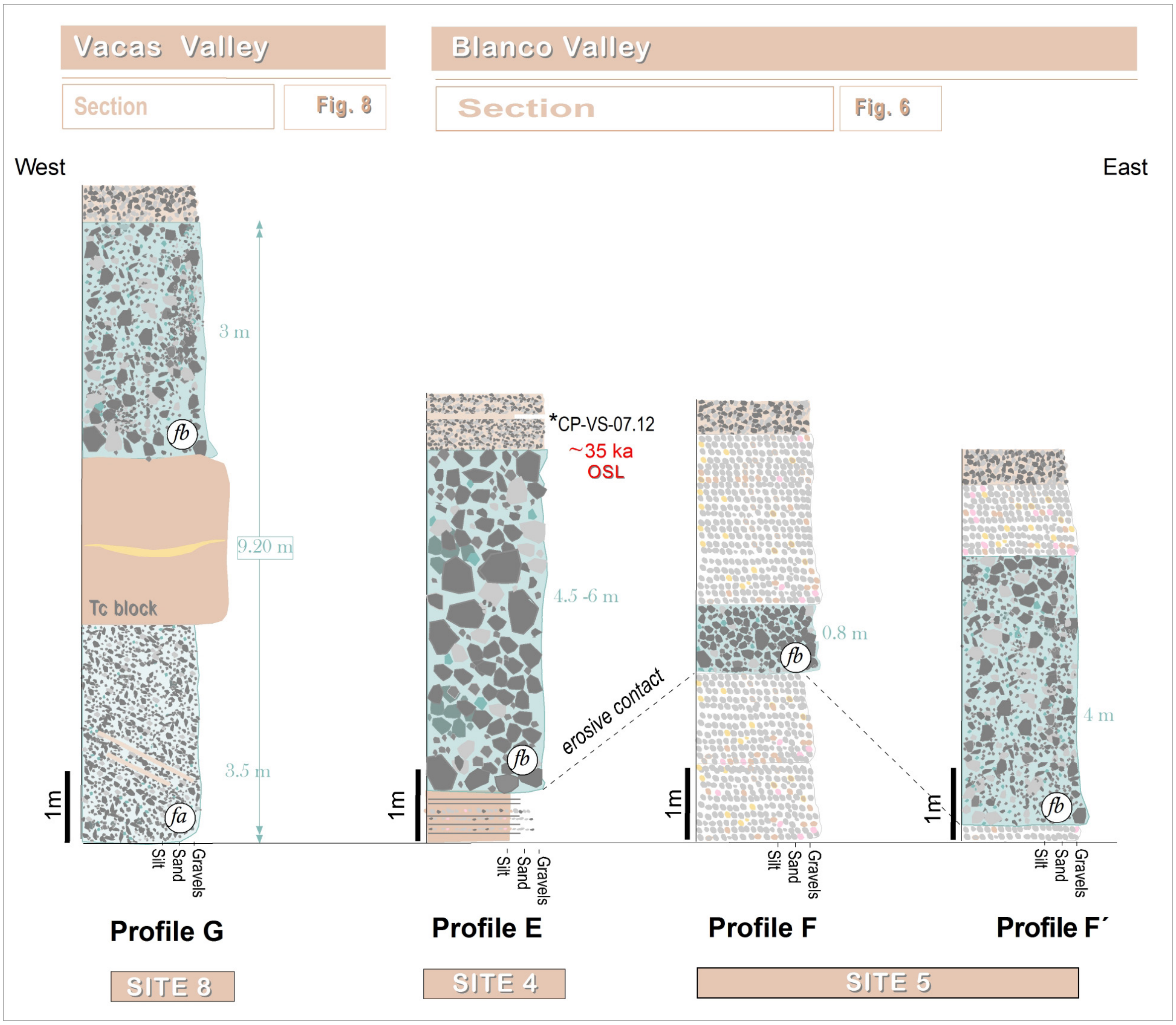

FIGURE 7 | Graph of sedimentological profiles described in sites 4 and 5 along the Blanco Valley (see pictures in the **Figure 6**) and profile G described in site 8 along the Vacas valley (see **Figure 8**). Tc block corresponds to the block of Tertiary rocks engulfing by the facie a (fa) and covered by the facie b (fb).

chaotic deposit (lithofacies a), similar to the deposit at site 2, marks the base of the section. The clasts are smaller (<0.5 m) and the matrix content is higher (40%) than at previously described sections. Some of the clasts are Tertiary siltstone and sandstone. The deposit is stratified, and the clasts are imbricated and inclined toward the west. A 2.7-m block of reddish Tertiary sedimentary rock separates this unit from 3 m of lithofacies b (**Figure 7**). The basal unit dips toward the west and east adjacent to the large Tertiary block; it appears that the block was flowing on this basal unit. The upper part of the chaotic deposit (lithofacies b) is massive and contains clasts of Carboniferous rocks 0.3–0.5 m in size. It is overlain at the top of the exposure by 0.6–1 m of alluvium.

Source Area

The source area of the chaotic deposit is not obvious. The composition of the deposit matches the widespread occurrence of Carboniferous rocks on the east slope of El Plata Peak (5,956 m asl), but the headwaters of the Angostura Valley lack a characteristic spoon-shaped scar. Furthermore, the chaotic deposits appear to be absent in the headwaters of the Angostura Valley (**Figures 3**, **9**). Different types of glaciers flow off this massif; rather, glaciers occupy the head of valleys of the BRB. In the Vallecitos Valley, Vallecitos, Rincon, Coloradas, and Stepanek (bare ice) glaciers are located above 4,700 m asl and cover a total area of 2.3 km^2, but the debris-covered glaciers flowing down along this valley have a greater area of 5.6 km^2 as with other dry environment mountains. Farther south, the only ice landform is the Lomas de los Morteritos Glacier in the headwaters of the Mulas Valley. This debris-covered glacier lies at 3,400 m asl, with a length of 2.7 km (**Figure 3**). In both valleys of the BRB, rock glaciers cover smaller areas (<0.86 km^2) and represent not more than 10% of glaciated areas in each sub-basin (**Table 3**).

Glacier ice cover in the headwaters of the Angostura Valley differs from north to south, with larger glaciers to the north and smaller ones and rock glaciers to the south. A bare ice glacier

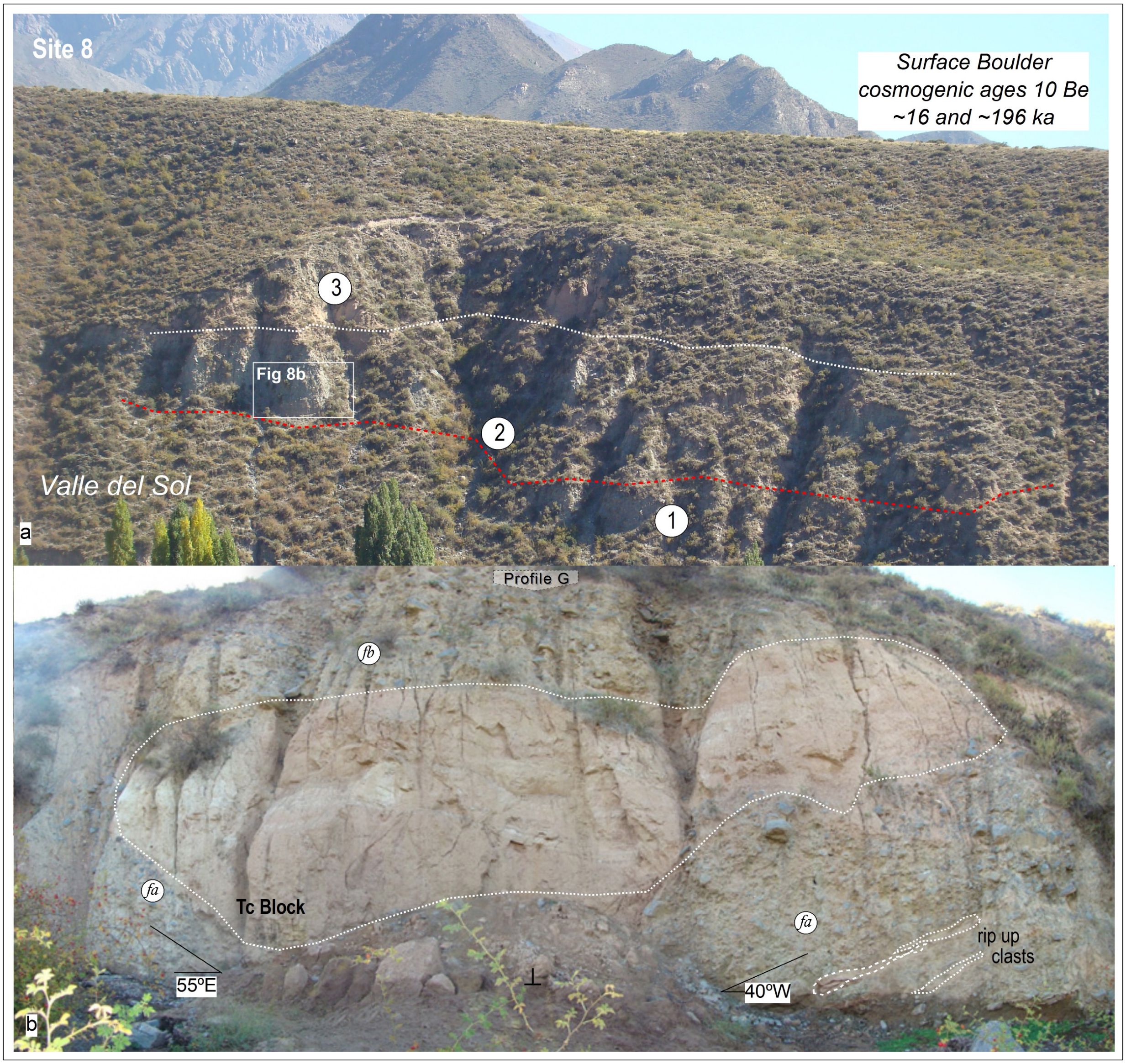

FIGURE 8 | Site 8 just in from of the Valle del Sol village. **(a)** Panoramic view of alluvial deposits along the Vacas Valley where 1. corresponds to alluvial deposits, 2. rock avalanche, and 3. alluvial deposits previously dated by cosmogenic nucleoids on surficial blocks (^{10}Be) ∼16 and ∼196 ka. **(b)** Detail of the rock avalanche deposit where a block of Tertian rocks (Tc block) is engulfed by the rock avalanches facies (*fa*) and facies (*fb*). Note that the basal layers are dipping in contrary directions containing rip up clasts.

is at the top of the northern headwaters, and two big debris-covered glaciers occupied the whole valley downstream, with practically no rock glaciers. This seems anomalous given that the southern headwaters initiate below the highest peak of the study area (El Plata, 5,656 m asl), where only a debris-covered glacier was identified.

There is no doubt that all the high valleys in the BRB supported glaciers at the LGM (Moreiras et al., 2017). However, the lack of a large glacier in the southern headwaters of the Angostura Valley is evidence that a rock avalanche was generated in this sector and removed the glacier during the collapse. The material detachment surely changed the original aspect of the slope preventing the further accumulation of snow/ice and the generation of a niche or circus what restricted the ensuing regrowth of a glacier. However, the debris-covered glacier just below this area could indicate the restoration of the glacial environment in this southern headwater of the Angostura valley.

Origin, Volume, and Emplacement of the Chaotic Deposit

The sedimentological and stratigraphic evidence presented above support the idea that the chaotic "cenoglomerate" is not a glacial deposit but rather the product of a rock avalanche. After the

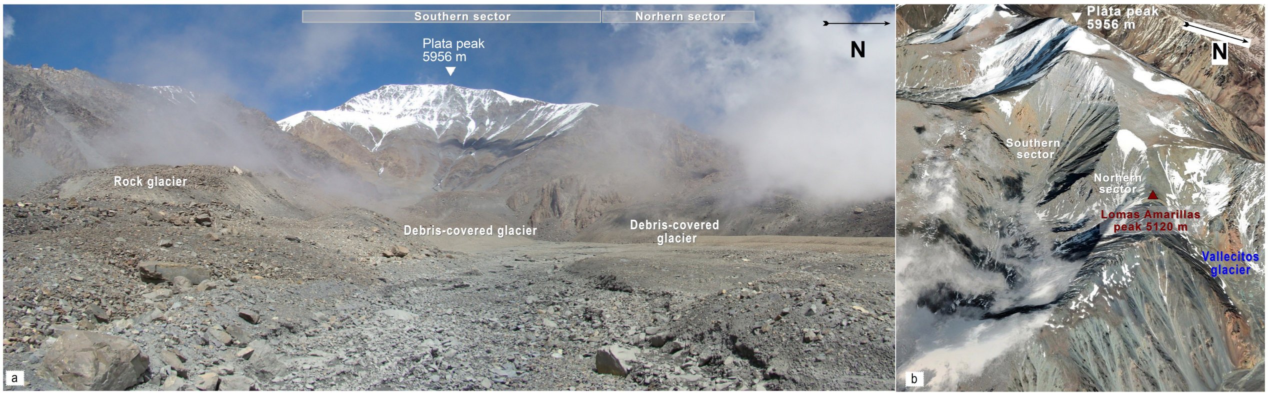

FIGURE 9 | Source area. **(a)** Picture of Plata peak showing predomination of ice covered glacier and debris rock glaciers in the southern sector of the headwater of the Angostura Valley where rock avalanche remains are lacking. **(b)** Google 3D stereographic view of the Plata peak without glaciers in the southern sector.

TABLE 3 | Areas occupied by different types of glaciers in the main sub-basins of the Blanco River basin.

Sub-basin	Area (km^2)	Bare ice glacier				Debris-covered glacier				Rock glacier			
		N	GA km^2	A %	GA/A	*N*	GA km^2	A %	GA/A	*N*	GA km^2	A %	GA/A
Vallecitos	53.1	11	2.3	26.3	0.043	9	5.59	63.9	0.105	17	0.86	9.8	0.02
Angostura	28	1	0.13	5.9	0.005	4	1.25	57.1	0.045	9	0.81	37	0.03
Las Mulas	43.6	0	–	–	0	1	2.29	100	0.053	0	–	–	0.0

N, number of landforms; GA, area covered by glacier type; A, percentage of area covered by glacier type in each subbasin; GA/A, ratio between area covered by glacier type (GA) and total area of the sub-basin.

rock mass collapsed, debris was channelized into the Angostura Valley and streamed down the Blanco River. Part of the streaming debris overtopped a topographic barrier and entered the southern parallel valley of the Vacas River (site 8) (**Figure 8**).

Assuming that the east face of El Plata Peak was the source area of the rock avalanche, the debris traveled at least 26.6 km over a vertical range of 4,700 m. The calculated fahrboschung of 0.17 indicates high mobility and an excessive travel distance compared to many other rock avalanches worldwide (Korup et al., 2007; Hewitt, 2009; Yang et al., 2019).

Only a rough estimate of the volume of the rock avalanche is possible because only isolated eroded remnants of the deposit exist and any material in the source area was removed. The maximum observed thickness of the rock avalanche deposit is 9.2 m, but at many sites < 0.6 m is exposed. Assuming a very conservative area covered by rock avalanche of 64,000 m^2, based on the surface of preserved deposits, and a mean thickness of the deposit of 5 m, a minimum volume of 3.2×10^5 m^3 was obtained. Other estimates, obtained by the mean thickness, travel distance (26.6 km), and assuming valley widths of 100 or 200 m, range from 1.46 to 2.9×10^7 m^3. These volumes are relatively small compared with those of neighboring rock avalanches, which reach up to 10^9 m^3 (Moreiras et al., 2015), and thus may be underestimates.

Age of Rock Avalanche

The Plata rock avalanche deposit overlies outwash and alluvium deposits and underlies alluvium along the Blanco River, neither of which has been previously dated. Polanski (1966) assumed a Late Pleistocene age based on the assumed association of the deposit with a dated tephra in overlying alluvial sediments. In contrast, Wayne (1984) considered that the deposit was a product of an Early Pleistocene glacial advance.

The rock avalanche deposit overlies alluvium, including silt and sand layers at sites 1, 2, and 3 (**Figures 4**, **5**). A sample of underlying fine sediments at site 3 (CP-VS03.12) yielded OSL ages of 39.7 ± 3.9 and 76.54 ± 6.81 ka (on feldspar) (CP-VS03.12), depending on the model used (**Table 2**). A second OSL sample collected from a sandy layer in alluvium overlying the rock avalanche deposit at site 4 (CP-SA07.12) yielded ages of 35.90 ± 2.89 ka or 50.35 ± 3.79 ka (on quartz), depending on the model used.

The dose rates for most terrestrial sediments are 2–4 Gy/ka (Aitken, 1985, 1998). The measured dose rate for quartz in our samples ranges from 2.2 to 3.1 Gy/ka and for feldspar from 2.9 to 3.9 Gy/ka (**Table 1**). Both quartz and feldspar mineral grains have been utilized. Quartz was favored initially, but due to the relatively low proportion of sensitive grains obtained in the first runs, feldspar experiments were added to the suite of analyses (Antinao et al., 2013). The ages obtained from feldspar by the MAM (Galbraith et al., 1999) were preferred for the CP-VS03.12 sample as a larger fraction of feldspars was sensitive compared to the fraction displayed by quartz. The age obtained from quartz was still preferred for the CP-SA07.12 sample since about 3–5% of the analyzed grains of the total feldspars showed saturation (i.e., the accumulated dose cannot be related to a finite artificial dose), indicating that these grains, although sensitive, have not been bleached. Coupled together, these data indicate that probably an analysis with a MAM would yield an equivalent dose identifiable with the event that buried the alluvial deposits (**Table 2**).

CONCLUSION

Wayne (1990) concluded that there were four glacial advances in the BRB, as supported by his interpretation of the deposits as tills. He noted glacial micromorphology on quartz grains, the presence of striated quartzite boulders, boulder fabrics that he attributed to glacial processes, valley walls polished by larger glaciers, and the large size of most of the cirques. However, according to this study, the Angostura till of Wayne and Corte (1983) and Wayne (1984), said to be a nearly monolithic deposit, is associated with a huge rock avalanche. Polanski (1966) and, later, Wayne (1990) attributed this event to a debris flow. However, the monolithic composition, with debris derived nearly entirely (98%) from the Carboniferous El Plata Formation (98%), the matrix content (20–40%), the dominance of subangular to angular blocks, the local presence of inverse grading, the absence of striations on clasts, and the presence of two related lithofacies are more consistent with a rock avalanche origin.

Rock avalanches are powerful mass movements resulting from the sudden and catastrophic failure of large rock masses that rapidly fragment and move as rapid flows downslope (Cruden and Varnes, 1996; Hungr and Evans, 2004; Strom and Korup, 2006; Hungr et al., 2014). The Plata rock avalanche mobilized at least 3.2×10^5 m^3 of debris and traveled up to 26.6 km from the source. The debris became channelized along the Blanco River but had enough energy to cross over to the Vacas Valley. A block 12 m wide and 5 m high floated on the streaming debris (**Figure 8**).

Since the pioneer work of Yarnold and Lombard (1989), typical facies models of rock avalanches describe a disturbed basal facies influenced by interactions with the substrate over which the landslide flows, overlain by a mixed zone with a higher content of finer material, and then a boulder cap known as a "carapace" (Prager et al., 2012; Weidinger et al., 2014; Wang et al., 2015; Dufresne et al., 2016; Strom and Abdrakhmatov, 2018; Zeng et al., 2019). This entire set of facies was not observed at any of the studied sections, but the lithofacies a at sites 2 and 8 share some similarities to the mixed zone mentioned above. Ripped-up clasts were observed as well in this basal facies. This weakly stratified facies resembles debris deposited by rock avalanches in the Tien Shan in Central Asia (e.g., Ornok, Yashilkul landslides; Strom and Abdrakhmatov, 2018). Lithofacies b has larger blocks and less matrix content than lithofacies a. Notably, at site 8, a large block of Tertiary rock at the base of facies b "rides" on much finer facies and debris. Although inverse grading is noted in lithofacies b (e.g., profile B at site 1), the typical carapace facies (Dufresne et al., 2016) was not observed, perhaps because it was subsequently removed by erosion.

Characterization of the rock avalanche deposit was helpful for understanding the provenance and the behavior of the landslide. The rock avalanche was initiated on the eastern slope of El Plata Peak, even though a typical source scar is lacking. The geomorphological study likewise reveals that the distribution of glaciers in the valleys of the BRB is not uniform. Even though the Plata Range is sufficiently high to support glaciers, they are poorly developed in the southern sector of the headwaters of the Angostura Valley. The lack of bare ice glaciers in this southern area could be explained by the generation of a great rock slope collapse. Even though the modified steep hillslope aspect of the east face of El Plata hindered the generation of a new glacier accumulation zone, the glacial environment could have been later restituted. A debris-covered glacier places just below the inferred source area of the rock avalanche and moraines associated with the LMG (∼18–25 ka) remain in this valley downstream.

The rock avalanche generated in the south face of the Aconcagua peak (∼11 ka) (Fauqué et al., 2009) modified the previous cirque area, generating a hanging wall glacier that remains until today. The lower Horcones inferior glacier, which is a reconstructed debris-covered glacier, is disconnected from the accumulation zone. This glacier is fed by snow avalanches coming from the south face of the Aconcagua peak. In the study area, the debris-covered glacier in the southern headwater of Angostura valley is disconnected from an "accumulation zone" in the eastern hillslope of the Plata peak (**Figure 9**). Besides that, a cirque morphology is absent in this hillslope.

Another evidence of the possible glacier contribution is that the Plata rock avalanche traveled 26.6 km, widely exceeding the distance of typical rock avalanches. This run-out is much longer than rock avalanches in the northern Plata Range (<10 km). The H/L ratio (∼0.17) is low, even if excess mobility is forced by the larger volume (Hsu, 1975; Hungr et al., 2005). A likely cause of this extraordinary run-out is that the rock avalanche incorporated glacier ice that melted and lubricated the debris material, increasing the erosional power and the distance traveled. Rock avalanches that overrun glaciers show more mobility (Evans and Clague, 1988; Sosio et al., 2012; De Blasio, 2014; Deline et al., 2015; Yang et al., 2019). The existence of a glacier in the headwaters of the Angostura Valley when the landslide happened is plausible as a moraine ∼40 ka was dated in the nearby Las Mulas basin. Similarly, the long run-out of Horcones rock avalanche in the Argentine Andes (13 km) has been attributed to the collapse of a rock mass onto a glacier below the south face of Aconcagua Peak (6,958 m asl) (Fauqué et al., 2009; Hermanns et al., 2015).

Optically stimulated luminescence dating of alluvial sediments above and below the rock avalanche deposit placed the event between about 40 and 36 ka. These ages are within the envelope of ^{10}Be ages of ∼16 and ∼169 ka previously obtained on boulders on the alluvial fan covering the rock avalanche in the Vacas Valley (site 8) (Moreiras et al., 2017). Evidence for climate forcing of the rock avalanche is weak as evidences for warmer or wetter conditions between 40 and 35 ka have not been found in the region. The collapse was possibly caused by an earthquake as alluvial deposits associated with the Plata rock avalanche are offset by the Rio Blanco and Salto faults belonging to the Carrera Fault system. A cluster of seven rock avalanches in the northern

Plata Range is likewise associated with the same fault system (Moreiras et al., 2015).

DATA AVAILABILITY STATEMENT

All datasets generated for this study are included in the article/supplementary material.

AUTHOR CONTRIBUTIONS

The author confirms being the sole contributor of this work and has approved it for publication.

FUNDING

This research was funded by the Universidad Nacional de Cuyo through Projects SeCTyP 2011-2013 06/A519 and ANLAC Program Res 571/15.

ACKNOWLEDGMENTS

We used QGis for data processing. OSL dating was done in the DRI lab. I thank J. Antinao for dating and P. Rodriguez, C. Lauro, and L. Mastrantonio for help with fieldwork. Gregory Carling and two reviewers helped to improve this manuscript.

REFERENCES

Abele, G. (1984). Derrumbes de montaña y morrenas en los Andes chilenos. *Rev. Geogr. Norte Grande* 11, 17–30.

Adamiec, G., and Aitken, M. J. (1998). Dose-rate conversion factors: update. *Ancient TL* 16, 37–50.

Aitken, M. J. (1985). *Thermoluminescence Dating*. San Diego, CA: Academic Press, 351.

Aitken, M. J. (1998). *Introduction to Optical Dating*. Oxford: Oxford University Press, 256.

Antinao, J. L., and Gosse, J. (2009). Large rockslides in the Southern Central An-des of Chile (32–34.5°S): tectonic control and significance for Quaternary landscape evolution. *Geomorphology* 104, 117–133. doi: 10.1016/j.geomorph.2008.08.008

Antinao, J. L., Huenupi, E., Baker, S., and Lewis, A. (2013). "Luminescence dating of alluvial deposits," in *Desert Research Institute Final Report*, (Vallecitos), 20.

Berger, G. W. (1988). "Dating quaternary events by luminescence," in *Dating Quaternary Sediments, Special Paper*, Vol. 227, ed. D. J. Easterbrook (Boulder, CO: Geological Society of America), 13–50.

Berger, G. W., Henderson, T. K., Banerjee, D., and Nials, F. L. (2004). Photonic dating of prehistoric irrigation canals at Phoenix. *Arizona. Geoarchaeol.* 19, 1–19. doi: 10.1002/gea.10101

Borgnia, M. (2004). *Neotectónica del Piedemonte Oriental del Cordón del Plata al Norte del río BLANCO, Provincia de Mendoza*. MSc thesis, Universidad de Buenos Aires, Buenos Aires. 43.

Brenning, A., Trombotto, D., and Schroeder, H. (2005). Zur verbreitung von blockgletschern in den semiariden anden (Chile/Argentinien, 32-35°S): Bedeutung, Regionale Trends und der Einfluss des Reliefs. *Berl. Geograph. Arbeiten* 100, 19–28.

Buk, E. (2002). "Hidrología de ambientes periglaciales. cuenca morenas coloradas–vallecitos, cordón del plata, cordillera frontal, mendoza," in *IANIGLA, 1973-2003: 30 Años de Investigación Básica y Aplicada en Ciencias Ambientales*, eds D. Trombotto and R. Villalba (Mendoza), 60–65.

Caminos, R. (1965). Geología de la vertiente oriental del Cordón del Plata, Cordillera Frontal de Mendoza. *Asoc. Geol. Argent. Rev.* 20, 351–392.

Casa, A. L. (2005). *Geología y Neotectónica del Piedemonte Oriental del Cordón del Plata en los Alrededores de El Santo*. Msc thesis. Universidad de Buenos Aires, Buenos Aires, 174.

Casa, A. L. (2009). Sistema de fallas de La Carrera (AR-86; AR-114; AR-115; AR-116; AR-156). In: atlas de deformaciones cuaternarias de los andes. proyecto multinacional andino: geociencia para las comunidades andinas. atlas de deformaciones cuaternarias de los andes. *Serv. Naci. Geol. Minería Publ. Geol. Mult.* 7, 118–123.

Casa, A. L., Cortés, J. M., and Borgnia, M. (2010). Evidencias de deformación pleistocena en el sistema de fallas de La Carrera (32° 40' – 33° 15' LS), Cordillera Frontal, Mendoza. *Revi. Asoc. Geol. Argent.* 67, 91–104.

Corte, A. E., and Espizúa, L. (1981). *Inventario de Glaciares de la Cuenca del Río Mendoza*. Mendoza: Instituto Argentino de Nivologia y Glaciología, 64.

Corte, A. E., and Grosso, E. (1993). "Geocriología," in *Geología y Recursos Naturales de Mendoza. XII Congreso Geologico Argentino y II Congreso de Exploración d Hidrocarburos*, Vol. 16, ed. V. A. Ramos (Medoza: Relatorio), 205–216.

Cortés, J. M., Casa, A., Pasini, M., Yamín, M. G., and Terrizzano, C. (2006). Fajas oblicuas de deformación neotectónica en precordillera y Cordillera Frontal (31°30'-33°30' LS): controles paleotectónicos. *Rev. Asoc. Geol. Argent.* 61, 639–646.

Cortés, J. M., Vinciguerra, P., Yamín, M., and Pasini, M. M. (1999). "Tectónica Cuaternaria de la fregión Andina del Nuevo Cuyo (28° - 38° LS)," in *Geología Argentina. Subsecretaría de Minería de la Nación*, Vol. 29, ed. R. Caminos (Anales: Servicio Geológico Minero Argentino), 760–778.

Cruden, D. M., and Hungr, O. (1986). The debris of the Frank slide and theories of rockslide-avalanche mobility. *Can. J. Earth Sci.* 23, 425–432. doi: 10.1139/e86-044

Cruden, D. M., and Varnes, D. J. (1996). Landslide types and processes. *U.S. Natl. Acad. Sci. Trans. Res. Board Special Rep.* 247, 36–75.

De Blasio, F. V. (2014). Friction and dynamics of rock avalanches travelling on glaciers. *Geomorphology* 213, 88–98. doi: 10.1016/j.geomorph.2014.01.001

Deline, P., Hewitt, K., Reznichenko, N., and Shugar, D. (2015). "Rock avalanches onto glaciers," in *Landslide Hazards, Risks and Disasters. Amsterdam*, eds F. John, J. F. Shroder, and T. Davies (Amsterdam: Elsevier), 263–319. doi: 10.1016/b978-0-12-396452-6.00009-4

Dessanti, R. N. (1946). Hallazgo de depósitos glaciales en las Huayquerías de San Carlos. *Rev. Asoc. Geol. Argenti. I* 1, 270–284.

Drewes, J., Moreiras, S., and Korup, O. (2018). Permafrost activity and atmospheric warming in the Argentinian Andes. *Geomorphology* 323, 13–24. doi: 10.1016/j.geomorph.2018.09.005

Drovandi, A., Zuluaga, J., Filippini, M., Consoli, D., Valdes, A., Nacif, C., et al. (2010). "Evaluación de la calidad del agua en el Embalse Potrerillos y Cuenca del Río Blanco, Provincia de Mendoza," in *Proceedings, III Congreso Internacional sobre Gestión y Tratamiento Integral del Agua*, Córdoba, 1–39.

Dufresne, A., Bösmeier, A., and Prager, C. (2016). Sedimentology of rock avalanche deposits – Case study and review. *Earth Sci. Rev.* 163, 234–259. doi: 10.1016/j.earscirev.2016.10.002

Dunning, S. A. (2006). The grain size distribution of rock-avalanche deposits in valley confined settings. *Italian J. Eng. Geol. Environ. Special Issue* 1, 117–121.

Espizúa, L. E. (1982). Glacier and moraine inventory on the eastern slopes of cordon del plata and cordon del portillo, central andes, argentina. in: tills and related deposits. *Proc. INQUA Sympos. Argent.* 1982, 381–395.

Espizúa, L. E. (1999). Chronology of late pleistocene glacier advances in the río mendoza valley, argentina. *Global Plane. Change* 22, 193–200. doi: 10.1016/s0921-8181(99)00036-3

Espizúa, L. E., and Bigazzi, G. (1998). Fission-track dating of the Punta de Vaca glaciation in the río mendoza valley, Argentina. *Q. Sci. Rev.* 17, 755–760. doi: 10.1016/s0277-3791(97)00056-5

Evans, S. G., and Clague, J. J. (1988). "Catastrophic rock avalanches in glacial environments. Landslides," in *Proceedings, 5th Symposium on Landslides*, Vol. 2, Lausanne, 1153–1158.

Fauqué, L., Hermanns, R., Hewitt, K., Rosas, M., Wilson, C., Baumann, V., et al. (2009). Mega-landslide in the southern wall of the Aconcagua and its relationship with deposits assigned to Pleistocene glaciations. *Rev. Asoc. Geol. Argent.* 65, 691–712.

Folguera, A., Etcheverría, M., Pazos, P., Giambiagi, L., Fauqué, L., Cortés, J., et al. (2004). Hoja geológica 3369-15, potrerillos, provincia de mendoza. *Serv. Geol. Min. Argent. Bolet.* 301:135.

Galbraith, R. F., Roberts, R. G., Laslett, G. M., Yoshida, H., and Olley, J. M. (1999). Optical dating of single and multiple grains of quartz from Jinmium rock shelter, northern Australia: part i, experimental design and statistical models. *Archaeometry* 41, 339–364. doi: 10.1111/j.1475-4754.1999.tb00987.x

Gates, W. C. B. (1987). The fabric of rockslide avalanche deposits. *Bull. Assoc. Eng Geol.* 24, 389–402. doi: 10.2113/gseegeosci.xxiv.3.389

Giambiagi, L. B., Ramos, V. A., Godoy, E., Alvarez, P. P., and Orts, S. (2003). Cenozoic deformation and tectonic style of the Andes, between 33° and 34° south latitude. *Tectonics* 22, 1041–1059. doi: 10.1029/2001TC001354

Groeber, P. (1951). La Alta Cordillera entre las Latitudes 34° y 29°30'. *Museo Argent. Bernard. Riv. Revi. Cien. Geol.* 1:352.

Groeber, P. (1955). Bosquejo paleogeográfico de los glaciares del Diamante y Atuel. *Rev. Asoc. Geol. Argent.* 9, 89–108.

Heredia, N., Farias, P., García-Sansegundo, J., and Giambiagi, L. (2012). The basement of the andean frontal cordillera in the cordón del plata (Mendoza, Argentina): geodynamic evolution. *Andean Geol.* 39, 242–257. doi: 10.5027/andgeoV39n2-a03

Hermanns, R., Fauqué, F., and Wilson, C. (2015). "36Cl terrestrial cosmogenic nuclide dating suggests late Pleistocene to early Holocene mass movements on the south face of Aconcagua mountain and in the Las Cuevas – Horcones valleys, Central Andes, Argentina," in *Geodynamic Processes in the Andes of Central Chile and Argentina*, Vol. 399, eds S. A. Sepúlveda, L. B. Giambiagi, S. M. Moreiras, L. Pinto, M. Tunik, G. D. Hoke, et al. (London: Geological Society of London), 345–368. doi: 10.1144/sp399.19

Hewitt, K. (1999). Quaternary moraines vs. catastrophic rock avalanches in the Karakoram Himalaya, Northern Pakistan. *Q. Res.* 51, 220–237. doi: 10.1006/qres.1999.2033

Hewitt, K. (2009). Glacially conditioned rock-slope failures and disturbance-regime landscapes, Upper Indus Basin, northern Pakistan. *Geol. Soc. Special Publ.* 320, 235–255. doi: 10.1144/sp320.15

Hewitt, K., Gosse, J., and Clague, J. J. (2011). Rock avalanches and the pace of late Quaternary development of river valleys in the Karakoram Himalaya. *Geol. Soc. Am. Bull.* 123, 1836–1850. doi: 10.1130/b30341.1

Hsu, K. J. (1975). Catastrophic debris streams (sturzstroms) generated by rockfalls. *Geol. Soc. Am. Bull.* 86, 129–140.

Hungr, O., Corominas, J., and Eberhardt, E. (2005). "Estimating landslide motion mechanism, travel distance and velocity," in *Landslide Risk Management, Balkema. Proceedings of the International Conference on Landslide risk Management*, ed. O. Hungr (Vancouver), 99–128.

Hungr, O., and Evans, S. G. (2004). Entrainment of debris in rock avalanches: an analysis of a long run-out mechanism. *Geol. Soc. Am. Bul.* 116, 1240–1252. doi: 10.1130/B25362.1

Hungr, O., Leroueil, S., and Picarelli, L. (2014). The Varnes classification of landslide types, an update. *Landslides* 11, 167–194. doi: 10.1007/s10346-013-0436-y

Huntley, D. J., and Wintle, A. G. (1981). The use of alpha scintillation counting for measuring Th-230 and Pa-231 contents of ocean sediments. *Can. J. Earth Sci.* 18, 419–432. doi: 10.1139/e81-036

Irigoyen, M. V., Buchan, K. L., and Brown, R. L. (2000). Magnetostratigraphy of Neogene Andean foreland-basin strata, lat 33°S, Mendoza Province, Argentina. *Geol. Soc. Am. Bull.* 112, 803–816. doi: 10.1130/0016-7606(2000)112<803:monafs>2.0.co;2

Irigoyen, M. V., Buchan, K. L., Villeneuve, M. E., and Brown, R. L. (2002). Cronología y significado tectónico de los estratos sinorogénicos neógenos aflorantes en la región de Cacheuta-Tupungato, Provincia de Mendoza. *Rev. Asoc. Geol. Argen.* 57, 3–18.

Janke, J. R., Bellisario, A. C., and Ferrando, F. A. (2015). Classification of debris-covered glaciers and rock glaciers in the Andes of central Chile. *Geomorphology* 241, 98–121. doi: 10.1016/j.geomorph.2015.03.034

Kleiman, L. E., and Japas, M. S. (2009). The Choiyoi volcanic province at 34°S-36°S (San Rafael, Mendoza, Argentina): implications for the Late Palaeozoic evolution of the southwestern margin of Gondwana. *Tectonophysics* 473, 283–299. doi: 10.1016/j.tecto.2009.02.046

Korup, O., Clague, J. J., Hermanns, R., Hewitt, K., Strom, A. L., and Weidinger, J. T. (2007). Giant landslides, topography, and erosion. *Earth Planet. Sci. Let.* 261, 578–589. doi: 10.1016/j.epsl.2007.07.025

Llambías, E. J., Kleiman, L. E., and Salvarredi, J. A. (1993). "). El magmatismo Gondwánico," in *Geología y Recursos Naturales de Mendoza. 12° Congreso Geológico Argentino y 2° Congreso de Exploración de Hidrocarburos*, ed. V. A. Ramos (Mendoza: Relatorio), 53–64.

Massone, H., Martinez, D., Vich, A., Londoño, M. Q., Trombotto, D., and Grondona, S. (2016). Snowmelt contribution to the sustainability of the irrigated Mendoza's oasis, Argentina: an isotope study. *Environ. Earth Sci.* 75:520.

Mejdahl, V. (1979). Thermoluminescence dating: beta-dose attenuation in quartz grains. *Archaeometry* 21, 61–72. doi: 10.1111/j.1475-4754.1979.tb00241.x

Moreiras, S. M. (2006). Chronology of a Pleistocene rock avalanche probable linked to neotectonic, Cordon del Plata (Central Andes). *Mendoza Argent. Q. Int.* 148, 138–148. doi: 10.1016/j.quaint.2005.11.009

Moreiras, S. M., Hermanns, R. L., and Fauqué, L. (2015). Cosmogenic dating of rock avalanches constraining quaternary stratigraphy and regional neotectonics in the argentine central andes (32° S). *Q. Sci. Rev.* 112, 45–58. doi: 10.1016/j.quascirev.2015.01.016

Moreiras, S. M., Páez, M. S., Lauro, C., and Jeanneret, P. (2017). First cosmogenic ages for glacial deposits from the Plata range (33° S): new inferences for quaternary landscape evolution in the Central Andes. *Q. Int.* 438, 50–64. doi: 10.1016/j.quaint.2016.08.041

Moreiras, S. M., and Sepúlveda, S. A. (2015). "Megalandslides in the andes of central chile and argentina (32°-34°s) and potential hazards," in *Geodynamic Processes in the Andes of Central Chile and Argentina*, Vol. 399, eds S. A. Sepúlveda, L. B. Giambiagi, S. M. Moreiras, L. Pinto, M. Tunik, G. D. Hoke, et al. (London: Geological Society of London), 329–344. doi: 10.1144/sp399.18

Murray, A. S., and Wintle, A. G. (2000). Luminescence dating of quartz using an improved single aliquot regenerative-dose protocol. *Radiat. Meas.* 32, 57–73. doi: 10.1016/s1350-4487(99)00253-x

Norte, F. (1995). *Condiciones Meteorológicas Favorables a la Contaminación Atmosférica en Mendoza*, eds E. Martinez Carretero and A. Dalmasso (Mendoza Ambiental), 197–206.

Polanski, J. (1953). Supuestos englazamientos en la llanura pedemontana de Mendoza. *Rev. Asoc. Geol. Argent.* 8, 195–213.

Polanski, J. (1961). Cenoglomerado El Quemado. *Rev. Asoc. Geol. Argent.* 15, 159–179.

Polanski, J. (1963). Estratigrafía, neotectónica y geomorfología del Pleistoceno pedemontano entre los ríos Diamante y Mendoza. *Rev. Asoc. Geol. Argent.* 17, 127–349.

Polanski, J. (1966). *Flujos Rápidos de Escombros Rocosos en Zonas áridas y Volcánicas*. Argentina: Universitaria de Buenos Aires, 67.

Polanski, J. (1972). Descripción Geológica de la Hoja 24a-b, Cerro Tupungato, Provincia de Mendoza. *Dir. Nacion. Geol. Min. Bolet.* 124:114.

Prager, C., Zangerl, C., and Kerschner, H. (2012). "Sedimentology and mechanics of major rock avalanches: implications from (pre-) historic sturzstrom deposits (Tyrolean Alps, Austria)," in *Landslides and Engineered Slopes, Protecting Society through Improved Understanding*, Vol. 2, eds E. Eberhardt, C. Froese, K. Turner, and S. Leroueil (Boca Raton, FL: CRC Press), 895–900.

Prescott, J. R., and Hutton, J. T. (1994). Cosmic ray contributions to dose rates for luminescence and ESR dating: large depths and long-term time variations. *Radiat. Meas.* 23, 497–500. doi: 10.1016/1350-4487(94)90086-8

Reznichenko, N. V., Davies, T. R. H., Shulmeister, J., and Larsen, S. H. (2012). A new technique for identifying rock avalanche-sourced sediment in moraines and some paleoclimatic implications. *Geology* 49, 319–322. doi: 10.1130/g32684.1

Rhodes, E. J. (2011). Optically stimulated luminescence dating of sediments over the past 200,000 years. *Annu. Rev. Earth Planet. Sci.* 39, 461–488. doi: 10.1146/annurev-earth-040610-133425

Rodríguez, E., and Barton, M. (1993). "El cuaternario de la llanura," in *Geología y Recursos Naturales de Mendoza. Relatorio del XII Congreso Geológico Argentino y II Congreso de Exploración de Hidrocarburos*, ed. V. Ramos (Mendoza), 173–194.

Sepúlveda, S. A., and Moreiras, S. M. (2013). Large volume landslides in the central Andes of Chile and Argentina (32°-34°S) and related hazards. *Bull. J. Eng. Geol. Environ.* 6, 287–294. doi: 10.4408/IJEGE.2013-06.B-26

Sosio, R., Crosta, G. B., Chen, J. H., and Hungr, O. (2012). Modelling rock avalanche propagation onto glaciers. *Q. Sci. Rev.* 47, 23–40. doi: 10.1016/j.quascirev.2012.05.010

Strom, A. L., and Korup, O. (2006). Extremely large rockslides and rock avalanches in the Tien Shan mountains, Kyrgyzstan. *Landslides* 3, 125–136. doi: 10.1007/s10346-005-0027-7

Strom, A. L., and Abdrakhmatov, K. (2018). "Structure and grain-size composition of large-scale bedrock landslides deposits," in *Rockslides and Rock Avalanches in Central Asia: Distribution, Morphology and Internal Structure*, ed. M. Le Fleur (Amsterdam: Elsevier), 458.

Trombotto, D. (1991). Untersuchungen zum Periglazialen Formenschatz und zu Periglazialen Sedimenten in der "Lagunita del Plata", Mendoza, Argentinien. *Heidelber. Geograph. Arbeit.* 90:171.

Trombotto, D. (2002). "Present cryogenic environment and palaeopermafrost in Southern South America," in *IANIGLA, 1973-2003: 30 años de Investigación Básica y Aplicada en Ciencias Ambientales. ZETA*, eds D. Trombotto and R. Villalba Mendoza, 65–70.

Trombotto, D., and Borzotta, E. (2009). Indicators of present global warming through changes in active layer-thickness, estimation of thermal diffusivity and geomorphological observations in the Morenas Coloradas rock glacier. Argentina. *Cold Regions Sci. Technol.* 55, 321–330. doi: 10.1016/j.coldregions.2008.08.009

Wang, Y. F., Cheng, Q. G., Lin, Q. W., Li, K., and Yang, H. F. (2018). Insights into the kinematics and dynamics of the Luanshibao rock avalanche (Tibetan Plateau, China) based on its complex surface landforms. *Geomorphology* 317, 170–183. doi: 10.1016/j.geomorph.2018.05.025

Wang, Y. F., Cheng, Q. G., and Zhu, Q. (2015). Surface microscopic examination of quartz grains from rock avalanche basal facies. *Can. Geotech. J.* 52, 167–181. doi: 10.1139/cgj-2013-0284

Wayne, W. J. (1984). The quaternary succession in the rio blanco basin, cordon del plata, mendoza province, argentina: an application of multiple relative-dating techniques. *Dev. Palaeontol. Stratigr.* 7, 389–406. doi: 10.1016/s0920-5446(08)70083-9

Wayne, W. J. (1990). The diamictons of rio blanco basin, Cordon del Plata, Mendoza. *Q. South Am. Antarct. Penin.* 2, 8–31.

Wayne, W. J., and Corte, A. E. (1983). Multiple glaciations of the Cordon del Plata, Mendoza, Argentina. *Palaeogeogr., Paleoclimato. Paleoecol.* 42, l85–l209.

Weidinger, J. T., Korup, O., Munack, H., Altenberger, U., Dunning, S. A., Tippelt, G., et al. (2014). Giant rockslides from the inside. *Earth Planet. Sci. Lett.* 389, 62–73. doi: 10.1016/j.epsl.2013.12.017

Yang, Q., Su, Z., Cheng, Q., Ren, Y., and Caid, F. (2019). High mobility of rock-ice avalanches: insights from small flume tests of gravel-ice mixtures. *Eng. Geol.* 260, 105–260.

Yarnold, J. C., and Lombard, J. P. (1989). "A facies model for large rock-avalanche deposits formed in dry climate," in *Conglomerates in Basin Analysis: A Symposium Dedicated to A.O. Woodford, Pacific Section*, Vol. 62, eds I. P. Colburn, L. Patrick, X. Abbott, and J. Minch (Tulsa, OK: SEPM), 9–31.

Zeng, Q., Zhang, L., Davies, T., Yuan, G., Xue, X., Wei, R., et al. (2019). Morphology and inner structure of Luanshibao rock avalanche in Litang, China and its implications for long-runout mechanisms. *Eng. Geol.* 260, 105–216.

Conflict of Interest: The author declares that the research was conducted in the absence of any commercial or financial relationships that could be construed as a potential conflict of interest.

frontiers
in Earth Science

ORIGINAL RESEARCH
published: 20 July 2020
doi: 10.3389/feart.2020.00295

Chronology and Geomorphological Activity of the Akdag Rock Avalanche (SW Turkey)

Cihan Bayrakdar[1], Tolga Gorum[2], Zeynel Çılğın[3], Christof Vockenhuber[4], Susan Ivy-Ochs[4] and Naki Akçar[5]**

[1] Department of Geography, Istanbul University, Istanbul, Turkey, [2] Eurasia Institute of Earth Sciences, Istanbul Technical University, Istanbul, Turkey, [3] Department of Geography, Munzur University, Tunceli, Turkey, [4] Laboratory of Ion Beam Physics, ETH Zürich, Zurich, Switzerland, [5] Institute of Geological Sciences, University of Bern, Bern, Switzerland

Edited by:
Reginald Leonhard Hermanns,
Geological Survey of Norway, Norway

Reviewed by:
Paula Hilger,
Western Norway University of Applied Sciences, Norway
Gianluca Vignaroli,
University of Bologna, Italy
Markus Schleier,
Independent Researcher, Weilheim, Germany

***Correspondence:**
Cihan Bayrakdar
cihanbyr@istanbul.edu.tr
Naki Akçar
akcar@geo.unibe.ch

Specialty section:
This article was submitted to Structural Geology and Tectonics, a section of the journal Frontiers in Earth Science

Received: *03 January 2020*
Accepted: *24 June 2020*
Published: *20 July 2020*

Citation:
Bayrakdar C, Gorum T, Çılğın Z, Vockenhuber C, Ivy-Ochs S and Akçar N (2020) Chronology and Geomorphological Activity of the Akdag Rock Avalanche (SW Turkey). Front. Earth Sci. 8:295. doi: 10.3389/feart.2020.00295

Large rock-slope failures are among the primary geohazards in high mountain areas. These rock avalanches and rockslides constitute most of the world's largest landslide deposits. This study focuses on the formation and geomorphological activity of the Akdag landslide complex located on the southern slope of Mount Akdag, SW Turkey. We employed detailed mapping in the field, spatial and morphometric analysis using GIS and remote sensing technologies, and surface exposure dating with cosmogenic ^{36}Cl to reconstruct the chronology of the landslide complex. For the analysis of cosmogenic ^{36}Cl, we collected 18 surface samples from calcareous boulders within the landslide deposit. Our field mapping shows that the Akdag rock avalanche is a large and active slope failure developed between carbonates and flysch. The rock-avalanche deposits cover an area of 9.8 km^2 and together with the primary and secondary slope failures which form the landslide complex, cover an area of 15 km^2. The Akdag rock avalanche is one of the largest (3×10^8 m^3) known bedrock landslides in Turkey. Cosmogenic ^{36}Cl exposure ages indicate that the main collapse occurred at 8.3 ± 1.4 ka (2σ), followed by secondary failures. We dated one of the latter to 1.1 ± 0.2 ka (2σ). Based on field evidence, we surmise that increased water discharge in the springs along the carbonate-flysch contact zone played a key role in the Early Holocene failure.

Keywords: cosmogenic ^{36}Cl exposure dating, rock avalanche, Mount Akdag, Western Taurus, Holocene

INTRODUCTION

Large bedrock landslides represent an important geomorphological process in terms of the evolution of hillslopes and fluvial and glacial systems in mountainous terrains around the world (Densmore and Hovius, 2000; Korup, 2002; Korup et al., 2005; Hewitt et al., 2008; Ivy-Ochs et al., 2009; Shulmeister et al., 2009; Davies and McSaveney, 2012; Deline et al., 2015; Crosta et al., 2017; Singeisen et al., 2020). Substantial rock-slope failures are frequently observed in mountain landscapes due to the high topographic relief and hillslope gradient; such failures are sensitive to changes in the climate and tectonic stress conditions (Agliardi et al., 2009; Huggel et al., 2012). On a global scale, extensive bedrock landslides are responsible for 1–10% of Late Pleistocene and Holocene erosion (>1 mm per ka) in tectonically active mountain belts (Korup et al., 2007, among others), and their density is amplified by high topographic relief in response to fluvial and glacial incision along inner gorges (Blöthe et al., 2015). Rock avalanches are characterized by large volume and long runouts due to their high energy and flow-like movement (e.g., Hungr and Evans, 2004).

Rock avalanche deposits are important markers to understand past climatic and geo-environmental changes in glaciated high mountainous terrain (Pánek, 2019). In addition, catastrophic rock-slope failures are strongly related to the location and orientation of faults, shear zones and bedding joints, as well as external triggering conditions (Ambrosi and Crosta, 2006; Stead and Wolter, 2015). Moreover, many studies have emphasized that large bedrock landslides observed after deglaciation are closely related to the decrease in ice load and changes associated with water table fluctuations (Gischig et al., 2011; McColl, 2012, 2015; McColl and Davies, 2013; Pánek, 2019). On the other hand, there may be delays in the reaction time of hillslope stability to paraglacial effects (McColl, 2012) leading to a significant relaxation time in mountain environments, which further underlines the importance of dynamic conditions due to the time-dependent changes of the conditional factors.

Periods of extreme precipitation and seismic triggering are also effective in rock-avalanche formation (Ivy-Ochs et al., 2017). Before the introduction of isotopic dating, it was generally accepted that most voluminous landslides in the Alps occurred immediately after deglaciation (Heim, 1932). As more Alpine rock-slope failures were dated, it became apparent that most of them occurred during Holocene; specifically, 6000 years or more after the glacier recession from the affected valleys (Prager et al., 2009; Ivy-Ochs et al., 2017). However, unlike the congeneric sections of the Alpine-Himalayan orogenic belt, there are no studies available on the nature and timing of rock avalanches at the Turkish syntax of the Alpine orogenic system. Limited studies on the occurrence and timing of bedrock landslides in the Pontide and Taurus mountains, which constitute the northern and southern margins of the Anatolian Orogenic Plateau, focus mainly on the northern margin of the plateau (i.e., Duman, 2009; Görüm, 2019).

Along the margins of the Anatolian Plateau, large bedrock landslides are more abundant on north-facing slopes of the Western and Eastern Pontides in the north of Turkey, where the slope and precipitation values are high (Görüm, 2019). Even though the southern margins of the orogenic plateau are similar to those of the Western and Eastern Pontides in terms of mean altitude, topographic gradient and precipitation values, the number of large bedrock landslides reported in the Taurus Mountains is limited (Görüm, 2019). Landslide deposits in this mountain belt are concentrated in the western sector, mainly in the Akdag Massif (**Figure 1**).

The Akdag Massif is characterized by autochthonous carbonates and shales overridden by allochthonous Jurassic and Cretaceous carbonates (**Figure 1**; Şenel, 1997). This massif was glaciated at least three times during Late Pleistocene (Bayrakdar, 2012; Sarıkaya et al., 2014). It is also karstified and bears large karstic depressions. Impermeable flysch deposit sequences underlie these karstic depressions. Karstic springs are located along the contact zone between the flysch and overlying carbonates. This contact area appears to be the major failure plane for most mass movements in the massif. The mass movements are concentrated on the eastern and southern slopes of the Akdag Massif, which creates a topographic asymmetry between the eastern and western slopes (Bayrakdar and Görüm, 2012).

The Akdag rock avalanche is one of the largest rock avalanches in the Western Taurus Mountains. Furthermore, Akdag is significant in terms of still being active. It is the source of many fatal debris flows in Saklikent Canyon, which is an important touristic site located downstream of the catchment area of the landslide complex. Our study gives new insights into the chronology and geomorphological activity of the Akdag rock avalanche and subsequent slope failures, with the aim of expanding the data catalog on Turkish rock avalanches and highlighting the complex interactions between glacial, karst and gravitational processes.

STUDY AREA

Geology

The Western Taurus constitutes an important part of the Alpine orogenic belt in the southwestern part of Anatolia. The study area was greatly affected by thrust faulting and napping movements. These movements made the structure of the rock units very complex (Şenel, 1997). The Beydag autochthonous carbonate platform, which is composed of Upper Cretaceous neritic limestone, underlies all units. The Elmalı formation (Eocene–Lower Miocene flysch), which is part of Yeşilbarak Nappe, tectonically overrides the Beydag autochthon.

The Madırkaya Formation is a member of the Lycian Nappes that consists of Middle Jurassic-Cretaceous neritic limestone (**Figures 1B,C**, **2**, and **3**; Şenel, 1997). This formation overlies the Yeşilbarak Nappe. In terms of active tectonics, the Akdag Massif is located on the western edge of the major geological structure known as the Isparta Angle in SW Anatolia, which is controlled by the Fethiye-Burdur fault zone (**Figure 1A**; Bozcu et al., 2007).

Geomorphology

Having a summit of 3014 m above sea level (a.s.l.) and bordered by faults on all sides, the Akdag Massif is stepped karst with flat surfaces at higher elevations (Doğu et al., 1999; Bayrakdar, 2012). Although it belongs to the Lycian Nappes, it lacks a thick carbonate stack (**Figure 1B**). Because thrust napping significantly shifted the stratigraphic location of the carbonates, these rocks are surrounded by insoluble clastic and ophiolitic rocks in some places (Şenel, 1997; Nazik and Tuncer, 2010; Bayrakdar, 2012).

For this reason, it is not possible to assert widespread karstification taking place with lateral and vertical continuity. In addition, active faults and continuous regional uplift prevent the establishment of a pronounced karstic base level at Akdag (Nazik and Tuncer, 2010; Bayrakdar, 2012). There are many uvalas and dolines above 2000 m a.s.l. due to the limestone lithologically having high solubility. The swallow holes and sinkholes within these karstic depressions have contributed to the formation of an improved underground drainage system since the beginning of karstification (Bayrakdar, 2012).

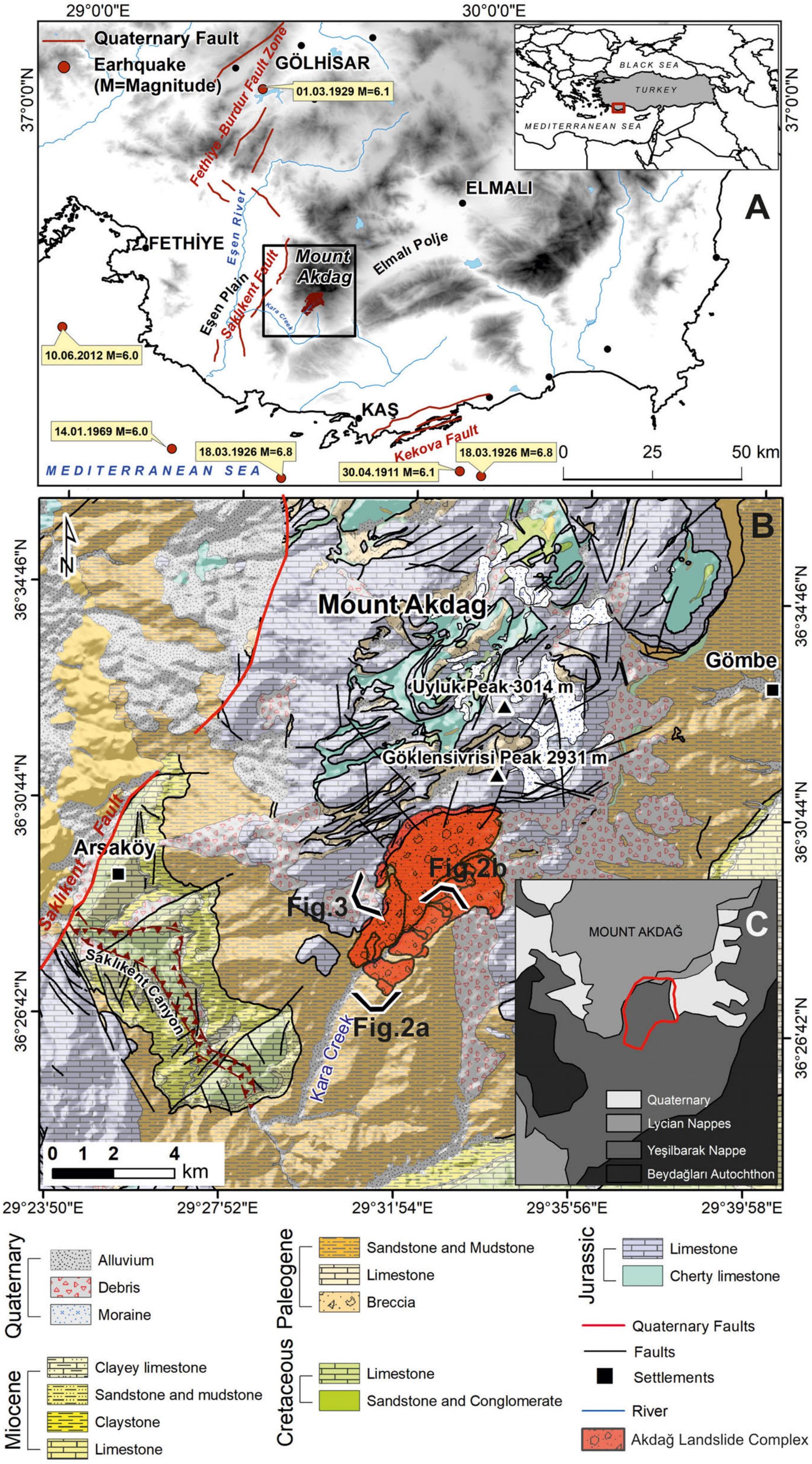

FIGURE 1 | (A) Location of Akdag Massif in southwest Turkey indicating active Quaternary faults and instrumental earthquakes and their magnitudes. **(B)** Generalized geology of Akdag Massif and its surroundings, SW Turkey (from Şenel, 1997). **(C)** Tectonic units of Mount Akdağ (from Şenel, 1997).

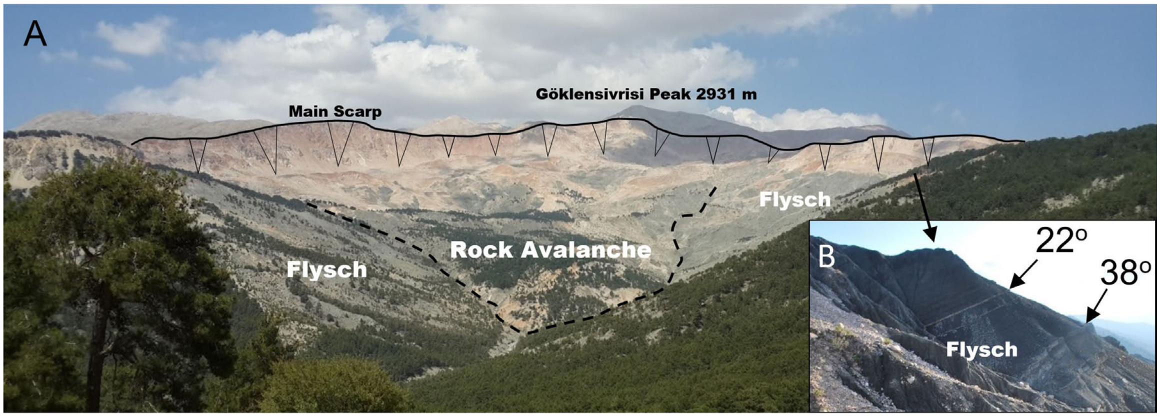

FIGURE 2 | (A) Main scarp and deposits of the rock avalanche within Akdag landslide complex, view toward north. **(B)** View of a flysch outcrop and its dip (in **Figure 1B**, viewpoint of photograph is marked).

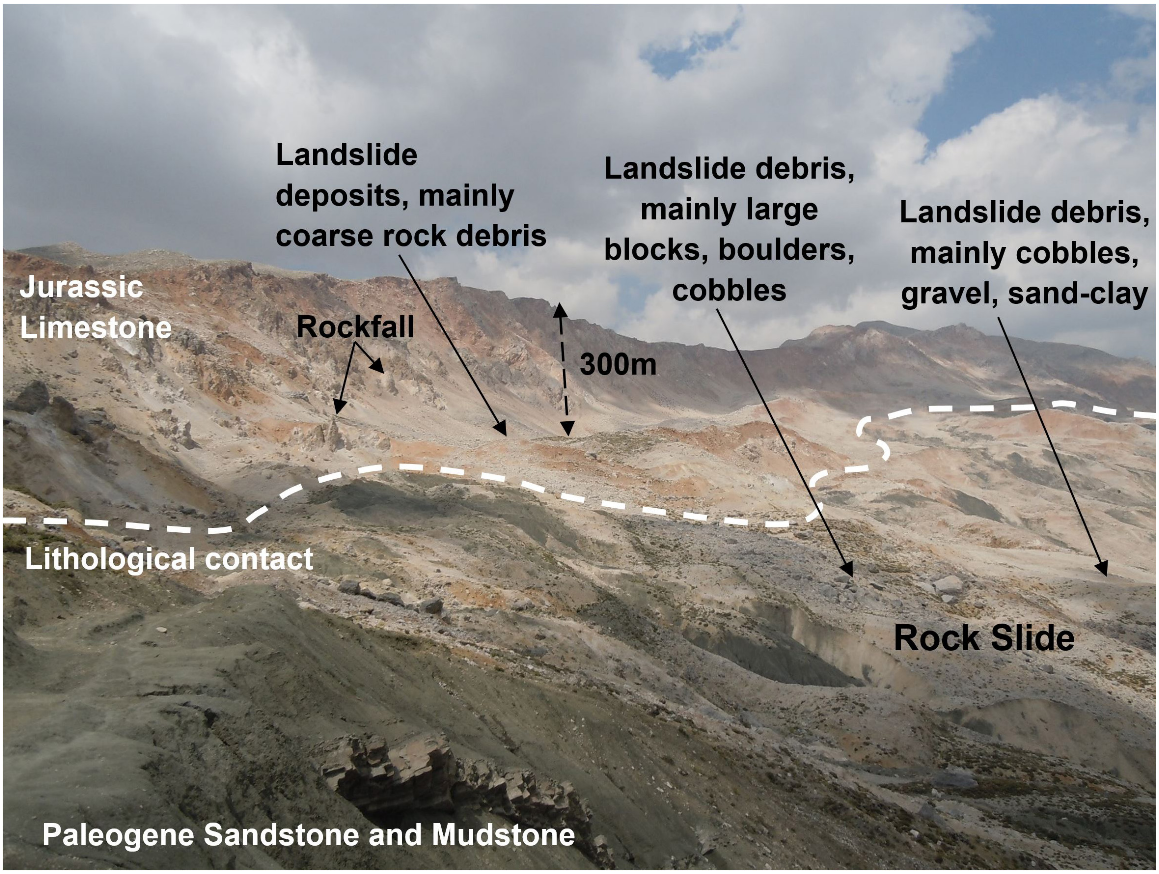

FIGURE 3 | Contact point between Jurassic limestone and Paleocene sandstone and claystone units near the head of the scarp zone of Akdag landslide complex (in **Figure 1B**, viewpoint of photograph is marked).

Mount Akdag was glaciated at least three times in Pleistocene and the associated glacial landforms were deposited by valley glaciers (Onde, 1952; Planhol and İnandık, 1958; Doğu et al., 1999; Bayrakdar, 2012; Sarıkaya et al., 2014). During the glacial advances, thick ice must have accumulated in the paleo-karstic depressions at elevations above 2500 m a.s.l. There are five glacial valleys with well-developed cirques in the Akdag Massif. These glacial valleys are in conformity with slightly inclined, wider-based paleo-karstic depressions at elevations of 2500 m, which are covered by large ground and lateral moraines. After approximately 2500 m, these valleys start to lose their glacial morphology and become narrower and finally end at 2000 m (Bayrakdar, 2012).

The first absolute ages for the glacial chronology of the Akdag Massif were provided by Bayrakdar (2012) using the OSL dating method, for which samples were collected from terminal and ground moraines. The ages of 20.2 ± 3.0, 17.7 ± 4.4, and 17.8 ± 3.6 ka were obtained from the central part of the Akdag Massif (Bayrakdar et al., 2017). Subsequently, Sarıkaya et al. (2014) showed three glaciations and reconstructed their chronology by surface exposure dating with cosmogenic ^{36}Cl. They dated the oldest advance as prior to 35.1 ± 2.5 ka, thus before the global Last Glacial Maximum (LGM; at 22.1 + 4.3 ka in the northern hemisphere, Shakun and Carlson, 2010). They revealed that during the LGM, the glaciers reached their largest extent (descending to 2050 m a.s.l) before 21.7 ± 1.2 ka. Later, approximately 15.1 ± 0.9 ka during the Late Glacial period (Clayton et al., 2006), the glaciers retreated and remained stationary for a short period of time (Sarıkaya et al., 2017). In addition to the glacial and karst geomorphology, mass movements play a significant role in the present geomorphological appearance of Mount Akdag.

Climate

At the present time, many secondary slope instabilities are active within the Akdag landslide complex and these masses are generally accelerated by extreme rainfall and sudden snowmelt (Bayrakdar and Görüm, 2012). The Akdag Massif confronts humid air masses coming from the Mediterranean (Bayrakdar, 2012) and when moist air from the southwest reaches Akdag it is forced to ascend the hillslopes, causing orographic precipitation due to adiabatic cooling. Higher elevations of the massif receive more rainfall; whereas karstic poljes on the lee side of the Akdag Massif receive less (e.g., Elmalı Polje 470 mm; **Figure 1A**). When precipitation data from the Kaş, Fethiye and Elmalı meteorological stations near Akdag (**Figure 1A**) are extrapolated to the massif, the annual mean precipitation reaches 1200 mm at elevations above 2000 m a.s.l. From the peaks of the massif downward, the precipitation values drop to 670 mm at approximately 1000 m a.s.l. In the winter, precipitation occurs largely as snowfall in areas above 2000 m a.s.l. (Bayrakdar, 2012).

MATERIALS AND METHODS

Geomorphological and Geomorphometric Data

A geomorphological map of the Akdag landslide complex (Görüm et al., 2017) was used to characterize the Akdag rock avalanche and secondary landslides that occurred during the period following the initial failure (**Figure 4**). In addition to geomorphological mapping, the geological map of Şenel et al. (unpublished) was used to extract lithological and structural information for further interpretation. This geological map was mainly used for determining the boundaries of pre-Quaternary units. The Quaternary units were mapped by processing high-resolution remote sensing images (e.g., unmanned aerial vehicle (UAV) derived orthophoto mosaics and GeoEye-2 satellite images) as well as extensive fieldwork.

To assess the potential role of conditional factors on the occurrence of the Akdag rock avalanche and the following secondary landslide events, we obtained the following terrain metrics from a 10 m DEM of the study area in SAGA GIS(c) (Conrad et al., 2015); abundance and depth of depressions and the topographic wetness index (TWI). The closed depression map was derived using compound analyses under the terrain analysis module. The Topographic Wetness Index (TWI), which is a measure widely used to describe the effect of topography on the location and size of saturated source areas of run-off generation, was also used as a proxy for regional soil moisture assessment. We used the SAGA topographic wetness index (Olaya and Conrad, 2009), which defines TWI as:

$$\mathrm{TWI} = \mathrm{In}\left(\frac{SCA_m}{\tan(\beta)}\right) \tag{1}$$

where TWI is the SAGA wetness index at a given point, SCA_{m} is the modified specific catchment area draining to that cell, and β is the slope angle of the point (Boehner and Selige, 2006). High TWI values represent wetter conditions. After the calculation of TWI values, we then reclassified the derived results using the mean plus standard deviation (1σ) to identify particularly high values in our study area.

Surface Exposure Dating

Many landslides have been dated by cosmogenic isotopes in Europe (Ballantyne, 1998; Ivy-Ochs et al., 2009; Prager et al., 2009; Akçar et al., 2012a; Singeisen et al., 2020, among others), North America (e.g., Nichols et al., 2006), South America (e.g., Hermanns et al., 2004) and Asia (e.g., Barnard et al., 2001). The top surfaces of boulders in a landslide deposit represent potential sample locations for cosmogenic nuclide dating (Ivy-Ochs and Schaller, 2010; Pánek, 2015). Apparent exposure ages from such surfaces may be older or younger than the true deposition age (e.g., Akçar et al., 2011).

The presence of inherited nuclides from pre-failure exposure may give exposure ages that are too old (e.g., Ivy-Ochs et al., 2009; Hilger et al., 2019). In general, inheritance occurs as a result of cosmogenic nuclide accumulation both at the surface and at depth in the bedrock before the collapse (e.g., Akçar et al., 2014). The exposure duration prior and after the collapse determines the contribution of inheritance to the overestimation of the exposure age; for instance, old landslides with short pre-failure exposure times would result in limited overestimation due to inheritance (Hilger et al., 2019). However, inheritance will make a significant contribution to the age overestimation in submillennial scale failures (Akçar et al., 2012a, 2014). As well as cosmogenic nuclide accumulation prior to failure, the reworking of previously exposed boulder surfaces can cause inheritance (Ivy-Ochs and Schaller, 2010). Underestimation of the true age is generally a result of post-depositional processes such as erosion, exhumation and toppling (e.g., Putkonen and Swanson, 2003). In addition, snow, sediment and/or vegetation cover can also cause "younger" ages than the true age (Ivy-Ochs et al., 2009).

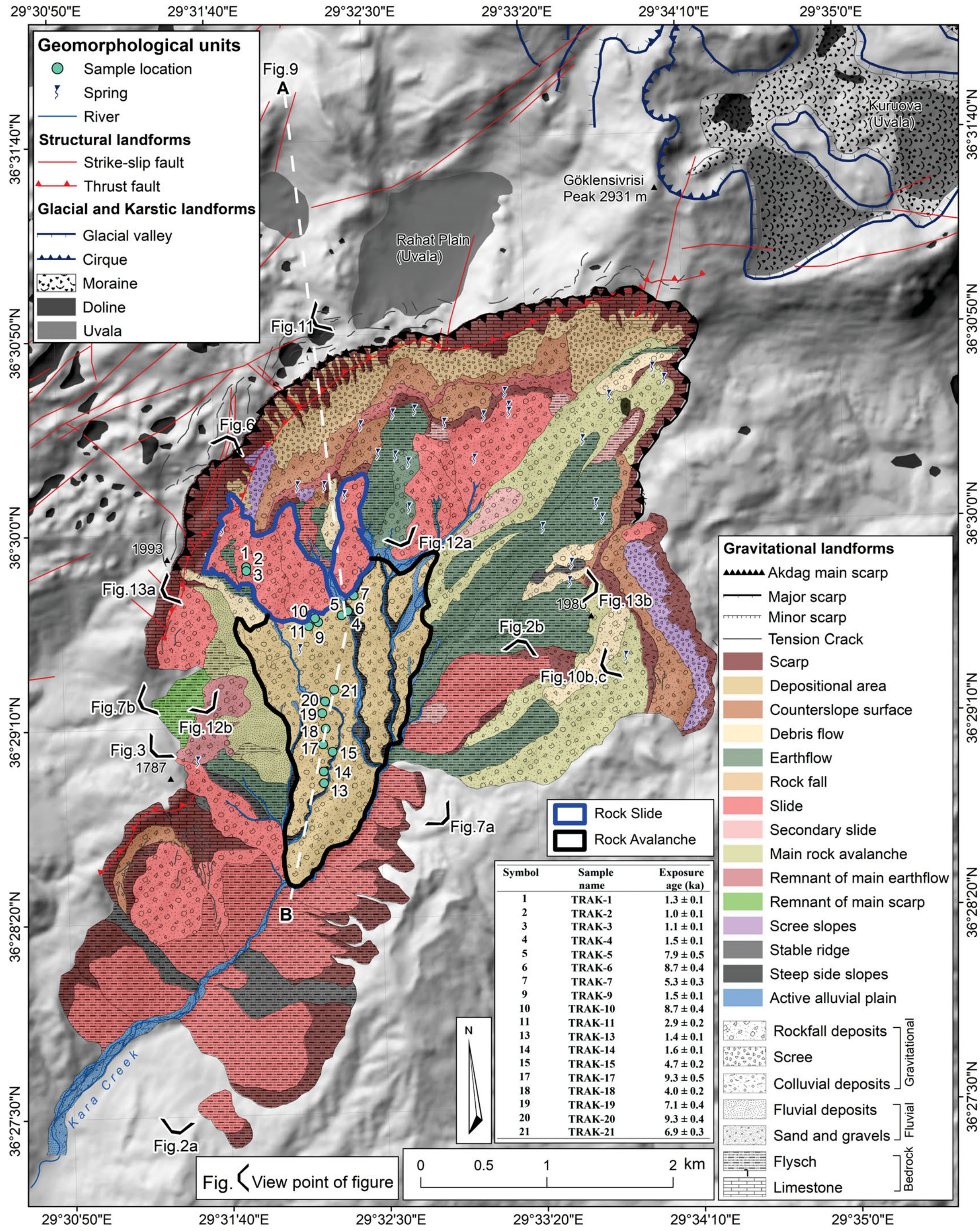

Symbol	Sample name	Exposure age (ka)
1	TRAK-1	1.3 ± 0.1
2	TRAK-2	1.0 ± 0.1
3	TRAK-3	1.1 ± 0.1
4	TRAK-4	1.5 ± 0.1
5	TRAK-5	7.9 ± 0.5
6	TRAK-6	8.7 ± 0.4
7	TRAK-7	5.3 ± 0.3
9	TRAK-9	1.5 ± 0.1
10	TRAK-10	8.7 ± 0.4
11	TRAK-11	2.9 ± 0.2
13	TRAK-13	1.4 ± 0.1
14	TRAK-14	1.6 ± 0.1
15	TRAK-15	4.7 ± 0.2
17	TRAK-17	9.3 ± 0.5
18	TRAK-18	4.0 ± 0.2
19	TRAK-19	7.1 ± 0.4
20	TRAK-20	9.3 ± 0.4
21	TRAK-21	6.9 ± 0.3

FIGURE 4 | Geological and Geomorphological map of Akdag landslide complex (modified after Görüm et al., 2017), sample locations and ^{36}Cl cosmogenic exposure ages. Line A to B indicates location of cross section given in **Figure 9**.

In this study, 18 surface samples were taken from boulders on the Akdag landslide complex (**Figures 4**, **5**). These samples were prepared at the Surface Exposure Dating Laboratory at the University of Bern following the preparation procedure described by Ivy-Ochs et al. (2004, 2009), based on the method of Stone et al. (1996) using isotope dilution (Elmore et al., 1997; Ivy-Ochs et al., 2004; Desilets et al., 2006). Before crushing, each sample was cut parallel to the surface to decrease the thickness down to 1,2 cm (**Table 1**). Afterward, the samples were crushed and sieved to 250–400 µm (micrometer) grain-size fraction. They were subsequently leached two times in 2 M HNO_3 overnight and thoroughly rinsed with ultrapure water (18.2 MΩ cm) and dried overnight to free the samples of any possible meteoric Cl. An aliquot of approximately 10 g of leached material from one

FIGURE 5 | (A) Picture of boulder TRAK-10. **(B)** Close-up view of sampled top boulder surface of TRAK-10.

sample per strip was analyzed for major and trace elements at SGS Mineral Services, Toronto, Canada (**Table 2**). The leached sample was spiked with ~2.5 mg of pure ^{35}Cl and dissolved with HNO_3 (**Table 1**). To precipitate AgCl, $AgNO_3$ was added. Sulfur in the sample, ^{36}S as an isobar of ^{36}Cl, was eliminated by precipitation of $BaSO_4$ to avoid its interference during the accelerator mass spectrometry (AMS) measurement. The ^{35}Cl- spike was used for the determination of total Cl concentration (^{35}Cl, ^{37}Cl) in the analyzed rock material (Ivy-Ochs et al., 2004, 2009). This required the calculation of (1) the ^{36}Cl concentration in the sample; (2) ^{36}Cl production rate through low-energy neutron capture by ^{35}Cl; and (3) subsurface production of non-cosmogenic ^{36}Cl. The concentrations of total Cl and ^{36}Cl were measured from one target at the ETH AMS facility by applying the isotope dilution technique (Synal et al., 1997; Ivy-Ochs et al., 2004). In this way, independent determination of total Cl on a separate sample aliquot was eliminated; this has led to crucial improvements in both the precision and sensitivity of ^{36}Cl methodology (Ivy-Ochs et al., 2004; Desilets et al., 2006). Sample ratios of ^{36}Cl/^{35}Cl were normalized to the ETH internal standard K382/4N, which has a value of $^{36}\text{Cl/Cl} = 17.36 \times 10^{-12}$ (normalized to the Nishiizumi standard in 2009), whereas the stable ^{37}Cl/^{35}Cl ratio was normalized to the natural ratio $^{37}\text{Cl}/^{35}\text{Cl} = 31.98\%$ of K382/4N standard and a machine blank. The sulfur correction of measured ^{36}Cl/^{35}Cl ratios was negligible (0.7% of ratios). Measured sample ^{36}Cl/^{35}Cl ratios were also corrected for a procedure blank of 8×10^{-15}, which amounted to a correction of less than 5% for the samples.

For the production rate of cosmogenic ^{36}Cl, we applied 48.8 ± 1.7 atoms g^{-1} of Ca a^{-1} at SLHL as the spallogenic production rate from Ca (Stone et al., 1996, 1998) and 162 ± 24 atoms g^{-1} of K a^{-1} from K (Evans et al., 1997). The Lal

TABLE 1 | Description of samples from Akdag landslide complex.

Sample name	Elevation (m a.s.l)	Latitude, °N (DD.DD) WGS84	Longitude, °E (DD.DD) WGS84	Boulder height (m)	Sample thickness (cm)	Shielding correction factor
Trak 1	1849	36.3028	29.3149	2.40	5	0.9904
Trak 2	1838	36.2951	29.3149	1.32	5	0.9904
Trak 3	1838	36.2950	29.3149	0.80	5	0.9904
Trak 4	1776	36.2933	29.3205	0.40	5	0.9627
Trak 5	1758	36.2938	29.3219	0.90	5	0.9550
Trak 6	1757	36.2939	29.3221	1.60	5	0.9550
Trak 7	1775	36.2943	29.3223	1.70	5	0.9166
Trak 9	1766	36.2938	29.3208	1.85	5	0.9336
Trak 10	1769	36.2939	29.3207	1.20	5	0.9466
Trak 11	1770	36.2937	29.3205	1.30	5	0.9500
Trak 13	1553	36.2855	29.3212	1.00	5	0.9645
Trak 14	1581	36.2858	29.3212	1.10	5	0.9717
Trak 15	1597	36.2903	29.3215	2.00	4	0.9732
Trak 17	1618	36.2905	29.3212	1.70	5	0.9665
Trak 18	1625	36.2909	29.3213	0.70	5	0.9639
Trak 19	1641	36.2913	29.3212	1.30	3	0.9662
Trak 20	1641	36.2916	29.3213	1.70	5	0.9662
Trak 21	1665	36.2919	29.3216	1.70	5	0.9467

TABLE 2 | Major and trace element data for the analyzed samples.

Sample name	Si (wt.%)	Al (wt.%)	Fe (wt.%)	Mn (ppm)	Ca (wt.%)	K (wt.%)	Ti (wt.%)	P (wt.%)	B (ppm)	Gd (ppm)	Sm (ppm)	U (ppm)	Th (ppm)
TRAK-1	0,18	0,06	<0.05	<3	39,9	<0.1	<0.01	0,041	20	0,2	<0.1	0,2	<0.1
TRAK-2	0,13	0,05	<0.05	<3	39,9	<0.1	<0.01	0,018	<10	1,9	2,5	11,8	1,6
TRAK-3	0,12	0,04	<0.05	4	39,9	<0.1	<0.01	0,019	<10	0,2	<0.1	0,1	<0.1
TRAK-4	0,23	0,09	<0.05	<3	39,4	<0.1	<0.01	<0.005	<10	0,2	0,1	0,1	<0.1
TRAK-5	0,24	0,1	<0.05	3	39,4	<0.1	<0.01	0,008	<10	0,1	<0.1	1,4	0,1
TRAK-6	0,17	0,05	<0.05	82	39,9	<0.1	<0.01	0,027	<10	0,2	0,2	<0.1	<0.1
TRAK-7	0,28	0,11	0,05	3	39,3	<0.1	<0.01	0,014	<10	0,1	<0.1	0,4	<0.1
TRAK-9	0,22	0,09	<0.05	3	40,1	<0.1	<0.01	<0.005	<10	0,1	<0.1	0,1	0,1
TRAK-10	0,26	0,1	<0.05	8	39,8	<0.1	<0.01	<0.005	<10	0,2	0,2	0,2	0,2
TRAK-11	0,16	0,08	<0.05	5	40,7	<0.1	<0.01	0,009	<10	<0.1	<0.1	1,6	<0.1
TRAK-13	0,13	0,05	<0.05	15	40,4	<0.1	<0.01	0,009	<10	0,2	0,4	0,5	0,4
TRAK-14	0,25	0,08	<0.05	7	31,7	<0.1	<0.01	<0.005	<10	<0.1	<0.1	2,6	<0.1
TRAK-15	0,11	0,05	<0.05	3	40,4	<0.1	<0.01	<0.005	<10	<0.1	<0.1	1,2	<0.1
TRAK-17	0,12	0,05	<0.05	3	40,3	<0.1	<0.01	<0.005	<10	0,2	0,3	1,3	1,1
TRAK-18	0,1	0,08	<0.05	<3	40,7	<0.1	<0.01	0,006	<10	<0.1	<0.1	0,3	<0.1
TRAK-19	0,17	0,08	<0.05	9	40,2	<0.1	<0.01	<0.005	<10	<0.1	<0.1	0,3	<0.1
TRAK-20	0,09	0,05	<0.05	<3	40,7	<0.1	<0.01	<0.005	<10	<0.1	<0.1	0,8	0,6
TRAK-21	0,15	0,07	0,76	55	39,9	<0.1	<0.01	0,009	<10	0,2	0,2	1,7	0,2

(1991)/Stone (2000) scheme was employed to scale the local ^{36}Cl production rates in order to calculate the ^{36}Cl exposure ages. A production rate of 5.3 ± 0.5 atoms (g^{-1} Ca) a^{-1} at SLHL due to muon capture was used (Stone et al., 1996, 1998). For ^{36}Cl production caused by the capture of thermal and epithermal neutrons, we applied a rate of 760 ± 150 neutrons g^{-1} a^{-1} above the surface following Liu et al. (1994) and Phillips et al. (2001) (see Alfimov and Ivy-Ochs, 2009 for further details). Major element, boron, gadolinium and samarium concentrations were used to determine the fraction of low-energy neutrons available for capture by ^{35}Cl to build ^{36}Cl (Fabryka-Martin, 1988; Phillips et al., 2001; Alfimov and Ivy-Ochs, 2009). Uranium and thorium concentrations were considered to determine the contribution of non-cosmogenic subsurface ^{36}Cl (Fabryka-Martin, 1988). In the calculation of exposure ages, topographic shielding (based on Dunne et al., 1999), sample thickness (using an exponential attenuation length of 160 g/cm^2), rock density (2.4 g/cm^3) and erosion rate (0.5 cm/ka) were considered. We selected this erosion rate according to: (1) saturated cosmogenic ^{36}Cl concentrations analyzed in massive bedrock limestone surfaces in Crete (Ivy-Ochs, Hetzel, Alfimov unpublished data) and (2) the depth of the original quarry marks on the building stones at Hattusha, the ancient Hittite capital in central Turkey (Akçar et al., 2009).

RESULTS

Morphometric Properties of the Akdag Rock Avalanche

The surface area of the Akdag landslide complex is approximately 15 km^2. The Akdag rock avalanche is a complex landslide area that developed in multiple stages and contains more than one landslide type, caused by a massive collapse in the southern sector of the mountain. The main rock avalanche covers an area of 9.8 km^2. The approximate volume of displaced material due to this large slope failure is 3×10^8 m^3, and the distance from the crown to the toe is approximately 4.5 km (**Figure 4**).

The rock avalanche occurred on the contact plane of tectonically discordant Jurassic limestone with Paleogene sandstone and claystone units (**Figures 3**, **4**). The failure was primarily affected by structural discontinuities, such as joints, cracks and faults apparent in the source area. Many of the tension cracks and fissures observed on the landslide deposits and behind the main scarp indicate that the landslide is currently in a relatively active state (**Figure 6**). The presence of newly developed failures within the landslide mass at different periods is one of the most important indicators showing that the slopes have not stabilized to date. The jagged morphology of the crown area and concave parts of the main scarp corresponding to rockfall and secondary slip indicate that the scarp becomes rejuvenated as it retrogrades, giving the landslide a retrogressive character (**Figures 4**, **6**). Moreover, the landslide complex is enlarging its extension with secondary failures (e.g., rockslides) which have been developing on the southern slopes of Akdag (Görüm et al., 2017).

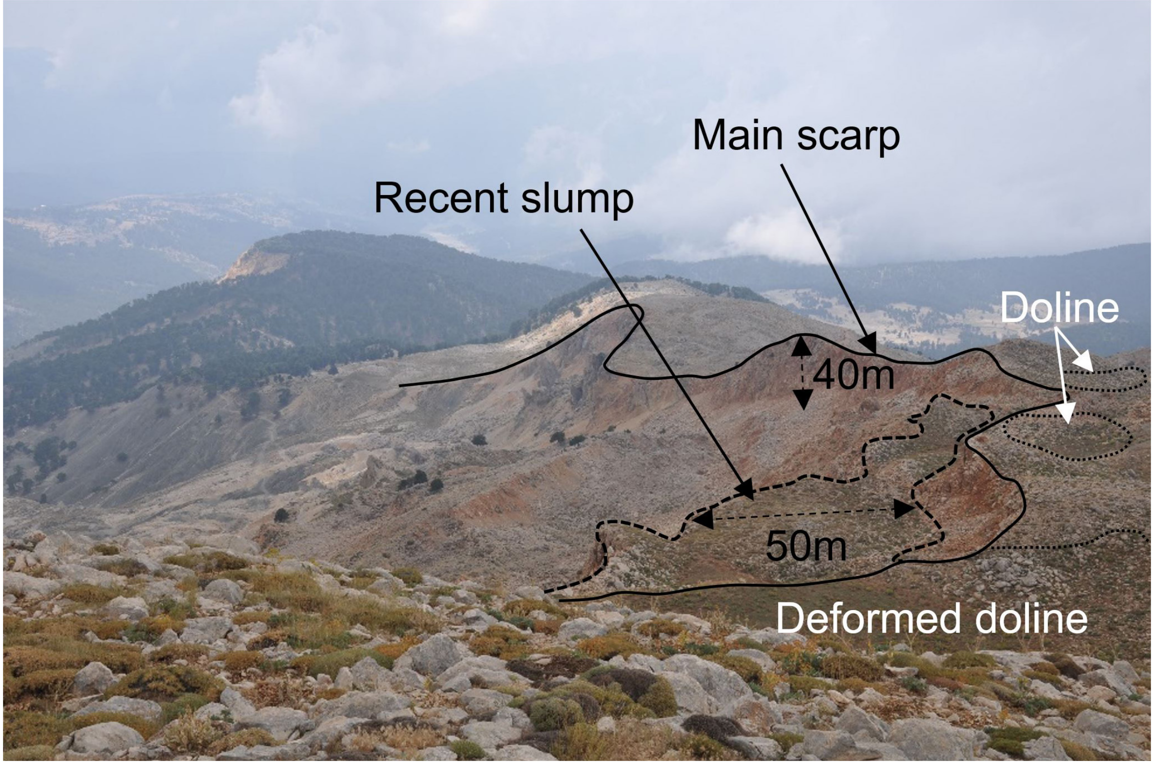

FIGURE 6 | Akdag main scarp and recent slumps inside the main scarp (in **Figure 4**, viewpoints of photographs are marked).

TABLE 3 | Cosmogenic ^{36}Cl exposure age parameters and results.

Sample name	Sample weight (g)	Carrier weight (mg)	Cl (ppm)	^{36}Cl (10^4 at.g^{-1})	Local production rate [at ^{36}Cl.g(rock).a^{-1}]	Exposure age (ka)
TRAK-1	68.9031	2.2593	63.80 ± 0.8	11.54 ± 6.9	88.54 ± 3.20	1.3 ± 0.1
TRAK-2	70.0194	2.2587	63.25 ± 1.0	8.77 ± 8.0	88.04 ± 3.19	1.0 ± 0.1
TRAK-3	70.3745	2.2542	79.49 ± 1.7	9.72 ± 8.6	91.54 ± 3.62	1.1 ± 0.1
TRAK-4	69.2951	2.2572	80.03 ± 1.3	13.03 ± 7.3	86.98 ± 3.47	1.5 ± 0.1
TRAK-5	69.1904	2.2542	93.50 ± 1.2	67.45 ± 3.8	88.28 ± 3.13	7.9 ± 0.5
TRAK-6	69.0953	2.2605	65.73 ± 1.0	69.51 ± 3.4	84.28 ± 3.17	8.7 ± 0.4
TRAK-7	68.3552	2.2623	48.69 ± 0.8	39.11 ± 3.9	81.34 ± 2.84	5.3 ± 0.3
TRAK-9	68.9534	2.2605	55.62 ± 1.1	11.50 ± 7.2	83.29 ± 2.97	1.5 ± 0.1
TRAK-10	69.1612	2.2638	54.67 ± 0.6	67.21 ± 3.0	82.90 ± 2.95	8.7 ± 0.4
TRAK-11	68.7688	2.2656	48.32 ± 1.0	22.29 ± 5.1	82.27 ± 2.85	2.9 ± 0.2
TRAK-13	69.2598	2.2626	58.80 ± 0.7	9.64 ± 7.1	72.38 ± 2.60	1.4 ± 0.1
TRAK-14	67.9544	1.9041	47.60 ± 0.8	9.03 ± 7.0	59.14 ± 2.20	1.6 ± 0.1
TRAK-15	69.3325	1.5066	38.72 ± 0.7	32.42 ± 3.9	71.58 ± 2.39	4.7 ± 0.2
TRAK-17	68.8696	2.2680	42.36 ± 0.9	64.61 ± 4.0	73.17 ± 2.48	9.3 ± 0.5
TRAK-18	68.8323	2.2536	38.72 ± 0.5	27.99 ± 4.2	72.97 ± 2.45	4.0 ± 0.2
TRAK-19	67.6867	2.2575	50.09 ± 1.3	51.54 ± 4.8	75.59 ± 2.58	7.1 ± 0.4
TRAK-20	69.2010	2.2677	31.79 ± 0.4	63.53 ± 3.1	72.68 ± 2.39	9.3 ± 0.4
TRAK-21	65.4889	2.2560	48.57 ± 0.7	48.98 ± 3.6	76.18 ± 2.62	6.9 ± 0.3

Surface Exposure Dating

Eighteen rock-surface samples were collected in Akdag from landslide deposits for cosmogenic nuclide surface exposure dating (**Table 1**). Major and trace elements measured in the collected rock surface samples are provided in **Table 2**. The cosmogenic nuclide data presented in **Table 3** are the amount of dissolved rock, the ^{35}Cl spike, total Cl concentration, ^{36}Cl concentration, local production rate of ^{36}Cl and the

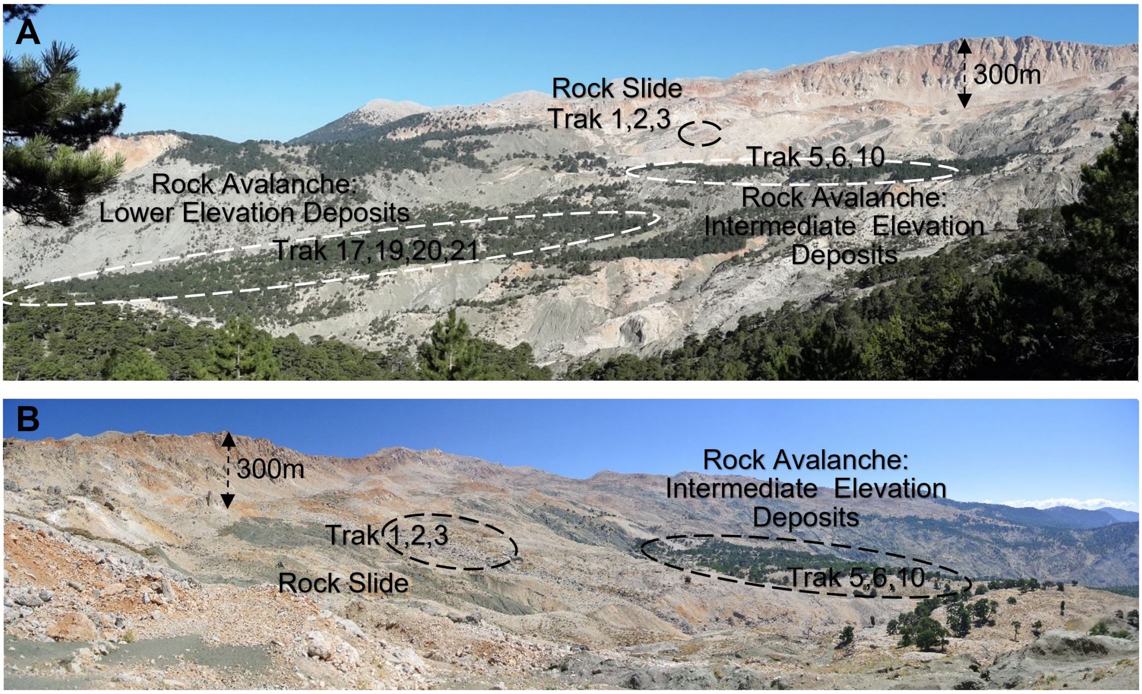

FIGURE 7 | Sampling sites for ^{36}Cl cosmogenic nuclide dating in the landslide complex. In **Figure 4**, viewpoints of photographs are marked. **(A)** Rock avalanche and rockslide. **(B)** Higher elevation deposits of rock avalanche and rockslide.

surface exposure age. The total Cl concentrations were between 31.8 ± 0.4 and 93.50 ± 1.2 ppm; and the measured ^{36}Cl concentrations were between 8.77 ± 8.0 × 10^4 atoms/g and 69.51 ± 3.4 × 10^4 atoms/g. Based on these data, we calculated ^{36}Cl exposure ages that ranged from 1.0 ± 0.1 to 9.3 ± 0.5 ka.

The deposits of the Akdag landslide complex were exposure-dated at two distinct landslide parts, consisting of a rockslide and the rock avalanche. The deposits of the latter form two topographical levels found at different levels: the intermediate elevation deposits and the lower elevation deposits (**Figure 7**). Cosmogenic ^{36}Cl exposure ages from the intermediate elevation deposits (Trak-4 to TRAK-11; **Figure 7**) of the Akdag landslide complex varied between 1.5 ± 0.1 and 8.7 ± 0.4 ka; and from the lower elevation deposits (TRAK-13 to TRAK-21; **Figure 7B**) they were between 1.4 ± 0.1 and 9.3 ± 0.5 ka, respectively. The lower elevation deposits form the lowest level of the toe of the landslide mass, which starts at 1650 m and ends at 1340 m a.s.l. then continues along a 1,900 m-long gently sloping surface. We interpret this area as being the oldest sliding section of the landslide mass, based on the exposure ages and field evidence. This part of the landslide mass has been severely dissected by streams with steep erosional slopes, indicating an absence of active movements (**Figures 4**, **8**). The oldest exposure ages are 9.3 ± 0.5 ka (TRAK-17) and 9.3 ± 0.4 ka (TRAK-20), which were collected from this level. In addition, exposure ages of 7.1 ± 0.4 (TRAK-19), 6.9 ± 0.3 (TRAK-21), 4.7 ± 0.2 (TRAK-15), 4.0 ± 0.2 ka (TRAK-18), 1.4 ± 0.1 ka (TRAK-13), and 1.6 ± 0.1 ka (TRAK-14) were also obtained from boulders on this deposit (**Figures 8**, **9**).

We explain the young exposure ages of 1.4 ± 0.1 ka (TRAK-13) and 1.6 ± 0.1 ka (TRAK-14) from the boulders situated at the lowest level of the main landslide close to the toe as follows: these boulders might belong to a younger landslide that occurred on the right lateral slope (western hillslope) of the valley which may have slumped onto the toe of the main rock avalanche body. An alternative explanation could be their exhumation due to active disintegration of the main landslide mass since failure. For this reason, the exposure ages from boulders TRAK-13 and TRAK-14 were excluded for further discussion. In addition, we argue that the young exposure ages from the boulders TRAK-15 and TRAK-18 are the result of either exhumation or surface weathering, which were not physically detectable in the field. Therefore, their exposure ages were also excluded.

Above this section, the intermediate elevation deposits of the rock avalanche are located at approximately 1750 m a.s.l. with an average width of 450 m. This level contains mounds with adjacent pits and a distorting trend toward the crown. The exposure ages of 8.7 ± 0.4 ka (TRAK-6), 8.7 ± 0.4 ka (TRAK-10), 7.9 ± 0.5 ka (TRAK-5), 5.3 ± 0.3 ka (TRAK-7), 2.9 ± 0.2 ka (TRAK-11) and 1.5 ± 0.1 ka (TRAK-4 and TRAK-9) were obtained from seven boulders from these intermediate elevation deposits (**Figure 8**). At this level, we argue that the boulders TRAK-4, 7, 9, and 11 are outliers because of exhumation. These boulders were more likely uncovered through the erosion of the matrix or exposed by secondary post-depositional processes (cf. Akçar et al., 2011) (e.g., **Figure 6**). After identifying outliers of the rock avalanche in the lower and intermediate elevation deposits, we calculated a weighted mean age of 8.3 ± 1.4 ka (2σ uncertainty) based

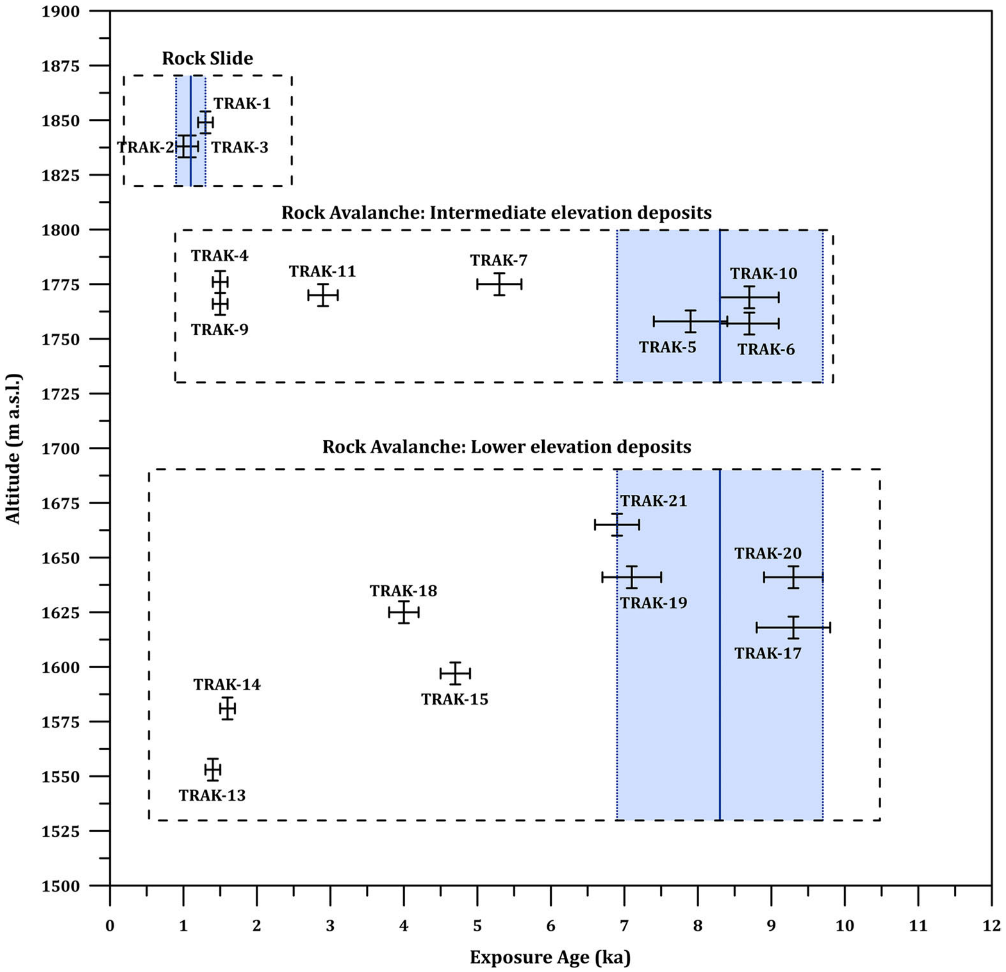

FIGURE 8 | Altitude versus cosmogenic ^{36}Cl exposure age plot. Plotted uncertainties are one sigma. Dark blue solid line indicates weighted mean ages of the rock avalanche and rockslide. Blue shaded area shows the two sigma solution space.

on the exposure ages from TRAK-5, 6, 10, 17, 19, 20, and 21, representing the entire rock avalanche body. Here, we note that the outliers plot beyond the two sigma solution space in **Figure 8**. The deposits of the secondary rockslide cover an area approximately 300 m below the crown corresponding to approximately 1850 m a.s.l., and consist of coarse debris varying from gravel to large blocks. Three surface samples collected from boulders at this site gave exposure ages of 1.1 ± 0.1 ka (TRAK-1), 1.3 ± 0.1 ka (TRAK-3), and 1.0 ± 0.1 ka (TRAK-2). Based on these exposure ages, we calculated a weighted mean age of 1.1 ± 0.2 ka (2σ uncertainty) for this rockslide (**Figure 8**).

DISCUSSION

Chronology of the Akdag Rock Avalanche and Its Plausibility

The active displacement within the Akdag landslide complex is manifested by several minor landslides along the crown of the major failure. For example, we studied one of the younger rockslides in the crown area which was dated to 1.1 ± 0.2 ka (2σ uncertainty). The toe of the rock avalanche deposits has been dissected and bears signs of disintegration as well as other geomorphic features within the complex (**Figure 4**). Our reconstructed chronology of the rock avalanche complex shows that the major collapse occurred at 8.3 ± 1.4 ka (2σ uncertainty), which we mapped as a rock avalanche. We consider that the mass of the major collapse has been actively moving since the major failure at 8.3 ± 1.4 ka. It should be noted that we cannot exclude mass wasting processes prior to 8.3 ± 1.4 ka; if the deposits were present, they were most likely overridden by a rockslide.

Surface exposure dating of landforms may sometimes be affected by inheritance (i.e., too old exposure ages) and/or exhumation (i.e., too young exposure ages) (Ivy-Ochs et al., 2007; Heyman et al., 2011, among others). However, for the following reasons, we argue that age overestimation due to inheritance in the Akdag rock avalanche is limited within the uncertainties, if present. In case of significant inheritance we would expect much older exposure ages due to the long pre-failure exposure of the study area.

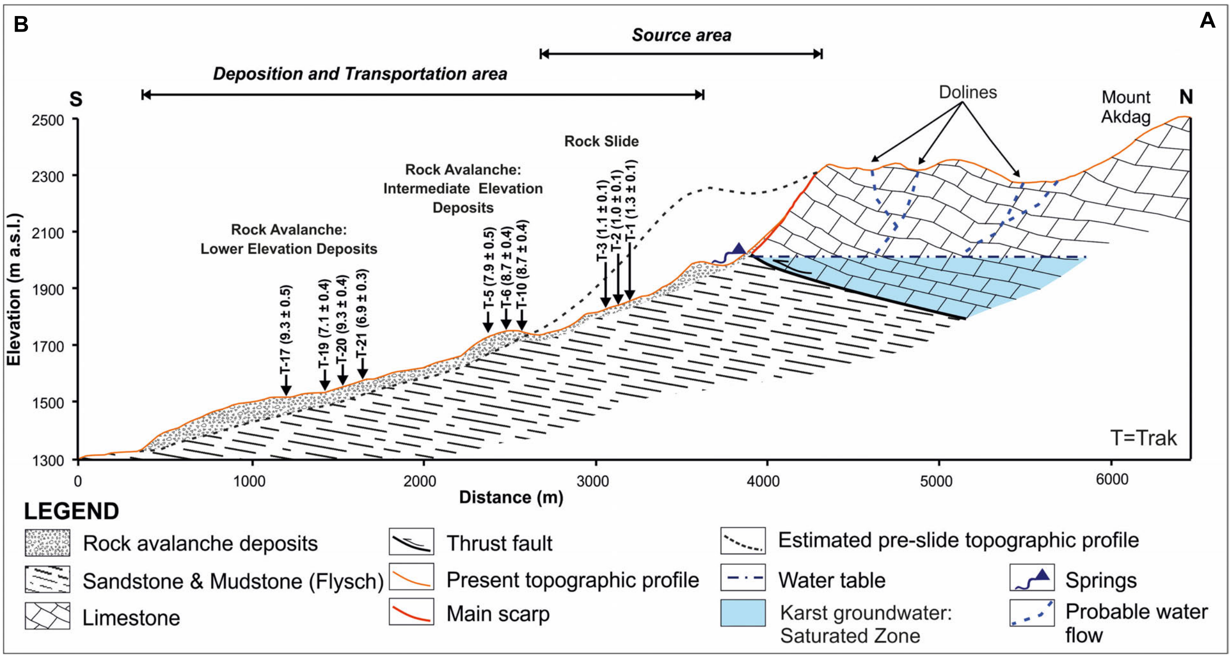

FIGURE 9 | Cross-section of Akdag rock avalanche and distribution of ^{36}Cl surface exposure ages (profile line is shown in **Figure 4** with a white dashed line).

The source area is beyond the extent of glaciations, thus the Jurassic limestone in the source area has been continuously exposed to cosmic rays during at least the last 40 ka (after Sarıkaya et al., 2014). Considering the existing chronology of the glaciations in Anatolia (Akçar et al., 2017), one could argue that the continuous exposure time is even longer, in the order of a few hundred thousand years. In both cases, the pre-collapse exposure time is long enough to cause significant inheritance. In addition, boulders which were transported on the passive carapace (Davies and McSaveney, 2009) during the collapse could certainly contain inherited cosmogenic ^{36}Cl (after Akçar et al., 2012b). Under these circumstances, we argue that we should have encountered at least one exposure age of around 20–30 ka among the 15 boulders which we sampled within the rock avalanche. It is thought that the lack of inheritance in our data might be a hint of active surface processes and/or mass wasting prior to 8.3 ± 1.4 ka.

Karstification of the Akdag Massif is still active today, which is observed in the Jurassic limestone bedrock to the north or the scarp (**Figures 3**, **6**). Similar environmental conditions are likely to have prevailed prior to the collapse, when karstification should have played a significant role in landscape degradation (Bayarı et al., 2019; Doğan et al., 2019; Nazik et al., 2019). For instance, repeated sinkhole and uvala formation and the collapse of cave systems would lead to the instantaneous removal of a few meters of rock at the surface, which would already be enough to remove the inherited cosmogenic ^{36}Cl acquired during the tens of thousands of years during the pre-collapse exposure time. In addition, repeated retrogressive wasting of the scarp area with smaller scale landslides during the pre-failure exposure time might also have contributed to the removal of inherited cosmogenic ^{36}Cl.

As well as inheritance, exhumation and/or post-depositional movement of the boulders can hinder the reconstruction of the chronology (cf. Akçar et al., 2011). In both lower and intermediate elevation deposits, eight boulders are plotted beyond the two sigma solution space. As previously explained, we argue that these boulders were exposed because of post-depositional factors, such as exhumation. In the lower elevation deposits, there is a gentle trend in the distribution of exposure ages with respect to elevation, i.e., exposure age becomes younger with decreasing elevation (**Figure 9**). This is in accordance with our field observations and interpretations. The margin (lower elevation) of the toe of the landslide mass is more unstable in comparison to the central parts (higher elevation). This indicates that post-depositional factors such as exhumation have had a potentially high effect on the boulders in this deposit. Boulders in the intermediate elevation deposits do not indicate any relationship between the elevation and exposure age (**Figure 9**) but they seem to have been affected by exhumation. They indicate a similar age distribution pattern as the lower elevation deposits; however, this resemblance does not indicate episodes of movement in the landslide mass.

The distribution of the cosmogenic ^{36}Cl exposure ages of the three boulders from the secondary rockslide shows a tight distribution (**Figure 9**). Recent slump activity has also affected the rock avalanche complex, supporting the hypothesis of a sudden secondary rock slide at 1.1 ± 0.2 ka. In these high elevation deposits, the boulders are not embedded in a matrix, which makes it unlikely that they have been shielded by sediment cover since their deposition. This field evidence points toward a lack of exhumation in this area and thus a well confined timing of failure. In general, exhumation and other post-depositional processes in an actively moving landscape have possibly more impact on boulders than inheritance.

Causes of Akdag Rock Avalanche and Landslide Complex

The interplay of lithology, structure and surface processes is clearly complex, as multi-scale conditional factors have a destabilizing effect on rock slopes. Massive rock-slope failures such as rock avalanches are closely related with preconditioning tectonic factors; more specifically, the internal structure of hillslopes (Hermanns and Strecker, 1999; Dortch et al., 2009; Korup and Dunning, 2015). Like several reported rock avalanches in other high mountain belts around the world, the location of Akdag landslide complex is not coincidental (e.g., Davies et al., 1999; Strom and Korup, 2006).

The effects of lithological characteristics and sedimentary structures play a significant role in setting up an environment prone to slope failures in the southern section of Akdag Massif. This also affects the development of shallow karstic processes on the upper part of the Akdag rock avalanche and has formed numerous karstic depressions in the upper sections of impermeable autochthonous units (**Figure 10A**). Since nappe movements in this area significantly change the stratigraphic position of limestone units, karstic features developed horizontally due to underlying impermeable rock units. The largest of these karstic depressions is the Rahat Plain (Uvala), which has an area of 553 m^2 immediately north of the Akdag rock-avalanche scarp (**Figures 10A**, **11A**). In the formation of Rahat Plain and nearby karstic depressions, secondary inactive faults might have played a role as well as the stratigraphic position of the Elmalı formation, which acted as an impermeable zone. This impermeable unit of sandstone, claystone and siltstones builds a karstic base level; thus preventing the vertical expansion of karstification and resulting in laterally extensive and shallow karstic depressions (**Figure 10A**).

At the base of these depressions are swallow holes that drain water into the ground. Mainly during the snowmelt period, the water at the base of these karstic depressions migrates underground. The discharge most likely flows vertically until it reaches contact with the clay layers. Because of the presumed inclination of the contact zone, drainage continues toward the south along the impermeable zone of claystone and siltstones and finally emerges within the landslide complex of the massif as karstic springs. We identified numerous karstic springs emerging at the limestone-claystone contacts in the Akdag landslide complex (**Figure 10B**). Although we have no information about the density of discontinuities within the bedrock, pore-water pressures, or level of the groundwater table at the time the Akdag rock avalanche occurred, we argue that these springs are one of the crucial factors in the formation of the Akdag rock avalanche, and that they had higher flow rates at the end of the Last Glaciation and beginning of Holocene based on the spatial distribution and depth of these karstic sources (**Figure 10**).

The main rock-avalanche scarp tends to retrogressively expand to the north. Together with continuing changes in stress of the shallow karstic process after the Akdag rock avalanche, secondary slope failures were initialized, such as the analyzed rockslide, which furthered the formation of this landslide complex (**Figures 5**, **11**). Although the main scarp of the Akdag rock avalanche has not yet reached the Rahat Uvala, it has already deformed many dolines behind it (**Figures 5**, **11**). These dolines and uvalas are filled with snow in the winter period. When the snow melts during the early spring, it contributes to an increasing groundwater level that drains into the main body of the rock avalanche through subsurface drainage. In the spring, subsurface drainage enhanced by snowmelt and rainfall emerges as karstic springs at the contact plane of the Elmalı formation, just 300 m below the main scarp (**Figure 10**). Karstic springs with high flow rates and floods caused by heavy rainfall trigger rapid erosion in sandstone, claystone, and siltstone, which are easily eroded and consequently cause deep gully erosion (**Figure 12**). During floods, they rapidly erode the Elmalı formation and transform into mudflows in the creeks. This rapid erosion taking place beneath the limestone units causes further slope instability and creates new mass movements and extensive gully erosion (**Figure 13A**). Secondary slope instabilities along the main scarp form counter slopes, creating temporary ponds which in turn increase the probability of sudden failure (**Figure 13B**).

Potential Triggering Factors

Seismic shaking is one of the main factors that trigger large bedrock landslides, including rock avalanches, in tectonically active mountain belts (Keefer, 1984; Weidinger et al., 2002; Dunning et al., 2007; Görüm et al., 2014). Keefer (1984) reports that even small earthquakes (i.e., Mw 4.0) may trigger landslides; moreover, earthquakes greater than 7.0 may induce tens of thousands of landslides (Tanyas et al., 2017). The Akdag Massif is located in a tectonically active region of SW Anatolia (**Figure 1**). The neotectonic evolution of SW Anatolia is characterized by the development of several extensional intermontane basins (e.g., Esen Basin on the foothills of Akdag Massif to the west) during Late Miocene–Quaternary (e.g., Ten Veen, 2004; Alçiçek, 2007). The extensional intermountain Esen Basin includes many short normal-faulting segments running in a NE–SW direction (Emre and Duman, 2011). This fault, with a total length of 23.5 km, is known as the Saklıkent Fault, which is defined as a Quaternary fault 7.5 km west of the Akdag rock avalanche (**Figure 1A**). The fault consists of two main segments, 9.1 and 14.4 km in length, respectively.

Based on the magnitude-length scaling relationship of Wells and Coppersmith (1994), we calculated the probable earthquake magnitudes that these fault segments and the entire fault could produce if they were ruptured at once. The results showed that possible earthquake magnitudes could be M_w = 6.1, 6.4 and 6.7. Considering these magnitudes, we estimated that the maximum ground acceleration (based on the empirical equation proposed by Ulusay et al., 2004 for Turkey) that these earthquakes can produce is from 158 to 235 (gal). Paleo-earthquakes of this magnitude could potentially provide sufficient ground acceleration to trigger the Akdag rock avalanche, although there is no paleo-seismic evidence that validates this assumption. Yet further paleo-seismological investigations need to be conducted

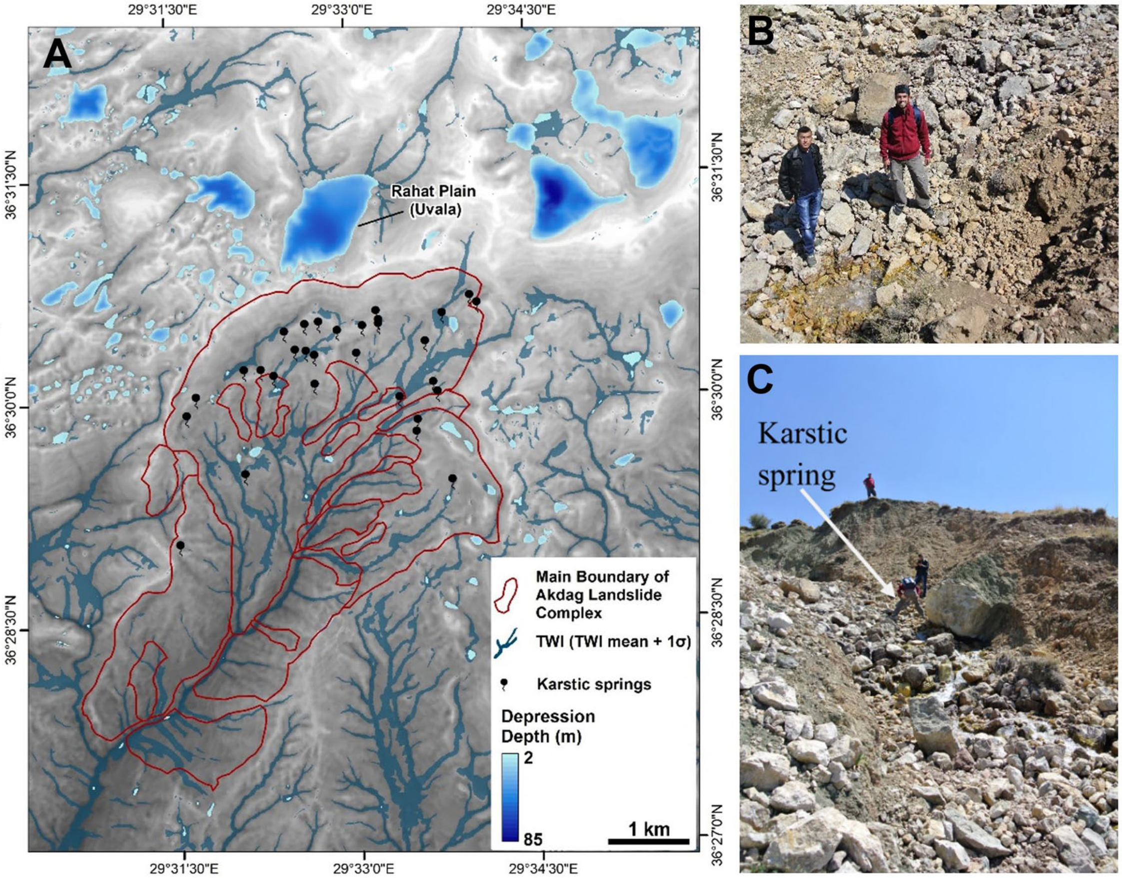

FIGURE 10 | (A) Distribution and depth of karstic depressions (TWI: topographic wetness index). **(B, C)** Head of a karstic spring on the eastern flank of the Akdag rock avalanche (In **Figure 4**, viewpoints of photographs are marked).

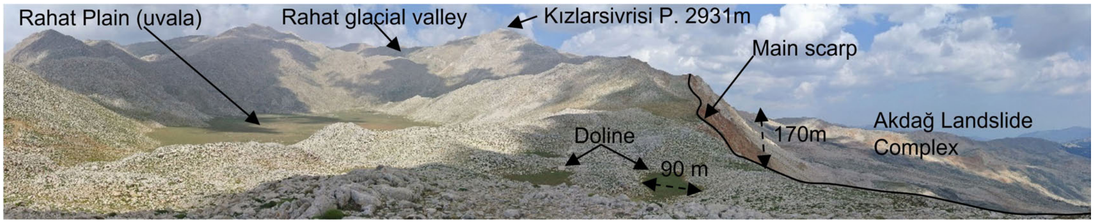

FIGURE 11 | Panoramic view of Rahat glacial valley, Rahat plain (uvala), and main scarp of the Akdag landslide south of Akdag Massif (in **Figure 4**, the viewpoints of photographs are marked).

with radiometric dating methods to clarify the role of past seismic events in the Akdag rock avalanche as a trigger factor.

Additionally, there were short cooling and warming periods during the Holocene according to research, including the study area and its near surroundings. On the basis of $\delta^{18}O$ measurements, we attempted to reveal the relationship between the landslide chronology and climate change. $\delta^{18}O$ measurements carried out in the Mediterranean (some locations close to the Akdag rock avalanche) and Black Sea basins e.g., Lake Sünnet (Ocakoğlu et al., 2013), Gölhisar (Eastwood et al., 2007), Soreq Cave (Bar-Matthews et al., 1999), Marmara Sea (Marino et al., 2009), Aegean Sea (Kotthoff et al., 2008), and Sofular Cave (Badertscher et al., 2011) indicate cooling events at 9.2, 8.9, 8.2 and 7.6 ka (Ocakoğlu et al., 2013). Among the locations mentioned above, Gölhisar is closest to Akdag, found 70 km north of the mountain. Although the $\delta^{18}O$ climate record from Gölhisar does not show a close relationship with Akdag landslide activity, isotopic fluctuations in this lake during the early-to-mid Holocene (8800–5100 ka) suggest oscillations between aridity and humidity (Eastwood et al., 2007). It can be asserted that specifically humid periods may have triggered the Akdag rock avalanche (**Figure 14**).

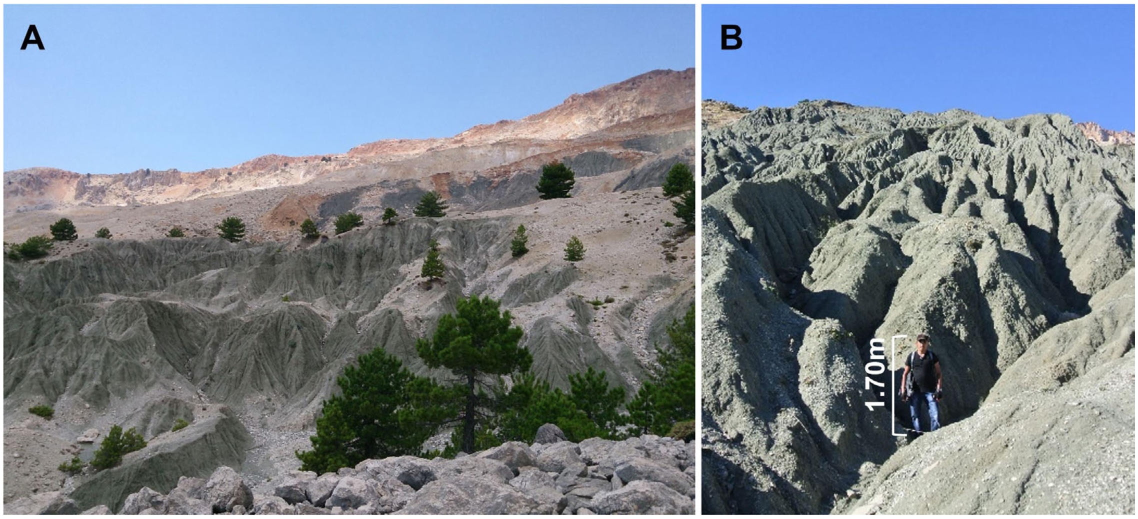

FIGURE 12 | (A) Different lithology and forms of erosion in the landslide. **(B)** Gully erosion (in **Figure 4**, the viewpoints of photographs are marked).

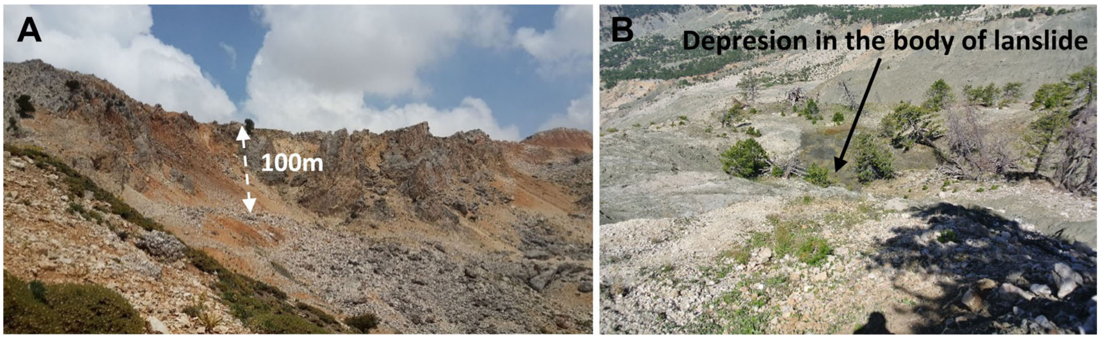

FIGURE 13 | (A) Rock slump on scarp due to slope instability. **(B)** Destruction of forest on Elmalı formation as a result of flow material in one of the secondary rock avalanches (in **Figure 4**, viewpoints of photographs are marked).

Besides the impact of past climatic events, today's climatic characteristics also cause landslide activity on Akdag. The landslide complex is found on the western part of the Teke Peninsula, surrounded by the Mediterranean. This area encounters moist air masses coming from the southwest over the Mediterranean. These air masses are confronted by the south and west slopes of Akdag Massif, as the first high and prominent mountain range on the peninsula. As the humid air ascends over the southern hillslope of the mountain where the Akdag rock avalanche is located, it is forced into lifting further and finally turns into orographic precipitation due to adiabatic cooling. The annual average precipitation reaches 1200 mm in this area (Bayrakdar, 2012), and sporadic heavy rainfall triggers many large and small landslides.

Based on the cosmogenic ^{36}Cl chronology, we concluded that the main rock avalanche occurred at 8.3 ± 1.4 ka (2σ), and a secondary rockslide at 1.1 ± 0.2 ka (2σ) (**Figures 9**, **10**). Moreover, although a clear relation between the exposure ages and the δ^{18}O climatic data cannot be established from the locations close to Akdag, a parallel relationship can be seen between the cooling periods and landslide activity. The age of 8.3 ± 1.4 ka (2σ) for the Akdag rock avalanche is more meaningful when correlated with global climate change during the Holocene (**Figure 14**). The Holocene thermal maximum was reached 9,000–5,000 years ago in the northern central Mediterranean region. The average July temperature is estimated to have been 1,2°C warmer than the recent pre-industrial period, consistent with glacier and marine records, and with transient climate model runs (Samartin et al., 2017). At the beginning of the Holocene, the increase in temperature may have triggered the Akdag rock avalanche by causing rapid melting of glaciers and snow. In particular, the glacier and snow in the glacio-karstic Kuruova uvala found to the northeast of the landslide complex may have produced enough melting water for the underground system to trigger a slope failure because the limestone strata dips toward the landslide complex (**Figure 4**).

A common pattern of landslide occurrence in previously glaciated areas is that many major landslides are of the order of 10 to 8 ka in age, with another cluster around mid-late Holocene at approximately 3–2 ka (Abele, 1997). These findings have been

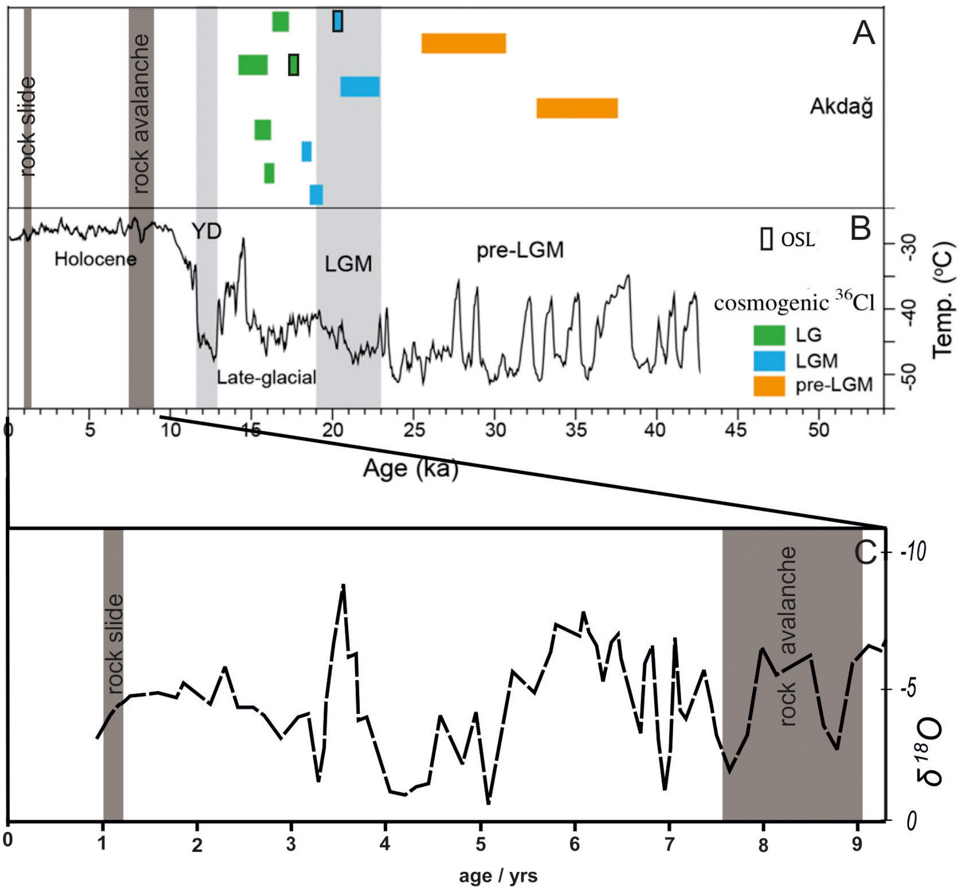

FIGURE 14 | Comparison between OSL dating (Bayrakdar, 2012; Bayrakdar et al., 2017) and cosmogenic surface exposure dating (Sarıkaya et al., 2014) for the Akdag Massif glacial chronology (Sarıkaya and Çiner, 2015). **(A)** Past surface temperatures gathered by drilling cores from Greenland GISP 2 (Alley, 2000). **(B)** Correlation between δδ18O climate data belonging to Gölhisar, located 70 km north of Akdag (Eastwood et al., 2007). **(C)** 36Cl exposure age of the rock avalanche and rockslide.

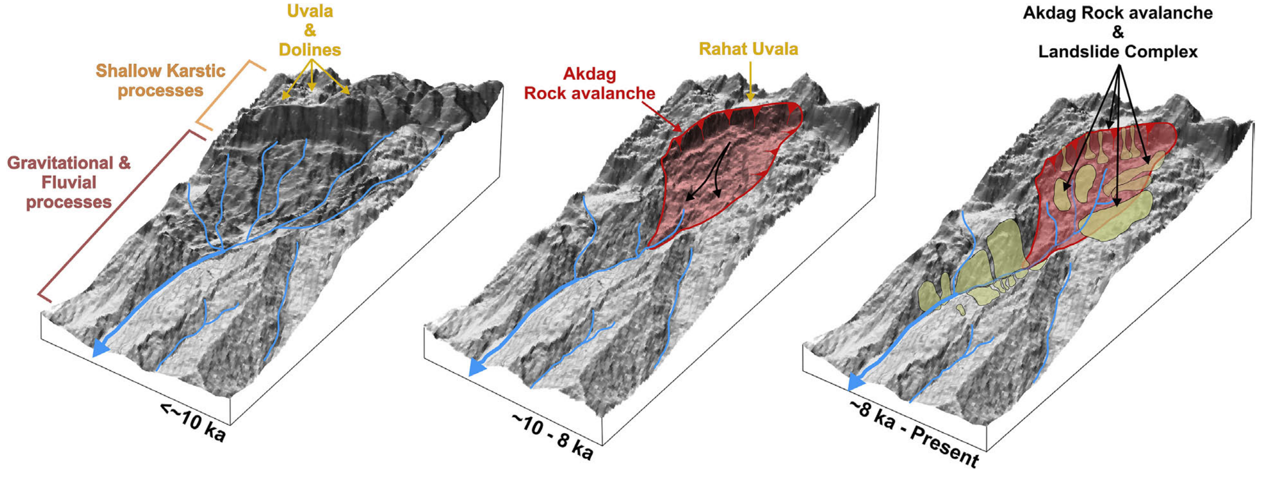

FIGURE 15 | Schematic three-dimensional diagram showing the eventual morphologic appearance before and after Akdag rock avalanche. Blue lines and arrows denote river network and flow direction, respectively.

both surprising and challenging for researchers in the European Alps, who had previously assumed that the relict large landslides were a remnant of deglaciation and not a phenomenon that had occurred under climatic conditions similar to the present (Abele, 1997). While some major landslides began occurring before deglaciation (Ambrosi and Crosta, 2006), and some were synchronous with deglaciation (Agliardi et al., 2001; Smith, 2001), the majority of documented cases indicate that large post-glacial failures typically occurred thousands of years after the retreat of the ice (McColl, 2012). Although the landslides mentioned here occurred in valleys that were glaciated during the Last Glacial (Clayton et al., 2006; Bayrakdar, 2012; Sarıkaya et al., 2014; Bayrakdar et al., 2017), the Akdag rock avalanche took place just beyond the maximum extent of the glaciers in this massif. The exposure ages have shown that the first landslide happened at c. 8.3 ka, and the second major failure came about at c. 1.1 ka. The instability after these major events led to sequential slope failures and formed the Akdag landslide complex (**Figure 15**).

CONCLUSION

Occurring on the southern slope of the Akdag Massif in the western Mediterranean region, the Akdag landslide is a complex phenomenon covering a surface area of approximately 9.8 km^2 that developed under the impetus of multiple factors and involves more than one type of movement. Because the slope failure was initiated at the point of contact between carbonates and flysch, the total mass of displaced material has been calculated as 300×10^6 m^3. This volume makes it the largest bedrock landslide known in the Western and Central Taurus mountains. The surface exposure ages show that there were two major events: the first is a rock avalanche dated to 8.3 ± 1.4 ka (2σ), and the second is a rockslide dated to 1.1 ± 0.2 ka (2σ). The rock avalanche event is closely related to karstic depressions in the upper parts of Akdag Massif and wetter conditions prevailing at the beginning of Holocene. The landslide is still active and is enlarging toward the sides and upper slopes.

Although the first major failure of the Akdag rock avalanche dates to early Holocene, the presence of new landslides observed in several field campaigns indicate that the landslide mass is currently active. As well as forested and residential areas, there are many important roads and water pipeline routes within the landslide area. Depending on the progress of landslide activity, the residential areas and roads are constantly in danger and frequently damaged causing loss of life, property and resources that cannot be recovered. Since the landslide areas may be characterized as a mountain basin providing a high input of debris into the river system, it heightens the effect of frequent torrents, especially in Saklikent Canyon, an important tourist site downstream of the basin. The fatal torrent in July 2014 triggered by a flash flood or heavy rainfall event in which two tourists died and nine people were seriously injured is only one example of the landslide geohazards posing a risk to tourists and local people (Görüm et al., 2017). In this respect, the landslide's long-term activity and the quantity of sediment flux need to be monitored. From this aspect, keeping track of current mass movements affecting the landslide, as well as the process understanding, is of great importance for local and national authorities to take preventive measures to counter landslide hazards and risks.

DATA AVAILABILITY STATEMENT

All datasets presented in this study are available upon request.

ETHICS STATEMENT

Written informed consent was obtained from the relevant individuals for the publication of any potentially identifiable images or data included in this article.

AUTHOR CONTRIBUTIONS

CB, TG, ZÇ, and NA designed the study. NA, CV, and SI-O performed the Cosmogenic Cl-36 exposure dating processing with input from CB. CB, TG, and NA wrote the manuscript with input by all co-authors. All authors interpreted and discussed the results.

ACKNOWLEDGMENTS

We would like to thank the Scientific Research Projects Coordination Unit of Istanbul University (Project number: ONAP 33594 [ID734]) for their support. We are most grateful to the Laboratory of Ion Beam Physics (accelerator mass spectrometry facility) operated by the Swiss Federal Institute of Technology, Zurich, Switzerland for the AMS measurements. We thank Dr. Nasim Mozafari for his collaboration during the sample preparation, Dr. Abdullah Akbaş and Dr. Ozan Kocadağlı for their assistance, and Mücahit Durmuş and Onur Yasan for their support during our fieldwork studies, and Graham H. Lee for proofreading. We sincerely thank the topic editors; Adrian Pfiffner, Tim Davies, John Clague, and Reginald Leonhard Hermanns and three referees for their instructive and thought-provoking comments on an earlier version of this manuscript.

REFERENCES

Abele, G. (1997). "Influence of glacier and climatic variation on rockslide activity in the Alps," in *Rapid mass movement as a source of climatic evidence for the Holocene*, Vol. 19, eds J. A. Matthews, B. Brunsden, B. Frenzel, B. Glaser, M. Weiß, and M. Palaoklimaforschung (Stuttgart: Gustav Fischer Verlag), 1–6.

Agliardi, F., Crosta, G., and Zanchi, A. (2001). Structural constraints on deep-seated slope deformation kinematics. *Eng. Geol.* 59, 83–102. doi: 10.1016/s0013-7952(00)00066-1

Agliardi, F., Crosta, G. B., Zanchi, A., and Ravazzi, C. (2009). Onset and timing of deep-seated gravitational slope deformations in the eastern Alps, Italy. *Geomorphology* 103, 113–129. doi: 10.1016/j.geomorph.2007.09.015

Akçar, N., Deline, P., Ivy-Ochs, S., Alfimov, V., Hajdas, I., Kunik, P. W., et al. (2012a). The 1717 AD rock avalanche deposits in the upper ferret valley (Italy): a datingapproach with cosmogenic 10Be. *J. Quat. Sci.* 27, 383–392. doi: 10.1002/jqs.1558

Akçar, N., Tikhomirov, D., Özkaymak, C., Ivy-Ochs, S., Alfimov, V., Sözbilir, H., et al. (2012b). 36Cl exposure of dating paleoearthquakes in the eastern mediterranean: first results from the western Anatolian Extensional Province, Manisa fault zone, Turkey. *GSA Bull.* 124, 1724–1735. doi: 10.1130/b30614.1

Akçar, N., Ivy-Ochs, S., Alfimov, V., Schlunegger, F., Claude, A., Reber, R., et al. (2017). Isochron-burial dating of glaciofluvial deposits: First results from the Swiss Alps. *Earth Surf. Process. Landf.* 42, 2414–2425. doi: 10.1002/esp.4201

Akçar, N., Ivy-Ochs, S., Alfimov, V., Yılmaz, ÝÖ, Schachner, A., Altıner, D., et al. (2009). First results on determination of cosmogenic 36Cl in limestone from the Yenicekale Complex in the Hittite capital of Hattusha (Turkey). *Quat. Geochronol.* 4, 533–540. doi: 10.1016/j.quageo.2009.09.002

Akçar, N., Ivy-Ochs, S., Kubik, P. W., and Schlüchter, C. (2011). Post-depositional ompacts on "Findlinge" (erratic boulders) and their implications for surface-exposure dating. *Swiss J. Geosci.* 104, 445–453. doi: 10.1007/s00015-011-0088-7

Akçar, N., Yavuz, V., Ivy-Ochs, S., Reber, R., Kubik, P. W., Zahno, C., et al. (2014). Glacier response to the change in atmospheric circulation in the eastern Mediterranean during the Last Glacial Maximum. *Quat. Geochronol.* 19, 27–41. doi: 10.1016/j.quageo.2013.09.004

Alçiçek, C. M. (2007). Tectonic development of an orogen-top rift recorded by its terrestrial sedimentation pattern: the Neogene Eşen Basin of southwestern Anatolia, Turkey. *Sediment. Geol.* 200, 117–140. doi: 10.1016/j.sedgeo.2007.04.003

Alfimov, V., and Ivy-Ochs, S. (2009). How well do we understand production of 36Cl in limestone and dolomite? *Quat. Geochronol.* 4, 462–474. doi: 10.1016/j.quageo.2009.08.005

Alley, R. B. (2000). The younger dryas cold interval as viewed from central greenland. *Quat. Sci. Rev.* 2013–2226.

Ambrosi, C., and Crosta, G. B. (2006). Large sackung along major tectonic features in the Central Italian Alps. *Eng. Geol.* 83, 183–200. doi: 10.1016/j.enggeo.2005.06.031

Badertscher, S., Fleitmann, D., Cheng, H., Edwards, R. L., Göktürk, O. M., Zumbühl, A., et al. (2011). Pleistocene water intrusions from the Mediterranean and Caspian seas into the Black Sea. *Nat. Geosci.* 4, 236–239. doi: 10.1038/ngeo1106

Ballantyne, C. K. (1998). Aeolian deposits on a Scottish mountain summit: characteristics, provenance, history and significance. *Earth Surf. Process. Landf.* 23, 625–641. doi: 10.1002/(sici)1096-9837(199807)23:7<625::aid-esp874>3.0.co;2-f

Bar-Matthews, M., Ayalon, A., Kaufman, A., and Wasserburg, G. (1999). The eastern Mediterranean paleoclimate as a reflection of regional events: soreq cave, Israel. *Earth Planet. Sci. Lett.* 166, 85–95. doi: 10.1016/s0012-821x(98)00275-1

Barnard, P. L., Owen, L. A., Sharma, M. C., and Finkel, R. C. (2001). Natural and humaninduced landsliding in the garhwal himalaya of northern India. *Geomorphology* 40, 21–35. doi: 10.1016/s0169-555x(01)00035-6

Bayarı, C. S., Klimchouk, A., Sarıkaya, M. A., and Nazik, L. (2019). "Aladağlar mountain range: a landscape-shaped by the interplay of glacial, karstic, and fluvial erosion," in *Landscapes and Landforms of Turkey*, eds C. Kuzucuoçlu, A. Çiner, and N. Kazancı (Cham: Springer), 423–435. doi: 10.1007/978-3-030-03515-0_22

Bayrakdar, C. (2012). *Akdağ Kütlesi'nde (Batı Toroslar) Karstlaşma-Buzul Ýlişkisinin Jeomorfolojik Analizi.* Unpublished PhD thesis., Ýstanbul University, Ýstanbul.

Bayrakdar, C., and Görüm, T. (2012). Yeşil göl heyelanı'nın jeomorfolojisi ve oluşum mekanizması. *Türk. Coğrafya Dergisi.* 1–10.

Bayrakdar, C., Güneç Kıyak, N., Turoğlu, H., Öztürk, T., and Canel, T. (2017). Akdag Kütlesi'nde (Batı Toroslar) Pleistosen buzullaşmalarının jeomorfolojik özellikleri ve optik uyarmalı lüminesans (OSL) ile yaşlandırılması. *Türk. Coğrafya Dergisi.* 27–37. doi: 10.17211/tcd.318170

Blöthe, J. H., Korup, O., and Schwanghart, W. (2015). Large landslides lie low: excess topography in the Himalaya-Karakoram ranges. *Geology* 43, 523–526. doi: 10.1130/g36527.1

Boehner, J., and Selige, T. (2006). "Spatial prediction of soil attributes using terrain analysis and climate regionalisation," in *SAGA – Analysis and Modelling Applications*, Vol. 115, eds J. Boehner, K. R. McCloy, and J. Strobl (Goettingen: Goettinger Geographische Abhandlungen), 13–28.

Bozcu, M., Yağmurlu, F., and Şentürk, M. (2007). Some neotectonic and paleosismological features of the fethiye-burdur fault zone, SWAnatolia. *Geol. Eng.* 2, 25–48.

Clayton, L., Attig, J. W., Mickelson, D. M., Johnson, M. D., and Syverson, K. M. (2006). *Glaciation of Wisconsin*. Wisconsin: Wisconsin Geological and Natural History Survey.

Conrad, O., Bechtel, B., Bock, M., Dietrich, H., Fischer, E., Gerlitz, L., et al. (2015). System for automated geoscientific analyses (SAGA) v. 2.1.4. *Geosci. Model Dev. Discuss.* 8, 2271–2312. doi: 10.5194/gmdd-8-2271-2015

Crosta, G. B., Hermanns, R. L., Dehls, J., Lari, S., and Sepulveda, S. (2017). Rock avalanches clusters along the northern Chile coastal scarp. *Geomorphology* 289, 27–43. doi: 10.1016/j.geomorph.2016.11.024

Davies, T. R., and McSaveney, M. J. (2009). The role of rock fragmentation in the motion of large landslides. *Eng. Geol.* 109, 67–79. doi: 10.1016/j.enggeo.2008.11.004

Davies, T. R., and McSaveney, M. J. (2012). *Mobility of Long-Runout Rock Avalanches. Landslides–types, Mechanisms and Modeling,* eds J. J. Clague and D. Stead. Cambridge: Cambridge University Press, 50–58.

Davies, T. R., McSaveney, M. J., and Hodgson, K. A. (1999). A fragmentation-spreading model for long-runout rock avalanches. *Can. Geotechnol. J.* 36, 1096–1110. doi: 10.1139/t99-067

Deline, P., Hewitt, K., Reznichenko, N., and Shugar, D. (2015). Rock avalanches onto glaciers. *Landslide Hazards Risks Disasters* 2015, 263–319. doi: 10.1016/b978-0-12-396452-6.00009-4

Densmore, A. F., and Hovius, N. (2000). Topographic fingerprint of bedrock landslides. *Geology* 28, 371–374. doi: 10.1130/0091-7613(2000)028<0371:tfobl>2.3.co;2

Desilets, D., Zreda, M., Almasi, P. F., and Elmore, D. (2006). Desilets, D., Zreda, MDetermination of cosmogenic Cl-36 in rocks by isotope dilution: innovations, validation and error propagation. *Chem. Geol.* 123, 185–195. doi: 10.1016/j.chemgeo.2006.03.001

Doğan, U., Koçyiğit, A., and Yeşilyurt, S. (2019). The relationship between Kestel Polje system and the Antalya Tufa Plateau: their morphotectonic evolution in Isparta Angle, Antalya-Turkey. *Geomorphology* 334, 112–125. doi: 10.1016/j.geomorph.2019.03.003

Doğu, A. F., Çiçek, I., Tunçel, H., and Gürgen, G. (1999). Akdag'ın jeomorfolojisi ve bunun beşeri faaliyetler Üzerine etkisi. *Türk. Coğrafyası Araşt. Uygul. Merkezi Dergisi.* 7, 95–120.

Dortch, J. M., Owen, L. A., Haneberg, W. C., Caffee, M. W., Dietsch, C., and Kamp, U. (2009). Nature and timing of large landslides in the Himalaya and Transhimalaya of northern India. *Quat. Sci. Rev.* 28, 1037–1054. doi: 10.1016/j.quascirev.2008.05.002

Duman, T. Y. (2009). The largest landslide dam in Turkey: tortum landslide. *Eng. Geol.* 104, 66–79. doi: 10.1016/j.enggeo.2008.08.006

Dunne, J., Elmore, D., and Muzikar, P. (1999). Scaling factors for the rates of production of cosmogenic nuclides for geometric shielding and attenuation at depth on sloped surfaces. *Geomorphology* 27, 3–11. doi: 10.1016/s0169-555x(98)00086-5

Dunning, S. A., Mitchell, W. A., Rosser, N. J., and Petley, D. N. (2007). The Hattian Bala rock avalanche and associated landslides triggered by the Kashmir Earthquake of 8 October 2005. *Eng. Geol.* 93, 130–144. doi: 10.1016/j.enggeo.2007.07.003

Eastwood, W. J., Leng, M. J., Roberts, N., and Davis, B. (2007). Holocene climate change in the eastern Mediterranean region: a comparison of stable isotope and pollen data from Lake Gölhisar, southwest Turkey. *J. Quat. Sci.* 22, 327–341. doi: 10.1002/jqs.1062

Elmore, D., Ma, X., Miller, T., Nueller, K., Perry, M., Rickey, F., et al. (1997). Status and plans for the PRIME Lab AMS facility. *Nucl. Instrum. Methods Phys. Res. Sect. B Beam Interact. Mater. Atoms* 123, 69–72. doi: 10.1016/s0168-583x(96)00621-0

Emre, Ö, and Duman, T. Y. (2011). *Active Fault Map Series of Turkey, Fethiye (NJ 35-16) Quadrangle. Serial Number* 13. Ankara-Turkey: General Directorate of Mineral Research and Exploration.

Evans, J. M., Stone, J. O. H., Fifield, L. K., and Cresswell, R. G. (1997). Cresswell, Cosmogenic chlorine-36 production in potassium feldspars. *Nttcl. Lnstrttm. Methods B* 123, 334–340. doi: 10.1016/s0168-583x(96)00714-8

Fabryka-Martin, J. T. (1988). *Production of Radionuclides in the Earth and Their Hydrogeologic Significance, with Emphasis on Chlorine-36 and Iodine-129.* PhD., University of Arizona, Tucson.

Gischig, V., Amann, F., Moore, J. R., Loew, S., Eisenbeiss, H., and Stempfhuber, W. (2011). Composite rock slope kinematics at the current Randa instability, Switzerland, based on remote sensing and numerical modeling. *Eng. Geol.* 118, 37–53. doi: 10.1016/j.enggeo.2010.11.006

Görüm, T. (2019). Tectonic, topographic and rock-type influences on large landslides at the northern margin of the Anatolian Plateau. *Landslides* 16, 333–346. doi: 10.1007/s10346-018-1097-7

Görüm, T., Bayrakdar, C., Avdan, U., and Çömert, R. (2017). Geomorphology of the mount akdag landslide, western taurus range (SW Turkey). *J. Maps* 2, 165–172. doi: 10.1080/17445647.2017.1280424

Görüm, T., Korup, O., van Westen, C. J., van der Meijde, M., Xu, C., and van der Meer, F. D. (2014). Why so few? Landslides triggered by the 2002 Denali earthquake, Alaska. *Quat. Sci. Rev.* 95, 80–94. doi: 10.1016/j.quascirev.2014.04.032

Heim, A. (1932). *Bergsturz und Menschenleben. Vierteljahrschr. Naturf. Ges*. içinde Zurich: Beer and Co, 218

Hermanns, R. L., Niedermann, S., Ivy-Ochs, S., and Kubik, P. W. (2004). Rock avalanching into a landslide-dammed lake causing multiple dam failure in Las Conchas valley (NW Argentina)-evidence from surface exposure dating and stratigraphic analyses. *Landslides* 2, 113–122.

Hermanns, R. L., and Strecker, M. R. (1999). Structural and lithological controls on large Quaternary rock avalanches (sturzstroms) in arid northwestern Argentina *Geol. Soc. Am. Bull.* 111, 934–948. doi: 10.1130/0016-7606(1999)111<0934:salcol>2.3.co;2

Hewitt, K., Clague, J. J., and Orwin, J. F. (2008). Legacies of catastrophic rock slope failures in mountain landscapes. *Earth-Sci. Rev.* 87, 1–38. doi: 10.1016/j.earscirev.2007.10.002

Heyman, J., Stroeven, A. P., Harbor, J. M., and Caffee, M. W. (2011). Too young or too old: evaluating cosmogenic exposure dating based on an analysis of compiled boulder exposure ages. *Earth Planet. Sci. Lett.* 302, 71–80. doi: 10.1016/j.epsl.2010.11.040

Hilger, P., Gosse, J. C., and Hermanns, R. L. (2019). How significant is inheritance when dating rockslide boulders with terrestrial cosmogenic nuclide dating?-a case study of an historic event. *Landslides* 16, 729–738. doi: 10.1007/s10346-018-01132-0

Huggel, C., Clague, J. J., and Korup, O. (2012). Is climate change responsible for changing landslide activity in high mountains? *Earth Surf. Process. Landforms* 37, 77–91. doi: 10.1002/esp.2223

Hungr, O., and Evans, S. G. (2004). Entrainment of debris in rock avalanches; an analysis of a long run-out mechanism. *Geol. Soc. Am. Bull.* 116, 1240–1252.

Ivy-Ochs, S., Kerschner, H., and Schluchter, C. (2007). Cosmogenic nuclides and the dating of lateglacial and early holocene glacier variations: the alpine perspective. *Quat. Int.* 16, 53–63. doi: 10.1016/j.quaint.2006.12.008

Ivy-Ochs, S., Martin, S., Campedel, P., Hippe, K., Alfimov, V., Vockenhuber, C., et al. (2017). Geomorphology and age of the Marocche di Dro rock avalanches (Trentino, Italy). *Quat. Sci. Rev.* 169, 188–205. doi: 10.1016/j.quascirev.2017.05.014

Ivy-Ochs, S., Poschinger, A. V., and Maisch, M. (2009). Surface exposure dating of the Flims landslide, Graubunden, Switzerland. *Geomorphology* 103, 104–112. doi: 10.1016/j.geomorph.2007.10.024

Ivy-Ochs, S., and Schaller, M. (2010). Examining processes and rates of landscape change with cosmogenic radionuclides. *Radioact. Environ.* 16, 231–294. doi: 10.1016/s1569-4860(09)01606-4

Ivy-Ochs, S., Synal, H. A., Roth, C., and Schaller, M. (2004). Ivy-Ochs, S., Synal, Initial results from isotope dilution for Cl and Cl-36 measurements at the PSI/ETH Zurich AMS facility. *Nucl. Instrum. Methods Phys. Res. Sect. B Beam Interact. Mater. Atoms* 223–224, 623–627. doi: 10.1016/j.nimb.2004.04.115

Keefer, D. K. (1984). Rock avalanches caused by earthquakes: source characteristics. *Science* 223, 1288–1290. doi: 10.1126/science.223.4642.1288

Korup, O. (2002). Recent research on landslide dams - a literature review with special attention to New Zealand. *Prog. Phys. Geogr. Earth Environ.* 26, 206–235. doi: 10.1191/0309133302pp333ra

Korup, O., Clague, J. J., Hermanns, R. L., Hewitt, K., Strom, A. L., and Weidinger, J. T. (2007). Giant landslides, topography, and erosion. *Earth Planet. Sci. Lett.* 261, 578–589. doi: 10.1016/j.epsl.2007.07.025

Korup, O., and Dunning, S. (2015). "Catastrophic mass wasting in high mountains," in *The Hıgh-mountain Cryosphere*, eds C. Huggel, M. Carey, and J. J. Clague (Cambridge: Cambridge University Press), 127–146. doi: 10.1017/cbo9781107588653.008

Korup, O., Schmidt, J., and McSaveney, M. J. (2005). Regional relief characteristics and denudation pattern of the western Southern Alps, New Zealand. *Geomorphology* 71, 402–423. doi: 10.1016/j.geomorph.2005.04.013

Kotthoff, U., Pross, J., Muller, U. C., Peyron, O., Schmiedl, G., Schulz, H., et al. (2008). Climate dynamics in the borderlands of the Aegean Sea during formation of sapropel S1 deduced from a marine pollen record. *Quat. Sci. Rev.* 27, 832–845. doi: 10.1016/j.quascirev.2007.12.001

Lal, D. (1991). Cosmic ray labeling of erosion surfaces: in situ nuclide production rates and erosion models. *Earth Planet. Sci. Lett.* 104, 424–439. doi: 10.1016/0012-821x(91)90220-c

Liu, B. L., Phillips, F. M., Fabrykamartin, J. T., Fowler, M. M., and Stone, W. D. (1994). Cosmogenic 36Cl accumulation in unstable landforms, 1. Effects of the thermal neutron distribution. *Water Resour. Res.* 30, 3115–3125. doi: 10.1029/94wr00761

Marino, G., Rohling, E. J., Sangiorgi, F., Hayes, A., Casford, J. L., Lotter, A. F., et al. (2009). Early and middle Holocene in the Aegean Sea: interplay between high and lowlatitude climate variability. *Quat. Sci. Rev.* 28, 3246–3262. doi: 10.1016/j.quascirev.2009.08.011

McColl, S. T. (2012). Paraglacial rock-slope stability. *Geomorphology* 15, 1–16. doi: 10.1016/j.geomorph.2012.02.015

McColl, S. T. (2015). "Landslide causes and triggers," in *Landslide Hazards, Risks and Disasters*, eds T. Davies and N. Rosser (Amsterdam: Elsevier Science), 17–42. doi: 10.1016/b978-0-12-396452-6.00002-1

McColl, S. T., and Davies, T. R. H. (2013). Large ice-contact slope movements: glacial buttressing deformation and erosion. *Earth Surf. Process. Landf.* 38, 1102–1115. doi: 10.1002/esp.3346

Nazik, L., Poyraz, M., and Karabıyıkoğlu, M. (2019). "Karstic landscapes and landforms in Turkey," in *Landscapes and Landforms of Turkey*, eds C. Kuzucuoğlu and A. Çiner (Cham: Springer), 181–196. doi: 10.1007/978-3-030-03515-0_5

Nazik, L., and Tuncer, K. (2010). Türkiye karst morfolojisinin bölgesel özellikleri. *Türk. Speleol. Dergisi* 1, 7–19.

Nichols, K. K., Bierman, P. R., Foniri, W. R., Gillespie, A. R., Caffee, M., and Finkel, R. (2006). Dates and rates of arid region geomorphic processes. *Geol. Soc. Am. Today* 16, 4–11.

Ocakoğlu, F., Kır, O., Yılmaz, ÝÖ, Açıkalın, S., Erayık, C., Tunoğlu, C., et al. (2013). Early to mid-holocene lake level and temperature records from the terraces of lake sünnet in NW Turkey. *Palaeogeogr. Palaeoclimatol. Palaeoecol.* 369, 175–184. doi: 10.1016/j.palaeo.2012.10.017

Olaya, V., and Conrad, O. (2009). "Chapter 12 geomorphometry in SAGA," in *Geomorphometry – Concepts, Software, Applications*, eds T. Hengl and H. I. Reuter (Amsterdam: Elsevier), 293–308. doi: 10.1016/s0166-2481(08)00012-3

Onde, H. (1952). "Formes Glaciaires dans le Massif Lycien de I'Akdağ," in *XIXe Congres Geologique International, Alger Fasc. XV* (Algiers: Association des Services Geologiques Africains Press), 327–335.

Pánek, T. (2015). Recent progress in landslide dating: a global overview. *Progr. Phys. Geogr. Earth Environ.* 39, 168–198. doi: 10.1177/0309133314550671

Pánek, T. (2019). Landslides and quaternary climate changes—The state of the art. *Earth-Sci. Rev.* 196, 102871. doi: 10.1016/j.earscirev.2019.05.015

Phillips, F. M., Stone, W. D., and Fabryka-Martin, J. T. (2001). An improved approach to calculating low-energy cosmic-ray neutron fluxes near the land/atmosphere interface. *Chem. Geol.* 175, 689–701. doi: 10.1016/s0009-2541(00)00329-6

Planhol, X., and İnandık, H. (1958). La limite de la glaciation quaternaire dans le massif du yeşil göl dağ (anatolie du sud-quest). *Review* 4, 33–35.

Prager, C., Ivy-Ochs, S., Ostermann, M., Synal, H., and Patzelt, G. (2009). Geology and dating of the Fernpass rockslide (Tyrol, Austria). *Geomorphology* 103, 93–103. doi: 10.1016/j.geomorph.2007.10.018

Putkonen, J., and Swanson, T. (2003). Accuracy of cosmogenic ages for moraines. *Quat. Res.* 59, 255–261. doi: 10.1016/s0033-5894(03)00006-1

Samartin, S., Heiri, O., Joos, F., Renssen, H., Franke, J., Brönnimann, S., et al. (2017). Warm Mediterranean mid-Holocene summers inferred from fossil midge assemblages. *Nat. Geosci.* 10, 207–212. doi: 10.1038/ngeo2891

Sarıkaya, M. A., and Çiner, A. (2015). Türkiye Geç Pleyistosen Buzullaşması ve Paleoiklimi. *Maden Tetkik ve Arama Dergisi* 151, 111–132.

Sarıkaya, M. A., Çiner, A., Haybat, H., and Zreda, M. (2014). An early advance of glaciers on Mount Akdağ, SW Turkey, before the global Last Glacial Maximum; insights from cosmogenic nuclides and glacier modeling. *Quat. Sci. Rev.* 88, 96–109. doi: 10.1016/j.quascirev.2014.01.016

Sarıkaya, M. A., Ciner, A., and Yıldırım, C. (2017). Cosmogenic S 36Cl glacial chronologies of the Late Quaternary glaciers on Mount Geyikdag in the eastern Mediterranean. *Quat. Geochronol.* 39, 189–204. doi: 10.1016/j.quageo.2017.03.003

Şenel, M. (1997). *1/100.000 ölçekli Türkiye Jeoloji Haritaları, Fethiye-L9 paftası*. Ankara: MTA.

Shakun, J. D., and Carlson, A. E. (2010). A global perspective on Last Glacial Maximum to Holocene climate change. *Quat. Sci. Rev.* 29, 1801–1816. doi: 10.1016/j.quascirev.2010.03.016

Shulmeister, J., Davies, T. R., Evans, D. J. A., Hyatt, O. M., and Tovar, D. S. (2009). Catastrophic landslides, glacier behaviour and moraine formation – A view from an active plate margin. *Quat. Sci. Rev.* 28, 1085–1096. doi: 10.1016/j.quascirev.2008.11.015

Singeisen, C., Ivy-Ochs, S., Wolter, A., Steinemann, O., Akçar, N., Yesilyurt, S., et al. (2020). The Kandersteg rock avalanche (Switzerland): integrated analysis of a late Holocene catastrophic event. *Landslides* 17, 1297–1317. doi: 10.1007/s10346-020-01365-y

Smith, K. (2001). *Environmental Hazards: Assessing Risk and Reducing Disaster*, Third Edn. London: Routledge.

Stead, D., and Wolter, A. (2015). A critical review of rock slope failure mechanisms: the importance of structural geology. *J. Struct. Geol.* 74, 1–23. doi: 10.1016/j.jsg.2015.02.002

Stone, J., Evans, J., Fifield, K., Cresswell, R., and Allan, G. L. (1996). Cosmogenic chlorine-36 production rates from calcium and potassium: radiocarbon. *Radiocarbon* 38, 170–171.

Stone, J. O. (2000). Air pressure and cosmogenic isotope production. *J. Geophys. Res. Solid Earth* 105 23753–23759. doi: 10.1029/2000jb900181

Stone, J. O. H., Evans, J. M., Fifield, L. K., Allan, G. L., and Cresswell, R. G. (1998). Cosmogenic chlorine-36 production in calcite by muons. *Geochim. Cosmochim. Acta* 62, 433–454. doi: 10.1016/s0016-7037(97)00369-4

Strom, A. L., and Korup, O. (2006). Extremely large rockslides and rock avalanches in the Tien Shan Mountains, Kyrgyzstan *Landslides* 3, 125–136. doi: 10.1007/s10346-005-0027-7

Synal, H. A., Bonani, G., Ender, R. M., Gartenmann, P., Kubik, P. W., Schnabel, C., et al. (1997). Status report of the PSI/ETH AMS facility. *Nucl. Instrum. Methods Phys. Res. Sect. B Beam Interact. Mater. Atoms* 123, 62–68. doi: 10.1016/s0168-583x(96)00608-8

Tanyas, H., Van Westen, C. J., Allstadt, K. E., Jessee, M. A. N., Gorum, T., Jibson, R. W., et al. (2017). Presentation and analysis of a worldwide database of earthquake-induced landslide inventories. *J. Geophys. Res. Earth Surf.* 122, 1991–2015. doi: 10.1002/2017jf004236

Ten Veen, J. H. (2004). Extension of Hellenic forearc shear zones in SW Turkey: the Pliocene–Quaternary deformation of the Eşe Çay Basin. *J. Geodynam.* 3, 181–204. doi: 10.1016/j.jog.2004.02.001

Ulusay, R., Tuncay, E., Sonmez, H., and Gokceoglu, C. (2004). An attenuation relationship based on Turkish strong motion data and iso-acceleration map of Turkey. *Eng. Geol.* 74, 265–291. doi: 10.1016/j.enggeo.2004.04.002

Weidinger, J. T., Wang, J., and Ma, N. (2002). The earthquake-triggered rock avalanche of Cui Hua, Qin Ling Mountains, PR of China—the benefits of a lake-damming prehistoric natural disaster. *Quat. Int.* 93, 207–214. doi: 10.1016/s1040-6182(02)00019-8

Wells, D., and Coppersmith, K. (1994). New empirical relationships among magnitude, rupture length, rupture width, rupture area, and surface displacement. *Bull. Seismol. Soc. Am.* 84, 974–1002.

Conflict of Interest: The authors declare that the research was conducted in the absence of any commercial or financial relationships that could be construed as a potential conflict of interest.

frontiers
in Earth Science

ORIGINAL RESEARCH
published: 11 August 2020
doi: 10.3389/feart.2020.00312

Anatomy of the Naga City Landslide and Comparison With Historical Debris Avalanches and Analog Models

Alfredo Mahar Francisco Lagmay [1,2]*, ***Carmille Marie Escape*** [1,2], ***Audrei Anne Ybañez*** [1], ***John Kenneth Suarez*** [1] ***and Genaro Cuaresma*** [1]

[1] UP Resilience Institute, University of the Philippines, Quezon City, Philippines, [2] National Institute of Geological Sciences, University of the Philippines, Quezon City, Philippines

Edited by:
O. Adrian Pfiffner,
University of Bern, Switzerland

Reviewed by:
Chong Xu,
China Earthquake Administration, China
Anke Verena Zernack,
Massey University, New Zealand
Lucia Capra,
National Autonomous University of Mexico, Mexico

****Correspondence:***
Alfredo Mahar Francisco Lagmay
mlagmay@nigs.upd.edu.ph

Specialty section:
This article was submitted to Structural Geology and Tectonics, a section of the journal Frontiers in Earth Science

Received: *31 March 2020*
Accepted: *02 June 2020*
Published: *11 August 2020*

Citation:
Lagmay AMF, Escape CM, Ybañez AA, Suarez JK and Cuaresma G (2020) Anatomy of the Naga City Landslide and Comparison With Historical Debris Avalanches and Analog Models.
Front. Earth Sci. 8:312.
doi: 10.3389/feart.2020.00312

Debris avalanches pose some of the most destructive geologic hazards that threaten both urban and rural populations around the world. On 20 September 2018, villages in Naga City, Cebu, Philippines, were devastated by a landslide that claimed 78 lives with 6 missing, joining other catastrophic landslides in the country like the 1628 Iriga and the 2006 Guinsaugon debris avalanches. Understanding the mechanism of these gargantuan landslides and their correct nomenclature are useful for hazard prevention and mitigation. In this study, we compare the deposit characteristics of the Naga City landslide with analog models and well-known historical debris avalanche events/deposits in the Philippines to understand factors that led to the landslide disaster in Naga City. Physical characteristics obtained from aerial and satellite imagery, ground surveys, recorded footage, borehole data, and lithologic maps provided a detailed dataset for analyzing the conditions that led to the mass movement and the observed characteristics of the Naga landslide deposits. Comparison with analog models of hummock formation and the description of historical debris avalanche deposits show striking similarities, which were used to demonstrate that the Naga landslide was a Rockslide-Debris Avalanche. The equations of Corominas (1996) and Dade and Huppert (1998) for long-runout rockfalls support this analysis. The Naga landslide event is an example of a well-documented debris avalanche, complete with all the characteristics of this type of rapid mass movement. It is consistent with the descriptions found in the literature with respect to its deposit features and mechanical behavior as defined by laboratory models and empirically-derived equations. This study helps us understand historical and future long-runout debris avalanches in order for scientists and authorities to find ways to save lives. Unfortunately, there was lack of appropriate hazards assessment on the site, which had warnings in the form of the development of fractures at the headscarp of the landslide, a month prior to the disaster.

Keywords: landslide, debris avalanche, hazard assessment, excessive runout, Fahrböschung, Naga landslide disaster, Naga Philippines

1. INTRODUCTION

On 20 September 2018, a massive landslide devastated Naga City, Cebu. The Naga City Landslide claimed the lives of 78 villagers and injured 18 while six people remained missing and are presumed dead. The majority of the fatalities were recovered at the landslide toe about 1.2 km from the 200 meter-high headscarp. This was due to the unexpectedly large landslide volume and unusually long-runout, which surprised villagers at the landslide toe (**Figure 1**). Despite early warnings from developing fractures near the headscarp a month prior to the disaster, no action was taken by villagers at the landslide toe in Sitio Sindulan, Barangay Tinaan and those in an adjacent area at the base of a cliff in Barangay Naalad (**Figure 1**). Only residents in Sitio Tagaytay, situated near the headscarp of the landslide, were evacuated by authorities the night before the mountain collapsed.

Discernible from the closed-circuit television (CCTV) footage that captured the event (see **Supplementary Video 1**, BJMP-NAGA, 2018) was mass movement that started as a translational slide. It also showed a landslide mass that initially moved as one intact block with no significant backward regression. The landslide lasted for a minute and traveled with a maximum velocity of 72 km/h. Fractures observed a month prior to the catastrophe (Lagmay, 2018; MGB, 2018; Catane et al., 2019) suggest that the sliding block started to move some time before

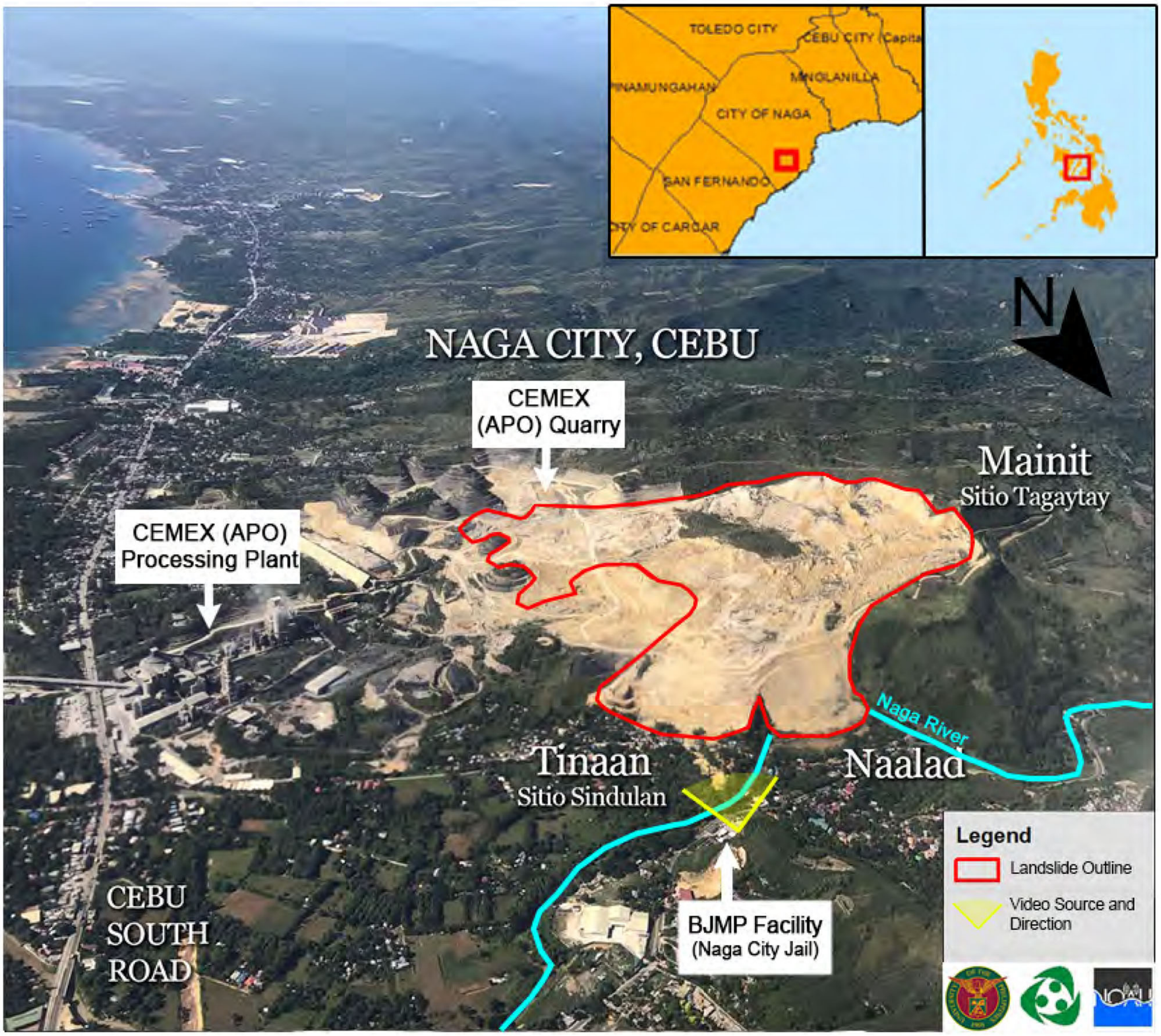

FIGURE 1 | Aerial image of the Naga landslide taken a month after the incident. Numerous houses in Sitio Sindulan, Barangay Tinaan and the village situated near the base of the cliff in Barangay Naalad were buried by the landslide debris.

the main collapse event, which happened in the early morning at 5:45 a.m. on 20 September 2018. The sliding mass moving as a whole, meant a larger volume was available, favoring increased runout of the landslide. Once in motion, the front of the sliding mass accelerated, stretching the limestone body to create a long-runout (L) relative to the collapse height (H) with a calculated H/L ratio of 0.17, which is a characteristic value of volcanic and non-volcanic debris avalanches (Ui, 1983; Siebert, 1984; Ui et al., 1986; de Vries and Delcamp, 2015).

Debris avalanches are catastrophic, large scale, mass wasting events with a fast moving body that can travel a long way relative to the collapse height, regardless of whether they are volcanic or non-volcanic in origin (de Vries and Delcamp, 2015). Though more commonly associated with volcanic mass wasting events, the use of the term debris avalanche also applies to non-volcanic landslides if they meet the criteria of having an amphitheater, hummocks, torevas, megablocks, jigsaw puzzle features (Ui, 1983) and a longer-runout compared to landslides. Debris avalanche deposits, irrespective of whether volcanic or non-volcanic in origin, exhibit similar characteristics (Ui, 1989). Well-known examples for volcanic debris avalanches are Mt. St Helens (Glicken, 1996), Jocotitlan (Siebe et al., 1992), Bezymiannyi (Belousov and Belousova, 1998) and Shiveluch (Ponomareva et al., 1998) volcanoes, whereas examples for non-volcanic debris avalanches are Guinsaugon (Lagmay et al., 2008; Futalan et al., 2010), Mt. Meager (Guthrie et al., 2012; Roberti et al., 2017), Blackhawk (Johnson, 1978; Ui et al., 2000), Sherman (McSaveney, 1978; Ui et al., 2000) and Luanshibao (Wang et al., 2018). Ui (1983) also demonstrated the similarity of the H/L ratio for volcanic and non-volcanic events and proposed that both types have similar mode of transportation related to gravitational sliding due to slope instability. Although a debris flow is another type of mass wasting event that has a long-runout, it can be differentiated from debris avalanches in the sense that their mobility is primarily controlled by the presence of water. The Naga City landslide was relatively dry and did not form debris flows at the distal portion of the deposits. Due to the morphological characteristics of the deposit field, the long-runout, the absence of debris flow deposits, and the initial slide movement of rock units, the Naga City landslide was classified as a rockslide-debris avalanche. Hungr et al. (2001) suggested that the distinction between rock avalanches and debris avalanches is gradational and subjective especially because there is a certain difficulty in separating welded materials (rock) from uncemented granular deposits (debris). The Carcar and Barili formations which comprised the collapsed Naga landslide material, are largely uncemented, soft to semi-hard and can crumble. The collapse started as a rockslide, but because of the extension and acceleration that leads to fragmentation, forms the block facies, matrix facies and other features that are distinctive of a debris avalanche, hence the classification.

Due to the high number of fatalities associated with the long reach of the landslide, it is important to analyze the conditions that contributed to the unusual runout of this event. To do this, we compared the Naga City disaster with two other known local debris avalanche events: The 1628 Iriga volcanic debris avalanche (Aguila et al., 1986; Paguican, 2012; Minimo and Lagmay, 2016) and the 2006 Guinsaugon debris avalanche (Lagmay et al., 2006; Evans et al., 2007; Catane et al., 2008). In this paper, we revisit the analysis of the landslide event and present new detailed field investigation. We explore the relationship of the volume with the runout length of the Naga landslide and compare the deposits with the worldwide dataset of debris avalanches (Corominas, 1996; Dade and Huppert, 1998) and existing analog models (Paguican et al., 2014). This is used to determine the emplacement mechanism of the landslide, which led to the fatal disaster in Naga City.

2. GEOLOGIC SETTING

The City of Naga is located at the southeastern coast of Cebu Islands, Philippines. Cebu is part of an island group, which along with Panay, Negros, Bohol, Leyte, and Samar comprise the Central Philippines region that has a common geologic history (Deng et al., 2015). These islands, including their adjacent sedimentary basins, namely Iloilo and Visayan basins (Aurelio and Peña, 2002), are underlain by a basement complex composed of Cretaceous to Eocene igneous and metamorphic rocks and Cenozoic volcanic and sedimentary units (Santos-Ynigo, 1951; Dimalanta et al., 2006; Deng et al., 2015). The region lies within the Philippine Mobile Belt (PMB), a deforming and seismically active zone, which is bound by subduction zones of opposite polarities (Gervasio, 1967; Lagmay et al., 2009). West of Panay is the east-dipping Early to Middle Miocene Negros Trench, whereas east of Samar is the west-dipping Pliocene Philippine Trench. The Philippine Fault Zone traverses this part of the Philippine Archipelago along Leyte (Allen, 1962) (**Figure 2**).

The oldest rock formation in Cebu is the Jurassic Tunglob Schist. It is overlain by the Cretaceous to Paleocene age Mananga Group, which consists of limestone, clastic sedimentary rocks, andesitic to basaltic pyroclastics and lava, calcareous mudstone, conglomerate and sandstone (Aurelio and Peña, 2010). Unconformably overlying the Mananga Group are a series of unconformable sedimentary and mostly calcareous formations that range in age from Late Eocene to Plio-Pleistocene age. Intruding into the Mananga Group at places is the Lutopan Diorite. In other areas of Cebu, the late Miocene Bulacao Andesite occurs as intrusive breccia and extrusive deposits of porphyritic andesite. Serpentinized ultramafic and mafic rocks occur as diapiric intrusions along major faults that cut across Cebu (Balce, 1977; Aurelio and Peña, 2010). The two youngest formations in the area of Cebu where the landslide took place and the subject of interest in this study, are the Late Miocene to Early Pliocene Barili and Plio-Pleistocene Carcar Formations, which are both calcareous in composition (Corby, 1951; Aurelio and Peña, 2010).

The nearest identified potentially active fault system from the Naga landslide is the Cebu Fault System, which is a northeast-trending fault system composed of two major structures: The

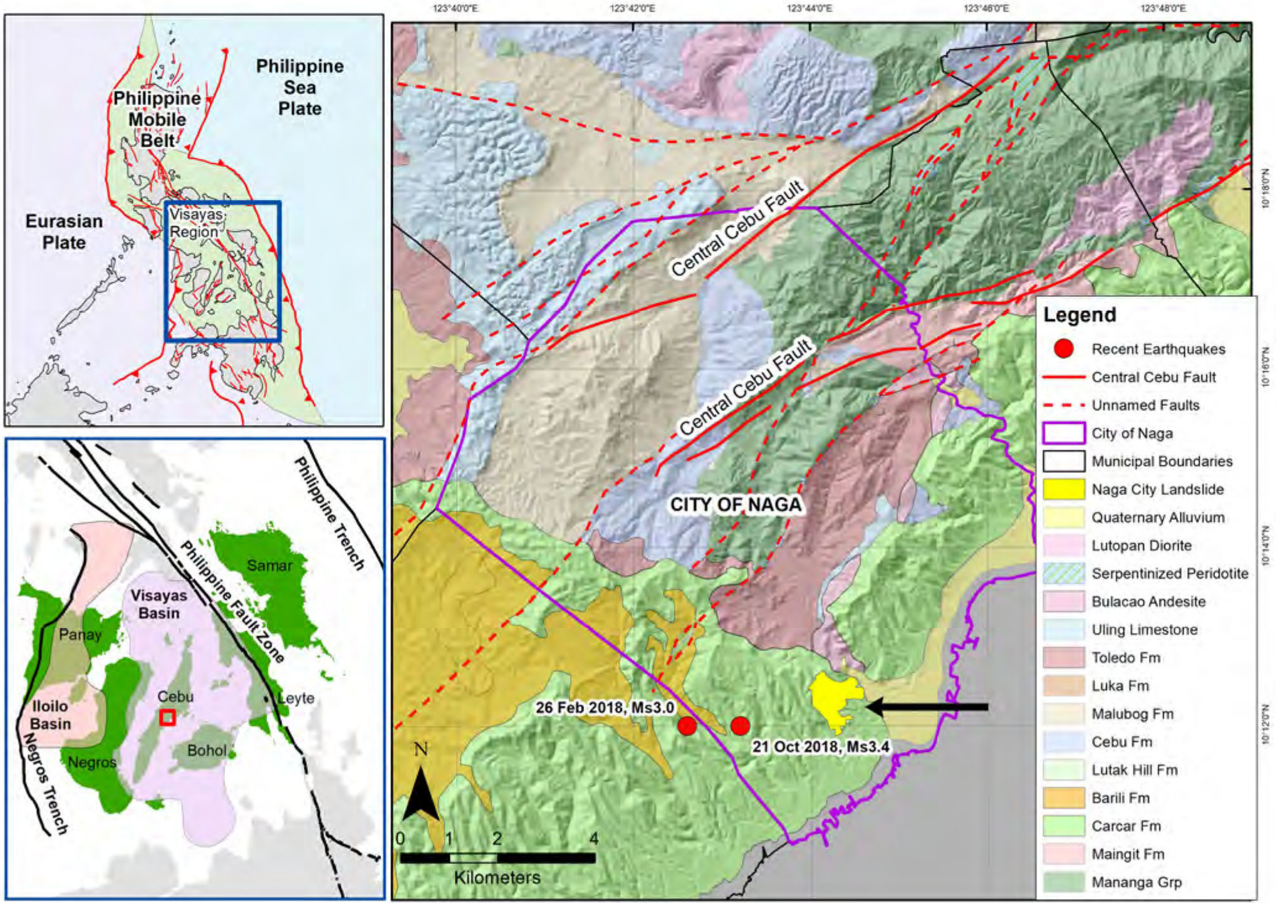

FIGURE 2 | The PMB is found within the convergent zone between the Philippine Sea Plate and the Eurasian Plate (adapted from Lagmay et al., 2009). The Visayas Region contains the Iloilo Basin and the Visayas Basin, wherein Cebu is located (adapted from Dimalanta et al., 2006). The City of Naga is located in central Cebu which is underlain by a basement complex of igneous, volcanic, sedimentary, and metamorphic rocks. Nearby is the active NE-SW trending Central Cebu Fault (PHIVOLCS) as well as numerous unnamed faults (MGB, 1983).

Central and the South Cebu faults (PHIVOLCS, 2016). The Central Cebu Fault passes through Naga City and is located 5.5 km west of the landslide. Other unnamed faults that were previously mapped (MGB, 1983) are consistent with the northeast trend of the Central Cebu Fault. Two earthquakes near the Naga Landslide area were recorded in 2018 by the Philippine Seismic Network with magnitudes 3.0 and 3.4, respectively. Both of these earthquakes were less than 33 km deep with the epicenters located within 3 km of the Naga landslide deposits (**Figure 2**).

3. METHODOLOGY

Satellite data from Planetscope and other aerial images were used to analyze the pre-event (8 September 2018) and post-event (21 September 2018) conditions of the Naga landslide. These orthorectified images contained 4 multispectral bands (blue, green, red, near-infrared), with a resolution of 3 m. The pre- and post-event satellite images were compared to identify the extent of the landslide deposit field. The change analysis was done a day after the landslide event and was used during the search and rescue phase of the disaster to identify buried houses at the distal portion of the debris field (GMA News and Public Affairs, 2018).

For better analysis, satellite images were augmented by crowd-sourced drone photo and video footages. The drone images were processed using digital photogrammetry to generate Digital Elevation Models (DEMs). In succeeding field surveys, a DJI Mavic 2 Pro drone equipped with a Hasselblad L1D-20c camera with a field of view (FOV) of about 77 deg, aperture of f/2.8-f/11 and shooting range of a minimum of 1 m was used to fill in gaps of the initial DEMs. The latter drone surveys were focused in the headscarp area, which was extremely difficult to access due to dangerous and harsh terrain created by the landslide event. Point clouds were created and transformed into a DEM and combined with the crowd-sourced data to create a post-event DEM of the entire landslide area. A 1 × 1 m Lidar pre-event DEM was used for change analysis of the topography. The pre- and post-event DEMs, with the same resolution, were used for the volume calculation.

Field data collection was conducted from November to December 2018, and in January and June 2019 to investigate the landslide area and vicinities. Lithologies, geological structures and morphology of the area were mapped. The consecutive field surveys were conducted to characterize the landslide deposit in detail.

Drill core data collected in the year 2010 was obtained as a supplement to field activities and were used for the generation of a 3-dimensional geologic model of the area. Contact relationships derived from the core data were used as the guiding base for 3D modeling in the Leapfrog Geo software. Core logs were assimilated across a directed core line which utilizes an implicit model to define boundaries between stratigraphic units and geologic structures. These surfaces were generated using a triangulated irregular network in between known data points and were projected along the lithologic boundaries.

The pre- and post-landslide high-resolution DEMs were used to compute the traveled horizontal distance (L) over a vertical height difference (H) to determine the angle of reach. Known as the Fahrböschung or Heim ratio (Heim, 1932), the reach angle was calculated from the high-resolution DEMs to demonstrate the efficiency of landslide motion. According to the analysis of Corominas (1996) on a global landslide dataset, movements showing the lowest angles of reach attain the farthest horizontal distance in relation to fall-height of the landslide. The mobility plot of Corominas (1996) showing H/L vs. volume was used in the analysis to determine the regression limits and confidence interval in the classification of the Naga landslide. The angle of reach was computed based on Equation (1):

$$\log(\frac{H}{L}) = -0.105 \log vol - 0.012 \qquad r^2 = 0.763 \tag{1}$$

where H is the vertical height difference and L is the horizontal projection of the distance. To be classified as a debris avalanche with a 95% mean confidence interval, the regression equation of Corominas (1996) requires a range of limits of -0.8607 and -0.6419, whereas for a translational slide, the range is from -0.7302 to -0.5454.

We also used the formula of Dade and Huppert (1998) to determine the area overrun by the landslide which has been demonstrated to be proportional to the potential energy of the debris mass. The long-runout scaling was computed using Equation (2):

$$A = (\lambda)^{\frac{1}{3}} (\frac{gMH}{\tau})^{\frac{2}{3}} \tag{2}$$

where A is the area overrun by the landslide, $\left(gMH\right)^{\frac{2}{3}}$ is the potential energy of the debris mass before failure, τ is the resisting shear stress and λ is the geometry parameter of the landslide. According to Dade and Huppert (1998), the magnitude of shear stress of resistance (τ) and ratio of landslide width and length (λ) limit the runout extent and is proportional to the area of the landslide footprint.

However, the relationship between the Fahrböschung angle and landslide volume is not as straightforward as it seems (Lucas et al., 2014). Therefore, the Naga landslide was further examined relative to two well-known debris avalanche deposits in the Philippines. These are the 1628 Iriga (Aguila et al., 1986; Paguican et al., 2012; Minimo and Lagmay, 2016) and the 2006 Guinsaugon (Lagmay et al., 2006; Evans et al., 2007; Catane et al., 2008) landslides, which also had long reaches relative to their collapse height. Additionally, a recent study of the 2018 Naga landslide classifying it as a low-angle translational block slide (Catane et al., 2019) was included in the comparative analysis. Landslide parameters used in the comparative analysis include debris volume, area covered, vertical height, and horizontal distance for each of these landslide events as described in the literature. Where other parameters are absent (i.e., Fahrböschung angle), these were measured in maps or computed using given associated values included in the respective publications. Through calculations using the Corominas (1996) and Dade and Huppert (1998) equations, the deposits of the three landslides were compared to determine their similarities and differences, if any. The comparative analysis was made to better understand the Naga landslide and its nomenclature. The presence of geomorphic and structural features characteristic of debris avalanche deposits which includes: (1) megablock structures; (2) jigsaw puzzle effects; (3) hummocks; and (4) an amphitheater at the source (Ui, 1983; Siebert, 1984; Andrade and de Vries, 2010; Davies et al., 2010; de Vries and Delcamp, 2015), was critical in the analysis.

Scaled analog models that investigated geomorphic features, in particular hummock formation, were also used to characterize the deposit features observed in the Naga landslide deposit and to interpret their formation. For example, hummocks, which were demonstrated through laboratory models to form by extension of large blocks during the collapse event were compared to the pinnacle hummocks pervasive in the Naga landslide debris field. Analog model structures associated with hummock formation, such as normal faults, horsts and grabens were compared with those found in the Naga landslide deposits.

The Naga City landslide's morphology, geology, structures, runout behavior (according to Corominas, 1996; Dade and Huppert, 1998), comparison with known debris avalanches of the Philippines and analog models for large-scale volcanic and non-volcanic collapses of Paguican et al. (2014) were then integrated in the analysis. This was done to gain insights on the kinematics and dynamics of debris avalanches and advance our understanding on their long-runout behavior to prevent or mitigate their impacts in future events.

4. RESULTS

4.1. Morphology

Planetscope satellite images taken a day after the landslide event reveal a striking land cover change (**Figures 3A,B**). The areas that exhibit the biggest difference in surface conditions are those within the scarp area at the elevated regions of the quarry site and the two lobes of the landslide deposit in Barangay Naalad and Sitio Sindulan, Barangay Tinaan (**Figure 3**). The region near the headscarp was vegetated as clearly seen from the pre-disaster satellite image (**Figure 3A**). After the collapse and mass movement, the underlying limestone was largely exposed and is seen in the post-disaster satellite imagery with high albedo. At the distal end of the landslide deposit in Barangays Tinaan

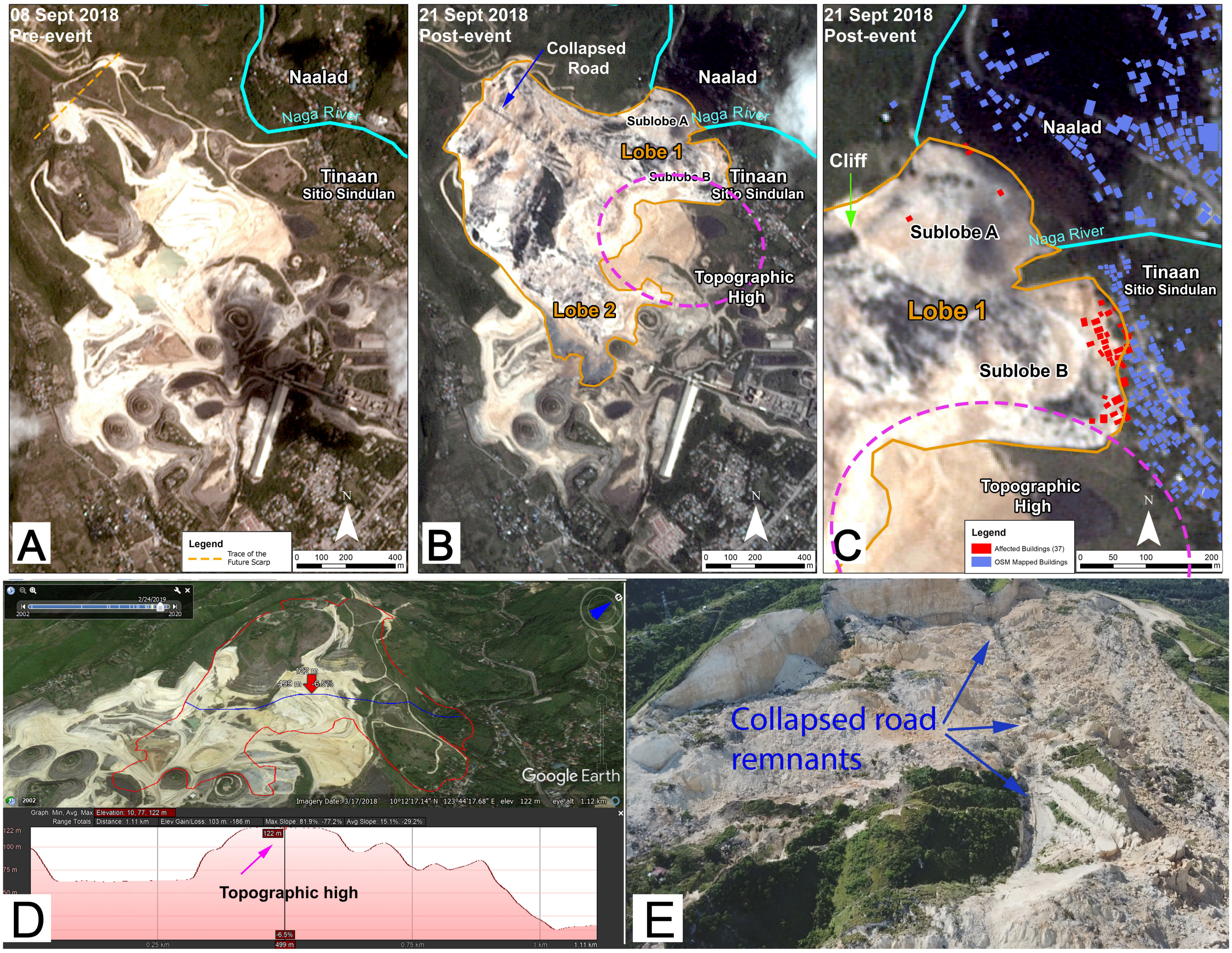

FIGURE 3 | Planetscope satellite images of the Naga landslide area **(A)** before and **(B)** after the Naga disaster **(C)** close up of the Lobe 1 with building footprints (OpenStreetMap contributors, 2017). There were 37 houses buried in Sublobes A and B. **(D)** Pre-event cross-section from Google Earth show the "topographic high" that disrupted/diverged the flow of the materials which caused the formation of Lobe 1 and Lobe 2. A natural cliff also caused the formation of Sublobe A and B. Another notable feature of the event is the **(E)** remnants of the road that collapsed and formed a seemingly linear feature.

and Naalad, 37 houses were buried in debris (**Figure 3C**). These residential areas at the toe of the landslide were buried up to 10 m as measured in the field and the DEMs. The Naga River was dammed as well. Quarried areas that were covered by the September 2018 Naga landslide deposit event did not show any significant change in NDVI values in pre- and post-disaster Planetscope imageries.

There are two lobes at the distal end of the landslide debris field. The first is located in the northern side (Lobe 1) whereas the second is in the southern side (Lobe 2). In between these lobes, is a topographic high that diverted flow toward two directions (**Figures 3B,D**). The topographic high has a maximum pre-event elevation of 120 masl whereas the areas which eventually became Lobe 1 and Lobe 2 only have maximum pre-event elevations of 55 and 80 masl, respectively. This elevated portion acted as a barrier along the landslide path and prevented the axial part of the landslide to equally spread further downslope. The diversion of flow effectively shortened the landslide runout to 830 m in the axial portion and caused the formation of a two-lobed landslide deposit field. The pre-event, frontal plane cross-section of the landslide area (**Figure 3D**) shows the topographic high that caused the diversion of materials. Furthermore, a natural cliff with an elevation of 60 masl dropping to 30 masl eventually caused the formation of sublobes A and B (**Figure 3C**). The collapse of this cliff and the overflow of landslide material from the top section can clearly be seen from the CCTV (see **Supplementary Video 1**, BJMP-NAGA, 2018). It may look like a waterfall or some dewatering has happened, but the deposits are dry and debris flows did not form. A significant amount of dust clouds was seen generated during mass movement, indicating relatively dry material. Debris flows would have also formed if there was a significant amount of water present.

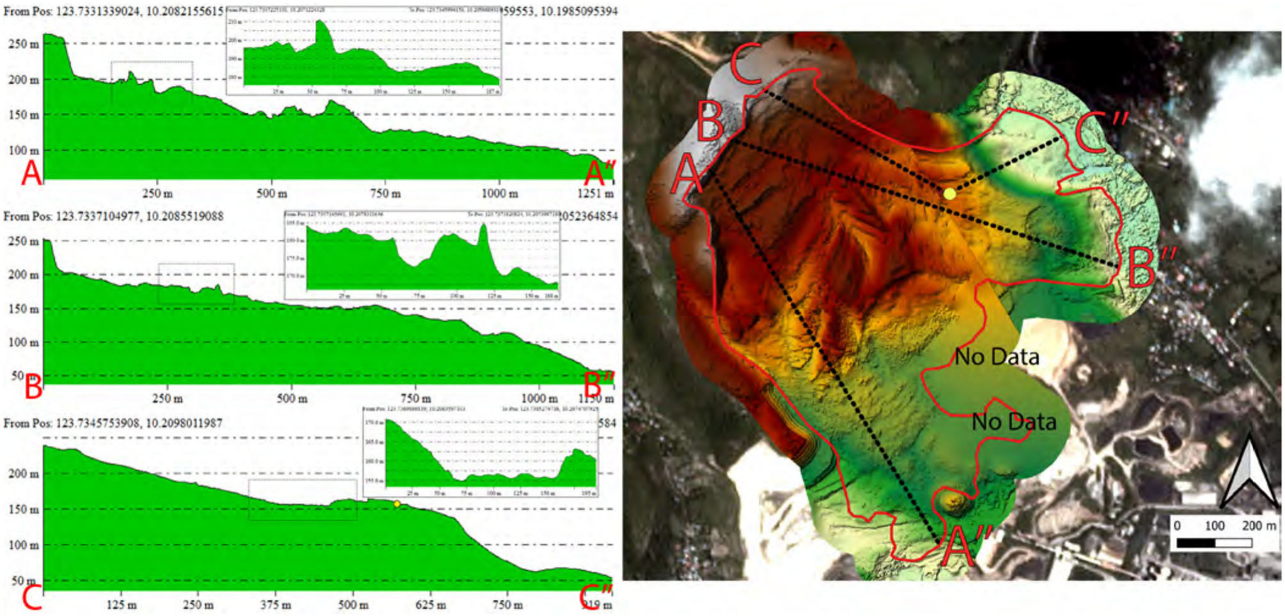

FIGURE 4 | Cross sections of the Naga landslide based on a DEM generated from drone images.

The post-event DEM used for detailed analysis of the Naga Landslide has a resolution of 33 × 33 cm. This post-event DEM was resampled to match the 1 × 1 m resolution of the pre-event LiDAR DEM to calculate the 11,000,000 m^3 volume of the Naga landslide. Cross-sections derived from the DEM, show prominent hummocks and rotated toreva blocks (**Figure 4**). Toreva blocks are commonly composed of one or more blocks that slide and retain the original stratigraphic sequence, whereas hummocks are mound features composed of block material in the surface with a form of conical shape and have a height of tens to hundreds of meters (Ui, 1983; Stoopes and Sheridan, 1992). Hummock sizes in the Naga deposit field decrease in dimension away from the headscarp, consistent with the descriptions in other debris avalanche deposits (Reiche, 1937; Ui, 1983; Crandell et al., 1989; Thompson et al., 2010; de Vries and Delcamp, 2015). The high-resolution DEM also reveals that the highest elevation of the failure is at 255 masl, whereas the elevation at the toe in Lobes 1 and 2 is 50 and 70 masl, respectively. In terms of maximum distance traveled from the headscarp, the landslide is measured at 1.1 km at Lobe 1 and 1.2 km at Lobe 2.

Noticeable in the debris field are large tilted blocks found at the medial to proximal section of the 1.2 km landslide (**Figure 5**). The tilted blocks or toreva blocks manifest as rows of broken material with their long axis perpendicular to the direction of the landslide. The largest blocks within the debris field have widths ranging from 120 to 350 m and traveled up to 220 m. Careful analysis of a linear feature (**Figures 3B,E**) that appears to divide the torevas in the proximal collapse zone of the landslide, reveal a road that subsided and whose parts were preserved as a large, intact landslide block (**Figure 3E**). The torevas at both sides of the road are found to be contiguous upon closer examination and indicate a single collapse event.

Pinnacle hummocks were also identified at the medial section of the Naga debris field. The sizes of the hummocks vary but are as large as 15 m in height and 10 m in width at its base. These hummocks appear as the remains of highly stretched blocks that have developed normal fault structures with horst and graben structures (**Figure 5**). High-standing hummocks are horst structures with adjacent grabens separated from them.

The distal portion of the deposit field is comprised of smaller blocks compared to the proximal and distal portions (**Figure 6**). The range of sizes of the blocks are 5 to 15 m and are surrounded by non-graded angular finer-sized fragments. These fragments vary from clay (<1/256 mm) to larger than gravel sizes (2–64 mm). In Lobe 1, the largest blocks are up to 6 m in size whereas in Lobe 2, blocks are up to 15 m.

Large mobilized intact blocks (MIB) are present in the proximal and medial portion of the landslide. Relatively smaller blocks compared to the MIBs, but still up to several meters in size, are scattered in the proximal and medial portions of the debris field with their sizes generally decreasing away from the headscarp. These blocks, no matter their size, commonly exhibit jigsaw cracks and are surrounded by a finer-grained matrix composed of fragmented limestone (**Figure 7**).

Other notable morphological features include; a linear headscarp that extends for about 734 m and largely intact MIBs that had been translated over an average distance of 225 m without being overturned. Houses and trees on top of these large blocks remain standing.

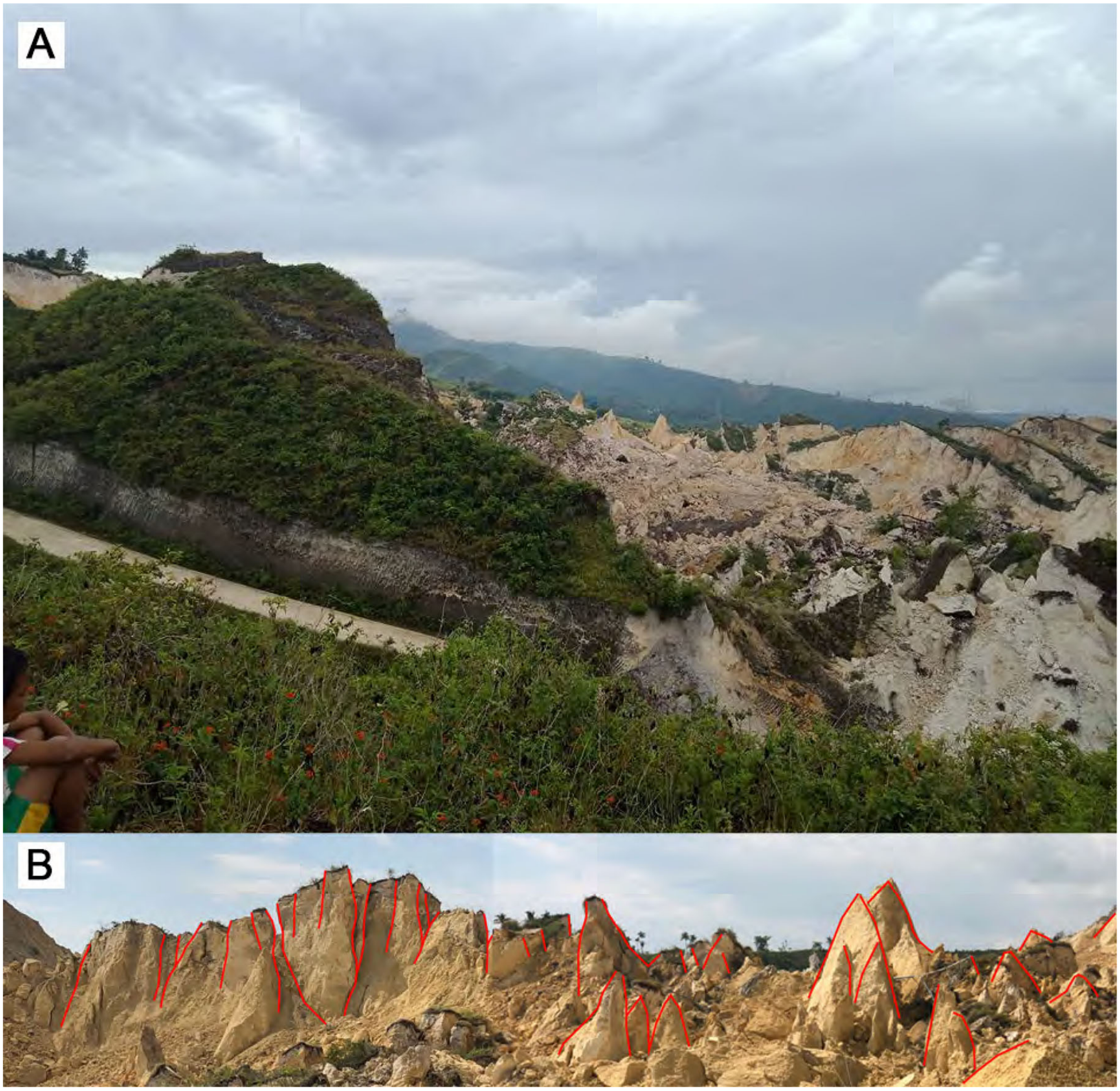

FIGURE 5 | (A) View looking north. Rotated toreva blocks at the proximal portion of the debris field (UP-CENVI, 2018). **(B)** View looking south-southeast. Horst and Graben structures and pinnacle hummocks formed due to faulting as the slide was extending.

4.2. Geology

The landslide area is composed of two geological formations as seen from the exposed amphitheater walls of the collapsed scarp. The lower part is the Barili Formation of Late Miocene to Early Pliocene age (Mines and Geosciences Bureau, 1981), which consists of a lower limestone member and upper marl member. The limestone is hard, light brown, coralline, locally porous or sandy, richly fossiliferous, whereas the marl is generally brown, slightly sandy poorly bedded and, fossiliferous with thin limestone interbeds (Del Rosario et al., 2005). In general, the bedded outcrops seen at the fringes of the landslide were classified as part of this formation. The Barili Formation is overlain by the poorly bedded to massive Plio-Pleistocene Carcar Formation, which according to the literature is composed of more coralline limestone and partly dolomitic.

The exposed calcareous formations within the landslide zone are more than 50 m thick and are underlain by a 3 m-thick sandstone/siltstone bed. This sandstone/siltstone bed, which is most likely the Marl component of the Barili Formation, is distinguished from the buff-colored limestone and appears in the quarry site of the Apo Tenement at 60 m elevation. Boulders of siltstone are also found in some areas of the debris field. The contact between the limestone and the sandstone/siltstone is clearly seen in some of the boulders within the avalanche deposit (**Figure 6D**).

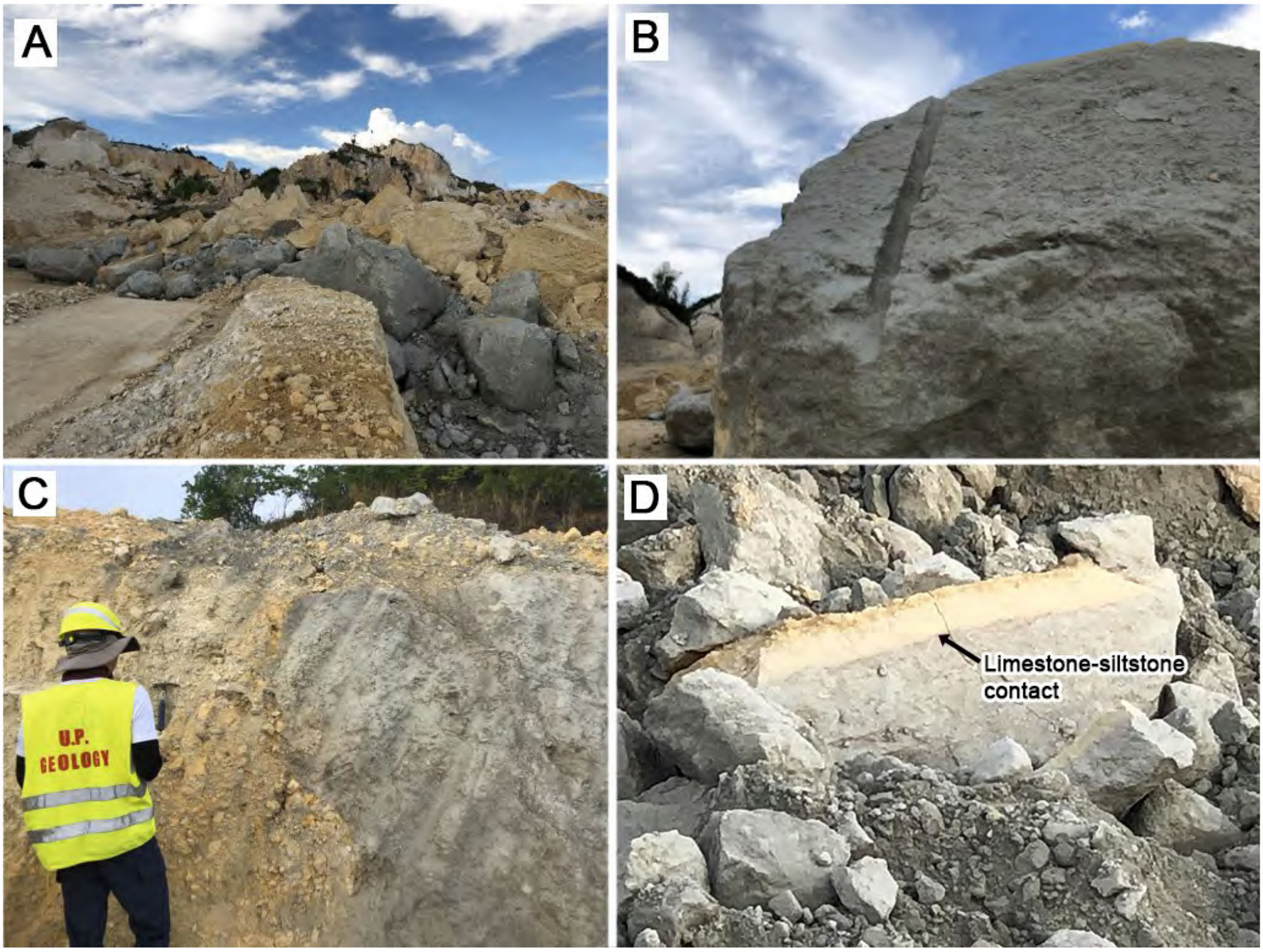

FIGURE 6 | (A) Sandstone/siltstone in the debris field of the landslide. **(B)** A drill hole mark is evident in a boulder. **(C)** Sandstone and limestone deposit. **(D)** The contact between the limestone and the siltsone is clearly seen in a boulder in the debris field.

4.3. Core Data

From April to May 2010, 12 boreholes within the Mineral Production Sharing Agreement (MPSA) 286 and 137 tenements of the Apo Land and Quarry Corporation were drilled and logged. Out of these, nine boreholes within the landslide area were used in this study. The elevations of these boreholes range from −0.5 to 242.7 masl with a drill depth of 40 to 121.5 m. The boreholes show limestone as the thickest and topmost lithology along the length of each core topped by a thin layer of topsoil. The limestone core logs are described as ranging from hard to soft with predominance of semi-hard to soft limestone descriptions. Sandstone with thickness ranging from 1.2 to 42.6 m underlie the limestone. Other lithologies described in the corelogs include lime, black clay, black shale, blackstone, gray and black pozzolan, green sands and soft clay. The Leapfrog plots reveal dipping beds with limestone above a less coherent layer of sandstone (**Figure 8**). The average dip angle of these layers is 7.65 deg with an average dip direction of N87.16°E toward the sea and in the direction of the landslide. This dipping bed and deposition plane between the sandstone and limestone beds is identified as the sliding plane where the landslide moved.

4.4. Structural Geology of the Landslide

The headscarp of the landslide is planar. Numerous measurements in different areas from top to bottom and north to south of this approximately 70 m-high and 734 m-wide planar structure show a northeast strike direction and a dip angle in the range of 58–90 deg. Slickenlines and slickensides (**Figure 9**) are also present on this plane with striations that have a rake angle of 69.9 deg. Striations with similar slickenlines are observed everywhere in this planar landslide head wall.

About 30 m at the back of the landslide scarp, faults were also observed. Generally, northeast-trending fractures are also present in the north and southern margins of the headscarp whereas numerous northeast-trending tension cracks were observed on top of the head wall that continue to widen (**Figure 10**). The entire area of Naga City has numerous faults that are mainly oriented northwest or northeast directions (**Figure 11**). These faults, however, maybe of various ages

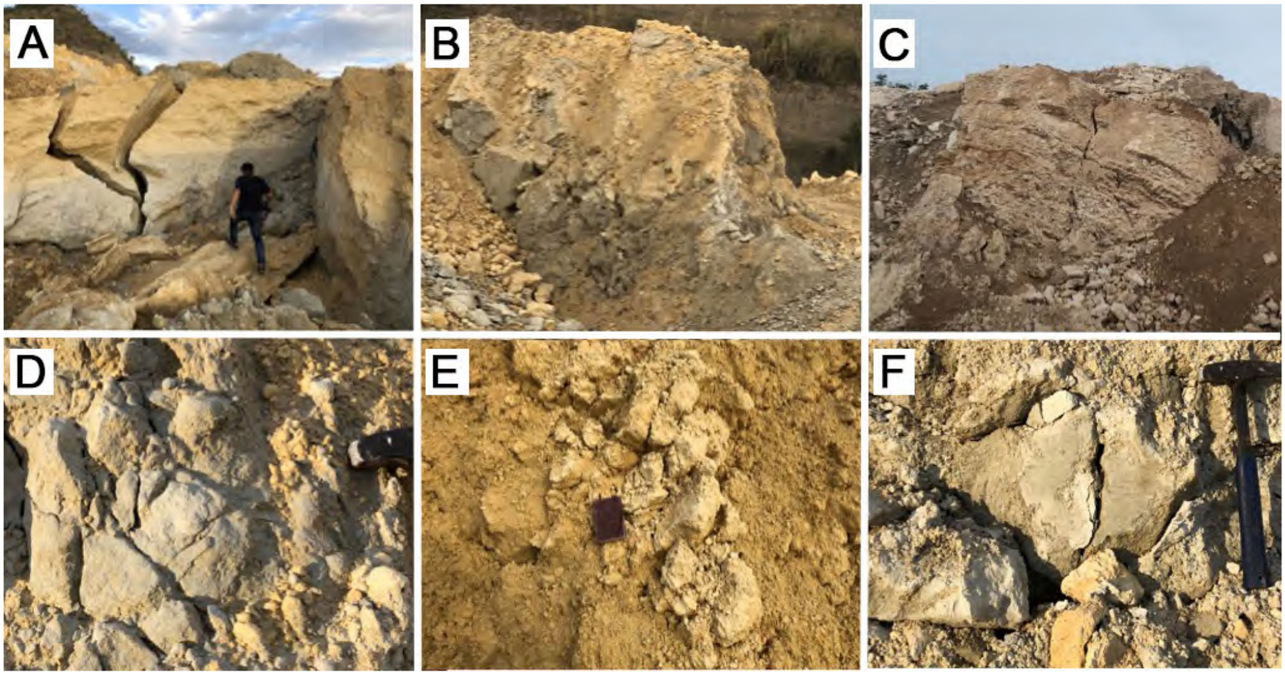

FIGURE 7 | (A–F) Boulders and blocks with jigsaw cracks.

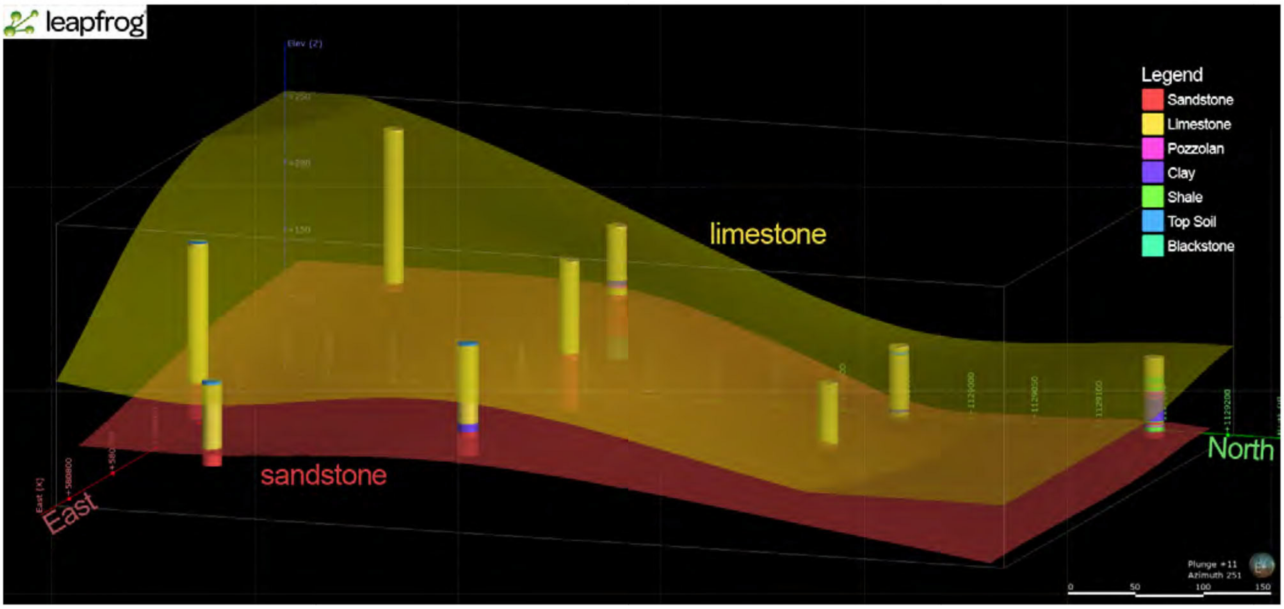

FIGURE 8 | Nine borehole data were modeled to show the lithology of the study area. A dipping layer of limestone lays on top of a sandstone layer.

given the range of rock types with various ages they cut through. Of particular interest are the set of fractures that have a general northeast direction, which correspond to the northward projection of the strike of the Naga landslide head wall (**Figure 12**).

4.5. Quantitative Classification of the Naga Landslide

The H/L ratio of the Naga landslide yields a Fahrböschung angle of 9 deg. Using this angle and the measured volume of 11,000,000 m^3 from DEMs, the Naga landslide deposit plots in the field of

FIGURE 9 | A N66°E fault plane at the landslide head showing slickensides and slickenlines with a 69.9° rake angle. Oblique slip movement is suggested by the direction and orientation of the slickensides.

debris avalanches together with 71 similarly classified events out of the 204 landslides in the global dataset used by Corominas (1996) (**Figure 13**). Based on the regression equations for each type of landslide, the 2018 Naga landslide event falls under the category of debris avalanches with a 95% confidence interval.

The range of shear strength of resistance for terrestrial avalanches is from 10 to 100 kPa (Dade and Huppert, 1998). According to the empirically-derived equations of Dade and Huppert (1998) and given the range of shear strength for avalanches, the Naga landslide with a measured collapse height of 200 m and volume of 11,000,000 m^3, classifies as a long-runout rockfall if its depositional area falls within 551,571–2,456,460 m^2. Our calculations of the area covered by the Naga landslide yields a value of 770,723 m^2, which is within this range. This power law relationship has a 2/3 exponent and is a best-fit regression line with a 95% confidence interval for 76 long-runout rockfalls or rock avalanches that were studied by Dade and Huppert (1998).

4.6. Comparative Analysis With Well-Known Philippine Debris Avalanches

The Naga landslide has a Fahrböschung angle of 9 deg (this study), which is less than the 16 deg Fahrböschung angle reported by Catane et al. (2019). The measured volume is 11,000,000 m^3 and is much lower than the 27,000,000 m^3 volume reported by Catane et al. (2019) (**Table 1**). Our estimate of the volume is based on the subtraction and cut and fill calculations of the pre-event and post-event high resolution DEMs. On the other hand, the volume of the Naga landslide reported by Catane et al. (2019) is from field estimates and terrain data derived from a 2013 Interferometric Synthetic Aperture Radar (InSAR), satellite images, and drone surveys.

For the Guinsaugon debris avalanche, Evans et al. (2007) reported a Fahrböschung angle of 12 deg and a volume of 15,000,000 m^3, whereas Lagmay et al. (2008), published a volume of 15,000,000 m^3 and a 10 deg Fahrböschung angle based on their reported H/L ratio. Lastly, the Iriga debris avalanche (DAD2) has a reported H/L ratio equivalent to a Fahrböschung angle of 6 deg (Paguican et al., 2012) and a volume of 1,500,000,000 m^3 (Aguila et al., 1986). Based on the reported volumes, H/L ratios and equivalent Fahrböschung angles, the Iriga, Guinsaugon, and Naga landslides, all fall within the debris avalanches category with a 95% confidence interval according to the Corominas (1996) classification with the exception of the parameters used in the report of Catane et al. (2019).

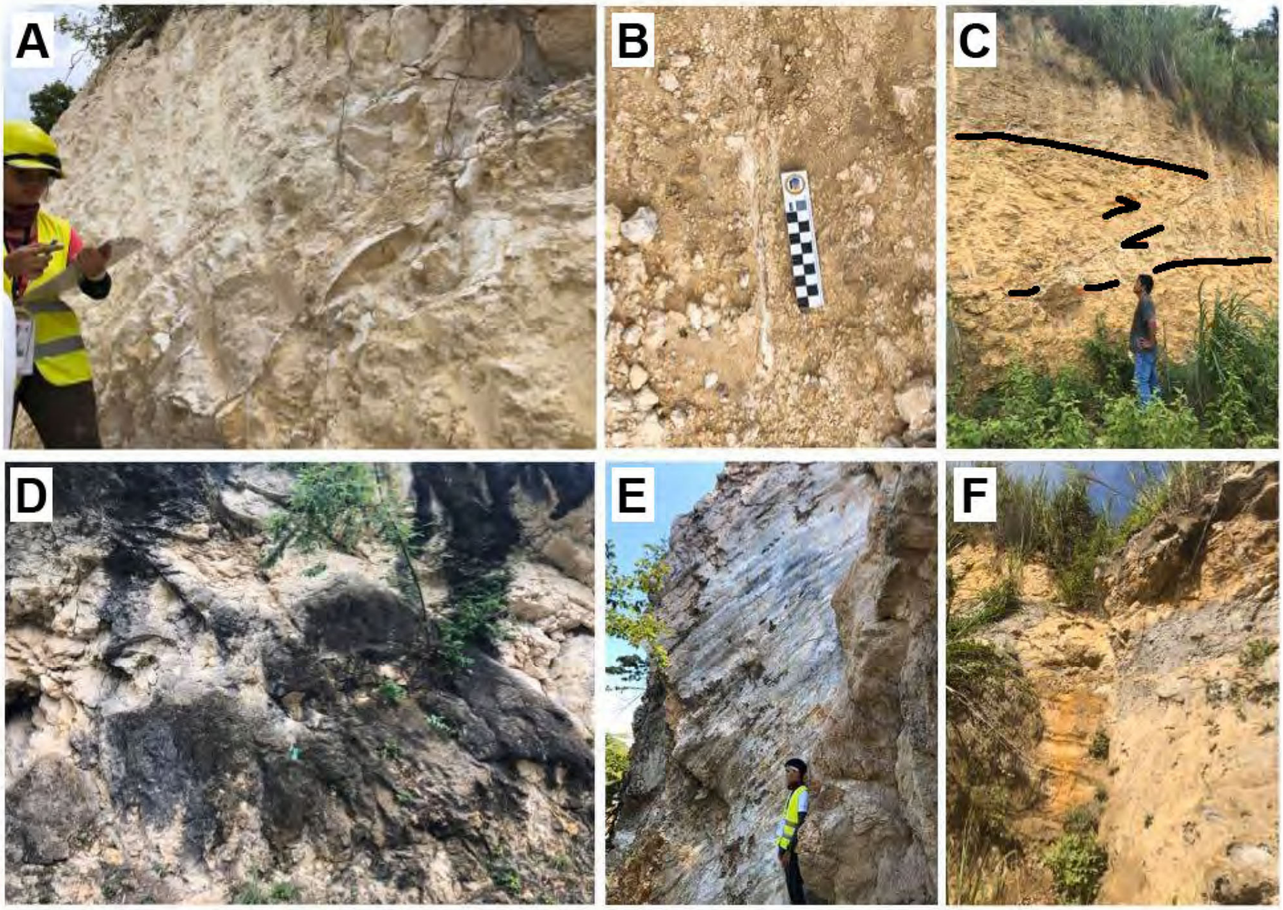

FIGURE 10 | (A–C) Faults at the margins of the headscarp. **(D–F)** Faults in areas farther from the landslide (please see **Figure 11**).

In terms of the equation used by Dade and Huppert (1998), the area covered by the Guinsaugon landslide as reported by Evans et al. (2007) and Lagmay et al. (2008) is within the range of the shear strength of resistance for the prediction of extent of runout for debris avalanches. Similarly, the area of the 1628 Iriga debris avalanche falls within the range of possible shear strength values of debris avalanches and consistent with the power-law relationship between the area and potential energy for long-runout rockfalls or rock avalanches. On the other hand, the area reported by Catane et al. (2019), when calculated using the equation of Dade and Huppert (1998), yields a value of 102 kPa, which is out of the range of shear strength values for debris avalanches.

4.7. Comparison With Analog Models

Scaled analog models were used by Paguican et al. (2014) to study hummock formation and explore their importance in understanding landslide kinematics and dynamics. These models have been used to characterize hummocks in terms of their evolution, spatial distribution, and internal structure from slide initiation to final stop. The models were designed to replicate large-scale volcanic collapses but are also relevant to non-volcanic settings.

The analog model structures of Paguican et al. (2014), in particular the rotated torevas and hummocks, are consistent with field observations of the Naga landslide and suggest a general brittle slide emplacement (**Figure 14**). The sliding block is composed of brittle limestone, which when extended during transport, forms hummocky structures. Inter-hummocks or those in between hummocks are more broken, finer-grained matrix facies derived from the excessive extension during transport (de Vries and Delcamp, 2015). Hummocks with faults that formed horst and graben structures were preserved within the proximal to medial portions of the Naga landslide deposit field. Thus, the existence of these features imply the presence of sufficient cohesion of the landslide material, such that they remained intact despite the downward movement and spreading.

5. DISCUSSION

5.1. Landslide Impact

The Naga landslide was an unfortunate event that caused fatalities because of its unexpected long-runout and vastly

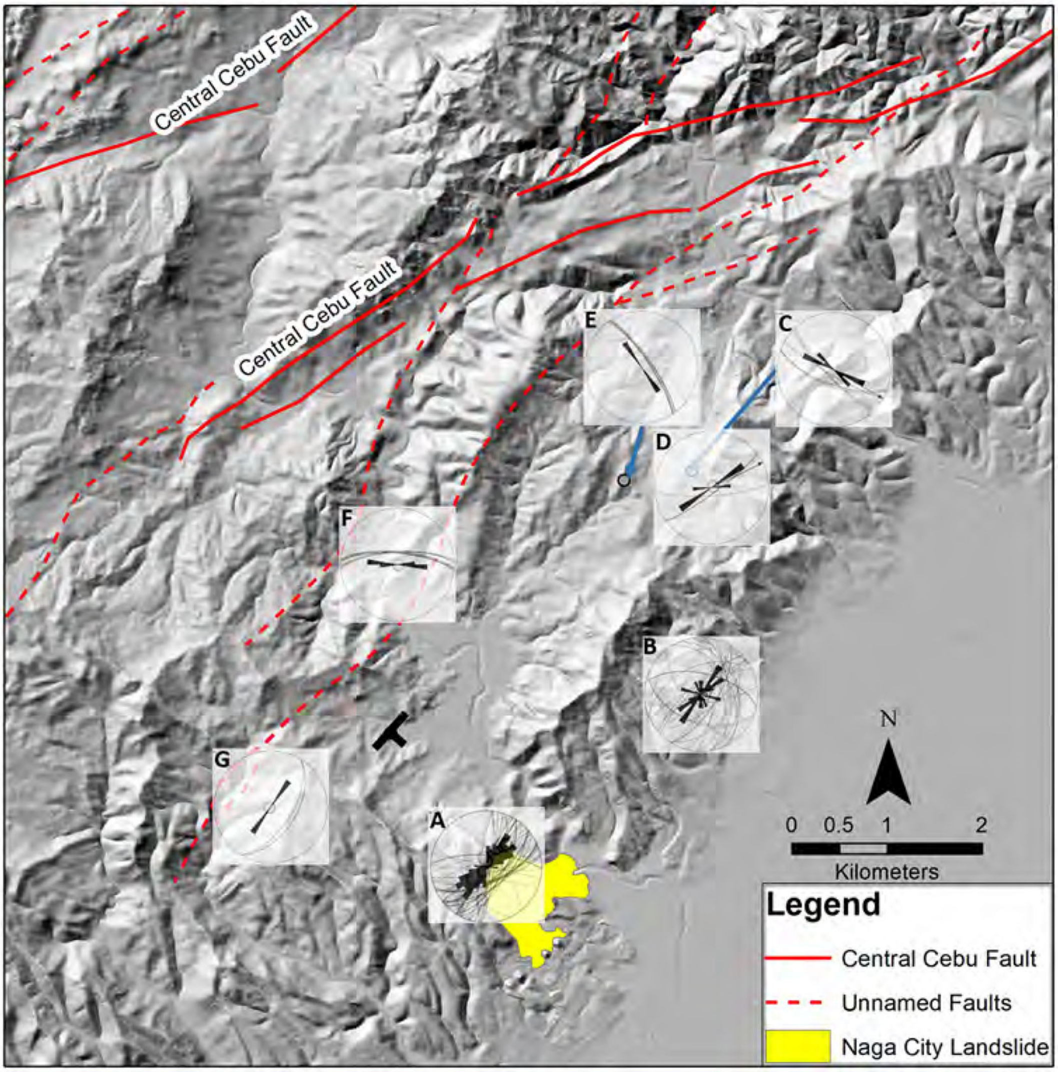

Location	Size	Max Value	Mean Vector	Ave. Length	Circ. Variance	Kappa Krumbein's axial mean; uncertainty is 1 standard error, for 95% confidence level multiply by 1.96
A	67	12.19512% between 031° and 040°	045.5° ± 12.7°	0.3412	0.6588	0.7236
B	28	17.85714% between 031° and 040°	035.2° ± 25.5°	0.2986	0.7014	0.6062
C	6	50% between 111° and 120°	120.2° ± 09.5°	0.9238	0.0762	6.5394
D	3	66.66667% between 051° and 060°	063.8° ± 18.0°	0.8621	0.1379	3.9107
E	7	100% between 141° and 150°	325.4° ± 02.2°	0.9988	0.0012	100
F	11	63.63636% between 091° and 100°	091.9° ± 02.4°	0.9919	0.0081	50.242
G	3	100% between 031° and 040°	032.0° ± 00.5°	1	0.0	5000

FIGURE 11 | Stereoplots and rose diagram plots of structural measurements in Naga City. **Figures 10A–C** found in rose diagram A. **Figure 10D** in rose diagram B. **Figure 10E** in rose diagram E. **Figure 10F** in rose diagram D.

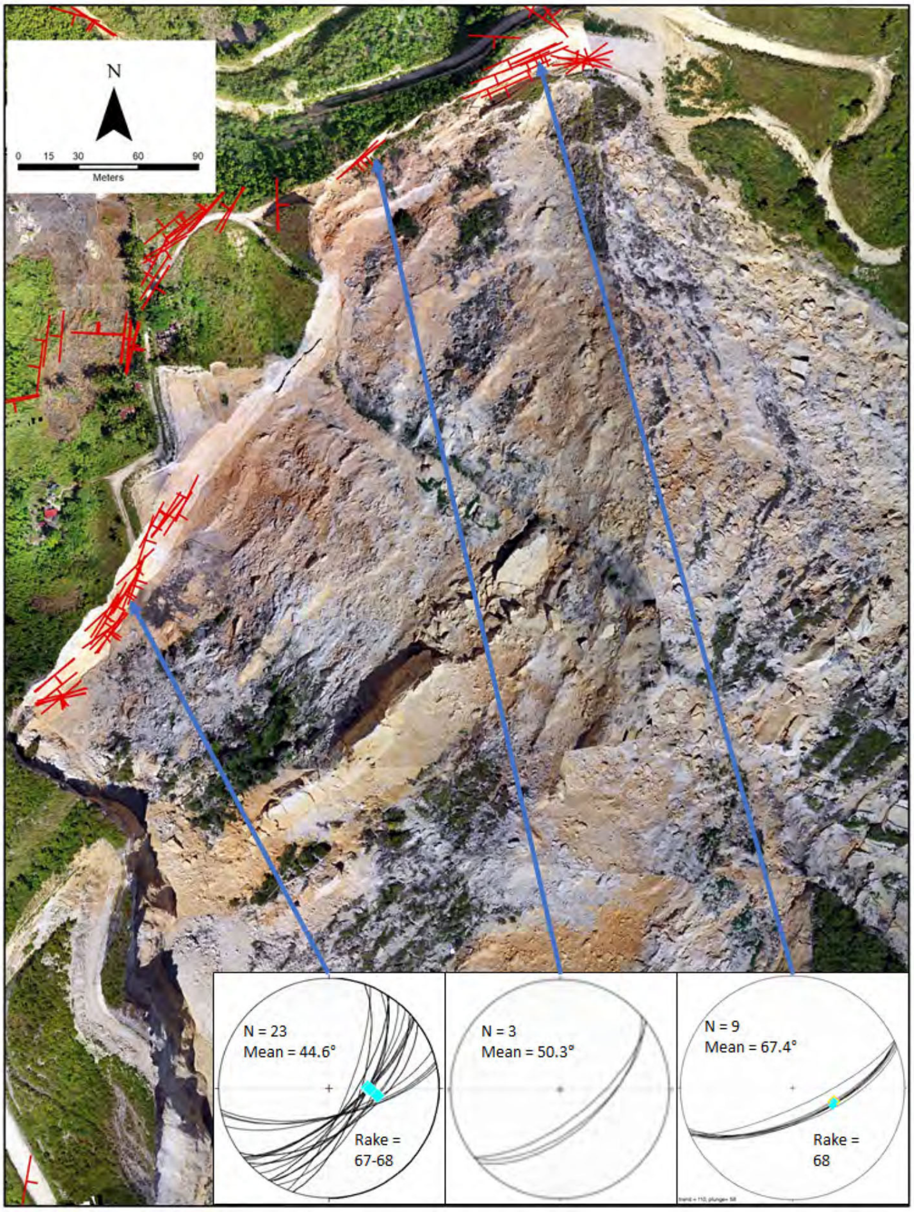

FIGURE 12 | Landslide head wall with fault measurements. The image is an orthomosaic map overlain on a DEM image.

underestimated impact. Destabilizing conditions and possible triggers that culminated into a massive landslide have been discussed by Catane et al. (2019). They conclude that there was no apparent trigger for the landslide, citing minimal rainfall and no earthquakes immediately prior or during the slide, even though a M_s 3.0 tectonic earthquake occurred on 26 February 2018 about 3 km away. However, the failure was attributed to a marginally stable slope along a low-angle surface. According to Catane et al. (2019), failure could have been due to progressive weakening of the slope mass or further modification and disturbance of the slope. We agree that there is no apparent trigger but note that there was a post-landslide tectonic earthquake with M_s 3.4 on 21 October 2018, which happened 1.5 km away from the landslide area (**Figure 2**). These may be related to the faults identified in the immediate area of the landslide as both are shallow earthquakes with depths less than 33 km (**Figure 11**).

From the viewpoint of disaster prevention and mitigation, the manifestation of structures ranging from hairline fractures to several centimeter-wide cracks, which developed a month prior to the event, is very important as it represented a clear warning sign. Due to these telling events, residents close to the headscarp were evacuated by authorities a day before the landslide occurred

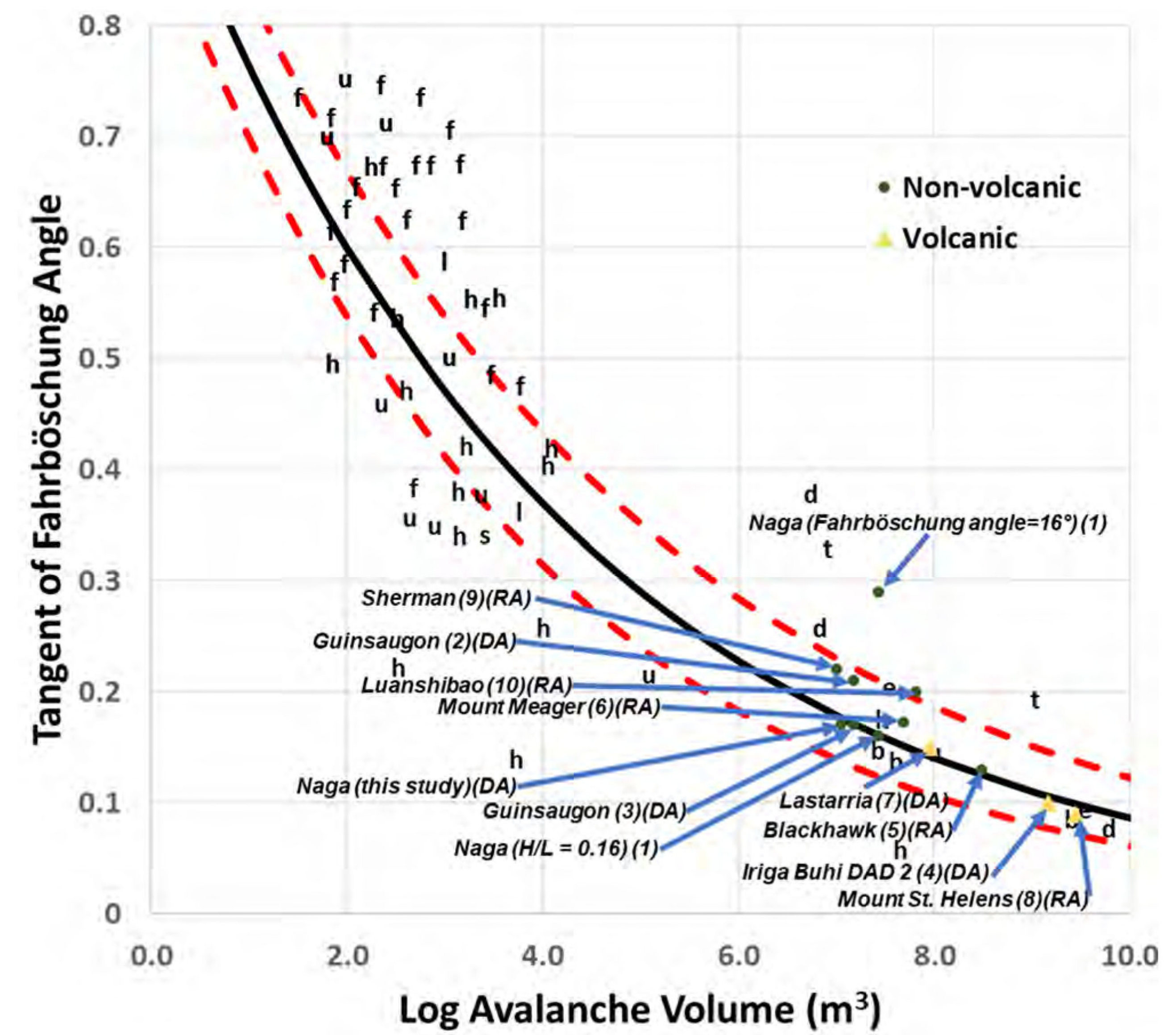

FIGURE 13 | Modified plot of debris flow and debris avalanche volume vs. tangent of reach angle for 71 events from Corominas (1996) and additional data. Labels correspond to the obstacles and topographic constraints of the path: f, dense forest: l, open forest; s, scree deposit; b, bends; d, deflections; t, toe thickening in a fan; h, channeling; w, opposing wall; u, unobstructed with free lateral extension. Black line represents the regression equation derived from the dataset whereas the red dashed lines show its corresponding upper and lower limits. Additional data are included to show how the Naga Landslide fits in the global context of debris and rock avalanches. References are as follows: (1) Catane et al., 2019, (2) Evans et al., 2007, (3) Lagmay et al., 2008, (4) Paguican et al., 2012, (5) Johnson, 1978, (6) Guthrie et al., 2012, (7) Naranjo and Francis, 1987, (8) Voight et al., 1983, (9) McSaveney, 1978, (10) Wang et al., 2018 whereas *DA* and *RA* stand for *Debris Avalanche* and *Rock Avalanche*, respectively.

but the more populated communities one kilometer downslope were not (MGB, 2018). The massive translation of part of the quarried mountain stretched the sliding body, which accelerated to create a long-runout landslide that buried houses far from its source relative to its collapse height. Had the residents in the distal areas been evacuated along with the residents in the areas near the headscarp, then unnecessary deaths could have been avoided.

A review of the 2018-2022 Local Disaster Risk Reduction and Management (DRRM) Plan of the City Government of Naga, certified by the Office of Civil Defense Region 7 based on their formal review along with the Technical Working Group composed of DRRM-mandated agencies, showed that the areas near the headscarp were highly susceptible to landslides while the distal areas buried by the Naga landslide were classified to have low susceptibility (CDRRMO of Naga City, Cebu, 2018). This may have been the basis for the evacuation of the highland areas proximal to the headscarp but not the hard hit lowland areas about 1.2 km away from source of the Naga landslide, which were mapped to have low susceptibility to landslide

TABLE 1 | Computational analysis of Naga Landslide and other known Debris avalanches.

Parameter	**NAGA (this study)**	**NAGA (Catane et al., 2019)**	**Guinsaugon (Evans et al., 2007)**	**Guinsaugon (Lagmay et al., 2008)**	**Iriga Buhi DAD 2 (Paguican et al., 2012)**
Height (m)	200	210	810	700	1,200
Length (m)	1,200	1,340	3,800	4,100	12,000
Volume (m^3)	11,000,000	27,000,000	15,000,000	15,000,000	**1,500,000,000
Area (m^2)	1,080,000	946,000	3,200,000	3,300,000	70,000,000
H/L	0.17	0.16	0.21	0.17	0.1
Fahrböschung angle (°)	9	16	12	*10	*6
$(gMH/\tau)^{\frac{2}{3}}$ at 10 kPa (m^2)	2,560,167	4,812,549	8,277,291	7,509,832	261,701,703
$(gMH/\tau)^{\frac{2}{3}}$ at 100 kPa (m^2)	551,571	1,036,832	1,783,288	1,617,944	56,381,923
$A = \lambda^{\frac{1}{3}}(gMH/\tau)^{\frac{2}{3}}$ at 10 kPa (m^2)	2,456,460	4,450,842	6,328,094	5,394,901	254,220,379
$A = \lambda^{\frac{1}{3}}(gMH/\tau)^{\frac{2}{3}}$ at 100 kPa (m^2)	529,228	958,905	1,363,347	1,162,296	54,770,120
$gMH/\tau)^{\frac{2}{3}}\tau$ (kPa)	34	102	28	21	69

**Measured from the respective publication, **From* Aguila et al. (1986).

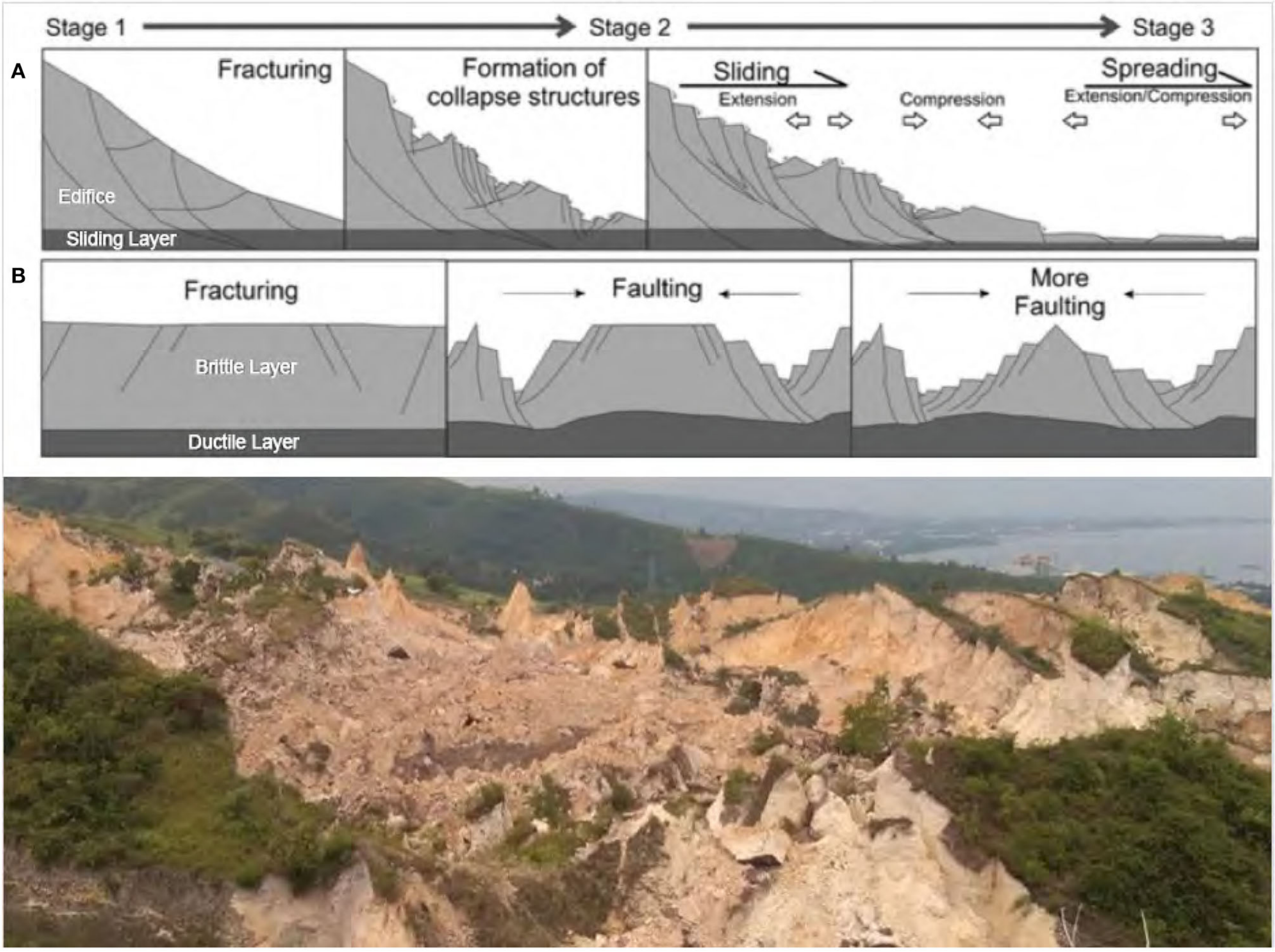

FIGURE 14 | Comparison of analog models of Paguican et al. (2014) with the Naga landslide hummocks and toreva blocks. **(A)** The different stages of avalanche emplacement showing an interpretation of hummock formation and **(B)** degree faulting.

hazards. This demonstrates clearly that landslide hazard maps are very important as basis for disaster prevention efforts. Such landslide susceptibility maps need to reflect the appropriate understanding of the kinematics of landslides, in particular debris avalanches.

5.2. Landslide Classification

Various geometric parameters of the Naga event measured using satellite imageries and DEMs derived from drone aerial photos made it possible to characterize the morphology of the Naga Landslide and calculate the H/L ratio, volume, Fahrböschung angle and the involved resisting shear stress during transport and emplacement. Based on these mentioned parameters and along with the description of the structural and geomorphic features of the landslide deposit, we were able to categorize the Naga landslide as a debris avalanche.

In general, there is another type of landslide that generates low H/L ratios. These are debris flows which also have a long-runout. Although lahar (mud flow and debris flow) deposits have textures and internal structures similar to the matrix facies of a debris avalanche deposit, debris flow or lahar deposits do not contain debris avalanche blocks which exhibit three-dimensional jigsaw puzzle features and preserved intact primary stratigraphy in hummocks (Sigurdsson et al., 2015). Large boulders within a debris flow deposit are generally surrounded by finer-grained material and concentrate toward the upper surface of the deposit, forming reverse grading. There are also no steep cliffs that form at the distal and lateral edges of a lahar deposit (Ui, 1989).

Several elements that characterize volcanic or non-volcanic debris avalanches are found within the Naga landslide debris field. These features include the presence of an amphitheatre wall (linear headscarp), hummocks, jigsaw cracks, and a long-runout (Ui, 1983; Siebert, 1984; Ui et al., 1986; Andrade and de Vries, 2010; Davies et al., 2010; de Vries and Delcamp, 2015). The Naga landslide is notable for its linear head wall, which is distinct from a horseshoe-shaped amphitheatre commonly found in volcanic debris avalanches (Mt. Galunggung, Mt. St.Helens Siebert, 1984 and Mt. Iriga Paguican et al., 2010).

As for the non-conical shape of the Naga landslide source, we attribute the linear headscarp to a northeast-trending fault, which is similar in orientation to the Central Cebu Fault and one of the principal orientations of fractures measured within Naga City. The large nearly vertical planar feature comprising the head wall of the Naga landslide has slickenlines and slickensides with a consistent rake angle of about 70 deg northeast. Together with other normal faults and thrust faults found at the uncollapsed back- and side-margins of the headscarp (**Figure 12**) we interpret this planar head wall as an oblique strike-slip fault, which served as a discontinuity and one of the planes of failure of the landslide. The other discontinuity, which acted as the sliding plane, is the interface between the limestone and the underlying sandy to silty sedimentary strata (**Figure 8**).

All of these can be used to classify the event as a debris avalanche. However, to acknowledge the initial movement which is a translational rockslide, the Naga City landslide is more specifically classified as a Rockslide-Debris Avalanche.

5.3. Excessive Runout

The long-runout characteristic of the Naga landslide relative to the collapse height which was checked using the empirically-derived equations of Corominas (1996) and Dade and Huppert (1998) reveal a classification fit for debris avalanches. The 9 deg Fahrböschung angle and volume plot used by Corominas (1996) indicates relative mobility of the Naga landslide and falls within the range found in debris avalanches. We also calculated a shear stress value (τ) of 34 kPa, which is in the range prescribed for long-runout landslides and consistent with the description for a debris avalanche in terms of excess distance traveled. Such long-runout events, according to Dade and Huppert (1998), happen in both terrestrial and extraterrestrial environments and should have overall resisting shear stress values (τ) ranging from 10 to 100 kPa.

5.4. Comparison With Known Philippine Debris Avalanches

The Naga debris landslide, in terms of its morphology, field deposit description and runout, was compared with the Iriga and Guinsaugon debris avalanches. The collapse of Iriga volcano resulted in two main debris avalanche deposits in the southwest and southeast. This has been reportedly caused by a non-volcanic trigger and was not accompanied by an eruption (Aguila et al., 1986). The deposits are characterized by the presence of an amphitheatre crater, torevas, hummocks of intact conglomerate, sand, and clay units, jigsaw cracked blocks and long runout and cover wide areas in low, waterlogged plains. The presence of intact conglomerates derived from the base of the volcano indicates a very deep failure plane. The younger debris avalanche deposit features discrete hummocks made of ignimbrite (Paguican, 2012).

The Guinsaugon rock slide-debris avalanche slid along intersecting fault planes and joints of the Philippine Fault (Catane et al., 2008; Lagmay et al., 2008) and resulted in a 4.1 km long and 1.52 km wide deposit characterized by a rock slide which transformed into a debris avalanche and consequent debris flows. The debris avalanche deposit comprised of pointed conical hummocks (pinnacle hummocks) and jigsaw-cracked blocks surrounded by a matrix of granular material which was described as a mix of sand and soil from the collapsed mass, whereas the low-lying area of the deposit was reported to have numerous pressure ridges in the southern part, which was interpreted as debris flows (Catane et al., 2008).

The proportion of cohesive material has been observed as an important factor in determining runout length, lateral spread, shape and orientation of individual hummocks in debris avalanches (Vallance and Scott, 1997; Zernack et al., 2009; Paguican, 2012). More cohesive material is associated with pinnacle hummocks and shorter runout debris avalanches compared to the generally circular-based and flat-topped hummocks formed in longer runout debris avalanches (Paguican et al., 2014). Pinnacle or conical hummocks, as called by many authors, are present in both the Guinsaugon and Naga Landslides but are more pronounced in the latter case. The numerous pinnacle hummocks found in the debris field of the Naga debris avalanche indicate cohesive material. Limestone material from the Naga landslide is more cohesive than those of the Guinsaugon and Iriga debris avalanches and is most likely the primary reason for the dominance of pinnacle hummocks in the Naga landslide debris field. Conical hummocks are also found in other debris avalanche deposits aside from these local events. They have been described in Guinsaugon (Catane et al., 2008), Mt. St Helens (Glicken, 1996), Jocotitlan (Siebe et al., 1992), Bezymiannyi (Belousov and Belousova, 1998) and Shiveluch (Ponomareva et al., 1998) volcanoes.

In addition, recalculation of the Fahrböschung angle of the Naga landslide puts it in the same class of landslide as the Iriga and Guinsaugon debris avalanches. The long-runout of the Naga event is likewise confirmed by the equation of Dade and Huppert (1998) on long-runout rockfalls, which is characterized by shear stress values indicative of excess mobility and consistent with calculations made for the Iriga and Guinsaugon debris avalanches.

5.5. Analog Laboratory Models

The Naga landslide is a mass wasting phenomenon that constitutes a catastrophic geologic hazard. However, it is incompletely understood in terms of its kinematics and dynamics. In particular, the physical basis for the extent of runout remains poorly understood. There are many hypotheses to explain the excessive travel distance of such long-runout landslides, which can have H/L ratios of 0.6 for small events, but can be as low as 0.1 for large events with volumes of several cubic kilometers (Heim, 1932; Erismann, 1979; de Vries and Delcamp, 2015). These include: (1) elastic release of fracture energy (Davies and McSaveney, 2009); (2) granular fluidization (Okura et al., 2000; Manzella, 2008; Pastor et al., 2009); (3) trapped air (Shreve, 1968); (4) water pore pressure (Iverson et al., 2000; Manzella, 2008; Pastor et al., 2009); (5) vibrations (Wang et al., 2010); or (6) sudden loss of strength as the material breaks (Quinn et al., 2011; Hungr et al., 2014).

The Naga landslide offers a unique opportunity to test relatively recent literature on the mechanism for the development of long-runout landslides or debris avalanches. Geological fieldwork and DEMs from drone surveys of the Naga debris field allows for a comparison with analog models, where a block of sand material slides down a plane and stretches to create an avalanche. These scaled models allow a sliding body to stretch and lengthen its lobes for increased runout. Downslope movement stops when the resistance of the material is greater than its depth which provides the force for the motion. These laboratory replications reveal that hummocks which form during avalanche events, are morphological expressions of brittle layer deformation due to the spreading. These features are remains of tilted and rotated blocks, whose morphology and distribution depends on the material properties, such as cohesion and viscosity of the sliding layer. Furthermore, its shape, size and density of occurrence can change depending on subsequent spreading, breakup or merging due to a change or restriction in topography (Paguican et al., 2014).

Based on the hummock categorization proposed in these models, the toreva blocks found at the proximal and medial zones of the Naga landslide are transverse in orientation to the direction of the landslide. Torevas, which are actually elongated hummocks are described in the experiments as first-order landslide material, formed during the initial stages of spreading. In the medial portion are pinnacle hummocks. Due to continuous stretching, hummocks will proceed to disaggregate especially at the front portion of the avalanche. In the distal portion of the Naga landslides where there were no topographic barriers (i.e., Lobes 1 and 2 areas), the landslide continued to accelerate and stretch, further disaggregating the larger blocks into fragments.

The transport mechanism for the Naga debris avalanche requires low basal shear resistance to have formed the observed features in the deposit field. Extension during transport produced faulted blocks, including horst and grabens (**Figure 5**). Greater extension leaves behind the blocks, which are pinnacle in shape in 2D view and pointed conical shapes in 3D view. But the calcareous Carcar and Barili formations, which are sedimentary rocks can also be comminuted. The finer granular matrix surrounding the jigsaw-cracked blocks and those found in inter-hummock areas, are the broken (clastic) Carcar and Barili formation sedimentary rocks, which underwent extensive stretching. The hummocky topography of the Naga landslide, therefore, reflects the dynamics of emplacement, particularly the lower basal friction which becomes smaller for larger debris avalanche deposits because of the volume effect. Because of the presence of hummocks, much of the shear of the moving mass is interpreted to have been concentrated at the basal portion (Davies et al., 2010; de Vries and Delcamp, 2015), which are difficult to find in the deposit field.

Following the analog model sequence, the Naga landslide started as a simple translational slide, where failure along a south-southwest dipping bed of siltstone allowed a large part of the mountain or block of limestone to move down. Features resulting from the extending sliding mass were classified as torevas, megablocks and hummocks with the larger fragments more prevalent in the proximal and medial portion of the debris field. In terms of deposit facies classification, there are the toreva-block, matrix, mixed and basal facies (de Vries and Delcamp, 2015). The debris-avalanche blocks observed in the field were large rocks, sometimes mega blocks that preserve the structure of the source. These megablock features are characteristically found at the proximal to medial area of the deposit (Godoy et al., 2017). A matrix of fine granular rocks surrounds the blocks and is composed of non-graded materials ranging from clay to larger than gravel-sized sediments. The matrix are also present in between hummocks where spreading was much more extensive leading to the formation of more granular collapse material.

Often when water escapes, landslides convert into debris flows. However, this does not appear to have happened in the Naga event as the limestone did not hold much water content and any drained rapidly. Furthermore, although it rained lightly in the morning of the disaster and the weeks prior to the landslide event, there was insignificant rainfall to have caused debris flows to form. While this study relied heavily on comparison with analog models, future work may explore and focus on numerical models to gain new perspectives on the initiation and runout of the landslide.

6. CONCLUSIONS

Analysis of satellite images, ground surveys, review of video footage, processing of borehole data, and identification of structural discontinuities reveal details on the conditions that culminated into rapid mass movement and the formation of the Naga Landslide. Comparison of the observations of the Naga Landslide deposits with known examples of debris avalanches show striking similarities. In particular, there is consistency with the descriptions found in the literature in terms of the presence of the following features: (1) Amphitheater crater; (2) Hummocks; (3) Jigsaw cracks in blocks; (4) Megablocks and (5) Long-runout (Ui, 1983; Siebert, 1984; Andrade and de Vries, 2010; Davies et al., 2010; de Vries and Delcamp, 2015). In addition, there is also consistency of the characteristics of the Naga landslide with empirically-derived equations describing debris avalanches and long-runout rockfalls (Corominas, 1996; Dade and Huppert, 1998).

The anatomy of the Naga landslide as described in this work and its comparison with analog models of Paguican et al. (2014) allows a description of the emplacement mechanism of the landslide. Following the analog model sequence, the Naga landslide started as a translational slide when a large block of limestone comprising the mountain slipped along a southwest dipping bed of sandstone/siltstone. Once in motion, the front of the sliding block then accelerated, further stretching the limestone body creating the debris avalanche. Jigsaw-cracked blocks surrounded by a non-graded matrix indicate an en masse flow with a main body with a low shear stress and an underlying sliding boundary with higher shear stress.

This study demonstrates that a debris avalanche and not a simple translational slide devastated villages in Naga City, Cebu on 20 September 2018. This type of landslide with excessive runout is known as one of the most destructive geologic hazards. It claimed the lives of 78 Filipinos with 6 missing and now joins other catastrophic landslides in the Philippines, including the 1628 Iriga and 2006 Guinsaugon debris avalanches. The Naga landslide was used to understand the emplacement mechanism of debris avalanches to advance the knowledge on how to prepare against such hazards. By comparing the deposits of the catastrophic collapse with analog models and well-known debris avalanches, we were also able to provide proper nomenclature, essential in the understanding of factors that led to the landslide disaster in Naga City. The results of this work are an important step to understand Rockslide-Debris Avalanches, necessary for future hazard assessment and risk mitigation. Warnings a month before the catastrophe in the form of hairline fractures that progressed to centimenters-wide cracks saved people living near the headscarp of the landslide. Unfortunately, the long-runout potential of the landslide was neither anticipated nor understood. Such understanding of long-runout events, which this study advances, is crucial in hazards and risk assessment.

DATA AVAILABILITY STATEMENT

The raw data supporting the conclusions of this article will be made available by the authors, without undue reservation, to any qualified researcher.

AUTHOR CONTRIBUTIONS

AL is the head of the investigative group for this study while the rest of the authors are members. CE, AY, and JS contributed in data gathering, modeling, analysis, and writing different parts of the manuscript. GC contributed in the calculations and computational results used in the study.

FUNDING

This study was funded by the UP Resilience Institute under the Office of the President of the University of the Philippines.

ACKNOWLEDGMENTS

The authors express their gratitude to the UP NOAH Researchers, especially Ms. Francesca Llanes, Ms. Feye Andal, Ms. Dianne Bencito, Ms. Krichi Cabacaba, Mr. Prince Goting, Mr. Marc Moises, Ms. Patricia Delmendo, Ms. Camille Cuadra, Ms. Girlie David, Ms. Lia Gonzalo, Mr. Joshua Abaygar, Ms. Trizia Muldong, Mr. Michael Ramos, Mr. Niño Joshua Tangaan and Mr. Archie Amba for their contributions to the entire report on the 2018 Naga Landslide event regarding information on topics not included or not the focus of this publication. We also would like to thank Dr. Benjamin van Wyk de Vries, Dr. Gioachino Roberti, Dr. Fabio Luca Bonali, and Dr. Malcolm Whitworth for virtual discussions and feedback on the analysis of the Naga Landslide. Last but not least, the authors also acknowledge the Center for Environmental Informatics (CENVI) for the additional drone image datasets used in this study.

SUPPLEMENTARY MATERIAL

The Supplementary Material for this article can be found online at: https://www.frontiersin.org/articles/10.3389/feart.2020.00312/full#supplementary-material

REFERENCES

Aguila, L., Newhall, C., Miller, C., and Listanco, E. (1986). Reconnaissance geology of a large debris avalanche from Iriga volcano, Philippines. *Philipp. J. Volcanol*. 3, 54–72.

Allen, C. R. (1962). Circum-Pacific faulting in the Philippines-Taiwan region. *J. Geophys. Res*. 67, 4795–4812. doi: 10.1029/JZ067i012p04795

Andrade, S. D., and de Vries, B. V. W. (2010). Structural analysis of the early stages of catastrophic stratovolcano flank-collapse using analogue models. *Bull. Volcanol*. 72, 771–789. doi: 10.1007/s00445-010-0363-x

Aurelio, M., and Peña, R. (2002). *Geology and Mineral Resources of the Philippines-Volume 1: Geology*. Quezon City: Mines and Geosciences Bureau, Department of Environment and Natural Resources, 391.

Aurelio, M., and Peña, R. (2010). *Geology of the Philippines*. Mines and Geosciences Bureau, Manila.

Balce, G. (1977). *An Introduction to the Stratigraphy of Cebu*. Technical report, Bureau of Mines.

Belousov, A., and Belousova, M. (1998). Bezymyannyi eruption on March 30, 1956 (Kamchatka): sequence of events and debris avalanche deposits. *Volcanol. Seismol*. 20, 29–47.

BJMP-NAGA (2018). *CCTV Video Captures Naga City Landslide*.

Catane, S., Cabria, H., Zarco, M., Saturay, R., and Mirasol-Robert, A. (2008). The 17 February 2006 guinsaugon rock slide-debris avalanche, Southern Leyte, Philippines: deposit characteristics and failure mechanism. *B. Eng. Geol. Environ*. 67, 305–320. doi: 10.1007/s10064-008-0120-y

Catane, S., Veracruz, N., Flora, J., Go, C., Enrera, R., and Santos, E. (2019). Mechanism of a low-angle translational block slide: evidence from the September 2018 Naga landslide, Philippines. *Landslides* 16, 1709–1719. doi: 10.1007/s10346-019-01212-9

CDRRMO of Naga City, Cebu (2018). *Naga City (2018) Local Disaster Risk Reduction and Management Plan 2018-2022 City of Naga, Cebu*. Technical report.

Corby, G. W. (1951). *Geology and Oil Possibilities of the Philippines*. Department of Agriculture and Natural Resources Technical Bulletin, Philippines.

Corominas, J. (1996). The angle of reach as a mobility index for small and large landslides. *Can. Geotech. J*. 33, 260–271. doi: 10.1139/t96-005

Crandell, D. R. (1989). Gigantic debris avalanche of Pleistocene age from ancestral Mount Shasta volcano, California, and debris-avalanche hazard zonation. U.S. G.P.O.; USGS Numbered Series; Books and Open-File Reports Section, 32. doi: 10.3133/b1861

Dade, W., and Huppert, H. (1998). Long-runout rockfalls. *Geology* 26, 803–806. doi: 10.1130/0091-7613(1998)026<0803:LRR>2.3.CO;2

Davies, T., and McSaveney, M. (2009). The role of rock fragmentation in the motion of large landslides. *Eng. Geol*. 109, 67–79. doi: 10.1016/j.enggeo.2008.11.004

Davies, T., McSaveney, M., and Kelfoun, K. (2010). Runout of the Socompa volcanic debris avalanche, Chile: a mechanical explanation for low basal shear resistance. *Bull. Volcanol*. 72, 933–944. doi: 10.1007/s00445-010-0372-9

de Vries, B. V. W., and Delcamp, A. (2015). "Volcanic debris avalanches," in *Landslide Hazards, Risks and Disasters*, eds J. F. Shroder and T. Davies (Cambridge, MA: Elsevier), 131–157. doi: 10.1016/B978-0-12-396452-6.00005-7

Del Rosario, R. Jr., Pastor, M., and Malapitan, R. (2005). "Controlled source magnetotelluric (CSMT) survey of Malabuyoc thermal prospect, Malabuyoc/Alegria, Cebu, Philippines," in *Proceedings World Geothermal Congress 2005* (Antalya), 24–29.

Deng, J., Yang, X., Zhang, Z.-F., and Santosh, M. (2015). Early Cretaceous arc volcanic suite in Cebu Island, Central Philippines and its implications on paleo-Pacific plate subduction: constraints from geochemistry, zircon U-Pb geochronology and Lu-Hf isotopes. *Lithos* 230, 166–179. doi: 10.1016/j.lithos.2015.05.020

Dimalanta, C., Suerte, L., Yumul, G., Tamayo, R., and Ramos, E. (2006). A Cretaceous supra-subduction oceanic basin source for Central Philippine ophiolitic basement complexes: geological and geophysical constraints. *Geosci. J*. 10:305. doi: 10.1007/BF02910372

Erismann, T. (1979). Mechanisms of large landslides. *Rock Mech*. 12, 15–46. doi: 10.1007/BF01241087

Evans, S., Guthrie, R., Roberts, N., and Bishop, N. (2007). The disastrous 17 February 2006 rockslide-debris avalanche on Leyte Island, Philippines: a catastrophic landslide in tropical mountain terrain. *Nat. Hazards Earth Syst. Sci*. 7:89–101. doi: 10.5194/nhess-7-89-2007

Futalan, K. M., Biscaro, J. R. D., Saturay, R. M., Catane, S. G., Amora, M. S., and Villaflor, E. L. (2010). Assessment of potential slope failure sites at Mt. Can-abag, Guinsaugon, Philippines, based on stratigraphy and rock strength. *Bull. Eng. Geol. Environ*. 69, 517–521. doi: 10.1007/s10064-009-0253-7

Gervasio, F. (1967). Age and nature of orogenesis of the Philippines. *Tectonophysics* 4, 379–402. doi: 10.1016/0040-1951(67)90006-6

Glicken, H. (1996). *Rockslide-Debris Avalanche of May 18, 1980, Mount St. Helens Volcano, Washington*. Technical report, US Geological Survey. doi: 10.3133/ofr96677

GMA News and Public Affairs (2018). GMANewsTV: 41 patay, 32 Nawawala Sa Killer landslide Sa Naga City, Cebu. https://www.gmanetwork.com/news/video/balitanghali/471381/41-patay-32-nawawala-sa-killer-landslide-sa-naga-city-cebu/video//

Godoy, B., Rodríguez, I., Pizarro, M., and Rivera, G. (2017). Geomorphology, lithofacies, and block characteristics to determine the origin, and mobility, of a debris avalanche deposit at Apacheta-Aguilucho Volcanic Complex (AAVC), northern Chile. *J. Volcanol. Geotherm. Res*. 347, 136–148. doi: 10.1016/j.jvolgeores.2017.09.008

Guthrie, R., Friele, P., Allstadt, K., Roberts, N., Evans, S., Delaney, K., et al. (2012). The 6 August 2010 Mount Meager rock slide-debris flow, Coast Mountains, British Columbia: characteristics, dynamics, and implications for hazard and risk assessment. *Nat. Hazards Earth System Sciences* 12, 1277–1294. doi: 10.5194/nhess-12-1277-2012

Heim, A. (1932). *Bergsturz und Menschenleben*. Fretz & Wasmuth.

Hungr, O., Evans, S., and Hutchinson, I. (2001). A review of the classification of landslides of the flow type. *Environ. Eng. Geosci*. 7, 221–238. doi: 10.2113/gseegeosci.7.3.221

Hungr, O., Leroueil, S., and Picarelli, L. (2014). The Varnes classification of landslide types, an update. *Landslides* 11, 167–194. doi: 10.1007/s10346-013-0436-y

Iverson, R. M., Reid, M., Iverson, N. R., LaHusen, R., Logan, M., Mann, J., et al. (2000). Acute sensitivity of landslide rates to initial soil porosity. *Science* 290, 513–516. doi: 10.1126/science.290.5491.513

Johnson, B. (1978). "Blackhawk landslide, California, USA," in *Rockslides and Avalanches. 1. Natural Phenomena. Developments in Geotechnical Engineering A*, ed B. Voight (Amsterdam: Elsevier), 181–196. doi: 10.1016/B978-0-444-41507-3.50008-8

Lagmay, A. (2018). *Assessment of the Tinaan, Naga City, Cebu Landslide and Preparation of Geohazard Assessment after the Landslide Disaster*. Technical report, Geosciences Foundation Incorporated.

Lagmay, A., Ong, J., Fernandez, D., Lapus, M., Rodolfo, R., Tengonciang, A., et al. (2006). Scientists investigate recent Philippine landslide. *Eos Trans. Am. Geophys. Union*. 3, 121–124. doi: 10.1029/2006EO120001

Lagmay, A., Tejada, L., Pena, R., Aurelio, M., Davy, B., David, S., et al. (2009). New definition of Philippine Plate boundaries and implications to the Philippine Mobile Belt. *J. Geol. Soc. Philipp*. 64, 17–30.

Lagmay, A., Tengonciang, A., Rodolfo, R., Soria, J., Baliatan, E., Paguican, E., et al. (2008). Science guides search and rescue after the 2006 Philippine landslide. *Disasters* 32, 416–433. doi: 10.1111/j.1467-7717.2008.01047.x

Lucas, A., Mangeney, A., and Ampuero, J. P. (2014). Frictional velocity-weakening in landslides on Earth and on other planetary bodies. *Nat. Commun*. 5, 1–9. doi: 10.1038/ncomms4417

Manzella, I. (2008). *Dry rock avalanche propagation: unconstrained flow experiments with granular materials and blocks at small scale*. Ph. D. thesis, Citeseer, Lausanne, Switzerland.

McSaveney, M. (1978). "Sherman glacier rock avalanche, Alaska, USA," in *Developments in Geotechnical Engineering*, Vol. 14, ed B. Voight (Amsterdam: Elsevier), 197–258. doi: 10.1016/B978-0-444-41507-3.50014-3

MGB (1983). *Geological Map of Pardo Quadrangle*.

MGB (2018). *Geological Investigation/Assessment Re: Cracks/Fissures in Limestones within Apo Land and Quarry Corporation (ALQC) Tenement in Sitio Tagaytay, Barangay Tina-an, Naga City, Cebu*. Technical report, Mines and Geosciences Bureau - Region 7.

Mines and Geosciences Bureau. (1981). Geosciences, 1981. Geologic Map of the Philippines: BMG, scale, 1(1,000,000):1. Mines and Geosciences Bureau, Philippines. Geosciences, 1981.

Minimo, L., and Lagmay, A. (2016). 3D Modeling of the Buhi debris avalanche deposit of Iriga Volcano, Philippines by integrating Shallow-Seismic Reflection and Geological data. *J. Volcanol. Geotherm. Res*. 319, 106–123. doi: 10.1016/j.jvolgeores.2016.03.002

Naranjo, J. A., and Francis, P. (1987). High velocity debris avalanche at Lastarria volcano in the north Chilean Andes. *Bull. Volcanol*. 49, 509–514. doi: 10.1007/BF01245476

Okura, Y., Kitahara, H., and Sammori, T. (2000). Fluidization in dry landslides. *Eng. Geol*. 56, 347–360. doi: 10.1016/S0013-7952(99)00118-0

OpenStreetMap contributors (2017). *Planet Dump*. Retrieved from: https://planet.osm.org, https://www.openstreetmap.org

Paguican, E. (2012). *The structure, morphology, and surface texture of debris avalanche deposits: field and remote sensing mapping and analogue modelling* (Ph.D. thesis). Clermont-Ferrand: Université Blaise Pascal U.F.R. Sciences et Technologies.

Paguican, E., Lagmay, A., van Wyk de Vries, B., and Quina, G. (2010). "Revisiting the historical debris avalanche deposit at the footslopes of Iriga Volcano, Philippines," in *Solid Earth-Basic Science for the Human Habitat-ILP's Second Potsdam Conference 2010* (Potsdam).

Paguican, E., van Wyk de Vries, B., and A.M.F. (2012). Volcano-tectonic controls and emplacement kinematics of the Iriga debris avalanches (Philippines). *Bull. Volcanol*. 74, 2067–2081. doi: 10.1007/s00445-012-0652-7

Paguican, E., van Wyk de Vries, B., and Lagmay, A. (2014). Hummocks: how they form and how they evolve in rockslide-debris avalanches. *Landslides* 11, 67–80. doi: 10.1007/s10346-012-0368-y

Pastor, M., Blanc, T., and Pastor, M. (2009). A depth-integrated viscoplastic model for dilatant saturated cohesive-frictional fluidized mixtures: application to fast catastrophic landslides. *J. NonNewtonian Fluid Mech*. 158, 142–153. doi: 10.1016/j.jnnfm.2008.07.014

PHIVOLCS (2016). *Active Fault Map of the Philippines*.

Ponomareva, V. V., Pevzner, M. M., and Melekestsev, I. V. (1998). Large debris avalanches and associated eruptions in the Holocene eruptive history of Shiveluch volcano, Kamchatka, Russia. *Bull. Volcanol*. 59, 490–505. doi: 10.1007/s004450050206

Quinn, P., Diederichs, M., Rowe, R., and Hutchinson, D. (2011). A new model for large landslides in sensitive clay using a fracture mechanics approach. *Can. Geotech. J*. 48, 1151–1162. doi: 10.1139/t11-025

Reiche, P. (1937). The Toreva-Block: a distinctive landslide type. *J. Geol*. 45, 538–548. doi: 10.1086/624563

Roberti, G., Friele, P., van Wyk de Vries, B., Ward, B., Clague, J. J., Perotti, L., et al. (2017). Rheological evolution of the Mount Meager 2010 debris avalanche, southwestern British Columbia. *Geosphere* 13, 369–390. doi: 10.1130/GES01389.1

Santos-Ynigo, L. (1951). *Geology and Ore Deposits of Central Cebu*. Philippine Bureau of Mines and Geosciences Report, 42–44.

Shreve, R. L. (1968). Leakage and fluidization in air-layer lubricated avalanches. *Geol. Soc. Am. Bull*. 79, 653–658. doi: 10.1130/0016-7606(1968)79[653:LAFIAL]2.0.CO;2

Siebe, C., Komorowski, J.-C., and Sheridan, M. F. (1992). Morphology and emplacement of an unusual debris-avalanche deposit at Jocotitlán volcano, Central Mexico. *Bull. Volcanol*. 54, 573–589. doi: 10.1007/BF00569941

Siebert, L. (1984). Large volcanic debris avalanches: characteristics of source areas, deposits, and associated eruptions. *J. Volcanol. Geotherm. Res*. 22, 163–197. doi: 10.1016/0377-0273(84)90002-7

Sigurdsson, H., Houghton, B., McNutt, S., Rymer, H., and Stix, J. (2015). *The Encyclopedia of Volcanoes*. San Diego, CA: Elsevier.

Stoopes, G. R., and Sheridan, M. F. (1992). Giant debris avalanches from the Colima Volcanic Complex, Mexico: implications for long-runout landslides (> 100 km) and hazard assessment. *Geology* 20, 299–302. doi: 10.1130/0091-7613(1992)020<0299:GDAFTC>2.3.CO;2

Thompson, N., Bennett, M. R., and Petford, N. (2010). Development of characteristic volcanic debris avalanche deposit structures: new insight from distinct element simulations. *J. Volcanol. Geotherm. Res*. 192, 191–200. doi: 10.1016/j.jvolgeores.2010.02.021

Ui, T. (1983). Volcanic dry avalanche deposits—identification and comparison with nonvolcanic debris stream deposits. *J. Volcanol. Geotherm. Res*. 18, 135–150. doi: 10.1016/0377-0273(83)90006-9

Ui, T. (1989). "Discrimination between debris avalanches and other volcaniclastic deposits," in *Volcanic Hazards*, ed J. H. Latter (Wellington: Springer), 201–209. doi: 10.1007/978-3-642-73759-6_13

Ui, T., Takarada, S., and Yoshimoto, M. (2000). "Debris avalanches," in *Encyclopedia of Volcanoes*, eds H. Sigurdsson, B. Houghton, S. McNutt, H. Rymer, and J. Stix (Cambridge, MA: Academic Press), 617–626.

Ui, T., Yamamoto, H., and Suzuki-Kamata, K. (1986). Characterization of debris avalanche deposits in Japan. *J. Volcanol. Geotherm. Res*. 29, 231–243. doi: 10.1016/0377-0273(86)90046-6

UP-CENVI (2018). *Landslide Image in Naga City Cebu*.

Vallance, J. W., and Scott, K. M. (1997). The Osceola Mudflow from Mount Rainier: Sedimentology and hazard implications of a huge clay-rich debris flow. *Geol. Soc. Am. Bull*. 109, 143–163. doi: 10.1130/0016-7606(1997)109<0143:TOMFMR>2.3.CO;2

Voight, B., Janda, R., Glicken, H., and Douglass, P. (1983). Nature and mechanics of the Mount St Helens rockslide-avalanche of 18 May 1980. *Geotechnique* 33, 243–273. doi: 10.1680/geot.1983.33.3.243

Wang, Q., Yao, Y., Li, J., and Huang, J. (2010). "Ground vibration characteristics of large rock landslide in Three Gorges Reservoir," in *2010 The 2nd Conference on Environmental Science and Information Application Technology* (Wuhan).

Wang, Y.-F., Cheng, Q.-G., Lin, Q.-W., Li, K., and Yang, H.-F. (2018). Insights into the kinematics and dynamics of the Luanshibao rock avalanche (Tibetan Plateau, China) based on its complex surface landforms. *Geomorphology* 317, 170–183. doi: 10.1016/j.geomorph.2018.05.025

Zernack, A. V., Procter, J. N., and Cronin, S. J. (2009). Sedimentary signatures of cyclic growth and destruction of stratovolcanoes: a case study from Mt. Taranaki, New Zealand. *Sediment. Geol*. 220, 288–305. doi: 10.1016/j.sedgeo.2009.04.024

Conflict of Interest: The authors declare that the research was conducted in the absence of any commercial or financial relationships that could be construed as a potential conflict of interest.

frontiers
in Earth Science

ORIGINAL RESEARCH
published: 17 September 2020
doi: 10.3389/feart.2020.00372

Surface Exposure Dating and Geophysical Tomography of the Royal Arches Meadow Rock Avalanche, Yosemite Valley, California

Marcus Pacheco[1], Alain M. Plattner[2]*, Greg M. Stock[3]*, Dylan H. Rood[4] and Christopher J. Pluhar[1]

[1] Earth & Environmental Sciences, California State University, Fresno, Fresno, CA, United States, [2] Geological Sciences, The University of Alabama, Tuscaloosa, AL, United States, [3] National Park Service, Yosemite National Park, El Portal, CA, United States, [4] Earth Science and Engineering, Imperial College London, London, United Kingdom

Edited by:
John Joseph Clague,
Simon Fraser University, Canada

Reviewed by:
Jeff Moore,
The University of Utah, United States
O. Adrian Pfiffner,
University of Bern, Switzerland

***Correspondence:**
Alain M. Plattner
amplattner@ua.edu
Greg M. Stock
greg_stock@nps.gov

Specialty section:
This article was submitted to
Quaternary Science, Geomorphology
and Paleoenvironment,
a section of the journal
Frontiers in Earth Science

Received: 01 April 2020
Accepted: 10 August 2020
Published: 17 September 2020

Citation:
Pacheco M, Plattner AM, Stock GM,
Rood DH and Pluhar CJ (2020)
Surface Exposure Dating and
Geophysical Tomography of the Royal
Arches Meadow Rock Avalanche,
Yosemite Valley, California.
Front. Earth Sci. 8:372.
doi: 10.3389/feart.2020.00372

Since the retreat of glaciers after the Last Glacial Maximum, rock avalanches have occurred intermittently in Yosemite Valley, California. We investigated the distal portion of the oldest of these, the Royal Arches Meadow rock avalanche, which has been partially buried by sediment aggradation. Cosmogenic ^{10}Be exposure ages of boulders within the deposit indicate that the rock avalanche occurred at 16.1 ± 0.3 ka, immediately after deglaciation and thus prior to most aggradation. The interface between the rock avalanche deposit and the underlying glaciofluvial sediments therefore provides an elevation marker of the valley floor at the time of deposition. To identify the elevation of this interface, we collected eight Ground Penetrating Radar (GPR) and five Electrical Resistivity Tomography (ERT) profiles across the rock avalanche. Both methods are sensitive to contrasts between the granitic avalanche deposit and the underlying sediments. By constraining ERT inversions with GPR interfaces that are continuous across the profiles, we identified a single interface, interpreted as the basal contact of the rock avalanche, that separates resistive material from conductive material underneath. The elevation of this approximately horizontal interface is between 1,206 and 1,209 m, roughly $10\,\mathrm{m}$ below the modern ground surface, indicating $\approx 10\,\mathrm{m}$ of sediment aggradation since deglaciation. Based on topographic expression and depth to this contact, we determined a minimum volume estimate of between $8.1 \times 10^5\,\mathrm{m}^3$ and $9.7 \times 10^5\,\mathrm{m}^3$, nearly three times larger than what would be estimated from surface expression alone. Our findings allow reconstruction of the sedimentation history of Yosemite Valley, inform hazard and risk assessment, and confirm that geophysical methods are valuable tools for three-dimensional investigations of rock avalanches, particularly those buried by younger sediments.

Keywords: rock avalanche, Yosemite Valley, cosmogenic nuclide exposure dating, near-surface geophysics, ground penetrating radar, electrical resistivity tomography

1. INTRODUCTION

Rock avalanches - streams of rapidly moving rock debris resulting from catastrophic failure of bedrock slopes - are among the most powerful geologic forces on earth, rapidly eroding extremely large masses of rock and causing dramatic and long-lasting landscape changes (e.g., Evans et al., 2006; Hovius and Stark, 2006; Korup et al., 2007; Hewitt et al., 2008; Hermanns and Longva, 2012). As a result of their large volumes and associated long runout distances, rock avalanches are also the source of some of the world's most destructive natural disasters, posing significant hazard and risk in mountainous environments (Evans et al., 2006).

Determining rock avalanche volumes is a key aspect of evaluating their hazard, as accurate volumes are needed to establish robust volume-frequency relationships (e.g., Evans, 2006) and are critical components of empirical equations governing rock avalanche mobility (e.g., Corominas, 1996; Dade and Huppert, 1998). Rock avalanche volumes are usually determined by field investigations or remote sensing methods, though in both cases accurate volumes can be elusive due to the inherent difficulty in establishing accurate deposit extents and thicknesses, post-event erosion of the deposit, cover by more recent debris, or a lack of sufficiently high resolution remote sensing data (Hutchinson, 2006; Hewitt et al., 2008). This situation is exacerbated in cases where rock avalanche deposits are partially buried by sediment aggradation, with an unknown but potentially substantial portion of the deposit volume hidden from view. Older rock avalanches may be particularly susceptible to this condition, in some cases prohibiting volume estimation entirely (e.g., Cordes et al., 2013; McColl, 2020). Partial burial can lead to an underestimation of volume, and thus inaccurate conclusions about frequency, runout, and overall hazard.

The need for determining accurate volumes for partially buried deposits has spurred application of geophysical methods to studies of talus deposits and rock avalanches. Previous studies in the Alps (Sass and Wollny, 2001; Otto and Sass, 2006; Sass, 2006; Socco et al., 2010), and in Yosemite Valley (Brody et al., 2015), showed the potential of geophysical methods, including electrical resistivity tomography, ground penetrating radar, and seismic refraction, for identifying basal contacts, deposit thickness, and associated stratigraphy. Near-surface geophysical investigations are well-suited for rock avalanches that possess a strong contrast in physical properties (e.g., electrical resistivity or dielectric permittivity) compared to the underlying substrate or, if applicable, overlying deposits. Weak contrasts, on the other hand, increase ambiguity, requiring additional information, for example from boreholes, to uniquely pinpoint contacts.

Here we use integrated geophysical imaging methods to investigate the basal contact, thickness distribution, and volume of the Royal Arches Meadow rock avalanche, a ≈ 16 ka, partially-buried rock avalanche deposit in Yosemite Valley. Our age determination is based on terrestrial cosmogenic ^{10}Be exposure dating of boulders on the surface of the rock avalanche (section 2). Ground penetrating radar profiles across the rock avalanche deposit revealed multiple interfaces and hence not a unique candidate for the basal contact (section 3.3). However, integrating our ground penetrating radar results with electrical resistivity tomography ultimately allows us to identify the rock avalanche base (section 3.4).

1.1. Physical Setting

Yosemite Valley is located in Yosemite National Park in the central Sierra Nevada mountain range of California, USA (**Figure 1A**). Yosemite Valley is approximately 12 km long and 1–2 km wide, with steep (including vertical to overhanging) cliffs nearly 1 km tall. These cliffs and associated waterfalls offer iconic scenery that draws more than 4 million visitors annually. The walls of Yosemite Valley are composed of late Cretaceous granitic rocks of the Sierra Nevada batholith (Bateman, 1992), primarily granites, granodiorites, and minor diorite. The cliffs in eastern Yosemite Valley, including those adjacent to the Royal Arches Meadow rock avalanche, are comprised of ≈ 88 Ma Half Dome Granodiorite (Peck, 2002).

Yosemite Valley was initially carved by river incision, but was subsequently deepened and widened by hundreds of meters during multiple Pleistocene glaciations (Matthes, 1930; Huber, 1987), mostly recently during the Last Glacial Maximum (LGM). Although the timing of LGM glacier retreat from Yosemite Valley is not precisely known (Wahrhaftig et al., 2019), results from elsewhere in the Sierra Nevada suggest that LGM deglaciation occurred between 18 and 16 ka (e.g., Rood et al., 2011; Phillips, 2017). Glacier retreat left behind a relatively flat valley floor comprised of glacial outwash, lacustrine and deltaic deposits, and fluvial silts, sands, and gravels (e.g., Matthes, 1930; Huber, 1987), with several meters of sediment aggradation of the valley floor in the Holocene (e.g., Cordes et al., 2013; Brody et al., 2015).

Rock slope failures, primarily in the form of rockfalls and rockslides, occur frequently from the glacially-steepened walls of Yosemite Valley (Stock et al., 2013). Sheeting (exfoliation) joints in the otherwise massive granite often form rockfall detachment surfaces (e.g., Stock et al., 2012). Smaller rockfalls of hundreds to thousands of cubic meters in volume occur on an annual basis in Yosemite Valley; larger failures up to tens of thousands of cubic meters in volume occur less frequently, but have been documented in the past 150 years (Wieczorek et al., 2000; Zimmer et al., 2012; Stock et al., 2013; Guerin et al., 2020). These events typically have modest runout distances, with deposition limited to the active talus slopes flanking the base of cliffs.

Yosemite Valley preserves several extremely large boulder deposits up to several million cubic meters in volume, considered to be rock avalanches resulting from catastrophic failure of the valley walls (Matthes, 1930; Wieczorek et al., 1999; Wieczorek, 2002; Stock and Uhrhammer, 2010). These deposits extend far beyond the base of active talus slopes onto the valley floor, where they manifest as laterally extensive, low-angle fields of angular boulders. At least six rock avalanche deposits have been identified in Yosemite Valley, all of which have occurred since LGM deglaciation. As the floor of Yosemite Valley is wide and flat, with low stream power to modify rock avalanche deposits, and erosion rates of the granitic boulders in the deposits are slow (on the order of tenths of a millimeter per year; Wahrhaftig et al., 2019), these rock avalanche deposits tend to be exceptionally well-preserved. A potentially confounding preservation factor is

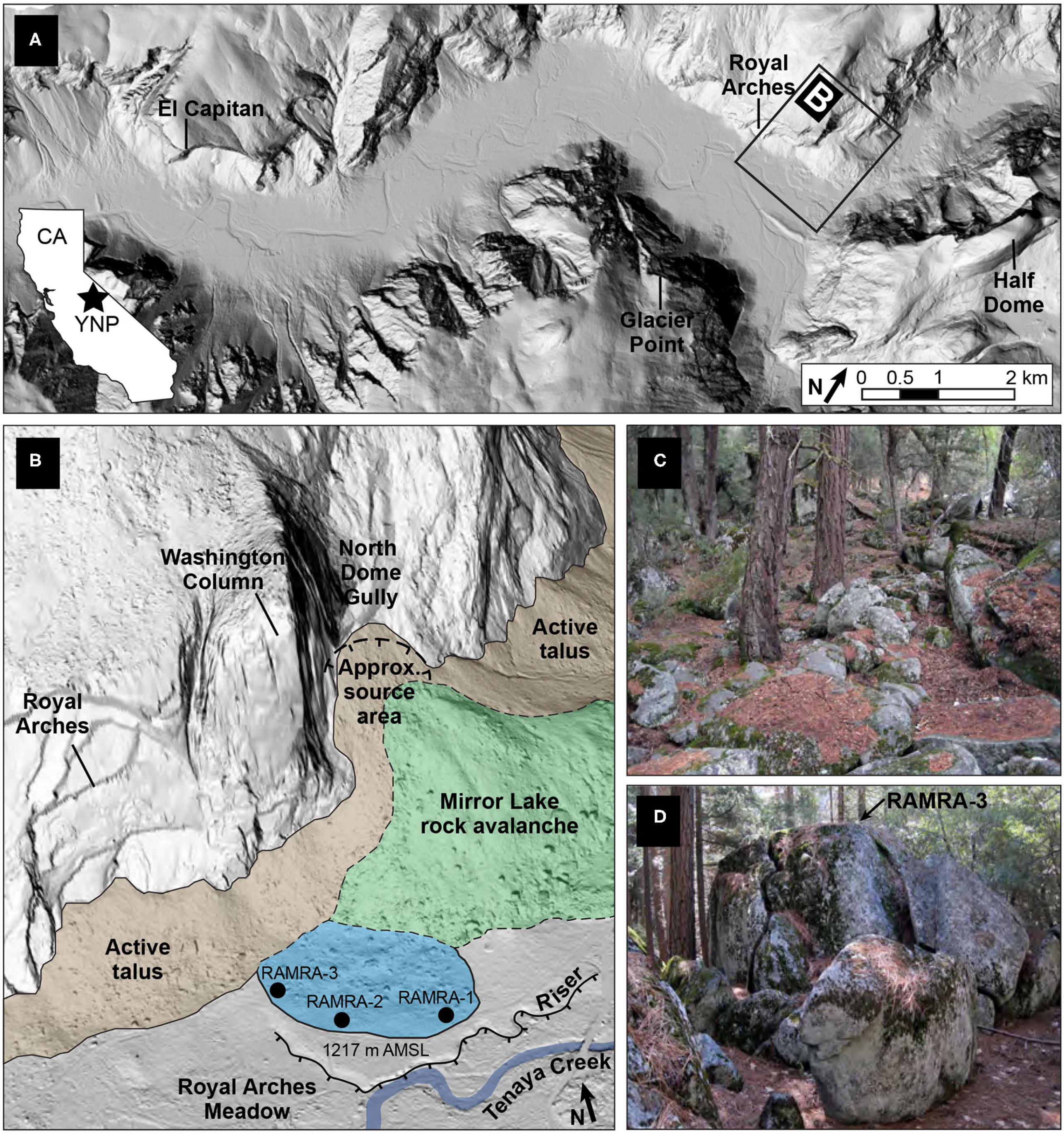

FIGURE 1 | Location and geologic setting of the Royal Arches Meadow rock avalanche. **(A)** Location of Royal Arches Meadow rock avalanche in eastern Yosemite Valley, Yosemite National Park (YNP), California (CA). **(B)** Oblique topographic hillshade, derived from 1 m filtered lidar data, showing the Royal Arches Meadow rock avalanche (blue), overlapping Mirror Lake rock avalanche (green), and active talus (brown), and terrace riser adjacent to Tenaya Creek. Black circles mark samples collected for cosmogenic ^{10}Be exposure dating. The width of the Royal Arches Meadow rock avalanche deposit is approximately 315 m. Extent of oblique view shown as box marked "B" in **(A)**. **(C)** Photograph showing bouldery topography typical of the exposed surface of the rock avalanche. **(D)** Photograph of a 3 m-tall boulder on the western margin of the rock avalanche sampled for cosmogenic ^{10}Be exposure dating (sample RAMRA-3).

that some of the older deposits appear to be partially buried by more recent sediment aggradation (e.g., Cordes et al., 2013) including younger talus deposits and other rock avalanches.

1.2. Royal Arches Meadow Rock Avalanche

The Royal Arches Meadow rock avalanche is located in eastern Yosemite Valley, at an elevation of 1,217 m above mean sea level

(AMSL), between a 420 m-tall rock tower named Washington Column to the north and Royal Arches Meadow and Tenaya Creek to the south (**Figure 1A**). The portion of the rock avalanche deposit proximal to the cliffs to the north is buried beneath debris from the more recent Mirror Lake rock avalanche (Wieczorek et al., 1999; Wieczorek, 2002), as well as aprons of active talus (**Figure 1B**). The distal portion of the deposit extending beyond this overlapping debris is therefore the primary focus of this study. This deposit has a lobate morphology, suggesting that it was topographically unconstrained as it spread out across the valley floor. The maximum length of the distal portion of the deposit is approximately 270 m, and the maximum width is approximately 315 m. Contrasting with the relatively steep (30°–35°) repose angles of the active talus slopes, the distal portion of the rock avalanche deposit is nearly flat, sloping only a few degrees to the south. The deposit has a hummocky morphology and a clast-supported surface cover of angular boulders (**Figure 1C**). Boulders exposed on the surface range from tenths of cubic meters to many hundreds of cubic meters in volume, with the largest boulders projecting up to 5 m above the mean deposit surface (**Figure 1D**). Finer-grained material between the boulders support dense trees and understory vegetation.

Along the southern margins of the rock avalanche deposit, the distribution of boulders on the surface becomes more dispersed, with many meters to tens of meters separating individual boulders. The intervening surfaces are composed of flat-lying sediments, presumed to be a mix of alluvium and colluvium; the isolated boulders appear to be embedded within these sediments, suggesting partial burial by sediment aggradation. Farther south, the topography is flat and comprises a fluvial terrace at 1,217m AMSL, the edge of which is a 5 m-tall terrace riser formed by lateral erosion of Tenaya Creek (**Figure 1B**). A cutbank in the terrace riser displays a layered stratigraphy of silts and sands with a capping coarse gravel deposit, interpreted to represent fine sediment deposition within small pro-glacial side channels and ponds followed by coarse sediment deposition resulting from migration of the main Tenaya Creek channel. The cutbank does not reveal angular clasts associated with the rock avalanche, indicating that the rock avalanche does not extend in the subsurface as far south as the terrace riser. Furthermore, the undeformed nature of the layered sediments exposed in the cutbank suggests that they post-date emplacement of the rock avalanche. The local topographic setting prohibits the rock avalanche deposit from acting as a natural dam (the deposit only extends partway across the valley), indicating that sediment aggradation occurred for reasons independent of rock avalanche emplacement.

Although the morphology of the Royal Arches Meadow rock avalanche clearly indicates it was sourced from the north wall of Yosemite Valley in the vicinity of Washington Column, an exact source area is not apparent. A likely explanation for this is that the rock avalanche originated from an edifice that later collapsed, generating the much larger-volume ($\approx 11 \times 10^6$ m^3) Mirror Lake rock avalanche (**Figure 1B**; Wieczorek et al., 1999; Wieczorek, 2002) and leaving behind a large depression in the valley wall immediately east of Washington Column known as North Dome Gully. We infer that the source area for the Royal Arches Meadow rock avalanche was located on a cliff formerly within the empty space in what is now the North Dome Gully (**Figure 1B**).

The ratio of the vertical fall height (H) and the horizontal runout length (L) of rock avalanches, the so called "Fahrböschung" (Hsü, 1975), and the arctangent of H/L, the so called "reach angle" (Corominas, 1996) are commonly used as indices of rock avalanche mobility. As the source area of the Royal Arches Meadow rock avalanche is no longer visible, it is not possible to precisely quantify the H and L parameters. However, given the general constraints on the likely source area, we estimate a maximum fall height of approximately 550 m and a maximum runout length of approximately 840 m, suggesting an H/L ratio of 0.65 As with the other rock avalanches in Yosemite Valley (Wieczorek et al., 1999), this relatively low mobility suggests that the Royal Arches Meadow rock avalanche does not display "excess" runout; rather, its large runout distance compared to the active talus is explained primarily by its potential energy (e.g., Dade and Huppert, 1998).

As the proximal portion of the rock avalanche is buried beneath younger talus and rock avalanche debris, we have not attempted to account for that volume. The exposed distal portion of the Royal Arches Meadow rock avalanche has a "bulked" volume (including porosity) of approximately 3.78×10^5 m^3, calculated by delineating the area of exposed boulders on the surface (54,186 m^2) and measuring the volume within this area that projects above the height of the adjacent, roughly planar, valley floor surface (1,217 m elevation). Importantly, this volume measurement assumes that the base of the rock avalanche is the modern valley floor surface, and that the entire volume of the distal portion is presently exposed. However, as described above, there is evidence that the Royal Arches Meadow rock avalanche is partially buried. Recognition that post-glacial aggradation likely strongly influences the surface expression of the rock avalanche was a primary motivation for integrated geophysical imaging of the deposit.

2. AGE OF THE ROYAL ARCHES MEADOW ROCK AVALANCHE

The intact deposit of the Royal Arches Meadow rock avalanche on the floor of Yosemite Valley confirms that it must be post-glacial in age, i.e., it was deposited after retreat of the LGM glacier from eastern Yosemite Valley. Several lines of field evidence, including overlapping deposition by the Mirror Lake rock avalanche and indications of substantial post-depositional aggradation of fluvial sediments adjacent to and within the distal portion of the deposit, suggest that it may be among the oldest of the rock avalanches in Yosemite Valley. To date the Royal Arches Meadow rock avalanche directly, we employed terrestrial cosmogenic ^{10}Be exposure dating of boulders on the surface of the deposit.

Terrestrial cosmogenic nuclide exposure dating, which utilizes the accumulation of cosmogenic nuclides in target minerals over time due to exposure to cosmic rays (e.g., Gosse and Phillips,

2001) offers a robust means of directly dating rock avalanche deposits, provided the exposed boulders were sufficiently shielded within the rock slope prior to failure and that they have not experienced substantial post-depositional burial or erosion. Cosmogenic nuclide exposure dating has been used to constrain the timing of rock avalanches in a variety of settings (e.g., Ballantyne and Stone, 2004; Mitchell et al., 2007; Moreiras et al., 2015; Nagelisen et al., 2015; McColl, 2020), and was previously used to obtain ages for two rock avalanches in Yosemite Valley (Stock and Uhrhammer, 2010; Cordes et al., 2013).

We collected three samples for cosmogenic ^{10}Be exposure dating from boulders on the surface of the Royal Arches Meadow rock avalanche deposit. We selected large boulders near the distal edge of the deposit that were solidly wedged against adjacent boulders (demonstrating that the boulders could not have rotated since emplacement), and sampled the tops of these boulders (**Figure 1D**) to simplify the exposure geometries and topographic shielding, and to minimize the potential for nuclide loss due to wildfire-induced boulder spallation. We did not correct for snow shielding. We assumed a boulder erosion rate of 0.0065 cm /yr (Wahrhaftig et al., 2019), likely a maximum value. Quartz sample preparation and accelerator mass spectrometer measurements were made at the Scottish Universities Environmental Research Center (SUERC) using standard procedures (Xu et al., 2015; Corbett et al., 2016). Model exposure ages were calculated using the CRONUS-Earth online calculator (Balco et al., 2008). The choice of reference production rate, scaling scheme, and erosion rate changes the ages by a maximum of 7.5 %, or approximately 1,200 years, which does not significantly affect our conclusions.

Results from the three samples are nearly identical (**Table 1**), yielding an error-weighted mean exposure age of 16.1 ± 0.3 ka (1σ), with a reduced chi-squared value of 0.4 and p-value of 0.96. This result confirms that the Royal Arches Meadow rock avalanche is Late Pleistocene in age. Given that the Royal Arches Meadow rock avalanche is located close to the inferred LGM terminus position (within 7 km), it is reasonable to assume that deglaciation had occurred there by ≈ 16 ka, and that the rock avalanche occurred immediately thereafter. As such, the Royal Arches Meadow rock avalanche presents an important marker of the elevation of the floor of Yosemite Valley immediately following deglaciation, providing insights into the post-glacial history of the valley. As much of this history involved aggradation of alluvial and colluvial sediments adjacent to, and on top of, the rock avalanche, the relationship between the rock avalanche and the former valley floor has been obscured. We thus turned to geophysical methods to investigate the position and morphology of the basal contact of the rock avalanche deposit.

3. GEOPHYSICAL INVESTIGATION

We used a combination of two non-intrusive geophysical methods—Electrical Resistivity Tomography (ERT) and Ground Penetrating Radar (GPR). GPR common-offset profiling consists of keeping transmitter and receiver antennae at a fixed offset and recording traces along a profile line (Jol, 2008). Electromagnetic wavelets emitted by the transmitter antenna at each measurement location get reflected by subsurface contrasts in dielectric permittivity (Neal, 2004) and recorded by the receiver antenna. A variety of factors, including change in lithology, grain size and orientation, and the water table affect dielectric permittivity (Olhoeft, 1998; Neal, 2004). This makes GPR a well-suited technique to investigate the interface between the granitic rock avalanche deposit and the underlying lacustrine, deltaic, and fluvial sediments. To detect structures within the subsurface, signals recorded by the GPR receiver antenna at each position along the profile are plotted next to each other to form a radargram. Since the vertical axis of a radargram shows the time since source wavelet transmission, subsurface radar wave velocity is required to extract depth information. This velocity can be obtained by conducting a "common midpoint," or a "wide angle reflection and refraction" survey, in which the separation between transmitter and receiver antenna is

TABLE 1 | Sample data and exposure ages for boulders on the Royal Arches Meadow rock avalanche.

Sample	SUERC[a] Sample ID	Latitude (°N)	Longitude (°W)	Elevation (m AMSL)	Sample thickness (cm)	Shielding factor[b]
RAMRA-1	b7146	37.743351	−119.56008	1,224	2	0.929307
RAMRA-2	b7147	37.743725	−119.56185	1,220	3	0.919873
RAMRA-3	b7149	37.744736	−119.56255	1,222	2.2	0.918220
Sample	**Mass quartz (g)**	**Be carrier[c] (g)**	**^{10}Be/^{9}Be ($\times 10^{-13}$)[d]**	**^{10}Be concentration (10^4 atoms /g SiO$_2$)**	**Exposure age (ka)**	
RAMRA-1	16.122	0.4460	1.52 ± 0.04	12.583 ± 0.370	16.0 ± 0.5	
RAMRA-2	17.168	0.4462	1.59 ± 0.04	12.366 ± 0.352	16.1 ± 0.5	
RAMRA-3	17.999	0.4458	1.69 ± 0.05	12.551 ± 0.368	16.2 ± 0.5	

Exposure ages calculated using the CRONUS web calculator, version 3 (Balco et al., 2008, https://hess.ess.washington.edu; version info – wrapper: 3.0.2, get_age: 3.0.2, muons: 1A, alpha = 1, validate: validate_v2_input.m - 3.0, const:3.0.4), assuming a rock density of 2.7 g /cm, *standard atmosphere, a boulder erosion rate of* 0.00065 cm/yr *(Wahrhaftig et al., 2019), and using the default calibration data set, reference production rate of* 3.92 ± 0.31 at/g /yr SLHL, *and Lifton-Sato-Dunai (LSDn or Sa) scaling scheme (Lifton et al., 2014; Phillips et al., 2016).*

[a] *Scottish Universities Environmental Research Center (SUERC) identification number.*

[b] *Calculated using the CRONUS online topographic shielding calculator Version 1.*

[c] *Carrier Be concentration of* 449 ppm.

[d] *Normalized to NIST standard with assumed* ^{10}Be/^{9}Be *value of* 2.79×10^{-11} *(Nishiizumi et al., 2007), and including* ≈ 2 % *background correction using blank sample CFG1313 (b7157) with background and sample uncertainties propagated in quadrature. All uncertainties are* 1σ.

successively increased (Annan and Davis, 1976; Davis and Annan, 1989).

In ERT surveys, electrical potential differences resulting from current injected into the ground reveal the spatially varying electrical resistivity of the subsurface. Measurements using multiple current- and potential-electrode pairs along a profile allow computer tomographic inversions to create vertical profiles showing the two-dimensional variation of electrical resistivity (e.g., Oldenburg and Li, 1999; Loke et al., 2013). We expected the electrical resistivity of the granitic rock avalanche debris to be an order of magnitude higher than the resistivity of the underlying sediments, posing a strong contrast in the physical parameter to which ERT is sensitive.

Neither of these two methods alone can pinpoint the basal contact of the rock avalanche. While GPR shows the boundaries of various units, it is not well-suited to differentiate between the unit materials. When several interfaces are present, standard GPR processing alone can not conclusively indicate which of these interfaces is the basal contact of the rock avalanche deposit. ERT, on the other hand, is sensitive to the materials of the units, but cannot by itself resolve sharp transitions. Moreover, ERT is typically underdetermined, meaning that different resistivity profiles may fit the data equally well. Additional constraints (regularization) must be provided, typically in the form of imposed smoothness (e.g., Günther et al., 2006; Loke et al., 2013). As a consequence, different regularization constraints may lead to different resistivity profiles (Oldenburg and Li, 1999). A-priori information of subsurface structure can be incorporated into ERT regularization. Here, we follow the approach of Doetsch et al. (2012) by removing smoothing constraints across interfaces obtained from GPR profiles that overlap with our ERT profiles.

3.1. Data Acquisition Strategy

We collected eight GPR and five ERT profiles (**Figures 2A,B**) crossing exposed parts of the rock avalanche, as well as the adjacent area covered by finer sediments. GPR profiles as well as "Wide Angle Reflection and Refraction" (WARR) data were acquired using a Sensors and Software PulseEKKO Pro (50 MHz) system between September and October 2018. The five ERT transects were collected in March 2018 with an Advanced Geosciences Inc SuperSting R1 system with 28 electrodes and 6 m electrode spacing, using Schlumberger and dipole-dipole electrode arrays. To increase the length of the ERT profiles, we used a roll-along strategy Loke et al. (2013). ERT and GPR profiles overlapped to allow for joint processing and interpretation.

3.2. Radar Wave Velocity

To determine the subsurface velocity, we collected "Wide Angle Reflection and Refraction" (WARR) data by transmitting and recording signals at increasing transmitter-receiver separation. The resulting radargram (**Figure 3C**), obtained after minimal processing using GPRPy (Plattner and Pacheco, 2019; Plattner, 2020) shows signals traveling directly from the transmitter to the receiver through air (air wave) and through the ground (ground wave) as straight lines, while signals reflected from horizontal interfaces appear as hyperbolae. The slope of the direct arrivals and the shape of the hyperbolae allow us to determine the subsurface velocity. We used the stacked amplitude procedure implemented in GPRPy to give best estimations for direct waves (**Figure 3B**) and reflected waves (**Figure 3A**). As expected, the air wave traveled at the speed of light in air (0.3 ns /m). The ground wave samples only the shallowest part of the subsurface. Its velocity is thus not necessarily representative of the deeper subsurface. The reflected arrivals (hyperbolae), on the other hand, travel down to an interface and hence provide an estimate of the average subsurface velocity between the interface and the surface. We therefore use the velocity obtained from the hyperbolae, 0.11 ± 0.01 m /ns, as subsurface velocity.

3.3. GPR Data Processing and Interpretation

Minimal GPR data processing using GPRPy (Plattner and Pacheco, 2019; Plattner, 2020) included a time-zero correction,

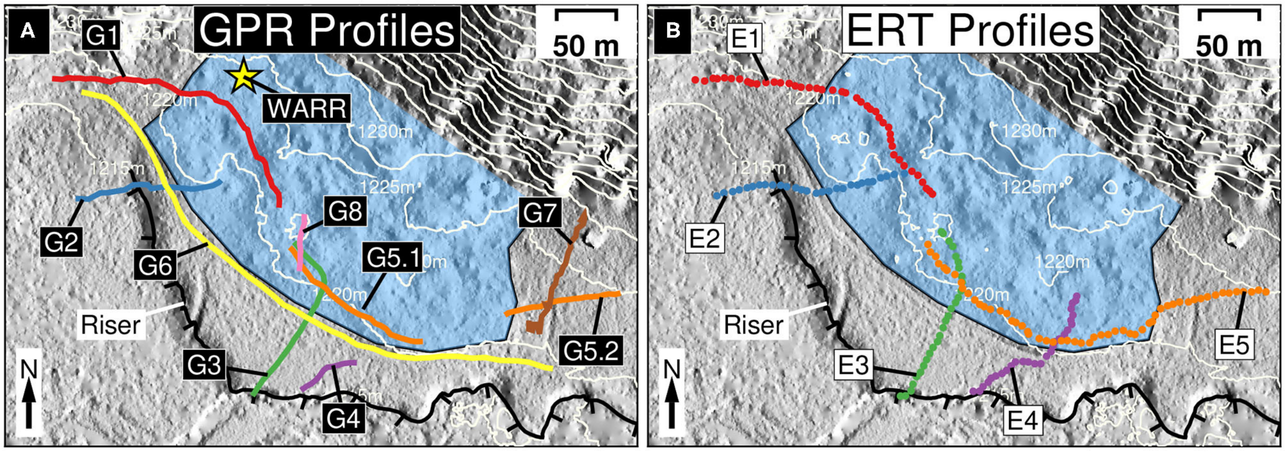

FIGURE 2 | (A) Map view of GPR profiles and WARR location. **(B)** Map view of ERT profiles. GPR and ERT profiles overlap to allow for joint processing and interpretation.

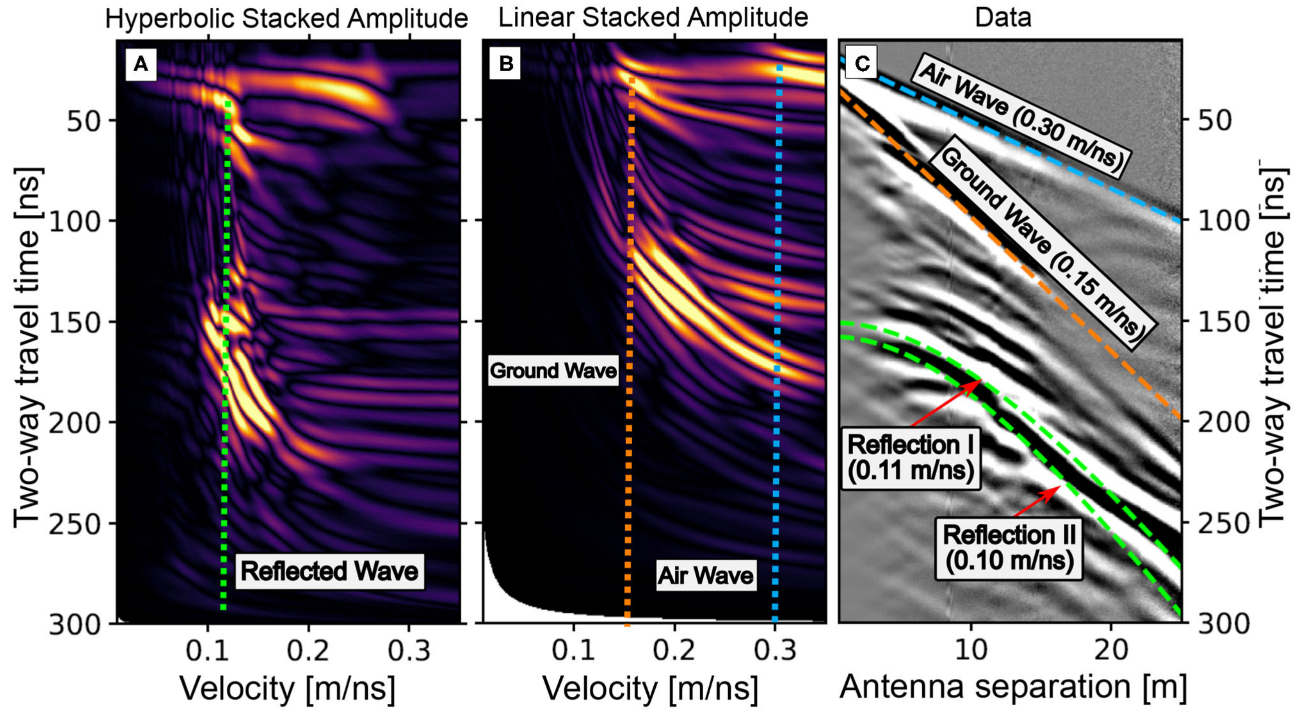

FIGURE 3 | (A) hyperbolic stacked amplitudes for the WARR data in **(C)**. Bright colors indicate velocities and depths (two-way travel time) of interfaces. **(B)** linear stacked amplitudes for the WARR data in **(C)**. Bright colors indicate velocities for direct waves. **(C)** WARR data with best-fitting lines and hyperbolae obtained from **(A,B)**.

filter (dewow and mean trace removal), T-power gain, f-k migration (Stolt, 1978) and topographic correction. Processing scripts including the parameters used are provided together with the raw data. For the time-to-depth transformation, we used a homogeneous velocity of 0.11 m /ns obtained from the WARR survey described in section 3.2 (Annan and Davis, 1976; Davis and Annan, 1989).

To identify candidates for the basal contact of the rock avalanche in the processed GPR data, we plotted GPR profiles in 3D (**Figure 4**) and identified interfaces that are consistent between the profiles and continue underneath the exposed rock avalanche as well as the surrounding area. The largest contributors to uncertainty of depth to a feature in GPR data are uncertainty in velocity, together with resolution caused by the signal wavelength. A velocity of 0.11 ± 0.01 m/ns, as obtained from our WARR survey (section 3.2), leads to a depth uncertainty of ≈ 10 %, hence ±1 m for an object buried at 10 m depth. Vertical resolution is typically limited by 1/4 of the wavelength (Jol, 2008), which, for a 50 MHz antenna and a velocity of 0.11 m/ns is ≈ 0.5 m. We took these uncertainties into account when reporting the following interfaces. We identified three candidates for the basal contact (**Figure 4D**): A relatively flat interface (parallel to the horizon) "*Alpha*" of elevation between 1,214 and 1,216 m above mean sea level, a deeper, nearly-horizontal interface "*Beta*" at an elevation of 1,206 to 1,209 m (**Figure 4E**), and "*Gamma*," which is visible in profiles G2 through G7 at an elevation of ≈ 1.205 m. Between interface *Alpha* and *Beta*, we observe scattering that is more prominent than below interface *Beta* (**Figure 4D**). The scattered texture close to the southeastern edge of G3, below *Beta* is an artifact of the migration processing step. The strong parallel lines at the topmost edges of the profiles result from radar waves directly traveling from the transmitter to the receiver (we used unshielded antennae).

3.4. GPR-Constrained ERT Inversion

To identify which of the previously identified candidates might be the basal contact of the rock avalanche, we removed smoothing constraints across interfaces *Alpha*, *Beta*, and *Gamma* in the ERT inversion of the corresponding profiles (Doetsch et al., 2012) using the open-source software BERT Günther et al. (2006), Rücker et al. (2017). This approach does not enforce but allows sharp transitions across the provided interface. We use profile E3 to illustrate the process (**Figure 5**), but other profiles showed similar patterns. For a granitic debris deposit overlying lacustrine, deltaic, and fluvial sediments, we expected electrically resistive material on top of conductive material. Indeed, inversion of the resistivity data with regular smoothing and no additional a-priori constraints revealed electrically resistive material (>5,000 Ωm) overlying relatively conductive material (<1,000 Ωm), but with a smooth transition (**Figure 5A**). For interface *Alpha*, resistive material is still present below the interface (**Figure 5B**). Interface *Beta* created a sharp transition between resistive and conductive material (**Figure 5C**), while interface *Gamma* lies

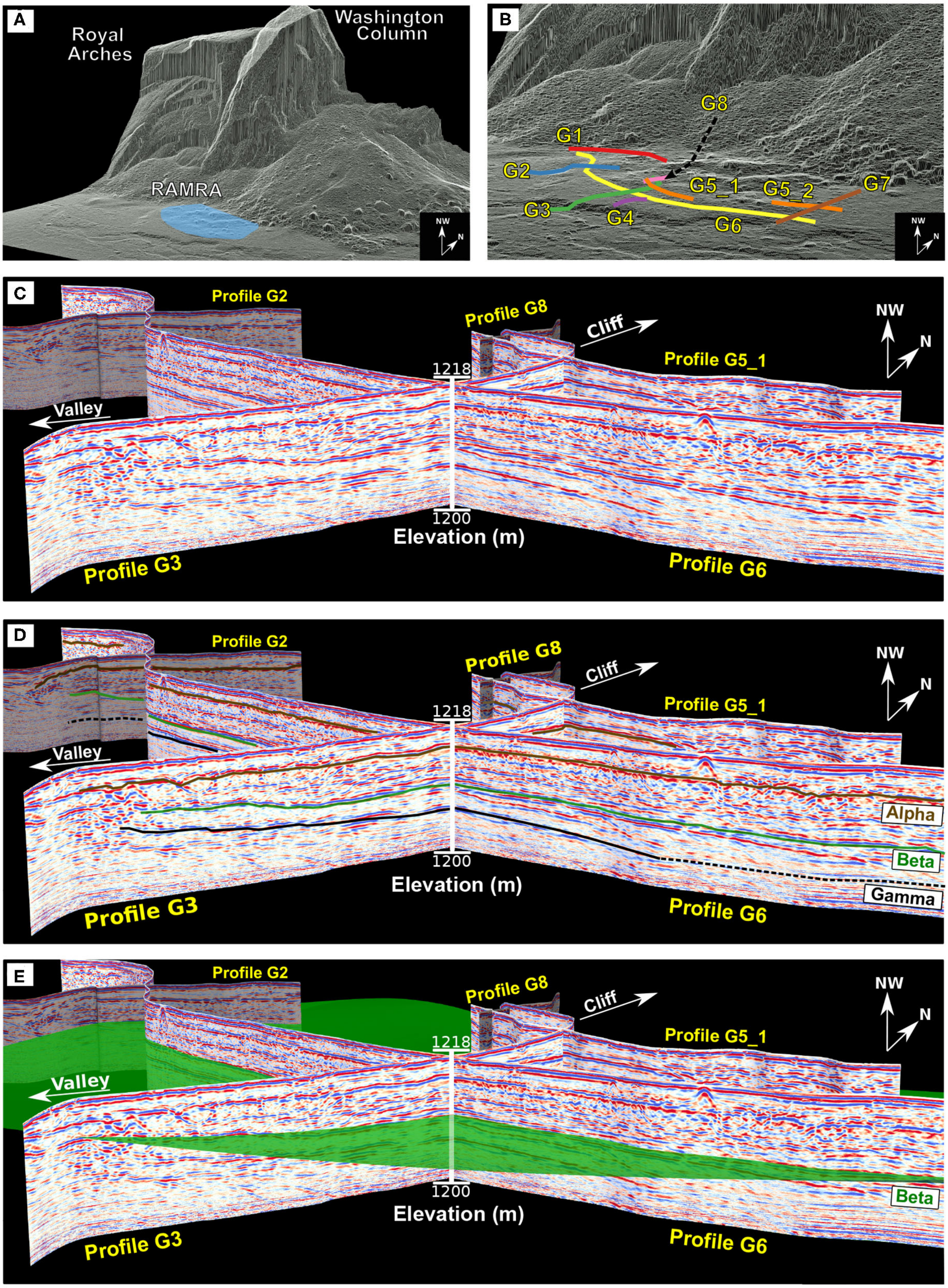

FIGURE 4 | (A) Location of the study area with respect to surrounding cliff faces. Extent of the Royal Arches Meadow rock avalanche (RAMRA) is shown in blue. **(B)** GPR profile arrangement within study area. **(C)** Oblique view of GPR profiles looking toward NW, **(D)** Identified interfaces *Alpha*, *Beta*, and *Gamma*, and **(E)** Interpolated surface for interface *Beta*.

below the transition of resistive to conductive material for most of the profile (**Figure 5D**). From our investigations, we were unable to identify the edge of the rock avalanche underneath the terrace riser. In our ERT profiles, we observed resistive material to within 10 m of the edge of the terrace, however, observations at the edge of the terrace riser did not reveal granitic boulders.

Identifying interfaces *Alpha*, *Beta*, and *Gamma* underneath the rough topography of the exposed rock avalanche was more challenging than underneath the adjacent smooth terrace. Interfaces in GPR profile G5.1 (**Figure 6A**) are less clear than in profiles G3 and G6 (**Figure 4**). In profile G5.1, we identified interfaces (**Figure 6B**) at elevations of ≈1,216 m (*Alpha*), ≈1,213 m (unnamed), and ≈1,207 m (*Beta*). Interface *Gamma* is not

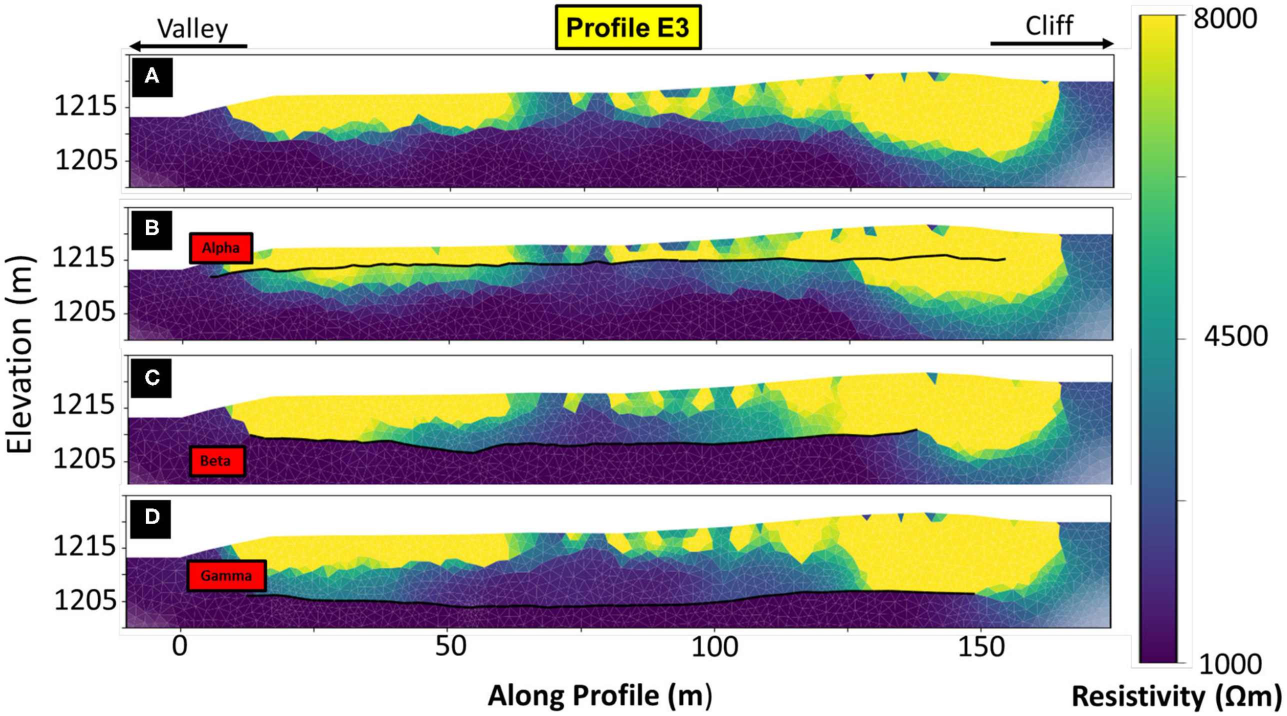

FIGURE 5 | ERT inversion results for profile E3 using smoothness regularization. **(A)** No additional a-priory information, smoothness applied everywhere. **(B)** No smoothing across interface *Alpha*. **(C)** No smoothing across interface *Beta*. **(D)** No smoothing across interface *Gamma*.

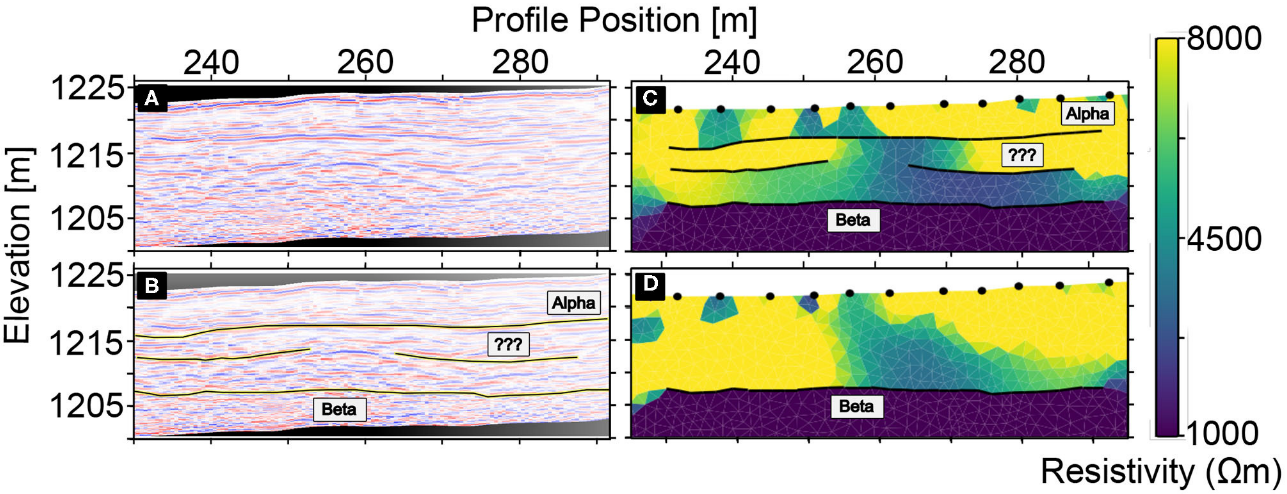

FIGURE 6 | (A) GPR profile G5.1. **(B)** Profile G5.1 with marked interfaces. **(C)** GPR-constrained ERT inversion result using all marked interfaces. **(D)** GPR-constrained ERT inversion result using only interface *Beta*.

visible in this GPR profile. Similar to the GPR-constrained ERT inversion for profile E3 (**Figure 5**), interface *Beta* creates the clearest separation between resistive and conductive materials (**Figures 6C,D**).

4. RESULTS AND IMPLICATIONS

We identified *Beta* as the interface between the rock avalanche deposit and the underlying sediments, which we interpret as the basal contact of the rock avalanche and thus the floor of Yosemite Valley at the time of the rock avalanche event. Our choice of *Beta* is based on the following observations: (1) of all three interfaces identified in the GPR data, *Beta* led to the clearest separation between electrically resistive and conductive material in GPR-constrained ERT inversions (**Figures 5**, **6**); and (2) in the GPR data, *Beta* separates a unit of visible scattering from a unit with little scattering underneath (**Figure 4**). We interpret that the scattering of radar waves is a result of randomly oriented clasts within the rock avalanche deposit.

Establishing the basal contact of the rock avalanche at between 1,206 and 1,209 m AMSL allows us to explore important metrics of the deposit and adjacent landscape. As discussed previously, the exposed distal portion of the deposit has a "bulked" volume of $\approx 3.8 \times 10^5$ m^3, assuming that the basal contact is at the elevation of the present valley floor elevation (1,217m AMSL). Using the newly established deeper basal contact, together with the existing area of the exposed portion of the rock avalanche deposit (recognized as a minimum area), yields a minimum deposit volume of between 8.1×10^5 m^3 and 9.7×10^5 m^3. This is a two- to three-fold increase compared to the previous volume estimation based solely on the surface expression of boulders. "Debulking" (correcting for an assumed 25% porosity) of the rock avalanche deposit (e.g., Hutchinson, 2006; Stock and Uhrhammer, 2010) leads to a minimum intact rock volume of between 6.1×10^5 m^3 and 7.3×10^5 m^3. As this is a minimum estimate and does not account for any volume in the proximal portion of the deposit buried underneath more recent talus, the actual volume of rock detached from the cliff was likely significantly larger. Although we were not able to reliably define the edges of the deposit in the subsurface, the lack of rock avalanche debris in the terrace riser adjacent to Tenaya Creek suggests that the total runout distance, though possibly larger than the extent of boulders on the surface, does not scale linearly with the increased volume (i.e., the runout distance is not two to three times longer). This implies that the rock avalanche had lower mobility than indicated by the surface expression of boulders alone.

Establishing the basal contact also allows the rock avalanche deposit to be used as a marker for the position of the floor of eastern Yosemite Valley at 16.1 ± 0.3 ka, immediately after deglaciation. Following emplacement of the rock avalanche, approximately 10 m of glaciofluvial sediment accumulated. As the rock avalanche deposit only extends partway across the valley, it likely did not act as a natural dam; sediment aggradation therefore must have occurred for reasons independent of rock avalanche emplacement. We conclude that the aggradation occurred in the latest Pleistocene as retreating glaciers produced prodigious sediment in the form of glacial outwash. This sediment was transported and deposited in alluvial fans and deltaic deposits in eastern Yosemite Valley, including in the vicinity of the Royal Arches Meadow rock avalanche. After aggradation ceased, Tenaya Creek has incised approximately 5 m into the alluvial sediments, as evidenced by the terrace riser and cutbank. This incision was likely driven by diminished sediment supply following full deglaciation. The geomorphic marker provided by the basal contact of the rock avalanche thus provides an important calibration point in reconstructing the post-glacial landscape evolution of Yosemite Valley.

5. CONCLUSIONS

Cosmogenic ^{10}Be exposure dating revealed that the Royal Arches Meadow rock avalanche occurred 16.1 ± 0.3 thousand years ago, shortly after deglaciation of eastern Yosemite Valley. We identified the basal contact of the Royal Arches Meadow rock avalanche at an elevation of between 1,206 and 1,209 m AMSL using a combination of ERT and GPR data. The adjacent terrace has a surface elevation of 1,217 m AMSL, indicating that approximately 10 m of sediment aggradation has occurred in this location since deglaciation. We estimate the volume of the Royal Arches Rock avalanche deposit to be at least between 8.1×10^5 m^3 and 9.7×10^5 m^3, of which only about a third is exposed on the surface. Integrated geophysical imaging greatly improves our understanding of the full extent and volume of the rock avalanche and serves as an important marker in the post-glacial evolution of the Yosemite Valley landscape.

ERT and GPR were well-suited geophysical methods to determine the basal contact of the Royal Arches Meadow rock avalanche deposit, because the granitic boulders in the deposit presented a strong contrast in electrical conductivity and dielectric permittivity compared to the underlying sediments. Many rock avalanche deposits in other parts of the world likely show similarly strong contrasts in these physical parameters, in particular if the avalanche debris is comprised of largely intact boulders deposited on sediments or soil. Our approach can hence be a general strategy for investigating rock avalanche deposits that are expected to be partly buried.

DATA AVAILABILITY STATEMENT

The geophysical datasets generated and analyzed for this study can be found on https://github.com/NSGeophysics/RAMRA_Data.

AUTHOR CONTRIBUTIONS

MP collected and processed the geophysical data. AMP collected ERT data, contributed to the geophysical data processing, and served as faculty advisor to MP. GMS characterized the rock avalanche deposit and collected the cosmogenic ^{10}Be samples. DR conducted cosmogenic ^{10}Be chemistry, accelerator mass spectrometry analyses, data reduction, and exposure age calculations. All authors interpreted the data. MP, AMP, and GMS wrote the manuscript, with contributions from DR and CP.

FUNDING

This material was based upon work supported by the National Science Foundation under Grant Nos. EAR-1550732 and EAR-2022671 to AMP.

ACKNOWLEDGMENTS

We thank Guohai Jia, Jukya and Ryuya Kimura, Mathieu Richaud, Amalie Larsen, and Jessie Shields for assistance with geophysical field work, and Jessica Jobe for assistance with deposit characterization and sampling for cosmogenic ^{10}Be dating. We appreciate helpful discussions with Elizabeth Haddon, Derek Booth and Brendon Quirk, and thank two reviewers and the editor. We thank the staff of the Scottish Universities Environmental Research Center (SUERC) for support during chemistry and accelerator mass spectrometry analyses. Dedicated to the memory of Jerry DeGraff (1947–2020).

REFERENCES

Annan, A. P., and Davis, J. L. (1976). Impulse radar sounding in permafrost. *Radio Sci*. 11, 383–394. doi: 10.1029/RS011i004p00383

Balco, G., Stone, J., Lifton, N., and Dunai, T. (2008). A complete and easily accessible means of calculating surface exposure ages or erosion rates from ↑10Be and ↑26Al measurements. *Quat. Geochronol*. 3, 174–195. doi: 10.1016/j.quageo.2007.12.001

Ballantyne, C. K., and Stone, J. O. (2004). The Beinn Alligin rock avalanche, NW Scotland: cosmogenic ↑10Be dating, interpretation and significance. *Holocene* 14, 448–453. doi: 10.1191/0959683604hl720rr

Bateman, P. C. (1992). *Plutonism in the Central Part of the Sierra Nevada Batholith, California*. U.S. Geological Survey Professional Paper 1483. doi: 10.3133/pp1483

Brody, A. G., Pluhar, C. J., Stock, G. M., and Greenwood, W. J. (2015). Near-surface geophysical imaging of a talus deposit in Yosemite Valley, California. *Environ. Eng. Geosci*. 21, 111–127. doi: 10.2113/gseegeosci.21.2.111

Corbett, L. B., Bierman, P. R., and Rood, D. H. (2016). An approach for optimizing in situ cosmogenic ↑10Be sample preparation. *Quat. Geochron*. 33, 24–34. doi: 10.1016/j.quageo.2016.02.001

Cordes, S. E., Stock, G. M., Schwab, B. E., and Glazner, A. F. (2013). Supporting evidence for a 9.6 ± 1 ka rock fall originating from Glacier Point in Yosemite Valley, California. *Environ. Eng. Geosci*. 19, 345–361. doi: 10.2113/gseegeosci.19.4.345

Corominas, J. (1996). The angle of reach as a mobility index for small and large landslides. *Can. Geotech. J*. 33, 260–271. doi: 10.1139/t96-005

Dade, W. B., and Huppert, H. E. (1998). Long-runout rockfalls. *Geology* 26, 803–806. doi: 10.1130/0091-7613(1998)026<0803:LRR>2.3.CO;2

Davis, J. L., and Annan, A. P. (1989). Ground-penetrating radar for high-resolution mapping of soil and rock stratigraphy 1. *Geophys. Prospect*. 37, 531–551. doi: 10.1111/j.1365-2478.1989.tb02221.x

Doetsch, J., Linde, N., Pessognelli, M., Green, A. G., and Günther, T. (2012). Constraining 3-D electrical resistance tomography with GPR reflection data for improved aquifer characterization. *J. Appl. Geophys*. 78, 68–76. doi: 10.1016/j.jappgeo.2011.04.008

Evans, S. G. (2006). "Single-event landslides resulting from massive rock slope failure: Characterising their frequency and impact on society," in *Landslides From Massive Rock Slope Failure*, eds S. Evans, G. Mugnzza, A. Strom, and R. Hermanns (Heidelberg: Springer), 53–73. doi: 10.1007/978-1-4020-4037-5_2

Evans, S. G., Mugnozza, G. S., Strom, A. L., Hermanns, R. L., Ischuk, A., and Vinnichenko, S. (2006). "Landslides from massive rock slope failure and associated phenomena," in *Landslides from Massive Rock Slope Failure*, eds S. Evans, G. Mugnzza, A. Strom, and R. Hermanns (Heidelberg: Springer), 3–52. doi: 10.1007/978-1-4020-4037-5

Gosse, J. C., and Phillips, F. M. (2001). Terrestrial in situ cosmogenic nuclides: theory and application. *Quat. Sci. Rev*. 20, 1475–1560. doi: 10.1016/S0277-3791(00)00171-2

Guerin, A., Stock, G. M., Radue, M. J., Jaboyedoff, M., Collins, B. D., Matasci, B., et al. (2020). Quantifying 40 years of rockfall activity in Yosemite Valley with historical Structure-from-Motion photogrammetry and terrestrial laser scanning. *Geomorphology* 356:107069. doi: 10.1016/j.geomorph.2020.107069

Günther, T., Rücker, C., and Spitzer, K. (2006). Three-dimensional modelling and inversion of dc resistivity data incorporating topography-II. inversion. *Geophys. J. Int*. 166, 506–517. doi: 10.1111/j.1365-246X.2006.03011.x

Hermanns, R. L., and Longva, O. (2012). "Rapid rock-slope failures," in *Landslides: Types, Mechanisms and Modeling*, eds J. Clague and D. Stead (Cambridge: Cambridge University Press), 59–70. doi: 10.1017/CBO9780511740367.007

Hewitt, K., Clague, J. J., and Orwin, J. F. (2008). Legacies of catastrophic rock slope failures in mountain landscapes. *Earth-Sci. Rev*. 87, 1–38. doi: 10.1016/j.earscirev.2007.10.002

Hovius, N., and Stark, C. P. (2006). "Landslide-driven erosion and topographic evolution of active mountain belts," in *Landslides from Massive Rock Slope Failure*, eds S. Evans, G. Mugnzza, A. Strom, and R. Hermanns (Dordrecht: Springer), 573–590. doi: 10.1007/978-1-4020-4037-5_30

Hsü, K. (1975). On sturzstroms-catastrophic debris streams generated by rockfalls. *Geol. Soc. Am. Bull*. 86, 129–140. doi: 10.1130/0016-7606(1975)86<129:CDSSGB>2.0.CO;2

Huber, N. K. (1987). *The Geologic Story of Yosemite National Park*. U.S. Geological Survey Bulletin 1595.

Hutchinson, J. (2006). "Massive rock slope failure: perspectives and retrospectives on state-of-the-art," in *Landslides from Massive Rock Slope Failure*, eds S. Evans, G. Mugnzza, A. Strom, and R. Hermanns (Heidelberg: Springer), 619–662. doi: 10.1007/978-1-4020-4037-5_32

Jol, H. M. (2008). *Ground Penetrating Radar Theory and Applications*. Amsterdam: Elsevier.

Korup, O., Clague, J. J., Hermanns, R. L., Hewitt, K., Strom, A. L., and Weidinger, J. T. (2007). Giant landslides, topography, and erosion. *Earth Planet. Sci. Lett*. 261, 578–589. doi: 10.1016/j.epsl.2007.07.025

Lifton, N., Sato, T., and Dunai, T. J. (2014). Scaling in situ cosmogenic nuclide production rates using analytical approximations to atmospheric cosmic-ray fluxes. *Earth Planet. Sci. Lett*. 386, 149–160. doi: 10.1016/j.epsl.2013.10.052

Loke, M. H., Chambers, J. E., Rucker, D. F., Kuras, O., and Wilkinson, P. B. (2013). Recent developments in the direct-current geoelectrical imaging method. *J. Appl. Geophys*. 95, 135–156. doi: 10.1016/j.jappgeo.2013.02.017

Matthes, F. E. (1930). *Geologic History of the Yosemite Valley. U.S. Geological Survey Professional Paper*, 504. doi: 10.3133/pp160

McColl, S. T. (2020). The anomalously old Bush Stream Rock Avalanche and its implications for landslide inventories in dynamic landscapes. *Front. Earth Sci*. 8:103. doi: 10.3389/feart.2020.00103

Mitchell, W. A., McSaveney, M. J., Zondervan, A., Kim, K., Dunning, S. A., and Taylor, P. J. (2007). The Keylong Serai rock avalanche, NW Indian Himalaya: geomorphology and palaeoseismic implications. *Landslides* 4, 245–254. doi: 10.1007/s10346-007-0085-0

Moreiras, S. M., Hermanns, R. L., and Fauqué, L. (2015). Cosmogenic dating of rock avalanches constraining quaternary stratigraphy and regional neotectonics in the Argentine Central Andes (32 S). *Quat. Sci. Rev*. 112, 45–58. doi: 10.1016/j.quascirev.2015.01.016

Nagelisen, J., Moore, J. R., Vockenhuber, C., and Ivy-Ochs, S. (2015). Post-glacial rock avalanches in the Obersee valley, Glarner Alps, Switzerland. *Geomorphology* 238, 94–111. doi: 10.1016/j.geomorph.2015.02.031

Neal, A. (2004). Ground-penetrating radar and its use in sedimentology: principles, problems and progress. *Earth-Sci. Rev*. 66, 261–330. doi: 10.1016/j.earscirev.2004.01.004

Nishiizumi, K., Imamura, M., Caffee, M. W., Southon, J. R., Finkel, R., and McAninch, J. (2007). Absolute calibration of ↑10Be AMS standards. *Nucl. Instrum. Meth. B* 258, 403–413. doi: 10.1016/j.nimb.2007.01.297

Oldenburg, D. W., and Li, Y. (1999). Estimating depth of investigation in DC resistivity and IP surveys. *Geophysics* 64, 403–416. doi: 10.1190/1.1444545

Olhoeft, G. R. (1998). "Electrical, magnetic and geometric properties that determine ground penetrating radar performance," in *Proc. of GPR'98, 7th Int'l Conference On Ground Penetrating Radar* (Lawrence, KS), 177–182.

Otto, J., and Sass, O. (2006). Comparing geophysical methods for talus slope investigations in the Turtmann valley (Swiss Alps). *Geomorphology* 76, 257–272. doi: 10.1016/j.geomorph.2005.11.008

Peck, D. L. (2002). *Geologic Map of the Yosemite Quadrangle, Central Sierra Nevada, California.* U.S. Geological Survey Geologic Investigation Series Map I-2751.

Phillips, F. (2017). Glacial chronology of the Sierra Nevada, California, from the Last Glacial Maximum to the Holocene. *Cuadernos Invest. Geogr*. 527–552. doi: 10.18172/cig.3233

Phillips, F. M., Argento, D. C., Balco, G., Caffee, M. W., Clem, J., Dunai, T. J., et al. (2016). The CRONUS-Earth project: a synthesis. *Quat. Geochron*. 31, 119–154. doi: 10.1016/j.quageo.2015.09.006

Plattner, A. (2020). GPRPy: Open-source ground penetrating radar processing and visualization software. *Lead. Edge* 39, 332–337. doi: 10.1190/tle39050332.1

Plattner, A. M., and Pacheco, M. (2019). *A Community-Developed Free Ground Penetrating Radar Software.* Near-Surface Views, Society of Exploration Geophysicists, 26.

Rood, D. H., Burbank, D. W., and Finkel, R. C. (2011). Chronology of glaciations in the Sierra Nevada, California, from ↑10Be surface exposure dating. *Quat. Sci. Rev*. 30, 646–661. doi: 10.1016/j.quascirev.2010.12.001

Rücker, C., Günther, T., and Wagner, F. M. (2017). pyGIMLi: An open-source library for modelling and inversion in geophysics. *Comput. Geosci.* 109, 106–123. doi: 10.1016/j.cageo.2017.07.011

Sass, O. (2006). Determination of the internal structure of alpine talus deposits using different geophysical methods (Lechtaler Alps, Austria). *Geomorphology* 80, 45–58. doi: 10.1016/j.geomorph.2005.09.006

Sass, O., and Wollny, K. (2001). Investigations regarding Alpine talus slopes using ground-penetrating radar (GPR) in the Bavarian Alps, Germany. *Earth Surf. Proc. Land*. 26, 1071–1086. doi: 10.1002/esp.254

Socco, L. V., Jongmans, D., Boiero, D., Stocco, S., Maraschini, M., Tokeshi, K., et al. (2010). Geophysical investigation of the Sandalp rock avalanche deposits. *J. Appl. Geophys*. 70, 277–291. doi: 10.1016/j.jappgeo.2009.12.005

Stock, G. M., Collins, B. D., Santaniello, D. J., Zimmer, V. L., Wieczorek, G. F., and Snyder, J. B. (2013). Historical rock falls in Yosemite National Park, California (1857-2011). *U.S. Geol. Survey Data Ser*. 746. doi: 10.3133/ds746

Stock, G. M., Martel, S. J., Collins, B. D., and Harp, E. L. (2012). Progressive failure of sheeted rock slopes: the 2009-2010 Rhombus Wall rock falls in Yosemite Valley, California, USA. *Earth Surf. Proc. Land*. 37, 546–561. doi: 10.1002/esp.3192

Stock, G. M., and Uhrhammer, R. A. (2010). Catastrophic rock avalanche 3600 years BP from El Capitan, Yosemite Valley, California. *Earth Surf. Proc. Land*. 35, 941–951. doi: 10.1002/esp.1982

Stolt, R. H. (1978). Migration by Fourier transform. *Geophysics* 43, 23–48. doi: 10.1190/1.1440826

Wahrhaftig, C., Stock, G. M., McCracken, R. G., Sasnett, P., and Cyr, A. J. (2019). *Extent of the Last Glacial Maximum (Tioga) Glaciation in Yosemite National Park and Vicinity, California*. U.S. Geological Survey Scientific Investigations Series Map 3414. doi: 10.3133/sim3414

Wieczorek, G. F. (2002). "Catastrophic rockfalls and rockslides in the Sierra Nevada, USA," in *Catastrophic Landslides: Effects, Occurrence, and Mechanisms*, eds S. G. Evans and J. V. De Graff (Geological Society of America Reviews in Engineering Geology), Boulder, CO. 165–190. doi: 10.1130/REG15-p165

Wieczorek, G. F., Morrissey, M. M., Iovine, G., and Godt, J. (1999). *Rock-Fall Potential in the Yosemite Valley, California.* U.S. Geological Survey Open-File Report 99. doi: 10.3133/ofr99578

Wieczorek, G. F., Snyder, J. B., Waitt, R. B., Morrissey, M. M., Uhrhammer, R. A., Harp, E. L., et al. (2000). Unusual July 10, 1996, rock fall at Happy Isles, Yosemite National Park, California. *Geol. Soc. Am. Bull.* 112, 75–85. doi: 10.1130/0016-7606(2000)112<75:UJRFAH>2.0.CO;2

Xu, S., Freeman, S. P. H. T., Rood, D. H., and Shanks, R. M. (2015). Decadal ↑10Be, ↑26Al and ↑36Cl QA measurements on the SUERC accelerator mass spectrometer. *Nucl. Inst. Methods B* 361, 39–42. doi: 10.1016/j.nimb.2015.03.064

Zimmer, V. L., Collins, B. D., Stock, G. M., and Sitar, N. (2012). Rock fall dynamics and deposition: an integrated analysis of the 2009 Ahwiyah Point rock fall, Yosemite National Park, USA. *Earth Surf. Proc. Land* 37, 680–691. doi: 10.1002/esp.3206

Conflict of Interest: The authors declare that the research was conducted in the absence of any commercial or financial relationships that could be construed as a potential conflict of interest.

frontiers in Earth Science

ORIGINAL RESEARCH
published: 30 September 2020
doi: 10.3389/feart.2020.543937

Rock Avalanche-Generated Sediment Mass Flows: Definitions and Hazard

Andrew Mitchell[1]*, *Scott McDougall*[1], *Jordan Aaron*[2] *and Marc-André Brideau*[3]

[1] *Department of Earth, Ocean and Atmospheric Sciences, The University of British Columbia, Vancouver, BC, Canada,* [2] *ETH Zürich, Zürich, Switzerland,* [3] *Westrek Geotechnical Services Ltd., Squamish, BC, Canada*

Rock avalanches can trigger destructive associated hazards following the initial collapse and fragmentation of a rock slope failure. One of these associated hazards occurs when the material derived from the initial collapse of the source zone impacts and mobilizes a mass flow composed of sediment from along the travel path. These mass flows can be grouped into radial impact areas that occur on relatively flat, open terrain (typically a floodplain), and more linear impact areas that occur in channelized terrain. Rock avalanche-generated sediment mass flows are an important consideration because they can significantly increase the area impacted by an event, thereby increasing the hazard area, especially in valley bottoms where there are likely more elements at risk. Existing runout prediction methods do not consistently account for the increase in the impact area from rock avalanche-generated sediment mass flows. Thus, there is a need for a simple data-supported method for estimating the extent of mass flow impacts resulting from an initial rock avalanche event with sediments along the potential travel path. This paper presents data from 32 rock avalanches and 23 rock avalanche-generated sediment mass flows from around the world, described using a consistent set of quantitative and qualitative attributes. A wide range of mass flow impacts were observed, with the sediment mass flow impact area or runout length exceeding the impact of the coarse, rocky debris in some cases. The area and length impacted by the coarse, rocky debris is estimated using multiple linear regressions considering the event volume and topographic features. The sediment mass flow dataset is used as input to develop an exponential distribution of the area or runout length of the sediment mass flow over that of the coarse, rocky debris. A decision tree framework is presented for estimating the extent of potential rock avalanches and potential rock avalanche-generated sediment mass flows for hazard and risk analysis, which is demonstrated by comparing the stochastic empirical predictions to those from numerical runout modeling.

Keywords: rock avalanche, runout, regression, stochastic prediction, mass flow, splash zone

Edited by:
Reginald Leonhard Hermanns,
Geological Survey of Norway, Norway

Reviewed by:
Thierry Oppikofer,
Geological Survey of Norway, Norway
Tim Davies,
University of Canterbury, New Zealand

***Correspondence:**
Andrew Mitchell
amitchell@eoas.ubc.ca

Specialty section:
This article was submitted to Structural Geology and Tectonics,
a section of the journal
Frontiers in Earth Science

Received: *18 March 2020*
Accepted: *31 August 2020*
Published: *30 September 2020*

Citation:
Mitchell A, McDougall S, Aaron J, Brideau M-A (2020) Rock Avalanche-Generated Sediment Mass Flows: Definitions and Hazard.
Front. Earth Sci. 8:543937.
doi: 10.3389/feart.2020.543937

INTRODUCTION

Rock avalanches are mass flows that can initiate complex hazard cascades. They are defined by their dominant characteristics: high velocity flow-like motion of a large volume (typically greater than 1 million m^3) of fragmenting rock that can travel several kilometers and run up opposing valley slopes (Hermanns, 2013; Hungr et al., 2014). A range of associated hazards must also be considered when making predictions about the potential impacts of a rock avalanche, such as air

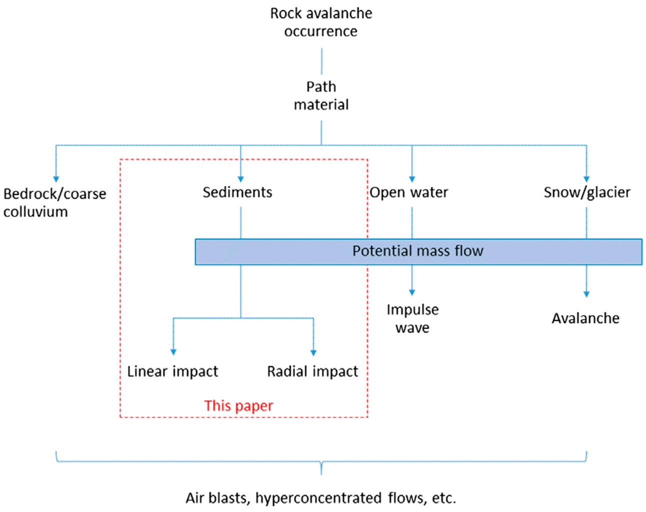

FIGURE 1 | Potential mass flows generated by rock avalanches. Note that multiple types of mass flows are possible in a single event (e.g., Bussmann and Anselmetti, 2010), depending on the nature and distribution of materials along the path.

blasts (e.g., Mathews and McTaggart, 1978; Zhuang et al., 2019) and floods caused by landslide dam impoundment and/or breach (e.g., Evans et al., 2011). A particularly destructive associated hazard involves the mobilization of surficial material from the travel path. When rock avalanches encounter sediments, open water or snow/ice along their path, a relatively fluid and mobile flow of these materials can be generated that extends beyond the margins of the coarse rocky flow. We refer to this process generally as a rock avalanche-generated mass flow (**Figure 1**). This paper specifically focuses on mass flows involving sediments.

One of the factors that can influence the mobility and impact area of rock avalanches is the mobilization of path sediments. In their report on the 1903 Frank Slide, McConnell and Brock (1904) described extensive "mud flats" fringing the deposit, derived primarily from alluvium that was "splashed" out of the valley floor. Heim (1932) observed similar zones (now often referred to as splash zones) surrounding rock avalanche deposits in the Alps, which he likened to the lateral moraines of a glacier and attributed to a "snowplow" style mechanism. Abele (1997) linked the apparent high mobility of some of these features, including the far-reaching Bonaduz Gravel deposits associated with the Flims rockslide, to the mechanism of rapid undrained loading of saturated path sediments. Other workers have expounded on this hypothesis (e.g., Hungr and Evans, 2004; Orwin et al., 2004; McDougall and Hungr, 2005; Crosta et al., 2009) and a large number of supporting case studies have been presented (see case study compilation and associated references later in this paper). Some laboratory flume and centrifuge experiments have also been carried out that shed further light on this mechanism (e.g., Steers, 2018; Furuya et al., 2019).

While these types of mass flows can be highly destructive, evidence of their presence is not as well preserved in the geomorphic and stratigraphic record as that of the coarse rocky debris. In their reexamination of the Frank Slide, Cruden and Hungr (1986) noted dense vegetation cover in the relatively fine-grained splash zones described by McConnell and Brock (1904). Another striking example of this sort of masking over time can be seen at the site of the 1965 Hope Slide (**Figure 2**). Panel **A** in **Figure 2** shows the northern distal splash zone of the 1965 Hope Slide (southwestern British Columbia) deposit. Panels **B** and **C** in **Figure 2** show aerial views of the site in 1965 and 2019, respectively; the splash zone is entirely overgrown in the 2019 imagery.

Since the evidence for rock avalanche-generated mass flows can be subtle and short-lived, it has led to inconsistencies in the ways that rock avalanche runout lengths and impact areas are measured. For example, the commonly used concept of the fahrböschung, or angle of reach, defined as the ratio of the difference in elevation from the highest point on the scarp to the toe of the deposit (H) to the horizontal path distance between those points (L), has long been used as a metric of rock avalanche mobility, and has been shown to be related to the volume of the rock avalanche (see Mitchell et al., 2020 for a summary). Inconsistencies in the inclusion or exclusion of rock-avalanche generated mass flows when assessing H and L can lead to multiple authors assessing different angle of reach values for the same cases.

This inconsistency is problematic when assessing rock avalanche hazard and risk because many empirical and numerical runout prediction methods that are used for this purpose (e.g., McDougall, 2017) are based on statistical analyses or model calibration approaches that implicitly rely on consistent case study data. Runout prediction methods that use case study datasets that include prehistoric events where distal mass flow impacts were not recognized, or datasets that are based exclusively on the mapped extents of coarse rocky deposits (e.g., Mitchell et al., 2020), may underestimate potential rock avalanche impacts unless suitable adjustments are made to the predictions. Furthermore, there is little information currently available in order to make a well constrained estimate of the likelihood of a mass flow occurring due to a rock avalanche.

To help address this issue, the objectives of this study were to:

- Highlight the importance of mass flows in rock avalanche hazard and risk assessment;
- Develop a consistent methodology for describing key quantitative and qualitative attributes of rock avalanche-generated mass flows involving sediments;
- Compile a dataset of case studies using the new methodology;
- Develop a probabilistic hazard assessment framework and preliminary statistical relationships to predict mass flow likelihood, impact areas and runout lengths.

A hypothetical mass flow runout prediction case is used to demonstrate the application of the new methodology.

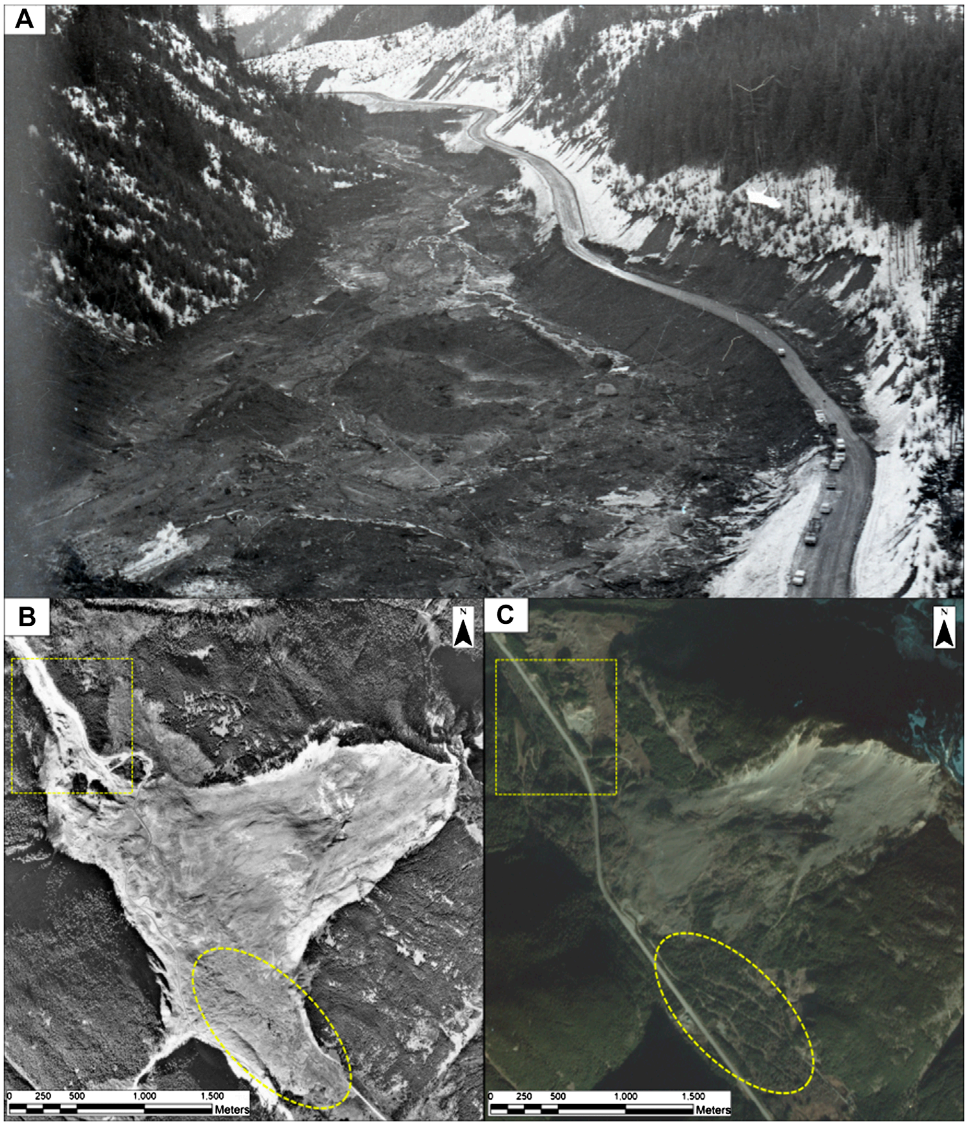

FIGURE 2 | (A) Rock avalanche-generated mass flow impact area (splash zone) at the northern margin of the Hope Slide [photo taken shortly after the event in January 1965, courtesy of British Columbia Ministry of Transportation and Infrastructure (BC MoTI)], **(B)** orthorectified airphoto of the impact area from 1965, and **(C)** orthorectified satellite image of the same area from 2019 (Planet, 2020). The approximate area shown in Panel **(A)** is indicated by the yellow rectangles in Panels **(B)** and **(C)**. The yellow oval highlights the revegetation of the Zone 2 impact area at the southern margin of the deposit.

METHODOLOGY

Definitions

To describe rock avalanche and associated sediment mass flow characteristics, we define three impact zones, as shown below. These zones can be identified based on their sedimentology, emplacement mechanism and relationship to the initial failed mass, and are based on concepts originally presented by Abele (1997) and Hungr and Evans (2004).

- Zone 1 Impact Area: The spatial area impacted by coarse, rocky debris. This area extends from the source, through the transport zone to the distal extent of continuous fragmented rock debris (**Figure 3**). In cases where a rock avalanche overrides sediments, the Zone 1 impact area may include *continuous* coarse debris rafted on top of the sediments. Typically, the Zone 1 impact area is all that is observable in aerial or satellite imagery of prehistoric events.
- Zone 2 Impact Area: The spatial area impacted by a rapid to extremely rapid (Hungr et al., 2014) mass flow generated by a rock avalanche impact (**Figure 3**). Zone 2 impacts occur coincidently with the deposition of the Zone 1 material; essentially they are different parts of the same event. In cases where a rock avalanche encounters sediments, the Zone 2 impact area may include *discontinuous* coarse debris rafted on top of the sediments, but these isolated blocks are

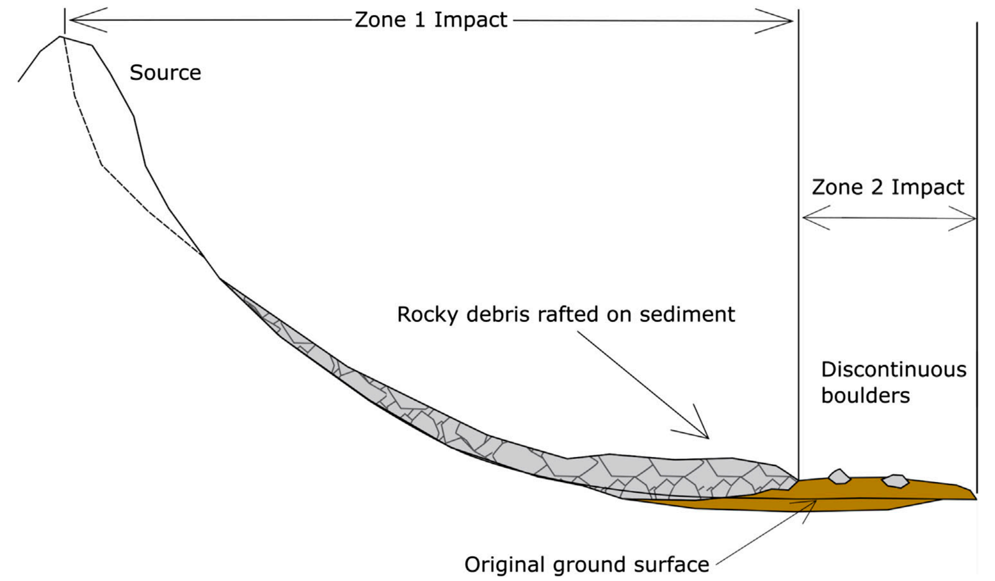

FIGURE 3 | Definition sketch showing Zone 1 and Zone 2 impacts from a rock avalanche.

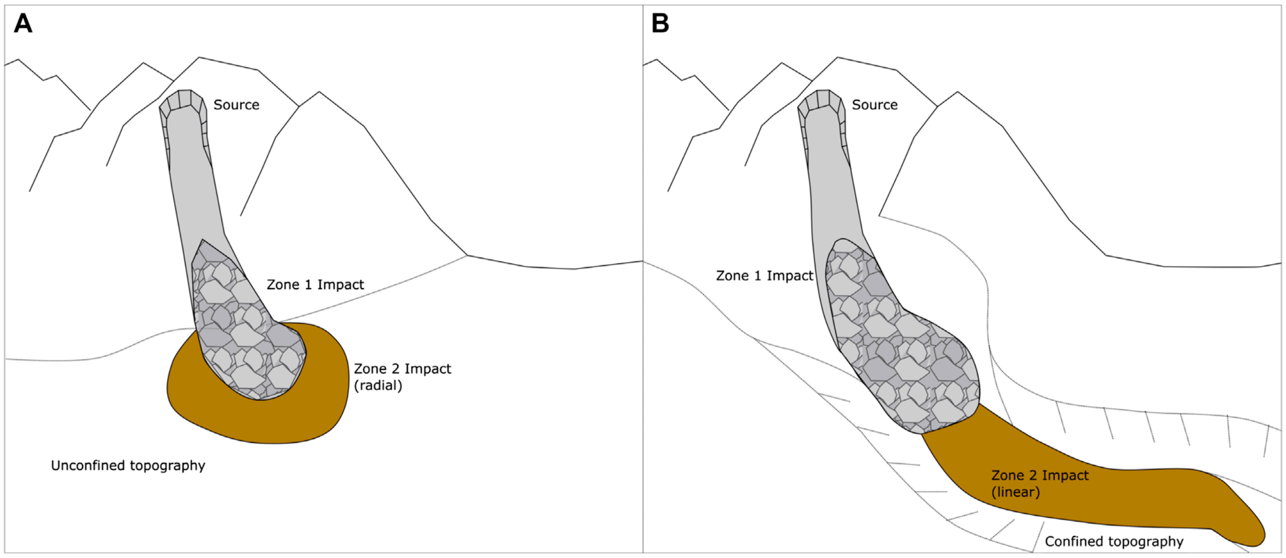

FIGURE 4 | Definition sketch showing **(A)** a radial Zone 2 impact zone, and **(B)** a linear Zone 2 impact zone.

considered a minor portion of the flow. Rock avalanches may also encounter coarse colluvium that is entrained into the flow, however these impacts will generally be indistinguishable from the Zone 1 impact area.

- Zone 3 Impact Area: The spatial area impacted as a result of a rock avalanche, but not triggered by the emplacement of fragmented rock debris and may be separated from the Zone 1 and Zone 2 impacts in time. For example, they may include the formation of a landslide dammed lake or aggradation/erosion of a downstream channel. These impacts may occur suddenly (e.g., through breach of a landslide dam) or over the course of many years.

Zone 2 impacts can be further subdivided into end-member events that have a radial impact zone (**Figure 4A**) or a linear impact zone (**Figure 4B**). Often mass flows have elements of the idealized radial and linear impact zones shown in **Figure 4**, which are examined in the *Hypothetical Example* and *Summary and Discussion* sections. Linear impact zones are sometimes referred to as debris flows or debris avalanches (Hungr et al., 2014). The

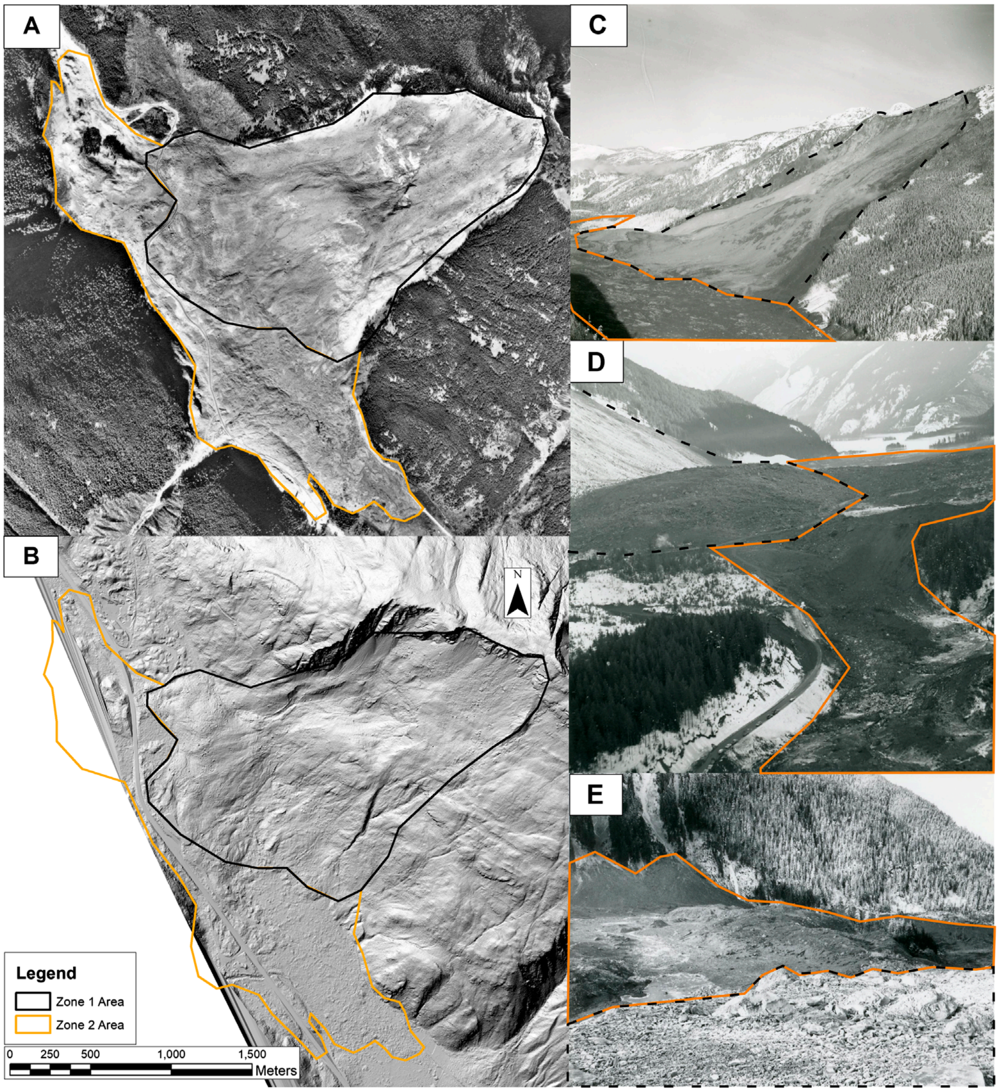

FIGURE 5 | Hope Slide **(A)** ortho image generated from aerial photographs taken in 1965, **(B)** bare-earth lidar hillshade from 2014 (data courtesy of BC MoTI), **(C)** oblique view of the slide, **(D)** oblique view of the west margin of the deposit area, and **(E)** view of the south side of the debris field showing the transition from Zone 1 to Zone 2 deposits (photos **C** through **E** courtesy of BC MoTI).

special term rockslide-debris avalanche was previously proposed for events with an entrainment ratio (ratio between entrained volume and initial failure volume) greater than 0.25 (Hungr and Evans, 2004).

As shown in **Figure 1**, mass flows involving water or snow and ice may also be generated by rock avalanches. Air blasts could also be considered a form of mass flow, just one involving a low density, low viscosity fluid. These impacts could be considered as part of Zone 2, however, the focus of this study is on mass flows primarily involving sediments. Likewise, systematic descriptions of Zone 3 impacts are beyond the scope of the present study; the definition of Zone 3 is included above for completeness, its relationship to landslide dam work referenced later in this paper, and for the potential future expansion of the general hazard assessment approach we propose.

Two "type case" examples are provided to illustrate the typical behavior of radial and linear rock avalanche-generated mass flows: the Hope Slide (**Figures 2**, **5**) and the McAuley Creek rock avalanche (**Figure 6**), respectively.

Hope Slide–Radial Impact Type Case

The Hope Slide occurred on January 9, 1965 in the Cascade Mountains of southwestern British Columbia and was described in detail by Mathews and McTaggart (1978). The event originated with a mass of rock releasing on a steeply dipping felsite sheet. The rock then fragmented and impacted the valley floor, burying approximately 3 km of BC Highway 3 and causing four fatalities (**Figures 5A,C**). The coarse rock avalanche debris deposited primarily at the base of the source slope, creating a series of irregular curved ridges near the middle of the deposit and

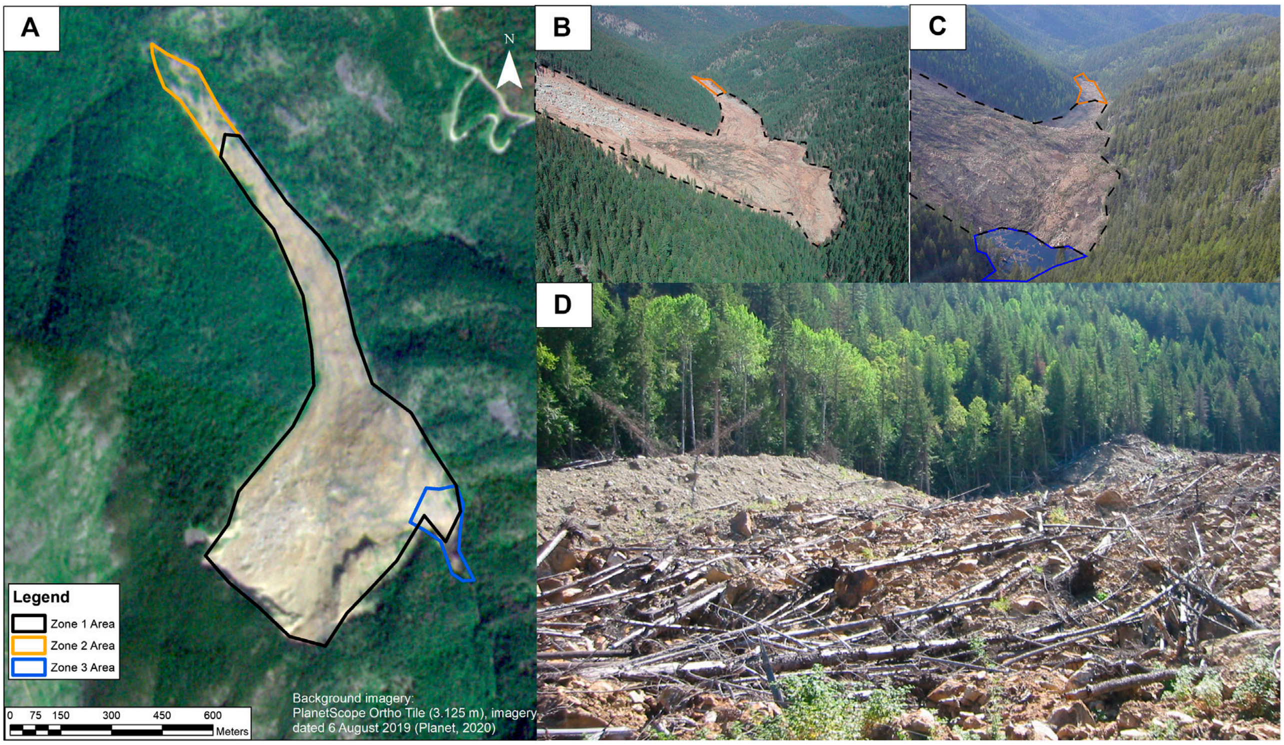

Background imagery:
PlanetScope Ortho Tile (3.125 m), imagery dated 6 August 2019 (Planet, 2020)

FIGURE 6 | McAuley Creek rock avalanche **(A)** impact area delineations on a satellite image from August 6, 2019 (Planet, 2020), **(B)** oblique view of the main deposition area with the tongue of more mobile material extending into the background from August 21, 2002 (photo courtesy Réjean Couture), **(C)** oblique view of the deposit area showing the transient landslide dammed lake from June 10, 2002 (photo courtesy Scott Paddington), and **(D)** a photo of the north margin of the deposit near the transition from what was mapped as Zone 1 and Zone 2.

irregular mounds elsewhere. The coarse debris was fringed by what was described as mud-rich debris (**Figures 5B,D,E**). Evidence of an air-blast was also noted, such as snow being dislodged from the branches of trees or the snow being covered by air-borne sediment, primarily near the mid-line of the landslide along the main direction of travel (Mathews and McTaggart, 1978).

The broad valley relative to the size of the Zone 1 deposit led to the formation of a radial fringe of sediment-rich debris in the Zone 2 area. However, the event did exhibit some characteristics of a linear Zone 2 impact, such as the opposite wall of the valley limiting the spread of debris to the west. A "mud flow" extending 5 km down the Nicolum River was also described by Mathews and McTaggart (1978). This area was not included in the estimate of the Zone 2 area given in **Table 2**, as it is not visible in the available imagery and we did not want to introduce inconsistency in the mapping methodology, described in detail in the Dataset Compilation section. While this flow was contained in the channel of the river, it did cause a bridge to become blocked, resulting in flow over Highway 3 at that location (Mathews and McTaggart, 1978). Further discussion on the applicable spatial resolution of this technique is included in the *Summary and Discussion*.

Since the event in 1965, vegetation has re-established over the Zone 2 impact area and Highway 3 has been reconstructed (**Figure 2**). Although much of the visual evidence has been lost in that 55-year period, there is evidence of the Zone 2 impact in the lidar hillshade image, where a rougher surface is visible relative to the surrounding valley floor (**Figure 5B**).

McAuley Creek–Linear Impact Type Case

The McAuley Creek rock avalanche occurred in an uninhabited area of southern British Columbia in late May or early June 2002 and was described in detail by Brideau et al. (2012). The basal failure surface and lateral release surfaces are thought to have developed from faults and shear bands present in the rock. The coarse rock avalanche debris deposited primarily at the base of the source slope, with the material thinning toward the distal edge of the deposit, and a more mobile lobe of material extending down the McAuley Creek valley (**Figures 6A,B**) (Brideau et al., 2012). The coarse debris formed a landslide dam that created a small, temporary lake upstream of the coarse deposit area (**Figure 6C**). The area the slide overran was a mature forest and many displaced trees were visible on the surface of the deposit (**Figure 6D**). Review of photographs from field investigations following the event showed there were progressively fewer large boulders in the deposit, and the surface texture visible in the aerial imagery became less rough toward the distal end of the flow. Vegetation regrowth visible in the 2019 satellite imagery (**Figure 6A**) was also used to help distinguish the transition from a primarily coarse, rocky deposit where slower vegetation regrowth is expected, to the finer sediment deposits where faster regrowth is expected.

The narrow valley relative to the size of the deposit and the formation of a linear lobe of sediment and organic-rich debris led to this event being classified as confined in the Zone 2 area. The lake visible in **Figure 6C**, but not in the 2019 imagery (**Figure 6A**), is an example of a transitory Zone 3 impact.

Dataset Compilation

A dataset of 32 historical and prehistoric rock avalanche events was compiled in order to derive statistical relationships to predict the length and area of Zone 2 (see subsequent sections for further details of this methodology). The cases included in this study were compiled from a literature review of rock avalanche case histories that overran sediments for a significant portion of their travel length (as opposed to bedrock or glacial ice/snow). Where available, pre- and post-event satellite images, aerial photographs, lidar topography, and published maps of deposits were used in the mapping. Published references were used to obtain information on the event volumes, source characteristics, substrate characteristics and deposit descriptions. Visible changes in deposit material and surface texture, along with published information, were used to determine if a Zone 2 impact was present, and if so, to map its extent. This dataset included a subset of cases where there is no strong evidence of a mass flow. The literature review attempted to collect all English language peer-reviewed case histories of events after 2010 to provide an unbiased sample for the estimation of the likelihood of a mass flow occurring given a rock avalanche occurring with sediment in the travel path. The cases without mass flow generation from before 2010 were described when there was sufficient information in the literature and air or satellite photos from a short time after the event to confidently determine there was not a mass flow associated with the rock avalanche. Cases of any age with insufficient data for detailed descriptions or mapping were excluded from the dataset.

Pre- and post-event satellite images of rock avalanches that occurred after 2010 were obtained from RapidEye (5 m pixel size) or PlanetScope (3.25 m pixel size) orthorectified images (Planet, 2020). DigitalGlobe satellite imagery was also accessed for all cases to examine recent land cover. The ASTER GDEM v2 was used for all elevations. For cases where the event pre-dated satellite imagery and aerial photographs were available, orthorectified images were generated using Agisoft Metashape v1.5 software (Agisoft, 2019). Where detailed deposit maps were available in the literature, they were used to aid in the mapping. Lidar imagery was available for some cases, for which it was also used for geomorphic interpretation of the different deposit zones.

The quantitative and qualitative attributes used in this study to describe the Zone 1 impact areas are consistent with the terms used in Mitchell et al. (2020). The attributes used to describe the Zone 1 and Zone 2 impact areas are shown in **Table 1**. For laterally confined events, the travel distance and fall height were mapped along the flow path, and for unconfined events the maximum distance was measured perpendicular to the margin of the Zone 1 deposit. There is some uncertainty in both the spatial extent of the deposits and the boundary between different deposit zones. This uncertainty is mainly controlled by the quality of available imagery and how soon after the event the imagery was collected. To qualitatively describe the degree of confidence in the mapped attributes, three spatial uncertainty classes were defined (ranging from well to poorly constrained), as shown in **Table 1**.

Hazard Assessment Framework

A statistical methodology for predicting the Zone 2 impact area has been developed based on the compiled rock avalanche dataset. As shown in **Figure 7**, the occurrence of a Zone 2 impact area of a given size is conditional on a number of factors described below, such as the Zone 1 impact area, and the probability of generating a mass flow given that a rock avalanche has occurred. Typically, a range of potential outcomes is examined, and continuous random variables are discretized using values chosen as representative for a range of probabilities. While the continuous random variables could theoretically be used, creating hazard maps and other practical tools for risk communication requires discrete values. This range of outcomes is represented as an event tree in **Figure 7**.

The event tree analysis requires the values of Zone 1 and Zone 2 impact areas (A_{Z1} and A_{Z2}) span the range of potential outcomes. The range of potential areas can be binned so each representative value, $a_{Z1,i}$ and $a_{Z2,j}$ is within one of the bins. For each of the $n \times m$ branches of the event tree shown in **Figure 7**, given a failure volume, v, and a runout path that encounters sediments, the probability of a certain representative Zone 2 impact area, a_{Z2}, being within a range of Zone 2 areas is:

$$P\left(a_{Z2,\,i,j}\right) = P(E) \times P\left(a_{Z1,i}\middle|E\right) \times P\left(E_{Z2}\middle|E, a_{z1,i}\right) \times P\left(a_{Z2,j}\middle|E, a_{Z1,i}, E_{z2}\right) \tag{1}$$

where $P(E)$ is the probability of a rock avalanche event with a volume of $V = v$ occurring; $P(a_{Z1,i}|E)$ is the probability of a certain Zone 1 impact area, $a_{Z1,i}$ being within the range of the ith bin of the plausible range of Zone 1 impact areas, given the rock avalanche occurs; $P(E_{Z2}|E,\ a_{Z1})$ is the probability of a mass flow occurring given the rock avalanche occurs and has a certain value of a_{Z1}; and, $P(a_{Z2,j}|E,\ a_{Z1,i},\ E_{Z2})$ is the probability of a certain Zone 2 impact area, $a_{Z2,j}$, being within the range of the jth bin of the plausible range of Zone 2 impact areas, given the rock avalanche occurs and has a certain value of a_{Z1}, and given a mass flow occurs.

An equivalent formulation for the probability of a certain Zone 2 runout distance, l_{Z2}, can be made by substituting l_{Z1} and l_{Z2} for all values of a_{Z1} and a_{Z2} in Equation 1. The choice of the number of representative values for the areas and lengths at which probabilities are estimated will depend on the desired granularity of the analysis, with more values providing more refined estimates, at the expense of increasing the number of branches on the event tree. The choice of values may also be informed by the locations of elements at risk (e.g., refining the estimates where smaller changes in runout length and impact area have a greater effect on the risk).

The methods used to estimate the above terms, with the exception of $P(E)$, are given in the following section.

TABLE 1 | Attributes used to describe the Zone 1 and Zone 2 impact areas for events in the dataset.

	Attribute	Units/descriptor	Source/comments
Quantitative	Volume[a]	10^6 m^3	Published references
	Fall height	m	ASTER GDEM v2
	Travel distance	m	Digitized path
	Total impacted area	m^2	Digitized deposit
Qualitative	Path topography	Unconfined	Visual interpretation of deposit shape and topographic features in the impacted area
		Laterally confined	
		Frontally confined[a]	
	Path substrate	Saturated	Published references, if available, or visual interpretation of landforms from aerial/satellite imagery
		Unsaturated	
		Bedrock[a]	
	Source geology[a]	Weak/weathered	Published references, if available, or estimated from publicly available geological maps
		Strong/fresh	
	Spatial uncertainty	Well constrained	Historical event with well-preserved deposit, high resolution imagery from less than one year post-event and/or any lidar topographic data and/or field mapping
		Moderately constrained	Historical event with well-preserved deposit, high resolution imagery from more than one year post-event, and/or any lidar topographic data and/or field mapping
		Poorly constrained	Prehistoric event with overgrown/eroded deposit and/or lidar topographic data and detailed field mapping
	Temporal uncertainty	Known	Date of event from eyewitness reports, daily satellite imagery and/or seismic signal
		Well constrained	Year of event from eyewitness accounts or aerial photographs
		Moderately constrained	Approximate age from radio carbon or cosmogenic nuclide dating
		Approximately constrained	General geologic/geomorphic evidence available (e.g., post-glacial)

[a]*Indicates attributes or descriptors that are only used for Zone 1 Impacts.*

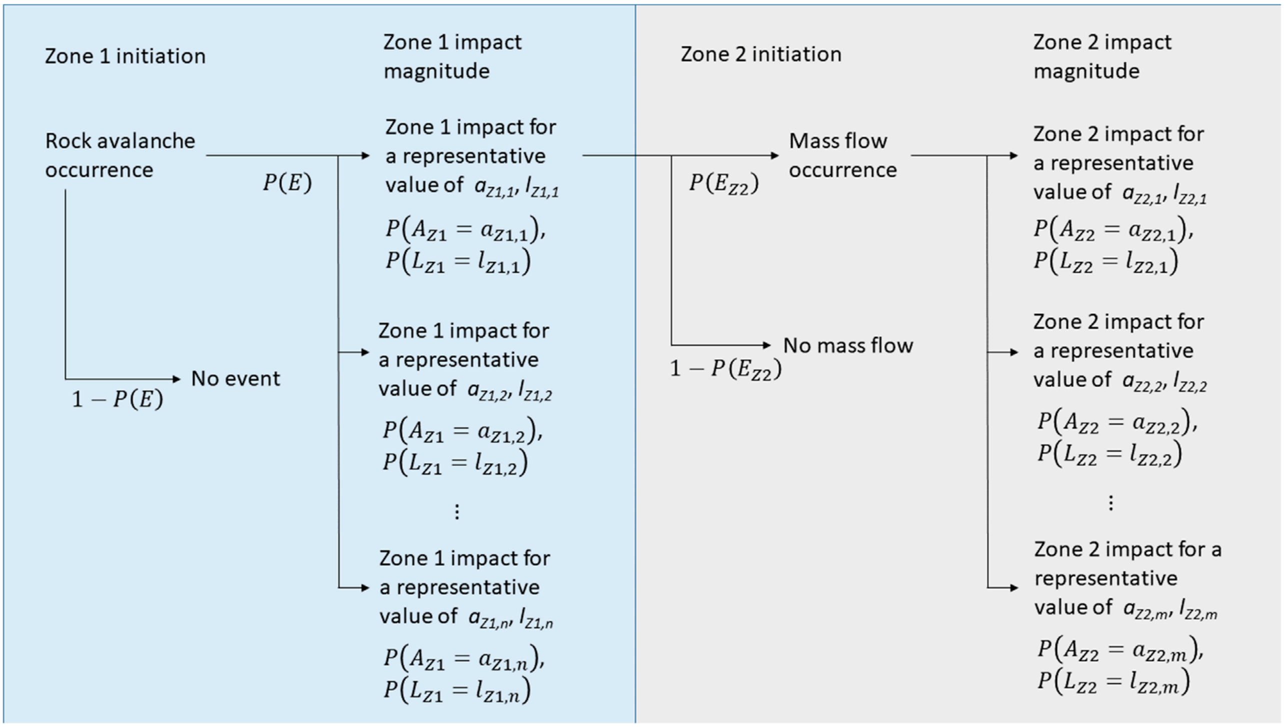

FIGURE 7 | Event tree for the estimation of Zone 2 impact area magnitudes. Note that only the top branch of the event tree is expanded. Terms shown are defined in the text.

Statistical Methods

The approach taken in this study is to work from an estimate of the Zone 1 impact area to estimate the potential Zone 2 impact area. The estimates of Zone 1 impacts are made using multiple linear regression of the dataset. The linear regression on a logarithmic transform of the variables is equivalent to a power law, which is consistent with previous research on rock avalanche impact area (e.g., Li, 1983; Hungr and Evans, 1993; Griswold and Iverson, 2008). The regression model for the Zone 1 impact area is:

$$\log A_{Z1} = \beta_0 + \beta_1 \log V + \beta_2 \log H_{Z1} + \varepsilon \tag{2}$$

where A_{Z1}, H_{Z1} are the Zone 1 total impact area and fall height, respectively; V is the event volume, in 10^6 m^3; β_0, β_1, β_2 are the regression coefficients; and, ε is the error term, assumed to be normally distributed with zero mean, $\varepsilon \sim N(0, \sigma^2)$.

The runout length is also estimated using multiple linear regression of the dataset. The path topography in the Zone 1 area was considered as an indicator variable, consistent with Mitchell et al. (2020). The regression model for Zone 1 runout is:

$$\log L_{Z1} = \beta_0 + \beta_1 \log V + \beta_2 \log H_{Z1} + \beta_3 C + \varepsilon \tag{3}$$

Where: L_{Z1} is the Zone 1 runout length; C is an indicator variable with a value of 1 if the Zone 1 path topography is laterally confined, 0 otherwise; and, All other terms are as defined before.

For hazard and risk assessment purposes, it is often useful to calculate runout exceedance probabilities (either as a runout length or an impact area). This can be achieved by expressing the results of the multiple linear regression in the form of survival functions. Assuming that the models in **Eqs 2** and **3** capture the range of potential outcomes of future events, and using the normally distributed error term, ε, the linear regressions can be rearranged as:

$$P(A_{Z1} \geq a_{Z1} | V = v,\ H_{Z1} = h_{Z1}) \\ = 1 - \Phi\left(\frac{\log a_{Z1} - \beta_0 - \beta_1 \log v - \beta_2 \log h_{Z1}}{\sigma}\right) \tag{4}$$

$$P(L_{Z1} \geq l_{Z1} | V = v,\ H_{Z1} = h_{Z1},\ C = c) \\ = 1 - \Phi\left(\frac{\log l_{Z1} - \beta_0 - \beta_1 \log v - \beta_2 \log h_{Z1} - \beta_3 c}{\sigma}\right) \tag{5}$$

Where: a_{Z1}, l_{Z1}, h_{Z1} and c are given values for Zone 1 area, Zone 1 runout distance, Zone 1 fall height, and Zone 1 lateral confinement (true or false), respectively; v is a given value of the event volume; and Φ is the cumulative distribution function for a standard normal variable.

The probability of a certain representative value of Zone 1 impact area or runout length, e.g., $P(a_{Z1,i}|E)$ in **Eq. 1**, can be found by calculating the difference between the probability of exceedance for the minimum and maximum value of the bin in which the representative value belongs. For example, if a Zone 1 impact area of 150,000 m^2 is selected as the representative value for the range from 100,000 to 200,000 m^2, then $P(a_{Z1\,=\,150{,}000}|E) = P(A_{Z1} \geq 100{,}000|\ldots) - P(A_{Z1} \geq 200{,}000|\ldots)$.

The next consideration is whether or not a rock avalanche-generated mass flow will occur. As part of compiling the dataset for this study, a literature review was conducted to find cases of rock avalanches that likely encountered sediments during the time in which we have high quality satellite imagery, to evaluate the surface conditions post-event. As a preliminary estimate of the probability of mass flow occurrence, $P(E_{Z2}|E, a_{Z1})$ in **Eq. 1**, the total number of events with published case histories that occurred after 2010 with an observable Zone 2 deposit was divided by the total number of events from the same time period in the dataset.

The estimates of $P(a_{Z2}|E, a_{Z1}, E_{z2})$ in **Eq. 1** were made by examining the ratio of the Zone 2 area to Zone 1 area for all cases with an observed Zone 2 impact. Several univariate distributions were fitted to the data using the maximum likelihood estimation method, implemented in the "fitdistr" function in R (R Core Team, 2020). The applicability of the univariate distributions tested was assessed using a Kolmogorov-Smirnov (KS) test. The KS test is used to assess if the fit distribution was different than the empirical distribution at a 95% confidence level. The same process was repeated with the ratio of Zone 2 runout length over Zone 1 runout length. The exponential distribution was then chosen for both the area and length ratios, as it meets the KS test criteria and it has the fewest number of parameters. The resulting probability density function for a given ratio of a_{Z2} over a_{Z1} is:

$$f\left(\frac{a_{Z2}}{a_{Z1}}\right) = \lambda * \exp\left(-\lambda \times \frac{a_{Z2}}{a_{Z1}}\right) \tag{6}$$

Where: λ is the scale parameter.

This equation can also be expressed as a survival function (Liu, 2012), which provides the probability of a ratio of Zone 2 to Zone 1 area, A_{Z1}/A_{Z2}, exceeding a given value, a_{Z2}/a_{Z1}. The survival function has the form:

$$P\left(\frac{A_{Z2}}{A_{Z1}} \geq \frac{a_{Z2}}{a_{Z1}}\right) = \exp\left(-\lambda \times \frac{a_{Z2}}{a_{Z1}}\right) \tag{7}$$

Estimates for the Zone 2 runout distance can be obtained by substituting L_{Z1}, L_{Z2}, l_{Z1} and l_{Z2} for all A_{Z1}, A_{Z2}, a_{Z1} and a_{Z2} in and 7.

As with the Zone 1 impact estimation, the probability of a certain representative value can be estimated by calculating the difference between the minimum and maximum value of the bin in which the representative value belongs.

RESULTS

Dataset

Zone 1 and Zone 2 impacts were mapped, and descriptive attributes were assigned to 32 cases. A summary of the quantitative attributes is provided in **Table 2**. The complete dataset with measurements and attributes for all events is included as **Supplementary Material**. Additional references and data sources for each event are also provided in the **Supplementary Material**, and shapefiles for each of the mapped deposits are available through the DesignSafe-CI

TABLE 2 | Summary of case histories.

Event (main reference)	Volume (10^6 m^3)	Zone 1				Zone 2			
		A (×10^4 m^2)	*L* (m)	*H* (m)	*C*[a]	*A* (×10^4 m^2)	*L* (m)	*H* (m)	*C*[a]
McAuley Creek (Brideau et al., 2012)	7.4	46.2	1,600	500	0	2.75	340	50	1
Zymoetz River (Boultbee et al., 2006)	1	45	1,220	610	0	19.7	2,820	610	1
Pink Mountain (Dufresne and Geertsema, 2019)	1	39.2	1,950	450	0	0	0	0	0
Mosque Mountain (Lu et al., 2003)	5	23.2	1,260	520	0	45.2	110	7	1
Mount Meager (Guthrie et al., 2012)	49	707	8,950	1,720	1	72.7	750	8	0
Harold Price (Dufresne and Geertsema, 2020)	1.6	63.7	2,660	730	1	9.68	2,010	110	1
Sutherland (Dufresne and Geertsema, 2020)	3	34.4	1,450	270	0	0	0	0	0
Little Salmon Lake (Brideau et al., 2010)	2	33.1	1,620	490	0	7.08	420	67	0
Nomash River (Hungr and Evans, 2004)	0.7	27.7	1,930	460	1	1.57	400	14	1
Mt Cayley Debris Avalanche 1984 (Evans et al., 2001)	0.7	59.7	3,460	1,180	1	18.2	3,130	370	1
Frank Slide (Cruden and Hungr, 1986)	37	341	3,080	760	0	57.0	400	2	0
Hope Slide (Mathews and McTaggart, 1978)	48	253	2,630	1,080	0	168	1,610	15	0
Cheam (Orwin et al., 2004)	180	117	6,420	1,050	0	583	1,690	15	0
Joffre Peak May 13, 2019 (Friele et al., 2020)[b]	1.9	127	4,000	1,200	1	1.75	420	37	1
Joffre Peak May 16, 2019 (Friele et al., 2020)[b]	3.1	115	3,650	1,300	1	17.7	2,190	130	1
Eagle Pass (Hungr and Evans, 2004)	0.1	12.9	950	570	0	0	0	0	0
Xinmo (Scaringi et al., 2018)[b]	4.5	154	2,600	1,120	0	0	0	0	0
Nayong (Zhu et al., 2019)[b]	0.8	219	640	270	0	2.85	170	20	0
Bondo (Walter et al., 2020)[b]	3.3	119	3,240	1,420	1	26.1	3,540	560	1
Santa Lucia (Duhart et al., 2019)[b]	7.2	209	5,890	1,050	1	229	3,800	180	1
Flims/Bonaduz (Calhoun and Clague, 2018)	11,000	6,369	13,650	1,670	0	223	14,640	31	1
Baige October 11, 2018 (Li et al., 2019)[b]	24	128	1,890	780	0	57.7	1,050	16	1
Baige November 3, 2018 (Li et al., 2019)[b]	9.1	76.8	1,950	790	0	34.3	1,230	20	1
Gaunling (Zhu et al. 2019)	1.8	17.1	1,260	380	1	1.02	280	38	1
West Salt Creek (Coe et al., 2016)[b]	55	236	4,530	670	1	0	0	0	0
Preonzo (Loew et al., 2017)[b]	0.21	36.4	1,820	1,240	0	0	0	0	0
Su Village (Ouyang et al., 2019)[b]	0.4	20.4	1,080	460	0	0	0	0	1
Round Top (Dufresne et al., 2010)	45	448	3,980	670	0	106	420	6	0
Matakitaki (Hancox et al., 2016)	18	164	1,690	390	0	62.3	280	2	0
Madison Canyon (Wolter et al., 2016)	20	110	1,600	400	0	0	0	0	0
Val Pola (Govi et al., 2002)	50	340	3,000	860	0	0	0	0	1
Goldau (Bussman and Anselmetti, 2010)	38	490	4,870	1,030	0	210	1,710	75	0

[a] *Lateral confinement (1 = true, 0 = false).*

[b] *Represents case histories that were considered for the calculation of* $P(E_{Z2}|E, a_{z1})$ (***Eq. 1***).

repository (https://www.designsafe-ci.org/data/browser/public/designsafe.storage.published//PRJ-2830).

The spatial extents of Zone 2 impacts vary widely, with impact areas ranging from unobservable at scale of imagery available to 2.23 m^2 × 10^7 m^2, and runout lengths up to 14,600 m. In one case (Santa Lucia) the Zone 2 impact area exceeds the Zone 1 impact, and in three cases (Zymoetz River, Bondo, and Flims) the Zone 2 runout length exceeds the Zone 1 runout. These observations highlight how considering only the impacts within Zone 1 could significantly underestimate the spatial extent of the hazard associated with a rock avalanche.

Statistical Analysis

The linear regression results for Zone 1 impact area and runout length are summarized in **Table 3**. The multiple linear regression for area predicted from volume and fall height (**Figure 8A**) shows a stronger association relative to the regression only using volume as the predictor, so the multiple linear regression results are used in the following analysis. The regression model for the Zone 1 runout distance (**Figure 8B**) shows a strong association between the runout distance, volume, fall height and whether or not the topography is laterally confined. These results are consistent with those reported in Mitchell et al. (2020). The effect of topographic confinement on the Zone 1 impact area was tested, but the uncertainty on the estimate was too high to be used for the regression equation (see **Supplementary Material**).

In the rock avalanche dataset, 13 events that ran out over sediment deposits were identified since 2010 that have satellite imagery and event descriptions (cases marked [b] in **Table 2**). These events were used for the preliminary assessment of the probability of a rock avalanche generating a mass flow of sediment, $P(E_{Z2}|E, a_{z1})$ in **Eq. 1**. Mass flows were noted in 9 of 13 events considered, giving a probability of approximately 0.7 based on this very limited dataset.

The ratios of Zone 2 area to Zone 1 area and Zone 2 runout length to Zone 1 runout length were calculated for all cases where a Zone 2 impact was mapped. The ratios between Zone 2 and Zone 1 impact areas range from 0.01 to 1.1, and the runout length ratios range from 0.08 to 2.3 (**Figure 9**). An exponential function was fitted to the data for the impact area and runout length ratios. Results of the KS tests are included in the **Supplementary Material** to confirm the applicability of the exponential function. The exponential survival functions of the Zone 2 to Zone 1 relationships are shown in **Figures 9A,B** for the impact area and runout length ratios, respectively. The calculated probabilities for the distributions fitted to the data are

TABLE 3 | Regression summary for Zone 1 impact area and runout and comparison to the estimates from Mitchell et al. (2020).

	Zone 1 impact area				**Zone 1 runout length**	
	Simple linear regression		**Multiple linear regression**		**Multiple linear regression**	
	This study	**Mitchell et al. (2020)**	**This study**	**Mitchell et al. (2020)**	**This study**	**Mitchell et al. (2020)**
Adjusted R^2	0.82	0.76	0.92	0.82	0.87	0.80
Coefficients	**Estimate (standard error)**	**Estimate (standard error)**	**Estimate (standard error)**	**Estimate (standard error)**	**Estimate (standard error)**	**Estimate (standard error)**
log(V)	0.547 (0.046)	0.516 (0.042)	0.472 (0.033)	0.441 (0.041)	0.168 (0.024)	0.139 (0.023)
log(H)	NA	NA	0.897 (0.145)	0.709 (0.171)	0.627 (0.098)	0.640 (0.098)
C	NA	NA	NA	NA	0.183 (0.045)	0.169 (0.037)
Intercept	5.582 (0.059)	5.537 (0.053)	3.081 (0.406)	3.617 (0.464)	1.405 (0.269)	1.412 (0.262)
σ	0.253	0.233	0.166	0.200	0.101	0.105

Note: Volume reported in 10^6 m^3, fall height reported in m, impact area reported in m^2, and runout length reported in m, NA indicates "not applicable".

relatively insensitive to the choice of distribution, except for small Zone 2/Zone 1 ratios. An exponential distribution has been used at this time as it is the simplest distribution that fits the data, and exponential distributions have been used previously to represent other natural geological processes/features, such as bed thickness (Straub et al., 2012) and joint spacing (Rives et al., 1992). As new data are added to this dataset in the future, the choice of distribution should be re-examined.

The data were also used to examine the potential effects of the descriptive topographic attributes on the Zone 2 impact area and runout distance. No strong associations could be found between the topography and either the impact area or runout distance within this dataset, however the number of data are limited (n = 14 and n = 9 for laterally confined and unconfined topography, respectively), and as such these results should be treated with caution. Details of the statistical comparisons are provided in the **Supplementary Material**, along with a cross validation to determine if any single case significantly affects the fitted distributions. As new data are added to the dataset it may be possible to fit separate distributions based on the descriptive attributes.

HYPOTHETICAL EXAMPLE

The application of the methodology presented in this paper for predicting potential impact areas is demonstrated here using a hypothetical case. The same case, a hypothetical rock avalanche site in Canada, was used for a numerical runout model benchmarking exercise in 2018 (Pastor et al., 2018). The potential rock avalanche scenario modeled had a volume of $8.3\ \text{m}^3 \times 10^6\ \text{m}^3$, the relief between the crest of the source zone and the valley bottom is approximately 1,380 m, and the valley bottom has potentially saturated fluvial and glaciofluvial deposits (Pastor et al., 2018).

The probabilities of the Zone 1 impact area of the event exceeding any value in a range of plausible impact areas were estimated using **Eq. 4**, the coefficients from **Table 3**, and the volume and fall height given above. Estimates of the probability of exceedance associated with a range of Zone 1 areas are shown in **Figure 10A**. From this information, representative values of the Zone 1 impact area can be selected, for example, points B, C, and D on **Figure 10A**, and using **Eq. 7**, the probability of exceedance for the Zone 2 impact areas associated with these representative Zone 1 impact areas can be estimated (**Figures 10B–D**).

The estimates shown in **Figure 10** can be used with the decision tree shown in **Figure 7** to calculate the probabilities of each Zone 1 and Zone 2 impact area scenario. For demonstration purposes, a conservative assumption can be made that the probability of the rock avalanche occurring and the probability of a mass flow being generated are 1. If the values for the Zone 1 and Zone 2 impact areas at the 0.9, 0.5 and 0.1 probability of exceedance levels shown in **Figure 10** are used as representative values for events with probabilities within the ranges of 1–0.8, 0.8–0.2, and 0.2–0, respectively, probabilities can be calculated for each branch on the decision tree, as shown in **Table 4**.

The estimated areas shown in **Table 4** can be mapped onto the topography by using the calculated representative values and by estimating the deposit width based on a geomorphic interpretation of the runout path. For example, considering the branch ending at $a_{Z2,2,2}$ in **Table 4**, the predicted Zone 1 area is $2.1\ \text{m}^2 \times 10^6\ \text{m}^2$. Since the topography below the source area is primarily unconfined, one can infer the deposit will spread laterally from the source, however a ridge along the upper part of the path on the west side of the travel path would limit spreading in that direction. For the purpose of this example, it was assumed that the widest point on the deposit would be approximately 50% greater than the source width, and the downslope end of the deposit would form a semi-circle, as shown in **Figure 11A**. For the prediction of potential Zone 2 impacts, a key question would be whether or not the flow could become channelized. Although the Zone 2 data could not be grouped by confined or unconfined cases (i.e., the topography was not a good predictor of the total Zone 2 impact area), the distribution of that area could vary substantially. For example, continuing along the branch ending at $a_{Z2,2,2}$ in **Table 4**, if the predicted Zone 2 impact area of $4.6\ \text{m}^2 \times 10^5\ \text{m}^2$ is distributed as a radial fringe around an approximately 1.2 km distance along the floodplain (**Figure 11A**), it would map as a 300 m wide area. Conversely, if the flow were to follow the

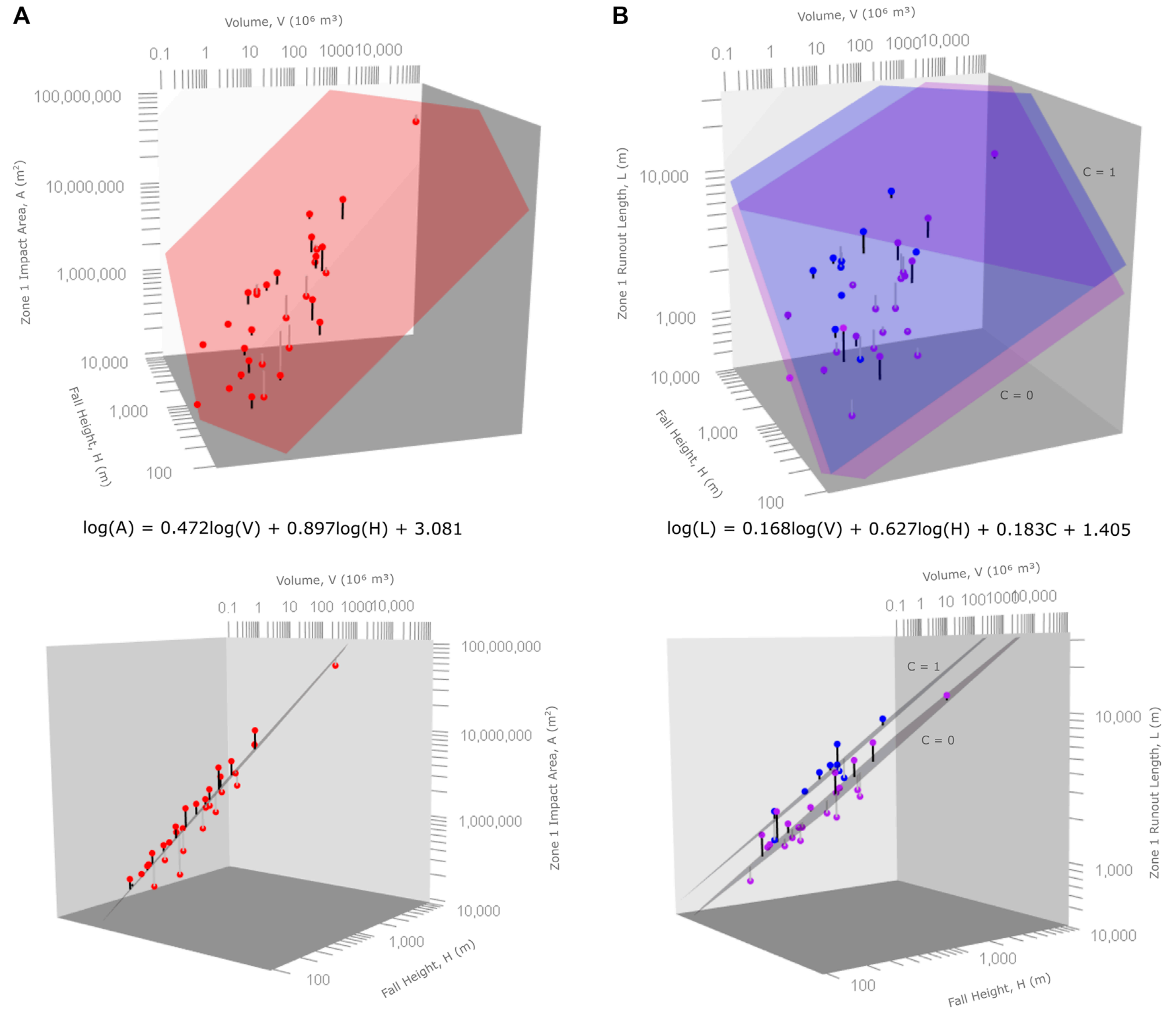

FIGURE 8 | Regression plots for **(A)** Zone 1 total impact area as a function of volume and fall height, plotted to show the variation in the measurements (top), and rotated to show the magnitude of the residuals (bottom), and **(B)** Zone 1 runout length as a function of volume, fall height, and lateral confinement, where $C = 1$ denotes laterally confined and $C = 0$ denotes laterally unconfined path topography, plotted to show the variation in the measurements (top), and rotated to show the magnitude of the residuals (bottom).

approximately 70 m–200 m wide river (flowing to the right on **Figure 11A**), the impact area would extend approximately 4 km downstream (flowing beyond the extents of the topography shown in **Figure 11A**).

Another application of these predictions is in the evaluation of numerical model results. This hypothetical benchmarking example was modeled using the Dan3D numerical model (Mitchell et al., 2018). The model was run using a range of rheological parameters sampled from a dataset of back-analyzed cases to represent a range of potential mobilities (Aaron and McDougall, 2019). The predicted impact areas from these model runs, shown in **Figure 11B** ranged from 4.1 $m^2 \times 10^6$ m^2 to 5.2 × 10^6 m^2 (Mitchell et al., 2018). These areas correspond to probabilities of exceedance of 0.04 and 0.01, respectively, for the Zone 1 impact area using Equation 4. The impact area near the source was also greater than would be expected due to the assumption of the slide mass instantaneously fluidizing, leading to rapid spreading and some of the material descending into a neighboring valley, also increasing the modeled impact area.

The prediction of the Zone 1 runout length (**Figure 11C**) shows the probability of the event reaching the end of the "low mobility" numerical model result being approximately 0.7, and the probability of the event reaching the "high mobility" numerical model result being approximately 0.4. These probabilities are significantly higher than those from the area prediction, which is interpreted to be related to the fact that this

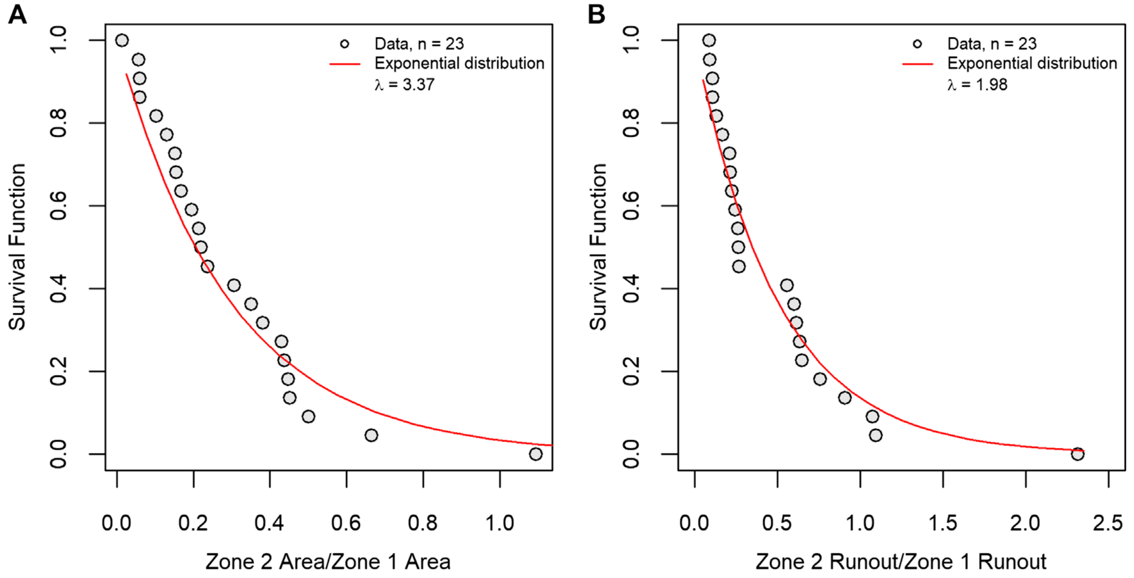

FIGURE 9 | (A) Relationship between Zone 2 and Zone 1 areas for events where a mass flow was observed, and survival function for the Zone 2 over Zone 1 areas, **(B)** relationship between Zone 2 and Zone 1 runout distance for events where a mass flow was observed, and survival function for the Zone 2 over Zone 1 runout lengths.

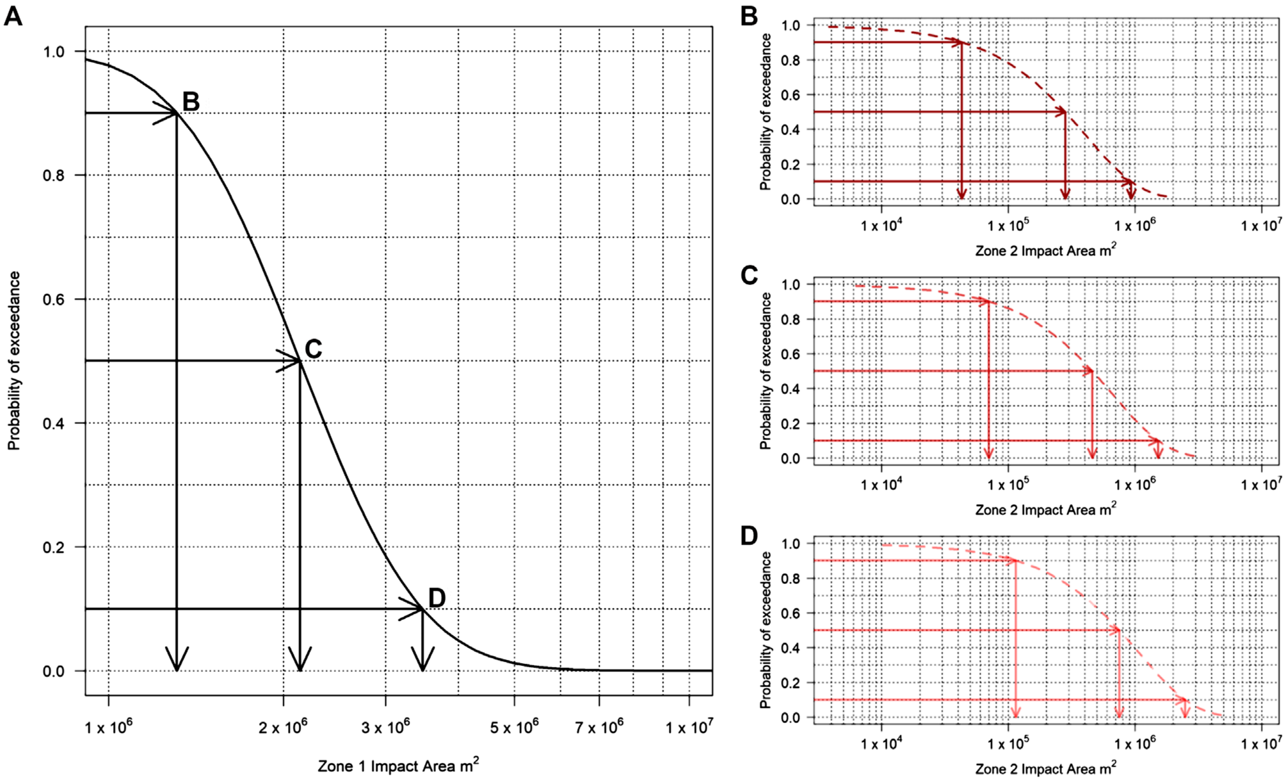

FIGURE 10 | Estimated probabilities of exceedance for a range of potential Zone 1 and Zone 2 impact areas for the hypothetical case, where points B, C, and D indicate representative Zone 1 impact areas for which Zone 2 impacts are estimated.

TABLE 4 | Summary of event tree calculation. Ranges of values corresponding to each representative value are given in brackets.

Zone 1 impacts		Zone 2 impacts		
$P(E) = 1$	$P(a_{Z1,1} = 1.3 \times 10^6\ \mathrm{m}^2) = 0.2\ (0 < A_{Z1} \le 1.5 \times 10^6\ \mathrm{m}^2)$	$P(E_{Z2}) = 1$	$P(a_{Z2,1} = 4.3 \times 10^4\ \mathrm{m}^2 \mid a_{Z1,1}) = 0.2\ (0 < A_{Z2} \le 9.1 \times 10^4\ \mathrm{m}^2)$	$P(a_{Z2,1,1}) = 0.04$
			$P(a_{Z2,2} = 2.8 \times 10^5\ \mathrm{m}^2 \mid a_{Z1,1}) = 0.6\ (9.1 \times 10^4\ \mathrm{m}^2 < A_{Z2} \le 6.5 \times 10^5\ \mathrm{m}^2)$	$P(a_{Z2,1,2}) = 0.12$
			$P(a_{Z2,3} = 9.4 \times 10^5\ \mathrm{m}^2 \mid a_{Z1,1}) = 0.2\ (6.5 \times 10^5\ \mathrm{m}^2 < A_{Z2})$	$P(a_{Z2,1,3}) = 0.04$
	$P(a_{Z1,2} = 2.1 \times 10^6\ \mathrm{m}^2) = 0.6\ (1.5 \times 10^6\ \mathrm{m}^2 < A_{Z1} \le 2.9 \times 10^6\ \mathrm{m}^2)$	$P(E_{Z2}) = 1$	$P(a_{Z2,1} = 7.0 \times 10^4\ \mathrm{m}^2 \mid a_{Z1,2}) = 0.2\ (0 < A_{Z2} \le 1.5 \times 10^5\ \mathrm{m}^2)$	$P(a_{Z2,2,1}) = 0.12$
			$P(a_{Z2,2} = 4.6 \times 10^5\ \mathrm{m}^2 \mid a_{Z1,2}) = 0.6\ (1.5 \times 10^5\ \mathrm{m}^2 < A_{Z2} \le 1.1 \times 10^6\ \mathrm{m}^2)$	$P(a_{Z2,2,2}) = 0.36$
			$P(a_{Z2,2} = 1.5 \times 10^6\ \mathrm{m}^2 \mid a_{Z1,2}) = 0.2\ (1.1 \times 10^6\ \mathrm{m}^2 < A_{Z2})$	$P(a_{Z2,2,3}) = 0.12$
	$P(a_{Z1,3} = 3.5 \times 10^6\ \mathrm{m}^2) = 0.2\ (2.9 \times 10^6\ \mathrm{m}^2 < A_{Z1})$	$P(E_{Z2}) = 1$	$P(a_{Z2,1} = 1.1 \times 10^5\ \mathrm{m}^2 \mid a_{Z1,3}) = 0.2\ (0 < A_{Z2} \le 2.5 \times 10^5\ \mathrm{m}^2)$	$P(a_{Z2,2,1}) = 0.04$
			$P(a_{Z2,2,2} = 7.7 \times 10^5\ \mathrm{m}^2 \mid a_{Z1,}) = 0.6\ (2.5 \times 10^5\ \mathrm{m}^2 < A_{Z2} \le 1.8 \times 10^6\ \mathrm{m}^2)$	$P(a_{Z2,2,2}) = 0.12$
			$P(a_{Z2,2,3} = 2.5 \times 10^6\ \mathrm{m}^2 \mid a_{Z1,3}) = 0.2\ (1.8 \times 10^6\ \mathrm{m}^2 < A_{Z2})$	$P(a_{Z2,2,3}) = 0.04$

hypothetical case study had an anomalously large fall height for a case without topographic confinement, compared to the other cases in the database. This issue is examined further in the *Summary and Discussion* section.

SUMMARY AND DISCUSSION

The spatial extents of impacts from rock avalanches can be amplified by mass flows of sediments along their travel path. These mass flows tend to have a finer texture than the deposit from the initial rock slope failure, so the evidence of their impacts is generally not as well preserved in the geomorphic and stratigraphic record (e.g., **Figure 2**). The impacts of these mass flows have not always been rigorously documented in the literature, and a consistent set of terminology and descriptive attributes has not been used to describe them. We have introduced a three-zone system to classify the different types of impacts resulting from a rock avalanche. Zone 1 refers to coarse rocky, debris, Zone 2 refers to mass flows associated with the immediate impact from the rock avalanche, and Zone 3 refers to impacts associated with a rock avalanche, but not generated directly from the impact, such as the formation of landslide dammed lakes or downstream channel aggradation/erosion as a result of the rock avalanche. The definition of a distinct mass flow impact area is a unique feature of this system, and the three-zone system provides the basis for the general rock avalanche hazard assessment system we propose. This work is complementary to recent work on landslide dams (a Zone 3 impact in our classification system), where researchers have described global datasets of landslide dams with consistent attributes (Fan et al., 2020; Oppikofer et al., 2020).

One of the outcomes of this study is a preliminary estimate of the likelihood of a sediment mass flow occurring. Sediment mass flows were generated in 9 of 13 cases from the post-2010 dataset, but given the limited size of this subset of cases, this preliminary result should be treated with caution. More generally, mass flow events of sediment, water or snow/ice are shown in **Figure 1** as distinct branches, however, these phenomena exist on a spectrum, with events potentially running out over multiple path materials (e.g., relatively small amounts of snow in the Hope Slide event, as described by Mathews and McTaggart, 1978), or multiple hazards occurring in a chain (e.g., the mass flow of the Goldau rock avalanche triggering a displacement wave in Lake Lauerz, as described by Bussman and Anselmetti, 2010). Within the hazard assessment framework proposed in this paper, the occurrence of a mass flow is assumed to be binary (Eq. 1). This may in reality be a more nuanced factor, where the degree of saturation, available surface or ground water, and velocity of the rock avalanche debris may result in substantial material entrainment and transformation into a mass flow (e.g., Hungr and Evans, 2004). The effect of slide impact velocity, a key consideration for the formation of landslide-generated impulse waves (e.g., Heller and Hager, 2010; Evers et al., 2019), is another potential area of future investigation. Other factors that could be investigated further are the depth of sediments (analogous to the still water depth for landslide-generated impulse waves, e.g., Heller and Hager, 2010) and the geotechnical properties of the sediment. Future work involving numerical modeling (e.g., Crosta et al., 2009) or physical modeling (e.g., Steers, 2018; Furuya et al., 2019) could help to better understand the mechanics of this process, and what distinguishes events without entrainment, with entrainment, and with entrainment and generation of a mass flow. The insights on physical controls for mass flow generation from physical and numerical modeling could help guide future field investigations by highlighting key information to be gathered in the field.

A classification system for the description of the Zone 2 impact area, which results from sediment mass flows, is proposed based on imagery, topography and field mapping (**Table 1**). This allows for a consistent mapping methodology to be applied across all cases. The attributes chosen to describe the events are meant to be simple, yet provide a meaningful division of the events. One challenge with this approach is determining a “representative” descriptor for each event, as there may be multiple descriptors that are applicable. For example, there were elements of confined and unconfined topography in the Hope Slide case, meaning judgment was required to determine which descriptor was most applicable to that case. As it will often be the case that multiple descriptors could apply, this application of judgment will be required by landslide practitioners.

Modern satellite imagery presents an opportunity to map future events systematically and track the changes within the different impact zones over time. With this approach, there are

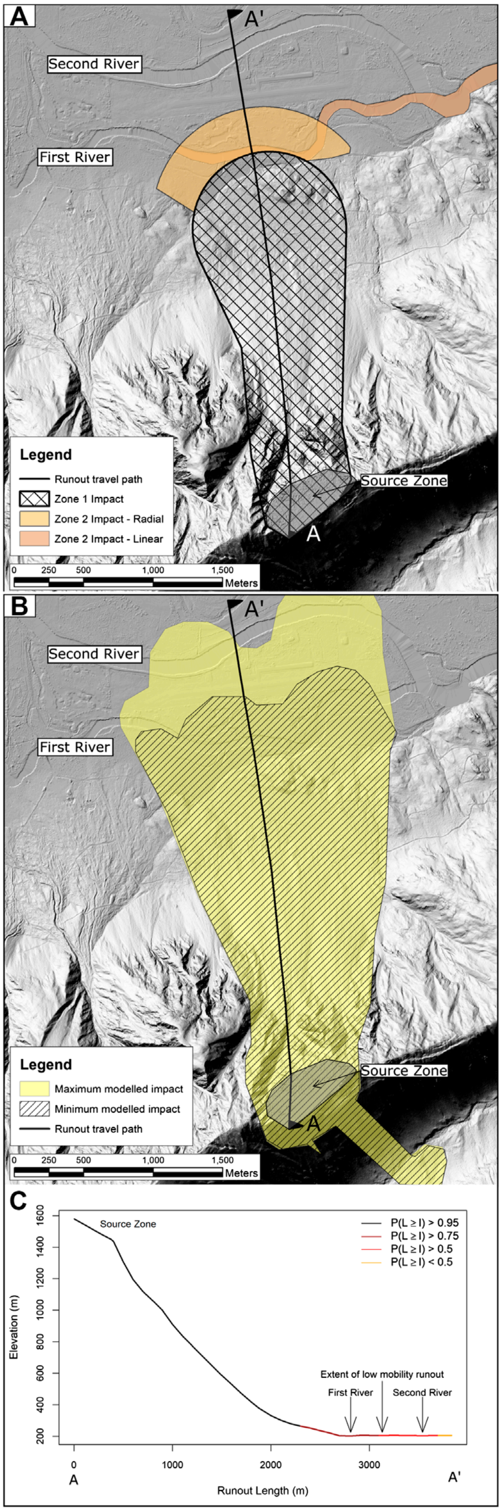

FIGURE 11 | (A) Interpreted Zone 1 and Zone 2 impact areas, with alternative Zone 2 impact areas considering radial or linear cases. **(B)** Topography of potential rock avalanche area with the maximum and minimum mobility cases from numerical modeling (Mitchell et al., 2018) and **(C)** the runout profile used for the empirical analysis, showing the probability of runout exceedance results along the travel path.

limitations to what can be seen from aerial or satellite imagery. This issue was highlighted by the 2019 Joffre Peak case described by Friele et al. (2020), in which the extent of the Zone 2 area estimated from the post-event PlanetScope ortho imagery was different from that observed during field mapping. This discrepancy was because there were areas where the mass flow of saturated sediments and organic material did not entirely remove the trees present in the impact area, meaning the full impact could not be observed clearly in the satellite images. This also demonstrates the variability in the intensity of Zone 2 impacts; whereas the vulnerability of an element at risk to a Zone 1 impact is generally assumed to be 1, the impact intensity may be more relevant to Zone 2 impacts. It is possible that mass flows were generated in more cases than reported here, however, the areal extent of the impacts was not observable with the resolution of imagery available (generally 3–5 m pixel sizes for satellite imagery). Hyperconcentrated flows that remain confined within a channel downstream of the Zone 1 and/or Zone 2 impact areas are especially challenging to identify from imagery. The methods for predicting Zone 2 impacts in this paper are relevant for impacts on the order of tens of meters or greater. The 2017 Bondo event highlights the limitations on the temporal resolution of this data, with several events occurring in quick succession following the main rock avalanche (Walter et al., 2020). The deposit area mapped from the first clear imagery following the event is in fact the accumulation of several events, meaning in this case we have somewhat over-estimated the Zone 2 impact area.

All cases were used to fit regression models to the observations of Zone 1 total impact area and runout length. The resulting regression models were consistent with the regression models for a dataset of 51 rock avalanches from the Canadian Cordillera (Mitchell et al., 2020). It should be noted that 14 of the cases included in the present dataset were also included in the Mitchell et al. (2020) dataset, however, the fact that the cases added for this analysis did not cause a statistically significant change in the regression coefficients (see **Table 3**) suggests that the regression methodology is generally applicable to rock avalanche runout. The relationship between total impacted area and debris volume found for this dataset (**Table 3**) shows a positive correlation with a strong linear association. The slope of the best-fit regression line for the simple area-volume relationship differs from previously published relationships that assume a slope of 2/3 for the regression analysis (based on geometric scaling relationships described by Hungr and Evans (1993) and Griswold and Iverson (2008). However, the geometric scaling relationships were developed using the deposit area as opposed to the total impacted area used in this study and, as a result, the assumptions used for the geometric scaling are not valid in the present case. Adding fall height as an additional independent predictor variable produced a stronger statistical relationship (**Eq. 2**; **Table 3**), consistent with the relationship for runout length.

Zone 2 impact areas were related to the Zone 1 impact areas for the statistical analysis using exponential functions fitted to the ratios of Zone 2 to Zone 1 impact area and runout length. With the data available, the descriptive attributes were not found to have a strong effect on the relationships, which may be in part due to the limited size of the dataset. Additional well constrained cases, especially cases that have well described substrate conditions, may allow for more refined predictions using more attributes. With additional well described case histories both the choice of distribution, and the potential to fit separate distributions for subsets of the dataset to incorporate descriptive attributes, should be re-examined. This is consistent with the findings of Mitchell et al. (2020), where the Zone 1 runout length was not found to be strongly influenced by substrate type, but more data may allow for these weaker effects to be quantified.

The application of the empirical runout prediction methods here requires geomorphic interpretation of the potential travel path for a rock avalanche and mass flow. To estimate the Zone 1 impacts, features such as topographic confinement, ridges or other barriers to flow need to be considered when selecting flow paths and expected deposit distributions for a given area estimate. Geomorphic mapping will also be required to evaluate if sediments are present to potentially form a mass flow. The analysis shown in **Figure 10** assumes a mass flow could occur at any of the representative values for the Zone 1 area estimates, however, evaluation of the potential travel path may reveal a minimum Zone 1 impact before a substantial volume of sediments would be encountered. Even in the absence of a strong statistical association between the Zone 2 confinement and impact area or runout length, the potential for a mass flow to have elements of confinement, even in generally unconfined topography, should be considered in a forward analysis. In the hypothetical example presented, when considering the spatial extent of the impacts, a practitioner would likely consider both a potential radial impact onto the flood plain and a linear impact following the river channel, and recognize that even if the impact zone is primarily radial, there could be downstream impacts extending kilometers beyond the distal end of the coarse, rocky debris, as an intermediate case between those shown on **Figure 11A**.

The potential for flooding resulting from a landslide dam, the potential for the breach of that dam (e.g., Fan et al., 2020; Oppikoffer et al., 2020), and downstream river bed aggradation/erosion could also be expected, and would result in a Zone 3 impact area.

The empirical-statistical analysis presented in this paper can also be used to evaluate numerical modeling results. The predictions from numerical models are subject to three main sources of uncertainty: the simplifications in the representation of the physical processes that are inherent in the model, errors in measurements of properties used for model definition or calibration, and the uncertainty regarding the parameters used in the model. One application of the empirical analysis presented here is evaluating the plausibility of sets of model parameters, considering the limitations of both the empirical and numerical analyses, for example, the calibration cases used for the regression and numerical models and the effects of model assumptions (e.g., instantaneous fluidization) on the results. Coupling the empirical and numerical analysis can also help constrain some of the uncertainties around the analyses. The empirical runout predictions for the hypothetical example suggest that the runout distance could be plausibly much further than the numerical model results indicate, however, the impact area estimates suggest that the numerical model results indicate cases with a low probability of exceedance. Our interpretation is that the combination of the high valley relief joining a low angle floodplain is unusual relative to the cases included in the dataset; most cases with similar fall heights entered more confined, gently sloping valleys, leading to narrower, longer deposits (e.g., Mount Meager, Joffre Peak, Bondo; **Table 2**). The numerical modeling helps by explicitly considering the 3D topography in the model to simulate the energy loss and spreading when the material encounters the valley bottom. It also provides insights on the likelihood of the flow becoming channelized. In this case, with the low incision of the rivers and the nearly 90° angle at which the flow intersects them, the presence of the rivers does little to affect the direction of the flow, which could lead to a higher likelihood being assigned to a radial impact as opposed to a linear one. The interpretation required to assess and synthesize the results of these analyses again highlights the continued importance of sound professional judgment.

Finally, it should be noted that the first term in **Eq. 1**, the probability of a rock avalanche occurring, is likely the biggest source of uncertainty in the entire hazard assessment framework presented (e.g., Oppikofer et al., 2018). This study has not addressed that uncertainty, and it remains an extremely important area for future research.

CONCLUSIONS

The potential for rock avalanches to generate mass flows of sediments has been recognized for a long time, but quantitative methods to estimate the impacts of these events have been lacking. We have proposed a methodology for consistently describing rock avalanches and the mass flows resulting from them, and compiled a dataset using the new methodology. The compiled data show that the impacts from mass sediment flows can have an even greater extent than the area impacted by coarse, rocky debris. The impact zone definitions presented in this work provide a framework for the consistent description and cataloging of rock avalanche events, particularly those that result in mass flows of sediment. Physical and numerical modeling may provide additional insights on the controlling factors for mass flow generation, which would in turn help guide refinements to the descriptive attributes defined in this study. Describing future events in a similarly consistent manner will allow for more refined estimates of the impact probabilities, and potentially reveal the effects of the qualitative factors. The development of a universal database of rock avalanche case histories is therefore an important subject of ongoing work.

A probabilistic hazard assessment framework has been presented and preliminary statistical relationships have been developed for the quantitative, probabilistic prediction of rock avalanche-generated mass flow likelihood, impact areas and runout distances. We propose survival functions developed from multiple linear regression for predicting Zone 1 impact areas and runout lengths, and survival functions developed from exponential distributions to predict the Zone 2 impact areas and runout lengths associated with a given Zone 1 prediction. The methodology uses an event tree approach to discretize the continuous survival functions associated with Zone 1 and Zone 2 impact areas to provide predictions that span the range of plausible impact areas for an event, while discrete predictions can be used to produce hazard area estimates or compare to numerical runout model results. The application of these relationships is appropriate for high-level screening exercises, and professional judgment is required in defining scenarios to be examined, such as when to consider potential channelized or unconfined flows. Future research will also be required to better define the probability of a rock avalanche occurring, as opposed to ongoing slow deformation or a rockslide that does not fail en masse, after a potential source zone is identified.

DATA AVAILABILITY STATEMENT

All datasets presented in this study are included in the article/**Supplementary Material**. The mapping datasets generated for this study can be in the DesignSafe-CI repository: https://www.designsafe-ci.org/data/browser/public/designsafe.storage.published/PRJ-2830.

AUTHOR CONTRIBUTIONS

AM led the preparation of the study, including compiling the dataset, developing the hazard assessment framework, developing and performing the statistical analysis, performing the hypothetical analysis, and drafting the manuscript. SM conceived the study and assisted with literature review and drafting the manuscript. JA assisted with compiling the dataset, developing the hazard assessment framework and statistical analysis, and drafting the manuscript. MB assisted with compiling the dataset, developing the hazard assessment framework, and drafting the manuscript.

FUNDING

We acknowledge the support of the Natural Sciences and Engineering Research Council of Canada (NSERC), funding reference number PGSD3—516701–2018.

ACKNOWLEDGMENTS

The authors would like to acknowledge the assistance of Natalia Nolde in reviewing the statistical methods section. We would also like to thank Scott Cosman and the BC Ministry of Transportation and Infrastructure for providing lidar data and imagery from the Hope Slide, and Réjean Couture and Scott Paddington for providing photos of the McAuley Creek rock avalanche. The authors have also benefited from conversations with Matthias Jakob and Matthieu Sturzenegger on the subjects discussed in this paper. The authors would also like to thank two reviewers whose constructive comments have improved the quality of the final manuscript.

SUPPLEMENTARY MATERIAL

The Supplementary Material for this article can be found online at: https://www.frontiersin.org/articles/10.3389/feart.2020.543937/full#supplementary-material

REFERENCES

Aaron, J., and McDougall, S. (2019). Rock avalanche mobility: the role of path material. *Eng. Geol.* 257, 105126. doi:10.1016/j.enggeo.2019.05.003

Abele, G. (1997). Rockslide movement supported by the mobilization of groundwater-saturated valley floor sediments. *Z. Geomorphol.* 41 (1), 1–20.

Agisoft (2019). *Metashape version 1.5*. St. Petersburg, Russia: Agisoft LLC.

Boultbee, N., Stead, D., Schwab, J., and Geertsema, M. (2006). The Zymoetz River rock avalanche, June 2002, British Columbia, Canada. *Eng. Geol.* 83 (1), 76–93. doi:10.1016/j.enggeo.2005.06.038

Brideau, M.-A., McDougall, S., Stead, D., Evans, S. G., Couture, R., and Turner, K. (2012). Three-dimensional distinct element modelling and dynamic runout analysis of a landslide in gneissic rock, British Columbia, Canada. *Bull. Eng. Geol. Environ.* 71 (3), 467–486. doi:10.1007/s10064-012-0417-8

Brideau, M.-A., Stead, D., Lipovsky, P., Jaboyedoff, M., Hopkinson, C., Demuth, M., et al. (2010). "Preliminary description and slope stability analyses of the 2008 Little Salmon Lake and 2007 Mt. Steele landslides, Yukon," in *Yukon exploration and geology 2009*. Editors K. E. MacFarlane, L. H. Weston, and L. R. Blackburn (Whitehorse, Canada: Yukon Geological Survey), 119–133.

Bussmann, F., and Anselmetti, F. S. (2010). Rossberg landslide history and flood chronology as recorded in Lake Lauerz sediments (Central Switzerland). *Swiss J. Geosci.* 103 (1), 43–59. doi:10.1007/s00015-010-0001-9

Calhoun, N. C., and Clague, J. J. (2018). Distinguishing between debris flows and hyperconcentrated flows: an example from the eastern Swiss Alps. *Earth Surf. Process. Landforms* 43 (6), 1280–1294. doi:10.1002/esp.4313

Coe, J., Baum, R. L., Allstadt, K. E., Kochevar, B. F., Schmitt, R. G., Morgan, M., et al. (2016). Rock-avalanche dynamics revealed by large-scale field mapping and seismic signals at a highly mobile avalanche in the West Salt Creek valley, western Colorado. *Geosphere* 12 (2), 604–631. doi:10.1130/ges01265.1

Crosta, G. B., Imposimato, S., and Roddeman, D. (2009). Numerical modelling of entrainment/deposition in rock and debris-avalanches. *Eng. Geol.* 109 (1–2), 135–145. doi:10.1016/j.enggeo.2008.10.004

Cruden, D. M., and Hungr, O. (1986). The debris of the Frank Slide and theories of rockslide-avalanche mobility. *Can. J. Earth Sci.* 23 (3), 425–432. doi:10.1139/e86-044

Dufresne, A., Davies, T., and McSaveney, M. J. (2010). Influence of runout-path material on emplacement of the round top rock avalanche, New Zealand. *Earth Surf. Process. Landforms* 35 (2), 190–201. doi:10.1002/esp.1900.

Dufresne, A., and Geertsema, M. (2020). Rock slide-debris avalanches: flow transformation and hummock formation, examples from British Columbia. *Landslides* 17 (1), 15–32. doi:10.1007/s10346-019-01280-x

Duhart, P., Sepúlveda, V., Garrido, N., Mella, M., Quiroz, D., Fernández, J., et al. (2019). "The Santa Lucía landslide disaster, Chaitén-Chile: origin and effects," in Proceedings of the 7th international conference on debris-flow hazards mitigation, Golden, CO, June 10–13, 2019 [abstract].

Evans, S. G., Delaney, K. B., Hermanns, R. L., Strom, A., and Scarascia-Mugnozza, G. (2011). "The formation and behaviour of natural and artificial rockslide dams; implications for engineering performance and hazard management," in *Natural and artificial rockslide dams.* Editors Evans, S. G., Hermanns, R. L., Strom, A., and Scarascia-Mugnozza, G. (Berlin, Heidelberg: Springer), Vol. 1–75.

Evans, S. G., Hungr, O., and Clague, J. J. (2001). Dynamics of the 1984 rock avalanche and associated distal debris flow on Mount Cayley, British Columbia, Canada; implications for landslide hazard assessment on dissected volcanoes. *Eng. Geol.* 61 (1), 29–51. doi:10.1016/s0013-7952(00)00118-6

Evers, F. M., Heller, V., Fuchs, H., Hager, W. H., and Boes, R. M. (2019). *Landslide-generated impulse waves in reservoirs, basics and computation*. 2nd Edn. Bern, Switzerland: Swiss Federal Office of Energy SFOE, VAW Mitteilung 254.

Fan, X., Dufresne, A., Siva Subramanian, S., Strom, A., Hermanns, R., and Tacconi Stefanelli, C. et al.(2020). The formation and impact of landslide dams - state of the art. *Earth Sci. Rev.* 203, 103116. doi:10.1016/j.earscirev.2020.103116

Friele, P., Millard, T. H., Mitchell, A., Allstadt, K. E., Menounos, B., and Geertsema, M. et al.(2020). Observations on the May 2019 Joffre Peak landslides, British Columbia. *Landslides* 17 (4), 913–930. doi:10.1007/s10346-019-01332-2.

Furuya, G., Hasegawa, M., and Wang, G. (2019). "Experimental study on squeezing-out phenomenon by landslide mass loading," in Proceedings of the 4th regional symposium on landslides in the adriatic-Balkan region, Sarajevo, Bosnia, October 23–25 2019, Paper 31.

Govi, M., Gullà, G., and Nicoletti, P. G. (2002). "Val pola rock avalanche of July 28, 1987, valtellina (Central Italian Alps)," in *Catastrophic landslides: effects, occurrence, and mechanisms*. Editors S.G. Evans and J.V. DeGraff (Boulder, Colorado: Geological Society of America), Vol. 15, 71–89.

Griswold, J. P., and Iverson, R. M., (2008). Report 2007-5276. Mobility statistics and automated hazard mapping for debris flows and rock avalanches (version 1.1. April 2014): U.S. Reston, VA: Geological Survey Scientific Investigation.

Guthrie, R. H., Friele, P., Allstadt, K., Roberts, N., Evans, S. G., Delaney, K. B., et al. (2012). The 6 August 2010 Mount Meager rock slide-debris flow, Coast Mountains, British Columbia: characteristics, dynamics, and implications for hazard and risk assessment. *Nat. Hazards Earth Syst. Sci.* 12 (5), 1277–1294. doi:10.5194/nhess-12-1277-2012

Hancox, G. T., Ries, W. F., Parker, R. N., and Rosser, B. (2016). Science Report 2015/042. Landslides caused by the MS 7.8 Murchison earthquake of 17 June 1929 in northwest south island, New Zealand. GNS science, Te pu Ao.

Heim, A. (1932). *Landslides and human lives (Bergstürz and menschenleben), Translated by: Skermer, N.* Vancouver, Canada: Bi-Tech Publishers.

Heller, V., and Hager, W. H. (2010). Impulse product parameter in landslide generated impulse waves. *J. Waterw. Port, Coast. Ocean Eng.* 136 (3), 145–155. doi:10.1061/(asce)ww.1943-5460.0000037

Hermanns, R. L. (2013). "Rock avalanche (sturzstrom)," in *Encyclopedia of natural hazards*. Editor P. Bobrowsky, Dordrecht, Netherlands, Springer.

Hungr, O., and Evans, S. G. (2004). Entrainment of debris in rock avalanches: an analysis of a long run-out mechanism. *Geol. Soc. Am. Bull.* 116 (9), 1240–1252. doi:10.1130/b25362.1

Hungr, O., and Evans, S. (1993). Geological survey of Canada open file report 2598. The failure behavior of large rockslides in mountainous regions.

Hungr, O., Leroueil, S., and Picarelli, L. (2014). The Varnes classification of landslide types, an update. *Landslides* 11 (2), 167–194. doi:10.1007/s10346-013-0436-y

Li, H.-b., Qi, S.-c., Chen, H., Liao, H.-m., Cui, Y.-f., and Zhou, J.-w. (2019). Mass movement and formation process analysis of the two sequential landslide dam events in Jinsha River, Southwest China. *Landslides*, 16 (11), 2247–2258. doi:10.1007/s10346-019-01254-z

Li, T. (1983). A mathematical model for predicting the extent of a major rockfall. *Z. Geomorphol.* 24, 473–482.

Liu, X. (2012). *Survival analysis: models and applications*. Chichester, UK: John Wiley & Sons.

Loew, S., Gschwind, S., Gischig, V., Keller-Signer, A., and Valenti, G. (2017). Monitoring and early warning of the 2012 Preonzo catastrophic rockslope failure. *Landslides* 14 (1): 141–154. doi:10.1007/s10346-016-0701-y

Lu, Z., Rollerson, T., and Geertsema, M. (2003). "The mosque mountain rockslide, sustut watershed," in 3rd Canadian Conference on Geotechnique and Natural Hazards, Northern British Columbia, Canada, June 8–10, 2003, 325.

Mathews, W. H., and McTaggart, K. C. (1978). "Hope rockslides, British Columbia, Canada," in *Rockslides and avalanches, volume 1 natural phenomena. Developments in Geotechnical Engineering*. Editor B. Voight (New York, NY: Elsevier), Vol. 14, 259–275.

McConnell, R. G., and Brock, R. W. (1904). "Report on the great landslide at Frank, Alberta," in *Part VIII, annual report, 1903, department of the interior dominion of Canada*, Study Edition. Editor D.M. Cruden (Edmonton, Canada: Edmonton Geological Society).

McDougall, S. (2017). 2014 Canadian Geotechnical Colloquium: landslide runout analysis - current practice and challenges. *Can. Geotech. J.* 54 (5), 605–620. doi:10.1139/cgj-2016-0104

McDougall, S., and Hungr, O. (2005). Dynamic modelling of entrainment in rapid landslides. *Can. Geotech. J.* 42 (5): 1437–1448. doi:10.1139/t05-064

Mitchell, A., McDougall, S., Nolde, N., Brideau, M.-A., Whittall, J., and Aaron, J. B. (2020). Rock avalanche runout prediction using stochastic analysis of a regional dataset. *Landslides* 17 (4): 777–792. doi:10.1007/s10346-019-01331-3

Mitchell, A. D., McDougall, S. D., and Aaron, J. B. (2018). "Benchmarking exercise: Dan3D with objective calibration methods," in Proceedings of the second JTC1 workshop, triggering and propagation of rapid flow-like landslides, Hong Kong, 3–5 December 2018. doi:10.5772/intechopen.75123

Oppikofer, T., Hermanns, R., Jaboyedoff, M., Brideau, M.-A., Jakob, M., and Sturzenegger, M. (2018). "Comparison between three rock slope hazard assessment methodologies using a case study from Norway," in Proceedings of Geohazards 7 Conference. Canmore, Canada, 8, 2018 , Paper 205.

Oppikofer, T., Hermanns, R., Jakobsen, V. U., Böhme, M., Nicolet, P., and Penna, I. (2020). Forecasting dam height and stability of dams formed by rock slope failures in Norway. *Nat. Hazards Earth Syst. Sci.* doi:10.5194/nhess-2020-135

Orwin, J. F., Clague, J. J., and Gerath, R. F. (2004). The cheam rock avalanche, fraser valley, British Columbia, Canada. *Landslides* 1 (4), 289–298. doi:10.1007/s10346-004-0036-y

Ouyang, C., An, H., Zhou, S., Wang, Z., Su, P., Wang, D., et al. (2019). Insights from the failure and dynamic characteristics of two sequential landslides at Baige village along the Jinsha River, China. *Landslides* 16 (7), 1397–1414. doi:10.1007/s10346-019-01177-9

Pastor, M., Soga, K., McDougall, S., and Kwan, J. S. H. (2018). "Review of benchmarking exercise on landslide runout analysis 2018," in Proceedings of the second JTC1 workshop, triggering and propagation of rapid flow-like landslides, Hong Kong, 3–5 December 2018.

Planet (2020). "Planet application program interface," in *Space for life on earth*. San Francisco, CA: Planet Labs.

R Core Team (2020). *R: a language and environment for statistical computing*, Vienna, Austria: R Foundation for Statistical Computing.

Rives, T., Razack, M., Petit, J.-P., and Rawnsley, K. D. (1992). Joint spacing: analogue and numerical simulations. *J. Struct. Geol.* 14 (8–9), 925–937. doi:10.1016/0191-8141(92)90024-q

Scaringi, G., Fan, X., Xu, Q., Liu, C., Ouyang, C., Domènech, G., et al. (2018). Some considerations on the use of numerical methods to simulate past landslides and possible new failures: the case of the recent Xinmo landslide (Sichuan, China). *Landslides* 15 (7), 1359–1375. doi:10.1007/s10346-018-0953-9

Steers, L. (2018). Static liquefaction of loose granular landslides. MSc thesis. Kingston (ON): Queen's University.

Straub, K. M., Ganti, V., Paola, C., and Foufoula-Georgiou, E. (2012). Prevalence of exponential bed thickness distributions in the stratigraphic record: experiments and theory. *J. Geophys. Res.* 117 (F2): F020.3. doi:10.1029/2011JF002034.

Walter, F., Amann, F., Kos, A., Kenner, R., Phillips, M., de Preux, A., et al. (2020). Direct observations of a three million cubic meter rock-slope collapse with almost immediate initiation of ensuing debris flows. *Geomorphology* 351, 106933. doi:10.1016/j.geomorph.2019.106933

Wolter, A., Gischig, V., Stead, D., and Clague, J. J. (2016). Investigation of geomorphic and seismic effects on the 1959 Madison Canyon, Montana, landslide using an integrated field, engineering geomorphology mapping, and numerical modelling approach. *Rock Mech. Rock Eng.* 49 (6), 2479–2501. doi:10.1007/s00603-015-0889-5

Zhu, Y., Xu, S., Zhuang, Y., Dai, X., Lv, G., and Xing, A. (2019). Characteristics and runout behaviour of the disastrous 28 August 2017 rock avalanche in Nayong, Guizhou, China. *Eng. Geol.* 259, 105154. doi:10.1016/j.enggeo.2019.105154

Zhuang, Y., Xu, Q., and Xing, A. (2019). Numerical investigation of the air blast generated by the Wenjia valley rock avalanche in Mianzhu, Sichuan, China. *Landslides* 16 (12), 2499–2508. doi:10.1007/s10346-019-01253-0

Conflict of Interest: MB is employed by Westrek Geotechnical Services Ltd.

The remaining authors declare that the research was conducted in the absence of any commercial or financial relationships that could be construed as a potential conflict of interest.

The reviewer TO declared a past co-authorship with one of the authors MB to the handling Editor.

frontiers in Earth Science

ORIGINAL RESEARCH
published: 14 October 2020
doi: 10.3389/feart.2020.537800

Numerical Simulation of the 2017 Xinmo Catastrophic Landslide Considering Entrainment Effect

Qin Chen[1]*, Gang Fan*[2] *and Jia-wen Zhou*[1]*

[1] *State Key Laboratory of Hydraulics and Mountain River Engineering, Sichuan University, Chengdu, China,* [2] *College of Water Resource and Hydropower, Sichuan University, Chengdu, China*

The mass movement process of the 2017 Xinmo catastrophic landslide was simulated using the discreet element method (DEM). Field investigation indicates that the basal entrainment is a typical feature of this landslide. Hence, the entrained colluvium on the sliding path is considered in the DEM model. According to the terrain elevation data before and after sliding, the slope geometry is divided into three parts: sliding bed, sliding body, and colluvium on the path. The blocks are generated in MATLAB and a fill-remove method has been used to produce the loose colluvium. The key parameter, contact friction angel, which controls the mobility of mass movement, has been obtained through displacement back analysis. The simulated deposit area and main sliding time coincide with actual landslide characteristics. Simulation results indicate that the colluvium is pushed to the bottom of the Songpinggou Valley by the sliding body. The local topography has a significant influence on the sliding direction. Some typical phenomena of substrate entrainment, including frontal plowing, mass spray, shear zones in substrate, thickened substrate, and basal abrasion, are observed in the DEM simulation. During the entrainment process, the frontal plowing, or the thrust, plays an important role in creating the substrate failure compared with basal abrasion. After the failure of the whole colluvium, the magnitude of thrust descends quickly but is still slightly larger than that of shear thrust. Entrainment of dry material on the slope leads to more friction energy consumption and reduces the mobility of mass movement. This work shows a good capability of simulating entrainment of dry materials using a discreet element method and highlights the significance of plowing relative to the basal abrasion under conditions of limited path material supply.

Keywords: landslide, mass movement, entrainment, dynamic analysis, discreet element method

Edited by:
Reginald Leonhard Hermanns,
Geological Survey of Norway, Norway

Reviewed by:
Jordan Balfour Aaron,
ETH Zürich, Switzerland
Marco Neri,
National Institute of Geophysics
and Volcanology, Section of Catania,
Italy

***Correspondence:**
Jia-wen Zhou
jwzhou@scu.edu.cn

Specialty section:
This article was submitted to
Structural Geology and Tectonics,
a section of the journal
Frontiers in Earth Science

Received: *03 March 2020*
Accepted: *13 August 2020*
Published: *14 October 2020*

Citation:
Chen Q, Fan G and Zhou J-w
(2020) Numerical Simulation of the
2017 Xinmo Catastrophic Landslide
Considering Entrainment Effect.
Front. Earth Sci. 8:537800.
doi: 10.3389/feart.2020.537800

INTRODUCTION

Rapid landslides often lead to catastrophic accidents and serious loss of life and property, because of their high velocity and long run-out distance (Pirulli, 2009; Yin et al., 2009; Zhou et al., 2013; Hu et al., 2020). Substrate entrainment is another typical feature of high-speed landslides (McDougall and Hungr, 2005; Zhou et al., 2016). As the loose deposition on run-out paths is entrained by sliding mass, the total volume of landslides increases rapidly, and the final volume of some landslides can reach several times their initial volume. For instance, on 9 April 2000, a catastrophic landslide took place at Yigong Town; the initial volume of the landslide was about 1.0×10^8 m^3, while the final volume reached 3×10^8 m^3 by scraping the ancient landslide deposits on the landslide path with a volume magnification factor of 2. The entrainment process is affected by many factors, such as topography, landslide volume, thickness of accumulation, water content, and compactness, so it is difficult to accurately predict the amplification effect of a landslide (Aaron and McDougall, 2019).

It is crucial for disaster prediction, prevention, and reduction to include entrainment in landslide dynamics models. However, there is little knowledge about entrainment, because landslides occur suddenly and the process of landslide motion is rarely recorded. Hence the insight into the entrainment effect is mainly based on laboratory experiments. According to the research purposes, experimental investigations are divided into two categories. One is to study the mechanism of entrainment (Barbolini et al., 2005; Sovilla et al., 2006; Lu et al., 2016). Based on the observation of the failure mode of the substrate, it is proposed that the plowing at the flow front and the basal abrasion occurred at the interface between flow mass and static path materials is two main mechanisms in the process of substrate entrainment. The other is to study the dynamic effect of entrainment, such as its influence on the velocity of landslide, the influence on the accumulation morphology of the landslide, etc (Mangeney et al., 2010; Dufresne, 2012). The mobility and runout of a landslide respond significantly to the nature of the substrate. A series of large-scale experiments have been conducted by Iverson et al. (2011) et al. and they suggest that increasing positive pore water pressure in wet substrate caused by debris flow significantly reduces the flowing resistance and leads to an increase of velocity and runout (Hungr and Evans, 2004; Wang et al., 2013; Zhou et al., 2016; Ouyang et al., 2017). For a dry substrate condition, both enhanced and reduced runout distance compared with results in a rigid path were observed under different experimental conditions (Mangeney et al., 2010; Dufresne, 2012), yet it is still difficult to explain the mechanism that the reduction of basal resistance operates under while entraining dry path materials in some particular situations. In addition, although we can accurately capture the movement characteristics of the landslide in these experiments, the results of the model experiments are limited to practical applications because the dynamic similarity between the model and the prototype cannot be strictly satisfied (Friedmann et al., 2006).

The numerical simulation technology can simulate a real-scale landslide which overcomes the disadvantages of scaled experiments. In addition, the scaled experiments provide insight to the mechanism of the entrainment effect, which contributes to developing a variety of mathematical entrainment models. At present, most of the entrainment models simulate the volume change of a landslide by adding a base erosion term to the hydrodynamics equation. These entrainment models can be divided into two categories: (1) empirical model (McDougall and Hungr, 2005; Cuomo et al., 2016) and (2) physical model (Luna et al., 2012; Ouyang et al., 2015). These entrainment models have a common feature, i.e., the failure of the substrate is caused by the shear force parallel to the basal surface, while the plowing at the flow front is ignored. Therefore, further validation is needed when these models are used.

The 2017 Xinmo catastrophic landslide is a typical rapid landslide with an obvious feature of volume enlargement due to basal entrainment. Many researchers had investigated the landslide movement using numerical simulation technology, including entrainment models (Chen and Wu, 2018; Hu et al., 2019; Huang et al., 2019; Liu et al., 2019), while a clear understanding of the entrainment process is still needed. In this paper, the three-dimensional distinct element code (3DEC) is applied to simulate the movement and the entrainment of the Xinmo Landslide. This paper is organized as follows: In Section "BACKGROUND," the background of the Xinmo Landslide is first introduced. Then, the DEM theory, geometry model establishment, and numerical parameters installation are illustrated in Section " METHOD AND MODEL." Section "RESULTS" gives the simulation results. The mechanism of frontal plowing and basal abrasion, and influence of substrate entrainment on the mobility of the Xinmo Landslide, is discussed in Section "DISCUSSION." The last section gives the conclusions of this paper.

BACKGROUND

On June 24, 2017, a catastrophic landslide took place in the Diexi Town, Maoxian County, Sichuan Province, at the southwest of China (**Figure 1**). It suddenly collapsed and rushed down the hill to the Xinmo Village at the slope's toe (**Figure 2a**), causing 10 fatalities, leaving 73 missing, and burying 64 buildings. The main reason for rock mass instability is that a large amount of rainfall in the two months before sliding and historical earthquakes in the area reduced the rock mass strength (Fan X. et al., 2017). The huge elevation difference and steep slope provided favorable conditions for the high-speed and long-distance movement of the landslide. According to field investigations and seismic acceleration records recorded by the Maoxian seismic station, the landslide runout extended 2,500 m horizontally and 1,200 m vertically (**Figure 3B**) in 120 s.

Based on the elevation variation by comparing pre- and post-failure DEM of the Xinmo Landslide, the slide range was divided into three areas (**Figure 3A**):

(1) Source area: The slip source area is located at the ridge of the Fugui Mountain on the left bank of Songpinggou River, a first-order tributary of the Minjiang River (**Figure 1B**). The elevation of the rear edge of the slip body is 3460 m a.s.l, the elevation of the shear opening location is about 3100 m a.s.l., and the average slope of the slip surface is about 47°. The length and width of the collapsed rock mass are about 260 and 370 m, respectively, with a maximum thickness of about 66 m. Due to the different accuracies and sources of the pre-failure terrain data, several organizations and researchers had carried out volume estimations of the source mass, and the volume range of the landslide

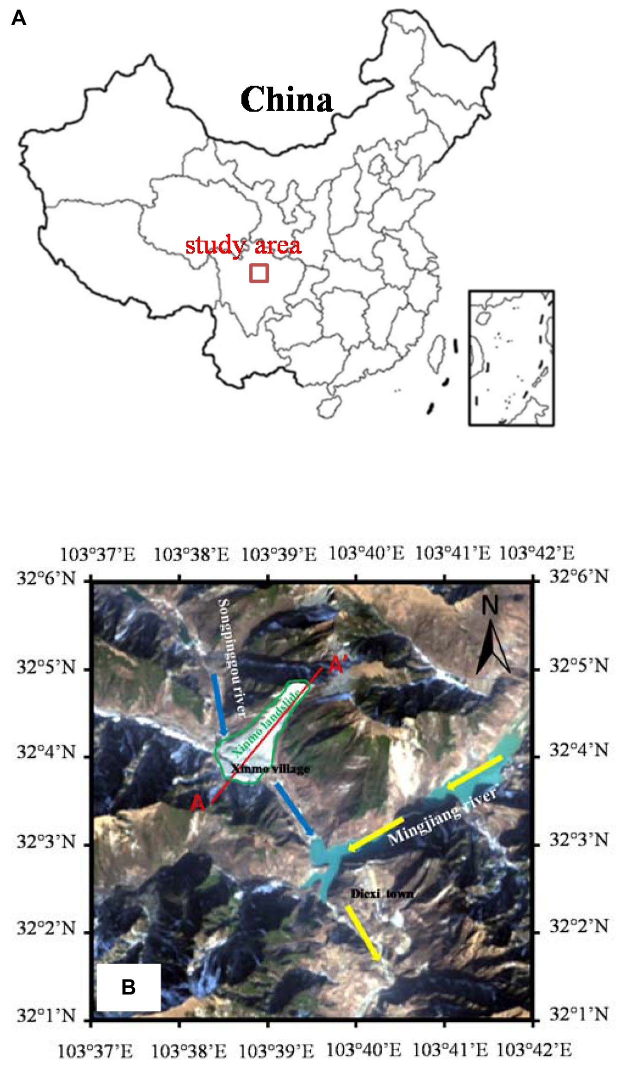

FIGURE 1 | Location of the 2017 Xinmo Landslide: **(A)** map of China and regional location of the study area. The small inset box in the lower right corner of the map of China is the South China Sea. **(B)** Landsat-8 image of the study area acquired on Jan. 19, 2018.

source mass is between 3.0 × 10^6 m^3 and 6.3 × 10^6 m^3 (Dai et al., 2019). The outcropping strata in this area is part of the Middle Triassic Zagunao Formation (T_2z), mainly consisting of metamorphic sandstone intercalated with slate (**Figure 4**). The occurrence of the beddings is N70°W/SW∠51°, which formed the bottom boundary of the sliding surface (**Figure 2b**). There are two sets of joints developed within the source mass, the occurrence of which are N7°E/NW∠71° and N40°E/NW∠29°, respectively (Fan J. R. et al., 2017). The former constitutes the lateral boundary of the sliding mass.

(2) Entrained area: As shown in **Figure 3A**, there is an apparent zone of depletion below the source area in which pre-existing loose colluvium of previous landslides induced by the Diexi Earthquake in 1933 were entrained and pushed by the sliding mass. The bedrock under the colluvium was exposed by strong entrainment and then covered again by the new landslide deposit (**Figure 2c**). The outcrop of bedrock at the slope's toe is still intact under the impact and erosion by flowing mass (**Figure 3A** shows there is no elevation difference before and after the landslide in the scrape area) and therefore entrainment of bedrock could be negligible. Entrainment of saturated colluvium by rock avalanche could change it to a debris flow and increase its volume and mobility. However, there is no liquefaction deposit observed according to field investigations, although there was two weeks rainfall prior to sliding (Huang et al., 2019). Hence, we deduce that the colluvium was in low water content during this event. The span of this area is 2,650–3,100 m a.s.l and the length and width are about 700 and 410 m, respectively. Considering about 7 × 10^5 m^3 new landslide deposits formed during this time, the net maximum scraper depth is about 30 m (Xu et al., 2017).

(3) Deposition area: The Deposition area is located below the elevation of 2,650 m a.s.l to the elevation of 2,300 m a.s.l. It is a fan-shaped accumulation, with a length of 1,600 m along the sliding direction and a maximum width of 1,080 m along the Songpinggou River. By comparing the terrain elevation changes before and after the landslide, the average accumulation thickness of the landslide is more than 10 m, and the maximum accumulation thickness is about 31 m. The final deposition volume is estimated between 6.4 × 10^6 m^3 and 13.81 × 10^6 m^3 (Dai et al., 2019). Due to the pre-existing terrain topography, the movement direction of the sliding mass moved eastward along a gully with NE strike (**Figure 2a**), resulting in the overall distribution of the deposition depth showing high in the East and low in the West (**Figure 3A**). The deposit can be divided into two parts by the scrape: the deposit on the slope and the deposit at the slope toe (**Figures 2d**, **3A**). Most of the deposit is located on the left riverbank, except for a small part that crosses the Songpinggou River.

METHOD AND MODEL

Numerical Method

The commercial three-dimensional distinct element code (3DEC) program, which has the capability to solve the problem of discontinuous deformation and failure of rock mass, is employed to simulate the run-out of the Xinmo Landslide. In 3DEC, the rock mass is simplified as a set of polyhedron blocks connected by specific contact models and the block could be deformable through meshing into finite-difference tetrahedral elements internally. The motion of each block is calculated by Newton's second law, the stress and strain of the block is solved by finite difference method, and the contact force between blocks is determined by the force-displacement law (Hart et al., 1988). The equilibrium of the block system is solved by repeat iteration calculation; **Figure 5** shows the calculation cycle in 3DEC.

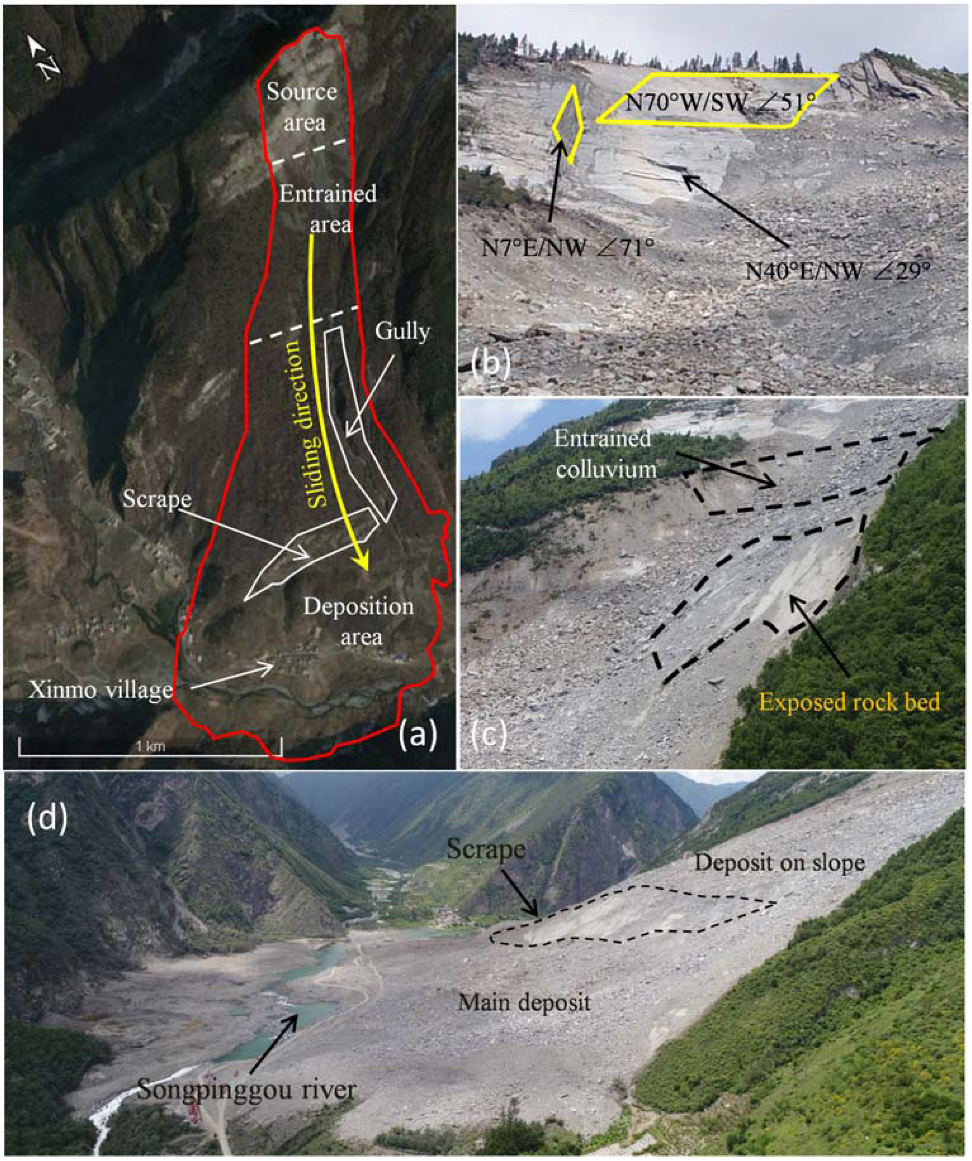

FIGURE 2 | Photos of the Xinmo Landslide before and after failure: **(a)** Pre-failure satellite image from Google earth on Jan. 9, 2016; **(b)** three sets of discontinuous (N70°W/SW∠51°, N7°E/NW∠71° and N40°E/NW∠29°) in the source area after failure taken on Oct 4, 2017; **(c)** scraped colluvium indicated by a schematic cross section and exposed bedrock in the entrained area taken on Jun. 29, 2017; **(d)** deposit of the Xinmo Landslide viewed from downstream taken on Jun. 29, 2017. Comparing **(a)** and **(d)**, the scrape at the foothill appears to be intact before and after the Xinmo landslide.

Numerical Model

According to the division of the slide range mentioned in the second section, the landslide model is also divided into three parts: sliding mass in source area, loose colluvium in the entrained area, and sliding bed. **Figure 6** shows the process of 3DEC landslide modeling including the following three steps:

(1) The first step is to build a two-dimensional model of the landslide and subdivide it into three areas. Add the boundary points of the source area and the entrained area in a rectangle area of 2910 × 1480 m, and use the Dismesh toolbox (Persson and Strang, 2004) in MATLAB to generate triangle meshes in each region, respectively. A total of 6,317 triangles are generated with an average side length of 40 m, including 159 in the source region, 296 in the entrained region, and 5816 in the outer region (**Figure 7**).

(2) The next step is to build a three-dimensional sliding bed and sliding body model. Taking the sliding bed as an example, two-dimensional triangles in the source area and entrained area are stretched into tri-prisms by two-dimensional linear interpolation based on the coordinates of the surface points after the landslide and using the coordinates of the surface points before the landslide

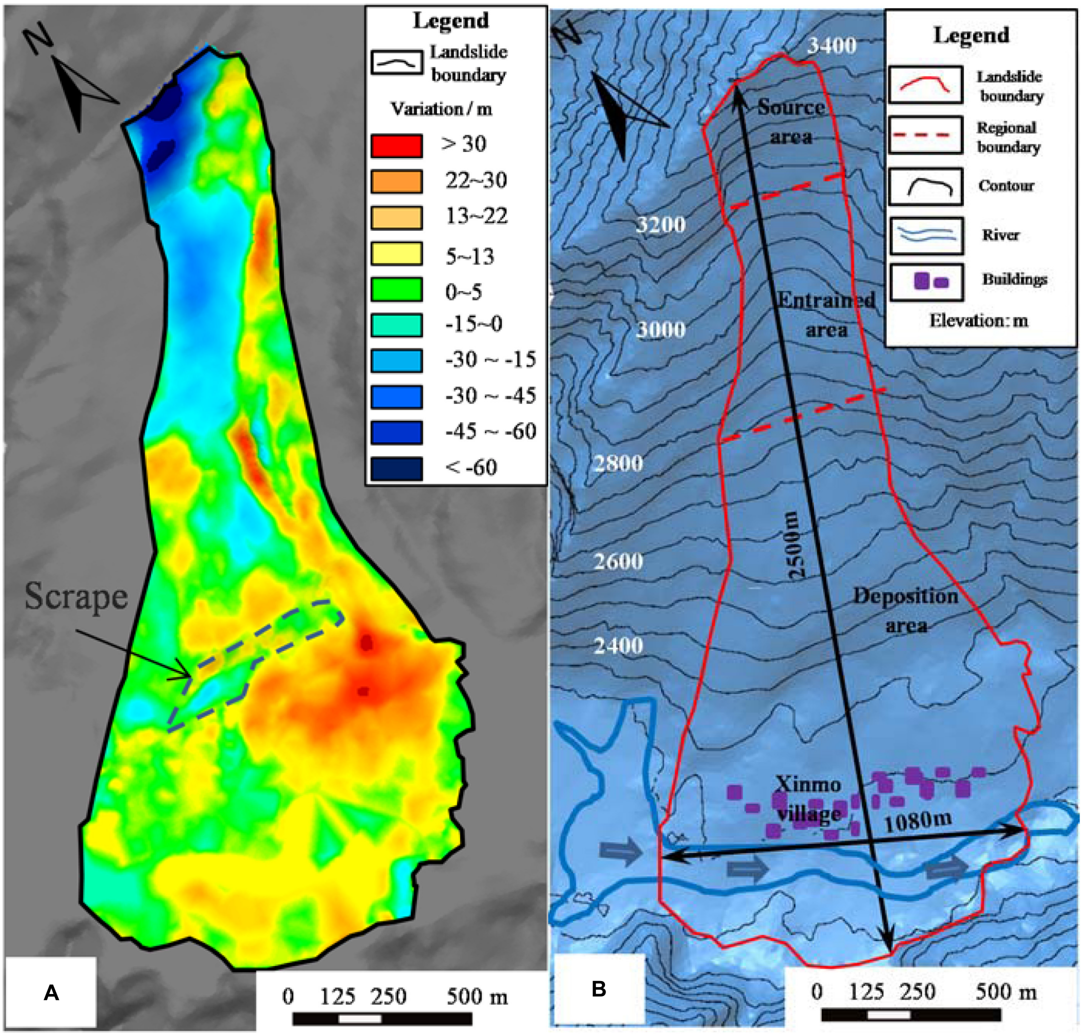

FIGURE 3 | Terrain conditions of the Xinmo catastrophic landslides: **(A)** elevation variation map of the Xinmo Landslide. Positive values indicate the thickness of deposit and negative values indicate reduction of surface elevation due source rock mass failure and entrainment of path materials. **(B)** digital elevation model of the Xinmo catastrophic landslide after sliding.

generates the tri-prisms consisting of the outer area. The sliding body could be obtained by the same way. After importing polyhedrons generated in MATLAB into 3DEC according to the syntax rules of 3DEC, three sets of discontinuities mentioned in Section 2 are used to cut the rock mass in the source area with spacing of 20 m. The sliding body volume of about 3.3×10^6 m^3 is calculated by adding the volumes of all the tri-prisms in the source area.

(3) In the last step, we use the fill-remove method to generate the entrained colluvium represented by the Voronoi polyhedrons which could be generated through Multi-Parametric Toolbox 3.0 (Herceg et al., 2013) in MATLAB. Only the colluvium above the bedrock was entrained, so a supply-limited condition is applied to construct the 3DEC slope geometry. As shown in **Figure 8**, a sufficient number of polyhedrons with an average 2.6-meter radius of inscribed sphere are created and placed above the sliding bed of the entrained domain in MATLAB, then translated into 3DEC blocks. Then, those blocks fall into the entrained area under gravity in 3DEC until this domain is filled and static. Finally, blocks outside the domain are removed. Input parameters used in this step are listed in **Table 1**. The gravity is set perpendicular to the slope surface of the entrained area and a high local damping coefficient is used, aiming to fill the domain quicker and within a shorter computing time. It should be noted that an initial static equilibrium must be satisfied by resetting the gravity vertically before run-out simulating. The inter-block contact friction angle of source mass is set as 51° before its failure and a high local damping coefficient of 0.7 is used to absorb kinetic energy during initial equilibrium of the model. Afterwards, the entrained domain is filled with 7,312 polyhedrons, with a total volume of 3.7 million cubic meters and a porosity of about 0.46.

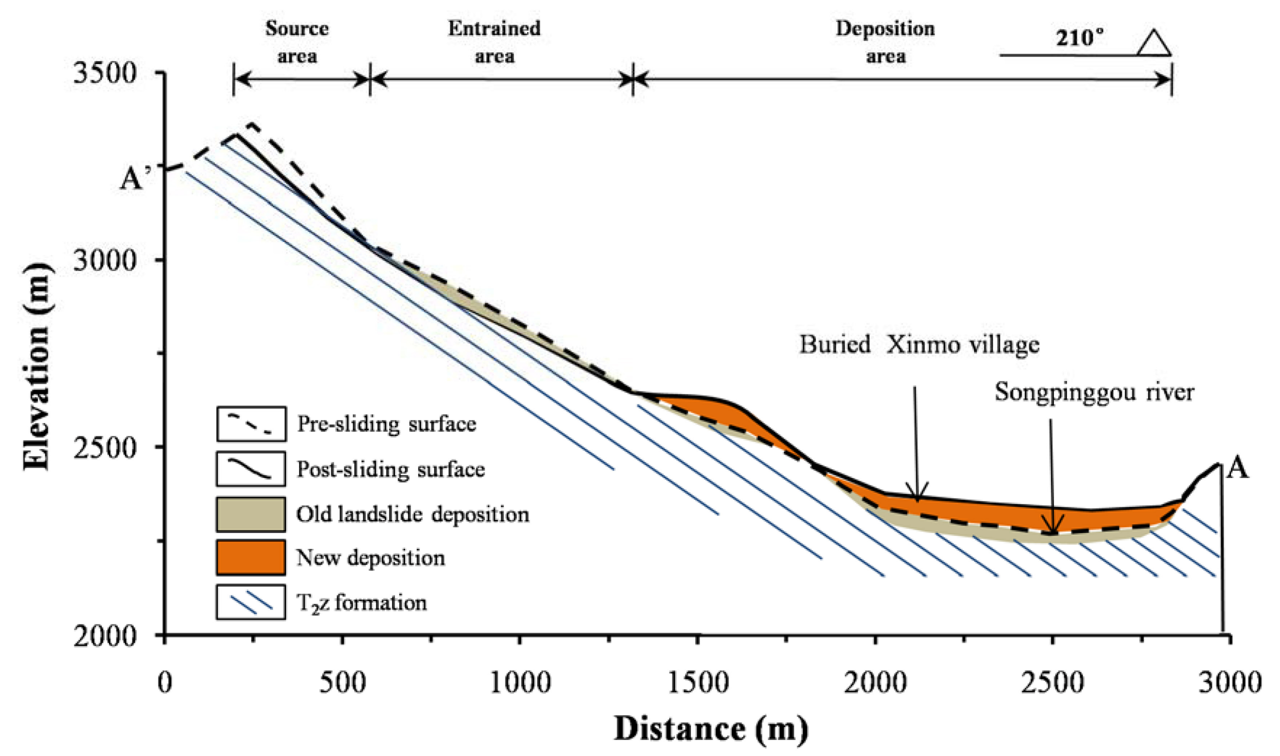

FIGURE 4 | The geological longitudinal profile of the Xinmo landslide along a typical cross section (Section A'-A in **Figure 1B**).

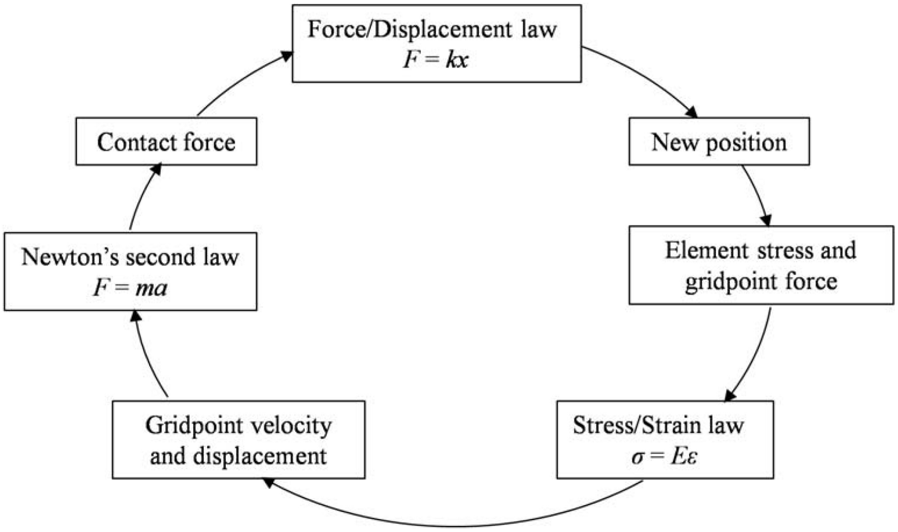

FIGURE 5 | Calculation cycle in the 3DEC (modified after Itasca Consulting Group Inc., 2016).

Figure 9 shows the slope geometry of the Xinmo Landslide with a maximum dimension of 2910 × 1480 × 1640 m and a total of 17026 blocks. The failure rock mass in the numerical model consists of two parts, i.e., the rock mass in the source area and the colluvium in the entrained area. Its total volume can be calculated as follows

$V_t = V_R \times (1+F_F) + V_E$ (1)

where V_{R} is the volume of the initial rockslide, F_{F} is the fractional amount of volume expansion due to the creation of pore space, and V_{E} is the volume of the entrained material. Considering that the porosity of crushed material ranges from 18 to 35% (Sherard et al., 1963), the total volume of deposition is estimated to be 7.6×10^6 to 8.16×10^6 m^3.

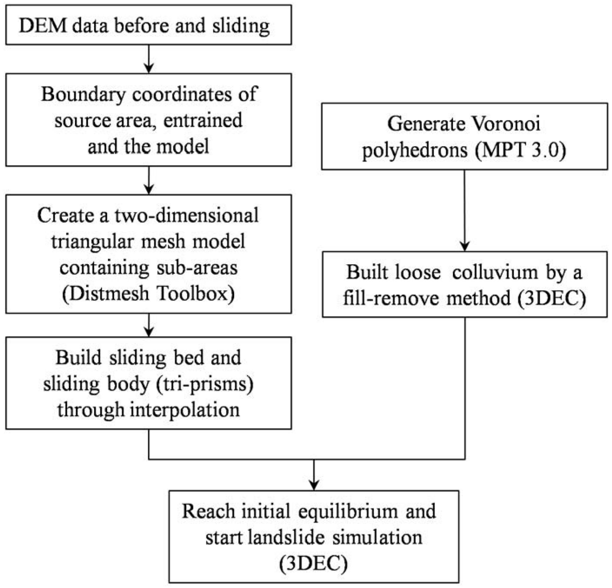

FIGURE 6 | Flowchart of numerical modeling for mass movement of landslides.

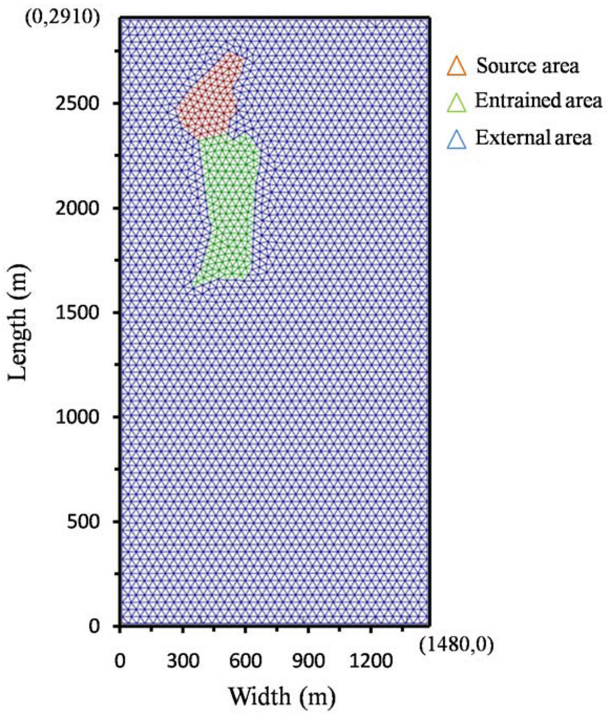

FIGURE 7 | Two-dimensional model of the Xinmo Landslide with three sub areas.

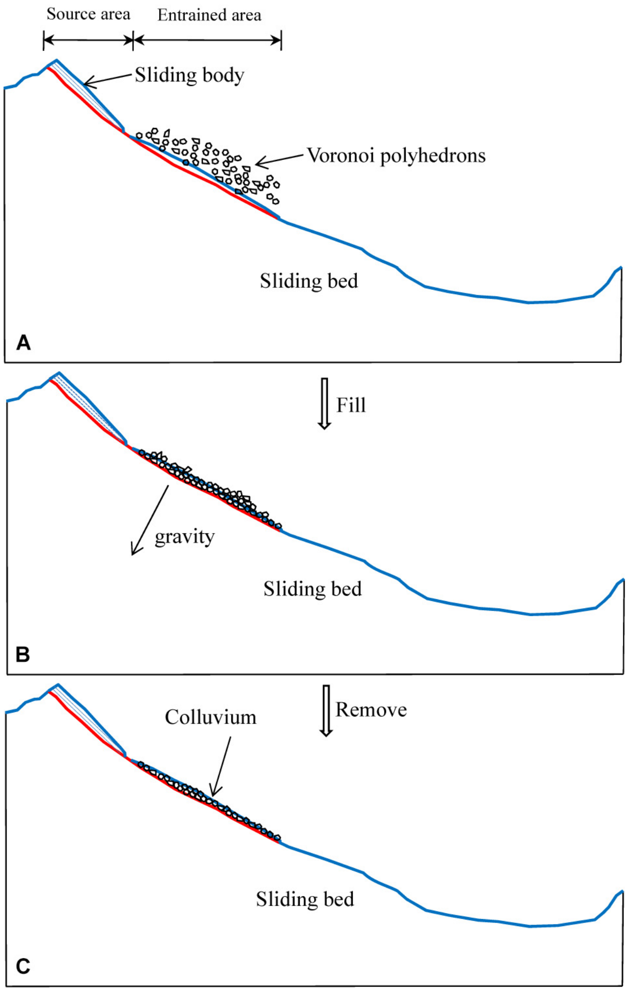

FIGURE 8 | The process of generating colluvium in 3DEC showed in 2D: **(A)** generate Voronoi polyhedrons enough to fill the entrained area above the slope surface; **(B)** Voronoi polyhedrons fall into the entrained area under gravity while the sliding bed is fixed; **(C)** remove blocks above the surface before sliding. The blue lines and red lines represent the slope surface before and after sliding, respectively. The gravity direction is perpendicular to the slope surface of the entrained area.

Determination of Parameters

In this simulation, all blocks are assumed to be rigid with the same density of 2,600 kg/m^3, and the Coulomb-slip joint model (Itasca Consulting Group Inc., 2016) is applied to contacts. **Table 1** lists the mechanical parameters of contacts used for numerical analysis. Joints in the source area are assumed to be in the residual state because block deformation were obtained before the slope failure (Dong et al., 2018; Intrieri et al., 2018). Therefore, the cohesion, the dilation angle, and the tensile strength of both contact materials are assumed to be 0.0 kPa, 0°, and 0.0 kPa, respectively. Teufelsbauer et al. (2009) found that the mechanical behavior of rapid granular flow is not sensitive to the contact stiffness. The contact stiffness k_n and k_s are set to a high value of 2 GPa to prevent excessive block overlap. The values of contact friction angle and damping coefficient have a significant influence on the block movements. The damping coefficient is not a parameter that is explicitly related to any physical mechanism, it is set to 0.0 during the sliding simulation (Li et al., 2012; Wu et al., 2017). The contact friction angle between sliding body and

TABLE 1 | Input parameters in 3DEC.

Parameters		Values
Density(kg/m^3)		2600
Inter-block friction angle(°)	Sliding body- sliding body	51*, 22
	Colluvium- colluvium	29
	Sliding body- sliding bed	51*, 22
	Colluvium- sliding bed	29
Contact stiffness (GPa)	Normal contact spring k_n	2
	Shear contact spring k_s	2
Contact tensile strength (kPa)		0
Contact dilation angle (°)		0
Joint spacing (m)		20
Local damping coefficient		0.7*, 0
Gravity (m/s^2)		(0, 5.8, −9.81)*, (0, 0, −9.81)
Time step (s)		8.7×10^{-4}

Note: values with '' are input while filling the entrained domain.*

sliding bed is 22° in dynamic evolution which is derived through back analysis based on the landslide geometry. Considering the colluvium was in low water content during this event, a constant contact friction angle, 29°, between colluvium and sliding bed is used. The friction angle of new contacts generated in the subsequent sliding are set to 22°. In the movement simulation, the time step is set as 8.7×10^{-4} s, and the numerical simulation is carried out in 1.3×10^6 steps. A standard desktop computer (Intel® Core$^{\mathrm{TM}}$ i7 CPU, 2.60 GHz × 6, and 16 GB RAM) has been adopted for the 2-day numerical simulation.

RESULTS

Evolutions of Sliding Mass Position

The movement simulation of the Xinmo Landslide is carried out for 120 s using a discrete element method. **Figure 10** shows the variations in position of the sliding mass over time. As shown in **Figure 10A**, the sliding body impacts the loose accumulation fiercely, and the frontal part of the sliding body climbs over the colluvium to the middle part of the entrained area after an elapsed time of 9 s. During this stage, the volume of the sliding mass increases obviously, owing to bulking. However, the colluvium in the lower part of the entrained area is not yet stable. After 11.2 s (**Figure 10B**), a few blocks reach the flat ground at the bottom of the Songpinggou Gully and their movement direction slightly deviates to the left along a pre-existing gully at the lower part of the slope. An integral-sliding of the old landslide deposits slide under the shoveling and scraping of the sliding mass can be seen from **Figure 10B**. **Figure 10C** (at 35 s) shows that the front of the landslide has been widened obviously after sliding out of the entrained area and reaches the scarp at the toe. From 35 to 52 s, the sliding mass glides to the bottom of the valley with a diffusion angle of about 60°, most of them stop at the slope toe after impacting the valley bottom and form a fan-shaped accumulation. Compare **Figure 10E** with **Figure 10F**, the landslide is essentially static except for a little debris moving on the scarp at 60 s. **Figure 10F** shows the final deposition after an elapsed time of 120 s. The landslide deposits are divided into two main parts, one portion is situated above the scarp and the other accumulates at the toe of the slope on the left bank of the river. The colluvium is entrained to the bottom of the Songpinggou Valley entirely and buried under the sliding mass, while the deposits on the scarps are all composed of the rock mass from the source area. In addition, few deposits cross the river or pile up in the pre-existing gully. The maximum run-out distance, L_s (measured from the rear edge of the source area to the distal edge of the deposits, seen in **Figure 10F**) in the numerical simulation is 2,450 m, which is close to the field investigation that was reported in Fan X. et al. (2017), 2,418 m. However, the maximum width, L_w, along the river, 1,400 m, is slightly larger than the field measurement value, 1,200 m (Fan X. et al., 2017).

Figure 11a shows the simulated deposit thickness; the maximum simulated deposit thickness is 55 m, which is larger than the actual thickness, 31 m. The average deposit thickness, 10.8 m, is close to the average value, 10 m, derived from field investigation (Wang et al., 2020). In this study, a uniform contact friction angle, 22°, between the sliding body and the sliding bed assumed is much smaller than the slope of the scraping area, which results in no blocks piling up in the entrained area and a higher deposit thickness than in reality in the area above the scrape. A comparison between simulated and actual deposit thickness along a typical cross section is shown in **Figure 11b**. The deposit thickness presents an increasing tendency from west to east due to the change of sliding direction (**Figure 10B**), which is consistent with reality, while a notable higher thickness is shown at the eastern end. The reason for this difference could be that the excessive block size cut by joints with an average space of 20 m would result in an uneven distribution of deposit. More reasonable simulation results could be obtained by using a block size closer to the actual value, but it would require a much longer computational duration.

Velocity Variations

The evolution of landslide propagation velocity has been analyzed in terms of the mean velocities of the whole mass, sliding body, and the entrained colluvium, as shown in **Figure 12**. Each of the velocity-time curves show two distinct peaks, indicating that the sliding body and accumulation have experienced two accelerations and decelerations due to the complex local topography and base erosion. Within 5 s from the instability of the sliding body, the gravitational potential energy of the sliding body and the elastic potential energy stored in contacts are rapidly converted into kinetic energy, and the velocity of the sliding body rapidly reaches its first peak value of 63.7 m/s (at 5.2 s). During the same time, the colluvium in the entrained area is impacted to accelerate. After 5 s, the impact reaction force exceeds the gravity of the sliding body, resulting in the deceleration of the sliding body, and the acceleration of the colluvium decreases (the velocity curve of colluvium changes from concave to convex). After 11.2 s, the velocity of the sliding body increases with little fluctuations for the second time since the general failure of the colluvium (**Figure 10B**). The second peak velocity, 55.8 m/s, of the sliding body and the second peak

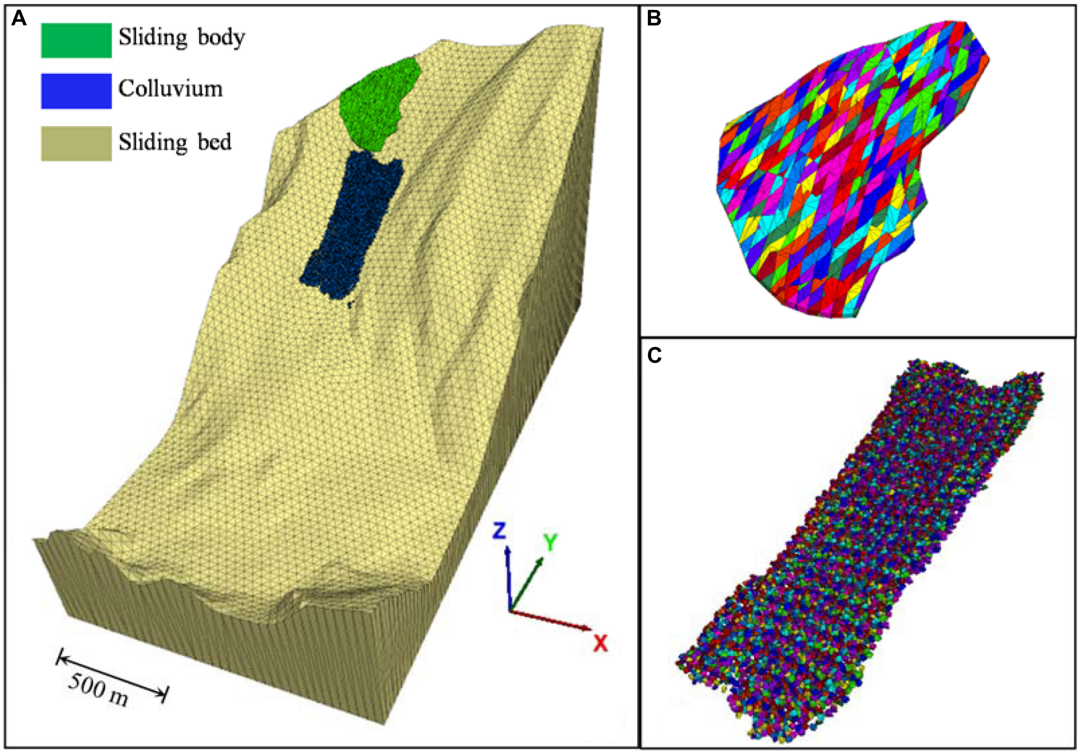

FIGURE 9 | Discrete element model of the Xinmo catastrophic landslide: **(A)** 3DEC model of the Xinmo Landslide; **(B)** simulated rock mass in the source area cut by three joint groups with an average space of 20 m and **(C)** simulated colluvium in entrained area as an assembly of Voronoi polyhedrons.

velocity, 39.9 m/s, of the colluvium occur at the same time (t = 25.3 s) and then decrease due to the flatter slope gradient. The velocity of the sliding body is always greater than that of the colluvium and pushes them to slide until they reach the same velocity. At 34.4 s, the colluvium slides down from the scarp at the lower slope, and gradually reaches the second peak velocity when they reach the bottom of the Songpinggou Valley. The average velocity of the sliding body also shows a slight decline a few seconds after the second acceleration of the colluvium because a big part of the sliding remains on the scarp (**Figure 10A**). Subsequently, the velocity of the landslide decreases slightly and the whole landslide motion stops in about 60 s.

It is more representative to use the overall velocity average curve to describe the whole landslide motion. The tendency of the whole mass average velocity curve is similar to that of the sliding body, and its two peaks (51.1 m/s at 5.2 s and 50.2 m/s at 26.0 s) are both smaller than those of the sliding body. The main sliding time could be estimated about 60 s from the average velocity curve of the whole mass when only a few blocks are in motion. Xu et al. (2017) analyzed the landslide movement according to the seismic signal of the Xinmo Landslide recorded by the Maoxian MXI station and suggested that the 120 s process of the landslide can be divided into three stages. In the first stage (about 40 s), some hanging rocks at the ridge collapsed and impacted the lower part of the source area, leading to the propagation of pre-existing cracks and the failure of the sliding body (Hu et al., 2018). The second stage, i.e., the main sliding, lasted 60 s from failure to stacking. Finally, some small-scale collapses occurred in the last 20 s until the event calmed down. In our study, only the main sliding was simulated, the time duration of the numerical simulation results correlates well with the measured data.

Figure 12B shows the evolutions of the average angular velocity of the sliding body and colluvium. There is some difference between the velocity curve and angular velocity, as the angular velocity curve has only one peak. However, the time when the angular velocity reaches the peak is equal to the time when the velocity reaches the second peak. After the beginning of the landslide, the angular acceleration of the sliding body and colluvium are close, but the colluvium is accelerated for a longer time and finally exceeds the sliding body. The change of angular velocity is not as sharp as that of velocity, and it still keeps a high value after the main sliding stage. When block motion changes from sliding to rolling, the friction energy consumption decreases and the block moves further. According to $V = \omega \times R$, the radius and peak angular velocity of the colluvium are about 2.6 m and 1.34 s, respectively, so the velocity of the pure rolling block is about 3.5 m/s and is far less than the actual peak velocity of 50.2 m/s. Therefore, sliding is the fundamental motion in this simulation.

Entrainment of the Colluvium

The amplified landslide volume caused by the substrate erosion is a typical feature of the Xinmo Landslide. Although many researchers considered the entrainment effect in numerical

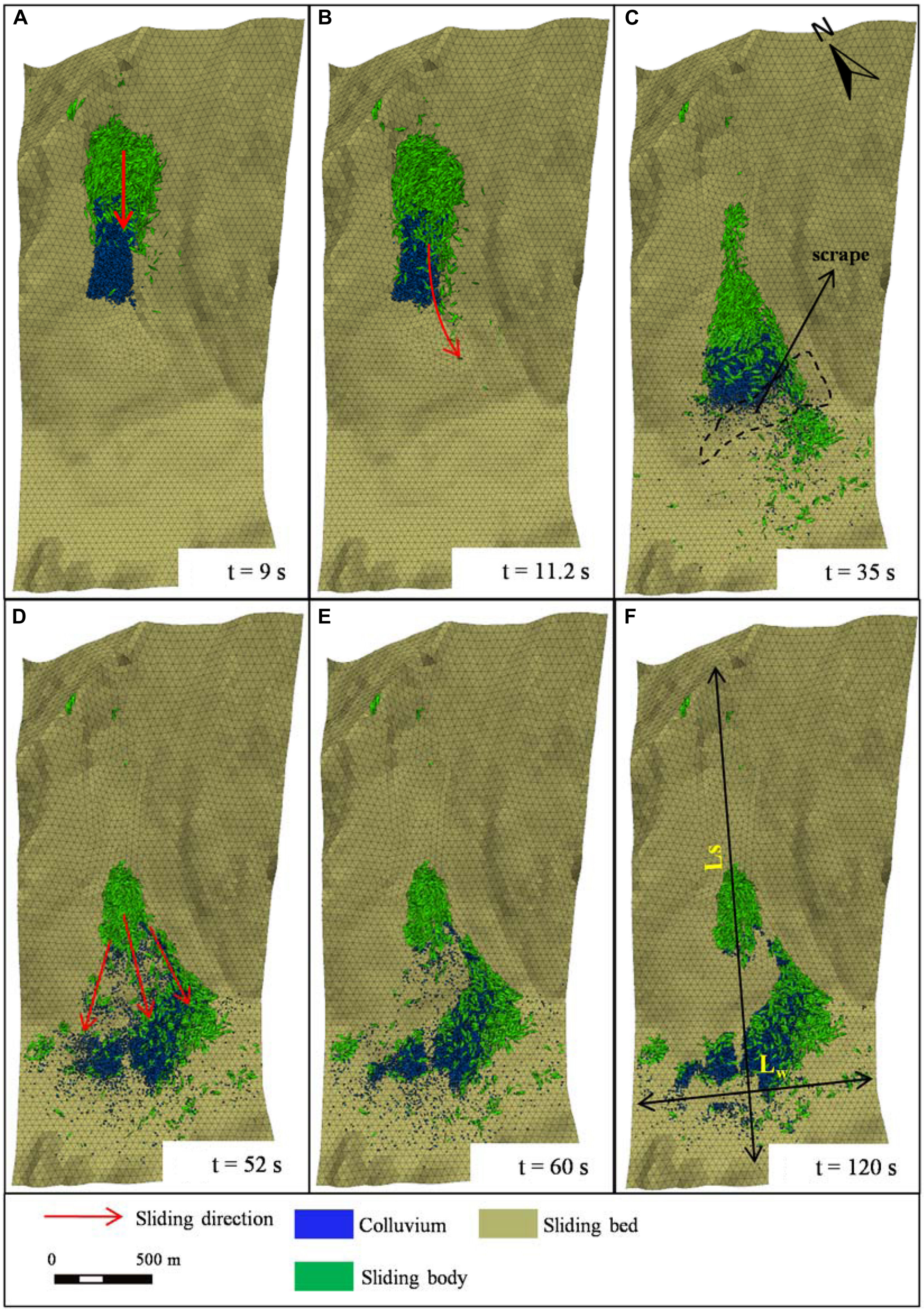

FIGURE 10 | Simulated sliding mass position at different times since the landslide initiation: **(A)** t = 9 s; **(B)** t = 11.2 s; **(C)** t = 35 s; **(D)** t = 52 s; **(E)** t = 60 s and **(F)** t = 120 s. L_S and L_W indicate the maximum length of the landslide along the direction of motion and down the river, respectively.

simulations of the Xinmo Landslide, the entrainment process was rarely analyzed (Chen and Wu, 2018; Hu et al., 2019; Huang et al., 2019; Liu et al., 2019). In order to understand the simulated erosion process, the failure and migration of the colluvium are stated here.

A typical profile A-A' is used to show the results aiming to observe the phenomenon clearly. The impact and entrainment process of the landslide is shown in **Figure 13**. At $t = 1.7$ s, the front of the sliding body plow into the colluvium and the failed colluvium generate an oblique upward velocity. It could also be seen that there is an obvious failure surface (the red dash) with an inclination angle ($\theta \approx 28°$) between failed and stable colluvium (**Figure 13A**). With the increase in the landslide displacement, the sliding mass becomes more broken and part of the fragments

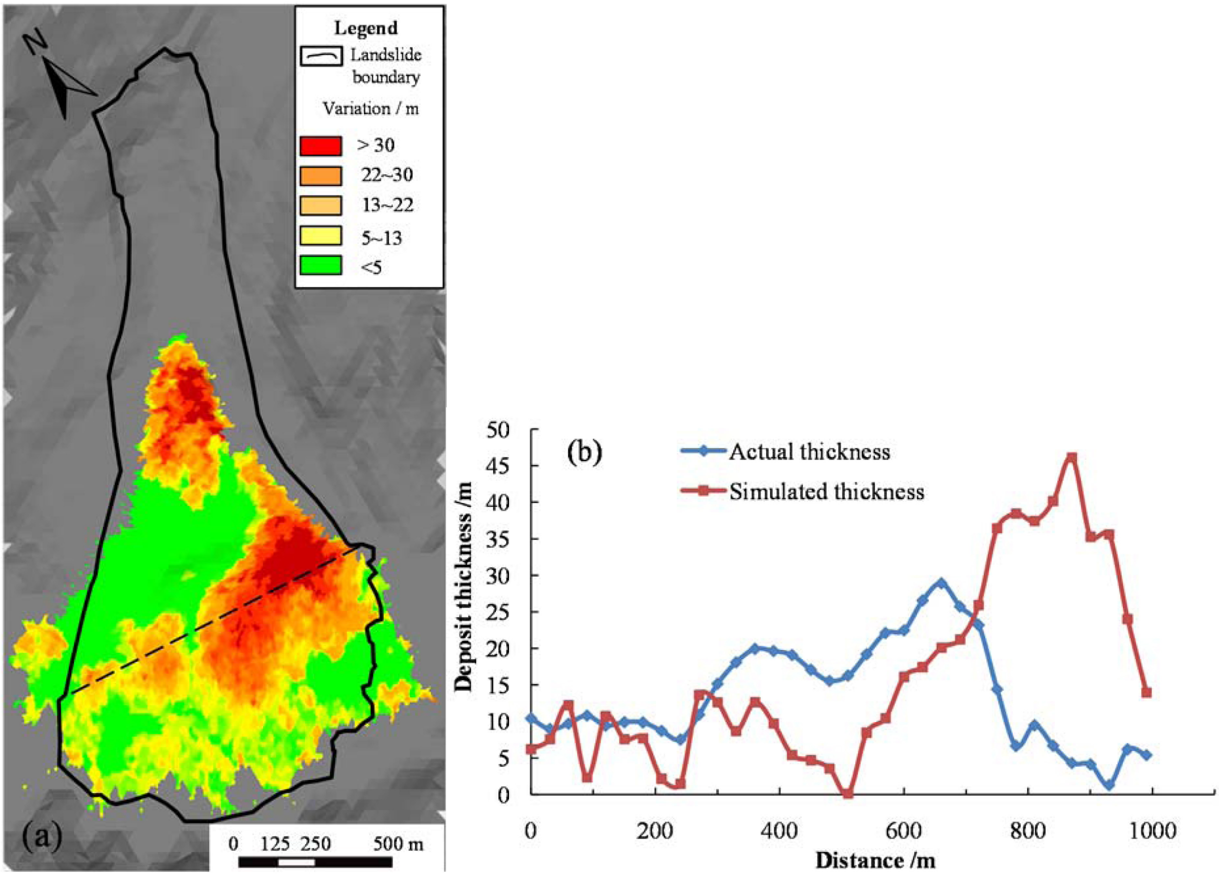

FIGURE 11 | Simulated deposit thickness distribution of the Xinmo Landslide. **(a)** the plan view and **(b)** simulated and actual thickness of the Xinmo Landslide deposit along a representative cross section which is shown in **(a)** as the dash line.

climb to the upside of the colluvium. At the front of the sliding mass, several blocks can be seen to be splashed and mixed with the sliding mass under the heavy impact. As the failure surface propagates towards the front of the accumulation, more and more colluvium is failed by the pushing of the sliding body, and the rear of the colluvium is compressed and thickened (**Figure 13B**). The phenomena, frontal plowing, mass spray, failure surface, and thickened substrate, observed in the DEM simulation, are very similar to the experimental ones (Dufresne, 2012; Lu et al., 2016). At $t = 26$ s, **Figure 13C** shows that the rear part of the sliding body becomes thinner and most of them are still located at the rear of the colluvium. Although the whole colluvium has already failed and slide as a whole with the sliding body, the back and upper sliding bodies still have a faster speed than the colluvium. This indicates that the entrainment process is not finished, and it will still last a few seconds to reach the same velocity as the sliding body after the failure of the whole colluvium.

DISCUSSION

In our study, the simulated movement distance, deposition pattern, and main sliding time of the Xinmo Landslide are in conformity with the field investigation and actual time based on landslide seismic signal analysis. In addition, some typical phenomena of substrate entrainment, including frontal plowing, mass spray, shear zones in substrate, thickened substrate, and basal abrasion, are observed in our simulation as found in the physical experiments of Dufresne (2012). The features of substrate entrainment in natural landslides should serve as constrains with numerical simulations. However, few documented entrainment processes or deeply buried substrate materials in landslide sediments limit insight into the natural phenomena. The agreement of the simulation results with those features of the phenomena observed in the laboratory during substrate entrainment can justify our simulation results to a certain extent, which in turn deepen the understanding of the complex physical phenomena.

Frontal erosion or plowing and basal abrasion are the two main forms of substrate failure (Hungr and Evans, 2004; Barbolini et al., 2005; Sovilla et al., 2006; Lu et al., 2016), both of which could be seen in our simulation (**Figure 13C**). At present, most entrainment models based on continuum mechanics simplify that the failure of the substrate material is caused by the shear force acting on the base surface (McDougall and Hungr, 2005; Luna et al., 2012; Ouyang et al.,

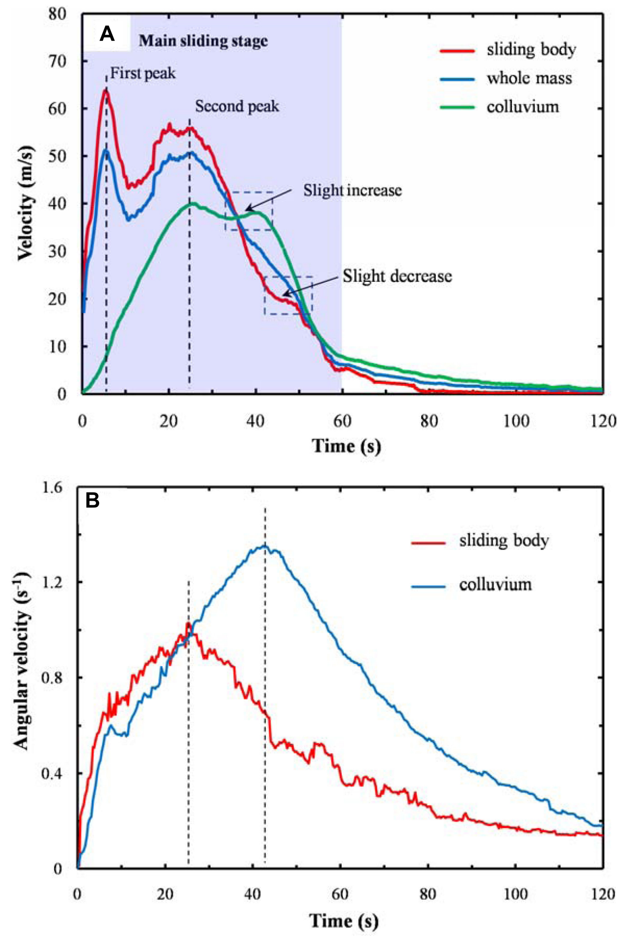

FIGURE 12 | Numerical results of the velocity evolution among the mass movement process: **(A)** evolutions of average velocity of sliding body, colluvium, and whole mass and **(B)** evolutions of average angular velocity of sliding body and colluvium. The velocity curves for the sliding body, the colluvium, and the whole body all have two distinct maxima. The angular velocity curves of both the sliding body and the colluvium have only one maximum value and the time at which the angular velocity reaches its maximum is the same as their respective times of reaching the second velocity maximum.

2015; Li et al., 2019). In our simulation, the front of the sliding body pushing the accumulation seems to be a significant factor leading to the failure of the colluvium, especially at the initiation of entrainment. In addition, the failure surface is always located in the front of the bulldozer, rather than parallel to the bottom of the sliding body (**Figures 13A,B**). The angle of about 28° between the failure surface and slope approximately equals to 30.5° (45°-29°/2), which indicates that the colluvium experiences a shear failure due to passive earth pressure.

According to the deformed base shape, we could divide the force acting on the base parallel to the direction of landslide movement into two parts: the thrust acting on the trailing edge and the shear acting on the upper surface of the sliding body (**Figure 14**). In order to find out the effect of thrust and shear force, we use the Fish language built in 3DEC to calculate the values of the two during the process of base entrainment. As the rear of the colluvium becomes flat (**Figure 13C**), the action position of thrust and shear force is not obvious, only the thrust and shear force from the beginning of the landslide to 17 s are calculated. **Figure 15** shows the calculation results. At the beginning of the entrainment process, the colluvium is impacted by the sliding body and the shear is zero. With the sliding body moving over to the surface of the colluvium, the shear begins to increase gradually, but the thrust is the main reason causing failure. For dry substrate materials, Barbolini et al. (2005) and Sovilla et al. (2006) also proposed that the predominant erosion mechanism observed in the experiments is plow, i.e., thrust, and the contribution to the erosion of shear is negligible. After the failure of the whole colluvium, the magnitude of thrust experiences a rapid decline but is still slightly larger than that of shear.

Detailed investigation of the morphology and internal structures of rock avalanche deposits could provide conditions for the exploration of the rapid motion of debris and constraints with the reliability of the numerical model. The colluvium in the front of the deposit simulated here also supports the plowing process (**Figure 10F**), but it is difficult to distinguish the new deposits from the path materials in this study because they are the products of the same kind of rock fragmentation. This phenomenon was observed in a similar landslide, the 2009 Jiweishan rock avalanche in Chongqing, China, wherein loose soil on the transport path was bulldozed to the very front and pushed passively by the rock debris, rather than remaining at the bottom and reducing frictional resistance between the debris and the ground through the deposit investigation and numerical simulation by Zhang et al. (2019).

To understand the role of entrainment of colluvium on landslide mobility, a simulation with no entrainment was conducted and its final deposit is shown in **Figure 16**. Here, the apparent friction coefficient (Φ_a), which is defined as slope of the line connecting the highest point (P_h) of the source mass and the most distal point (P_d) of the deposit, is used as a parameter to quantify the mobility of the rock avalanche. The equivalent friction coefficient (Φ_e) is equal to the height difference divided by the horizontal distance difference between the center of gravity of the source mass (C_s) and deposit (C_d), which can represent the consumption of potential energy in the mass due to friction (Heim, 1932). The equivalent friction coefficient could be obtained easily using Fish code to derive the center of mass of the failing mass and the deposit in 3DEC. **Table 2** shows the kinematic parameters of simulation results for different substrate conditions. The higher Φ_e under the erodible bed condition indicates that entrainment of path materials is an energy-consuming process and reduced the mobility. The similar Φ_a in both conditions is the result of opposite hill blocking.

Mangeney et al. (2010) found that the mobility of granular collapse increases on erodible slopes when the inclination angle exceeds a critical angle,$\theta_c \approx \theta_r/2$ ($\theta_r$is the response angle of substrate material). In this study, a contact friction angle of 29° was achieved, which is close to inclination angle of the slope and place in which the colluvium in critical stable is used, but the mobility of the landslide was reduced contrary to their

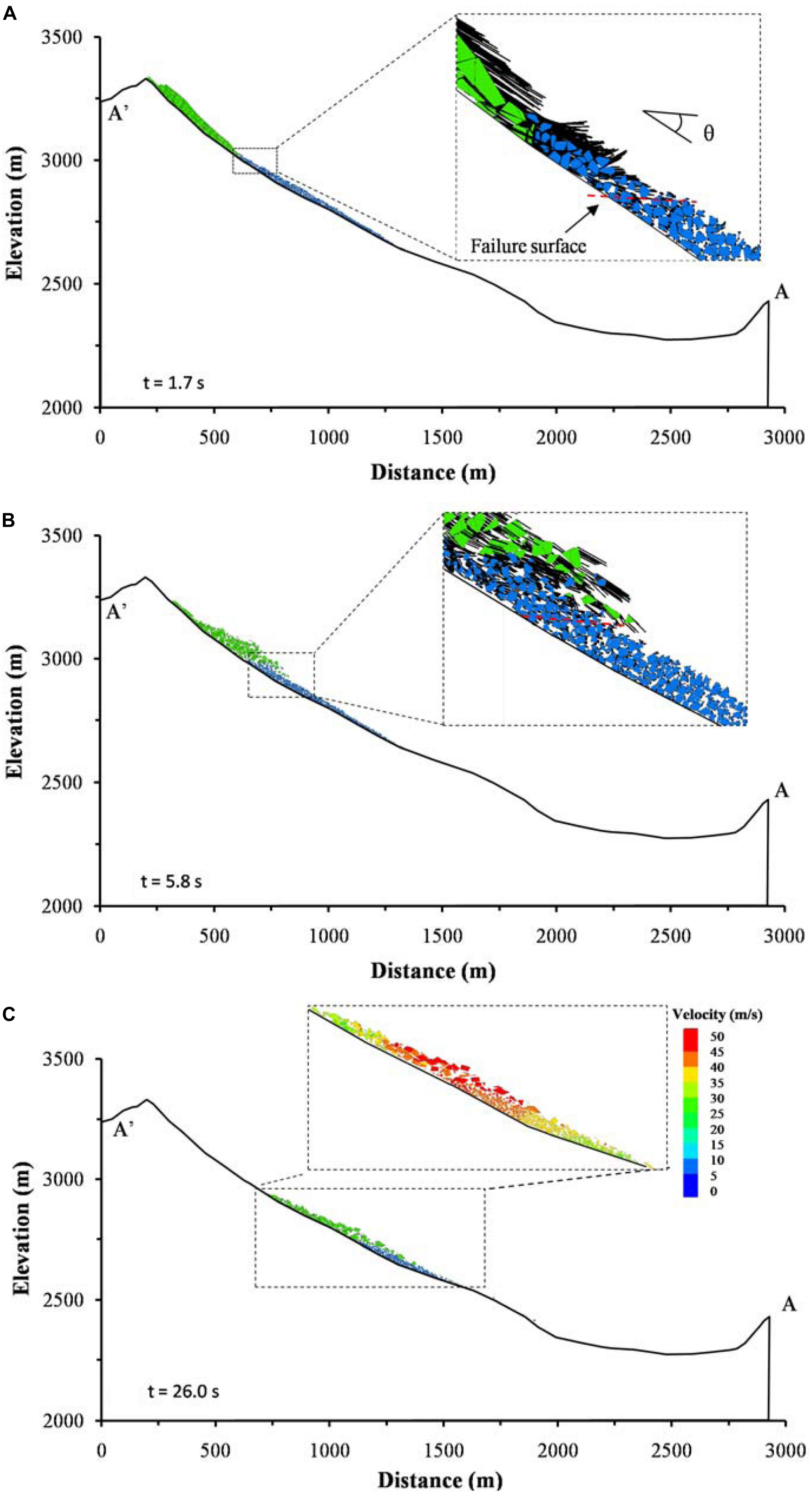

FIGURE 13 | Entrainment process at different times: **(A)** frontal plowing and substrate failure; **(B)** thickened substrate under compression; and **(C)** completely displaced colluvium indicated by the moving leading edge with a velocity more than 15 m/s. An interface (red dash line) between failed and static colluvium with an inclination angle ($\theta \approx 28°$) with respect to the base of the substrate under the plowing of the sliding mass can be seen at the beginning of the entrainment process.

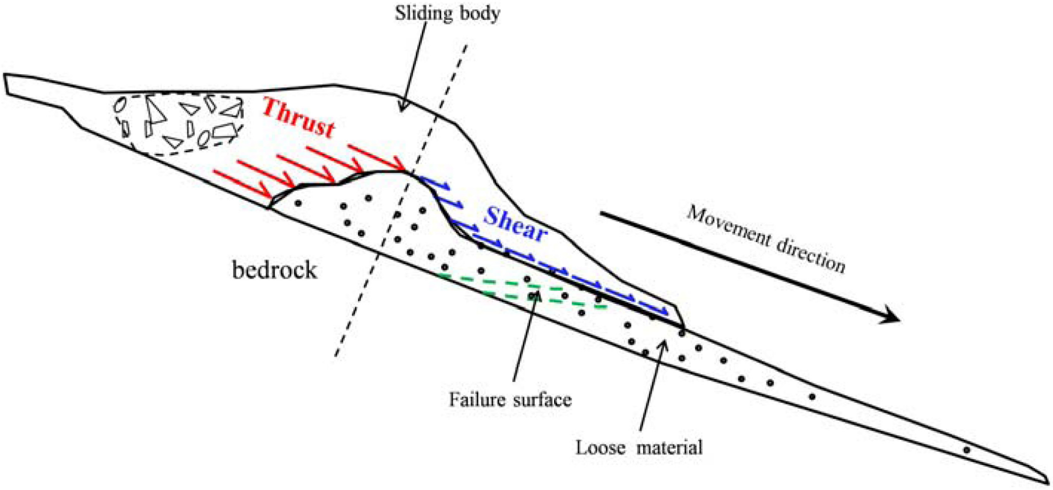

FIGURE 14 | Sketch diagram of the thrust and shear force acting on loose material alone sliding direction in a supply limited condition. The sliding body applying the thrust and shear force is divided into two parts, separated by a plane which passes through the ridge line of deformed path materials and is perpendicular to the movement direction.

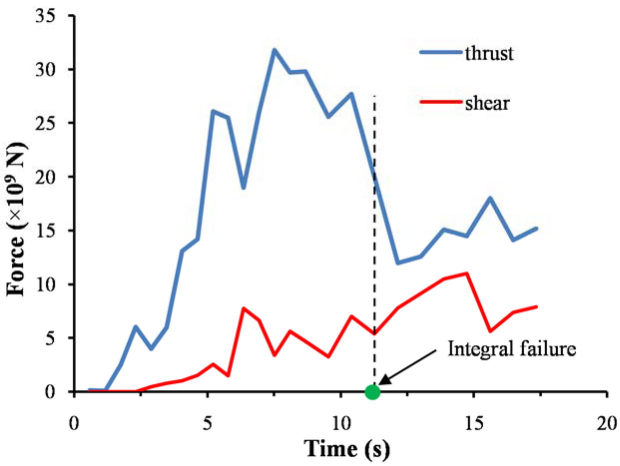

FIGURE 15 | Evolution of thrust and shear force during the entrainment process. The magnitude of the thrust decreases abruptly at the time of integral failure of the substrate but remains higher than the magnitude of shear.

experimental results. A significant decrease of average velocity at the initiation of entrainment could be seen in **Figure 8A** as a result of momentum transfer to accelerate stationary bed material by frontal plowing (Iverson and Ouyang, 2015). In Mangeney's experiments, there seem to be no difference between frontal velocities at the beginning of the slump between rigid and erodible path conditions which is dominated by a pressure gradient instead of plowing, yet a steady frontal flow on erodible bed occurred after a deceleration phase increased the runout distance. We infer that plowing at onset of entrainment inhibits flowing, but a promotion of mobility is caused by basal abrasion. In our simulation, plowing is the dominant entrainment mechanism compared to basal abrasion, according to a previous discussion. The reverse responses of mobility to path entrainment may be related to different initial geometries of flowing mass and substrate. In addition, it should be noted that the friction coefficient between sliding mass and sliding bed, 22°, used in both simulations, which derived from back

FIGURE 16 | Simulated deposit of the Xinmo Landslide in rigid bed condition. Part of the blocks sliding out of the model range is not shown.

TABLE 2 | Kinematic parameters of simulation results in different substrate conditions.

	Erodible bed	Rigid bed
P_h (m)	(518.6, 2646.9, 3416.7)	(518.6, 2646.9, 3416.7)
P_d (m)	(846.8, 197.3, 2314.9)	(1077.0, 265.5, 2296.7)
C_s (m)	(556.7, 2572.2, 3296.0)	(556.7, 2572.2, 3296.0)
C_d (m)	(912.3, 1073.0, 2429.3)	(1106.2, 675.5, 2316.6)
Φ_a	0.448	0.457
Φ_e	0.563	0.496

Note: C_s is the center of gravity of the source mass excluding substrate materials, C_d is the center of gravity of the deposit consisting of source mass and substrate material. Part of blocks sliding out of the model range in rigid bed condition is not considered here.

analysis of traveling distance in erodible substrate condition, is smaller than that of colluvium, a critical value maintaining its static on the slope. Plowing of the static colluvium of a higher strength is hence another explanation of the reduced mobility. Nevertheless, those parameters installed here may be reasonable according to the friction weakening with increasing sliding velocity that probably explains the unexpectedly long runout of giant landslides (Lucas et al., 2014). Moreover, the predicted potential landslide impacting areas in the same region using the friction coefficient obtained from back analysis of landslides that already occurred could be overestimated when entrainment of path material is not included.

The LS-RAPID landslide dynamics computer software based on the liquefied model proposed by Sassa et al. (2010) has successfully analyzed the long run-out landslides with characteristics of substrate liquefaction and mass amplification induced by earthquakes or rainfall. Wang et al. (2020) conducted the simulation of the Xinmo Landslide using different dynamic models and their results suggested that the liquefied model is not suitable for the Xinmo rock avalanche because there is no liquefaction condition according to the field investigation. In our study, pore pressure is not taken into account and a constant friction angle is used considering the low water content of the colluvium in the path, even if there was a long time of rainfall before the slope failure (Li et al., 2012). For different base material types, there will be different dominant failure modes, so the appropriate numerical method and entrainment model should be chosen cautiously when entrainment of substrate is included.

CONCLUSION

Taking the June 24, 2017 Xinmo Landslide in Maoxian County, Sichuan Province as an example, the displacement, velocity, and entrainment process of the landslide are investigated using a 3D Distinct Element Code (3DEC) program. Several conclusions can be summarized as follows:

(1) Topography has a great influence on the movement direction of landslide. A pre-existing gully at the lower part of the slope changes the main sliding direction, resulting in the thickness of the deposit being higher in the East and lower in the West.

(2) The landslide undergoes two decelerations: the first one is due to impacting the colluvium, and the second one is affected by the terrain. The average velocity of the landslide reaches the first peak value of 51.1 m/s at 5.2 s and the second peak of 50.2 m/s at 26 s. It lasts about 120 s from the overall instability of the landslide to the ceasing of the movement and the main sliding stage lasts for 60 s, which coincides with the time deduced from the seismic signal of the landslide.

(3) The entrainment process could be divided into two stages. In the first stage, the predominant erosion mechanism is plow and the contribution of the basal abrasion is negligible. In the second stage, the magnitude of thrust experiences a rapid decline but is still slightly larger than that of shear after the failure of the whole colluvium. The colluvium is always in the front and the lower part of the sliding body, which was pushed to the bottom of Songpinggou Gully by the sliding body. Entrainment of dry material on the slope leads to more friction energy consumption, although total potential increases and reduces the mobility of mass movement.

In the DEM model, the loose colluvium is represented by rigid Voronoi blocks stacked under gravity and its failure and displacement under entrainment with overlying sliding mass is determined by the Coulomb-slip contact model. This work shows good capability of simulating entrainment of dry materials in a supply limited condition using a discreet element method, wherein both frontal plowing and basal abrasion of substrate are simulated. However, frontal plowing was not included in most entrainment models using the continuum approaches due to the simplification of the physical process. Our study highlights the significance of plowing relative to the basal abrasion under conditions of limited path material supply and future explorations of improved entrainment models incorporating the plowing characteristics are needed.

DATA AVAILABILITY STATEMENT

The raw data supporting the conclusions of this article will be made available by the authors, without undue reservation, to any qualified researcher.

AUTHOR CONTRIBUTIONS

J-wZ did the conceptualization, review, and editing. QC did the methodology, collected the resources, and prepared the original draft. QC and GF did the validation. GF and J-wZ did the investigation and funding acquisition. All authors have read and agreed to the published version of the manuscript.

FUNDING

This research was funded by the National Key R&D Program of China (2017YFC1501102), the

National Natural Science Foundation of China (41977229 and 41907247), and the Sichuan Youth Science and Technology Innovation Research Team Project (2020JDTD0006).

ACKNOWLEDGMENTS

Critical comments by the reviewers greatly improved the initial manuscript.

REFERENCES

Aaron, J., and McDougall, S. (2019). Rock avalanche mobility: the role of path material. *Eng. Geol.* 257:105126. doi: 10.1016/j.enggeo.2019.05.003

Barbolini, M., Biancardi, A., Cappabianca, F., Natale, L., and Pagliardi, M. (2005). Laboratory study of erosion processes in snow avalanches. *Cold Reg. Sci. Technol.* 43, 1–9. doi: 10.1016/j.coldregions.2005.01.007

Chen, K. T., and Wu, J. H. (2018). Simulating the failure process of the Xinmo landslide using discontinuous deformation analysis. *Eng. Geol.* 239, 269–281. doi: 10.1016/j.enggeo.2018.04.002

Cuomo, S., Pastor, M., Capobianco, V., and Cascini, L. (2016). Modelling the space–time evolution of bed entrainment for flow-like landslides. *Eng. Geol.* 212, 10–20. doi: 10.1016/j.enggeo.2016.07.011

Dai, K., Xu, Q., Li, Z., Tomás, R., Fan, X., Dong, X., et al. (2019). Post-disaster assessment of 2017 catastrophic Xinmo landslide (China) by spaceborne SAR interferometry. *Landslides* 16, 1189–1199. doi: 10.1007/s10346-019-01152-4

Dong, J., Zhang, L., Li, M. H., Yu, Y. H., Liao, M. S., Gong, J. Y., et al. (2018). Measuring precursory movements of the recent Xinmo landslide in Mao County, China with Sentinel-1 and ALOS-2 PALSAR-2 datasets. *Landslides* 15, 135–144. doi: 10.1007/s10346-017-0914-8

Dufresne, A. (2012). Granular flow experiments on the interaction with stationary run-out path materials and comparison to rock avalanche events. *Earth Surface Proces. Landf.* 37, 1527–1541. doi: 10.1002/esp.3296

Fan, J. R., Zhang, X. Y., Su, F. H., Ge, Y. G., Tatolli, P., Yang, Z. Y., et al. (2017). Geometrical feature analysis and disaster assessment of the Xinmo landslide based on remote sensing data. *J. Mount. Sci.* 14, 1677–1688. doi: 10.1007/s11629-017-4633-3

Fan, X., Xu, Q., Scaringi, G., Dai, L., Li, W., Dong, X., et al. (2017). Failure mechanism and kinematics of the deadly June 24th 2017 Xinmo landslide, Maoxian, Sichuan, China. *Landslides* 14, 2129–2146. doi: 10.1007/s10346-017-0907-7

Friedmann, S. J., Taberlet, N., and Losert, W. (2006). Rock-avalanche dynamics: insights from granular physics experiments. *Int. J. Earth Sci.* 95, 911–919. doi: 10.1007/s00531-006-0067-9

Hart, R., Cundall, P. A., and Lemos, J. (1988). Formulation of a three-dimensional distinct element model—Part II. Mechanical calculations for motion and interaction of a system composed of many polyhedral blocks. *Int. J. Rock Mech. Min. Sci. Geomech. Abstracts* 25, 117–125. doi: 10.1016/0148-9062(88)92294-2

Heim, A. (1932). *Landslides and Human Lives*. Vancouver: Bitech Publishers.

Herceg, M., Kvasnica, M., Jones, C. N., and Morari, M. (2013). "Multi-parametric toolbox 3.0," in *Proceeding of 2013 European Control Conference*, Zurich: IEEE Press, 502–510.

Hu, K., Wu, C., Tang, J., Pasuto, A., Li, Y., and Yan, S. (2018). New understandings of the June 24th 2017 Xinmo Landslide. Maoxian, Sichuan, China. *Landslides* 15, 2465–2474. doi: 10.1007/s10346-018-1073-2

Hu, Y. X., Chen, M. L., and Zhou, J. W. (2019). Numerical simulation of the entrainment effect during mass movement in high-speed debris avalanches. *Arab. J. Geosci.* 12:14.

Hu, Y. X., Yu, Z. Y., and Zhou, J. W. (2020). Numerical simulation of landslide-generated waves during the 11 October 2018 Baige landslide at the Jinsha River. *Landslides* 17, 2317–2328. doi: 10.1007/s10346-020-01382-x

Huang, D., Li, Y. Q., Song, Y. X., Song, Y. X., Xu, Q., and Pei, X. J. (2019). Insights into the catastrophic Xinmo rock avalanche in Maoxian county, China: combined effects of historical earthquakes and landslide amplification. *Eng. Geol.* 258:105158. doi: 10.1016/j.enggeo.2019.105158

Hungr, O., and Evans, S. G. (2004). Entrainment of debris in rock avalanches: an analysis of a long run-out mechanism. *Geol. Soc. Am. Bull.* 116, 1240–1252. doi: 10.1130/b25362.1

Intrieri, E., Raspini, F., Fumagalli, A., Lu, P., Conte, S. D., Farina, P., et al. (2018). The Maoxian landslide as seen from space: detecting precursors of failure with Sentinel-1 data. *Landslides* 15, 123–133. doi: 10.1007/s10346-017-0915-7

Itasca Consulting Group Inc. (2016). *3DEC users' Manual (version 5.2)*.

Iverson, R. M., and Ouyang, C. (2015). Entrainment of bed material by Earth-surface mass flows: review and reformulation of depth-integrated theory. *Rev. Geophys.* 53, 27–58. doi: 10.1002/2013RG000447

Iverson, R. M., Reid, M. E., Logan, M., and Lahusen, P. (2011). Positive feedback and momentum growth during debris-flow entrainment of wet bed sediment. *Nat. Geosci.* 4, 116–121. doi: 10.1038/ngeo1040

Li, P., Shen, W., Hou, X., and Li, T. (2019). Numerical simulation of the propagation process of a rapid flow-like landslide considering bed entrainment: a case study. *Eng. Geol.* 263:105287. doi: 10.1016/j.enggeo.2019.105287

Li, W. C., Li, H. J., Dai, F. C., and Lee, L. M. (2012). Discrete element modeling of a rainfall-induced flowslide. *Eng. Geol.* 149, 22–34. doi: 10.1016/j.enggeo.2012.08.006

Liu, W., Wang, D., Zhou, J., and He, S. (2019). Simulating the Xinmo landslide runout considering entrainment effect. *Environ. Earth Sci.* 78:585.

Lu, P. Y., Yang, X. G., Xu, F. G., Hou, T. X., and Zhou, J. W. (2016). An analysis of the entrainment effect of dry debris avalanches on loose bed materials. *SpringerPlus* 5:1621.

Lucas, A., Mangeney, A., and Ampuero, J. (2014). Frictional velocity-weakening in landslides on Earth and on other planetary bodies. *Nat. Commun.* 5:3417. doi: 10.1038/ncomms4417

Luna, B. Q., Remaître, A., Van Asch, T. W. J., Malet, J. P., and van Westen, C. J. (2012). Analysis of debris flow behavior with a one dimensional run-out model incorporating entrainment. *Eng. Geol.* 128, 63–75. doi: 10.1016/j.enggeo.2011.04.007

Mangeney, A., Roche, O., Hungr, O., Mangold, N., Faccanoni, G., and Lucas, A. (2010). Erosion and mobility in granular collapse over sloping beds. *J. Geophys. Res.* 115:F03040. doi: 10.1029/2009JF001462

McDougall, S., and Hungr, O. (2005). Dynamic modelling of entrainment in rapid landslides. *Can. Geotech. J.* 42, 1437–1448. doi: 10.1139/t05-064

Ouyang, C., He, S., and Tang, C. (2015). Numerical analysis of dynamics of debris flow over erodible beds in Wenchuan earthquake-induced area. *Eng. Geol.* 194, 62–72. doi: 10.1016/j.enggeo.2014.07.012

Ouyang, C., Zhou, K., Xu, Q., Yin, J., Peng, D., Wang, D., et al. (2017). Dynamic analysis and numerical modeling of the 2015 catastrophic landslide of the construction waste landfill at Guangming, Shenzhen, China. *Landslides* 14, 705–718. doi: 10.1007/s10346-016-0764-9

Persson, P. O., and Strang, G. (2004). A simple mesh generator in MATLAB. *SIAM Rev.* 46, 329–345. doi: 10.1137/s0036144503429121

Pirulli, M. (2009). The Thurwieser rock avalanche (Italian Alps): description and dynamic analysis. *Eng. Geol.* 109, 80–92. doi: 10.1016/j.enggeo.2008.10.007

Sassa, K., Nagai, O., Solidum, R., Yamazaki, Y., and Ohta, H. (2010). An integrated model simulating the initiation and motion of earthquake and rain induced rapid landslides and its application to the 2006 Leyte landslide. *Landslides* 7, 219–236. doi: 10.1007/s10346-010-0230-z

Sherard, J. L., Woodward, R. J., and Gizienski, S. (1963). *Earth and Earth-Rock Dams: Engineering Problems of Design and Construction*. New York, NY: John Wiley & Sons Inc, 722.

Sovilla, B., Burlando, P., and Bartelt, P. (2006). Field experiments and numerical modeling of mass entrainment in snow avalanches. *J. Geophys. Res.* 111:F0300.

Teufelsbauer, H., Wang, Y., Chiou, M. C., and Wu, W. (2009). Flow–obstacle interaction in rapid granular avalanches: DEM simulation and comparison with experiment. *Granul. Matter* 11, 209–220. doi: 10.1007/s10035-009-0142-6

Wang, G., Huang, R., Chigira, M., Wu, X., and Lourenço, S. D. N. (2013). Landslide amplification by liquefaction of runout-path material after the 2008 Wenchuan (M 8·0) Earthquake. China. *Earth Surface Process. Landf.* 38, 265–274. doi: 10.1002/esp.3277

Wang, W., Yin, Y., Yang, L., Zhang, N., and Wei, Y. (2020). Investigation and dynamic analysis of the catastrophic rockslide avalanche at Xinmo, Maoxian, after the Wenchuan Ms 8.0 earthquake. *Bull. Eng. Geol. Environ.* 79, 495–512. doi: 10.1007/s10064-019-01557-4

Wu, J. H., Lin, W. K., and Hu, H. T. (2017). Assessing the impacts of a large slope failure using 3DEC: the Chiu-fen-erh-shan residual slope. *Comput. Geotech.* 88, 32–45. doi: 10.1016/j.compgeo.2017.03.002

Xu, Q., Li, W., Dong, X., Xiao, X., Fan, X., and Pei, X. (2017). The Xinmocun landslide on June 24, 2017 in Maoxian, Sichuan: characteristics and failure mechanism. *Chin. J. Rock Mech. Eng.* 36, 2612–2628.

Yin, Y. P., Wang, F. W., and Sun, P. (2009). Landslide hazards triggered by the 2008 Wenchuan earthquake. Sichuan, China. *Landslides* 6, 139–152. doi: 10.1007/s10346-009-0148-5

Zhang, M., Wu, L., Zhang, J., and Li, L. (2019). The 2009 Jiweishan rock avalanche, Wulong, China: deposit characteristics and implications for its fragmentation. *Landslides* 16, 893–906. doi: 10.1007/s10346-019-01142-6

Zhou, J. W., Cui, P., and Hao, M. H. (2016). Comprehensive analyses of the initiationand entrainment processes of the 2000 Yigong catastrophic landslide in Tibet, China. *Landslides* 13, 39–54. doi: 10.1007/s10346-014-0553-2

Zhou, J. W., Cui, P., and Yang, X. G. (2013). Dynamic process analysis for the initiation and movement of the Donghekou landslide-debris flow triggered by the Wenchuan earthquake. *J. Asian Earth Sci.* 76, 70–84. doi: 10.1016/j.jseaes.2013.08.007

Conflict of Interest: The authors declare that the research was conducted in the absence of any commercial or financial relationships that could be constructed as a potential conflict of interest.

frontiers
in Earth Science

ORIGINAL RESEARCH
published: 29 January 2021
doi: 10.3389/feart.2020.580293

Radiocarbon Dating for the Reconstruction of the 1717 CE Triolet Rock Avalanche in the Mont Blanc Massif, Italy

Irka Hajdas[1]*, *Ursula Sojc*[1], *Susan Ivy-Ochs*[1], *Naki Akçar*[2] *and Philip Deline*[3]

[1]*Institute of Particle Physics, ETH Zurich, Zurich, Switzerland,* [2]*Institute of Geological Sciences, University of Bern, Bern, Switzerland,* [3]*EDYTEM Lab, CNRS, Université Savoie Mont Blanc, Chambéry, France*

The Arp Nouva peat bog located in the upper Ferret Valley in the Mont Blanc massif was critically evaluated since published radiocarbon dates have led to controversial conclusions on the formation of this swamp. Radiocarbon dating of woody fragments from three pits of up to 1 m depth was used to discuss the question of whether the historically documented rock avalanche occurring in 1717 CE overran the peat bog or settled prior to its formation. For the deepest samples in the pits, calibrated radiocarbon ages between 1,652 and 1950 CE (95.4%; confidence level) were obtained, which fit very well into the time frame of the historical documented 1717 CE rock avalanche event. It can, therefore, be concluded that the Arp Nouva peat bog was formed by blockage of the Bella Combe torrent by the rock avalanche deposits. Furthermore, careful sample preparation with consequent separation of woody fragments from the bulk peat sample has shown that the problem of too old ^{14}C ages can be circumvented. This work demonstrates that a combined geomorphological and geochronological approach is the most reliable way to reconstruct landscape evolution. The key to successful ^{14}C dating is careful sample selection and the identification of the material that might not be ideal for chronological reconstructions.

Keywords: radiocarbon dating, peat, rock avalanche, Mont Blanc massif, Val Ferret, Triolet

Edited by:
Steven L. Forman,
Baylor University, United States

Reviewed by:
Vincenzo Amato,
University of Molise, Italy
Cristina Maria Pinto Gama,
University of Evora, Portugal

***Correspondence:**
Irka Hajdas
hajdas@phys.ethz.ch

Specialty section:
This article was submitted to Quaternary Science, Geomorphology and Paleoenvironment, a section of the journal Frontiers in Earth Science

Received: *06 July 2020*
Accepted: *23 December 2020*
Published: *29 January 2021*

Citation:
Hajdas I, Sojc U, Ivy-Ochs S, Akçar N and Deline P (2021) Radiocarbon Dating for the Reconstruction of the 1717 CE Triolet Rock Avalanche in the Mont Blanc Massif, Italy. Front. Earth Sci. 8:580293. doi: 10.3389/feart.2020.580293

INTRODUCTION

Not all changes in the landscape caused by mass movements can be reconstructed from historical accounts. Such records help to understand the mechanisms behind the events. Some cases, however, might remain confounded despite historical information. On September 12, 1717 CE, a rock avalanche occurred on the Mont Blanc massif's south flank in the upper part of Val Ferret (**Figure 1**). As described by Porter and Orombelli (1980), the written records spoke of the Triolet catastrophe, which was described as a collapse of ice and rock onto the Triolet Glacier. The sudden collapse sent masses of rocks mixed with water and ice down the valley, filling it with debris. Pastures and settlements were destroyed, and seven men were killed as well as 120 cows (Porter and Orombelli, 1980, and references therein).

This tragic rock avalanche was recounted for a few decades with the early historical report written by a local inhabitant Michael-Jospeh Pennard. However, over time, the event's memories became obscured, leading to various speculations for the nature of deposits filling the valley (Porter and Orombelli, 1980 and references therein). De Saussure (1786), who visited the valley in 1781,

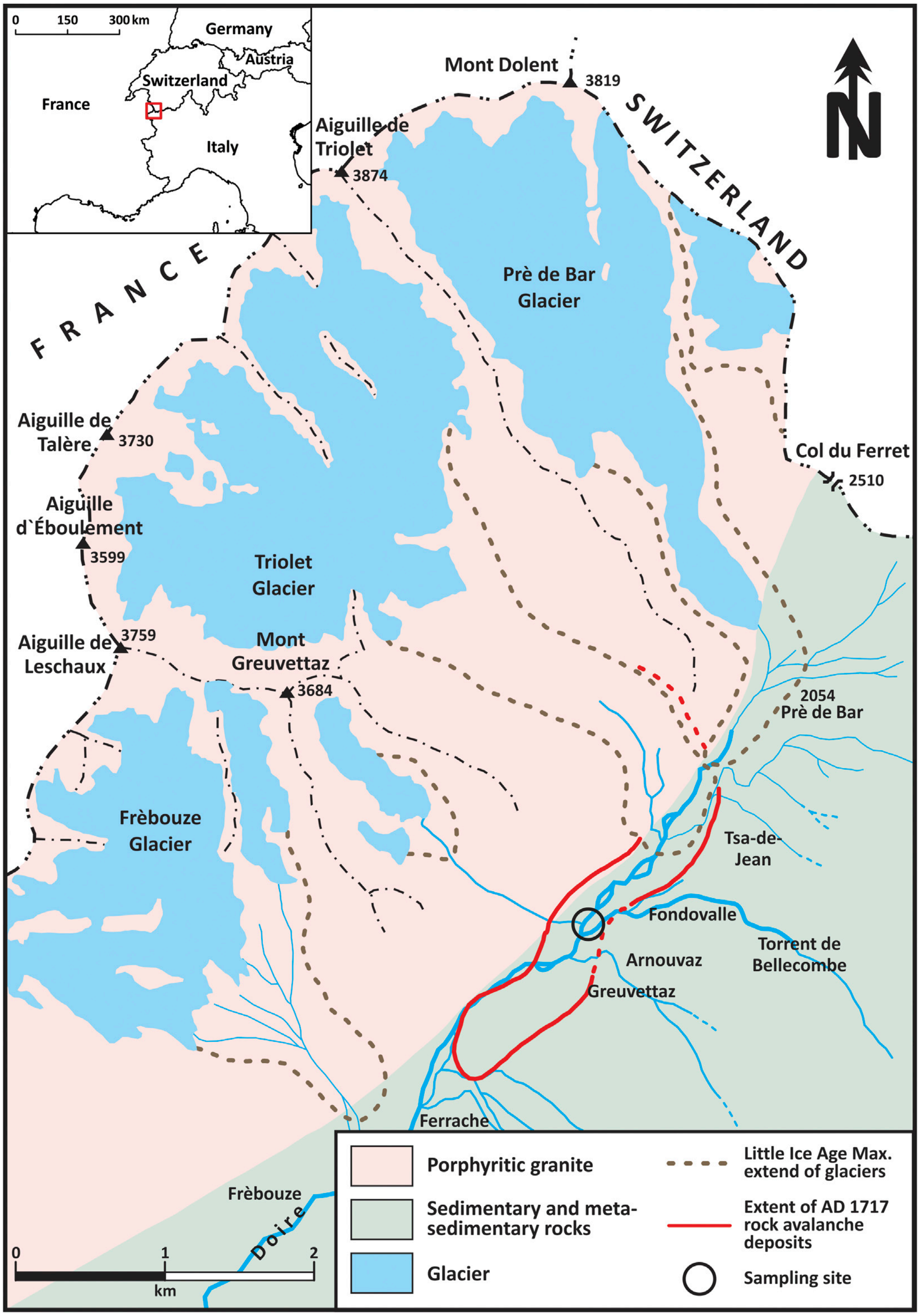

FIGURE 1 | Location of the study site, Arp Nova plain in the Ferret Valley, Italy (45.871341157559634, 7.05089817967189). Figure modified after Akçar et al. (2012).

attributed it to the rock avalanche but later in the 19th-century glacial deposits (Agassiz 1845) and a glacial outburst flood (Virgilio 1883) have been proposed. In the 20th century, both glacial and rock avalanche scenarios were active. Sacco (1918) advocated for 16th-19th century glacial drift, Zienert (1965) for late-glacial glaciers activity, and Mayr (1969) argued for mixed sources: rock avalanche and the glacial movement. Porter and Orombelli (1980) revisited the site. They described the boulder deposits as mostly angular and non-sorted, with the largest specimen as high as 20 m (4 × 12 × 20 m) on the Triolet deposit surface about 100 m for the terminus (Photo 3 in Porter and Orombelli 1980). They estimated that the 2 km-long and 500 m-wide valley was filled with debris raising its level by 4–6 m. Their estimated volume of rocks mixed with ice and snow was 6–20 million m^3, which collapsed from the elevation of 1860 m and traveled with the velocity of 125–160 km/h, covering a horizontal distance of 7 km. To support their observations, Porter and Orombelli (1980) used chronological tools of dendrochronology and lichenometry. Most notable were the dates of trees, all of which colonized the valley after a few decades. However, the Porter and Orombelli (1980) scenario, which excludes glacial activity as a source of geomorphological changes, has been debated. Aeschlimann (1983) applied radiocarbon dating on peat sampled on the valley floor covered by the Triolet deposit and obtained an age of 885 ± 60 BP (^{14}C years Before Present; Stuiver and Polach 1977). In consequence, he prescribed the older deposits to past glacial activity. In their response, Orombelli and Porter (1988) highlighted the inconsistency of radiocarbon ages on peat. The authors pointed out the possibility of the re-deposition of old peat from nearby locations, which could have happened during the catastrophic mass movement. The potential of hard water effect has been suggested as a possible explanation for the old ages. Hard water effect (depleted ^{14}C content or too old ^{14}C ages) can be expected when plants growing underwater incorporate dissolved CO_2 of a mixed ^{14}C signal, typically older than the atmosphere (Deevey and Stuiver, 1964).

Orombelli, Porter, and Aeschliman revisited the site in 1984 and took additional samples from the peat bog near the boulder accumulation of Arp Nuova (location P2 **Figure 1**; Orombelli and Porter, 1988). The sample was split in two and submitted to two laboratories, Paris and Zurich, which yielded different ages: 105 ± 70 BP (Paris) and 1,020 ± 65 BP (University of Zurich) did not resolve the debate (Orombelli and Porter, 1988). An additional sample taken from the same location in 1986 was analyzed by a ^{14}C laboratory in Rome and resulted in 2,320 ± 150 BP. Such a spread of ages pointed to a problem of ^{14}C dating peat at that location. Therefore the conclusions of Aeschlimann (1983), mostly based on ^{14}C age, were not supported. As Orombelli and Porter (1988) stressed, the importance of accurate interpretation of the geomorphological data cannot be underestimated, considering the geological hazard in the highly popular resort region of Mont Blanc.

In a further attempt to resolve the dispute, Deline and Kirkbride (2009) revisited the site. They proposed a smaller extent of the 1717 CE rock avalanche deposit in the valley with possibly, mixed deposits of an earlier rock avalanche that partly covered older moraines (Deline and Kirkbride, 2009). To describe the deposits' complex geomorphology, they divided the Val Ferret into distal, central, and proximal sectors. The proximal one, Arp Nouva, has also been divided into three subsectors, with granitic boulders dispersed across the valley. A new sampling at the Arp Nuova peat bog developed onto granitic rock avalanche deposit and radiocarbon dating at ^{14}C laboratory in Lyon provided ages ranging from 1,030 ± BP to modern (**Table 1** in Deline and Kirkbride (2009). Deline and Kirkbride (2009) suggested that the valley's deposits have a dual origin: Lateglacial moraines and two ca. 1,000 and 1717 CE rock avalanches for which they downscaled by ca. 50% of the volume estimate of rock debris proposed by Porter and Orombelli (1980). The differentiation between the deposition of the boulders is now possible with the cosmogenic nuclide exposure dating. The atoms of ^{10}Be produced and accumulated in the rock exposed to cosmic rays give a measure of exposure time. In their study, Akçar et al. (2012) and Akçar et al. (2014) sampled 19 granitic boulders (1.3–6 m high) located in the upper Ferret Valley and measured the ^{10}Be concentration. 17 of the boulders resulted in apparent ages close to the 18th century. They strengthened the Porter and Orombelli scenario of the 1717 CE rock avalanche deposit covering the whole valley floor, without Lateglacial moraines. The remaining two boulders that delivered apparent ages of ca 10–11 ka were sampled from Lateglacial deposits of the Ferret glacier.

Although the analysis of ^{10}Be delivered conclusive evidence for the rock avalanche being the source of the boulders, the discrepancy observed in radiocarbon ages of peat samples from the Arp Nouva peat bog remained unresolved. Therefore, another sampling campaign was planned in 2013 and completed as part of a master thesis. Various fractions of sediment were ^{14}C dated, and wood was considered to be the best choice. Our results illustrate the importance of a clear selection and description of the carbon source used for radiocarbon dating.

STUDY SITE

The Arp Nouva in the upper Ferret Valley is located on the southern, Italian flank of the Mont Blanc massif, on the border with Switzerland and France (**Figure 1**). The Ferret Valley is one of the Aosta Valley tributaries, with Triolet and Pré de Bar glaciers at its north-east. The Triolet glacier is now a partly debris-covered cirque glacier surrounded by steep rock walls with peaks exceeding 3,500 m a.s.l., from which rockfalls detach. The upper Ferret Valley floor is characterized by chaotic boulder accumulations with several ridges on the plain of Greuvetta and the Biche forest, and the sizable morainic complex of the Triolet glacier upstream (**Figure 2**; Deline and Kirkbride, 2009; Akçar et al., 2012).

MATERIALS AND METHODS

Sampling and Sample Selection

Four spatially distributed pits were dug on Arp Nouva near the Bellecombe torrent (**Figure 3** and **Supplementary Figure S1**). The depth in the sections varied between 60–100 cm (**Figures**

TABLE 1 | Results of the AMS analysis obtained on samples selected from organic rich layers and on Total Organic Carbon TOC of various fractions of sediments. F^{14}C is the concentration measured in the sample, corrected for fractionation and normalized to the 1950 value, and the corresponding ^{14}C age. The δ^{13}C values was measured on the graphite. The mass C is the final carbon content of the sample. The first sample contained only 70 μg of C (#) and was analyzed as CO_2 using gas ion source (GIS). Calendar ages corresponding to the measured F^{14}C concentration. Calibration and a phase model was performed using the OxCal calibration with INTCAL13 calibration curve (Reimer et al., 2013). The postmodern ages were calibrated using the CALIBomb and with the data for the Northern Hemisphere (Hua et al., 2013; Levin et al., 2013).

Lab no.	Pit no.	Depth (cm)	Sample code	Material/ Fraction	F^{14}C	±1 σ	^{14}C age BP	±1 σ	δ^{13}C (%)	Mass C (mg)	Calibrated ranges CE (95%conf. level)	Phase model calibrated ranges CE (95%conf. level)
ETH-52685	2	10–13	VF-27	Woody fragments	1.249	0.004	−1787	25	−29.4	0.55	1959, 1961, 1981–1983	
ETH-52685	2	10–13	VF-27	Bulk	1.268	0.003	−1910	21	−29.70	0.99	NA	
ETH-52685	2	10–13	VF-27	<150 μm	1.208	0.004	−1,520	25	−28.60	0.38	NA	
ETH-52685	2	10–13	VF-27	150–500 μm	1.217	0.003	−1,581	21	−26.90	0.99	NA	
ETH-52686	2	28–30	VF-28	Woody fragments	0.99	0.003	84	25	−25.8	0.93	1,691–1924	1701–1931
ETH-52686	2	28–30	VF-28	Bulk	0.936	0.005	532	47	−25.60	0.58	NA	
ETH-52686	2	28–30	VF-28	<150 μm	0.641	0.004	3,573	55	−22.40	0.50	NA	
ETH-52686	2	28–30	VF-28	150–500 μm	0.914	0.005	722	41	−26.70	1.00	NA	
ETH-52687	2	43–45	VF-29	Woody fragments	0.985	0.003	124	25	−29.1	0.99	1,679–1940	1,693–1894
ETH-52688	2	74	VF-30	Woody fragments	0.983	0.003	142	28	−24.5	0.99	1,669–1946	1,667–1867
ETH-52689	2	74	VF-31	Root	1.542	0.005	−3,479	26	−28	1	1963, 1968–1970	
ETH-52681	3	53	VF-23	Needle	1.054	0.001	−423	72	−24.6	0.07 (#)	1956–1957, 2003–2012	
ETH-52683	3	53	VF-25	Woody fragments	0.978	0.003	175	25	−23.1	0.98	1,661–1950	1,661–1950
ETH-52691	4	90	VF-33	Woody fragments	0.987	0.003	104	26	−27.9	0.88	1,683–1931	
ETH-52692	4	90	VF-34	Woody fragments	0.977	0.003	191	25	−25.1	0.78	1,654–1950	
ETH-52693	4	90	VF-35	Woody fragments	0.975	0.003	205	25	−21	0.99	1,649–1950	
ETH-52691-92-93	4	90		Mean value VF 33-34-35			169	15			1,667–1950	1,671–1953
ETH-52694	4	100	VF-36	Woody fragments	0.976	0.003	194	26	−27.4	0.99	1952–1950	1,649–1806
ETH-52694	4	100	VF-36	Bulk	0.838	0.005	1,421	48	−25.4	0.56	NA	

4A–C). Overall, 36 samples were collected from undisturbed, enriched organic layers. Our study's focus was on material deposited deeper than 30 cm, which would most likely contain the oldest deposit. The sample sections showed a succession of greyish laminated fine sediment, peat layers, and gray silty gravel (**Figures 4A–C**).

Radiocarbon Dating

In the ETH laboratory, samples were frozen to prevent microbial activity and the building of mold and fungus. Eight samples from three profiles were chosen for the analysis (for details, see **Supplementary Figure S2**). Most of the samples contained many visible roots; thus, the selection of wood fragments was essential. They were placed in glass beakers filled with DW and left for at least 24 h to disintegrate. Occasionally, the beakers were placed for 15 min in an ultrasonic bath to speed up the process. The sieving of samples was performed using sieves of mesh 500 and 125 μm. Pieces of wood were picked from a fraction of >500 μm. In one (V-23), a very small plant fragment (needle) was found and selected as a separate sample. One unidentified sample (V-27) of wood/root and one clearly identified as a large root (V-31) were picked for analysis (**Supplementary Figures S3–S5**). The fine fraction was saved for potential analysis. The wood fragments and one macrofossil were treated with Acid-Base-Acid to remove carbonates and humic acids, which might contaminate with old and young carbon (Hajdas, 2008). The clean material was weighed (ca. 2 mg of wood = ca. 1 mg·C) and wrapped in Sn cups for combustion in an Elemental Analyzer and a subsequent graphitization in the AGE graphitization system (Nemec et al., 2010). A set of standards (oxalic acid OXA II) and background material (phthalic anhydride) were graphitized to accompany the unknown samples' AMS analysis. The resulting graphite samples were pressed into the aluminum cathodes for the AMS isotopic analysis. The very small sample (V-23) was analyzed as CO_2 using the gas ion source (Ruff et al., 2010). The $^{14}C/^{12}C$ and $^{13}C/^{12}C$ ratio was measured on graphite samples

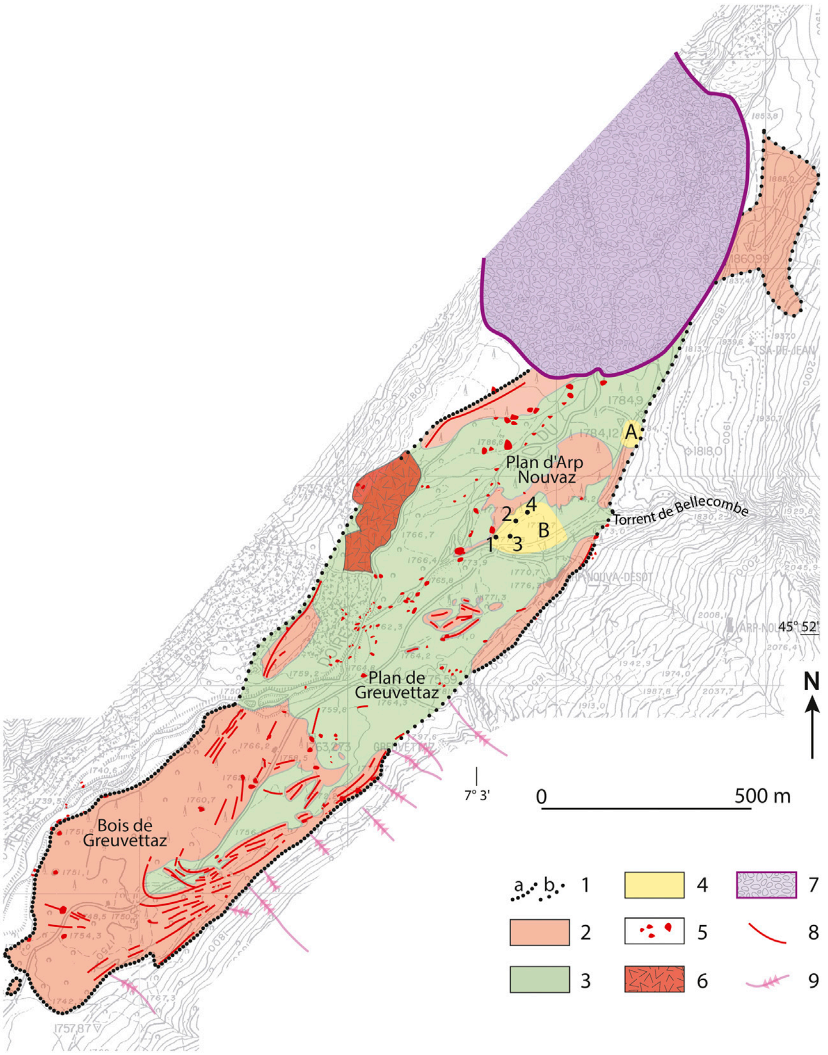

FIGURE 2 | Geomorphological map of the rock avalanche deposit of 1717 CE. 1: Limit of the deposit [**(A)**: recognized; **(B)**: inferred]; 2: chaotic block deposit; 3: alluvial deposit; 4: peat bog; 5: megablocks; 6: local rockfall deposit; 7: Holocene moraine complex of Triolet Glacier; 8: granitic ridges; 9: snow avalanche couloir; **(A)**: peat bog sampled by Aeschlimann (1983), **(B)**: peat bog sampled by Orombelli and Porter (1988), and Deline and Kirkbride (2009); 1–4: location of pits from this study (Topographic map: 1:10,000 with 10 m contour interval. Archivi topocartografici della Regione Autonomo Valle d'Aosta—permit no. 52–18/08/1999).

using the dedicated ^{14}C AMS instrument MICADAS (Synal et al., 2007).

RESULTS

Table 1 summarizes the results of the AMS ^{14}C analysis. The F^{14}C is a concentration of ^{14}C measured in the samples normalized and corrected for fractionation (δ^{13}C). Conventional radiocarbon ages were calculated using Libby's half-life for ^{14}C (Reimer et al., 2004; Stuiver and Polach, 1977). The δ^{13}C values used for correction of F^{14}C (see Reimer et al., 2004) were measured on graphite samples. Radiocarbon ages were calibrated (**Table 1**) using the OxCal software (Ramsey and Lee, 2013) and the INTCAL13 calibration curve (Reimer et al., 2013). In addition to simple calibration, a Bayesian model of OxCal was used to calibrate all the samples with F^{14}C < 1 and positive ^{14}C ages (**Figures 5** and **Supplementary Figure S6**). The samples with F^{14}C > 1 indicate the post-1950 source of carbon (modern). The corresponding calendar ages were obtained using the Bomb Peak ^{14}C data (Hua et al., 2013; Levin et al., 2013) and the online calibration software http://calib.org/CALIBomb/.

DISCUSSION

The results of ^{14}C dating obtained for various fractions selected from the bulk samples indicate the different carbon pools present in the profiles. The top 30 cm show consistently modern ages, i.e., F^{14}C > 1 for all the subsamples of VF27 (10–13 cm). The very close agreement between sub-samples ^{14}C signature suggests no sources of old reworked carbon deposited in

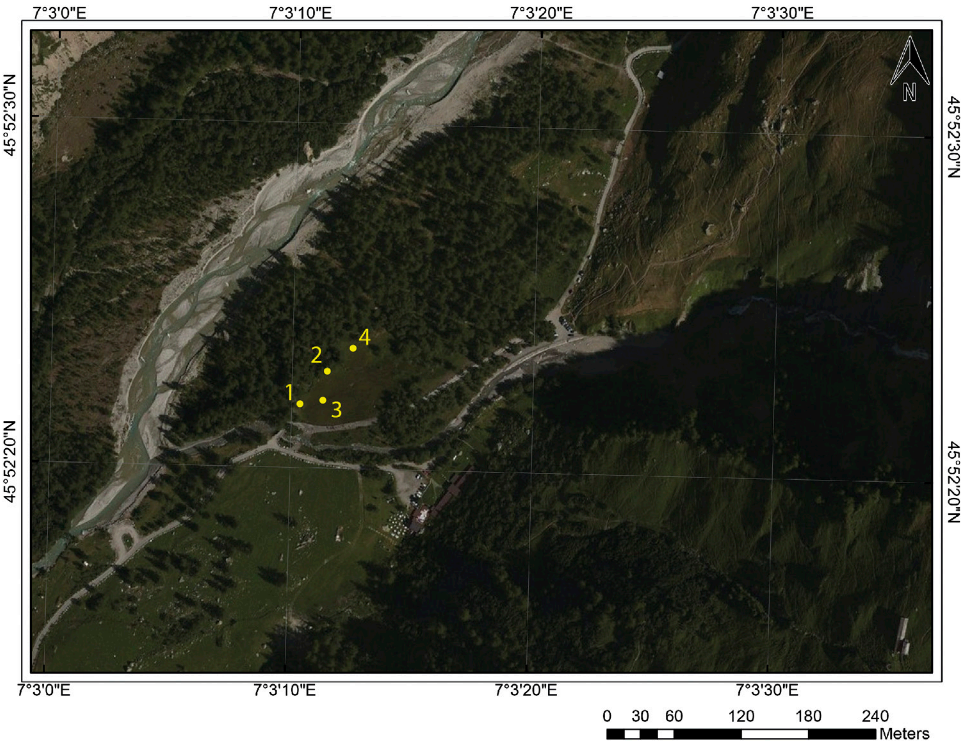

FIGURE 3 | Sample location of the four pits (Arp Nouva). A boulder was found at the bottom of the pit Arp Nouva -3. The woods around the pits constitutes of larch trees.

the top 10 cm layer. This is not the case for samples deeper than 30 cm as in all profiles, bulk and fine fraction show presence of old carbon (V28, V29, and V36). However, the newly obtained radiocarbon ages on woody fragments selected from the peat layers in Arp Nouva show a bimodal distribution. The very small sample V-23 (tiny needle) and the V-27 and V-31 wood/root samples resulted in negative radiocarbon ages ($F^{14}C > 1$). The remaining samples had radiocarbon ages between 84 ± 25 BP and 205 ± 25 BP. The negative radiocarbon ages of the root V-31 and the wood/root fragment V-27 are not surprising as the valley's meadows are overgrown with trees (**Supplementary Figure S1**). The root V-31 was chosen on purpose to demonstrate the presence of modern carbon deep in the soil, the fact that explains the modern (negative ^{14}C age) date obtained by Deline and Kirkbride (2009). The presence of roots of all sizes and probably ages is indisputable. The second negative age was obtained on a much smaller woody fragment (V-27), which could also be a fragment of the large root, however unrecognizable using binocular investigation. The needle V-23 was selected in the hope that it might date the deposit. However, the calendar age of 1956–1957 or 2003–2012 indicates that this small macrofossil was modern. It was probably contamination introduced to the sample during the digging of the pit in 2013. The sample V-27, which was challenging to identify as either wood or root, has the post-1950 ^{14}C concentration, which would support identification as root. However, no radiocarbon ages older than 230 BP were observed (205 ± 25 BP), and the oldest age of the wood is limited to the late 17th century, at the earliest. Although this limit slightly predates the 1717 CE rock avalanche, such an effect can be expected when wood fragments are dated. The small wood fragments found in the organic-rich sections were deposited over the years, but their origin might be the blast in 1717 CE that killed the trees. One could expect older ages of the wood if the trees grew for some time before the event. The fact that we have not yet found much older ages of wood does not exclude such a possibility. However, radiocarbon ages as old as 885 ± 60 BP (Aeschlimann, 1983) or older (Orombelli and Porter, 1988) cannot be explained by the old wood effect. Such discrepancy must have another reason, and the most probable explanation is the presence of old carbon in sediments deposited along with fresh organic matter.

Similar to Akçar et al. (2012) and Akçar et al. (2014), our results support the conclusion of Porter and Orombelli (1980) and Orombelli and Porter (1988) that the entirety of the blocky deposits was left during the 1717 CE event. The peat layers deposited in the Ferret Valley near the locations, which were investigated in the past, are now consistently dated to maximum 370 years (1,652–1950 CE; 95.4% confidence level). The radiocarbon ages on fragments of the wood date the deposit to the late 17th/early 18th century. More precise dating is not possible due to the wiggly nature of the calibration curve, which results in multiple calendar intervals corresponding to the measured ^{14}C ages of wood

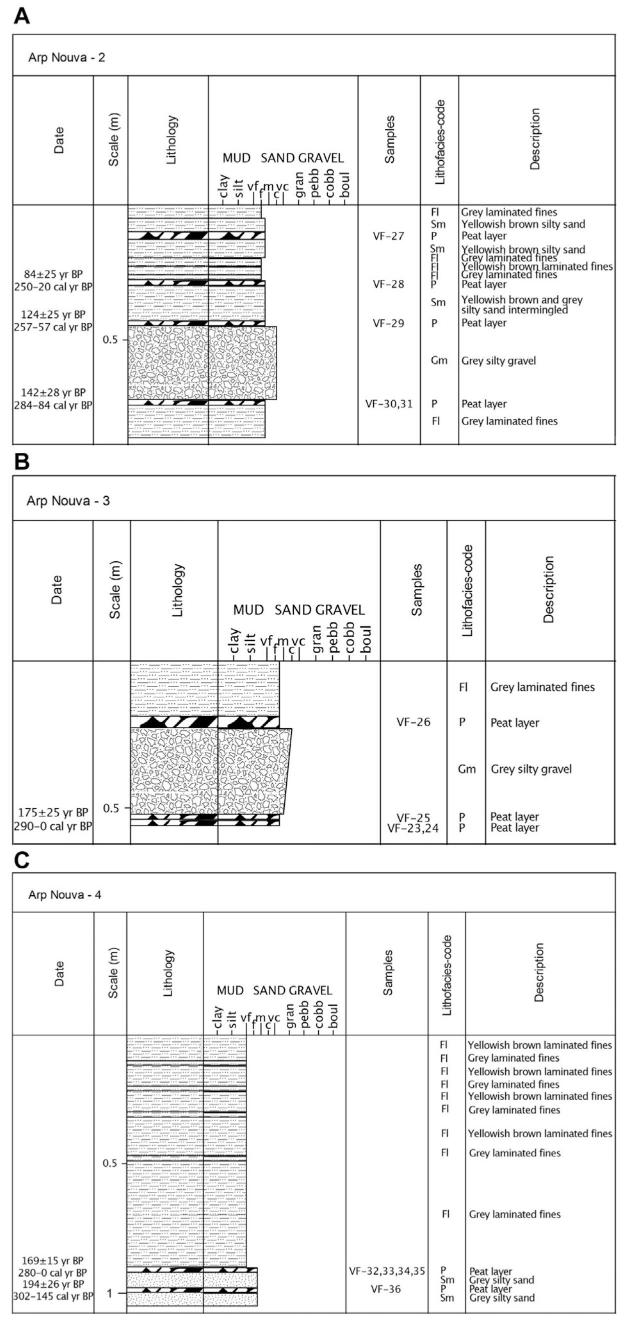

FIGURE 4 | Samples and the description of soil profiles from the pits: **(A)** Arp Nouva-2, **(B)** Arp Nouva-3 and **(C)** Arp Nouva-4.

(**Supplementary Figure S5**). Sometimes, Bayesian models of OxCal might help to obtain a more precise chronology (Ramsey and Lee, 2013; Ramsey, 2017). However, due to the limited number of samples, the effect is not so apparent; a bigger pool of ages could improve the fit (**Figure 5**).

Nevertheless, our results allow us to explain the discrepancies in ages observed by Porter and Orombelli (1980), Aeschlimann (1983) and Orombelli and Porter (1988). After being able to investigate the composition of the samples, we are convinced that the scatter in previously published ^{14}C ages is most probably due to the material chosen for dating performed in the past. From this perspective, it is admirable to read the efforts of scientists involved in the dispute. At that time, AMS facilities were scarce, and most ^{14}C dating has been performed using conventional counting techniques. This method required at least a gram of carbon, therefore substantially larger bulk samples.

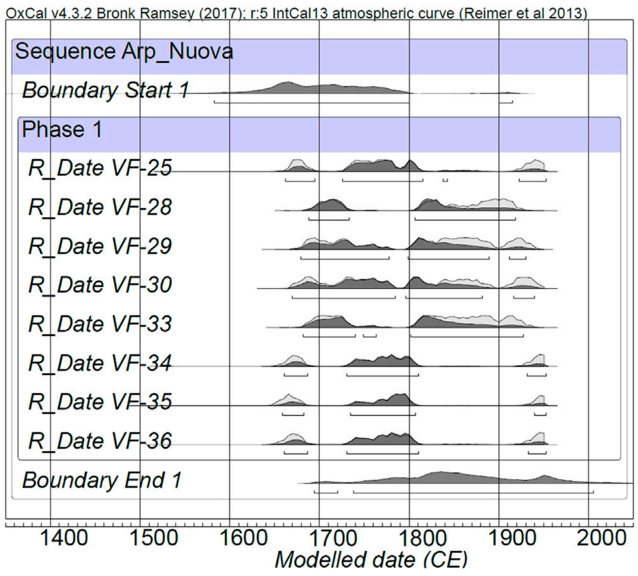

FIGURE 5 | Calendar age intervals as a result of calibration. ^{14}C ages of wood fragments from Arp Nova pits calibrated using the phase model of OxCal. Dark gray areas show posterior probability distributions resulting from the Bayesian phase model of OxCal. The light gray areas show the standard (unmodelled) probability distributions.

Nowadays, we can measure samples as small as 70 μg of carbon (VF-23), which allows us an in-depth analysis of the sources of carbon. The capacity and potential of the new AMS facilities allows for detailed ^{14}C dating of multiple profiles. Independent of the sites' location, the atmospheric ^{14}C signal corresponding to the dated event must be unraveled from the dated record. Wood and macro remains of terrestrial plants are the material of choice. Nevertheless, the application of multiple chronological methods is the best solution in dating deposits of unknown date. Our study supports and is supported by the results obtained by cosmogenic "*in-situ*" method applied to the boulders (Akçar et al., 2012; Akçar et al., 2014). Moreover, both dating methods are consistent with the dendrochronological investigations of Porter and Orombelli (1980), showing the potential of a multi-disciplinary approach.

CONCLUSION

The Ferret Valley, which is the site of the historic 1717 CE rock avalanche deposit, was revisited in 2013 and new samples were collected in the hope of resolving the controversy surrounding past inconsistent radiocarbon ages. Only woody fragments were chosen for the latest analysis. Results of radiocarbon dating of such well-defined material do not show radiocarbon ages older than 250 BP. Thus, the old radiocarbon ages (885–2,320 BP) can be explained by the choice of material. Our study highlights the importance of sample selection and illustrates the potential of the radiocarbon dating method.

DATA AVAILABILITY STATEMENT

The raw data supporting the conclusions of this article will be made available by the authors, without undue reservation.

ETHICS STATEMENT

Written informed consent was obtained from the individuals for the publication of any potentially identifiable images or data included in this article.

AUTHOR CONTRIBUTIONS

All authors listed have made a substantial, direct, and intellectual contribution to the work and approved it for publication.

ACKNOWLEDGMENTS

Participants of the field trip and helped to dig the pits: Olivia Steinemann Anne Claude, Loren Eggenschwiler, Regina Reber, Serdar Yesilyurt, André Roveyaz, Fabian Christener, and Melaine le Roy. Colleagues at the Laboratory of Ion Beam Physics, ETH for support with laboratory preparation and AMS analysis.

SUPPLEMENTARY MATERIAL

The Supplementary Material for this article can be found online at: https://www.frontiersin.org/articles/10.3389/feart.2020.580293/full#supplementary-material.

REFERENCES

Aeschlimann, H. (1983). *Zur Gletschergeschichte des italienischen Mont Blanc Gebietes Val Veni–Val Ferret–Ruitor*. Switzerland: Zurich University

Agassiz, L. (1845). "Les glaciers et le terrain erratique du revers meridional du Mont-Blanc," in *Nouvelles excursions et séjours dans les glaciers et les hautes regions des Alpes de M. Agassiz et de ses compagnons de voyage*. Editor E. Desor (Neuchatel: Kissling)

Akçar, N., Deline, P., Ivy-Ochs, S., Alfimov, V., Hajdas, I., Kubik, P., et al. (2012). The AD 1717 rock avalanche deposits in the upper Ferret Valley (Italy): a dating approach with cosmogenic Be-10. *J. Quat. Sci.* 27, 383–392. doi:10.1002/jqs.1558

Akçar, N., Ivy-Ochs, S., Deline, P., Alfimov, V., Kubik, P. W., Christl, M., et al. (2014). Minor inheritance inhibits the calibration of the Be-10 production rate from the AD 1717 val ferret rock avalanche, European Alps. *J. Quat. Sci.* 29, 318–328. doi:10.1002/jqs.2706

Deevey, E. S., and Stuiver, M. (1964). Distribution of natural isotopes of carbon in linsley-pond and other new-England lakes. *Limnol. Oceanogr.* 9 (1), 1–11

Deline, P., and Kirkbride, M. P. (2009). Rock avalanches on a glacier and morainic complex in haut val Ferret (Mont Blanc massif, Italy). *Geomorphology* 103, 80–92. doi:10.1016/j.geomorph.2007.10.020

Hajdas, I. (2008). The Radiocarbon dating method and its applications in Quaternary studies. *E&G Quat. Sci. J.* 57, 2–24. doi:10.3285/eg.57.1-2.1

Hua, Q., Barbetti, M., and Rakowski, A. Z. (2013). Atmospheric radiocarbon for the period 1950–2010. *Radiocarbon* 55, 2059–2072. doi:10.2458/azu_js_rc.v55i2.16177

Levin, I., Kromer, B., and Hammer, S. (2013). Atmospheric Delta (CO2)-C-14 trend in Western European background air from 2000 to 2012. *Tellus Ser. B Chem. Phys. Meteorol.* 65 (1), 20092. doi:10.3402/tellusb.v65i0.20092

Mayr, F. (1969). Die postglazialen Gletscherschwankungen des Mont Blanc-Gebietes. *Zeitschrift für Geomorphology* 8 (Suppl.), 31–57

Nemec, M., Wacker, L., and Gaggeler, H. (2010). Optimization of the graphitization process at age-1. *Radiocarbon* 52, 1380–1393. doi:10.1017/s0033822200046464

Orombelli, G., and Porter, S. C. (1988). Boulder deposit of upper val Ferret (courmayeur, Aosta Valley) - deposit of a historic giant rockfall and debris avalanche or a late-glacial moraine. *Eclogae Geol. Helv.* 81, 365–371

Porter, S. C., and Orombelli, G. (1980). Catastrophic rockfall of september 12, 1717 on the Italian flank of the Mont Blanc massif. *Zeitschrift für Geomorphologie Stuttgart* 24, 200–218

Ramsey, C. B., and Lee, S. (2013). Recent and planned developments of the program oxcal. *Radiocarbon*. 55, 720–730. doi:10.1017/s0033822200057878

Ramsey, C. B. (2017). Methods for summarizing radiocarbon datasets. *Radiocarbon* 59, 1809–1833. doi:10.1017/rdc.2017.108

Reimer, P., Brown, T., and Reimer, R. (2004). Discussion: reporting and calibration of post-bomb C-14 data. *Radiocarbon* 46, 1299–1304. doi:10.1017/s0033822200033154

Reimer, P. J., Bard, E., Bayliss, A., Beck, J. W., Blackwell, P. G., Ramsey, C. B., et al. (2013). Selection and treatment of data for radiocarbon calibration: an update to the international calibration (IntCal) criteria. *Radiocarbon* 55, 1923–1945. doi:10.2458/azu_js_rc.55.16955

Ruff, M., Szidat, S., Gaggeler, H. W., Suter, M., Synal, H. A., and Wacker, L. (2010). Gaseous radiocarbon measurements of small samples. *Nucl. Instrum. Methods Phys. Res., Sect. B.* 268, 790–794. doi:10.1016/j.nimb.2009.10.032

Sacco, F. (1918). I ghiacciai italiani del gruppo del Monte Bianco. Bolletino del Comitato Glaciologico Italiano, 3: 21–102.

Saussure, H.-B. (1786). Voyages dans les Alpes précédés d'un essai sur l'histoire naturelle des environs de Genève. Tome second. Barde, Manguet & Compagnie, Genéve, XVI-641 p.

Stuiver, M., and Polach, H. A. (1977). Reporting of C-14 data - discussion. *Radiocarbon*. 19, 355–363

Synal, H. A., Stocker, M., and Suter, M. (2007). MICADAS: a new compact radiocarbon AMS system. *Nucl. Instrum. Methods Phys. Res. Sect. B Beam Interact. Mater. Atoms* 259, 7–13. doi:10.1016/j.nimb.2007.01.138

Virgilio, F. (1883). Sui recenti studi circa le variazione periodiche dei ghiacciai. *Bolletino del Club Alpino Italiano*. 50, 50–70

Zienert, A. (1965). Gran Paradiso—Mont Blanc: prähistorische und historische Gletscherstände. *E&G Quat. Sci. J.* 16, 202–225

Conflict of Interest: The authors declare that the research was conducted in the absence of any commercial or financial relationships that could be construed as a potential conflict of interest.

Advantages of publishing in Frontiers

OPEN ACCESS
Articles are free to read
for greatest visibility
and readership

FAST PUBLICATION
Around 90 days
from submission
to decision

HIGH QUALITY PEER-REVIEW
Rigorous, collaborative,
and constructive
peer-review

TRANSPARENT PEER-REVIEW
Editors and reviewers
acknowledged by name
on published articles

Frontiers
Avenue du Tribunal-Fédéral 34
1005 Lausanne | Switzerland

Visit us: www.frontiersin.org
Contact us: frontiersin.org/about/contact

REPRODUCIBILITY OF RESEARCH
Support open data
and methods to enhance
research reproducibility

DIGITAL PUBLISHING
Articles designed
for optimal readership
across devices

FOLLOW US
@frontiersin

IMPACT METRICS
Advanced article metrics
track visibility across
digital media

EXTENSIVE PROMOTION
Marketing
and promotion
of impactful research

LOOP RESEARCH NETWORK
Our network
increases your
article's readership